

AD-A238 325



DTIC  
S ELECTE D  
JUL 19 1991  
C

(2)

AGARD-CP-493

AGARD-CP-493

# AGARD

ADVISORY GROUP FOR AEROSPACE RESEARCH & DEVELOPMENT

TRUP ATTELLE - 92000 - NEUILLY SUR SEINE - FRANCE

**AGARD CONFERENCE PROCEEDINGS No.493**

## **Missile Aerodynamics**

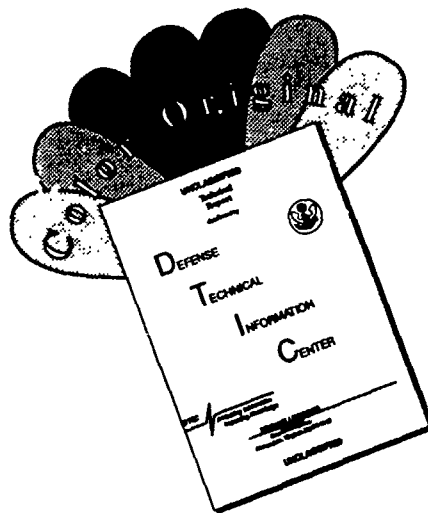
**(L'Aérodynamique des Missiles)**

NORTH ATLANTIC TREATY ORGANIZATION



**DISTRIBUTION AND AVAILABILITY  
ON BACK COVER**

# DISCLAIMER NOTICE



THIS DOCUMENT IS BEST QUALITY AVAILABLE. THE COPY FURNISHED TO DTIC CONTAINED A SIGNIFICANT NUMBER OF COLOR PAGES WHICH DO NOT REPRODUCE LEGIBLY ON BLACK AND WHITE MICROFICHE.

AGARD-CP-493

NORTH ATLANTIC TREATY ORGANIZATION  
ADVISORY GROUP FOR AEROSPACE RESEARCH AND DEVELOPMENT  
(ORGANISATION DU TRAITE DE L'ATLANTIQUE NORD)

AGARD Conference Proceedings No.493

# Missile Aerodynamics

(L'Aérodynamique des Missiles)

Accession For	
NTIS GRA&I	<input checked="" type="checkbox"/>
DTIC Tab	<input type="checkbox"/>
Unannounced	<input type="checkbox"/>
Justification	
By	
Distribution/	
Availability Codes	
Dist	Avail and/or Special
A-1	



91-05380



91 7 17 143

Papers presented and discussions held at the Symposium of the Fluid Dynamics Panel  
in Friedrichshafen, Germany, 23rd-26th April 1990.

## The Mission of AGARD

According to its Charter, the mission of AGARD is to bring together the leading personalities of the NATO nations in the fields of science and technology relating to aerospace for the following purposes:

- Recommending effective ways for the member nations to use their research and development capabilities for the common benefit of the NATO community;
- Providing scientific and technical advice and assistance to the Military Committee in the field of aerospace research and development (with particular regard to its military application);
- Continuously stimulating advances in the aerospace sciences relevant to strengthening the common defence posture;
- Improving the co-operation among member nations in aerospace research and development;
- Exchange of scientific and technical information;
- Providing assistance to member nations for the purpose of increasing their scientific and technical potential;
- Rendering scientific and technical assistance, as requested, to other NATO bodies and to member nations in connection with research and development problems in the aerospace field.

The highest authority within AGARD is the National Delegates Board consisting of officially appointed senior representatives from each member nation. The mission of AGARD is carried out through the Panels which are composed of experts appointed by the National Delegates, the Consultant and Exchange Programme and the Aerospace Applications Studies Programme. The results of AGARD work are reported to the member nations and the NATO Authorities through the AGARD series of publications of which this is one.

Participation in AGARD activities is by invitation only and is normally limited to citizens of the NATO nations.

The content of this publication has been reproduced directly from material supplied by AGARD or the authors.

Published October 1990

Copyright © AGARD 1990  
All Rights Reserved

ISBN 92-835-0589-1



Printed by Specialised Printing Services Limited  
40 Chigwell Lane, Loughton, Essex IG10 3TZ



## Foreword

The previous AGARD Fluid Dynamics Panel Symposium on missile aerodynamics (AGARD Conference Proceedings No.336) was held at Trondheim, Norway in September 1982. Since that time, substantial experimental and theoretical work has been conducted in an attempt to improve the fundamental understanding of the aerodynamics of missiles, to provide comprehensive data bases and to develop semi-empirical and computational prediction methods. Whilst significant progress has been made, the performance requirements of many types of missile have, at the same time, tended to widen significantly to cover, for example, higher speeds, increased agility and longer range. In addition, the use of unconventional shapes for weapons is now being considered more often. Consequently, new problems are being posed and thus, after eight years, it was considered appropriate to hold another symposium on missile aerodynamics to (i) review current progress and achievements, (ii) highlight outstanding problems and (iii) establish pointers for planning future research programmes.

To this end, the Symposium addressed many aspects of the aerodynamic design and performance of missiles for the subsonic through to the hypersonic flight regimes and reviews covering the stability and control of tactical missiles and progress made in the field of store carriage and release were also presented. 31 papers were accommodated in seven sessions with contributions from Canada, France, Germany, Turkey, United Kingdom and United States. The sessions were:-

- Overview (3 invited papers)
- Analysis and Predictive Methodologies: Computational Methods/Validation (5 papers)
- Analysis and Predictive Methodologies: Empirical Tools and Experimental Techniques (5 papers)
- Flow Separation and Interference Effects (3 papers)
- Unconventional Shapes and Projectiles (5 papers)
- Propulsion, Base Flows and Jet Reaction Controls (5 papers)
- Aerothermodynamics and Hypersonics (5 papers)

The Symposium ended with a substantial and worthwhile discussion period which began with a preliminary assessment given by the Technical Evaluator. These proceedings include a record of the discussion. The Technical Evaluation Report is available as AGARD Advisory Report AR-298.

P.R.Fagnell  
Programme Committee Chairman

## Avant-Propos

Le dernier symposium sur l'aérodynamique des missiles organisé par le Panel AGARD de la Dynamique des Fluides s'est tenu à Trondheim en Norvège en septembre 1982 (voir compte-rendu de conférence AGARD No. 336). Depuis lors, d'importants travaux théoriques et expérimentaux ont été réalisés en vue d'élargir le domaine des connaissances de l'aérodynamique des missiles, de fournir des bases de données complètes et d'élaborer des méthodes de prévision semi-empiriques et statistiques. Bien que des progrès importants aient été réalisés dans ce domaine, l'enveloppe des performances exigées a tendance à s'élargir, pour inclure, par exemple, l'accroissement de la vitesse et la manoeuvrabilité, ainsi que l'extension de la portée. En outre, les formes de missiles exotiques sont de plus en plus à envisager.

Par conséquent, de nouveaux problèmes se posent et, huit ans après, le Panel AGARD de la Dynamique des Fluides a jugé opportun d'organiser un deuxième symposium sur ce sujet afin de (i) faire le point des travaux en cours et des résultats déjà obtenus, (ii) définir les problèmes qui restent à résoudre, et (iii) poser des repères en vue de la planification des futurs programmes de recherche.

A cette fin, le symposium a examiné différents aspects de la conception aérodynamique et les performances des missiles, pour des régimes de vol allant du subsonique à l'ypersonique. Des exposés portant sur la stabilité et le contrôle des missiles tactiques et sur les progrès réalisés dans le domaine de l'emport et du largage des charges externes ont également été présentés. En tout, quelques 31 exposés ont pu être donnés par des conférenciers du Canada, de la France, de l'Allemagne, de la Turquie, du Royaume-Uni et des Etats-Unis lors des 7 sessions du symposium, à savoir:

- préambule (3 communications sur invitation)
- l'analyse et les méthodologies de prévision: les méthodes de calcul/validation (5 communications)
- l'analyse et les méthodologies de prévision: les outils empiriques et les techniques expérimentales (5 communications)
- le décollement de l'écoulement et les effets de sillage (3 communications)
- les formes et les projectiles peu conventionnels (5 communications)
- la propulsion, les écoulements de culot et les commandes par jets de gaz (5 communications)
- l'aérothermodynamique et l'ypersonique (5 communications)

Le symposium s'est terminé par un échange de vues soutenu et très valable, avec, en guise d'introduction, une évaluation préliminaire présentée par l'expert technique du symposium. Ce compte-rendu comprend le texte du débat. Le rapport d'évaluation technique est édité sous la forme du Rapport Consultatif AGARD AR-298.

P.R.Bignell  
Président du Comité de Programme

## Fluid Dynamics Panel

**Chairman:** Dr W.J. McCroskey  
Senior Staff Scientist  
US Army Aero Flightdynamics  
Directorate — Mail Stop N258-1  
NASA Ames Research Center  
Moffett Field, CA 94035-1099  
United States

**Deputy Chairman:** Professor Ir J.W. Slooff  
National Aerospace Laboratory NLR  
Anthony Fokkerweg 2  
1059 CM Amsterdam  
Netherlands

### PROGRAMME COMMITTEE

Mr P.R. Bignell (Co-Chairman)  
BAe PLC, Sowerby Research Centre  
Naval Weapons Division  
FPC 266, P.O. Box 5  
Filton  
Bristol BS12 7QW  
United Kingdom

Professor J.J. Ginoux  
Director  
von Kármán Institute for Fluid Dynamics  
Chaussée de Waterloo 72  
B-1640 Rhode-Saint-Genèse  
Belgium

Mr L.H. Ohman  
High Speed Aerodyn. Lab. — U66  
National Aeronautical Establishment  
National Research Council  
Montreal Road  
Ottawa, Ontario K1A 0R6  
Canada

M. l'Ing. Gen. C. Thery  
B.P. 72  
ONERA  
92322 Châtillon  
France

Dr W. Schmidt  
Deputy Director, DORNIER 328 Program  
Dornier GmbH, EY  
P.O. Box 1420  
D-7990 Friedrichshafen 1  
Germany

Dr R.A. Graves, Jr (Co-Chairman)  
Director, Aerodynamics Div.  
Mail Code RF  
NASA Headquarters  
Washington D.C. 20546  
United States

Dr Ing. G. Bucciantini  
Aeritalia-Società Aerospaziale Italiana  
Gruppo Aerei Difesa  
Corso Marche 41  
10146 Torino  
Italy

Professor Dr T. Ytrehus  
Institute of Applied Mechanics  
The University of Trondheim  
The Norwegian Inst of Technology  
N-7034 Trondheim — NTH  
Norway

Dr J. Simon  
CASA — Project Division  
Aerodynamic Department  
Avda John Lennon s/n  
GETAFE  
28065 Madrid  
Spain

Professor Dr C. Çiray  
Aeronautical Eng. Department  
Middle East Technical University  
Inönü Bulvarı AK: 06531  
Ankara  
Turkey

### PANEL EXECUTIVE

Dr W. Goodrich

**Mail from Europe:**  
AGARD—OTAN  
Attn: FDP Executive  
7 rue Ancelle  
92200 Neuilly sur Seine  
France

**Mail from US and Canada:**  
AGARD—NATO  
Attn: FDP Executive  
APO New York 09777

Telephone: 33 (1) 4738-5775  
Telex: 610176 (France)  
Telefax: 33 (1) 4738-5799

# Contents

	Page
Foreword	iii
Avant-Propos	iv
Fluid Dynamics Panel	v
	Reference
<b>SESSION I — OVERVIEW</b>	
Chairman: W.Schmidt	
Some Trends in Missile Aerodynamics by R.G.Lacau and M.Robert	1
Review of the Spring 1988 AGARD FMP Symposium by H.A.Torode	2
Store Carriage, Integration and Release by A.B.Haines	3
<b>SESSION II — ANALYSIS AND PREDICTIVE METHODOLOGIES: COMPUTATIONAL METHODS/VALIDATION</b>	
Chairman: S.Lekoudis	
Pressure Measurements on Slender Bodies at Supersonic Speeds and Development of Flow Separation Criteria for Euler Codes by J.Hodges, L.C.Ward and T.J.Birch	4
Computation of Viscous Supersonic Flows by Y.Noguchi, J.M.R.Graham and R.Hillier	5
Supersonic Tactical Missile Computations Using Euler's Equations with Crossflow Separation Modeling by F.J.Priolo and A.B.Wardlaw, Jr	6
Aerodynamic Design of Pegasus™ — Concept to Flight with CFD by M.R.Mendenhall, D.J.Lesieutre, S.C.Caruso, M.F.E.Dillenius and G.D.Kuhn	7
Application of Euler and Navier-Stokes Codes to Missile Type Bodies with High L/D Ratios by D.J.Jones, J.Evans, F.J.Priolo, W.Sturek and A.B.Wardlaw	8
<b>SESSION III — ANALYSIS AND PREDICTIVE METHODOLOGIES: EMPIRICAL TOOLS AND EXPERIMENTAL TECHNIQUES</b>	
Chairman: C.Çiray	
NUFA: A Semi-Empirical Method for the Prediction of Isolated Weapon Aerodynamics by S.McDougall, A.J.Press and P.S.Barratt	9
A Semi-Empirical Prediction Method for Missile Aerodynamics by K.-W.Bock	10
Aerodynamic Characteristics of Cylindrical Bodies with Pointed and Truncated Conical Noses by V.Ati	11

	Reference
<b>Retarded Store Interference</b> by M.E. Wood and R. Partington	12*
<b>A Wind Tunnel Rig for the Measurement of Magnus Force and Moment on Spinning Models</b> by N. Corby and J.B. Berry	13*

**SESSION IV – FLOW SEPARATIONS AND INTERFERENCE EFFECTS**  
Chairman: J.J. Ginoux

<b>Systematic Investigations of Body-Wing-Tail Interference at High Angles of Attack</b> by K. Hartmann and D. Nikoletsch	14
<b>Supersonic Vortex Flows Around a Missile Body – Basic Experiment and Euler Numerical Computation</b> by J. Lordon, J.-C. Fare and D. Pagan	15
<b>Asymmetric Supersonic Flow around Cones with Noncircular Sections</b> by O.A. Kandil, T.-C. Wong and C.H. Liu	16

**SESSION V – UNCONVENTIONAL SHAPES AND PROJECTILES**  
Chairman: G. Bucciantini

<b>Comparison de Différentes Méthodes de Calcul Appliquées à un Fuselage de Section Lenticulaire</b> par P. d'Espinay	17
<b>Three Dimensional Flow Calculations for a Projectile with Standard and Dome Bases</b> by J. Sahu and C.J. Nietubicz	18
<b>The Aerodynamic Characteristics of Long Rod Projectiles</b> by P.G.C. He ring	19*
<b>Navier-Stokes Predictions of Static and Dynamic Aerodynamic Derivatives for High L/D Finned Projectiles</b> by P. Weinacht and W.B. Sturek	20
<b>Numerical Modelling of Sabot Aerodynamics</b> by R.C. Krishna, J.M.R. Graham and R. Hillier	21*

**SESSION VI – PROPULSION, BASE FLOWS AND JET REACTION CONTROLS**  
Chairman: L.H. Ohman

<b>Overview of Propulsion Concepts for Tactical Missiles</b> by F.C. Zarlingo	22
<b>Prévision des Coefficients Aérodynamiques de Missiles Munis de Prises d'Air</b> par P. Champigny, D. Baudin et P. Gonidec	23
<b>Computation of Axisymmetric Base Flow with Different Turbulence Models</b> by F. Magagnato	24
<b>Results of GARTEUR Action group AG09 on "Flow Past Missile Afterbodies"</b> by J. Delery and B. Wagner	25
<b>Experimental Aerodynamics for Hot Gas Jet Reaction Control Systems</b> by H. Schilling, R. Friedrichs and D. Christ	26

---

\* Printed in classified publication CP 493(S).

	Reference
<b>SESSION VII — AEROTHERMODYNAMICS AND HYPERSONICS</b>	
Chairman: T.Ytrehus	
<b>Laminar/Turbulent Flow Transition Effects on High-Speed Missile Domes</b> by U.G.Hingst	27
<b>Investigations of Aerothermodynamic Effects on Axisymmetric Bodies at High Mach Numbers</b> by J.D.Regan and T.J.Rooke	28
<b>Thermal Imaging on Missiles in Hypersonic Flow</b> by H.Schöler	29
<b>Chordwise and Spanwise Centers of Pressure of Missile Fins</b> by D.J.Lesieutre and M.F.E.Dillenius	30
<b>Computational Models with Advanced Thermochemistry for the Analysis of Missile/Plume Flowfield Interactions</b> by S.M.Dash, N.Sinha and B.J.York	31
<b>Round Table Discussion</b>	RTD

## SOME TRENDS IN MISSILE AERODYNAMICS

by

R.G. LACAU and M. ROBERT  
**aerospatiale** - Division Engins Tactiques  
 2, rue Béranger - 92320 Châtillon - France

### SUMMARY

The objective of this paper is to highlight the requirements for the next generation of tactical missiles, the corresponding new aerodynamic problems, and the new wind tunnel testing techniques and computational methods. A special attention is focused on : unconventional shapes as airbreathing missiles, stealth considerations, pyrotechnical lateral jet control, high angles of attack and non rigid airframe. The computational codes presented are based on the resolution of the Euler equations ; they are illustrated by numerous industrial examples.

### 1. INTRODUCTION

This paper provides a general review of trends in tactical missile aerodynamics. The paper contents four parts.

The first part is related to new requirements in tactical missiles. They are given for each missile family with associated new aerodynamics problems.

The second part describes some of these problems facing the aerodynamicist :

- unconventional shapes which result from the use of side intakes on axisymmetric fuselage (ramjet missiles), the packaging of submunitions, the better integration on an aircraft,...
- stealth considerations,
- pyrotechnical lateral jet control which is highly suitable for : antitank, very short range missiles or missiles which use this system during a limited operating time,
- high angles of incidence which are encountered when a missile is fired vertically in a turnover phase to intercept a sea-skimming missile,...
- deformed shapes which result from loading.

Each problem will be described with his aerodynamic effects.

The third part presents non-classical wind tunnel testing relative to pyrotechnical lateral jet, and flowfield investigation.

The fourth and last part is dedicated to computational fluid dynamics (CFD). This approach is essential to :

- treat complicated configurations as airbreathing missiles,
- determine load distributions for structural calculations, local flow field properties (e.g. velocity profiles at an inlet face),...
- provide with important insights into the understanding of complex flow mechanisms.

Not so long, in 1982 (previous AGARD symposium on missile aerodynamics), only the linearized potential solvers were able to compute complete missile configurations. Since that time, remarkable progress have been done in numerical methods particularly for the Euler equations and grid generation, allowing today to compute inviscid nonlinear flow fields around complex 3D configurations. To demonstrate the capabilities of Euler codes we present several industrial examples.

### 2. NEW REQUIREMENTS IN TACTICAL MISSILES

#### 2.1 The antitank missiles

For the 3rd generation of antitank missiles, development work is taking place in two directions :

- the renewal of the actual series of medium range (2 km) and long range (4 km) missiles,
- the improvement of short range (25 m to 600 m) missiles.

There will probably never be any great changes made to the shapes which will remain conventional, that means, cylindrical cruciform with folding stabilizers at the rear. Nevertheless, for certain of these future antitank missiles (ERYX, ACMP) an original construction method has been adopted :

- motor at the front and hollow-charge warhead at the rear, thus enhancing warhead efficiency,
- force-type flight control system, enabling launching at reduced speed (launching possibilities within confined areas) and a possibility of guidance at low speed (efficiency at very short ranges). This new flight control system will produce lateral jets, causing complex three-dimensional flow patterns (fig. 1).

## 2.2 The anti-ship missiles

In the future, due to the foreseen developments of anti-missile systems, it will be necessary to develop missiles with a greater range and a greater target penetration capability. These results can be obtained by increasing the missile speeds ( $Mach > 2$ ) and by bringing them over the targets at very low heights with terminal maneuvering at high load factors.

In the range of speeds and altitudes to be covered, the most satisfactory means of propulsion is the ramjet engine. This is the type of propulsion selected for the successor of the EXOCET. The choice of this type of propulsion has the effect of giving the missile an unconventional shape, due to the existence of air intakes (fig. 2).

## 2.3 The surface-to-air missiles

As the surface-to-air missiles have demonstrated their efficiency against attacking aircraft (i.e. the FALKLANDS campaign and the IRAN-IRAK war), the attacking aircraft must now be equipped with jamming counter-measures to confuse surface-to-air missiles, and air-to-surface missiles that can be launched beyond the range of the anti-aircraft defences. For these reasons, future surface-to-air missiles must be able to intercept not only high performance aircraft but also supersonic missiles having diving or surface-skimming flight paths, a high degree of maneuverability and which are launched out of defensive range.

The response to these threats necessitates :

- vertical launching and turning over in all directions (reduction of launching sequence time),
- a supersonic speed,
- a very high degree of maneuverability (50 g). In order to obtain such maneuverability, but above all a very short response time so as to render the evasive actions of the enemy aircraft ineffective, a very advanced technical solution has been selected for the ASTER missile, which is being designed in France (fig. 3). This consists in a force-type flight control by lateral jets, which provides very short response time, operating in conjunction with a conventional aerodynamic flight control that makes the most important contribution to the maneuverability.

These new characteristics will lead to very high angles of incidence and complex three-dimensional flow patterns due to lateral jets.

## 2.4 The air-to-air missiles

The development of the threat that can be anticipated at the end of this century necessitates the definition of new missiles able to be fired from aircraft flying at very high incidence ( $35^\circ$  and perhaps more) and capable of hitting very maneuverable targets that may be dispersed throughout a very large range of altitude.

In order to fulfil this requirement, work is actually being undertaken in two directions :

- renewal of the present-day missiles. Examples : AMRAAM for long ranges, ASRAAM for short ranges, both types being developed within an international framework ;
- development of a light missile capable of fulfilling requirements for long range interception missions and dogfights. Example : the MICA missile which is being developed in France (fig. 4). This missile is small, of low weight, very compact (long chord wings), and provided with a mixed flight control system incorporating both aerodynamic control surfaces and jet deflector control surfaces, which allows very great variations of attitude. The choice of long chord wings and rear control surfaces enables high angles of incidence while allowing the missile to be slung directly against the underside of the aircraft.

## 2.5 The air-to-surface missiles

About air-to-surface missiles, the object is to launch them from an aircraft beyond the range of the enemy defences.

Among long range and highly accurate missiles we can mention the ASMP which is certainly a weapon unique in the world. It is propelled by a ramjet engine with an integrated booster, and equipped with a pair of two-dimensional lateral air intakes. Its shape is therefore unconventional (fig. 5). Flight control is aerodynamic, by means of rear control surfaces.

A new generation of cluster-type air-to-surface weapons is being prepared for future requirements for instance APACHE in France. This modular subsonic missile is designed to carry sub-projectiles suited to designated fixed or moving targets at a range of several tens of kilometers, while allowing the launching aircraft to remain out of range of the ground-to-air defence systems of these targets. These missiles will no longer have a symmetrical shape and they will have long folding wings (fig. 5). Their shape will be designed by taking geometrical constraints into consideration in association with the reduction of the Radar Cross-Section (RCS).



### 3. NEW PROBLEMS FACING THE AERODYNAMICIST

#### 3.1 Unconventional shapes

##### 3.1.1. Bodies with side intakes

Two classes of missiles are concerned :

- ramjet or ramroked missiles
- turbojet missiles.

The number, shape and position of the air intakes must be chosen taking into account the following aspects (Ref. 1, 2) :

- internal performance : thrust,
- external aerodynamics : drag, lift-to-drag ratio,
- operational constraints : overall dimensions (airplane carriage), discretion,...
- autopilot : skid-to-turn or bank-to-turn control.

Several configurations are illustrated fig 6.

- With a single intake :

- nose intake has high pressure recoveries but bad integration. It is no longer used.
- chin intake is well suited for bank-to-turn flight control (well adopted for long range missions). It uses the windward upstream part of the missile nose as supersonic compression ramp.
- annular intake has a better integration than the precedent but its performance is the poorest,
- vertical intake is an excellent solution. Compactness is good (the detection, attack and propulsion functions are separated) and performance is high.
- top mounted intake is an optimum solution for RCS (the intake is hidden from the ground based radar) but is limited in incidence.

- With two lateral intakes (e.g. ASMP)

A missile configuration with two lateral air intakes is well adapted for a bank-to-turn control. The intakes are located diametrically opposed or inclined towards the bottom. The first case is the best for supplying the chamber and for incrementing the normal force. The second case is the best for internal performance.

- With four intakes (e.g. ANS, SA6)

A missile configuration with four lateral air intakes is well suited for skid-to-turn control. However, at high incidence the leeward intakes reach their operation limit, and the lift-to-drag ratio of these configurations is not optimal (two intakes are sufficient to give lift, the other two induce drag).

For all these intakes the shape may be : axisymmetric, half axisymmetric, rectangular (classical or inverted),... (fig. 7).

The longitudinal location is a compromise between : the flowfield around the fuselage, the diffuser length, the center of pressure and the attachment points on the fuselage, but the normal force is only slightly modified.

It is possible to increase the performance of such intakes by adding wings or strakes to the fuselage.

#### a) External aerodynamics (Ref. 3, 4)

Concerning external aerodynamics, airbreathing missiles may be classified in two families :

- configurations with nose, chin or annular intakes. These intakes influence only fuselage's drag,
- configurations with lateral intakes. These intakes influence fuselage's lift, stability and drag.

##### • Lift and stability

Generally lateral intakes increase lift :

- intake span influences mainly lift. Note that air intake aerodynamics behaves like the long-wing aerodynamics,
- length of the intake nacelle influences mainly the center of pressure,
- intake type influences lift and stability. For example rectangular intakes and fairings produce higher lift than axisymmetric intakes.
- intake roll position is also important. The lift is maximal if the intakes are in an horizontal position (fig. 8 taken from ref. 3).

##### • Drag

Figure 9 (ref. 4) presents the different drag components of an airbreathing missile with four axisymmetric air intakes at Mach 2 at sea level. We note the important contribution of the air intakes which represents in this case 38 % of the total drag :

- |                                 |                 |
|---------------------------------|-----------------|
| 9 % for inlets                  | } pressure drag |
| 15 % for the fairing boat-tails |                 |
| 14 % for the friction drag      |                 |

To optimize drag we must do the thrust-drag balance.

##### • Control surfaces efficiency, hinge moments

Generally control surfaces are located on the fairings. Therefore theoretical prediction of the control forces and hinge moments is very difficult.

### b) Flow field around the fuselage

The study of this flow field is necessary to determine the best intake location. To obtain high performances, low velocity fields are sought and low energy fields (boundary layers, vortices) are avoided.

A delicate problem concerns the ogival nose vortices that develop on the leeward side of the missile at angles of attack beyond  $5^\circ$ . These vortices cause major total pressure losses in air intakes. With four-intake configurations, there will be always one or two intakes affected by these low-energy regions. It should be noted that longitudinal strakes upstream of the air intakes modify the natural development of the boundary layer around the fuselage at incidence and make it possible to move the vortices away from the intakes.

### c) Internal aerodynamics

Once we have defined the stream tube captured by the air intake, characterized by mean values in the inlet plane (Mach, incidence, side-slip,...) it is possible to study the intake in a uniform flow field and consequently to study it isolated. But this quick cheap method is not perfect and studies with air intakes on the fuselage are imperative during the development process.

### 3.1.2. Non-circular bodies

Two classes of missiles are concerned :

- subsonic modular stand-off-missiles with square or rectangular cross-sections
- supersonic/hypersonic air-breathing missiles with elliptical or triangular,... cross-sections.

A typical subsonic modular stand-off-missile is presented fig. 10. The layout shows a square cross-section body with the wing mounted at the top of the body to allow unrestricted installation of the submunitions.

The sharp corners of the body produce flow separations and vortex sheets inducing non-linear lift. Thus a square body provides much more normal force than a circular body with the same cross-section area. When the body is rolled the flow patterns change, they become unsymmetrical inducing lateral forces and moments, but become symmetric again when the roll angle reaches  $45^\circ$ .

Typical supersonic/hypersonic air-breathing missiles are presented fig. 11 (Ref. 5-8). Their objectives are :

- optimum integration of the intakes in the fuselage flow field,
- low drag,
- high lift-to-drag ratio,
- low RCS,
- good integration under aircraft.

Different shapes are possible : waveriders, elliptical, triangular, square,... Figure 11 presents two types of examples :

- the waveriders which are designed for a minimum drag (streamlines on the leeward side are not deflected) and for a maximum lift (shock wave is limited by the leading edges).
- the lenticular shape which is designed for a high lift-to-drag ratio at constant surface cross-section and for high lift at incidence (the sharp leading edges generate vortices). Figure 11 presents an ONERA study.

### 3.2 Stealth considerations

The main class of missiles which may be concerned by low radar signature (RCS) and low infrared signature (IRS) are missiles with relatively long flight times :

- subsonic stand-off missiles
- supersonic airbreathing missiles.

The RCS depends on many factors : the area, the shape, the presentation angle, the nature of materials, etc. The figure 12 shows the RCS of the B-52, the B-1B, and the US Air Forces future stealth bomber, and reveals the spectacular reduction achieved. As a reduction in RCS by one order of magnitude means an 80 % decrease in radar detection, the immense importance of such research becomes manifest, particularly since quite simple steps can produce significant results.

To reduce the RCS, there are essentially two ways :

- shape the airframe to deflect the radar signals (fig. 13 - Ref. 9),
- use composite materials that absorb radar signals.

Today, it can be asserted that considerable know-how has been gained in studying shapes for greater stealth, having regard for such constraints as space, carrying capacity,...

For the aerodynamicist the main design recommendations are :

- avoid sharp angles and surface irregularities,
- avoid straight leading edges,
- suppress reflective surfaces (depends on the observation direction).

that means :

- design smooth profil for the lifting surfaces and the fuselage, smooth the junction body/wings,
- use elliptic fuselage, sweep and curve the leading and trailing edges.

Air intakes are also significant sources of radar returns. To reduce them it is recommended to :

- smooth the intake duct
- shape the lips

- treat duct walls with radar absorbent material
- flush subsonic intakes with the fuselages.

Concerning the infrared signatures for subsonic missiles, they are essentially in the rear part. In order to minimize them, a shield can be installed around the jet pipe with or without auxiliary intakes admitting cold air to mix the hot flux.

### 3.3 The pyrotechnical lateral jet control

#### a) Limitation of moment control and advantages of pyrotechnical force control

The conventional control of missiles consists in responding to a lateral acceleration command by controlling the flight control surfaces creating the moment. This moment produces an angular movement of the missile resulting in a change of incidence which creates an aerodynamic lift force ensuring the desired maneuver.

The two disadvantages of this type of control are :

- a time delay between the steering command and execution of the order, related to a number of "intermediaries" and parameters governing the angular movement required to create the lateral acceleration (missile moment of inertia, aerodynamic damping moment) ; this applies to any type of moment control (aerodynamic or jet controls),
- an aerodynamic control force which is proportional to the dynamic pressure, i.e. to the air density and speed, and then a lack effectiveness at launching (low speed) and at high altitude (low air density).

But the use of a propulsive force at the missile center of gravity overrides these two disadvantages, thus enabling :

- to considerably reduce response time, and as a result, the passing distance from difficult targets, particularly, highly maneuvering targets,
- very low speed and high altitude maneuvers.

However, pyrotechnical force control has certain constraints :

- used as single means of control, its operational domain is limited by its powder consumption. In particular, with a gas generator associated to a distribution system towards the nozzles, powder consumption remains the same whichever the maneuver (null or maximum),
- the missile cannot be used following the propulsion phase of this system,
- the missile must be organized to obtain a nearly fixed center of gravity during use of the system,
- the definition of the missile's aerodynamic configuration must take account of interaction effects created by the jets.

For all of these reasons, the purely pyrotechnical force control technology is highly suitable for antitank and very short range missiles, or for missiles which only use this system in the final guidance phase (thus limiting operating time) with an associated aerodynamic control system (thus limiting the required power level).

Note that the use of moving wings at the center of gravity, which is also a type of force control, but aerodynamic, presents limitations (capacity of actuators, altitude effect, low speed effect, etc.) which do not allow the control levels provided by pyrotechnical force control.

#### b) Aerodynamic interactions due to a lateral jet

The transverse ejection of a lateral jet into an external flow results in a highly complex flow field (figure 14) leading to a set of interactions which can be classified in two categories (figure 15) :

- local interactions,
- downstream interactions.

The local interactions (figure 16) are related to the jet obstacle effect which, at supersonic speeds, produces upstream of the nozzle a detached shock and a separation of the boundary layer forming a shock generating an overpressure zone. Just immediately downstream of the nozzle, the external flow around the jet produces a depression zone. The distribution of the pressures around the nozzle, for a nozzle located on a wingless fuselage and near the center of gravity, produces a low resulting force which is generally opposed to the thrust of the nozzle (unfavorable interaction) and a slight nose up moment in the maneuver direction.

The downstream interactions (figure 17) are due to the highly vortical character of the flow downstream of the jet. Far from the exit section, the jet wake takes the form of two contra-rotating vortices resulting from the curvature of the jet and its rounding by the external flow. Thus, the speeds induced by these vortical structures affect the lifting surfaces placed downstream, generally producing a loss of lift and moments.

The total sum of these interactions result in :

- an interaction force which is added to the lateral propulsive force and which can affect efficiency of the propulsion system,
- "disturbing" pitch and roll moments which should not affect the controllability of the missile.

To design a missile controlled by lateral jets, it is therefore necessary :

- to optimize the aerodynamic shape of the missile with respect to the two preceding criteria,
- to achieve a complete model of the interactions required for the control studies.

### 3.4 Very high angles of attack

Very high angles of attack occur during vertical launch (fig. 18) :

- at the beginning of the trajectory when the missile has a low forward speed and the launch platform is travelling or with lateral wind,
- at the turn over maneuver to intercept sea-skimming missiles or aircrafts.

A typical vertical launch trajectory is shown in fig. 19 (Ref. 10). Within approximately the first second, the missile pitches at about 300 deg/s and the angle of attack can be as high as 50°-60°. Under these conditions, the missile can be subjected to asymmetric flow separations, inducing highly non-linear out-of-plane side force and moment.

An extensive review of available information on asymmetric vortex shedding from bodies of revolution compiled by Ericson and Reding is available in reference 11. From this reference we can note :

- asymmetric flow separation occurs generally between 30° and 60°,
- significant side forces occur only for subsonic cross flow,
- the magnitude of the side force is Reynolds number dependent,
- the phenomenon is nose and roll angle dependent.

To remove the dependence on roll angle of the out-of-plane force or to reduce it, various systems are proposed :

- excrescences very close to the tip of the nose to generate reliable and repeatable out-of-plane force at all roll angles,
- air jets to control asymmetric force (Ref. 12),
- a short section of the nose, free to rotate, with strakes, allows to reduce the magnitude (Ref. 13).

### 3.5 Non rigid airframes

The last problem concerns some types of missiles, as the air-air, which have long bodies ( $L/D > 20$ ) and with light structures constituted for example by composite materials. In this case, the missiles relatively flexible are deformed by the aerodynamic forces inducing changes in aerodynamic characteristics which may reduce missile stability and maneuverability (fig. 20 - Ref. 14).

## 4. NEW WIND TUNNEL TESTING TECHNIQUES

### 4.1 Lateral jets

The use of lateral jets as a control means has needed new wind tunnel test techniques to identify the aerodynamic characteristics of such a missile. In the same way, the base jets may affect the stability of missiles at the very high angles of incidence now encountered (vertical launch). The measurement of these aerodynamic interactions brings up three main problems :

#### • The simulation of the jets

The best representation of real effects of lateral jets is got with powder gases obtained by minipropulsion units mounted in the model. The study and the manufacture of these specific units - that must respect the adaptation ratio of the nozzles in flight, in comparison with the static pressure feasible in the wind tunnel - are very expensive ; the use of powder blocks brings to very long occupation times of the wind tunnels (safety problems, installation and removal operations for each propulsion unit, i.e. for each point of the flight domain to explore), and so to very large costs.

So the use of compressed air to simulate jets has appeared very attractive, and many wind tunnels offer now continuous supply lines. The characteristics of such compressed air being different from those of real powder gases, the research of a similarity criterion has to be made to respect at best physical phenomena and effects. This technique is very often used, generally in addition to some punctual tests with real propulsion units.

#### • The weight principle

The support of the model sustains both aerodynamic and propulsive component forces. Two techniques can be used :  
- it is first possible to measure the only aerodynamic forces and moments ; the propulsion unit and the nozzles must be then directly connected to the sting and uncoupled with the external aerodynamic model that is mounted on the strain-gage balance (fig. 21). This measurement technique permits to adapt the balance to the aerodynamic loads only, and so to obtain a good precision. Furthermore, the deformations or vibrations are weak, the propulsive forces loading only the sting, that is more rigid than the balance. The inconvenience of the technique concerns the needful looseness between the nozzles and the model, specially for small sizes.

- it is also possible to measure the gross-aerodynamic forces and moments (aerodynamic and propulsive). Propulsion unit and nozzles are then connected to the model, the manufacturing of which is more easy. But dynamic responses are then bigger, for instance at the time of the ignition of the powder-block, because the strain gage-balance is, by definition, a flexible mounting ; it measures then, in addition of aerodynamic and propulsive components, the inertial forces and moments due to the movements of the model ; the measuring capacity of the balance must be adapted to these loads, to the detriment of the precision.

#### • The correction of inertial forces and moments

It may be necessary to correct these inertial components in the two following cases :

- either when the combustion time is too short, so that these dynamic responses cannot get damped ; it is then very difficult to extract a mean value that represents only the external forces and moments applied on the model,

- or when one is actually interested in these transient or dynamic phenomena (ignition of the propulsion, command switchings,...).

Then, the model must be equipped with accelerometers, that permit to subtract the inertial forces from the gross-forces measured by the balance. Industrial wind-tunnel tests of this type have been already realized for some last years (Ref. 15) and will be a valuable implement in many unsteady studies, regarding for instance missiles in autorotation.

#### 4.2 Flowfield investigation

The advent of Computational Fluid Dynamic has created new requirements in measurement techniques in wind-channels. Theorists and "Numerists" have to know the physical phenomena so as to develop adequate flow modelings and to get some experimental data for their validation. Therefore, even if visualisation techniques are still rather employed (hydrodynamic, oil, schlieren techniques...), the actual need consists now of quantitative measures, not only of the gross-forces, but also of the velocity and pressure characteristics on the model skin and in the whole flowfield.

Many new techniques have emerged during the past decade and are now currently used for the research, as the following ones :

- the non intrusive techniques, as the laser velocimeter system, to measure the flow velocity and its fluctuations. The example given in figure 22 presents a detailed exploration by Laser Doppler Velocimetry of the separated flow behind a cylindrical after body with jet (Ref. 16).
- the RAMAN diffusion to identify different species in the flow (for instance air and powder gaz).

The improvement of instrumentation and data acquisition permits also such testings in an industrial context, for validations of numerical codes on complete configurations of missiles, or for particular studies of vortex downstream of wings or lateral jets ; It is now possible through, among other developments :

- new electronic pressure transducer switches (PSI), that allow a quicker acquisition cadence, and so a larger number of measurement points than when using scanivalves,
- five-hole probes of very small size, that allow detailed investigations of the flowfield (velocity module and direction, pressure).

The example given in figure 23 shows a detailed exploration with a five-hole probe of the separated cross-flow around a fuselage at one longitudinal station (Ref. 17).

### 5. NEW PREDICTIVE TOOLS : THE EULER SOLVERS

The Euler equations represent the most complete set of equations modelling the evolution of a non-viscous and non-conducting fluid. They admit weak solutions with jumps, among which physical discontinuities are modelled such as shock waves and vortex sheets.

Important progress has been made these last ten years for solving the 3D Euler equations. Moreover, the access to fast vector computer makes Euler calculations feasible and cost-effective, thus opening a new way for the prediction of missile aerodynamics. However care must be taken since the model does not take into account the viscous effects even if it computes vortex sheets.

To compute steady flows with Euler equations two ways are possible :

- to solve the steady equations. In this case, the equations are hyperbolic in space and a space-marching technique is used. This procedure is valid only for supersonic flows (e.g. code SWINT Ref. 18 and code SUP Ref. 19, 20),
- to solve the unsteady equations. In this case, the full three-dimensional flow variables are advanced in time until an asymptotic limit is reached. This procedure is valid for any speed range. But if the flow is everywhere supersonic, a pseudo-unsteady marching procedure can be used in which the steady solution is obtained in a plane using an upwind scheme and driving the time derivatives to zero, then proceeding to the next plane, sweeping the domain in the flow direction (e.g. code FLU3C, Ref 21, FLU3M, Ref 22). In this way, the memory requirement is kept to a minimum and computing time is reduced.

In tables 1 and 2 of the present paper, we have summarized the capabilities of 13 codes and some details on their models. From table 1, we note that there are two programs, SWINT and FLU3C, which have computed all types of configurations but only in supersonic. These two codes can also calculate flow separation.

**Remarks about flow separation calculation :** Flow can separate from sharp edges (leading and tip edges of wings) or smooth surfaces. It is now well known that Euler codes can calculate sharp edge separation without any modification. The common explanation is that numerical dissipation which locally generates entropy in such distorted regions is responsible for the phenomenon. For smooth surface separation, the problem is more complicated. Some authors (Rizzi, Newsome) showed separated flows without any modification of the codes. But the results are strongly dependent on the mesh used. With a very fine grid separation can even disappear. Another approach consists in applying a local treatment (Kutta-like condition) that rotates the body surface velocity vectors near separation points to make them parallel with a given separation line (called forced separation technique). The results obtained with both sharp edge and smooth surface separation are very similar to experimental measurements except near the center

of the vortices. Much theoretical work has to be done to explain why we get such nice results with perfect gas models. From an engineer point of view, we can say that "it works" and can give useful qualitative and quantitative results in aircraft, missile and even car aerodynamics.

To demonstrate the capabilities of Euler codes, we present some industrial examples in supersonic.

#### a) Configurations calculated with FLU3C :

##### • Conventional missile

Figure 24 presents for Mach number 2 the normal force coefficient and the center of pressure as a function of incidence. The computation-test agreement is good and results are even a few better than semi-empirical ones. Figure 25 presents a visualization of the surface pressure and shows in particular the body area influenced by the lifting surfaces.

##### • Boosted configuration

This configuration concerns the ASTER missile, which can be seen in figure 26 with a visualization of the surface pressure coefficients. Several configurations were tested, differing by the booster dimensions (chord length, span and apex position of the tail). The computation-test data comparison (table of figure 26) shows a good absolute agreement. Moreover there is an excellent relative agreement for the configuration variations, that underlines the advantage of this method for dimensioning complex shapes.

##### • Long wing missile

Figure 27 shows the isobar lines on the ASTER surface as well as a transverse plane (Mach 2.5 and incidence  $10^\circ$ ). On the transverse plane, we note the vortical structures produced by the tip edges of the long wings. Figure 28 shows the computation-experimentation comparison for the pressure on the long wing ; the agreement is very good from an industrial point of view.

##### • Missile with side jet controls :

The interaction of a supersonic jet coming out of the missile surface with the external supersonic flow gives a very complicated flow. The vorticity requires at least the Euler equations and though they do not enable to find all the real effects (separation upstream of the jet,...) they provide us with interesting information on the structure of the flow (see figure 29).

The figure 30 and 31 show the variations of the normal force coefficient as a function of the incidence respectively for a horizontal wing (+ configuration) and a leeward wing (x configuration) in a body-wing configuration. The computation provides a good representation of the changes in the normal force coefficient  $C_N$  as a function of incidence, and in particular, the difference at a given incidence between values with and without jet.

Figure 32 shows the pressure distribution on the surface of the ASTER and the isobar lines in a transverse plane located just downstream of the nozzle. This figure indicates the complexity of the flow and shows the obvious usefulness of these computations in understanding physical phenomena ; in particular, it illustrates the favorable overpressure of the detached shock on the fins.

Figure 33 illustrates the effect of altitude on the shape and position of the primary shock. Note that the computations and experiment results are in good agreement.

##### • Airbreathing missile

Figure 34 presents the pressure distribution on the surface of the ANS at Mach 2 and incidence  $4^\circ$  and the surface grid used for this computation. This example illustrates the capability of FLU3C to compute very complex configurations.

#### b) Configurations calculated with FLU3M

Even if very complex geometries can be calculated with FLU3C, it has some limitations due to its monodomain grid strategy.

But to treat certain very complex general geometries and to make refinements in interesting regions without refining the whole domain, it is necessary to adopt a multiblock grid strategy. In general the multiblock grid should be made of several structured, possibly overlapping or patched domains. This choice considerably simplifies the mesh construction and allows the same generality as unstructured grids. Such multiblock grid strategy is used in the Euler code FLU3M (Ref. 22).

##### • Lateral jet calculation (Ref. 23)

This case is related to the computation of a subsonic pocket experimentally exhibited in the wake of the jet. This phenomenon could not be captured with a coarse grid. Figure 35 presents the multiblock structure and the refined domain which has been included in the coarse grid. Figure 36 shows the Mach number distribution in the flowfield obtained with both grids (coarse grid and refined grid). As we can see, only the refined grid is able to capture the subsonic region.

##### • Supersonic air-intake calculation

This last case concerns the computation of inlet internal flowfield including the presence of the inner boundary layer bleed (an internal trap). Its complicated shape necessitates to use a multiblock grid. Figure 37 shows the multiblock approach with a discontinuous two-domain grid and the Mach number contours in a limited region of

the inlet, around the entry section of the inner boundary layer bleed. The computation-experiment (schlieren visualization) comparison is good even if the calculation does not take into account the viscous effects.

All these applications emphasize what Euler codes can bring to industrial studies.

In conclusion, Euler codes appear as powerful analysis tools for complex external and internal 3D flows, extending the capabilities of the semi-empirical methods. But there is still much progress to do in :

- understanding and modelling of flow-separation on smooth bodies,
- development of robust and cost-effective Euler codes for subsonic and transonic flows,
- mesh optimisation.

## 6. CONCLUSION

The challenge for the 2000's is to develop long range, high speed, highly maneuverable and highly penetrative missiles.

Among the aerodynamics problems involved in the design of these new missiles, there are :

- unconventional shape aerodynamics,
- aerodynamic interactions due to pyrotechnical lateral jet,
- high angle of attack aerodynamics.

All these problems received much attention during these last years but they are not yet completely solved.

With regards to the predictive methods, the most important progress have been made in numerical methods for solving the Euler equations and in grid generation linked to CAD system for meshing realistic configurations. Today Euler solvers are able to compute very complex geometries opening a new way for the prediction of missile aerodynamics. But before they could be among the principal tools for missile designers, they need a great deal of work in all areas from mesh generation (grid optimisation,...) to finding better ways of treating flow separation, and an increasing of computer speed.

Even if computation takes more and more place in the missile aerodynamic studies, the wind tunnel tests will remain necessary for the complete modelisation of the aerodynamic characteristics, for complex configurations such as airbreathing missiles, and for specific studies (lateral jets,...). Experimentation and calculation stay complementary and progress must continue to be done in both domains.

## REFERENCES

1. LARUELLE G., « Supersonic Missile Air Intakes : Design and Development criteria », La Recherche Aérospatiale n° 1987-6
2. LARUELLE G., « Intake Aerodynamics », Missile Intakes, VKI, Lecture series 1988-04
3. HAYES C., « Aerodynamic characteristics of a series of twin-inlet air-breathing missile configurations »  
I : Axisymmetric inlets at supersonic speeds - NASA TM 84558  
II : Two-dimensional inlets at supersonic speeds - NASA TM 85559
4. CHAMPIGNY P., « Problèmes liés à l'aérodynamique externe des missiles aérobies », Missile Aerodynamics, AGARD - CP - 336, 1982
5. KRIEGER R.J., « Summary of design and performance characteristics of aerodynamic configured missiles », AIAA paper 81-286
6. RASMUSSEN M.L. and DANIEL D.C., « Aerodynamics of cone-derived waverider missile configurations », AGARD - CP - 336
7. SCHINDEL L.H., « High lift/drag ratio hypersonic missiles » AGARD - CP - 336
8. SCHINDEL L.H., « Waveriders », Tactical Missile Aerodynamics, volume 104, Progress in Astronautics and Aeronautics Published by AIAA, 1986
9. AVIATION WEEK, October 30, 1989, p. 24.
10. DILLENUS M.F.E., PERKINS S.C., « Survey on nonlinear effects » AGARD-R-754, 1988
11. ERICSON L.E., REDING J.P., « Asymmetric vortex shedding from bodies of revolution », Tactical Missile Aerodynamics, volume 104, Progress in Astronautics and Aeronautics Published by AIAA, 1986
12. MUNDEL A.R., « Low speed wind tunnel tests on the use of air jets to control asymmetric forces and moments occurring on aircraft at high incidences » RAE Technical Memorandum Aero 1984
13. MOIR I.C.M., PECKHAM D.H., SMITH J.S., « Low speed wind tunnel tests of a device for reducing the out-of-plane forces on a pointed slender body of revolution at high angles of incidence ». RAE Technical Memorandum Aero 1992, 1984
14. CRONVICH L.L., « Missile Aerodynamics », Johns Hopkins APL Technical Digest, July-September 1983, Vol 4, No. 3
15. DREVET J.P., ROBERT M., « Mesure des efforts instantanés sur une maquette soumise a des variations rapides de commande » AGARD-CP-429, 1987

16. LACAU R.G., DESNOYER D., DELERY J., « Analyse au velocimètre laser de l'écoulement en aval d'arrière-corps de missiles », AGARD C.P. 336, 1982
17. LORDON J., FARE J.C., PAGAN D., « Ecoulements tourbillonnaires supersoniques autour d'un fuselage de missile. Expérience de base et modélisation », AGARD Missile Aerodynamics, 1990
18. WARDLAW A.B., BALTAKIS F.P., SOLOMON J.M. and HACKERMAN L.B., « An inviscid computational method for tactical missile configuration » NSWC - TR - 81 - 457, 1981
19. LORDON J., GUILLEN P., MORTEL P., LACAU R.G., « Calcul d'écoulements supersoniques autour de missiles tactiques » 23ème Colloque d'Aérodynamique Appliquée, 1986
20. GUILLEN P. and LORDON J., « Numerical simulation of separated supersonic flows around tactical missile bodies », AGARD CP No 437, 1988
21. BORREL M., MONTAGNE J.L., DIET J., GUILLEN P., LORDON J., « Upwind scheme for computing supersonic flows around a tactical missile », La Recherche Aérospatiale No 1988-2
22. GUILLEN Ph., DORMIEUX M., « Design of a 3D Multidomain Euler Code », Computational Mechanics Institute, Supercomputing in Fluid Flow, Boston 1989
23. DORMIEUX M., GUILLEN P., ABGRALL R., « Numerical simulation of transverse jet flows by a non reactive two species multidomain Euler flow solver » AIAA paper No 90-0126

#### TABLE REFERENCES

1. WHITFIELD D.L. and JANUS J.M. « Three-dimensional unsteady Euler equations solution using flux vector splittings », AIAA paper No 84-1552
2. EBERLE A., « Euler solution for a complete fighter aircraft at sub and supersonic speed », AGARD - CP - 412, 1986
3. CHATTOT J.J., KOCK C. and ELSAESSER E., « Solution of the EULER equations for missiles configurations », Proceedings of the six GAMM - Conference on Numerical Methods in Fluid Mechanics, volume 13, 1986, Vieweg
4. BORREL M., MONTAGNE J.L., « Numerical study of a non-centered scheme with applications to aerodynamics », AIAA paper n° 85 - 1497, 1985
5. LORDON J., GUILLEN P., MORTEL P., LACAU R.G., « Calcul d'écoulements supersoniques autour de missiles tactiques », 23ème Colloque d'Aérodynamique Appliquée, 1986
6. BELK D.M. and WHITFIELD D.L. « Three-dimensional Euler solutions on blocked grids using an implicit two-pass algorithm », AIAA paper n° 87-0450
7. WARDLAW A.B., PRIOLO F.G. and SOLOMON J.M., « An inviscid multiple zone method for supersonic tactical missiles », NSWC - TR - 85 - 484, 1985
8. DAYWITT J.E., BRANT D. and BOSWORTH F., « Computational technique for three-dimensional inviscid flow fields about reentry vehicles », SAMSO TR - 79 - 5, 1978
9. WARDLAW A.B., BALTAKIS F.P., SOLOMON J.M. and HACKERMAN L.B., « An inviscid computational method for tactical missile configuration » NSWC - TR - 81 - 457, 1981
10. WARDLAW A.B., NSWC TR-86-506, 1986



## CAPABILITIES OF EULER CODES FOR MISSILES

UP: ONE CIRCULAR FINNED SECTION  
 2CF: TWO CIRCULAR FINNED SECTION  
 3CF: THREE CIRCULAR FINNED SECTION  
 DO: DOUBLE DIAMETER

CODE NAME	ORIGIN	REF #	DATE	MACH	CONVENTIONAL			INCONVENTIONAL			MINUTES
					1CF	2CF	DO+3CF	CLASSICAL	BOOSTED	CONVENTIONAL	
EAGLE	USAF (USA)	1	1967	<1	C	C	C	C	C	ELIPTIC	OPEN (OXRD)
EUPLEX	MB	2	1984	<1	C	C	C	C	C	C	C
EULBAG	DOCMET (FRG)		1982	<1	C	C	C	C	C	C	C
EULERO	MATRA (FR)	3	1983	<1	C	C	C	C	C	C	C
EULBAG	DOCMET (FR)		1986	<1	C	C	C	C	C	C	C
FLUJ3C	CHESA (FR)	4	1986	<1	C	C	C	C	C	C	C
KODIAK	USAF (USA)	5	1986	<1	C	C	C	C	C	C	C
MISSILE	USAF (USA)		1972	<1	C	C	C	C	C	C	C
MUSE	NSWC (USA)	7	1985	<1	C	C	C	C	C	C	C
SANDAC	SANDIA (USA)	9	1986	<1	C	C	C	C	C	C	C
SWINT	NSWC (USA)	8	1982	<1	C	C	C	C	C	C	C
WINGA2	NSWC (USA)		1983	<1	C	C	C	C	C	C	C
ZEUS	NSWC (USA)	10	1986	<1	C	C	C	C	C	C	C

Configuration type has been completed / For no C Configuration type could be completed

TABLE 1

## EULER CODES FOR MISSILES

CODE NAME	EQUATIONS		METHOD	NUMERICAL SCHEME			MESH		NOTES ABOUT SEPARATION KUTTA CONDITION 1
	STEADY OR UNSTEADY (1)	CONSERVATIVE OR NON-CONSERVATIVE FORM (1)		IMPLICIT OR EXPLICIT (1)	CENTERED OR NON-CENTERED (1)	ORDER OF ACCURACY TIME SPACE (1)	STRUCTURE OR NON-STRUCTURE (1)	MACH	
EAGLE	U	C	FV	I	NC	1 2	S	*	
EUPLEX	U	C	FV	E+I	NC	1 2 1-4	NS	*	
EULBAG	U	C	FV	E	C	2 2	S	*	SSS
EULEND	U	C	FV	E	C	2 2	S	*	SSS
EULSSM	S	C	FV	I	C	1 2	NS	/	
FLUJ3C	U	C	FV	E	NC	2 2	S	*	SSS
KODIAK	S	C	FV	E	NC	1 2	S	/	
MISSILE	S	C	FD	E	C	1 2	S	/	
MUSE	S	C	FD	E	C	1 2	S	/	SSS
SANDAC	S	C+NC	FD	E	NC	1 2	S	/	
SWINT	S	C	FD	E	C	1 2	S	/	SSS
WINGA2	U	C	FV	E	C	2 2	S	*	
ZEUS	S	C	FV	E	NC	1 2	S	/	SSS

(1) Only the first letter(s)

(2) \* for YES

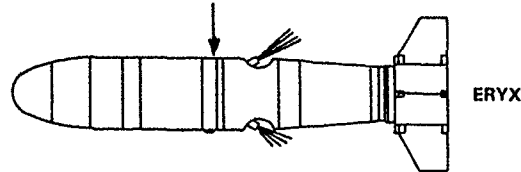
/ for NO

SSS Separation on Smooth Surface with Kutta Condition

TABLE 2

Requirements :

- launches from confined-spaces
- shorter ranges



ERYX

Missile with lateral jet control

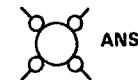
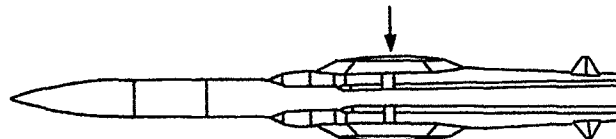
Aerodynamic problem :

- Jet interaction with external flow

SOME TRENDS IN FUTURE ANTITANK MISSILES AND  
RESULTING NEW AERODYNAMIC PROBLEMS  
Figure 1

Requirements :

- Increased range ( $> 100$  km)
- low time-to-target
- improved penetrativity



ANS

Airbreathing ramjet missile

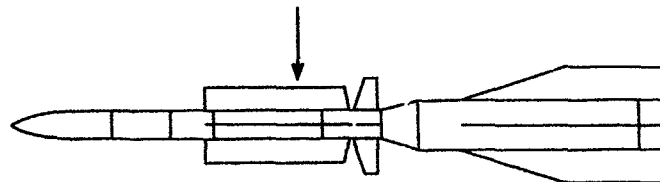
Aerodynamic problems :

- unconventional shape
- airframe-inlet interference
- aerodynamic heating
- etc.

SOME TRENDS IN FUTURE ANTI-SHIP MISSILES AND  
RESULTING NEW AERODYNAMIC PROBLEMS  
Figure 2

Requirements :

- launch sequence
- high maneuverability
- fast control response



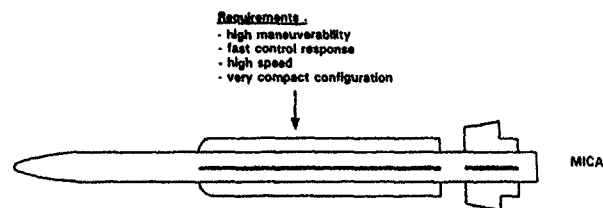
ASTER

- Vertically launched missile with quick turn-over
- Combined control systems (aerodynamic control and jet control)

Aerodynamic problems :

- high angle-of-attack aerodynamics
- lateral jet interaction with external flow

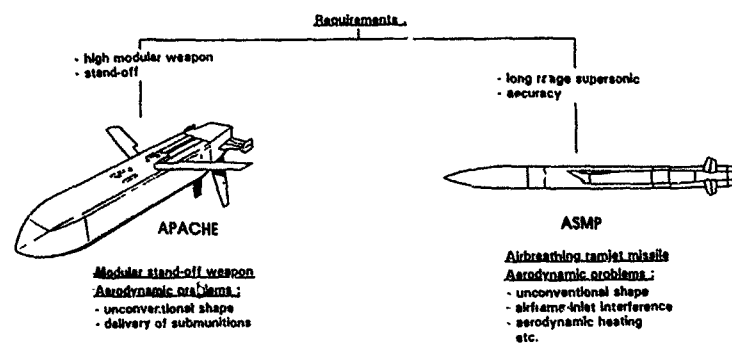
SOME TRENDS IN FUTURE GROUND/SURFACE-TO-AIR MISSILES  
AND RESULTING NEW AERODYNAMIC PROBLEMS  
Figure 3



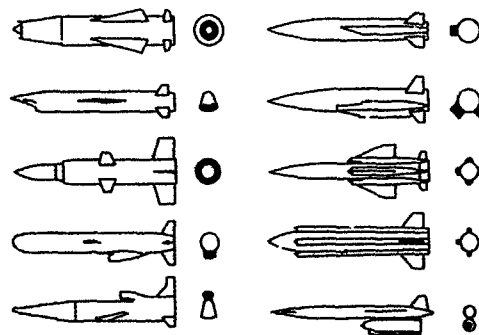
- Missiles with long wings
- Combined control systems (aerodynamic control and jet-deflector control)

**Aerodynamic problem:**  
High angle-of-attack aerodynamics ( $> 20^\circ$ )

### SOME TRENDS IN FUTURE AIR-TO-AIR MISSILES AND RESULTING NEW AERODYNAMIC PROBLEMS Figure 4

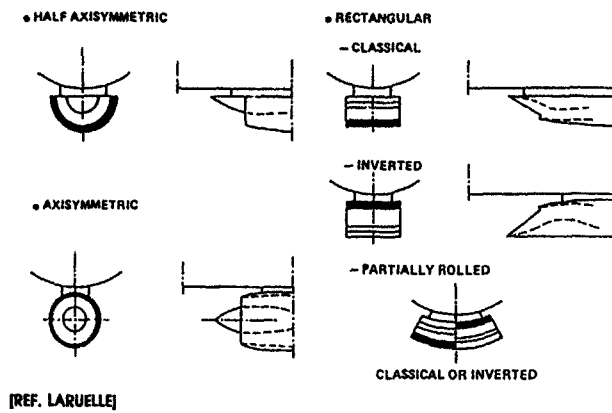


### SOME TRENDS IN AIR GROUND / SURFACE MISSILES AND RESULTING NEW AERODYNAMIC PROBLEMS Figure 5

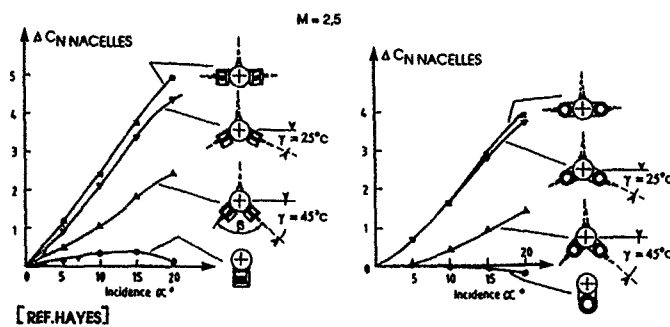


(REF. JEL)

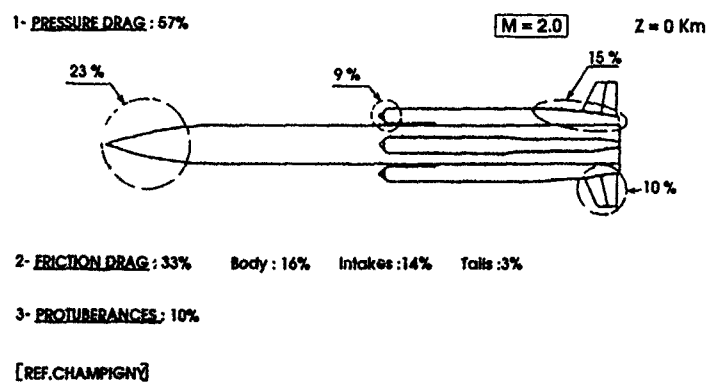
### INTAKE POSITIONS Figure 6



VENTRAL INTAKES  
Figure 7



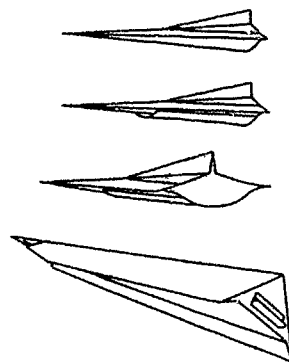
TWIN INTAKES : INCREMENTAL NORMAL FORCE  
Figure 8



DIFFERENT DRAG COMPONENTS OF AN AIRBREATHING MISSILE  
Figure 9



APACHE - MODULAR STAND-OFF-MISSILE  
Figure 10

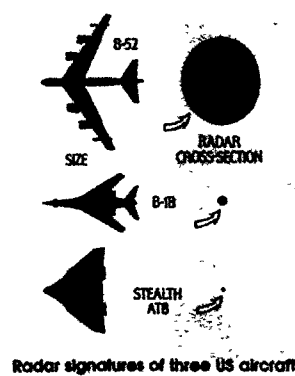


Waverider configurations  
(SCHINDLER - RASMUSSEN)



Lenticular configuration  
(ONERA)

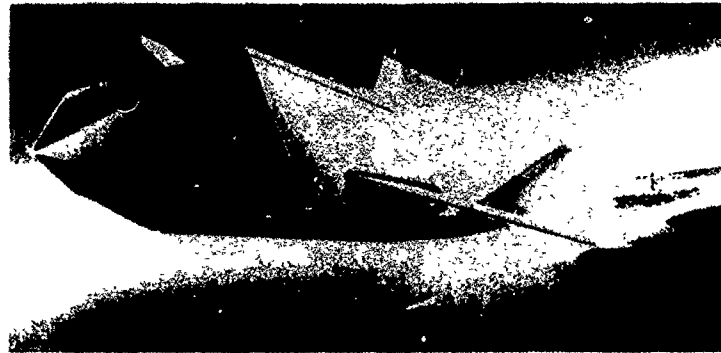
CONFIGURATIONS WITH NON CIRCULAR CROSS-SECTIONS  
Figure 11



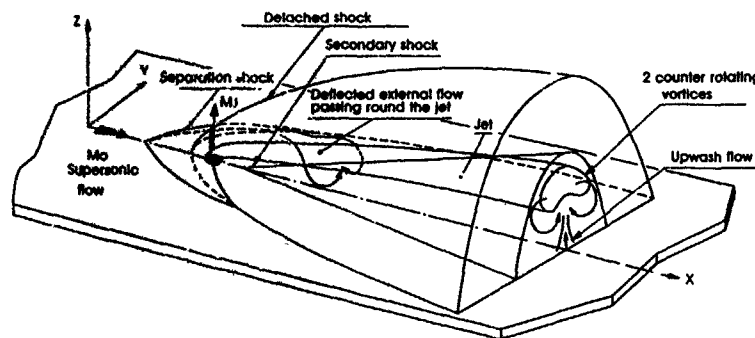
COMPONENT	PRIMARY SOURCE	SECONDARY SOURCE
FUSELAGE	SPECULAR	CREEPING
WING	EDGE	MULTIPLE, CREEPING
RADOME COMP.	SPECULAR	EDGE, TIP
INLET	SPECULAR	EDGE
EXHAUST	SPECULAR	EDGE
VERTICAL TAIL	SPECULAR	EDGE, MULTIPLE, CREEPING, GAPS
HORIZONTAL TAIL	EDGE	MULTIPLE, GAPS, CREEPING

Sources of RCS

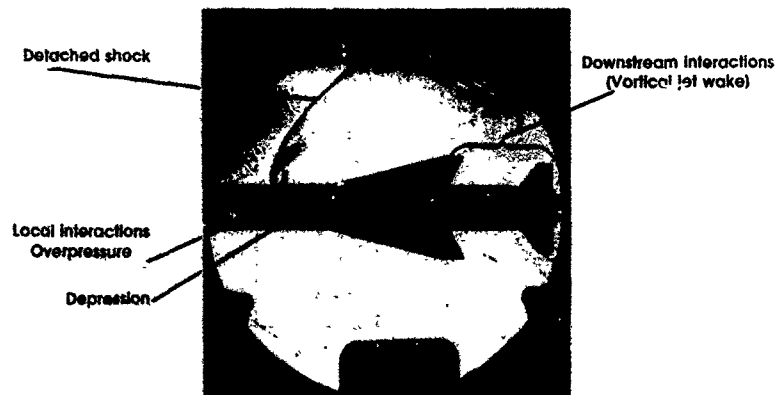
RCS - RADAR CROSS-SECTION  
Figure 12



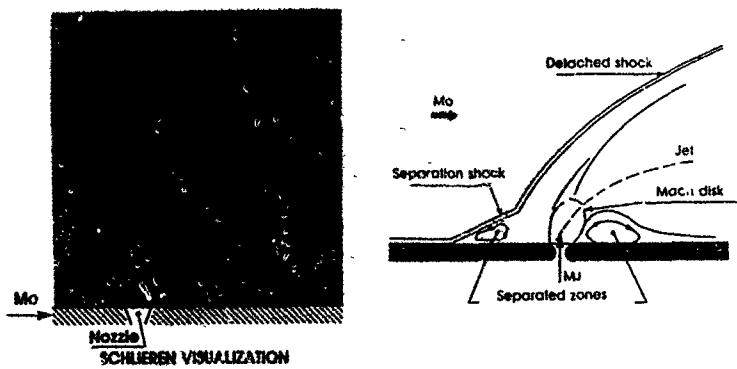
LOW OBSERVABLE CONFIGURATION  
TEXAS INSTRUMENTS CONCEPT (ARTIST'S SKETCH)  
Figure 13



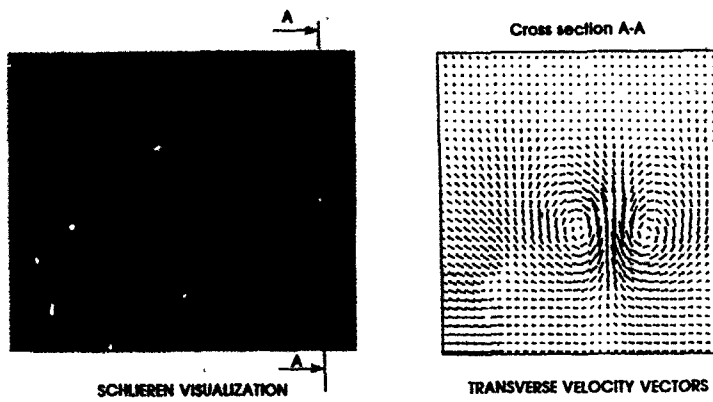
LATERAL JET IN AN EXTERNAL SUPERSONIC FLOW  
THREE DIMENTIONAL FLOW FIELD DESCRIPTION  
Figure 14



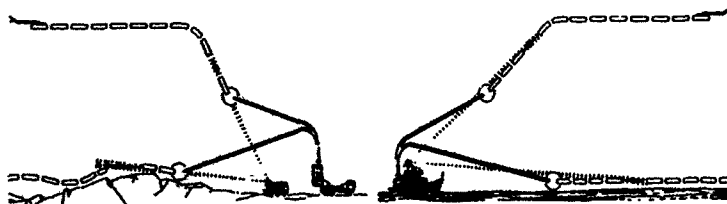
SCHLIEREN VISUALIZATION LATERAL JETS CONTROL  
JET/EXTERNAL FLOW INTERACTIONS  
Figure 15



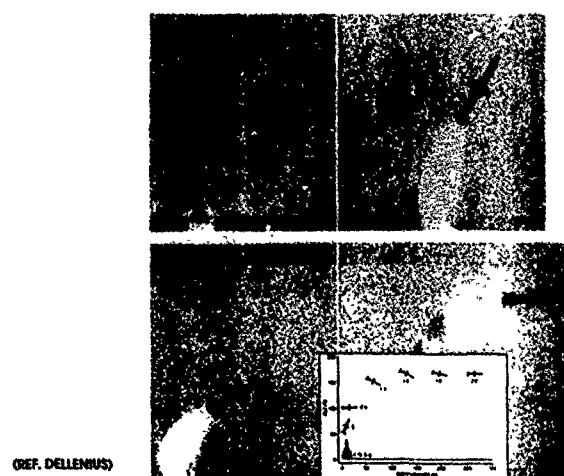
LATERAL JET IN AN EXTERNAL SUPERSONIC FLOW  
LOCAL INTERACTIONS  
Figure 16



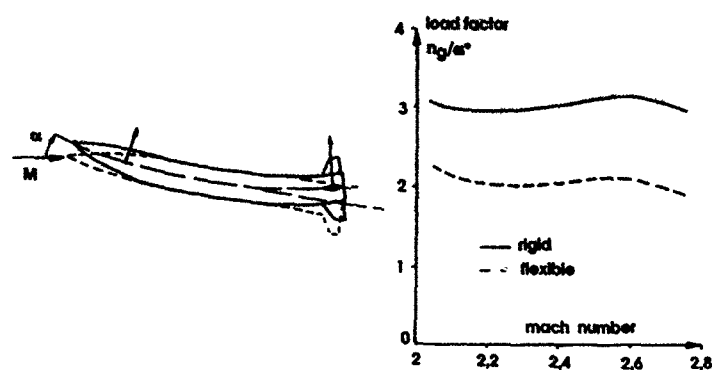
LATERAL JET IN AN EXTERNAL SUPERSONIC FLOW  
DOWNSTREAM INTERACTIONS  
Figure 17



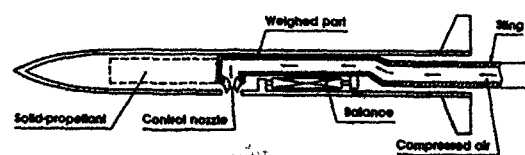
VERTICAL LAUNCH  
Figure 18



TYPICAL VERTICAL LAUNCH MISSILE TRAJECTORY  
DURING INITIAL TURN  
Figure 19

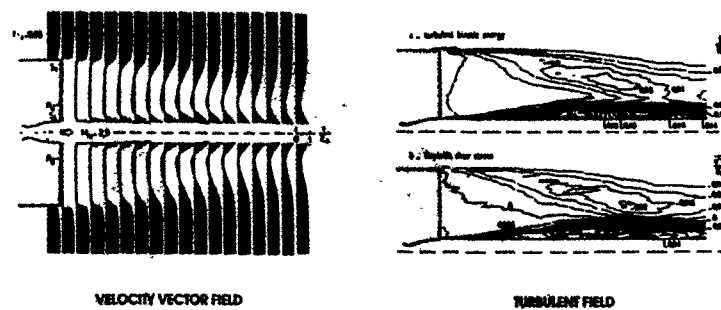


EFFECT OF MISSILE FLEXIBILITY ON MANEUVERABILITY  
Figure 20

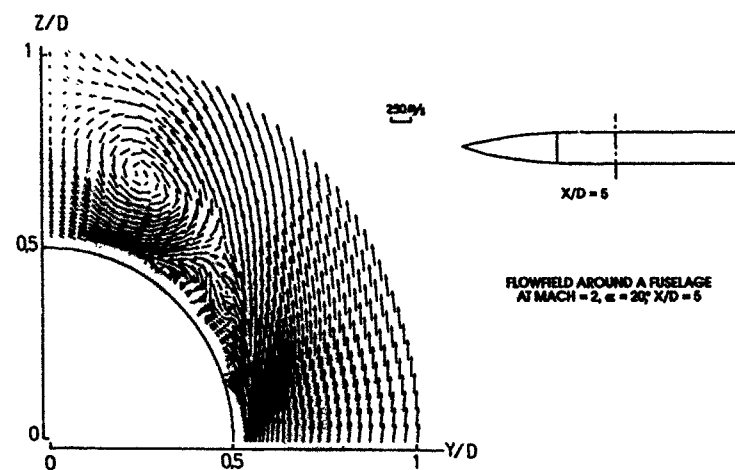


WIND TUNNEL SET UP  
Figure 21

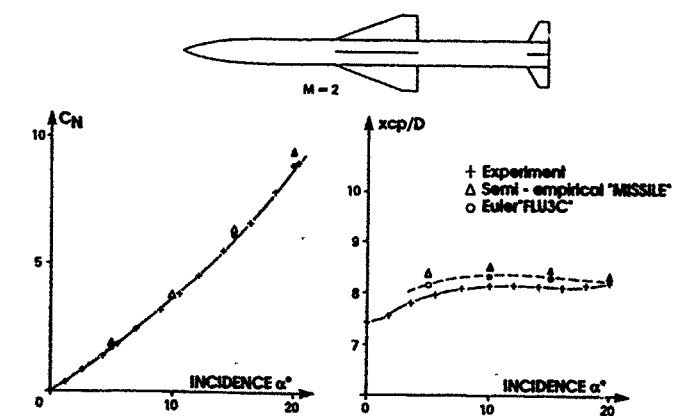




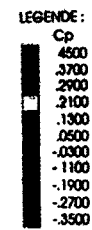
BASE FLOW BEHIND A CYLINDRICAL AFTER BODY WITH JET  
MEASUREMENTS BY LASER DOPPLER VELOCIMETRY  
Figure 22



CROSS-FLOW VELOCITY PLOT  
MEASUREMENTS BY A FIVE-HOLE PROBE  
Figure 23



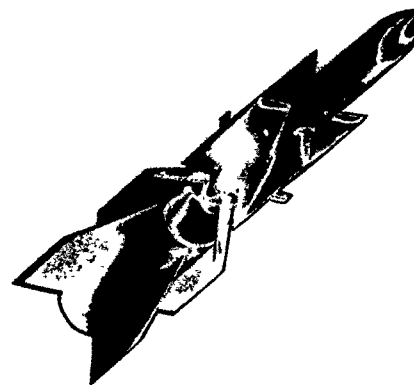
NORMAL-FORCE AND CENTER-OF-PRESSURE COEFFICIENTS  
FOR A BODY-WING-TAIL AT MACH 2.0  
Figure 24



SURFACE PRESSURE DISTRIBUTION ON A WING-BODY-TAIL  
AT MACH 2,  $\alpha = 20^\circ$  - EULER COMPUTATION (FLU3C)  
Figure 25

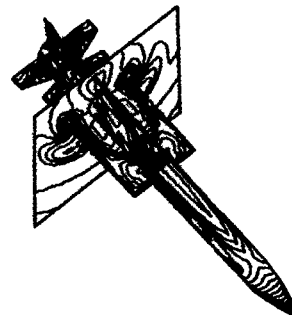
Config	Mesh	Incidence	DCR CN	$\Delta C_{DND}$
1	2	5	9 %	0.4
1	2	10	2 %	0.48
1	2.5	5	3 %	0.1
2	2.5	5	1 %	0.18
3	2.5	5	3 %	0.20
4	2.5	5	4 %	0.20
5	2.5	5	0.4 %	0.15
6	2.5	5	4 %	0.15
1	2.5	10	4 %	0
3	2.5	10	2 %	0.05

Comparison with experiment

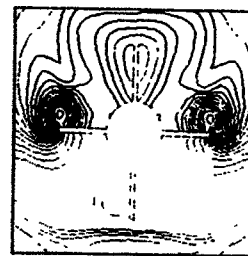


pressure distribution

ASTER 15 - EULER COMPUTATION (FLU3C)  
Figure 26

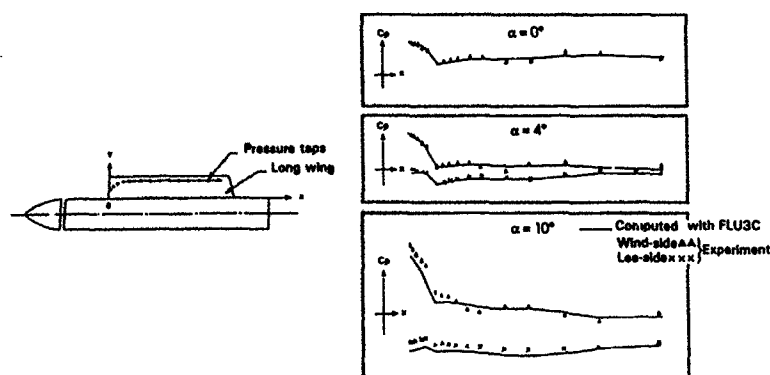


Missile - cross-flow plane

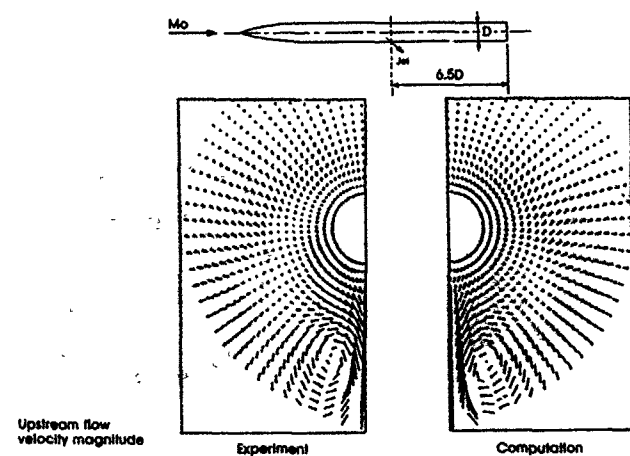


Cross-flow plane

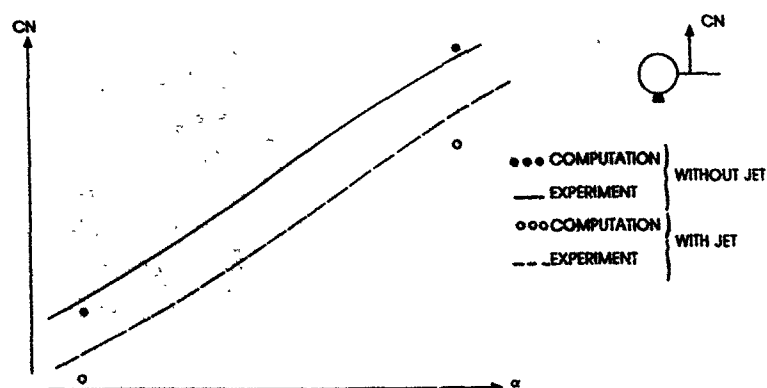
ISOBAR PATTERN - ASTER MISSILE AT MACH 2.5, 10 deg INCIDENCE  
Figure 27



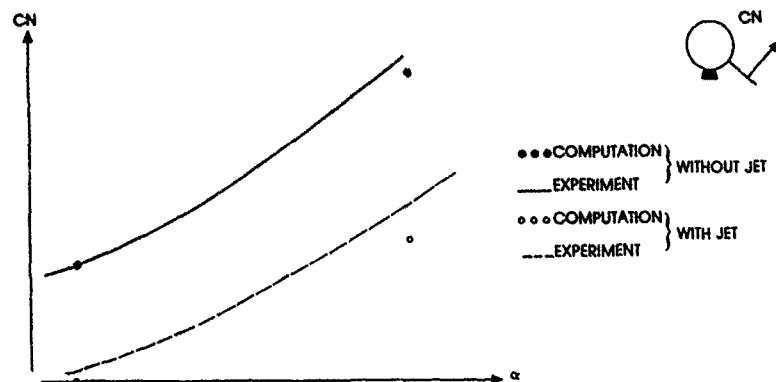
CALCULATED AND MEASURED SURFACE PRESSURES ON A LONG WING  
MISSILE ASTER (MACH 2.5)  
Figure 28



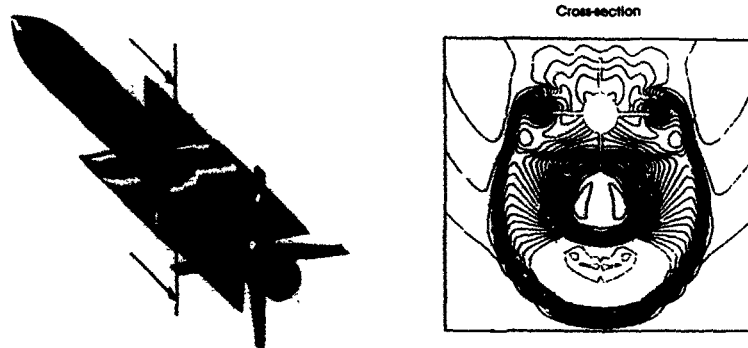
LATERAL JET IN AN EXTERNAL SUPERSONIC FLOW  
VELOCITY VECTORS IN THE TRANSVERSE PLANE LOCATED 6.5D  
BEHIND THE NOZZLE  
Figure 29



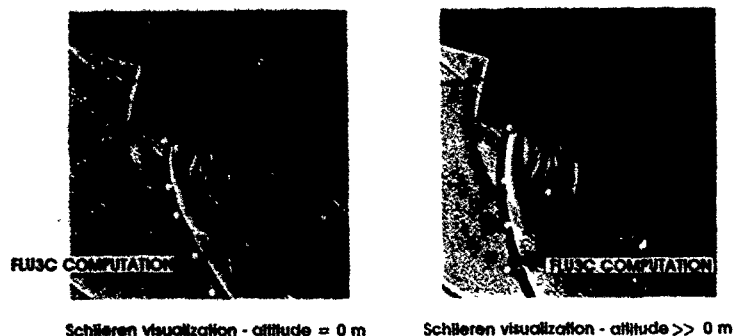
WING-BODY MODEL (C+ SHAPED WINGS -  $Mo = 2$ )  
NORMAL FORCE COEFFICIENT OF A HORIZONTAL WING  
Figure 30



WING-BODY MODEL ("x" SHAPED WINGS-  $M_o = 2$ )  
 NORMAL FORCE COEFFICIENT OF LEEWARD WING  
 Figure 31



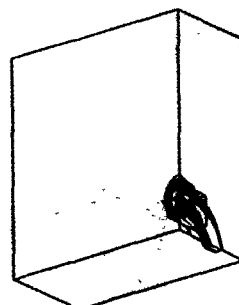
ASTER MISSILE ( $M_o = 2$  -  $\alpha = 12^\circ$  - WITH LATERAL JET)  
 PRESSURE DISTRIBUTION - FLUC3C COMPUTATION  
 Figure 32



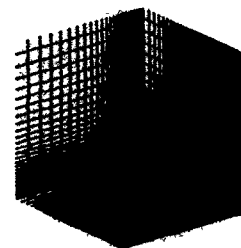
ASTER MISSILE ( $M_o = 2$  -  $\alpha = 12^\circ$  - WITH LATERAL JET)  
 DETACHED SHOCK LOCATION - COMPARISON BETWEEN  
 FLUC3C COMPUTATION AND EXPERIMENT  
 Figure 33



MESH AND SURFACE PRESSURE DISTRIBUTION  
MISSILE ANS - MACH 2,  $\alpha = 4^\circ$   
Figure 34

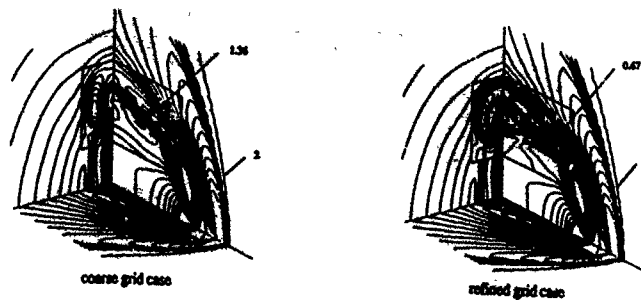


multidomain structure

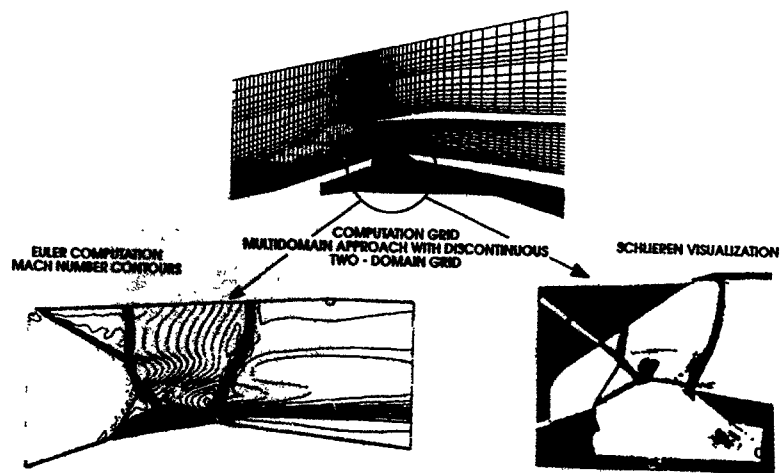


computational grid - grid in the refined area: 45x41x49

LATERAL JET FLOW  
MULTIDOMAIN APPROACH - GRID REFINEMENT IN THE FLOWFIELD  
Figure 35



LATERAL JET FLOW - EULER COMPUTATION  
GRID REFINEMENT EFFECT IN THE FLOWFIELD  
MACH NUMBER CONTOURS  
Figure 36



SUPERSONIC AIR INTAKE - INTERNAL FLOWFIELD  
COMPARISON BETWEEN EULER COMPUTATION AND EXPERIMENT  
Figure 37

# REVIEW OF THE SPRING 1988 AGARD FMP SYMPOSIUM

by

H.A. Torode  
Attack Weapons Dept.  
Royal Aerospace Establishment  
Farnborough, Hampshire GU14 6TD  
United Kingdom

## SUMMARY

The AGARD Flight Mechanics Panel held its 71st symposium in Ankara, Turkey during the period 9 to 12 May 1988 (Ref 1 & 2). The symposium was entitled "The Stability and Control of Tactical Missile Systems" and was classified NATO Secret. This topic was last sponsored by AGARD through the Fluid Dynamics Panel in 1982 (ref 3), but several subsequent symposia have also contained significant relevant information on underlying technologies (see References).

## INTRODUCTION

The symposium was first proposed in an FMP Pilot Paper in 1984, and was subsequently refined by several members of the Flight Mechanics Panel (notably Mr R. O. Anderson and Mr V. Hoehne of US) and was ultimately proposed to and authorised by the AGARD National Delegates Board in March 1987. The definitive proposal and meeting theme was built around the following issues:

"With recent advances in missile seekers and processors, aid in the analysis of missile dynamic motions and the associated control subsystem design, missile manoeuvre envelopes have expanded rapidly. It is therefore appropriate and timely that the stability and controllability of such missiles be examined, and this symposium will provide a forum for the interchange of ideas, and discussion of the different techniques currently involved in dealing with the various aspects of this subject. The presentations will cover a wide selection of topics, from prediction, simulation and test, through to a look at current development experience. The subject of the symposium would be limited to tactical missiles, encompassing air-to-air, air-to-ground, and ground-to-air, but not ballistic missiles."

The programme committee, co-chaired by Monsieur F. Mary (France) and Mr S. Metres (US), solicited papers by invitation and, as expected, created considerable interest from the Fluid Dynamics fraternity. Dr. K.J. Orlik-Ruckemann (Canada) of the AGARD Fluid Dynamics Panel joined the Programme Committee and undertook the organisation of Session 1. Guidance and Control was also seen as a driving technology and a significant input for Session 2 was solicited from the AGARD Guidance and Control Panel, in the form of a survey paper on their own symposium on a closely allied subject in the same timeframe (see Paper 9 and Ref 11).

The final programme consisted of 26 technical papers (from 5 NATO nations) plus two keynote addresses and the overview paper. The symposium received some 140 registrations and was attended by members of 12 NATO nations.

This paper summarises the technical aspects of the symposium in respect of the individual papers and their collective fulfilment of the meeting theme above. It is organised as follows. Under section 2 the individual unclassified papers are commented upon. (Classified presentations, denoted by \*, are not discussed in this unclassified document). Discussion has not been attempted in Session or presentation order owing to the breadth of the technical fields covered. Instead, the papers have been regrouped under more numerous sub-headings to reflect better the interrelation between the presentation material (Fig 1). Paper numbers are cross referenced under sub-headings. The Closing Discussion is reviewed in Section 3. Section 4 attempts to collect the impressions of the meeting as an entity and to comment on its effectiveness in covering the perceived field. The views expressed herein are the sole responsibility of the author.

## 2. REVIEW OF TECHNICAL PAPERS

### 2.1 Aerodynamic Prediction Codes (Papers 1,3, and 4)

In paper 1 CHAMPIGNY gave a wide ranging review of the computational methods applied for aerodynamic prediction in France. It covered panel methods, Euler codes and semi-empirical methods with detailed illustrative examples of the varied strengths of each technique, accompanied by the customary, unparalleled OGERA graphics. It was of interest to note that panel methods (methodes de singularites) maintain a strong following in France particularly when applied

to provisional, project style studies. More developed ("higher order" panel methods) continued to show promise, even when applied to non-circular and non-classical configurations. Their principle limitation remains the lack of ability to handle body vortices and therefore body lift. The Euler code presented (FLU3C) also showed considerable promise. Although limited to axisymmetric examples in fully supersonic flows, the ASTER configuration showed very good agreement with subsequent measurement. The fine computational meshes used in the examples clearly make computations of all but the most definitive of shapes prohibitive.

FORNASIER (paper 3) continued by describing in detail the development of the Franco/German HISSS panel code (also referenced above). This panel code appears unique in its capability of handling both fully subsonic and fully supersonic flows. The author describes in some detail the precautions necessary to provide the correct functioning of a panel code in supersonic flow. Examples were shown of the versatile options available in the software including treatment of fixed wakes, non-circular bodies and most notably intake flows with both sub and supercritical (or superinclined) intake angles. The performance of the code in supersonic regime appeared most encouraging. Subsonically the major limitation (apart from flow criticality), was again noted as the lack of treatment of body vortices leading to poor incidence performance particularly for bodies alone. It was candidly agreed that 5 degrees of flow onset angle remained the limit for precise calculation, although presented results often showed good performance above this low limit, illustrating a high degree of configuration dependency in this type of calculation.

Amongst semi-empirical codes the US Missile DATCOM is perhaps one of the most comprehensive. JENKINS (paper 4) gave a status report covering the basic concepts of the component prediction technique and the subsequent assembly of the subject configuration with consideration of the appropriate interference effects. While accepting that such an approach remained part art part science he demonstrated its integration with new "engineering" features such as experimental data substitution and the ability to radatum estimations on that inputted data. As with pure numerical codes, present limitations appear to be centred on vortex representations, in this case the precision of tracking of shed vortices and their downstream development.

## 2.2 High Incidence Dynamics (Papers 6,7 and 8)

FUCHS (paper 6) showed how higher order Fourier series expansions could be used, sometimes in conjunction with more conventional Taylor series techniques, to isolate higher order derivatives from dynamic experiments. He demonstrated how expansion to second order permitted the identification of several high incidence effects into characterising derivatives, as well as several incidental advantages over classical techniques (including the ability to isolate  $C_{mq}$  from  $C_{m\dot{\alpha}}$ ). Using a "Eurofighter" aircraft style example, he was able to show the methods success in quantifying such effects as that of vortex breakdown on aircraft motion at high incidence and/or body rates. Subsequent discussion noted that there was, even so, a limit to what could be achieved through extended linear expansion for incorporating higher order dynamics and that ultimately the severity of the ensuing motion invalidates linear superposition assumptions. In future a fully non linear approach may be required.

In a wide ranging, review style paper, ERICSSON described a variety of complex flow mechanisms which can dominate high incidence dynamics. He stressed that given a high incidence condition, remarkably low body rates can often result in significant cross coupled motions. He also noted that many (but not all) of these phenomena bring about increases in static stability (stiffness) at the same time as reductions in dynamic stability (damping); therefore stable oscillations and limit cycles often result. During the paper and questioning it was stressed that such behaviour are often the result of complex interactions between fluid dynamic processes of different genre and that complete representation of all these aspects would be necessary if sub scale modelling were to be successful.

MENDENHALL (paper 8) concentrated on one particular fluid dynamic process, the effect of fore body vortex shedding on fin effectiveness and missile loads during rapid high incidence manoeuvres. Using a space marching vortex cloud technique within an Euler solution he pursued the consequences of vortex interaction and lag through to the prediction of unsteady non linear fin load cycles. The net effect of these interactions on the ensuing motion was not addressed (a pity in this forum) and thus no comparisons with observed behaviour were available.

## 2.3 Wind Tunnel Experiments (Papers 5\*,16,17 and 18).

Internal carriage of stores has received a considerable re-evaluation in recent years as the operational limitations of external carriage have become more severely evident. SAWYER (paper 16) described an experimental programme using a well conceived group of conceptual models with differing metric elements to investigate carriage within a cavity. A variety of configurations were considered (but at zero incidence only), with each exhibiting at least one



serious shortcoming, these being diversely internal and external aerodynamic or acoustic environment. Thus far reported no attempts at configuration tuning had been made. The author felt that there was a poor likelihood of finding a configuration that would be free from all problems, or even capable of offering an acceptable mix. It was agreed during discussion that the closing of such a cavity was only a partial solution to some of these problems when viewed in an operational context. The way forward was therefore unclear with future developments eagerly awaited.

NASA Ames/Langley contributed a paper given by ALLEN on the assembly of the tri-service/NASA MISSILE3 database which essentially encompasses the entire operational regime for a wide variety of classically configured missiles. The paper concentrated on the wind tunnel automation and techniques necessary to even contemplate the acquisition of such a huge body of data. It was also suitably illustrated with several cases where the gathered data had shown trends which had not been found in comparison with current CFD codes. The investment in such a programme was warmly applauded by the audience who were able to offer numerous suggestions as to how this database might be further expanded in future, to the benefit of the entire community.

MAZZUCA described in generic terms the Italian approach to wind tunnel testing of missiles. The paper provides a comprehensive checklist for one contemplating such a programme but lacked any results or examples. The author showed the value of investment in tunnel automation and the resulting efficiency of tunnel usage.

#### 2.4 Configuration and Control (Papers 9\*,12,13,15,22 and 28)

Paper 12 by RANDALL described some interesting applications where careful integration of a sensor and its strategy with aerodynamic configuration could offer some simple lower cost options. The case considered was the use of a simple sensor (e.g. an IR sensor) with a single axis field of view thus requiring "twist to track" control to maintain the target in the field of view simultaneous with the conventional trajectory guidance. The author showed how modern control theory could be used to optimise the resulting control law and the ensuing trajectory. He further postulated the use of a non-cruciform ("anisotropic") aerodynamic configuration combining aircraft like bank-to-turn guidance with twist-to-track orientation during a terminal manoeuvre. It was perhaps unfortunate that the paper concentrated on the mathematical optimisation of the tracking rather than the more practical, yet less determinate, optimisation of using configurational aerodynamics to compensate for limited sensor sophistication, in order to achieve a cost effective weapon.

In his first paper (13) GAZZINA discussed the methodologies for controlling unstable missiles and highlighted some of the limitations imposed by this class of vehicle. His tutorial style paper used clear mathematics carefully simplified to highlight its basic conclusions. There was a clear parallel with the case of control of statically unstable aircraft, particularly since longitudinal motion only was considered, without any real involvement of guidance aspects.

Sensor development will always remain a driving technology in missile guidance. PETIT (paper 15) traced the miniaturisation of the 3 axis ring laser gyro to the present point where it now becomes feasible for use in small high performance missiles.

KLABUNDE (Paper 22) addressed the problem of establishing the robustness of a multi-variable control system through the use of the structured singular value approach. The Monte-Carlo eigenvalue search technique used appeared innovative and, as presented, removes much of the conservatism of the basic approach. The author anticipated that this technique (or developments thereof) will provide an efficient means to analyse the robustness of large multivariable systems. To date a precision of +10% had been demonstrated on a sample system of order 25. He also maintained that the technique was applicable to nonlinear systems although how this is achieved without local linearisation about the chosen operating point is not clear. The written paper is largely concerned with the strict demonstration of the control theory. It is perhaps unfortunate that the clear simple example used in the verbal presentation was not included.

In his second paper (28) GAZZINA reminded us that an analytical approach to configuration studies can still provide simple, visible results which are often obscured by complex parametric simulations. Using a series of simplifying assumptions (e.g. manoeuvres only in the terminal phase), he succeeded in extracting analytic solutions for the entire flight profile of an air-to-air interception. This enabled him to consider concisely the relative operational merits of winged and wingless weapons in this class. His input data showed marked dependency of normal force characteristics to static stability margin for the wingless case. The result suggested that these reflected strongly in the lift dependant and trim drags. Ultimately direct comparisons were made at equal levels of (neutral) stability. The authors initial premise was that the analytic approach added visibility to complex scenarios. As such it was a pity that his results were not more expansive in considering a more varied selection of operational profiles.

## 2.5 Direct Force Control

Many missile applications now demand powerful, precise control in conditions of low dynamic pressure, where aerodynamic controls have severe limitations. Only one author discussed integration of aerodynamic and direct force based motivators. The need for careful siting of control jets was stressed, to minimise aerodynamic interference, or indeed to turn it to positive advantage, which appears a possibility particularly at higher Mach numbers. The continuous use of jet thrusters appears wasteful of limited gas resources for non critical flight phases. The combining of jet and aerodynamic control either through scheduling, or the employment of jets as a high bandwidth control to enhance response time. Thruster and thrust vector controls of various forms were examined in detail in papers 11\*, 14\* and 21. Further more limited references to their evaluation were also made in papers 19, 23, 27 and 30\*.

DANIELSON (paper 21) described the design and development of a deployable, four vane, thrust vector controller. (A rotating ball-in-socket nozzle vectoring system is also discussed in the written text). The development programme concentrated on mechanisation aspects, the durability and continuing effectiveness of the vanes in an erosive, aluminised propellant stream clearly being the design driver. Excessive hinge moment were also cited as leading to undesirable hysteresis effects, but this appeared to be configuration specific.

## 2.6 Aeroelasticity (Papers 10 and 25).

Aeroelastic prediction has also benefited from recent advances in CFD aerodynamic codes. The symposium two presentations on advanced techniques for the prediction of non linear dynamic behaviour of canard controls on an air-to-air missile. Both noted a significant computational inconvenience in realigning data from separate aerodynamic and structural grid matrices.

DILLENUS (paper 10) described current work to combine a NASTRAN type code with an aerodynamic (supersonic panel) code to create a optimisation tool for a composite control fin structure, incorporating a variety of design constraints. A key feature was the use of local principal axes as design variables in an otherwise unvaried structure. This choice impacts uniquely on the stiffness matrix which is used initially to evaluate the deformation of a first approximation lay up. Aerodynamic load and structural displacement are then compare iteratively to converge onto a compatible solution. This can be treated as an end in itself or evaluated against the constraints for reentry and optimisation of the design. The recent results presented showed good convergence and considerable promise, although much still needs to be considered before a solution can be optimised for the full flight envelope. The ultimate aim is to reduce fin loads and actuator size and power ratings.

SEPAHY, in paper 25 (presented by R.Randell) also discussed the possibilities of an extension to NASTRAN type solvers, in this case, to consider kinematic nonlinearities. He described a two techniques, time simulation and local linearisation to an equivalent system; both techniques well known to control system engineering. One was left with the impression that the linearisation process still required a considerable degree of intuition and the author notes that the time simulation technique currently provides a more accurate result, albeit with higher computing overheads. A test case considers the effect of introducing hinge backlash into an all-moving canard control surface. The nonlinear methods predict an additional dynamic mode and a radical redistribution of modal energy. Unfortunately, the experimental evidence offered did not extend to the nonlinear case, and was therefore unable to corroborate these interesting effects. The programme is ongoing.

## 2.7 Test and Evaluation (Papers 19,20,23, and 24).

Paper 19 by DOHERR et al was an excellent illustration of the major recent strides made in raising the parameter identification technique to a effective engineering tool. The case studied, that of a jet controlled, aerodynamic lifting guided shell/submunition was clearly related to a serious developmental programme demanding practical results. Nonetheless, the identification of this diminutive vehicle appeared practically challenging and laden with pitfalls for the unwary. The careful integration of a varied suite of high precision instrumentation into a very compact vehicle, launched from and imprecisely initialised platform (under a hovering helicopter) was particularly impressive. It was equally complemented by the methodical modification and application of the DFVLR interpretation of the Maximum Likelihood method, which in this case included nonlinear modelling, and caters for both process and measurement noise. The preliminary results presented were limited but nonetheless impressive, and lead one to speculate on the impact this technique could soon have on the investigation of other highly nonlinear vehicles.

BUB (paper 20) presented the findings of a recent AGARD/FMP working group activity to attempt to quantify the validity of missile system simulations (Ref 7). This endeavour emerged as much philosophical as technical and the paper concentrated on the strict semantics definition of various validation processes. This text is recommended to anyone concerned with simulation, primarily as a

sound strategy against which to judge his own procedures and preparations. The significance of such work is easily underestimated particularly when such model systems are required to migrate within corporate or even international usage where retention of confidence is a prime requisite. The utility of a procedure such as presented will only be demonstrated by usage. A questioner also drew attention to the further applicability of these approaches in respect of "expert systems".

STEVENS (paper 23) described a technology demonstrator programme leading to test firings of a controlled but unguided missile vehicle, and highlighted the role of hardware-in-the-loop (HWIL) simulation as an effective systems integration tool. Problems which were isolated through simulation included the out of tolerance variation of actuator characteristics, confirmation of adequate gas reservoir capacity and evolution of autopilot control laws. It was perhaps surprising that a problem that did escape the net (although preliminarily evaluated) was that of body structural modes and lack of appropriate structural filters. An interesting side issue, barely touched upon, was the value of these tests as a focal point for the combined engineering workforce, all of whom were simultaneously involved in the corporate simulation activity.

Papers concerning test and evaluation usually stress their successes. It is an unfortunate fact that such a paper's value is most often proportional to the authors willingness to discuss what did not go according to plan. This paper was delivered in a frank, narrative style enabling the recipient to share in what was clearly a valuable exercise with many lessons learned.

DESLANDES (paper 24) was the only speaker to address stores separation, focusing on the important point that prevention of physical contact with the parent aircraft was a necessary but by no means sufficient criteria for a successful missile launch. Having described some of the advanced features of the current MBB separation prediction method, he showed two case studies where launch trajectories cleared the airframe but nonetheless suffered disturbances sufficient to impair guidance system performance and sensor lock. It should be accepted that the second case represented an extreme flight condition (in incidence) but it was all the more impressive to note the good agreement of the prediction method. Also noted in the paper was the utility of a launch control system in suppressing the disturbance and retrieving a marginal launch. This paper highlighted the need for careful systems integration in this sensitive area.

#### 2.8 Project descriptions. (Papers 27 and 30\*)

MAZZUCA (Paper 27) described the extensive modifications made to the Sparrow IIIB missile to enable it to be used in the ground-to-air role as Aspide. This role change demanded a considerable expansion of the original flight envelope, particularly in Mach number and dynamic pressure ranges. The need to improve low speed manoeuvrability immediately post launch led to the interesting example of retrospective reduction of static stability (see also Paper 13 by GAZZINA). It says much, both for the original design and the subsequent astute development that this major revision has been pursued successfully.

#### 3. SUMMARY OF CLOSING DISCUSSION.

The closing discussion was arranged as a forum of selected authors drawn from the various fields which had formed the subject matter of the symposium. These were F. Mary (TPC and Chairman), M. Mendenhall (Aerodynamics), A. Gazzina (Configurational Design), P. Letang (Project Development), H. Schilling (Aeroballistics), and G. Stevens (Test and Evaluation). As a catalyst to discussion and audience questions this panel was first asked to consider, within their own fields:

" In what directions will future operational requirements and guidance developments drive overall missile configurational design and development".

This was a broad issue, to which the panel could, perhaps, have been given a little more advanced warning. Their initial reactions centred largely on two themes:

- 1). That the overriding new requirement on missile systems was rapidity of reaction and control response. This led to complex dynamic flight situations which in themselves were extending aerodynamic prediction tools to the limit.
- 2). With ever increasing demands on cost control, the many sub systems which now make up an advanced weapon need careful integration and rigorous testing. New techniques of evaluation and analysis will be required to handle the rapidly approaching prospects of onboard "expert" guidance systems.

The first of these issues quite naturally lead to a discussion of the interleaved roles of aerodynamic prediction and control system simulation. The fluid dynamicists present pointed out, with numerous case studies, occasions when aerodynamic predictions had been oversimplified, or worse still, been neglected or ignored until too late in a project's development. Nonetheless it was conceded that there were numerous practical areas where aeroprediction remains in its infancy, and required practised interpretation. In this situation practical testing through wind tunnel rigs remains a necessary step for several issues. The following areas were defined as requiring further efforts:

- a) Improved prediction of roll characteristics
- b) Greater flexibility in store separation prediction.
- c) Limitations in respect of angle of attack. (and the configuration dependence of such limits).
- d) Capacity to consider non-classical shapes. (e.g. Noncircular/bluff bodies, and body vortices)

One course of action offered was the use of empiricism embedded in computational codes to inject test data where effects could not be modelled analytically (provided those mechanisms are adequately understood). Accepting that there often existed mechanisms which were not defined, there was also a body of opinion which suggested that, in such cases, the employment of a simple (e.g. panel) method was often the most appropriate, if only because in a project wide sense the results were accorded the appropriate margins of uncertainty. All agreed that modern requirements and the guidance performance presently available to satisfy them laid severe demands on configurational prediction and design. Full envelope, nonlinear, dynamics modelling of the airframe as well as the systems now needed to be carried into the systems integration phase. The future now demanded closer-than-ever collaboration between aerodynamicists and control engineers and as such, technical meetings of this nature were invaluable.

The second central theme identified in discussion was perhaps of more central interest to the Flight Mechanics Panel. Development cycle costs are currently rising against the trends of more accurate predictions and more rigorous testing. The costs of a programme interruption due to inadequate validation (ultimately resulting in a test failure) are now so high that there is no place for complacency in success. Valuable data is often discarded as surplus to requirements and could, if properly analysed, hold the key to the timely solution of a future problem. This aspect was considered to be the strongest, as well as the simplest, means of reducing test times and unexpected delays. Secondly, sophisticated analysis tools, such as parameter estimation and hardware in the loop testing must be pursued to the point where they make economic as well as technical sense.

The natural tendency to compartmentalise the disciplines required to produce an advanced weapons system drives heavily against the policy of integrated design. "Smart" weapons require the abilities of their seekers to be preserved (and their limitations respected) in their onboard environment. These demands and the constraints imposed by the parent aircraft must be integrated into the proposed weapon airframe at the earliest possible stage if a rational development is to result.

The highly sophisticated, and rapidly developing fields of image processing and target recognition remain driving technologies, but they cannot be expected to ease the problems of configurational designers. While onboard computing capability will undoubtedly increase dramatically in the foreseeable future, operational requirements will demand that advantages in target recognition must be complemented by advances in missile agility and effectiveness. Detailed dialogue, commencing at the earliest possible stage was again seen as the key to successful integration. Attendees from the flight control field expressed their satisfaction with a new appreciation of configurational problems as a result of this symposium.

#### 4. SYMPOSIUM ASSESSMENT

This symposium was conceived, and was described in the pilot paper as "a forum for the interchange of ideas and discussion of the various different techniques currently involved with the various aspects of missile stability and control". It was clearly accepted at the outset that the subject matter would cover a wide selection of topics and discuss their interrelation and integration within the context of the overall design problem. In the first keynote address, NIELSON traced the history of missile aerodynamics, and accompanied this with a list of key topics, meritorious of further research in that field. BISMUT, the second keynote speaker set the symposium into this context with a review of the issues anticipated to be central to the discussions. The audience proved to be a blend

of aerodynamicists, control technologists and test and evaluation engineers which provided the variety of viewpoint necessary to stimulate good discussion. As a Flight Mechanics Panel initiative, it was therefore anticipated that dialogue between these disciplines would review their strengths and weaknesses in addressing the overall design problem.

Presentations on aerodynamics proved to be a large part of the programme occupying the whole of the first day, and this may have left the impression of over-emphasis on this area. The papers of Session 1, and the wind tunnel experiments of papers 16 to 18 gave a very thorough overview of the aerodynamics field and stressed the impact of rapidly varying dynamics on overall configurational design capabilities. There was nonetheless a serious omission in that the field of carriage and release of externally carried store remained unaddressed; leaving the paper by SAWYER et al, on internal carriage, as the only paper on aerodynamic store/airframe integration. While accepting that many aerodynamic aspects required to be covered, the reviewer feels that the basic needs of the symposium could well have been covered by, perhaps two or three review style papers, highlighting the implications of the critical aerodynamic aspects.

The areas of the programme encompassing configurational and control technologies spread over a wide range of issues during days 2 and 3. The interaction between control requirements and configurational design was the key area where modern guidance and control strategies meet the real world of operational demands and system integration. Most papers in these sections, albeit well presented and topical, tended to concentrate on detailed individual technologies and did not define their impact on the overall design issues and mission effectiveness. Only the papers by RANDELL and GAZZINA attempted to highlight the opportunities and constraints that their technologies imbued on the ultimate capabilities of the overall system.

There was a justifiably strong core of emphasis on the use of direct force control which must now be recognised as an established option in high manoeuvrability missiles, particularly in regimes of low dynamic pressure. Among a group of excellent presentations on this topic only one referred to the integration of direct and aerodynamic force motivators. Clearly this is a promising area for further work. The proper integration of direct thrust and aerodynamic control is clearly a fruitful area for further research, offering considerable returns.

Regrettably, these sessions left the fields of guidance strategies and control law implementation virtually unaddressed. Possibly the programme committee had been cautious in this area, being aware of the near concurrent AGARD GCP meeting in the same field.

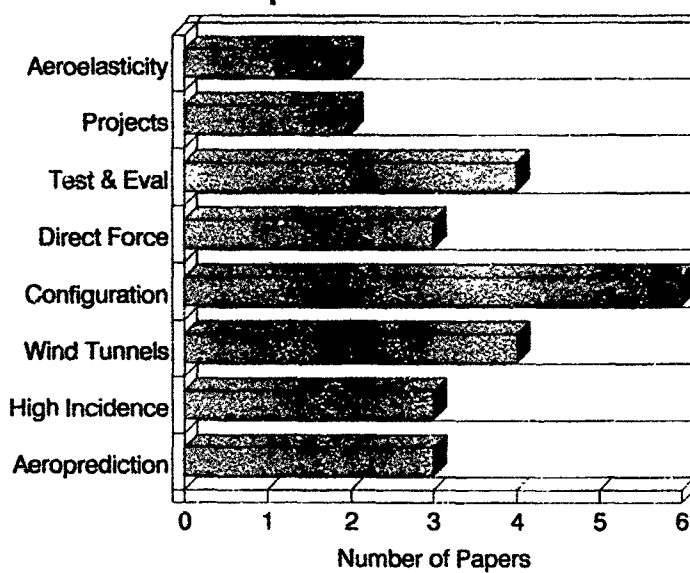
The final sessions concentrated on test, evaluation and projects and did much to redress the overall balance of the meeting. In particular, papers by DOHERR et al (on parameter estimation), STEVENS (on hardware-in-loop testing) and DESLANDES (on store separation testing) contributed valuable, practical experience in these areas of vital interest. Additional and contrasting contributions on such topics would have complemented the value of the interchanges in these areas, which well characterise the complex issues facing system and store/airframe integration. For the future, detailed joint studies and/or collaboration could be expected to expedite progress, or at least ease communication channels in any of these fields particularly in support of numerous international projects.

The two project orientated papers provided good examples of their type, largely because they contained innovative technological aspects and showed clearly how these had been progressed and controlled within the overall project management.

## AGARD REFERENCES

1. CP336 Missile Aerodynamics  
FDP Symposium, Sept 1982 (NR)
2. AR107 Lag and other effects of External Stores  
FDP Working Group, 1977 (NR)
3. CP386 Unsteady Aerodynamics - Fundamentals and  
Applications to Aircraft Dynamics  
FMP/FDP Symposium, May 1985
4. CP389 Stores Airframe Aerodynamics (NR)  
Fluid Dynamics Panel Symposium, Oct 1985
5. AR206 Validation of Missile System Simulation  
FMP Working Group, 1985
6. AG300 Store Separation Flight Testing  
Vol 5  
AGARDograph, 1986
7. CP388 Guidance, Control and Positioning of Future  
Precision Guided Stand-Off Weapon Systems,  
GCP Symposium, 1986 (NS)
8. Rep754 FDP Short Course on Missile Aerodynamics  
Von Karman Institute, March 1987
9. CP435 Guidance and Control of Precision Guided  
Weapons, GCP Symposium, 1988 (NS)

topic distribution



## STORE CARRIAGE, INTEGRATION AND RELEASE

A B Haines  
Chairman, Aerodynamics Group Committee  
Royal Aeronautical Society  
4 Hamilton Place, London W1V 0BQ, UK

**SUMMARY**

An international conference on 'Store Carriage, Integration and Release' organised by the Royal Aeronautical Society was held at Bath, UK on April 4-6 1990. The conference was attended by 140 delegates from 11 different countries. All the papers presented at the conference can be obtained from the Conference Department, Royal Aeronautical Society but the present paper summarises the highlights of the conference and is intended to give a balanced view of recent developments and prospects for the future in both design and prediction.

**1 INTRODUCTION**

An international conference on 'Store Carriage, Integration and Release', organised by the Royal Aeronautical Society was held in Bath on April 4-6 1990. The conference was well attended with 140 delegates from 11 different countries. 29 papers were presented by speakers from 8 countries. A full list of the papers is given at the end of this paper; all can be obtained by application to the Conference Department at the Royal Aeronautical Society, 4 Hamilton Place, London W1V 0BQ.

The aim of the present paper is to give a balanced view of recent developments and future prospects in both design and prediction, based on the papers from the conference. The sessions of the conference can be listed as follows:

- 1 General reviews of the present and future scene as seen by
  - (a) an 'elder statesman' in the subject: Charles Epstein<sup>1</sup>, formerly of USAFL, Eglin and NATO Headquarters, Brussels and now Vice President of Armcom Inc.
  - (b) an airframe aerodynamic designer: David Shaw<sup>2</sup>, Assistant Chief Aerodynamicist - Fluid Motion, BAe (Military Aircraft), Warton. and
  - (c) a launcher designer: Mr D Griffin<sup>3</sup>, Chief Engineer, Frazer Nash Defence Systems Ltd.
- 2 'New' design concepts:
  - (a) Internal carriage,
  - (b) Improved launch systems,
  - (c) Active Control during launch
- 3 Mathematical modelling for predictions of store release.
- 4 Development and application of experimental and engineering level prediction methods for installed drag, carriage loads, effects on aircraft stability and store release trajectories.
- 5 The RAE Tornado flight research programme to provide data for evaluation of prediction methods: aircraft flow fields, store carriage loads and release trajectories.
- 6 Application of CFD to problems of store carriage and release: design and prediction.

The first day of the conference was therefore devoted to design and new concepts (items 1 and 2 above) and the remainder of the conference to progress in developing, applying and evaluating prediction methods (items 3-6 above).

**2 DESIGN CONCEPTS: AIRCRAFT/STORE CARRIAGE**

Charles Epstein<sup>1</sup>, throughout his career first at USAFL Eglin, then at NATO Headquarters and then as Program Manager of the USAF Low Observables Weapons Program, has emphasised the need for aircraft/store compatibility. This has also been the constant theme of AGARD FDP Working Parties and conferences; ideally, aircraft and weapons should be designed together as a single entity. There have been many reasons why progress towards this ideal has been slow: in practice, aircraft have to carry many different stores of varying shape and size; many of these stores have been stockpiled for many years and there is a reluctance to abandon them. However, genuine progress has been made. It is no longer the norm, as it was 10-20 years ago, to carry all the stores on aerodynamically dirty multiple racks or carriers. Standards of aerodynamic cleanliness have been greatly improved and there has been a trend towards carrying as many of the stores as possible under the fuselage rather than on pylons below the wing. Shaw in his review<sup>2</sup> listed the pros and cons of alternative schemes. He noted that carrying the stores on pylons below the wings not only generally gave the highest installed drag: it could lead to a loss in longitudinal stability for an aircraft with a low tail; it could cause flutter problems and it could make jettison of light stores difficult; jettison loads could give wing response problems and asymmetric carriage could lead to rolling moment-g limits on pull-out. However, underfuselage carriage on pylons is not necessarily a panacea: there can be directional stability problems. Regard simply for aerodynamics can lead the engineer to favour an installation in which the stores are semi-buried in the bottom of the fuselage: lowest drag, negligible effects on stability, smallest installed loads, no flutter or aeroelastic problems and, in general, satisfactory jettison and release characteristics. However, installation accessibility with such a scheme can be poor and the cavities cut into the aircraft fuselage rarely fit more than one type of weapon. One must conclude that, to date, the best all-round compromise has been achieved with conformal carriage. Generally, this implies that the stores are carried in tandem and are fitted snugly below the bottom of the fuselage and, in this sense, conformal carriage has been practised extensively on aircraft such as the F-14, F-15E and Tornado. Indeed, one could claim that the store installations on the F-15E in particular exploit many of the recommendations put forward in earlier AGARD reports. The F-15E, now in production, is able to carry up to 12 bombs in two rows of 3 on conformal fuel tanks located on each side of the aircraft fuselage. The complete arrangement, ie aircraft + fuel tanks + weapon racks, has been designed with regard to its longitudinal distribution of cross-sectional area and, as a result, the performance improvements are similar to those obtained in the 1970s in a research programme with the F-4B. Epstein<sup>1</sup> noted, for example, that this arrangement on the F-15E had given more than 230 NM increase in low-altitude dash, more than 100

NM radius increase at supersonic speeds, a 450 NM radius increase while carrying three 2000 lb bombs, and an increase of over 1.5 hours of on-station time; the installed drag of the conformal tanks was about 50% less than that of two pylon-mounted tanks and also, the conformal tanks hold 28% more fuel. Although not mentioned at the Bath conference, one could add at this point that conformal carriage is not necessarily limited to installations on the fuselage: the F-16XL is an example of where it is possible to mount weapons in tandem in a semi-conformal arrangement snugly against the wing lower surface again showing, as confirmed by flight tests, very low values of installed drag.

Conformal carriage or at least, an approach to conformal carriage, is therefore practised on existing aircraft but, looking to the future, there appears to be a trend in the US but not yet in Europe, towards - or, should one say, back to - internal carriage. The potential advantages are obvious - no store drag and a low radar signature or at least a low signature on the way to the target. In passing, one must wonder about the implications of the fact that when the aircraft reaches the target area - the most difficult part of the flight - the bomb bay must be opened to release the weapons and it is quite possible for the radar signature to increase by as much as two orders of magnitude.

Internal carriage has been chosen as the primary method of store carriage on the USAF, A-12 and B-2. Internal carriage brings its own aerodynamic problems. Both NASA Langley<sup>3</sup> and AEDC Tullahoma<sup>4</sup> have been studying these problems in major long-running research programmes; highlights of both programmes were presented to the Bath conference and are to be found in papers 4 and 5.

Floyd Wilcox<sup>5</sup> of NASA Langley discussed the effects of cavity geometry on the flow in the cavity. The primary factor in determining the type of flow is the length/depth ratio,  $L/h$ . In a deep cavity with  $L/h < 11$ , the external flow passes over the cavity with hardly any expansion into the cavity: this is termed 'open cavity flow'. With a shallow cavity,  $L/h > 13$ , on the other hand, the flow expands into the cavity, impinges on and attaches to the cavity floor (ie bomb bay roof) and then exits at the rear; this is termed 'closed cavity flow'. The corresponding pressure distribution shows a decrease in pressure in the forward region where the flow is expanding into the cavity, an increase in pressure as the flow impinges on the floor, a pressure plateau as the flow passes along the floor and then a further increase in pressure as the flow exits ahead of the rear face. In the transitional range,  $11 < L/h < 13$ , as  $L/h$  changes from 13 towards 11, the impingement and exit shocks first coalesce to form a single shock: transitional-closed flow and then, as  $L/h$  is decreased further, the high pressure region at the rear vents to the low pressure region at the front and the flow is then turned by a series of weak expansion and compression waves: transitional-open flow. Clearly, the pressure fields associated with closed or transitional-closed flows exert more severe interference on the stores when they are ejected or released and examples are included by Floyd Wilcox showing how the store normal force and pitching moment can vary appreciably with distance below the cavity when the flow is of the transitional-closed type but where there is hardly any variation for open cavity flow.

Closed cavity flow, ie a shallow cavity, is however of major practical interest: if one has to increase the depth of the cavity to avoid these adverse interference effects, this is equivalent to saying that one is increasing the volume of the aircraft and thus, increasing its drag. The important

feature of the research at NASA Langley is therefore that the adverse effects can be alleviated significantly by allowing air to bleed from the rear to the front of the cavity either through a chamber below a porous floor or through pipes let into the floor. Again, from volume considerations, the second of these schemes is potentially more attractive but, in the research to date, it has not been uniformly successful at all Mach numbers in the test range up to  $M = 2.65$ : this may merely indicate that further research is needed to establish the design rules for the size of the pipes. When it is successful, the improvements in the variation of both store pitching moment and yawing moment as the store leaves the cavity are dramatic.

The research<sup>4</sup> at AEDC, which has concentrated on the aeroacoustic characteristics of cavity flow, shows however that even open cavity flow can lead to problems. Typical acoustic spectra for a deep cavity show that both the model and broadband amplitudes are at their greatest near the downstream wall of the cavity where the steady pressure reaches a maximum. Characteristic tones are clearly visible in these spectra and it is disturbing to find that, even in this example with open cavity flow, the amplitude of these tones can be as high as 170 dB. As noted<sup>1</sup> by Epstein, 'these high acoustic levels, approximating the levels of a jet engine exhaust at 20 feet or a booster rocket, can cause serious structural problems to both the aircraft and weapon structure, and may be catastrophic for sensitive store avionics.' A main aim of the research at AEDC has been to find some means of alleviating these high acoustic levels. Some success has attended the use of sawteeth or flap type spoilers mounted at or near the leading edge of the cavity. Earlier work<sup>30</sup> by Clark of AFATL had shown that the combination of a leading edge sawtooth spoiler and a rear bulkhead ramp was the most effective device but Dix in his paper<sup>4</sup> at the Bath conference pointed out that the internal ramp requires a cavity length that is longer than otherwise required and is therefore not regarded with favour by the structural designer. Results in the Bath paper show that, at subsonic speeds, a sawtooth spoiler with a height -  $3 \times$  boundary layer thickness placed at the front of the cavity on its own was effective in reducing both the tones and the overall sound pressure level. It also creates a benign flow field over more of the length of the cavity and also, it gives a favourable nose-down pitching moment on a store when it is released. Unfortunately, however, these spoilers appear to lose their effectiveness at supersonic speeds. The paper also shows the interaction between spoiler effectiveness and different types of cavity door.

The test programmes at both NASA Langley and AEDC have created a very large data bank of experimental data which is now available for correlation. This exercise should help to improve prediction methods: at present, for example, one can make a tolerable attempt at predicting modal frequencies but there is no easily applicable method for predicting modal amplitudes. Doubts persist as to whether the data are subject to scale effect (note: scale, not necessarily to be equated to Reynolds number).

Further research is therefore still required but Epstein<sup>1</sup> suggested that practical questions rather than aerodynamics may ultimately pose the more serious problems hindering the successful use of internal carriage. At present, there appears to be little activity on the practical issues to match the effort on aerodynamics. To quote some of these practical questions, 'how are the stores to be mounted in the cavity, how will the desired store be selected at any time for release, how will the bomb racks be moved around to allow for different size stores to be carried and, if more than one



layer of stores is used, how will the upper stores be ejected without hitting the lower racks?

Whether one should adopt internal carriage on a new high performance aircraft depends on a judgement regarding acceptable levels of aircraft radar cross-section. Again, to quote Epstein, 'internal carriage is not necessarily required to obtain 'Low Observable' standards even with existing weapons.' Designers are however considering - and in some cases - adopting internal carriage to achieve 'Very Low Observability' but even here, there are trade-offs to be considered.

### 3 DESIGN CONCEPTS: LAUNCHER DESIGN

There is no doubt that safe separation of stores from a cavity is more likely to occur if the stores are ejected with a high end-of-stroke velocity and a reasonable nose-down pitch rate. The trend to internal carriage will therefore increase the need, already present, for improved launchers giving high end-of-stroke velocities coupled with low peak accelerations over the ram stroke. Several papers<sup>3,6,7,8</sup> at the conference drew attention to the typical acceleration versus time curves of present-day launchers. Griffin<sup>3</sup> noted that missile structural strength or gyro tolerance generally set the limit to the peak allowable acceleration and the aircraft installation is often the primary factor in determining the length of the ram stroke. This leaves the launcher designer with the task of optimising the launcher performance to give a ratio of peak to mean acceleration as close as possible to 1:1; present-day launchers fall well short of this ideal.

Several papers<sup>3,6,8</sup> discussed how to improve launcher designs in this important respect. Long-term, the most significant paper may prove to be that given by Holder<sup>8</sup> of Attack Weapons Department, RAE Farnborough. This described the early stages of a research programme aimed at exploring the possible use of liquid propellants. These would offer a number of important advantages: reduced maintenance, reduced costs and, most significantly, the ability to change the rate of flow during the stroke and thus to modify the shape of the force, ie acceleration versus time curve. Research to date has concentrated on finding a suitable liquid propellant and addressing the crucial issue of repeatability. Factors affecting performance are still being addressed and much remains to be done. Eventually, it is hoped to produce a ram powered by a liquid propellant and to establish, using the ignition of the bulk fluid, full pressurisation curves for the operation of the ram. The final phase will be to try to perform open and closed loop control of the liquid supply to vary the burning rate with ram stroke and hence to be able to generate a particular response by altering the control mechanism.

This work with liquid propellants is being watched with interest by the manufacturers but it has to be viewed as a long-term development. In the meantime, both Frazer-Nash<sup>7</sup> and ML Aviation<sup>6</sup> described their present design strategy. Frazer-Nash highlighted how they have used mathematical modelling including dynamic simulations; ML Aviation presented the design of a high-pressure nitrogen-powered eject launcher developed in association with MBB and Matra: this would be suitable to meet the priorities of an internal carriage installation but would involve significant penalties, eg 15% in weight and 25% in volume compared with existing launchers which are thought to be more than adequate for aircraft such as Tornado, '18 or EFA.

Griffin<sup>3</sup>, in his general review of launcher design philosophy, pleaded for the launcher requirements to be considered at a much earlier stage in the design of a new aircraft or a new weapon. The essential requirements are to provide full control and restraint to the store in yaw, pitch and roll throughout the ejector stroke but too often in practice, these have had to be compromised because the launcher designer has been faced with a situation in which both the aircraft and weapon designs have been frozen without discussion with the launcher designer. Griffin showed a picture of his idealised ejectable missile/launcher interface: still designed to cope with rail launch in addition to store ejection as this is seen to be a continuing requirement. It is however idealised in the sense of including spigot features on the missile directly under both ram feet: such spigots or pegs on Sky-Flash provide 'a quantum improvement in missile alignment, load capability and constraint, during ejection'. Missile interface limitations on past launchers/weapons are considered to be the greatest single problem facing eject launcher designers. Complex geometry and, in particular, excrescences on the missile such as strakes containing the RF avionics systems have been a serious embarrassment. In practice, compromises will always be necessary and so, whatever recommendations are made in an idealised world, problems in release will be encountered in the real world even with the best launcher designs: hence, the importance of the next design concept - the use of active control, ie an autopilot in the launch phase.

### 4 DESIGN CONCEPTS: ACTIVE CONTROL DURING LAUNCH

A complete session of the Bath conference was devoted to the concept of using active control in the launch phase - a valuable concept that has already proved itself in practice, eg in the certified releases<sup>12</sup> of Skyflash from Tornado, but which is, of course, limited to releases of guided weapons; it is of no use for an inert bomb.

Deslandes<sup>9</sup> of MBB presented a clear example of the value of this concept. In this case, without active control, high weapon roll rates were induced by the aircraft flowfield, accentuated if the aircraft was manoeuvring in a turn. In a 45° turn at M = 0.8, computer predictions suggested that the weapon would roll so fast that the upper rear fin would collide with the launcher at the start of the release and that the roll motion would saturate the missile gyro; as a result, when full guidance was activated, one would be left with a bank error of 15° making it very dubious whether the missile would perform its operational task. Indeed, the predictions suggested that it was only when the aircraft was flying straight in a restricted incidence range between 2° and 6° that there would be no degradation of the weapon flight control system. Performance therefore fell well short of the customer's requirements. Activation of the full guidance mode of the missile during the launch phase gave only a marginal improvement but development of a special software package with enhanced roll control solved the problem. This autopilot was activated from 0.05 to 1.0 seconds after hook-off during which time the missile moved forward from the carriage position to a location about 50 ft ahead of the aircraft. The software package was designed to accept ±15° roll deflection authority (rather than ±5°) applied to all surfaces and ignored all pitch and yaw commands. The roll-rate peak rates now remained below the gyro limitation and the missile was controlled into the horizontal hook-up position compensating correctly for the 45° initial bank angle of the aircraft; a clear separation was predicted. These computer

predictions were subsequently confirmed in flight trials. The customer requirements were now fully met. Deslandes<sup>9</sup> concluded that active control was an attractive, feasible solution in cases where, without active control, flow disturbances are leading to an unacceptable limitation of the operating envelope, where hardware changes are difficult or impossible to implement but where software changes can be introduced cheaply and quickly into the missile guidance system.

The required type of autopilot is likely to vary according to the missile/aircraft combination. In the case just described, the problem lay in the missile rolling motion; in the case<sup>10,12</sup> of Skyflash on Tornado, the problem arose because, under certain conditions, the missile could experience a large nose-up pitching moment which, if uncontrolled, could lead to a collision between the missile and the nose of the aircraft fuselage. Two active control modes in pitch were developed, one based on pitch rate and the other on pitch attitude. For this particular application, pitch attitude proved to be the better choice; the pitch rate control gave excessive nose-down pitching moments for releases under benign conditions whereas pitch attitude gave satisfactory results, ie safe separations, for releases under both adverse and benign conditions. BAe, in two papers<sup>10,12</sup> at the conference, argued convincingly that the certified Skyflash envelope was an 'excellent achievement which would not have been possible without a reliable flight control system active during the release'.

Use of active control clearly adds to the complexity of making accurate predictions of the release characteristics by means of ground-based experiments. Mrs Wood<sup>11</sup> of ARA described how this challenge had been met successfully with the 2-sting rig at ARA. With an 1/11 scale model, it was not possible to move the missile wings during the test and so the loads due to the action of the autopilot had to be estimated by a simplified representation of the control system and then fed into the TSR computer as corrections to the measured loads. Further corrections to these loads were needed to allow for the missile rocket motor thrust and also for the fact that, during the release, the missile Mach number was greater than the aircraft Mach number and, as a result, the missile shock patterns in a test conducted at the aircraft Mach number are incorrect. In addition, as is normal practice with the TSR, corrections had to be made to allow for the dynamic incidence and damping derivative terms. For practical reasons, the TSR trajectories were commenced at the end of ejector stroke (EOS) and the EOS conditions were either matched to flight in cases where the firings had already taken place, or to conditions calculated using the BAe mathematical model<sup>12</sup> (see below in §5) in cases where the flight data did not yet exist. Despite the necessarily indirect approach, trustworthy pre-flight predictions of the trajectories were achieved but as with any ground-based experimental (or theoretical) prediction to be successful, one requires an adequate representation of the missile control system, control aerodynamics and the performance of both the rocket motor and launcher.

##### 5. USE OF MATHEMATICAL MODELS FOR PREDICTION OF STORE RELEASE CHARACTERISTICS

Two papers at the conference highlighted the value of a mathematical model for the prediction of store release trajectories. First, Akroyd<sup>12</sup> of BAe (Military Aircraft) when describing the certification exercise for the Skyflash on Tornado concluded that 'the use of mathematical models based on wind tunnel data gives accurate trajectory

simulations which has led to a significant reduction in the required flight test programme'. The model was comprehensive: it included the missile mass characteristics, the rocket motor thrust profile, the launcher performance, the free air aerodynamic data for the missile, a model of the aerodynamic interference data based on measured flow fields and also grid loads measured with the ARA TSR and finally, the flight control system as transfer function blocks connecting missile wing deflection outputs to missile angular body rate/attitude input. The model was used to define the flight test programme. In general, the flight test data were in reasonable agreement with the model predictions but as the flight test programme continued, modifications, significant but never large, were introduced into the mathematical model to improve the match. For convenience, the modifications were mostly made to the aerodynamic pitching moment term although, in fact, it is likely that the wide variability in launcher performance (strongly dependent on temperature) was at least partly responsible.

The second relevant paper in the context of mathematical modelling was that given by Wolffelt<sup>17</sup> and his colleagues at SAAB. It was generally recognised that this was one of the two outstanding papers at the conference (the other being the review<sup>24</sup> of CFD developments by Kraft and Belk, see §8). The SAAB approach starts from the thesis that all ground-based experimental techniques and all theoretical methods have their limitations but all can - and should - be used to develop and validate the mathematical model. Clearly, all TSR and drop tests in a wind tunnel should attempt to reproduce as closely as possible the conditions in the relevant flight release but when a mathematical model is available, the tests will still be useful even when a perfect correspondence with the flight conditions is not possible. The model can be used to predict the release in the tunnel test; if good agreement is obtained, this helps to create the confidence that the model can be used to predict the flight release. Both the SAAB and BAe models discussed above are being 'based on wind tunnel data' but there is a subtle change of emphasis. The SAAB approach lays considerable stress on the value of wind tunnel drop tests. These are planned with the specific aim of evaluating and refining the mathematical model. As noted above, they do not necessarily simulate any particular flight release. Technically, these drop tests can be complex and expensive but SAAB are convinced that they provide the best means of validating the flow-field representation in the model and that then, there will be no need to tune the model to give agreement with particular flight tests. Experience has confirmed these hopes - provided one really knows the initial conditions for the release. Accurate knowledge of the end-of-stroke velocities is absolutely vital. Regarding the expense of the special drop tests, Wolffelt<sup>17</sup> noted that, for the clearance of releases of external fuel tanks from the JAS 39 aircraft, the reduction in costs of the flight test programme already corresponds almost exactly with the cost of the tunnel tests and ultimately, as the programme proceeds with the deletion of further flight tests, there will be clear profit.

The SAAB mathematical model is comprehensive; it includes all the modules mentioned when discussing the BAe model and also, a special collision control algorithm since experience had shown that without such a feature, collisions were difficult to detect. The input data for the model were blended and selected not by a computer but by an intelligent engineer directing a computer! SAAB emphasise that it is important to obtain a complete picture of the interference effects in the carriage

position - from tests on models with a faithful representation of the full-scale geometry. An example was quoted where the missile control surface efficiency was changed dramatically by these interference effects. The results were for the Skyflash missile for which two of the four wings mounted half way along the body provide the roll control. With the missile in isolation, the direct effect of these controls tends to be offset by the effects of the swirl on the tail fins but in and near the carriage position, the presence of the aircraft pylon tends to destroy this offsetting effect. Differences are also observed between port and starboard results because of the relative direction of the aircraft-induced sidewash to the wings providing the control. This detailed point was not mentioned by any other speaker at the meeting and is a good example of the careful thinking underlying the development of the model.

The value of a mathematical model was demonstrated by an example where the release trajectory predicted using the model appeared to be completely safe whereas, in a CTS test using the ARA TSR, it was very different and clearly a hazardous release. Flight tests subsequently showed that the safe release prediction by the model was correct. The explanation for the discrepancy between the two predictions lay in the very rapid change in store pitching moment with a small vertical displacement of the store from the carriage position. In the TSR test, the trajectory had to start from a point a small but finite distance below carriage; otherwise, due to rig vibration, a collision would occur. As noted earlier, the mathematical model can be used - and was used - to predict both the tunnel and flight trajectories and this confirmed that the difference between them was due to the small error in starting condition. One could of course add that an alternative solution to this difficulty, once one had been aware of the pitching moment data, would have been to derive some corrections to the measured loads to allow for the difference in starting conditions, and then feed these into the trajectory calculations in the TSR computer, in the manner described earlier for the corrections in the CW release tests.

As a final point about the SAAB presentation, it ended with an impressive video showing how the release predictions are handled at a graphics workstation. A program described as a 'synthetic projector' has been written and this enables the release to be viewed from any angle and for the angle of view to be varied during a release without disturbing the store motion.

#### 6. DEVELOPMENT AND APPLICATION OF ENGINEERING-LEVEL PREDICTION METHODS

As would be expected, the conference included a number of papers describing further refinements in the empirical prediction methods and application of these methods in new situations such as releases from a hovering helicopter.

Dillenius<sup>18</sup> reviewed progress at the Nielsen organisation with NEAR methods. The application of these methods to the carriage and launch of Pegasus from a B-52 is to be described in another paper<sup>31</sup> at this AGARD meeting. General experience has shown that these methods can be a reliable guide to release characteristics particularly if, at supersonic speeds, corrections for non-linear effects are included when determining the positions of shock waves in the flow fields. Poorer agreement would be expected when using the methods to calculate carriage loads because of the likelihood of more severe viscous effects and so perhaps the most encouraging example in the paper<sup>18</sup> by Dillenius is the comparison between prediction

and experiment for the variation of store normal force and pitching moment with vertical displacement of a store below an open cavity. The NEAR methods correctly predicted the reversals in normal force and pitching moment which occur close to the cavity in contrast to the smooth monotonic behaviour for a store below a closed solid body.

Isaacs<sup>22</sup> described recent improvements in the RAENEAR code and presented many comparisons with experiment. Recent refinements have improved the agreement and reasonable results are often achieved in supercritical conditions at low incidence. Isaacs points out that many of the remaining discrepancies are due to strong viscous effects in the real flow and hence, similar discrepancies would be expected to be present even if the predictions were made by the more expensive panel or Euler methods. Also, the RAENEAR predictions would be expected to be more accurate for cases where the installations had been designed<sup>25</sup> to eliminate separations in, for example, the wing-pylon junction.

A parallel paper<sup>23</sup> by Bailey of the BAe Sowerby Research Centre presented results from a recent study in which the semi-empirical supersonic NUFA (SNUFA) method was used to predict store captive trajectory loads and store load distributions. SNUFA requires the input of a flow field and, in this study, the flow fields were obtained either experimentally or with the use of either the BAe (Warton) Mk II Supersonic Panel Program or two Euler codes developed at BAe (Filton). The results showed that the quality of the SNUFA predictions depended critically on the quality of the flow fields and, in this respect, both the panel method and the Euler codes had their weaknesses. The panel method had the great advantage that complex configurations could be modelled with ease but the assumption of potential, linearised theory meant that the shock waves in the flow field were not positioned correctly (ie corrections such as those introduced into the NEAR programs were needed). The results using the Euler codes were encouraging but showed the need for a finer grid; it is hoped that, in the future, it will be possible to use a full multiblock method to calculate the flow field.

Another paper<sup>15</sup> from the BAe Sowerby Research Centre described the development of a prediction method for modelling store releases from a hovering helicopter. This was achieved by coupling together a number of existing codes and modifying and improving these where necessary. Encouraging results have been obtained but further developments are needed. For example, the program currently calculates time-averaged induced velocities rather than instantaneous induced velocities. Modifying the program to calculate instantaneous induced velocities could improve trajectory predictions if, at the same time, some control of blade position at store release were also incorporated. This would provide a means of controlling the interaction of the tip vortex with the store. Another limitation at present is that the distorting effect of the fuselage on the rotor wake is not being modelled.

Finally, in this brief survey of empirical methods, mention should be made of the paper<sup>13</sup> by Ross of RAE Bedford describing the further development of the RAE method for predicting installed drag. Recent experimental programmes have extended the data base at transonic and supersonic speed, and attempts have been made to improve the accuracy of the prediction method in the difficult Mach number range between  $M = 0.95$  and  $M = 1.2$ . The paper highlighted some examples of where, in this range, any empirical method will inevitably have its limitations in predicting the variation of installed drag with Mach number. Unexpected variations have been found, particularly for very

thin wings. It is believed that these results are genuine and not caused by tunnel wall interference but almost certainly, a CFD approach would be needed to predict them.

#### 7 THE RAE TORNADO FLIGHT RESEARCH PROGRAMME

A complete afternoon at the Bath conference was devoted to the presentation and discussion of a wide-ranging UK research programme in which measurements are being made in flight of store carriage loads, store release trajectories and the flow fields through which the stores pass immediately after release. The aim is to provide high quality flight data that can be used for the evaluation of all available ground-based prediction methods, both experimental and theoretical. Two papers<sup>19,20</sup> from RAE described

- (i) the aircraft being used for the tests - a Tornado,
- (ii) the specially instrumented stores - inert BL755s, equipped with internal 5-component strain gauged balances, and mounted on the shoulder underfuselage pylons,
- (iii) the special instrumentation developed for the tests such as the rigs for the flow-survey rakes,
- (iv) the test programmes and how the data are being recorded and reduced.

Results from this important programme are only just becoming available; the analysis of the data has only just started. Staff at six different sites in the UK are cooperating in the analysis and in the comparison of the data with the prediction methods. The workshop-style unscripted discussion at the conference provided a snapshot of this activity at this point in time. Suggestions and comments in the discussion will help in the planning of further tests when flying resumes later in 1990. To date, carriage loads have been measured for 4, 3, 2 and 1-store arrangements on the shoulder underfuselage pylons and store releases have been photographed for 4, 2 and 1-bomb configurations with all releases being from the rear port station. It is clear that this programme will provide plenty of data for future AGARD conferences.

#### 8 APPLICATION OF CFD TO STORE CARRIAGE AND RELEASE

There has been considerable progress in the last few years in the development and application of CFD to problems of store carriage and release. At the very least, CFD can now be used as a guide to good design but in an exciting review paper<sup>24</sup> by Kraft of AEDC/Calspan and Belk of AFATL Eglin, much stronger claims are made. To quote: 'Dramatic advances have been made in various CFD methods that now permit good engineering simulation of the carriage and release of weapons from advanced aircraft configurations. The introduction of CFD into the weapons integration process ... portends a significant change in the manner in which stores are integrated with airframes ... weapon integration can now be examined before the design is frozen. Modifications to the location and orientation of hard points for weapon attachment can be evaluated ... For existing aircraft, the use of CFD techniques presents a significant opportunity to reduce the time needed to certify stores for safe separation .... Release effects can be determined within a few weeks using computational methods.'

These are strong claims. How has the progress been made? The paper<sup>24</sup> by Kraft and Belk suggests that the vital contributory factors are:

#### (1) Advances in grid generation for complex intersecting geometries

Two primary techniques are being used. First, the EAGLE code: a multiblock approach; this is a general, three-dimensional elliptic grid generation code developed by Thompson<sup>32</sup> with recent extensions by Kim<sup>33</sup> and Tu<sup>34</sup> who have demonstrated solution adaptive grid generation on blocked grids. This code was developed originally under USAF funding but is now widely available in the US. Second, the CHIMERA approach by which one mesh may be embedded entirely or partially within another and which allows each subdomain to be meshed independently with no requirement for continuity of grid lines from one grid to another. Communication between grids is established solely through grid boundaries.

Examples of the use of both techniques are included in the Kraft and Belk paper<sup>24</sup>. The CHIMERA approach is particularly suitable for external store problems. The sub-grid around the store, once optimised, can be placed in any relative position in the aircraft flow field and NASA Ames have now produced a program<sup>29</sup> known as  $\chi$ -MOTION in which CHIMERA grids move relatively to each other in order to calculate transient flow fields around bodies in relative motion. Meakin<sup>29</sup>, in another paper at the Bath conference, described the application of the  $\chi$ -MOTION program to the prediction of the transient flow around the space shuttle vehicle both in its ascent from subsonic to transonic conditions and during the release of the space rocket boosters.

#### (2) Advances in flow solver algorithms

Codes are available based on the solution of both the Euler and the Reynolds-averaged Navier-Stokes equations. The derivation and refinement of upwind algorithms has greatly improved the resolution of shock waves in the flow fields. Also, in the context of store separation problems, Kraft and Belk place particular emphasis on the value of implicit methods. In general, in the past, the preference has been for explicit methods on the grounds of simplicity, low cost per time step and smaller requirements for computer memory. However, the timescales involved in store separation are very large compared with the time step required for a stable solution from an explicit method: typically,  $10^6$  time steps required to drop a store a few centimeters. Implicit time-accurate viscous calculations have however been demonstrated with Courant numbers as high as  $10^4$  rather than  $O(1)$  and, as a result, simulation of a store drop can be done in hundreds rather than millions of time steps. The change to implicit methods has therefore been a most important factor in reducing computing costs for store release calculations.

#### (3) Use of incremental techniques for prediction of store release

Methodologies have been developed at AEDC whereby, instead of having to undertake CFD calculations of the absolute flow fields and store loads, one merely uses CFD to calculate the incremental effects on the flow field and store loads having already determined the basic aircraft flow field by either a wind tunnel test or a CFD calculation. These increments are then introduced into a trajectory generation program developed as an extension of the Influence Function Method (IFM), described in papers at earlier conferences. Somewhat surprisingly, it is claimed that when an IFM free-stream prediction with its associated linearisation error is subtracted from an IFM interference flow prediction also including linearisation errors, the resulting delta

coefficients are close to the true values that would be observed in an experiment. Also, by using delta coefficients in the trajectory prediction code, one only needs a CFD calculation with the store in the carriage position as opposed to a series of calculations with the store at many different points in its trajectory. With these simplifications, the calculations for predicting store release become cost-effective on present-day computers as an engineering tool.

(4) Extensive experimental programs for CFD evaluation

Finally and significantly, AEDC in recent years, has undertaken major experimental programmes planned with the specific aim of providing data that can be used for the evaluation of the new CFD methods.

The paper<sup>24</sup> by Kraft and Belk contained various examples demonstrating the capability of the CFD methods. These included:

- (a) Mach number contours in the flow field around a wing-pylon-weapon configuration. These were obtained from Reynolds-averaged Navier-Stokes calculations and the results show the detail of the flow, eg in the boundary layer and in the wake behind the pylon.
- (b) Pictures of the streamlines close to the undersurface of a 3-body configuration showing good agreement between the results of Navier-Stokes calculations and the evidence from oil flow tests.
- (c) Pressures at a point on the side of a shoulder body in a 3-body configuration, each body fitted with low aspect ratio cruciform fins at the rear. Euler multiblock calculations were successful in forecasting the main trends with Mach number in the experimental results in the transonic range ( $M = 0.80$  to  $M = 1.20$ ).
- (d) Finally, a comparison between prediction and experiment of the release trajectory of a weapon released from a pylon on the outboard side of one of the conformal fuel tanks on the F-15E. These predicted results were obtained entirely by CFD without making the simplifications described above. The flow field around the complete aircraft + conformal fuel tanks + pylons + stores was calculated and the predicted trajectory showed good agreement with experiment. This was a far from trivial case: on release, the weapon initially hung up close to the carriage position but yawed notably: these features in the experimental results were faithfully reproduced by the calculations: an impressive result.

Despite this success, Kraft and Belk conclude<sup>24</sup> that 'even with these advances in CFD techniques, aerodynamic predictions of a quality sufficient to enable accurate trajectory predictions are beyond the capabilities of current methods in a totally robust manner.' Nevertheless, they 'can be used confidently in a preliminary design stage to assess the influence of the airframe design on the quality of store separation.' The paper ends with a summary of the on-going CFD development tasks being undertaken at AEDC and AFATL.

The paper from AEDC/AFATL has been summarised in some detail because it clearly gives a good idea of what is being achieved at the frontiers of progress. It can be regarded as a guide to what is going to be possible more generally in the future but three other papers are worth mentioning as illustrations of what can be achieved today:

- (i) Stanniland of ARA showed<sup>25</sup> how the ARA Multiblock/BAE Euler CFD method has been used successfully to design improved underwing pylon installations.
- (ii) Clarkson of BAE (MA), Brough, presented<sup>26</sup> examples of where the BAE panel trajectory program, TSPARV, has been used successfully to predict release trajectories for complex cases. For example, the method is capable of modelling the complex store interaction effects in a ripple release and hence, in determining release sequencing/intervals for satisfactory release. It is noteworthy that a run with TSPARV only costs £500 - far cheaper than the more advanced CFD methods or a flight test programme.
- (iii) Finally, Carroll Dougherty, who introduced the CHIMERA grid concept to an AGARD audience in Athens in 1985, presented<sup>27</sup> further examples of its use. The calculations are effective in showing the physics of the unsteady flow around a store in the release from a simple wing.

## 9 CONCLUDING REMARKS

To sum up, the highlights of the conference can be listed as follows:

- 1 Progress in solving the aerodynamic problems of internal carriage
- 2 Long-term prospects for launchers giving mean-to-peak acceleration ratios closer to unity,
- 3 The success of applications of active control during release,
- 4 The value of mathematical modelling for predictions of store release,
- 5 Steady progress in refining empirical methods of prediction and in the application of these methods to new problems,
- 6 A major flight research programme,
- 7 Dramatic progress in CFD developments for at least 3 US establishments.

## REFERENCES

1-29 are papers from the Royal Aeronautical Society Conference on 'Store Carriage, Integration and Release' held in Bath, UK, April 1990.

- 1 Epstein C S, 'Carriage and release of stores on tactical military aircraft - past, present and trends for the future', Paper no 1.
- 2 Shaw D E, 'Weapon delivery systems - an aircraft designer's perspective', Paper no 2.
- 3 Griffin D, 'Designing for air carriage and ejection launch - a launcher designer's perspective', Paper no 3.
- 4 Dix R E, 'Cavity aeroacoustics', Paper no 4
- 5 Wilcox F J, 'Experimental measurements of internal store separation characteristics at supersonic speeds', Paper no 5
- 6 Evans R R, 'The engineering aspects of carriage and launch units for agile fighter aircraft', Paper no 6.

- 7 Vibert A J, Dunkley K J, 'Simulation of system dynamics during missile release from launchers', Paper no 7.
- 8 Holder I J, 'Liquid propellant powered weapon launchers', Paper no 8.
- 9 Deslandes R, 'Role of separation autopilots for modern missile concepts', Paper no 9.
- 10 Povey P G, 'Implementation of launch attitude control in Skyflash', Paper no 10.
- 11 Wood M E, 'Release of powered missiles with active control systems using the two sting rig - launch trajectories of Skyflash from Tornado', Paper no 11.
- 12 Akroyd G, 'Use of active control for safe separation of stores from aircraft', Paper no 12.
- 13 Ross J A, 'The prediction of the installed drag of stores', Paper no 13.
- 14 Baskaran V, Jerney C, 'Aircraft store carriage and release studies at the Aeronautical Research Laboratory, Australia', Paper no 14.
- 15 Figueiredo H M, 'A hovering helicopter store release prediction method', Paper no 15.
- 16 Mendenhall M R, 'Report on missile aerodynamics conference (Nielsen), Monterey, October/November 1988', Paper no 16.
- 17 Wolffelt K, 'A philosophy for the SAAB approach to aircraft-store separation problems', Paper no 17.
- 18 Dillenius M F E, 'Engineering level predictions for external store separation and submunition aerodynamics', Paper no 18.
- 19 Foster G W, 'In-flight measurements on a Tornado aircraft for store carriage and release research', Paper no 19.
- 20 Driffil P J, 'The collection of an airborne stores database for comparison with predictive methods. Part 1 - carriage loads', Paper no 20.
- 21 Torode H, 'The collection of an airborne stores database for comparison with predictive methods. Part 2 - release characteristics', Paper no 21.
- 22 Isaacs D, 'The prediction of carriage loads and change in aircraft longitudinal stability for pylon-mounted stores at subsonic speeds', Paper no 22.
- 23 Bailey R, 'Some results of a study of methods currently available for the prediction of aircraft flowfields and store loads at supersonic speeds', Paper no 23.
- 24 Kraft E M, Beik D, 'Advances in the use of CFD for weapon integration', Paper no 24.
- 25 Stammland D R, Baxendale A J, 'The use of CFD methods to aid the aerodynamic design and analysis of wing/pylon/store installations', Paper no 25.
- 26 Clarkson C D S, 'Prediction of store carriage/release behaviour using computational fluid mechanics (or higher order magic)', Paper no 26.
- 27 Dougherty F C, 'Computational store separation simulation', Paper no 27.
- 28 Morgan K, 'The simulation of store separation using unstructured grids and adaptive remeshing', Paper no 28.
- 29 Meakin R L, 'Transient flow field responses to unsteady manoeuvring of aerodynamic bodies', Paper no 29.
- 30 Clark R L, 'Weapons bay turbulence reduction techniques', AFFDL-TM-75-147-FXM, December 1975.
- 31 Mendenhall M R, Lesieutre D J, Caruso S C, Dillenius M F E, 'Aerodynamic design of Pegasus-concept to flight with CFD', AGARD FDP Symposium on 'Weapon Aerodynamics', Friedrichshafen, Germany, April 1990, Paper no 7.
- 32 Thompson J F, 'A composite grid generation code for general three-dimensional regions - the EAGLE code', AIAA Journal, Vol 26, No 3, March 1988, p 271.
- 33 Kim H J, Thompson J F, 'Three-dimensional adaptive grid generation on a composite block grid', AIAA Paper 88-0311, January 1988.
- 34 Tu Y, Thompson J F, 'Three-dimensional solution -adaptive grid generation on composite configurations', AIAA Paper 90-329, January 1990.

**PRESSURE MEASUREMENTS ON SLENDER BODIES AT SUPERSONIC SPEEDS AND DEVELOPMENT OF  
FLOW SEPARATION CRITERIA FOR EULER CODES**

J. Hodges  
L.C. Ward  
T.J. Birch  
Weapon Systems Aerodynamics Division  
Royal Aerospace Establishment  
Bedford MK41 6AE, UK

**SUMMARY**

Surface pressure measurements on a cylindrical body with a tangent-ogive nose are described. The Mach number range is 0.7 to 4.5 with incidence angles up to 26°. The high density of the measurements has allowed surface pressure contours to be constructed and detailed flow features can be observed. The measurements have suggested the use of a 2-element approximation to represent the line along which flow separation occurs. Calculations have been made using a space-marching Euler code (ZEUSB) both with and without forcing flow separation. Comparisons with experimental data are presented which show that forcing flow separation significantly improves both the surface pressure and force predictions. Conclusions are drawn regarding the use of a 2-element separation line representation within Euler codes.

**LIST OF SYMBOLS**

$C_l$	total rolling moment coefficient
$C_n$	total normal force coefficient
$C_{np}$	control panel normal force coefficient (ie normal to panel surface)
$C_p$	pressure coefficient, ie $(p - p_\infty)/q$
$C_{pmin}$	minimum value of $C_p$ (see Fig 7)
$C_{pvac}$	pressure coefficient when $p = 0$
$D$	maximum body diameter (1 calibre)
$M$	freestream Mach number
$p$	surface pressure
$p_\infty$	freestream static pressure
$q$	dynamic pressure
$Re$	freestream Reynolds number
$X$	distance from nose along body axis
$X_a$	distance from nose to upstream row of pressure taps
$X_b$	distance from nose to downstream row of pressure taps
$X_{cp}$	value of $X$ for longitudinal centre of pressure position
$X_n$	length of cylindrical extension piece
$\theta$	total angle of incidence (degrees)
$\lambda$	body roll angle
$\phi$	angular position on body surface relative to windward generator (positive anticlockwise)
$\phi_m$	value of $\phi$ at $C_{pmin}$
$\phi_{mc}$	value of $\phi_m$ for an infinite cylinder

**1 INTRODUCTION**

Traditionally, the aerodynamic loads on a missile shape have been obtained from

wind-tunnel tests and semi-empirical prediction methods. The combination of falling computer costs and the inability of semi-empirical methods to handle some new configurations has led to Computational Fluid Dynamic (CFD) methods being applied to missiles. For conventional shapes CFD methods are more expensive to run than semi-empirical methods but they can provide more accurate predictions and additionally supply flowfield information.

The Royal Aerospace Establishment (RAE) has conducted a series of tests to produce a data-base of experimental forces and moments on a variety of body, body-wing, and body-control configurations at Mach numbers from 2.5 to 4.5 (Ref 1) in order to support enhancements of semi-empirical methods. These data have also been used to carry out a limited assessment of CFD methods, but measurements of surface pressures and/or flowfield data are required for more thorough validation of such methods.

A short experiment has shown that reliable pressure measurements can be obtained at high Mach number using existing models and equipment (Ref 2). Consequently a longer and more comprehensive series of tests has been planned. Fig 1 illustrates the three phases of pressure measurements currently being performed at Mach numbers from 0.7 to 4.5. The models have a very high density of pressure taps, the limit being set by space within the various model components rather than by the number of pressures that can be connected to the pressure switches at any one time. All new model components are compatible with model parts used in the data-base tests, thereby allowing for possible future extensions to the planned programme.

In addition, surveys of the external flow using pitot and yawmeter probes are underway, initially on the plain cylindrical body. It is hoped that such studies will be continued for some of the body/wing/control combinations.

Most current CFD methods applied to missiles are based on the Euler equations. Unfortunately the Euler solution for the flow on the leeward side of a missile body at incidences higher than about 6° is not realistic, with flow separation and the resulting body vortices not being correctly modelled. Navier-Stokes methods with appropriate turbulence models will provide realistic predictions but with a heavy cost in computing resources on current machines. Until there are further major increases in computer speed and memory, Euler methods which incorporate an empirical separation model could be more attractive.

This paper gives a general description of the experimental work for measuring the surface pressures, presents some of the data, and describes the progress being made at RAE towards the development of empirical formulae for cross-flow separation locations on missile-type bodies. These formulae are intended for use in conjunction with a separation model incorporated within an Euler code. Initial comparisons between prediction and measurement have allowed several conclusions to be drawn relating to the extent and shape of imposed flow separation lines, and have shown the improvements in predictions which can be obtained by forcing flow separation.

## 2 EXPERIMENTAL PRESSURE MEASUREMENTS

### 2.1 Model, test equipment, and wind tunnel

The surface pressures on the cylindrical body were measured using two rings of pressure taps located at different axial stations along an 8-calibre long body (Fig 2). A 3-calibre power-law sharp nose (virtually identical with the profile of a tangent ogive) was fitted to the body by means of various length extension pieces. This had the effect of repositioning the measurement stations relative to the nose apex within the range  $3.5 \leq X/D \leq 14.5$  in 1-calibre steps. Each pressure-tap ring consisted of 80 taps, individually spaced  $4.5^\circ$  apart in roll. 43 consecutive taps of each ring (aligned with one another along common body generators) were connected to the ports of two commercially available 48-way pressure scanning switches mounted within the model.

The surface pressures over the nose profile were measured using a physically different nose built to the same geometry, having pressure tap rings every 0.2 of a calibre within the range  $0.2 \leq X/D \leq 4$  from the nose apex, and at relative orientations of  $45^\circ$ . As for the body, the circumferential angle between recorded pressures was every  $4.5^\circ$ , in this case being achieved by rolling the model.

For both of these tests carborundum grit was applied to the nose at  $0.27 \leq X/D \leq 0.35$  in order to promote boundary-layer transition.

The RAE 3ft x 4ft (0.914m x 1.219m) continuously-running wind tunnel was used for tests at freestream Mach numbers of 2.5, 3, 3.5, 4 and 4.5. Most of these tests were performed at a constant Reynolds number of  $13.1 \times 10^6/\text{m}$  ( $4 \times 10^6/\text{ft}$ ), and at nominal model incidences from  $-2^\circ$  to  $18^\circ$ , in steps of  $2^\circ$ . Additional data were recorded for some conditions at nominal model incidences up to  $26^\circ$ , though  $19^\circ$  was taken to be the maximum incidence in most cases. At Mach numbers of 3 and 4.5 some data were taken at freestream Reynolds numbers of  $6.6 \times 10^6/\text{m}$  and  $19.7 \times 10^6/\text{m}$  ( $2 \times 10^6/\text{ft}$  and  $6 \times 10^6/\text{ft}$ ), both with and without the boundary-layer trip applied.

The tests at Mach numbers of 0.7, 1.45 and 1.8 were performed in the RAE 8ft x 8ft, (2.438m x 2.438m) continuously-running wind tunnel at a freestream Reynolds

number of  $6.6 \times 10^6/\text{m}$  and nominal model incidences from  $-2^\circ$  to  $22^\circ$ , in steps of  $2^\circ$ .

### 2.2 Accuracy of the results

A discussion of the problems associated with the measurement of the very low surface pressures encountered at high Mach number is presented in Ref 2. It is worth noting that the pressure levels that require to be measured can be as low as 1.7 mbar (0.05 inches of mercury absolute), for a freestream Reynolds number of  $6.6 \times 10^6/\text{m}$  at Mach 4.5.

Fig 3 shows a comparison between values of  $C_p$  measured for the three freestream Reynolds numbers of 6.6, 13.1 and  $19.7 \times 10^6/\text{m}$  at Mach 4.5,  $X/D = 4.5$  and a nominal model incidence of  $19^\circ$ . After the preliminary tests described in Ref 2, doubts had been voiced about whether the lowest pressures recorded were genuine, or just the lowest that the equipment could handle. It is clear from the close similarity of the curves in Fig 3 that at the lowest Reynolds number (and in particular at the lowest pressure), the results are consistent with those at the other two Reynolds numbers.

Thus at the usual test Reynolds number of  $13.1 \times 10^6/\text{m}$  no equipment limit appears to have been reached.

### 2.3 Flow symmetry

With only 43 of the 80 pressure taps of each body ring connected to the pressure switches, a complete  $360^\circ$  roll coverage of the surface pressures around the body requires data to be taken at two model roll angles  $180^\circ$  apart. This would not be necessary if flow symmetry across the incidence plane could be assumed, with substantial savings in both wind-tunnel running time and costs. During the earlier tests (Ref 2) some data were recorded at model roll angles of  $-90^\circ$ ,  $0^\circ$  and  $90^\circ$ , for  $X/D = 5.5$ , a model incidence of  $19^\circ$ , and at Mach numbers of 2.5, 3.5 and 4.5. The results are shown in Fig 4. No obvious asymmetry is apparent, the small differences that appear between the port and starboard pressures are either within the resolution of the test, or can be explained by a small error in the setting of the body zero roll angle. It was therefore decided not to roll the body during the present tests, and assume flow symmetry. Likewise, flow symmetry was assumed during the tests to measure the nose pressures.

### 2.4 Experimental data comparisons at Mach 3

Fig 5 shows comparisons between the results of the present test and those of Ref 3 around bodies having virtually the same geometry, a common Mach number of 3, model incidences of  $8^\circ$ ,  $12^\circ$  and  $16^\circ$ , and  $X/D$  values of 4.5 and 6.5. In general the agreement is fairly reasonable. However, the occasionally complex shape of the curves as revealed by the present data can not be appreciated from the sparseness of the data from Ref 3. Use of these data alone would increase the chances of fortuitous agreement with theoretical



predictions, and the correct modelling of all the surface flow features could not be verified. This highlights the danger of using sparse experimental data to validate a theoretical method.

## 2.5 Sample contour plots of $C_p$ at Mach 2.5 and 4.5

Fig 6 shows contour plots of  $C_p$  covering the X/D range from 0.2 to 14.5 for half of the body surface (circumferential angles from windward to leeward), at incidences of 12° and 16° at Mach 2.5, and 12° at Mach 4.5.

For Mach 2.5 and 12° of incidence, from windward at each X/D station on the cylindrical body the pressure decreases to a minimum followed by a pressure rise causing flow separation. For X/D values up to about 8 there is a local high pressure region around the most leeward generator. Between these two areas is a second low pressure region. From contour plots at other incidences (eg at 16°), this low pressure region is shown to move forwards as the incidence increases, having initially appeared at around 6° to 8° of incidence. It seems certain therefore that it is created by one of the pair of vortices shed from the body. Possibly a secondary separation occurs slightly to windward of this second minimum value of  $C_p$  at some values of X/D. Similar patterns have been observed before, for example on a conically pointed circular cylinder at Mach 2.3 (Ref 4).

At Mach 4.5 there is no evidence of a cross-flow shock associated with flow separation, at either the 12° of incidence shown or at any other test incidence angle. In general, the pressures on the body leeside remain fairly constant at all incidences, the body vortex having only a minimal effect. This is confirmed from Schlieren observations which show that both leeside vortices appear to be weak, diffuse, and further away from the body than at lower Mach numbers.

An understanding of the complex nature of the leeside flow requires more than just surface pressure measurements, however detailed. Ideally, surface oil-flow pictures, coupled with boundary-layer and flow-field measurements are needed. Currently, the RAE is undertaking pitot probe and yawmeter surveys of the external flow over the leeside of a body with the same geometry as used in these surface pressure tests, at Mach numbers from 0.7 to 4.5. Some data have been acquired, and are in the process of being analysed.

The contour plots of Fig 6 show that the length of body that is influenced by the nose decreases as both incidence and Mach number increase. Thus at high values of X/D (eg X/D > 13 at Mach 2.5, or X/D > 8 at Mach 4.5, both at 12° of incidence), a contour pattern showing no apparent nose effects emerges, suggesting that this is close to the flow pattern that would be observed on an infinitely long cylinder.

## 3 FLOW SEPARATION

### 3.1 Location of flow separation from measured pressures

Typical single station pressure distributions were shown in Fig 5. If cross-flow separation occurs, it is associated with the pressure rise immediately to leeward of the pressure minimum. In some cases flow separation is triggered by a cross-flow shock, and flow separation can be assumed to be located at the shock position. In other cases (particularly at high Mach number or at low incidence angles) the pressure rise is more gentle and the circumferential location of flow separation is not obvious. Various criteria for obtaining separation locations from measured pressure distributions have been suggested (eg Ref 5), but the authors know of none which can be applied consistently over the ranges of Mach number and incidence covered by the present tests. Although the cross-flow separation line would not coincide with the minimum pressure line, it would be expected to follow the same trends (Ref 6).

As the object of this exercise was to investigate the effects of adding a semi-empirical separation line option into an Euler code, it was felt that absolute accuracy in defining the location of flow separation would not be as important as consistency across the Mach number and incidence test ranges. As each of the measured pressure distributions has a well defined minimum, its position has therefore been taken as an indication of the separation location.

Fig 7 shows values at  $C_{pmin}$  of the circumferential angle,  $\phi_m$ , for  $M = 3.5$  and various angles of incidence. Up to X/D = 6.5 the spread of these data at each station is only about  $\pm 5^\circ$ , ie relatively independent of incidence when compared with the data at X/D values greater than 6.5. The data for other Mach numbers show the same trends, suggesting that the minimum pressure line (and therefore the corresponding separation line) can be approximated by two discrete elements. The forward element is part of a common curve. When that curve reaches a particular value of  $\phi_m$ , ( $\phi_{mc}$ ), which is dependent on the angle of incidence, the minimum  $C_p$  line (and presumably the corresponding separation line) continues at a constant value. Thus the aft elements are straight lines at constant values of  $\phi$ .

The value  $\phi_{mc}$  is achieved at a distance sufficiently far along the body for the nose to have no further effect, ie  $\phi_{mc}$  is the minimum  $C_p$  location which would be achieved on an infinitely long cylinder, and thus should be dependent only on the cross-flow Mach number,  $M_{sin\theta}$ . Fig 8 shows a plot of  $\phi_m$  at X/D = 14.5 against  $M_{sin\theta}$  for all the Mach number and angle of incidence combinations which exhibited flow separation. Most of the points fall within a band only 4° wide. For values of  $M_{sin\theta} < 0.5$ , the crossflow remains subsonic, allowing the nose to influence the flow over the entire body.

#### 4 COMPARISONS WITH PREDICTIONS

##### 4.1 Prediction method

###### 4.1.1 ZEUSB

The prediction method used for the calculations is ZEUSB, a UK development of the NSWC space marching Euler code, ZEUS (Ref 7). Extensions to ZEUS incorporated within ZEUSB include:

- a) a parametric geometry input scheme developed by British Aerospace (Ref 8)
- b) the calculation of individual control panel loads (RAE)
- c) the inclusion of a model of flow separation from the body, originally developed at the University of Salford under RAE funding (Ref 9).

The separation model was incorporated into ZEUS for the half flowfield case (ie where flow symmetry is assumed) by NSWC and extended to the full flowfield case by RAE.

All the present calculations used an unclustered grid consisting of 72 cells between the body and the bow shock, and circumferential spacing of  $2.5^\circ$ . Thus half flowfield calculations used a  $72 \times 72$  grid, and full flowfield calculations a  $72 \times 144$  grid.

###### 4.1.2 Separation model

Although full details of the Salford separation model are available in Ref 9, it is felt that a brief description here of its implementation would be useful. Within the ZEUSB code the size of the step between computing planes in the axial direction is calculated from the flow variables, and a two-dimensional grid constructed around the configuration at the new axial location. The two cells adjacent to the body surface and nearest to the imposed separation location are identified, and at all the remaining cells the Euler solution is calculated. In the two cells, pressure and density are obtained by averaging neighbouring values in the circumferential direction and the flow speed is obtained by using the condition of constant total enthalpy. The velocity components in the two cells are then obtained using empirically defined flow directions. These flow directions have radial components away from the body, and circumferential components towards each other in order to force separation. Other flow variables can be derived and the next axial step size is calculated.

##### 4.2 Comparisons for body alone configuration

###### 4.2.1 Surface pressures

In order to assess the ability of the Euler code ZEUSB to predict flow features for the body alone configuration discussed earlier, contours of calculated and measured surface pressures have been compared. Fig 6 showed the experimental measurements for Mach 2.5 and  $12^\circ$  angle of

incidence, and Fig 9 the ZEUSB results with no separation modelling. The agreement is good on the windward side of the body and on the whole of the nose section, but is poor on the leeward side of the cylindrical section ( $X/D > 3$ ). The prediction shows the flow expanding beyond the observed minimum pressure line with recompression through a strong crossflow shock. There is no indication in the prediction of flow separation from the body or of a suction under a body vortex.

A ZEUSB calculation was performed with separation forced along a line derived from the experimental measurements (as described in Section 3). The line consisted of two straight-line elements, one in the region  $2 < X/D < 7$  and the other parallel to the body axis in the region  $X/D > 7$ . The forward element starts at  $X/D = 2$  because the measurements indicate no flow separation ahead of this point.

The leeside prediction (Fig 10) shows a large area of low pressure caused by the high velocities under a body vortex. Although this feature is spread over a larger area than is observed in the measurements, its presence provides a significant improvement over the prediction without separation modelling.

Another feature observed in Fig 10 is the location of the minimum pressure line. The forward element of the forced separation line ( $2 < X/D < 7$ ) matches the predicted minimum pressure line. However, the aft element ( $X/D > 7$ ) lies to the leeward of the predicted minimum pressure line. It appears that the forced separation model has behaved as required for the forward element, but the slope discontinuity at  $X/D = 7$  has caused a problem. Having initiated the flow separation for  $X/D < 7$ , the calculation has produced a pressure minimum and a flow separation along a continuation of the forward element of the imposed separation line, with a second separation being forced along the aft element of the imposed line.

A calculation was performed with separation forced along the forward element ( $2 < X/D < 7$ ) only and this overcame the above problem, producing surface pressures in closer agreement with experiment. A calculation with separation forced along a shortened version of the forward element ( $3 < X/D < 6.5$ ) provided further improved results (Fig 11). By comparing Fig 11 with Figs 6 and 10 it can be seen that the predicted vortex suction is more localised, although its position does not match that deduced from experiment very well. The calculated minimum pressure line beyond  $X/D = 6.5$  is in good agreement with experiment.

This prediction probably gives the best agreement with experiment that could be expected from an Euler method with a simple forced flow separation model. There are areas of the leeside flow where the agreement is not good, but these can be attributed to the lack of viscous terms in the calculation. The separation modelling has achieved its main objective of modelling the gross effects of the real vortical flow.

The imposed separation line ( $3 < X/D < 6.5$ ) is in the region where separation location is relatively unaffected by the incidence of the body. It was therefore considered worthwhile carrying out calculations for the body alone configuration at Mach 2.5 and a range of incidences, using the same forced separation line.

Fig 12 shows measured and calculated surface pressure contours for the body alone configuration at Mach 2.5 and  $8^\circ$  of incidence. Although the quantitative agreement could be better, the observed flow features have been represented in the prediction. The minimum pressure and the vortex suction are both in approximately the correct locations. However, the calculated minimum pressure is lower and the vortex suction weaker than observed experimentally.

Fig 13 shows calculated surface pressure contours for the body alone configuration at Mach 2.5 and  $16^\circ$  of incidence. This figure can be compared with Fig 6 which shows the corresponding experimental measurements. The predictions show a localised vortex suction a little further along the body than is seen in the measurements. However, after the forcing of flow separation ceases at  $X/D = 6.5$ , the separation does not continue in the same way as it did at  $12^\circ$  of incidence. In contrast, the calculated leeside flowfield at  $16^\circ$  of incidence quickly reverts to that expected with no separation modelling, and features a strong crossflow shock.

There is an explanation for the behaviour at  $16^\circ$  of incidence. The value of  $M_{\sin\theta}$  for this case is 0.689, so that just above the surface near  $\phi = 90^\circ$  the crossflow is supersonic. Therefore the forced flow separation in the region  $3 < X/D < 6.5$  cannot influence the calculated flow further along the body in the region where flow separation is likely to occur. Thus in the region  $X/D > 6.5$ , the calculated flow near  $\phi = 90^\circ$  knows nothing of the forced flow separation further forward, and therefore behaves as it would in a calculation with no forced separation.

In contrast, at  $8^\circ$  of incidence the value of  $M_{\sin\theta}$  is 0.348 so that the cross-flow remains subsonic and the forced separation can trigger separation further along the body.  $M_{\sin\theta} = 0.5$  corresponds to the change in the nature of the flow for an infinite cylinder.

For all three incidence angles ( $8^\circ$ ,  $12^\circ$ ,  $16^\circ$ ) the forced separation has introduced a body vortex into the half flowfield calculation and thus improved the modelling of the vortical leeside flow, at least qualitatively. At  $16^\circ$  of incidence, the predicted leeside flow can be further improved by forcing separation along the whole cylindrical section of the body, as shown in the lower half of Fig 13.

A general conclusion that can be drawn from the above discussion is that, having initiated a flow separation in a calculation at some forward station, it is

only necessary to force separation at stations further aft if the local Mach number normal to the separation line is greater than unity.

#### 4.2.2 Forces

Measured forces have been compared with those predicted by ZEUSB both with and without forced separation. In all calculations with forced separation, only the shortened version of the forward element of the separation line has been used.

Fig 14 shows calculated and measured values of normal force coefficient,  $C_n$ , for a range of incidences at Mach 2.5. The results of the calculations without forced separation are in good agreement with the measurements at low angles of incidence ( $\theta < 6^\circ$ ) and at high angles of incidence ( $\theta > 14^\circ$ ). However, for incidences in the range  $6^\circ < \theta < 14^\circ$ , the normal force predictions are significantly below the measurements because they do not include a vortex suction contribution. Although body vortices are still present in the real flow at the higher angles of incidence, their effect at the body surface is felt over a relatively small area, and so the vortex suction contribution to normal force is reduced. Also, the predicted leeside pressures, although not in agreement with experiment, integrate fortuitously to provide forces that are in agreement with experiment.

With separation forced along the line described above, there is a significant improvement in the normal force predictions for the range  $6^\circ < \theta < 14^\circ$ , because the body vortices and their suction at the body surface are now being modelled. At incidences above  $14^\circ$ , as only the forward element of the separation line is being used, the modelling is incomplete. Also the vortex suction may have been slightly overestimated.

Fig 15 shows the corresponding centre of pressure positions. Without separation modelling the calculations are in poor agreement with experiment for incidences below  $12^\circ$ , but at higher angles the agreement with experiment is good. With forced separation, the vortex suction on the cylindrical section of the body is modelled, and as a result the centre of pressure moves towards the base of the body. A significant improvement in the agreement between prediction and experiment is seen for  $\theta < 12^\circ$ . For higher incidences, the extent of the calculated vortex suction is overestimated and the centre of pressure is moved too far aft.

#### 4.3 Comparisons for body-control configuration

Further calculations were made on a body-control configuration to assess the modelling of the interaction between body vortices and undeflected control panels. The configuration chosen is shown in Fig 16. In the experiment two opposite control panels were instrumented with strain-gauge balances. The measurements of panel load against angle of incidence with the instrumented controls at right angles to the incidence plane are displayed in Fig 17. Also shown in Fig 17

are results of ZEUSB calculations with and without forced flow separation from the body along the line described above.

The predictions without forced separation are in good agreement with experiment up to about 6° of incidence. At higher incidences the panel loads are overestimated.

With forced separation there is a significant improvement in the agreement with experiment at angles of incidence below 16°. At incidences up to 12° the agreement with experiment is good.

Figs 18 and 19 show comparisons of calculated loads with measurements for various roll angles at Mach 2.5 and 12° of incidence. This is the incidence for which the imposed separation line was tuned, so it would be hoped that these calculations should give reasonable agreement with experiment.

Fig 18 shows the load on a control panel as the configuration is rolled through 360° (the panel being in the leeward position at zero roll). When the panel is within 60° of the windward position ( $120^\circ < \lambda < 240^\circ$ ), the ZEUSB calculations (both with and without separation modelling) produce panel loads in excellent agreement with measurement. Outside this region the results of the calculations with forced separation remain in good agreement with experiment, while those without separation are poor. In particular, the calculations without forced separation have not predicted the sign reversal seen in the measured panel loads near the leeward position. With separation modelling, this feature is predicted.

Fig 19 shows corresponding comparisons of overall rolling moment,  $C_l$ , a notoriously difficult parameter to predict. Once again, the results of the calculations with separation modelling are in much better agreement with experiment than those without. The latter results do not even show the correct trends.

## 5 CONCLUSIONS

The surface pressures on a cylindrical body and tangent-ogive nose have been measured for a Mach number range from 0.7 to 4.5, and at angles of incidence up to 26°. Data were recorded for circumferential angles around the model from 0° to 180° in 4.5° steps, and at axial stations from 0.2 to 14.5 calibres. This paper shows that:

1. The pressure measurements are of high accuracy, and the coverage is sufficiently dense to show many features which would otherwise be missed.

2. The measurements suggest that for any given Mach number the flow separation line can be approximated by two elements, the forward element being independent of incidence, and the aft element being independent of  $X/D$ . For values of  $M \sin \alpha > 0.5$ , the aft element represents the flow separation line that would be observed on an infinite cylinder.

The flow separation model within the Euler code ZEUSB has been provided with a realistic separation line derived from the experimental measurements. Comparisons have been made between experimental data for surface pressures, total loads and control panel loads, and the computed results using ZEUSB both with and without separation modelling. The following conclusion has been reached.

3. Forcing flow separation within an Euler code can improve predicted surface pressures by introducing a vortical flow into the solution. The prediction of both overall and control panel loads can also be significantly improved.

The separation lines discussed in the present study have been associated with cylindrical bodies having 3-calibre tangent-ogive noses. However, the following conclusion is generally applicable to separation modelling in Euler codes using cell-centred schemes.

4. Having initiated a flow separation in a calculation at some forward station, it is only necessary to force separation at stations further aft if the local Mach number normal to the separation line is greater than unity.

The results described here are encouraging and justify further work on empirical formulae for separation lines which can be used within Euler codes. In particular, further calculations are required to be performed in order to fully verify conclusion 4.

## REFERENCES

1. J. Hodges and L.C. Ward. The RAE experimental data-base for missiles at high Mach number and its use in assessing CFD methods. AGARD-CP-428 (1987); RAE Technical Memorandum Aero 2096 (1987).
2. L.C. Ward. The experimental pressure distribution at one location around a body at Mach numbers from 2.5 to 4.5. RAE Technical Memorandum Aero 2120 (1987).
3. Emma Jean Landrum. Wind-tunnel pressure data at Mach numbers from 1.6 to 4.63 for a series of bodies of revolution at angles of attack from -4° to 60°. NASA TM X-3558 (1977).
4. S.J. Boersen. Reynolds number effects on pressure and normal force distributions along conically pointed circular cylinder at free-stream Mach number of 2.3. NLR TR 75124 U (1975).
5. L.H. Jorgensen and E.W. Perkins. Investigation of some wake vortex characteristics of an inclined ogive-cylinder body at Mach number 2. NACA Report 1371 (1958).
6. E.W. Perkins and D.M. Kuehn. Comparison of the experimental and theoretical distributions of lift on a slender inclined body of revolution at  $M = 2$ . NACA TN 3715 (1956).

7. A.B. Wardlaw and S.F. Davies. A second order Godunov method for tactical missiles. NSWC TR 86-506 (1986).

8. D.P. Hills. An evaluation of the ZEUS computer program. BAE Report JS 11303, Vol. 2 (1989).

9. C.M. Kwong and D.F. Myring. Fusiform body separated flowfield calculation using Euler and boundary layer methods. Royal Aeronautical Society Conference. The prediction and exploitation of separated flow. 18-20 April 1989.

Copyright © Controller, HMSO London 1990

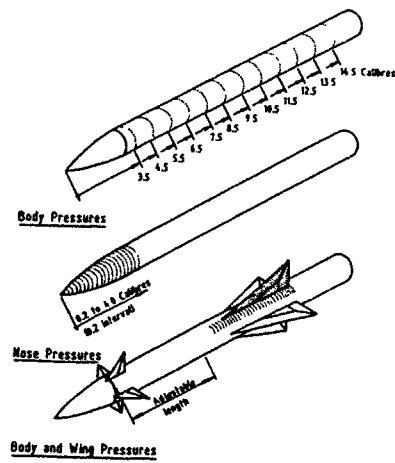
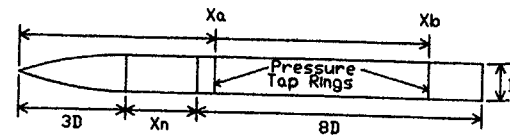
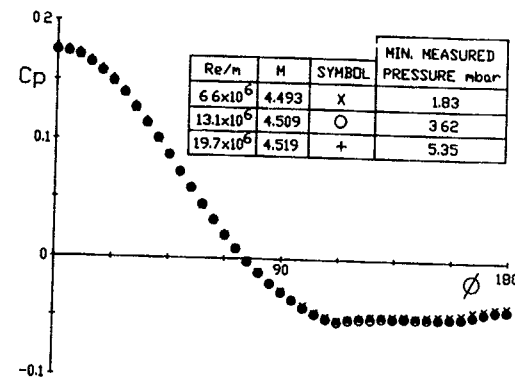
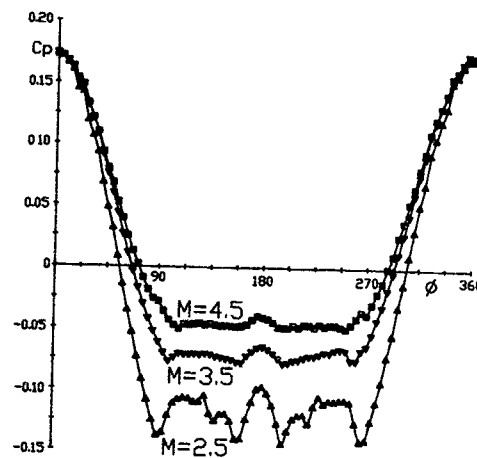


Fig 1 Pressure measurement programme



$X_n$	$X_a$	$X_b$
0D	3.5D	9.5D
1D	4.5D	10.5D
2D	5.5D	11.5D
3D	6.5D	12.5D
4D	7.5D	13.5D
5D	8.5D	14.5D

Fig 2 Model for measuring body surface pressures

Fig 3 Pressure measurement check at  $M = 4.5$ ,  $X/D = 4.5$ ,  $\theta = 19^\circ$ Fig 4 Flow symmetry at  $M = 2.5, 3.5, 4.5$  and  $X/D = 5.5$ ,  $\theta = 19^\circ$

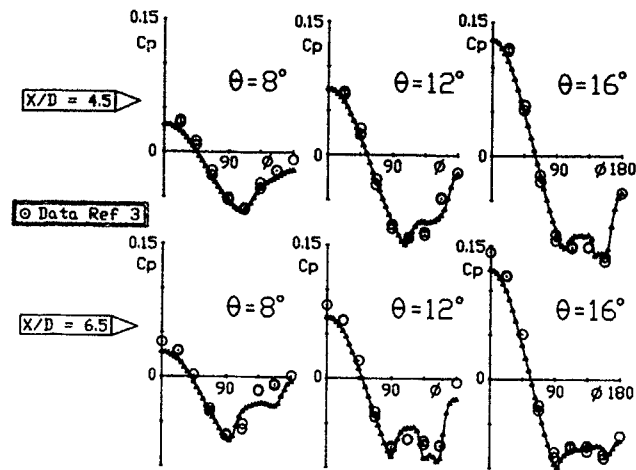
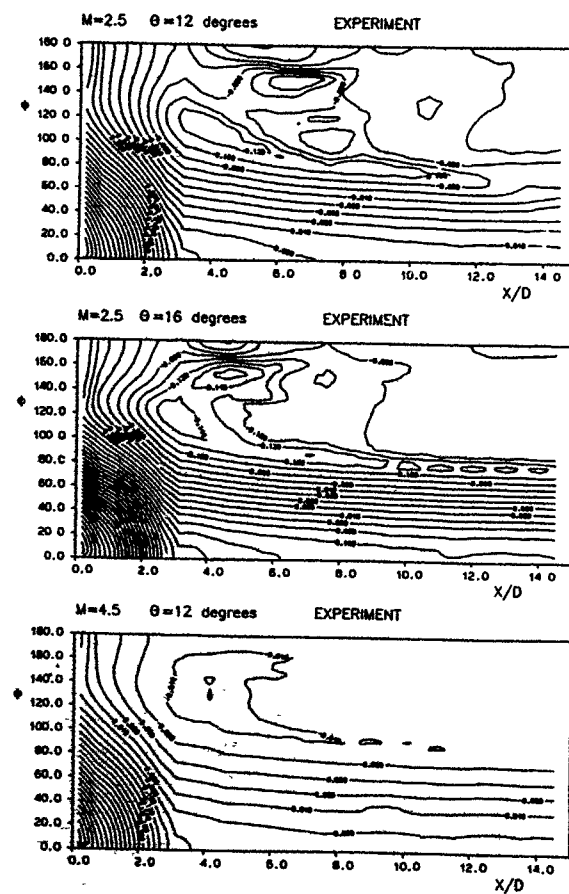
Fig 5 Data comparisons at  $M = 3$ 

Fig 6 Measured pressure contours

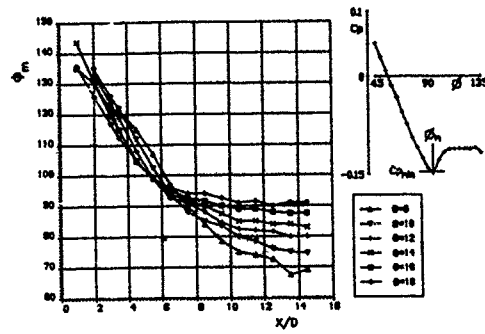
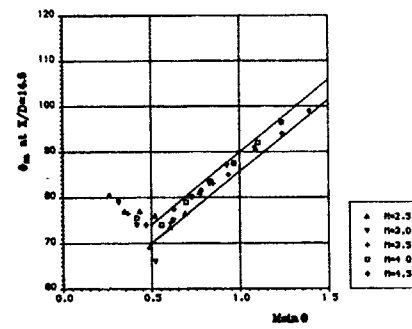
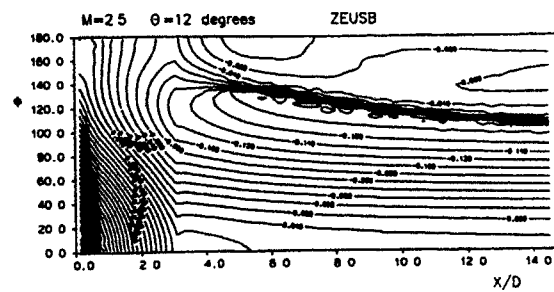
Fig 7 Minimum pressure locations at  $M = 3.5$ Fig 8 Correlation of minimum pressure locations at  $X/D = 14.5$ 

Fig 9 ZEUSB calculation; no separation

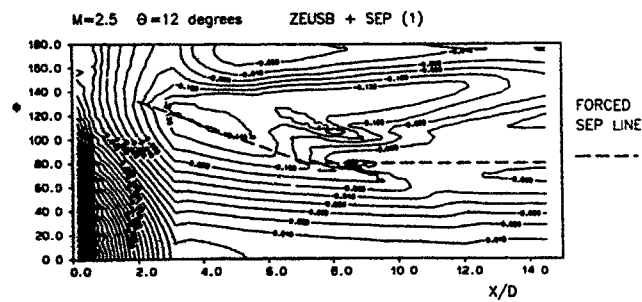


Fig 10 ZEUSB calculation; forced separation 1

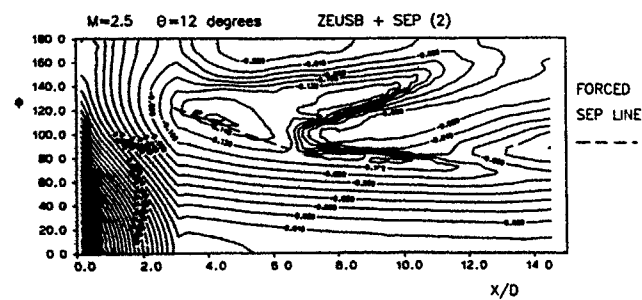


Fig 11 ZEUSB calculation; forced separation 2



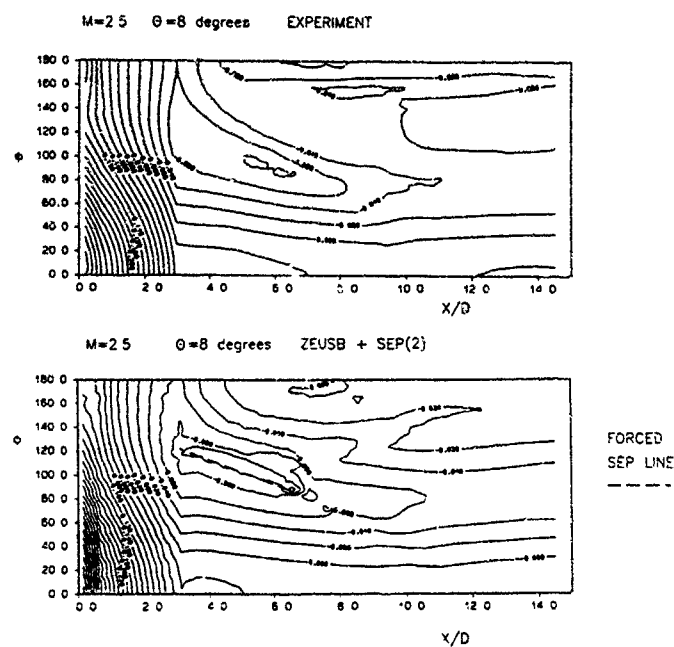


Fig 12 Comparison between experiment, and ZEUSB calculation with forced separation

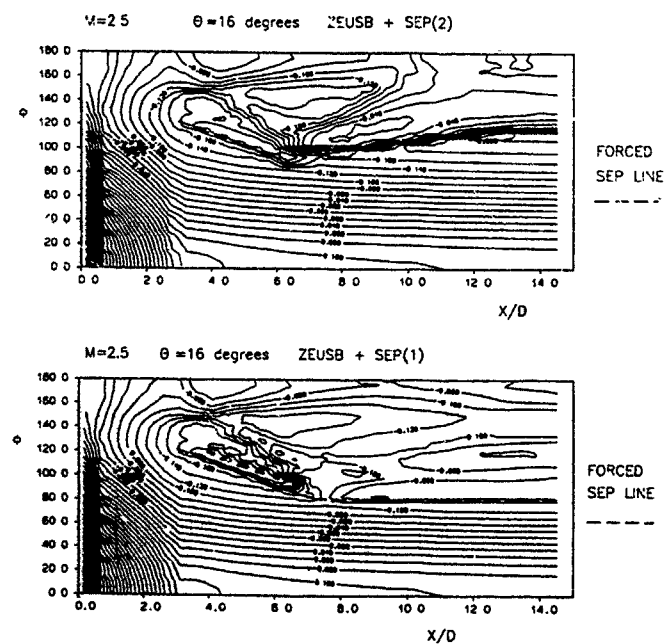


Fig 13 ZEUSB calculation; forced separation

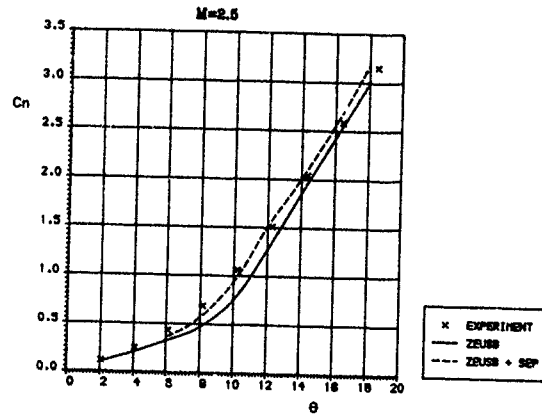


Fig 14 Normal force comparisons; body alone

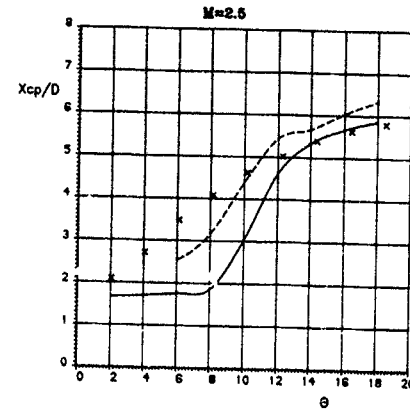


Fig 15 Centre of pressure comparisons; body alone

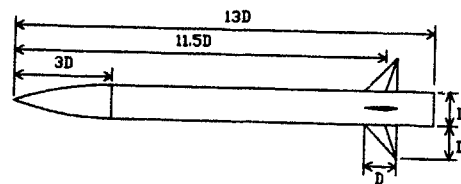


Fig 16 Body and cruciform control configuration

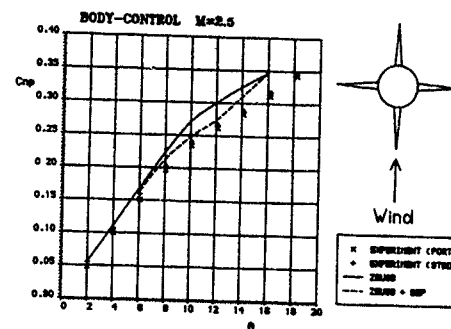


Fig 17 Control normal force comparison with incidence angle

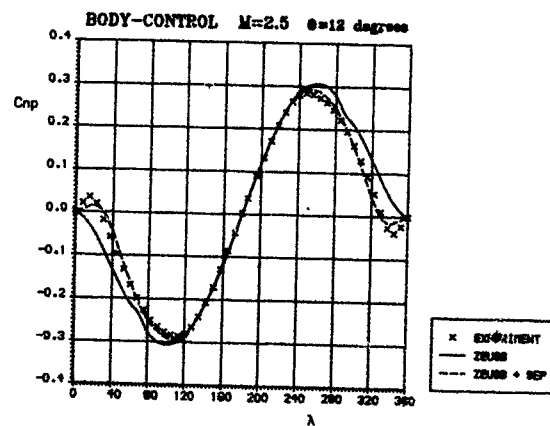


Fig 18 Control normal force comparison with roll angle

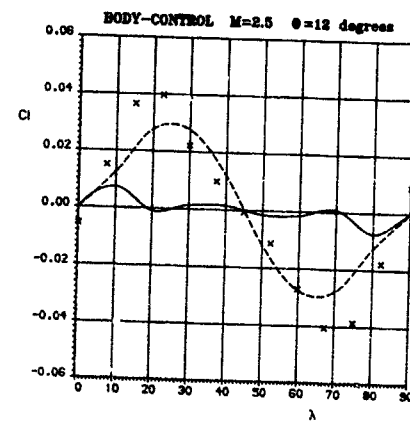


Fig 19 Total rolling moment comparison with roll angle

## COMPUTATION OF VISCOUS SUPERSONIC FLOWS

Y. NOGUCHI, J.M.R. GRAHAM and R. HILLIER

Department of Aeronautics  
Imperial College of Science, Technology and Medicine  
Prince Consort Road  
London SW7 2BY  
England, U.K.

1 SUMMARY

This paper describes finite difference computations aimed at the prediction of the viscous flow field around projectiles and slender bodies at transonic and low supersonic speeds. Following a step by step validation process to ensure reliability in the computer program development, the code is tested with an axi-symmetric body of revolution at a free stream Mach number of 1.4 and length based Reynolds number of  $Re_x = 1.0 \times 10^7$ . Results using Baldwin-Lomax and Johnson-King turbulence models are shown.

2 LIST OF SYMBOLS

Cf Local skin friction Coefficient.  
Cp Pressure coefficient.  
E,F Flux vectors in  $\xi$  and  $\eta$  directions.  
H Axi-symmetric source term.  
L Reference length.  
M Mach number.  
Q Vector of conservative variables.  
Rex Reynolds number based on reference length L.  
Re<sub>θ</sub> Reynolds number based on momentum thickness θ.  
S Viscous & heat conduction vector.  
T Temperature.  
U,V Velocity in X and Y direction.  
X,Y Cartesian co-ordinate axes.  
δ Boundary layer thickness.  
δ\* Displacement thickness.  
ξ,η Computational co-ordinate axes.  
θ Momentum thickness.  
ρ Density.

Subscripts  
w Wall condition.  
∞ Free stream value.

3 INTRODUCTION

A project to develop a computer code to calculate the flow field around projectiles at transonic and/or low supersonic speed has been in progress for nearly 3 years. The long term objective of the project is to calculate spinning projectiles at incidence. In order to achieve this objective, a structured sequence of validation tests have been carried out. They are:

- \* Inviscid code development and validation against analytical data.
- \* Laminar viscous code and validation against classical boundary layer theory.
- \* Introduction of simple turbulence models and validation against good and reliable experiments.

The axi-symmetric compressible thin-layer approximation of the Navier-Stokes equations in conservation law form in general curvilinear co-ordinates is:

$$\frac{\partial Q}{\partial t} + \frac{\partial E}{\partial \xi} + \frac{\partial F}{\partial \eta} + H = \frac{1}{Re} \left( \frac{\partial S}{\partial \xi} \right)$$

The equations are solved by the Warming and Beam (Ref. 1) explicit time marching scheme. The method uses central differencing in the regions where the eigenvalues of the Jacobian are negative and upwind differencing in the regions where the eigenvalues are positive. This scheme captures shocks more sharply than the MacCormack method which, in effect, uses central differencing everywhere. The equations are transformed for use with a general curvilinear co-ordinate system. In order to damp high frequency oscillations fourth order numerical dissipation terms suggested by Warming and Beam are added.

All the results presented here are calculated with the far field boundary sufficiently far away from the body to allow the free stream condition to be used at the boundary. When the far boundary was taken close to the solid body and the bow shock penetrated the boundary, it caused a large error in body surface pressure prediction, even when a characteristic based boundary condition was used.

The algebraic turbulence model due to Baldwin and Lomax (Ref. 2) is one of the most widely used turbulence models for compressible flow computations because of its simplicity. The model has been applied for a variety of flows including separated flows. However the method incorporates no 'history effects' and may not be adequate for regions of large pressure gradient.

Johnson and King (Ref. 3) introduced a turbulence closure model which added some 'history effects' to the simple algebraic eddy viscosity model. An ordinary differential equation is introduced to relate the maximum Reynolds shear stress development in the streamwise direction to account for convection and diffusion effects.

In this paper both models are applied to a waisted body of revolution, for which Winter et. al. (Ref. 4) have made a series of detailed measurements of surface pressure, boundary layer profiles and skin friction.

Finally, we have used this project to develop our computing ability on personal computers, the bulk of the work being performed on a Compaq Deskpro 386/25 with a Weitek floating point co-processor.

#### 4 VALIDATION TESTS

We have followed a step by step validation process to ensure reliability in the computer code development. Inviscid validation tests were conducted against analytical solution of cones and cone-cylinders at various cone angles and Mach numbers.

The basic laminar 2-D code has been validated against the flat plate boundary layer of Van Driest (Ref. 5) with zero pressure gradient with and without heat transfer. Initial tests with various co-ordinate systems for the adiabatic case showed that at the very least 15 mesh points are needed to predict velocity and temperature profiles with reasonable accuracy at the downstream end of the boundary layer. Even more points may be necessary for cases with heat transfer. Figure 1 shows the co-ordinate system used for the cold wall case where the wall temperature is fixed at the free stream value. This case is a much severer test than the adiabatic wall case because of the larger temperature variation across the boundary layer and the reversal of the temperature gradient near the wall. The free stream Mach number is at  $M_\infty = 4.0$ . There are 37 mesh points within the boundary layer at the point close to the downstream end. The arrow indicates the station where the velocity and temperature profiles are compared with theory. In Figure 2 the dotted lines represent the analytical solution of Van Driest. The agreement between the results are very good, and a similar accuracy was achieved for the adiabatic wall case.

The first turbulent test was carried out with the Baldwin-Lomax algebraic turbulence model. A turbulent flat plate boundary layer with zero pressure gradient, at a free stream Mach number of 4.0, is calculated and compared with

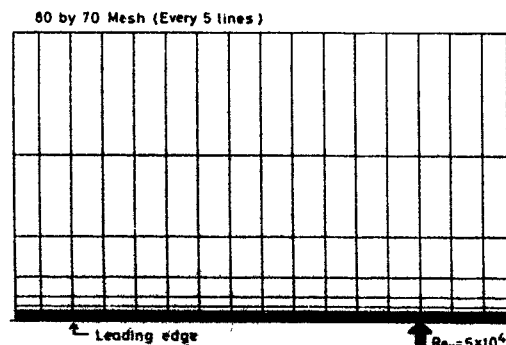


FIGURE 1. Co-ordinate system for laminar flat plate boundary-layer: Cold wall case  $M_\infty = 4.0$ ,  $T_w = T_\infty$ .

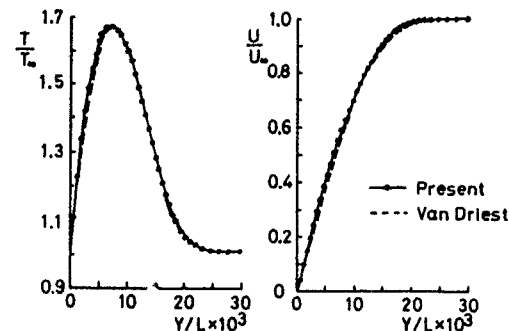


FIGURE 2. Velocity and temperature profiles of laminar flat plate boundary-layer at  $Re_x = 5 \times 10^4$ .

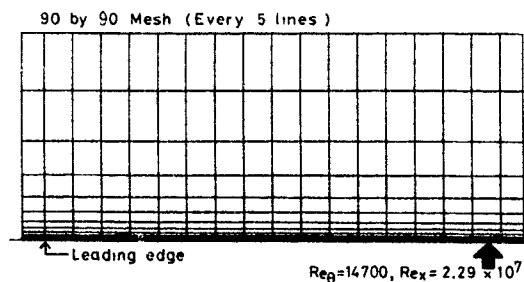


FIGURE 3. Co-ordinate system for turbulent flat plate boundary layer with zero pressure gradient: Adiabatic wall case  $M_\infty = 4.0$ ,  $T_\infty = 310^\circ \text{ K}$ .

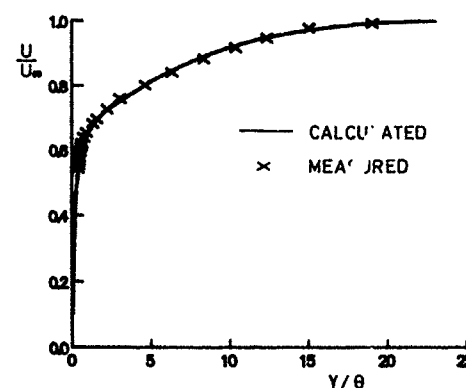


FIGURE 4. Velocity profiles of turbulent flat plate boundary layer at  $Re_x = 14700$ : Adiabatic case  $M_\infty = 4.0$ ,  $T_\infty = 310^\circ \text{ K}$ .

the experiments of Maybey et. al. (Ref. 6). They measured profiles at 5 streamwise stations and paid a great deal of attention for achieving near adiabatic conditions. The experimental profiles are also given in great detail e.g. 50 points in a profile. The co-ordinate system used computationally is shown in Figure 3 and the arrow indicates the point where the comparison is made. Although the calculated momentum thickness is approximately 20% larger than the experiments at a given X-station, the growth rates of the boundary layer are very similar. This discrepancy may be caused by a difference in transition position. The velocity profile comparisons, therefore, are made at momentum thickness based Reynolds number rather than length based Reynolds number  $Rex$ . The profile at  $Re_\theta = 14700$  ( $Rex = 2.29 \times 10^4$ ) is shown in Figure 4. The crosses represent the measured profile which agrees very well with the calculated profile. The skin friction prediction also agrees well with the experiments.

#### 5 WAISTED BODY OF REVOLUTION

We now extend the validation tests to the boundary-layer with pressure gradient. There are several choices of experimental data for such a purpose. However the test flow should be attached, because at this stage the validation should be carried out without the added complication of separation. The flow should be at a moderate Mach number, because the ultimate purpose of the project is to predict the flow field around projectiles at transonic speed, not at subsonic or high supersonic speed. And preferably the flow field should be axi-symmetric since it represents projectiles and also a two dimensional planar flow field is likely to be more difficult to create accurately in an experiment.

Winter, Rotta and Smith (Ref. 4) carried out definitive experiments to measure the boundary-layers on an axi-symmetric waisted body which is shown in Figure 5. The body is 1524mm long. The conical nose has a half angle of 20 degrees. This is followed by a shape defined by a quartic curve which joins the cubic giving approximately constant convergence. A mirror image of this cubic provides the final flare and a quartic fairing curve joins the converging and diverging region. The flow is attached and measurements at various Mach numbers and Reynolds numbers were carried out. The case chosen for the present validation test is with the free stream Mach number at  $M_\infty = 1.4$  and the length based Reynolds number of  $Rex = 1.01 \times 10^7$ .

At first, only the cone part up to  $X/L = 0.11$  is calculated using the Baldwin-Lomax model. The turbulence model was switched on at the same location as the transition trip in the experiments ( $X/L = 0.085$ ). The grid used for this part has 90 points in the X direction ( $X/L = 0$  to  $0.11$ ) and 80 points

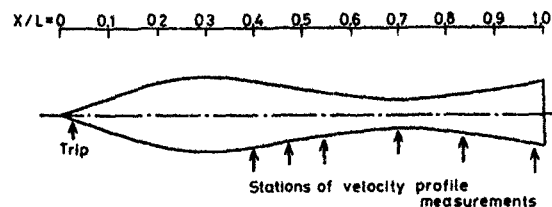


FIGURE 5. Geometry of Waisted body of Winter et. al.

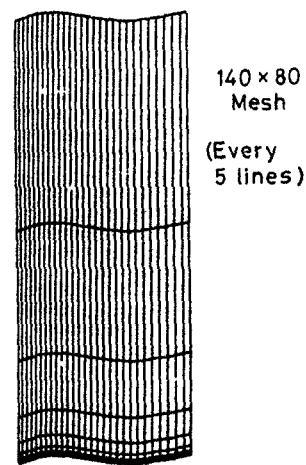


FIGURE 6. Co-ordinate system for Waisted body of Winter et. al. at,  $M_\infty = 1.4$ ,  $T_\infty = 290^\circ K$  and  $Rex = 1.01 \times 10^7$

in the Y direction. The result at  $X/L = 0.1$  is then used as a starting condition to calculate the downstream part of the body using both the Baldwin-Lomax model (BLM) and the Johnson-King model (JKM).

The co-ordinate system used for the afterbody calculation has 140 points in the X direction and 80 in the Y direction as seen in Figure 6. The grid is generated to distribute at least 35 mesh points within the boundary layer at around  $X/L = 0.5$ . We consider this to be the number needed to calculate turbulent boundary layers with reasonable accuracy. The present grid has 44 points within the boundary layer. The results with a mesh which has 120 by 70 points are compared with the present results. This grid has 38 points within the boundary layer at the same streamwise location. Both results are almost identical and this suggests that the number of mesh points seems to be adequate and the results are more-or-less mesh independent. Approximately 25000 time steps are required to obtain a converged solution.

Figure 7 shows the computed surface pressure, compared with experiments, for BLM, JKM and an inviscid calculation. The results of the BLM and JKM are almost identical and they fall on a single line. The dotted line represents the inviscid results which is very close to the viscous results. Agreement with experiment is also very good, providing a further validation of the inviscid part of the code and also ensuring that the pressure field is correctly modelled for the viscous calculation. The results show a region of major favourable pressure gradient from the nose to  $X/L=0.4$ , followed by adverse pressure gradient. The close agreement between the viscous and inviscid results suggests that the boundary layer displacement thickness is relatively small and hence the viscous effect on the pressure is small.

The momentum thickness developments along the body are shown in Figure 8. The solid and dotted lines represent the BLM and JKM results respectively and the crosses represent the experiments. All the following figures are also presented in the same way. Figure 9 shows the displacement thickness development along the body. Both figures 8 and 9 show the discrepancy between BLM and JKM is rather small, and in general, the agreement between the calculated results and the experiment is reasonably good.

The skin friction coefficient is probably the most difficult boundary layer parameter to calculate and to measure with reasonable accuracy. It is evaluated from the velocity gradient at the wall using the velocity value at the first mesh point from the wall; a higher order interpolation would change predicted values by up to +15%. Figure 10 shows the skin friction. The dashed line represents the skin friction of the forebody. The two dots at  $X/L=0.05$  and  $0.1$  are the calculated values from the  $1/7$  power law on a cone as quoted by Winter et. al. Both BLM and JKM give

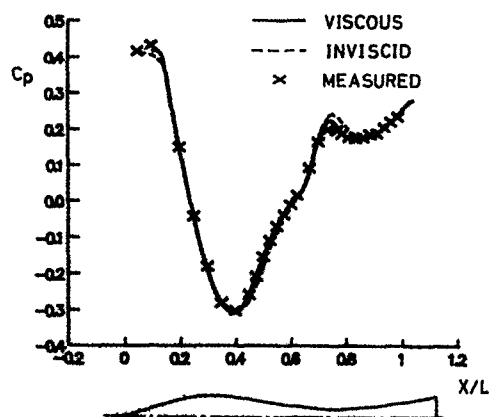


FIGURE 7. Surface pressure comparison between BLM, JKM & inviscid calculations and experiment.

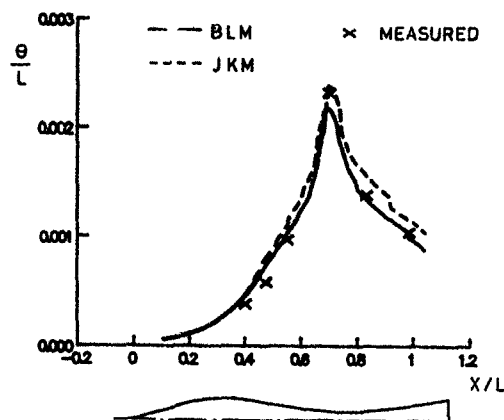


FIGURE 8. Momentum thickness comparison between BLM, JKM and experiment.

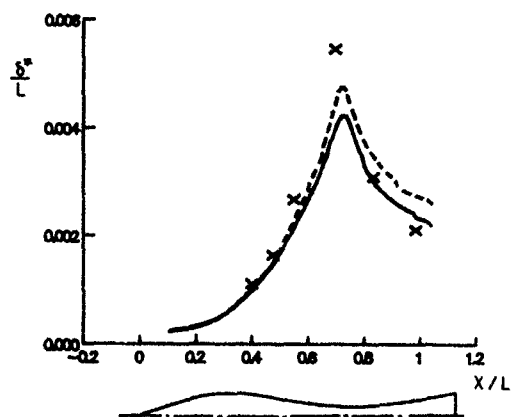


FIGURE 9. Displacement thickness comparison between BLM, JKM and experiment.

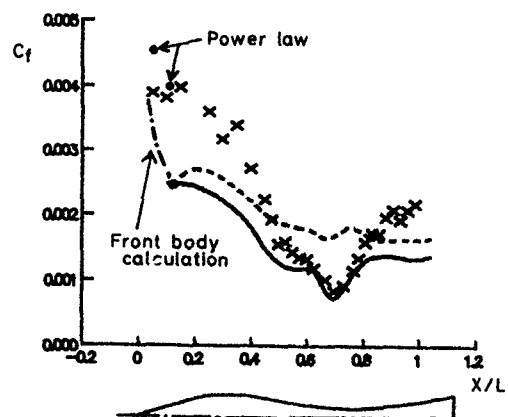


FIGURE 10. Skin friction coefficient comparison between BLM, JKM and experiment.

results which are much lower than the experiments in the conical nose region. The experiments also show larger variation in the skin friction, generally. The BLM of the two methods gives the better reproduction of the trends.

Figure 11 shows the velocity profiles at various  $X$  stations. The calculated and measured velocity profiles agree reasonably well at  $X/L=0.4$  where the pressure gradient reverses from favourable to adverse. At  $X/L=0.475$  which is the beginning of the adverse pressure gradient, the agreement between the calculations and the experiment is still reasonable. However, for the further downstream stations at  $X/L=0.55$  and  $0.7$  the discrepancies between the calculated and the measured profiles are large. The computed profiles appear to be more sensitive to the pressure gradient than are the experimental ones, perhaps indicating an overestimate of the Reynolds stresses by both turbulence models. The calculated profiles at  $X/L=0.833$  which are in the second favourable pressure region again agree reasonably well. However, at the last station at  $X/L=0.983$  the disagreement among the profiles are large although this is also close to the model trailing edge. The discrepancy between the two models, the BLM and JKM, are relatively small when compared with the discrepancy with the calculated and the measured results.

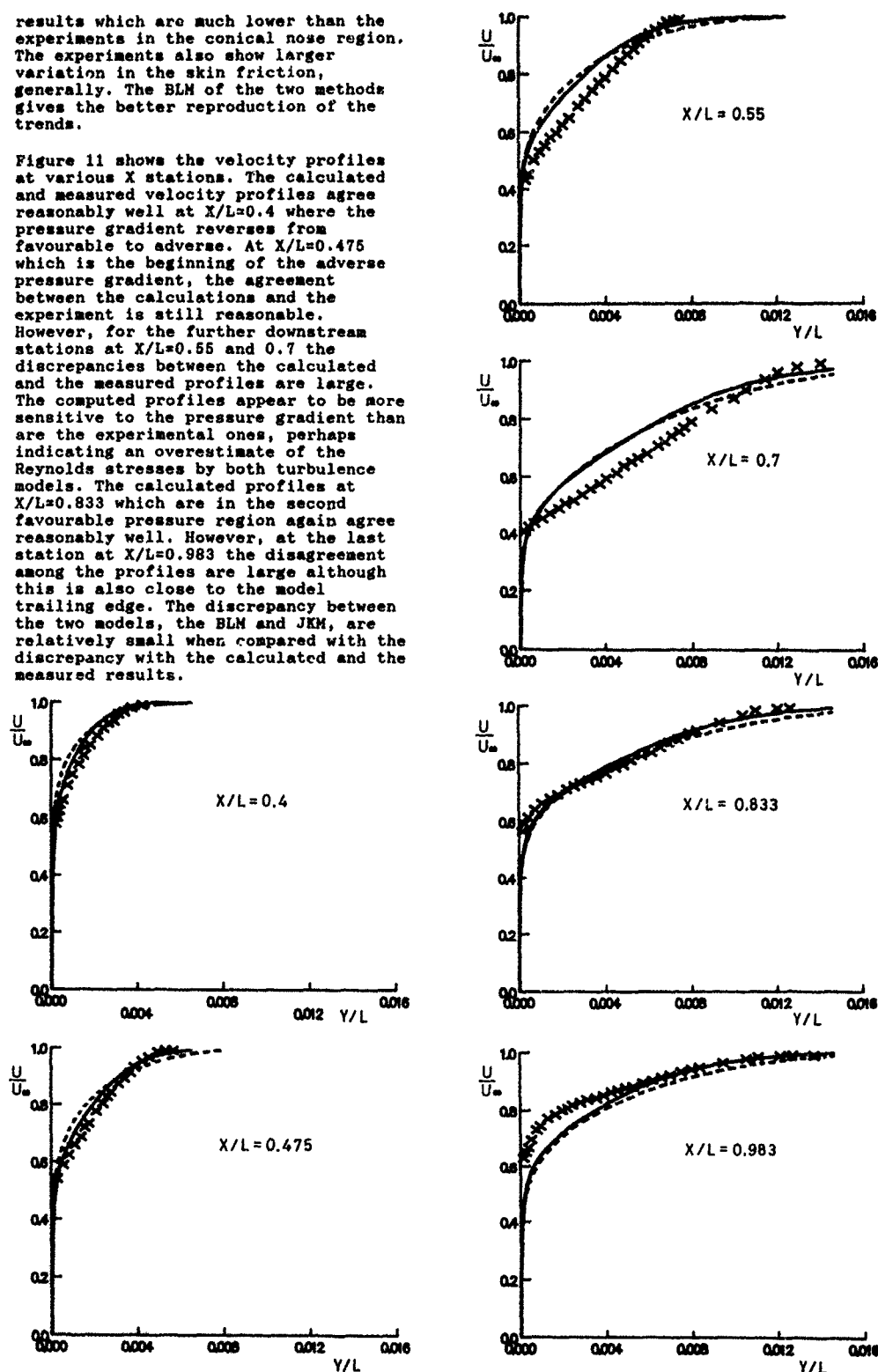


FIGURE 11. Velocity profile comparison between BLM, JKM and experiment. (For notation see FIGURE 8.)

It is still too early in the study to give definite comments on the JKM calculations and is not clear yet why the history effect included in the JKM does not give a better representation than the simpler BLM. A further study should be carried out with progressively severer pressure gradient, but it may be very difficult to find suitable experimental cases.

#### 6 CONCLUDING REMARKS

A computer code to calculate laminar and turbulent flows around projectile shaped body has been developed. The code underwent rigorous step by step validation stages. All of the validation tests against analytical results have given confidence with the code. However, it became more difficult to validate turbulent flows, especially with pressure gradient, because of the difficulties in finding appropriate and reliable experimental cases. The code has been tested with the waisted body of Winter et. al. This body seems to be ideal for testing the code and its turbulence models in non-separated flows. In the present study both Baldwin-Lomax and Johnson-King turbulence models are used. Both models produced very similar results, and are in reasonable agreement with the experiments, although we consider that extensive validations are still required for flows with pressure gradient.

#### 7 ACKNOWLEDGEMENT

This work has been carried out with the support of (RARDE) Procurement Executive, Ministry of Defence.

#### 8 REFERENCES

1. Warming, R.F. and Beam, R.M., "Upwind Second Order Difference Scheme and Applications in Aerodynamic Flows", AIAA Journal, 14, 9, 1976, p. 1241.
2. Baldwin, B.S. and Lomax, H., "Thin Layer Approximation and Algebraic Model for Separated Turbulent Flows", AIAA Paper 78-0257, 1978.
3. Johnson, D.A. and King, L.S., "A Mathematically Simple Turbulence Closure Model for Attached and Separated Turbulent Boundary Layers", AIAA Journal, Vol. 23, 1985, p 1684.
4. Winter, K.G., Rotta, J.C. and Smith, K.G., "Studies of the Turbulent boundary layer on a Waisted Body of Revolution in Subsonic and Supersonic Flow", ARC R & M no. 3633, 1970.
5. Van Driest, "Investigation of Laminar Boundary Layer in Incompressible Fluids using the Crocco Method", NACA Tech. Note 2557, 1952.
6. Mabey, D.G., Meier, H.U. and Sawyer, W.G., "Experimental and Theoretical Studies of the Boundary Layer on a Flat Plate at Mach Numbers from 2.5 to 4.5", RAE Tech. Report 74127, 1974.



# SUPERSONIC TACTICAL MISSILE COMPUTATIONS USING EULER'S EQUATIONS WITH CROSSFLOW SEPARATION MODELING

F. J. PRIOLO and A. B. WARDLAW, JR.

Aerospace Engineers  
Information and Mathematical Sciences Branch  
NAVAL SURFACE WARFARE CENTER  
White Oak, Silver Spring, Maryland 20903-5000  
USA

## ABSTRACT

The space-marching Euler solver, ZEUS, is coupled with a separation model to predict the fully three-dimensional separated flows for supersonic tactical missiles. ZEUS incorporates a multiple zone, gridding technique and a second-order extension of Godunov's method. The separation model assumes a vortex sheet leaves the surface at the experimentally observed separation point. Computations are performed on missiles which have bodies of circular and elliptic cross sections at incidences high enough to exhibit boundary layer separation. Results show that the separation model was most effective in improving predictions on missiles with circular bodies at Mach numbers below 3.5; but, at higher Mach numbers, predicted loads are not significantly affected. Qualitatively, calculated and measured flow field structures exhibit improved agreement which increases the accuracy of the predicted body and fin loads, however, quantitative flow field differences remain. For elliptic bodies, inviscid solutions are in close agreement with measured surface pressures except near the shoulder where calculations display a crossflow shock. Inclusions of the separation model diminishes the strength of the inviscid crossflow shock in the vicinity of the shoulder but has little influence on the missile loads.

## NOMENCLATURE

$A^k$	area of control volume edge lying in the $x = x^k$ plane.
$d$	diameter
$C_M$	pitching moment coefficient, (pitching moment / $q_\infty S L$ )
$C_N$	normal force coefficient, (normal force / $q_\infty S$ )
$C_{N,fin}$	fin normal force coefficient
$C_l$	rolling moment coefficient, (rolling moment / $q_\infty S d$ )
$C_p$	pressure coefficient, $(p - p_\infty) / q_\infty$
$C_v$	side force coefficient, (side force / $q_\infty S$ )
$\vec{F}$	flux vector [Eqs. (1)]
$H_0$	stagnation enthalpy
$L$	reference length
$M_\infty$	free stream Mach number
$\vec{n} = (n_x, n_y, n_z)$	vector normal to the cell edge [Eqs. (1)]
$ \vec{n} $	cell edge area
$p$	pressure
$q_\infty$	free stream dynamic pressure
$R_\pm$	upper and lower supersonic streams for the Riemann problem (Fig. 3)
$S$	reference area
$s$	wall cell immediately windward of the crossflow separation point (Fig. 2)
$\vec{U}$	flux vector [Eqs. (1)]
$(u, v, w)$	Cartesian velocity components
$(x, y, z)$	Cartesian coordinates with $z$ along the missile axis
$\alpha$	angle of attack (degrees)
$\beta_a, \beta_c$	axial and crossflow plane angles defining the streamline direction immediately leeward of the separation point (Fig. 2)
$\delta$	canard deflection angle, positive with leading edge up
$\delta_f$	flow direction angle (Fig. 3)
$\gamma$	ratio of specific heats

$\kappa'$	difference limiter [Eqs. (3)]
$\phi$	crossflow plane angle measured clockwise from the leeward pitch plane
$\phi_a, \phi_c$	axial and crossflow plane angles defining the streamline direction immediately windward of the separation point (Fig. 2)
$\rho$	density
Subscripts	
$n, m, k$	cell center (Fig. 4)
1, 2, 3, 4	canard panel number as defined in Fig. 10
$\infty$	ambient conditions

## 1. INTRODUCTION

The inviscid shock layer for tactical missiles in supersonic flight can be approximated by numerically solving the Euler equations. This approach does not depend on an extensive data-base such as semi-empirical methods and other traditional predictive methods. Solutions to the Euler equations provide detailed flow field properties, aerodynamic coefficients and load distributions. For missiles in supersonic flight, Euler's equations are best solved using a space-marching procedure. Under these conditions, the equations are hyperbolic, and the missile's flow field can be determined from known flow conditions at a cross-sectional plane near the nose tip which is marched down the length of the missile. Euler's equations can convect vorticity and determine the circulation generated by shocks; but, viscous phenomenon, such as vortex shedding from the surface of smooth bodies, must be empirically modeled.

The prediction of flow separation and the formation of vortices is important for an effective treatment of tactical missiles. Vortices exert a significant and non-linear influence on missile aerodynamics. They are generated by sharp lifting surfaces and from body boundary layer separation. Changes in incidence alter the vortex trajectories as well as the number of vortices present, as shown in Fig. 1. The penalties for neglecting separation for missile shapes are poor force and moment predictions on circular bodies and fins. To remedy this situation, body boundary layer separation can be simulated by modifying boundary conditions near the experimentally observed separation line.

Vortex shedding from smooth bodies in inviscid flows has been studied for many years. Smith<sup>1,2</sup> developed a model in which vortex sheets are shed into otherwise irrotational flow;

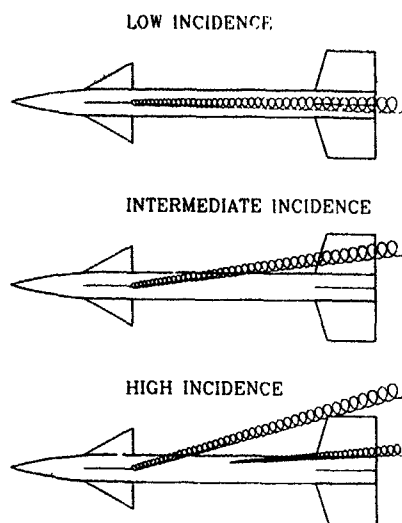


Figure 1. Vortex structures in a tactical missile flow field at different incidences.

however, this model was restricted to conical flow. The discrete vortex method of Mendenhall<sup>3</sup> predicted both symmetric and asymmetric vortex shedding from bodies at incidence. Fiddes<sup>4</sup> incorporated Smith's model to conical flow by using slender body theory for the irrotational flow and fitting the complex spiraling vortex sheets with point vortices.

In addition to potential flows, separation modeling has also been used in conjunction with Euler's equations. These separation models are usually based on the assumption that a slip surface leaves the body along the separation line. The velocity normal to this surface is zero, and across this surface, the pressure is continuous but other variables may not be. Also, the separation line is prescribed empirically.

One method of implementing this type of separation model, suggested by Klopfer and Nielsen<sup>5</sup> for tangent ogive bodies, does not try to capture property jumps across the slip surface. Here, the pressure and density at the separation point are determined by interpolation which, together with the constant total enthalpy constraint, allow the velocity magnitude to be ascertained. The velocity direction is empirically prescribed (at a constant circumferential angle) which completes the definition of the properties at the separation point. This approach has been applied to missile shapes by Wardlaw et al.<sup>6</sup> and Guillen and Lordon<sup>7</sup> where the separation line lies between grid points and the velocity vector is aligned with the separation line. In a similar vane, Kwong and Myring<sup>8</sup> have developed a forced separation model coupled with a time-dependent Euler solver and have applied this to bodies of revolution. In this model, the vortex sheet is assumed to leave the surface at the experimentally observed separation point. At the cells adjacent to the wall immediately upstream and downstream of the separation point, a velocity jump is imposed across the vortex sheet with mean values computed for the pressure and density. The velocity components are determined at each of the two cells by prescribing a streamline direction, as shown in Fig. 2, and imposing the constant total enthalpy condition. Away from the surface, the vortex sheet is captured by the numerical scheme (see Sect. III for more details).

A second method, developed by Marconi,<sup>9,10</sup> uses Smith's model together with the Euler equations to predict separated flow on conical bodies at supersonic speeds. This method captures the tangent velocity and entropy jump across the slip surface. Along the body, the slip surface is modeled using a double point at the separation location. The point representing the windward side of the slip surface is computed using the Euler equations differenced in a one-sided manner away from the separation surface. At the leeward point, the crossflow velocity is set to zero, and a small pressure plateau is imposed

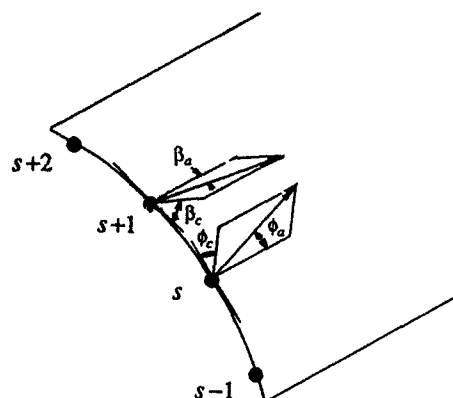


Figure 2. Flow angle parameters in 3-D forced separation model.<sup>8</sup>

along the surface leeward of the separation point. Both primary and secondary separation are modeled.

Another approach to separation modeling is the clipping technique of Baltakis et al.<sup>11</sup> Here, separation is allowed to occur in conformance with the leeward circulation level. This circulation is introduced by limiting (i.e. setting an upper bound) the crossflow velocity near the surface.

The separation models described above produce a qualitatively correct picture of the flow field for circular bodies. However, the ability of separation models to quantitatively define the flow field remains to be demonstrated.

In the present study, the separation model of Kwong and Myring (Ref. 8) is incorporated into the space-marching Euler solver, ZEUS.<sup>12-16</sup> ZEUS is applied to various tactical missile shapes and is evaluated for its ability to predict measured surface pressures and flow field profiles. Computations are performed on missiles which have bodies of circular or elliptic cross sections at incidences high enough to exhibit boundary layer separation. Results are compared with measured surface pressures, flow field profiles, and force and moment data, as well as some of the previous work of Refs. 8-11. A brief description of the ZEUS computational algorithm is provided in Sec. II, and an outline of the forced crossflow separation model is given in Sec. III. Sec. IV discusses results while Sec. V outlines conclusions drawn from this study.

## II. COMPUTATIONAL PROCEDURE

The ZEUS code combines a multiple zone gridding technique with a second order extension of Godunov's method, an upwind scheme based on the Riemann problem for steady supersonic flow. It is cast in control volume form and consists of a predictor and corrector step. The predictor step advances the primitive variables using Euler's equations in non-conservation form. Derivatives are computed using a limited central differencing procedure. The corrector step modifies Godunov's method by assuming linear property variations within each control volume. This program is devoid of explicit artificial viscosity and is robust.

Some details of ZEUS are given below with a more elaborate description found in Refs. 13 and 14.

### A. ZONE STRUCTURE

The ZEUS program uses a multiple zone structure which provides a convenient framework from which to compute shapes having sharp edged fins. The crossflow plane is

divided into several quadrilateral zones, and a simple, separate transformation is applied to each. Zone boundaries are taken to coincide with the body, canard and tail surfaces, and the bow shock allowing fin thickness and fin deflections to be accurately modeled.

### B. NUMERICAL SCHEME

For steady supersonic flow, the Riemann problem represents the confluence of two, two dimensional supersonic streams, as illustrated in Fig. 3. At the point of intersection, shocks or expansion fans form which turn both streams to a common direction. The two final streams need not feature the same density or velocity, and a slip line generally forms between them. The direction of the slip line is the one producing the same pressure in both streams. If the two streams forming the Riemann problem have similar properties, a closed form linear solution can be obtained. Alternatively, an approximate Riemann problem<sup>17</sup> can be constructed which has a closed form solution.

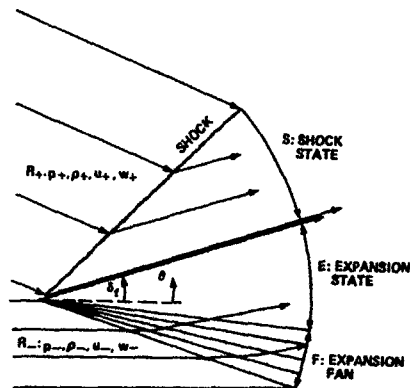


Figure 3. The supersonic Riemann problem consists of two intersecting supersonic streams,  $R_+$  and  $R_-$ .

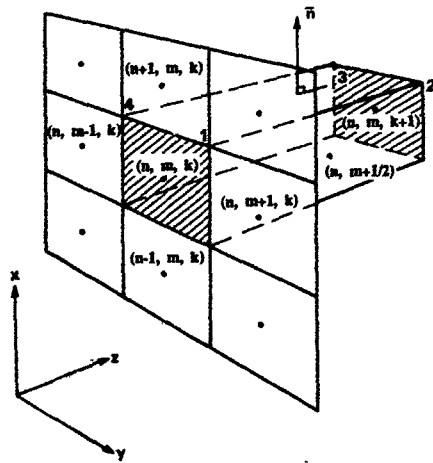


Figure 4. Control volume nomenclature.

Using the notation of Fig. 4, mass and momentum conservation through a control volume can be expressed as:

$$\bar{U}_{n,m}^{k+1} = \bar{U}_{n,m}^k - \bar{F}_{n+\frac{1}{2},m} + \bar{F}_{n-\frac{1}{2},m} - \bar{F}_{n,m+\frac{1}{2}} + \bar{F}_{n,m-\frac{1}{2}} \quad (1a)$$

where:

$$\bar{U}_{n,m}^k = A_{n,m}^k \begin{bmatrix} \rho w \\ \rho w^2 + p \\ \rho w u \\ \rho w v \end{bmatrix}_{n,m} \quad (1b)$$

$$\bar{F}_{n+\frac{1}{2},m} = \begin{bmatrix} \rho V \\ \rho w V + n_x p \\ \rho u V + n_y p \\ \rho v V + n_z p \end{bmatrix}_{n+\frac{1}{2},m} \quad (1c)$$

$$V = \bar{n}_{n+\frac{1}{2},m} \cdot (u, v, w)_{n+\frac{1}{2},m} \quad (1d)$$

Here,  $\bar{U}$  is the flux in the  $z$ -direction which passes through the shaded cell ends while the  $\bar{F}$ 's are the fluxes associated with the remaining cell edges. Equations (1) are closed using the constant total enthalpy condition and the perfect-gas equation of state that yield the constraint

$$H_0 = \frac{p}{\rho(\gamma-1)} + \frac{1}{2}(u^2 + v^2 + w^2) \quad (2)$$

The ZEUS code integrates Euler's equations using a second order Godunov method. Godunov's original method<sup>18</sup> is first order accurate and usually cast in a control volume form. Properties within each cell are assumed constant and fluxes  $\{\bar{F}\}$  appearing in Eq. (1) at cell edges are calculated using the Riemann problem.

Godunov's method is extended to second order by adding a predictor step to determine properties at  $z^k + \Delta z/2$  and linearly extrapolating these properties to the cell edge. The property slopes for both the predictor step and the linear extrapolation are computed using limited differences which prevent oscillations near shocks. These differences are calculated in the following manner:

$$\frac{\partial f}{\partial \xi} = \begin{cases} 0 & \text{if } c_1 < 0 \\ c_2 & \text{if } c_1 \geq 0 \end{cases} \quad (3a)$$

where:

$$c_1 = (f_{n+1,m} - f_{n,m})(f_{n,m} - f_{n-1/2}) \quad (3b)$$

$$c_2 = \frac{\text{sgn}(f_{n+1,m} - f_{n,m})}{\Delta \xi} \min \left\{ \frac{|f_{n+1,m} - f_{n-1,m}|}{2}, \kappa' |f_{n+1,m} - f_{n,m}|, \kappa' |f_{n,m} - f_{n-1,m}| \right\} \quad (3c)$$

Here,  $f$  is some dependent variable differentiated with respect to some independent variable  $\xi$  and  $1 \leq \kappa' \leq 2$ .

Near shocks and other discontinuities, the limiter reduces all slopes to zero and the scheme collapses to the first order Godunov method.

### C. BOUNDARY CONDITIONS

ZEUS is based on a finite volume formulation. Therefore, grid points do not lie on the boundary, but rather the cells adjacent to the wall have an edge lying along the boundary. Properties along cell edges adjacent to the wall are computed by extrapolating predicted properties to the wall using the cell slope normal to the wall. These edge properties do not satisfy the tangent flow boundary conditions and must be turned using either an oblique shock or Prandtl-Meyer expansion to satisfy the wall boundary conditions. The flow is tangent to the wall, and only the post-turn pressure influences the flux at the edge lying on the wall.

The outer zone boundary is determined by tracking the domain of dependence of the numerical solution using information contained in the Riemann problem.

### D. SPECIAL PROCEDURES

Artificial viscosity and other special procedures are not required by the ZEUS code. However, free parameters do occur in the difference limiters. In the program,  $\kappa'$  of Eqs. (3) is set to 0 at cells next to fin surfaces, 1 at interior cells and 2 at boundary cells in smooth flow regions. These values of  $\kappa'$  do not require adjustment from one problem to the next.

### III. CROSSFLOW SEPARATION MODELING

The separation model of Ref. 8 is incorporated into the ZEUS program to model boundary layer separation for bodies of revolution. At large Reynolds numbers, the separated boundary layer can be regarded as a vortex sheet embedded in an inviscid flow. Therefore, this model is constructed based on the following physical conditions for a vortex sheet:

1. zero velocity component normal to the sheet
2. continuous pressure across the sheet
3. constant total enthalpy for steady flow
4. a jump in tangential velocity across the sheet

In the crossflow plane, the separation model is applied to the wall cells  $s$  and  $s+1$  which are immediately windward and leeward of the separation point, respectively, as shown in Fig. 2. Here, the vortex sheet is assumed to leave the surface at the experimentally observed separation point lying between cells  $s$  and  $s+1$ . A velocity jump is imposed across the vortex sheet with mean values of the fluid properties computed at the two cells in the following manner:

$$F_s = \frac{1}{2} (F'_{s-1} + F'_{s+1}) \quad (4a)$$

$$F_{s+1} = \frac{1}{2} (F'_s + F'_{s+2}) \quad (4b)$$

Here,  $F$  denotes either  $p$  or  $\rho$ . The  $+$  and  $-$  subscripts denote the leeward and windward directions, respectively. The  $'$  superscripts denote old values.

The flow velocities are determined at each of the two cells by prescribing a streamline direction and imposing the constant total enthalpy constraint. The direction of the streamline at the wall cell on the windward side (cell  $s$ ) of the separation line is specified by the angles,  $\phi_a$  and  $\phi_c$ , as shown in Fig. 2. Similarly, at the wall cell on the leeward side (cell  $s+1$ ), the streamline is specified by the angles,  $\beta_a$  and  $\beta_c$ . Once this vortex sheet has left the body surface, it is captured by the numerical scheme.

### IV. COMPUTED RESULTS AND DISCUSSION

The ZEUS program, coupled with the separation model of Ref. 8, has been applied to missile-shaped bodies of circular and elliptic cross sections. Calculations included bodies alone and bodies with lifting surfaces. Results were achieved using

a marching step size of 90% of the CFL limit. In some cases, mesh effects were compared by halving and doubling the mesh size. Computations featuring canards or a tail were run using multiple zones; otherwise, a one zone model was employed. The streamline angles,  $\phi_c$ ,  $\phi_a$ ,  $\beta_a$ ,  $\beta_c$  were taken as  $20^\circ$ ,  $20^\circ$ ,  $20^\circ$  and  $5^\circ$ , respectively.

### A. BODIES ALONE

Experiment and computations for a tangent-ogive/cylinder body<sup>19</sup> with a nose fineness ratio of 4 and a length of 7 calibers are shown in Figs. 5-7 for  $M_\infty = 3.5$ ,  $4.0$  at  $\alpha = 10^\circ$ ,  $15^\circ$ . The measured flow field and surface pressure distributions at  $M_\infty = 3.5$  and  $\alpha = 10^\circ$  are illustrated in Fig. 5. A crossflow shock is located on the leeside of the body followed by a vortex which is primarily the product of boundary layer separation. The  $10^\circ$  incidence curve is marked with letters A, B and C.

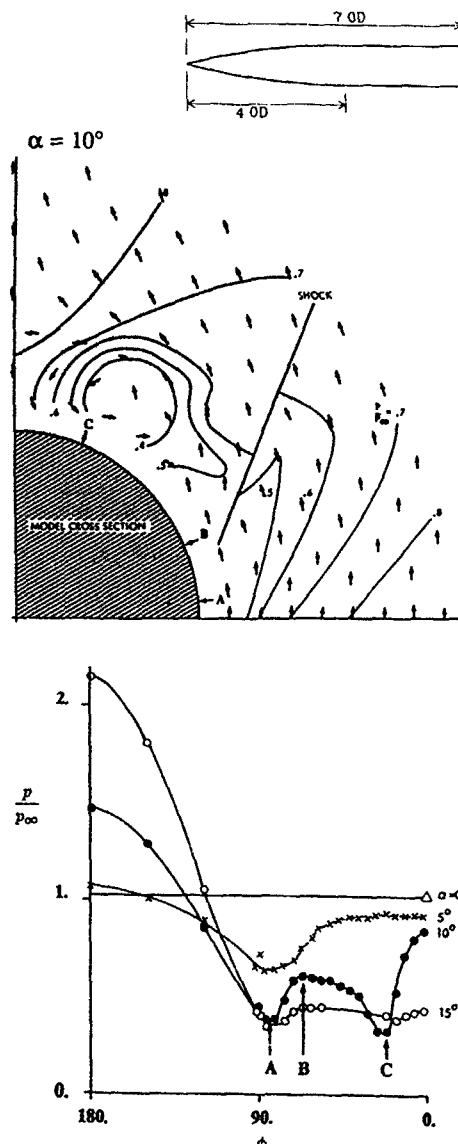


Figure 5. Measured<sup>19</sup> crossflow plane isobars and velocity directions on the leeside of a tangent-ogive/cylinder for  $M_\infty = 3.5$ ,  $\alpha = 10^\circ$  and  $z/d = 6.5$ . Measured surface pressure distribution is also shown at various incidences.

By comparing both figures, it is evident that the rise in surface pressure between points A and B occurs beneath the crossflow shock. Separation occurs downstream of the crossflow shock, and beneath the vortex at point C, a suction peak forms. This suction peak diminishes as the vortex lifts off the body with increasing incidence or distance down the body, as indicated by the  $\alpha = 15^\circ$  curve. By contrast, the calculated inviscid flow field at  $\alpha = 15^\circ$ , overlaid on the experimental data as shown in Fig. 6, exhibits a crossflow shock which is too far leeward followed by a vortex that is too small. As illustrated in Fig. 7, application of the separation model produces a leeward flow field dominated by a large vortex which brings the calculated flow field structure into qualitative agreement with experiment. However, quantitative differences remain. The computed vortex is miss-located, and the crossflow shock, visible in the experiment, is missing from the computed flow field. Computed surface pressures, which are also shown in Fig. 7, agree closely with experiment only on the windward side of the body. However, the separation model reduces discrepancies elsewhere.

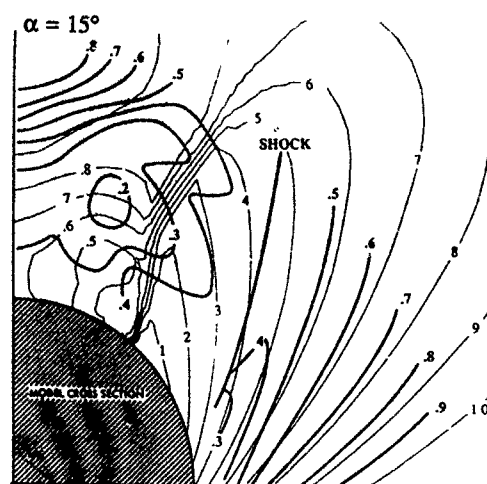


Figure 6. Computed (inviscid ZEUS, 72 x 72 mesh) and measured<sup>19</sup> crossflow plane isobars on the tangent-ogive/cylinder of Fig. 5 at  $M_\infty = 3.5$ ,  $\alpha = 15^\circ$  and  $z/d = 6.5$ .

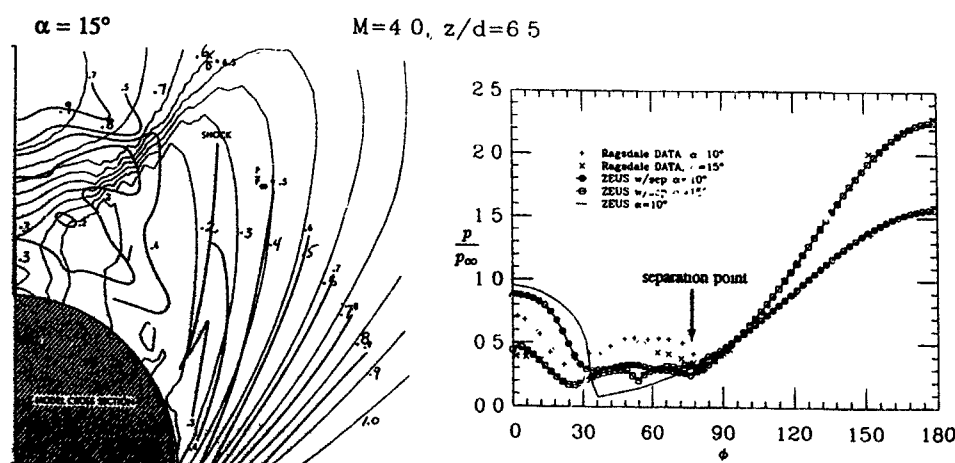
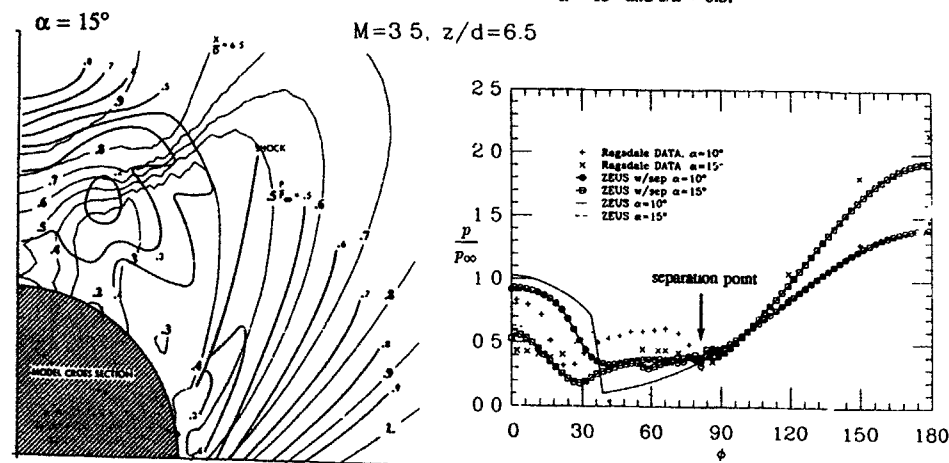


Figure 7. Computed (ZEUS w/separation model, 72 x 72 mesh) and measured<sup>19</sup> crossflow plane isobars on the tangent-ogive/cylinder of Fig. 5 at  $M_\infty = 3.5$  and  $4.0$ ,  $\alpha = 15^\circ$  and  $z/d = 6.5$ . Computed and measured surface pressure distributions are also compared for  $\alpha = 10^\circ$  and  $15^\circ$ .

The three-dimensional separated flow over a tangent ogive/cylinder body<sup>20</sup> with a nose fineness ratio of 3 and a length of 14.5 calibers was computed for  $M_\infty = 2.5$  at  $\alpha = 12^\circ$ ,  $16^\circ$  and  $M_\infty = 4.5$  at  $\alpha = 12^\circ$ . The separation line was estimated from the experimental surface pressure distribution by Hodges.<sup>20</sup> Fig. 8 illustrates surface pressure distributions at four axial stations for  $M_\infty = 2.5$  at  $\alpha = 16^\circ$ . Separated results are compared with experiment, inviscid ZEUS calculations and Ref. 8. As expected for all cases, the inviscid results agree well with experiment on the windside of the body; however, as the flow expands around the leeward of the body, the pressure decreases below measurement, and a crossflow shock occurs. With the separation model added, ZEUS computations typically emulate the viscous results in the vicinity of the separation

point. Leeward of the separation point, in the region under the main vortex, however, the pressures are somewhat under-predicted. At  $z/d = 8.5$ , computations with separation modeled display a vortex trapped near the surface and a reverse crossflow shock under the vortex as indicated by the arrow. The predicted vortex is too strong, as indicated by the large dip in the pressure distribution behind the reverse crossflow shock, which is not observed experimentally. Downstream at  $z/d = 14.5$ , however, this discrepancy subsides as the vortex lifts away from the surface. The vortex formation and lift off is illustrated in Fig. 9 at three axial stations using computed isobars. The primary vortex and the reverse crossflow shock locations are marked. A mesh dependency is seen in the leeward flow field using ZEUS. Similar results are observed for  $M_\infty = 2.5$ ,  $4.5$  at  $\alpha = 12^\circ$  which are not shown here.

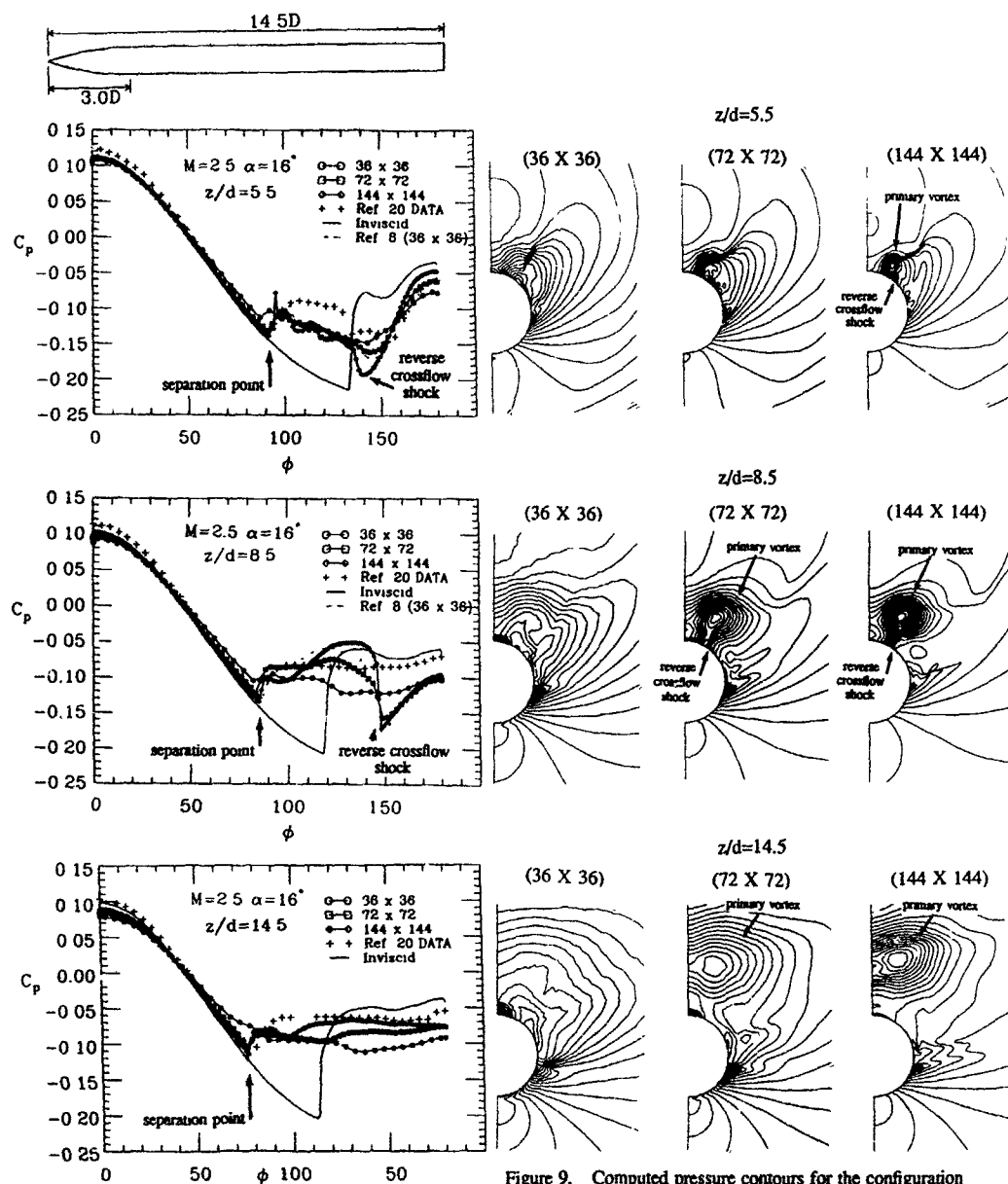
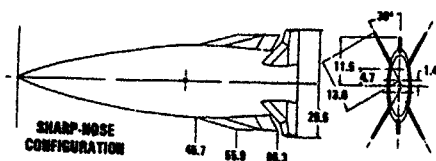


Figure 8. Surface pressure distribution for a three caliber tangent ogive/cylinder for  $M_\infty = 2.5$ ,  $\alpha = 16^\circ$  and  $z/d = 5.5, 8.5, 14.5$ . Results compare ZEUS with separation model, inviscid ZEUS, inviscid Euler<sup>8</sup> and measurement.<sup>20</sup> Windward plane is  $\phi = 0^\circ$ .

Figure 9. Computed pressure contours for the configuration of Fig. 8 for  $M_\infty = 2.5$  and  $\alpha = 16^\circ$  using ZEUS w/separation model. Computations are for a (36 x 36), (72 x 72) and (144 x 144) mesh at  $z/d = 5.5, 8.5$  and  $14.5$ . Note the primary vortex and reverse crossflow shock.

Figure 10. Monoplane elliptic missile configuration.<sup>21</sup>

Computations were performed on a model<sup>21</sup> with a 2:1 elliptic cross section, as shown in Fig. 10. Here, the separation line was estimated from the measured surface pressure distribution. Fig. 11 illustrates the surface pressure distribution at three axial stations at  $M_\infty = 2.5$  and  $\alpha = 20^\circ$ . Computed results, with and without the separation model, are compared with experimental data,<sup>21</sup> separated Euler calculations<sup>10</sup> and Navier-Stokes results.<sup>24</sup> Windward of the separation point ( $\phi \approx 90^\circ$ ), all methods are in good agreement. At the shoulder, both experiment and the Navier-Stokes calculation feature separation. This phenomenon is absent for the inviscid calculation which experiences a pressure over-expansion at the shoulder and a leeside crossflow shock. Improvements in the leeside pressure distribution near the shoulder are observed when separation modeling is included. Furthermore, the separated ZEUS results are in reasonable agreement with the separated solutions of Ref. 10 in predicting the leeside pressure plateau. At stations  $z/L = .6$  and  $.95$ , measured results and the Navier-Stokes solution

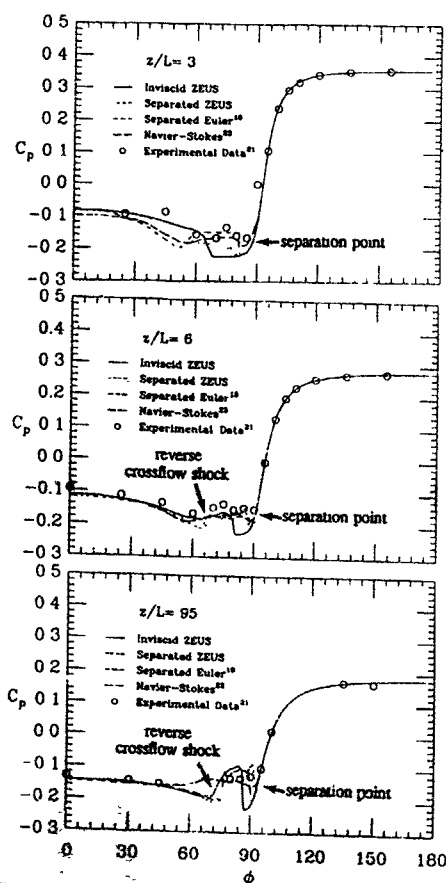
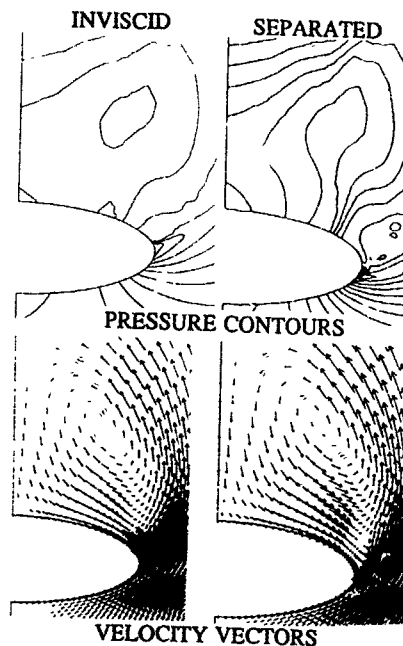
Figure 11. Computed and measured  $C_p$  vs.  $\phi$  for the body alone configuration of Fig. 10 at  $M_\infty = 2.5$ ,  $\alpha = 20^\circ$  and  $z/L = .3, .6, .95$ . Calculations are for ZEUS with and without separation, Euler with separation<sup>10</sup> and Navier-Stokes.<sup>24</sup>

exhibit leeside separation. On the other hand, for the Euler solutions, a sharp shock occurs at the primary separation point while a supersonic reverse crossflow shock appears beneath the vortex. A dip in the pressure distribution is observed behind the reverse crossflow shock which is similar to the results for the circular bodies. This suction peak indicates a predicted vortex which is too close to the surface. Separation modeling reduces the magnitude of the shock at the separation point, but the leeside vortex location is unaffected. Computed crossflow isobars and velocity vectors are illustrated in Fig. 12 for  $M_\infty = 2.5$ ,  $\alpha = 20^\circ$  and  $z/L = .95$ . Separation modeling only affects the solution near the primary separation point.

Figure 12. Computed pressure contours and velocity vectors for the body alone configuration of Fig. 10 at  $M_\infty = 2.5$ ,  $\alpha = 20^\circ$  and  $z/L = .95$ . Calculations are for ZEUS with and without separation modeling.

## B. FINNED BODIES

The missile shape<sup>22</sup> shown in Fig. 13 was computed at  $M_\infty = 2.5$  and  $3.5$ ,  $\alpha \leq 20^\circ$  and  $\phi = 0^\circ$ . The missile is characterized by a 2.25 caliber tangent ogive nose, a 3.7 caliber forebody and cruciform canards in line with a cruciform tail. Solutions were calculated using separation lines estimated at  $\phi = 90^\circ$  and  $270^\circ$ . These separation lines began behind the canards and terminated just ahead of the tail. The rolling moment and side force comparisons are illustrated in Fig. 13 with canards 2 and 4 asymmetrically deflected  $5^\circ$ . Comparisons are made with measured data<sup>22</sup> and inviscid ZEUS calculations.<sup>16</sup> Previously, inviscid ZEUS results indicated that non-linear trends of the  $C_l$  vs.  $\alpha$  curves were accounted for; however, discrepancies occurred between measured and calculated  $C_l$ , as shown in Fig. 13. This lack of agreement is likely a result of inappropriately computed body vortices. The inviscid solution generates such vortices by virtue of crossflow shocks instead of boundary layer separation which occurs in the viscous case. By modeling the appropriate mechanism for generating body vortices, i.e. using a body boundary layer separation model, improved accuracy in  $C_l$  and  $C_y$  is achieved, as shown in Fig. 13 for  $M_\infty = 2.5$ . At  $M_\infty = 3.5$ , inclusion of the separation model has little effect on computed  $C_l$  and  $C_y$ . Fig. 14 displays computed isobars and axial vorticity contours at two axial stations between the canards and the tail ( $z/L = 11$  and  $30$ ) at  $M_\infty = 2.5$ ,  $\alpha = 18^\circ$  with and without the separation model. Inclusion of the separation model eliminates the leeside crossflow shocks which alters the strengths and trajectories of the leeside body vortices.

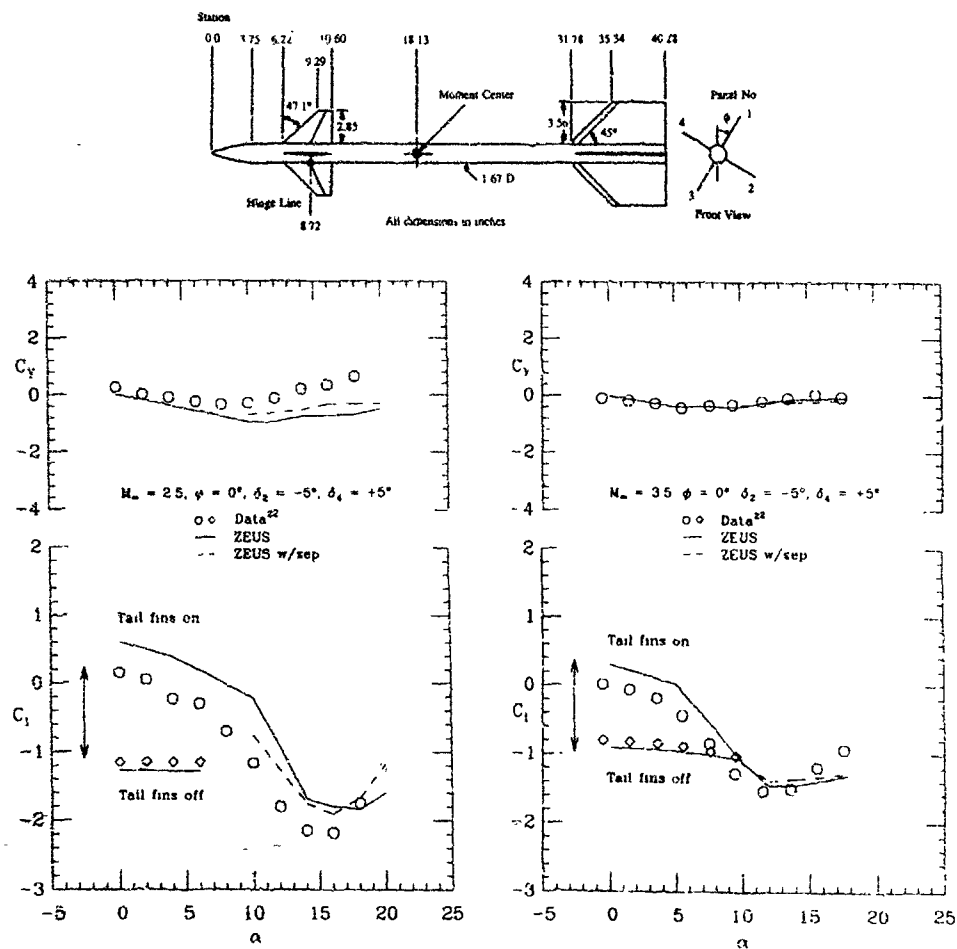


Figure 13. Computed and measured  $C_l$  vs.  $\alpha$  and  $C_y$  vs.  $\alpha$  for the canard/body/tail configuration<sup>22</sup> for  $M_\infty = 2.5$  and  $3.5$ ,  $\phi = 0^\circ$  and canards 2 and 4 deflected asymmetrically  $5^\circ$ .

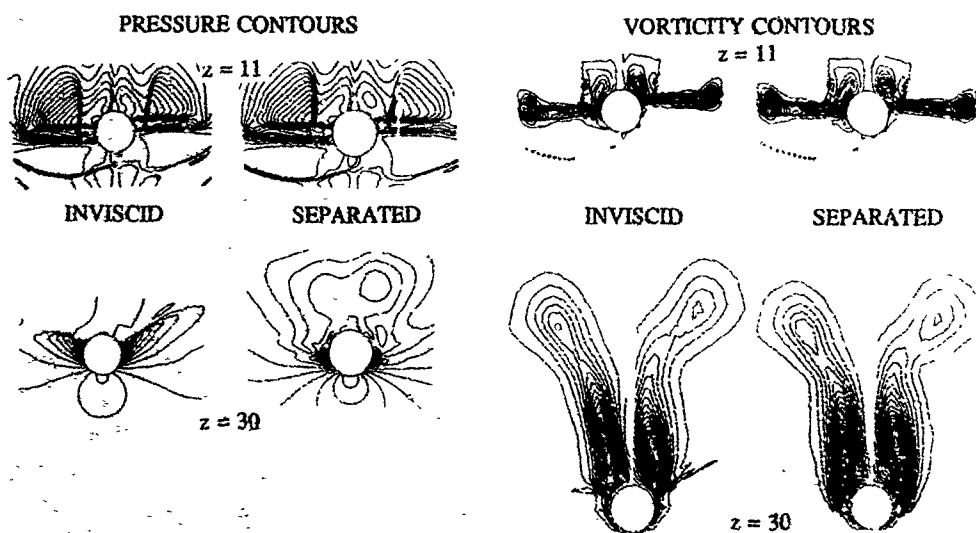


Figure 14. Computed pressure and axial vorticity contours for the configuration of Fig. 13 (looking downstream) with canards 2 and 4 deflected asymmetrically  $5^\circ$  for  $M_\infty = 2.5$ ,  $\phi = 0^\circ$  and  $\alpha = 18^\circ$  at  $z = 11$  and  $30$ . Calculations are for ZEUS with and without separation modeling.



Fig. 15 compares measured and computed  $C_{N_{fin}}$  as a function of roll angle on a body-tail missile<sup>23</sup> at  $M_{\infty} = 2$  and  $4.5$  and  $\alpha = 10^\circ$ . The model, which is shown in Fig. 15, is characterized by a nose fineness of 3, a body length of 12 calibers and fins with a span of 5 calibers. The separation line for these calculations was estimated from the measured data of Hodges<sup>20</sup> for a tangent ogive body with a nose fineness of 3. At  $M_{\infty} = 2$ , inviscid computations on circular bodies produce a crossflow shock not present in experiment. As a result, the inviscid fin load calculations over-predict experiment especially on the leeward side of the body. By modeling crossflow separation and, thus, more accurately computing the leeward vortices, improved fin load predictions are obtained on the leeward side of the body. At  $M_{\infty} = 4.5$ , the inviscid leeward fin force predictions only slightly over-estimate experiment. Inclusion of the separation model marginally improves computed fin loads; however, the change in sign of the fin force at  $165^\circ$  is well predicted.

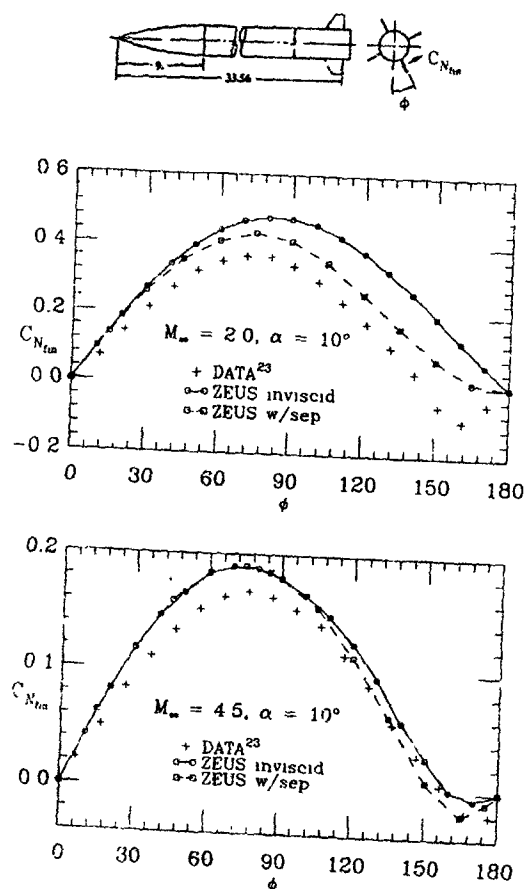


Figure 15. Computed and measured  $C_{N_{fin}}$  with the fin at various roll positions for the body/wing configuration.<sup>23</sup> Conditions are for  $M_{\infty} = 2$  and  $4.5$  at  $\alpha = 10^\circ$ . Calculations are for ZEUS with and without separation modeling.

Fig. 16 compares measured and computed  $C_{N_{fin}}$  as a function of roll angle for a body-tail missile<sup>20</sup> with twice the tail span as the model in Fig. 15. This model has an overall length of 13 calibers, a nose fineness of 3 and fins with a span of 1.0 caliber. Ambient conditions are  $M_{\infty} = 3.5$  and  $\alpha = 12^\circ$ . The separation line is estimated from the experimental surface pressure distribution of Hodges<sup>20</sup>. Computed and measured fin loads agree well on the windward side of the body; however, inviscid fin load calculations are higher than experiment on the leeward side of the body in the vicinity of the body vortices. Inclusion of the separation model improves the computed fin loads in this region. Fig. 17 illustrates  $C_l$  as a function of roll angle for the model of Fig. 16. Inviscid computations and experiment are in reasonable agreement over the full range. Therefore,  $C_l$  predictions are only slightly improved when the separation model is applied. Comparison of the results in Figs. 15-17 suggests that better results are obtained on fins with larger spans. An increased fin span diminishes the portion of the fin which is influenced by the boundary layer.

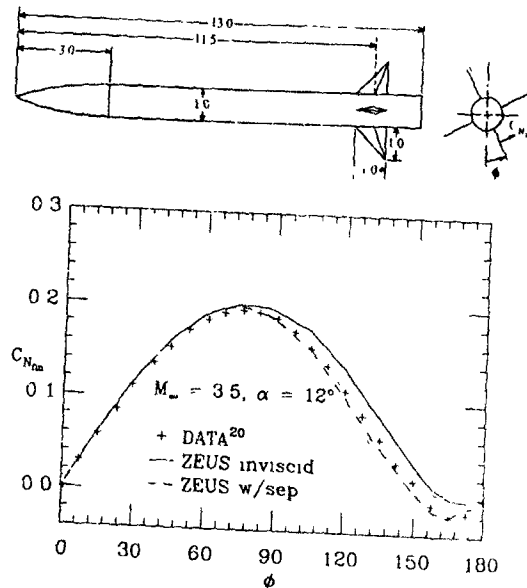


Figure 16. Computed and measured  $C_{N_{fin}}$  with the fin at various roll positions for the body/wing configuration.<sup>20</sup> Conditions are for  $M_{\infty} = 3.5$  at  $\alpha = 12^\circ$ . Calculations are for ZEUS with and without separation modeling.

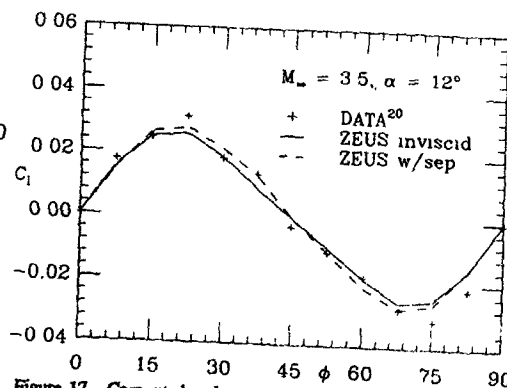


Figure 17. Computed and measured  $C_l$  with the fin at various roll positions for the configuration of Fig. 16. Conditions are for  $M_{\infty} = 3.5$  at  $\alpha = 12^\circ$ . Calculations are for ZEUS with and without separation modeling.

Finally, computations were performed on the elliptic body<sup>21</sup> of Fig. 10 with the lifting surfaces. Predicted surface pressures with and without separation modeling, shown in Fig. 18, compare favorably. This suggests that the inclusion of the wings and the tail has a dominate effect on the leeside flowfield which leads to the minimal influence of the separation model. This is further illustrated by the crossflow isobars and velocity vectors in Fig. 19. Addition of the separation model changes  $C_N$  and  $C_M$  by less than 1% (not shown here).

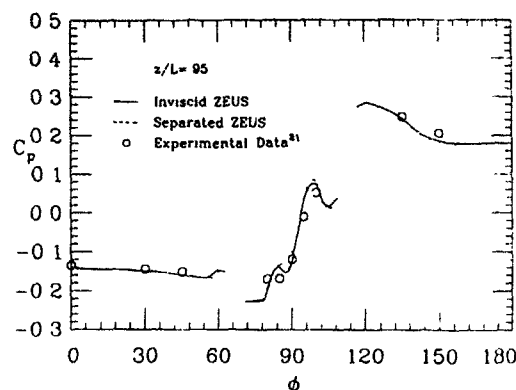


Figure 18. Computed and measured  $C_p$  vs.  $\phi$  for the body/wing/tail configuration of Fig. 10 at  $M_\infty = 2.5$ ,  $\alpha = 20^\circ$  and  $z/L = .95$ . Calculations are for ZEUS with and without separation modeling.

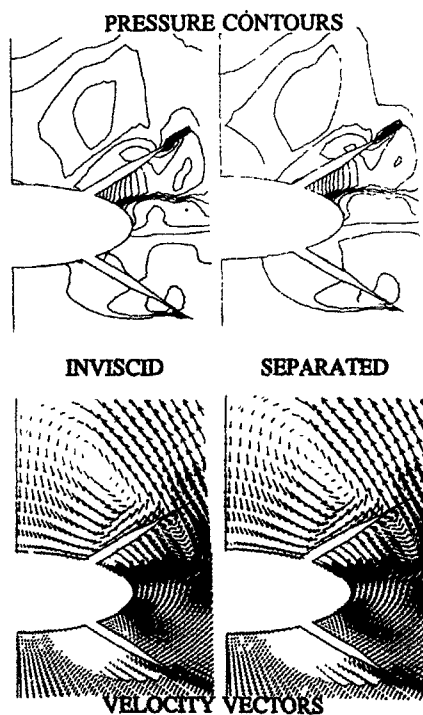


Figure 19. Computed pressure contours and velocity vectors for the body/wing/tail configuration of Fig. 10 at  $M_\infty = 2.5$ ,  $\alpha = 20^\circ$  and  $z/L = .95$ . Calculations are for ZEUS with and without separation modeling.

## V. CONCLUSIONS

A separation model has been coupled to a space marching Euler code and applied to missiles with circular and non-circular bodies. The separation model was most effective in improving predictions on missiles with circular bodies at Mach numbers below 3.5. An examination of the calculated flow field indicates that the separation model destroys the crossflow shock, which occurs in the inviscid calculation, and produces a large leeside vortex bringing the computed flow field structure into qualitative agreement with experiment. This improved flow field description increases the accuracy of the predicted body and fin loads. However, quantitative differences remain between the predicted and measured flow field. At higher Mach numbers a similar change in flow field structure is introduced by the separation model. Here, pressures on the leeside of the model are low, and the predicted loads are not significantly affected by the separation model.

Inviscid predictions for missiles with elliptic bodies (minor axis parallel to the pitch plane) agree well with experiment even in the absence of a separation model. Here, the crossflow shock, which develops in the inviscid solution, is located near the shoulder ( $\phi = 90^\circ$ ) as is the experimentally observed separation point. Predicted and measured surface pressures are in close agreement except near the shoulder where the inviscid predictions are much lower than experiment. This discrepancy is caused by an expansion at the shoulder, followed by a crossflow shock which occurs in the inviscid solution. Experimentally, these phenomena are replaced by boundary layer separation. The separation model diminishes the strength of the crossflow shock and increases the pressure in this region but has little influence on the missile loads.

## REFERENCES

1. Smith, J. H. B., "Remarks on the Structure of Conical Flow," *Progress in Aeronautical Sciences*, Vol 12, 1972, pp. 241-271.
2. Smith, J. H. B., "Theoretical Modeling of Three-Dimensional Vortex Flows in Aerodynamics," *Aeronautical Journal*, 1984, pp. 101-116.
3. Mendenhall, M. R., "Predicted Vortex Shedding From Noncircular Bodies in Supersonic Flow," AIAA Paper 80-1559, 1980.
4. Fiddes, S. F., "A Theory of the Separated Flow Past a Slender Cone at Incidence," AGARD CP-291, 1981, pp. 30-1 to 30-14.
5. Klopfer, G. H. and Nielsen, J. N., "Euler Solutions of the Body Vortices of Tangent Ogive Cylinders at High Angles of Attack and Supersonic Speeds," AIAA Paper 81-0361, Jan. 1981.
6. Wardlaw, A. B. Jr., Baltakis, F. P., Solomon, J. M. and Hackerman, L. B., "An Inviscid Computational Method for Tactical Missile Configurations," NSWC TR 81-457, Dec. 1981.
7. Guillen and Lordon, "Numerical Simulation of Separated Supersonic Flows About Tactical Missile Bodies," AGARD CP-437, Paper 23, 1988.
8. Kwong, C. M. and Myring, D. F., "Fusiform-Body Separated Flow Field Calculation Using Euler and Boundary Layer Equations," Royal Aeronautical Society Conference on the Prediction and Exploitation of Separated Flows, Paper No. 27, April 1989.
9. Marconi, F., "The Spiral Singularity in the Supersonic Inviscid Flow Over a Cone," AIAA Paper 85-1665, 1985.
10. Marconi, F., "Fully Three-Dimensional Separated Flows Computed With the Euler Equations," AIAA Paper 87-0451, Jan. 1987.
11. Baltakis, F. P., Wardlaw, A. B. Jr. and Allen, J. M., "Leeside Crossflow Modeling in Euler Space-Marching Computations," NSWC TR 86-342, Nov. 1986.
12. Wardlaw, A. B. Jr. and Davis, S. F., "A Second Order Godunov Method for Tactical Missiles," AGARD, 58th Meeting of the Fluid Dynamic Panel Symposium of Applications of Computational Fluid Dynamics in Aeronautics, April 1986.
13. Wardlaw, A. B. Jr. and Davis, S. F., "A Second Order Godunov Method for Supersonic Tactical Missiles," NSWC TR 86-506, Dec. 1986.

14. Wardlaw, A. B. Jr. and Priolo, F. J., "Applying the ZEUS Code," NSWC TR 86-508, Dec 1986.
15. Priolo, F. J. and Wardlaw, A. B. Jr., "Supersonic Non-Circular Missile Computations," AIAA Paper 88-0278, Jan 1988.
16. Priolo, F. J. and Wardlaw, A. B. Jr., "Induced Roll Computations for Conventional Missile," AIAA Paper 89-0331, Jan 1989 (accepted to the *Journal of Spacecraft & Rockets*).
17. Davis, S. F., "Simplified Second Order Godunov-Type Methods," *SIAM Journal on Scientific and Statistical Computing*, Vol. 9, May 1988, pp. 445-473.
18. Godunov, S. K., "A Finite Difference Method for the Numerical Computation of Discontinuous Solutions of the Equations of Fluid Dynamics," *Mat. Zh.*, 47, 1959, pp. 271-290.
19. Ragsdale, W. C., "Flow Field Measurements Around an Ogive-Cylinder at Angles of Attack up to 15 Degrees for Mach Numbers 3.5 and 4," NOLTR 72-198, Aug. 1972.
20. Hodges, J., RAE Bedford, England, Private Communications.
21. Allen, J. M., Hernandez, G. and Lamb, M., "Body-Surface Pressure Data on Two Monoplane-Wing Missile Configurations With Elliptical Cross Sections at Mach 2.50," NASA TM-85645, Sept 1983.
22. Blair, A. B., Jr., Allen, J. M., and Hernandez, G., "Effect of Tail-Fin Span on Stability and Control Characteristics of a Canard-Controlled Missile at Supersonic Mach Numbers," NASA TP 2157, June 1983.
23. Allen, J. M., Shaw, D. S., and Sawyer W. C., "Analysis of Selected Data From the Tri-Service Missile Database," AIAA Paper 89-0478, Jan. 1989.
24. Newsome, R. W. and Adams, M. S., "Vortical Flow over an Elliptical-Body Missile at High Angles of Attack," *Journal of Spacecraft & Rockets*, Vol. 25, No. 1, Jan-Feb 1988, pp. 24-30.

## AERODYNAMIC DESIGN OF PEGASUS<sup>TM</sup> Concept to Flight with CFD

Michael R. Mendenhall, Executive Vice President  
Daniel J. Lesieur, Research Engineer  
Steven C. Caruso, Research Engineer  
Marnix F. E. Dillenius, Vice President  
Gary D. Kuhn, Senior Research Scientist

Nielsen Engineering & Research, Inc.  
510 Clyde Ave.  
Mountain View, CA 94043  
USA

### 1. SUMMARY

Pegasus<sup>TM</sup>, a three-stage, air-launched, winged space booster is currently under development to provide fast and efficient commercial launch services for small satellites. The aerodynamic design and analysis of the vehicle has been conducted without benefit of wind tunnel and subscale model testing using only computational aerodynamic and fluid dynamic methods. All levels of codes, ranging in complexity from empirical database methods to three-dimensional Navier-Stokes codes, were used in the design. This paper describes the design and analysis requirements, the unique and conservative design philosophy, and the analysis methods considered for the various technical areas of interest and concern.

### 2. LIST OF SYMBOLS

AR	aspect ratio
c	mean aerodynamic chord
$C_D$	drag coefficient
$C_{L,R}$	rolling-moment coefficient
$dC_L/d\beta$	lift-coefficient
$C_{m,\alpha}$	pitching-moment coefficient
$dC_m/d\alpha$	yawing-moment coefficient
$dC_y/d\beta$	normal-force coefficient
$dC_N/d\alpha$	side-force coefficient
$dC_y/d\beta$	gravitational acceleration
g	altitude
h	reference length
l	Mach number
$M_\infty$	dynamic pressure
$q_\infty$	time
t	axial coordinate measured from the nose
x	lateral coordinate
y	vertical coordinate
z	angle of attack
$\alpha$	angle of sideslip
$\beta$	angle of roll
$\phi$	taper ratio

#### Subscripts

cp	center of pressure
m	center of moments

### 3. INTRODUCTION

Pegasus (Fig. 1) is an air-launched space booster designed to satisfy launch requirements for small payloads in a variety of missions. The objective of this privately financed development program is to provide reliable space launch services at a low cost on a near-term schedule. Under this joint venture between Orbital Sciences Corporation and Hercules Aerospace Company, the design approach is based on a conservative development using conventional techniques while exploiting state-of-the-art technology and experience. Most of the aerodynamic design is based on proven, existing vehicles; therefore, no wind tunnel tests were included in the program, and readily available computational codes were used for all aerodynamic analyses.

As part of this development philosophy, the authors formed a design team responsible for aerodynamic analysis and support for a number of different technical areas including trajectory requirements, aerodynamic loading distributions, stability and control, and aerodynamic heating. The flight conditions considered included carriage and launch from the B-52 parent aircraft, transonic flight at high angles of attack, supersonic flight over the entire angle of attack range, and hypersonic flight to first-stage burnout. For this entire flight regime, it was necessary to select and validate appropriate prediction methods, estimate the level of accuracy achieved, and limit the flight envelope as necessary based on experience and engineering judgement.

The purpose of this paper is to discuss the computational techniques used, from engineering methods (empirical database/theoretical codes) to computational fluid dynamics (CFD) methods, and the results obtained from each level of prediction method. Though specific codes will be described, it is not the purpose of the paper to evaluate individual codes, but to evaluate the approach of using a number of different codes for detailed aerodynamic design of a new flight vehicle for which no test data exist.

### 4. BACKGROUND

#### 4.1 Pegasus Mission

To gain the advantages of increased payload performance and operational flexibility, Pegasus is carried aloft beneath the wing of a B-52 bomber or a modified conventional commercial transport aircraft. The performance improvements over ground launch are a result of both the aircraft forward velocity and the initial launch altitude. Launch at 40,000 feet contributes to lower dynamic pressure, lower drag, and lower structural and thermal stresses. The reduced atmospheric pressure range encountered by the first stage permits optimization of the first-stage nozzle. All things considered, a winged air-launch vehicle has a significant payload mass fraction advantage over conventional ground launches.

In level flight at Mach 0.8 and 40,000 feet, Pegasus is released from the carrier aircraft and allowed to free-fall for 5 seconds. After first-stage ignition, Pegasus begins a 2.5-g pull-up maneuver using wing lift and thrust while accelerating through the transonic speed regime and maximum dynamic pressure. When first-stage burnout occurs after 82 seconds, the vehicle has reached Mach 8.7 at an altitude of over 200,000 feet. The first-stage, which includes all the aerodynamic lifting surfaces, is separated from the second and third stages at this time. A typical baseline flight profile is illustrated in Figure 2.

For purposes of this paper, the end of the aerodynamic analysis is denoted by first-stage separation. At this high altitude, the low dynamic pressure makes the aerodynamic forces and moments negligible compared to thrust and inertial forces.

#### 4.1 Geometry

A sketch of the complete configuration is shown in Figure 1. The blunt nose body is cylindrical with a constant diameter of about 4 feet over the total body length of 50 feet. A fairing between the wing and the body and a slight expansion near the tail to accommodate the nozzle of the first stage rocket engine are the only modifications to the cylindrical shape. The wing, a clipped delta planform, is mounted on top of the fuselage, slightly aft of mid-length. The wing span of 22 feet is dictated by the available

clearance from the B-52 aircraft and is the same as the X-15 research aircraft. The graphite composite wing has a modified double wedge airfoil section. The position of the wing is critical to minimize the pitching moment variation due to the large center of gravity travel during first-stage burn.

The tail section is composed of clipped delta planform horizontal stabilizers and vertical rudder. These all-movable surfaces are also double wedge sections made of graphite composite structure. Other important details of the geometry which must be considered in the aerodynamic analysis are the interaction of the wing and tail surfaces and the contours and corners produced by the wing-body fairing.

Though significantly different from the X-15 geometry, there are a number of similarities between the configurations that are dictated by the B-52 carriage and launch requirements (Fig. 1(b)). Given these similarities, the aerodynamic characteristics of Pegasus can be compared with measured and predicted X-15 aerodynamics to provide a realistic check of the computational results.

#### 4.2 Aerodynamic Requirements

A typical baseline mission profile for Pegasus is shown in Figure 2 to illustrate the aerodynamic requirements. Note that the aerodynamic portion of the flight involves only the first 80 seconds of the mission. Briefly, launch from the B-52 occurs at  $M = 0.8$  at a low angle of attack. The angle of attack immediately increases to nearly 20 degrees as Pegasus accelerates through the transonic regime to supersonic speed. During this part of the mission, Pegasus is gaining altitude using both rocket thrust and wing lift. By  $M = 3$ , the angle of attack is down to 5 degrees, and by  $M = 6$  it is nearly zero degrees. Different missions will dictate different angle of attack and Mach number schedules.

A flight envelope is illustrated by the solid curve in Figure 3, and the names of various computer codes are shown to illustrate their range of applications. The codes noted on this figure are discussed in a later section. Before a decision about appropriate aerodynamic prediction methods can be made, the aerodynamic requirements for the various technical areas are needed. A minimum set of requirements is shown in Figure 4. For trajectory simulations, the longitudinal and lateral aerodynamic characteristics must include effects of control surface deflections since trim calculations are required throughout the trajectory. Some of the other items in Figure 4 are specific to Pegasus; for example, the wing fairing shock interference is of interest because of a specific vehicle component, and the B-52 pylon carriage loads and separation trajectories are required because of the nature of the launch. The number of flow conditions shown for each requirement is a conservative estimate based on preliminary design considerations. In reality, items such as the longitudinal and lateral aerodynamic matrices were calculated a number of times as the design changed, therefore, the 1400 flow conditions shown were calculated as many as four different times.

#### 4.3 Aerodynamic Design Philosophy

Economics and accuracy were under constant consideration during the computational aerodynamic analyses. In some cases, the number of calculations required dictated the codes and methods that could be used; for example, even if it were technically possible, the aerodynamic matrices could not be developed using CFD methods because of the cost and time involved. These matrices of aerodynamic characteristics had to be calculated using simpler, faster engineering methods. However, certain of the calculations involving flow separation and shock wave interference are too complex for simple methods, and these results can only be obtained using modern CFD techniques involving solutions of the Navier-Stokes equations. In other cases, intermediate methods such as panel methods and solutions of the Euler equations were sufficient to provide the design details required.

Additional considerations in the aerodynamic design philosophy were code availability, ease of use, engineering capability, and confidence level. Obviously, codes that are difficult to acquire and use cannot be considered for a design study like Pegasus because of the time constraints involved. Also, there is generally little time available for code development and training; therefore, reliable

codes familiar to the design group are a necessity. Finally, since no wind tunnel data are available for guidance, there must be a high degree of confidence in the prediction methods so that a large amount of time is not spent validating the selected codes. Missile designers and analysts have noted that the aerodynamic design of a new vehicle may be limited by the highest level of code with which the aerodynamics design group is familiar. The objective of the Pegasus effort was to use the highest level code required for the specific task.

In this commercial design effort, time became an important factor for some items. The basic aerodynamic analysis had to be completed quickly in the conceptual design stage so that the design effort could move on toward final design. As geometric modifications were made, rapid aerodynamic evaluation was necessary so that performance characteristics were available in a timely manner for mission analysis.

After the preliminary aerodynamic design, there is generally more time available for aerodynamic support. For example, the calculation of aerodynamic heating and aerodynamic loads for structural design require the use of more complex methods, but the timing, though still important, is not as critical. Similarly, very detailed fluid mechanic analysis of certain flow characteristics may require a significant effort using modern CFD methods, but the results of this study, though important for the final design, may be carried out over a longer period of time after the final aerodynamic design is fixed. The method-selection process for this design effort will be described in greater detail in the next section.

### 5. TECHNICAL DISCUSSION AND RESULTS

A number of different aerodynamic design and analysis codes were applied to Pegasus; the portions of the flight envelope considered by various codes are shown in Figure 3. The different codes used are identified in Figure 5, and descriptions of each code are presented in the following paragraphs. Since it is important to see the relationship between the specific aerodynamic task and the code or codes selected, sample results will be presented and discussed at the same time the prediction methods are described.

#### 5.1 Preliminary Design

As noted above, speed and accuracy are important considerations for the codes used for preliminary design purposes. A number of possible codes are available for this task, but as discussed in Reference 1, not all codes are applicable to the configuration and flow conditions of interest for this investigation. Since no experimental data on Pegasus was to be available, a conservative approach was taken for the analysis and a number of different codes were selected for the preliminary aerodynamic design phase.

Two independent engineering codes for preliminary design analysis, MISL3 (Refs. 2 and 3) and Missile DATCOM (Ref. 4 and 5), were used in parallel to predict the longitudinal and lateral aerodynamic characteristics of Pegasus over the first part of the flight envelope below Mach 5. Between Mach 4 and 8, the S/HABP (Ref. 6) and MADM (Ref. 7) codes were selected.

MISL3 is a semiempirical code which uses a combination of theoretical methods with nonlinear corrections for the body and an extensive experimental data base for wing and tail fin loads. The data base inherently includes viscous and compressibility effects as well as fin-body gap effects. The code emphasizes high angles of attack and transonic speeds, important flow regimes for Pegasus. Mutual interference between control surfaces is also considered in the data base, another important feature for the anticipated flight profile. To provide some confidence in the applicability of this code, MISL3 has been validated by comparison of measured and predicted aerodynamic characteristics with a number of different configurations (Refs. 2, 3, 8, and 9). The range of application of the flow parameters in the MISL3 data base is

$$\begin{aligned} 0.5 &\leq M_{\infty} \leq 5.0 \\ -45.0 &\leq \alpha \leq 45.0 \\ 0.0 &\leq \phi \leq 90.0 \\ 0.25 &\leq AR \leq 4.0 \\ 0.0 &\leq \lambda \leq 1.0 \end{aligned}$$

Missile DATCOM is based on the body buildup method and includes a number of prediction methods for each component of the configuration. It was developed specifically for preliminary design applications, and it has also been validated by numerous comparisons with experimental data (Refs. 4, 9 and 10). Even though MISL3 and Missile DATCOM use some similar approaches, they are independent codes with individual strengths and weaknesses. For example, Missile DATCOM predicts axial force or drag much better than MISL3, but MISL3 predicts vortex-induced forces and moments at high angles of attack better. The body loads in Missile DATCOM have proved to be more accurate than those from MISL3 in subsonic flow.

Both of these codes should provide independent predictions of Pegasus aerodynamics. Throughout the preliminary aerodynamic analysis, both codes were run in parallel for all flow conditions and the results were compared. Since some of the flight regime involves high angles of attack where vortex-induced nonlinearities can dominate the aerodynamic characteristics, there is likely to be some disagreement between the results from the two codes. When this occurs, higher level codes can be used to predict a limited number of results to help resolve the differences. These higher level codes are described in a following section.

Predicted static longitudinal aerodynamic characteristics of the complete Pegasus configuration with control surfaces undeflected are shown in Figure 6 for the range of Mach numbers. Results from both MISL3 and Missile DATCOM are shown. Agreement is very good for the entire range of Mach numbers at moderate angles of attack, but there is some disagreement above  $\alpha = 10^\circ$ , a good indication that predicted vortex effects are different between the two codes. The final aerodynamic characteristics are determined by a combination of the two results, giving consideration to the respective strengths of both codes. One use of these aerodynamic results is for trajectory simulations; therefore, the calculations were repeated for a range of horizontal tail deflection angles to complete the longitudinal aerodynamic matrix.

A matrix of Pegasus lateral aerodynamic characteristics was generated by varying the sideslip angle and the rudder deflection angle. Roll control information was generated by computing the effects of differential deflection of the horizontal tail surfaces.

Verification of the above approach for longitudinal aerodynamic characteristics was essential to build confidence in the calculation procedure. Experimental results are available on a similar configuration at  $M_\infty = 2$  in Reference 12, and comparisons of measured and predicted lift, drag, and center of pressure are shown in Figure 7 for a range of angles of attack up to the maximum angle permitted for the Pegasus mission. The comparisons are in very good agreement over the entire range of angles of attack. Since the longitudinal center of pressure was not in as good agreement as the force coefficients, a sensitivity study was performed to illustrate the effect of moving the moment center an amount equal to 10-percent of the mean aerodynamic chord. It is apparent that this is approximately the magnitude of the error in the predicted center of pressure.

The two previous codes have an upper limit of Mach 5; therefore, another code was required for the higher Mach number ranges. Missile DATCOM has a hypersonic option which was used at selected flow conditions; however, other codes are more appropriate to this flow regime. S/HABP and MADM (Refs. 6 and 7) were applied to Pegasus for Mach numbers between 4 and 8. Note that there is also an overlap in the Mach region at which preliminary design codes were used to be certain of continuity of results. MADM is a major upgrade of the S/HABP code and includes additional capability to improve the pressure prediction at supersonic speeds. Both codes are panel codes that use impact methods to predict pressure distributions on arbitrary configurations. The disadvantages with these codes are the absence of wing tail vortical interference effects and the requirement that the user select the appropriate force calculation procedure from the many options. However, it is possible to validate the codes with experimental or other predicted results to enhance the use of the method. Since the angles of attack at the higher Mach numbers is very low and it is expected that the aerodynamic characteristics will be well behaved, MADM was the only code used for these

calculations. The MADM results were compared with MISL3 and Missile DATCOM results between Mach 4 and 5 to test for consistency and accuracy.

Predicted lift and drag coefficients at  $M_\infty = 8$  are shown in Figure 8 for a range of angles of attack far beyond that expected during flight. An impact-panel representation of Pegasus is also shown in the figure. No data on a similar configuration in this Mach range are available for comparison purposes.

## 5.2 Engineering Methods

The next level of code available for aerodynamic calculations is a panel method. For Pegasus, the high angles of attack experienced at both subsonic and supersonic speeds add the requirement that vortex-induced effects be included. These vortex effects are those associated with vortex shedding from the body ahead of the wing SUPDL, an improved version of the NWCDM-NSTRN supersonic code described in Reference 11, was immediately available for analysis over the Pegasus flight envelope up to Mach 3. A subsonic version, SUBDL, was also available for use in the limited flight regime between launch and the onset of transonic flow.

SUPDL represents the components of the configuration with distributions of singularities derived from supersonic linear theory. The body is modeled with linearly varying supersonic line sources and doublets to account for volume and angle of attack effects, and the lifting surfaces and body interference regions are modeled with planar supersonic lifting panels. Nonlinear fin loads associated with leading edge and side edge separation at high angles of attack are included. Other important nonlinearities from forebody and afterbody separation vortices are included as is the interference effect of the wing trailing vorticity on the tail fins. SUPDL also has the capability of predicting the aerodynamic characteristics of the configuration under constant pitch, yaw, and roll rates. This is particularly useful for obtaining damping derivatives to a first approximation.

The predicted distribution of aerodynamic loads from both SUBDL and SUPDL are easily converted for use in the structural analysis code NASTRAN. This information on the wing and tail fins at a number of different flow conditions was provided to the structural designers. Predicted loading distributions on the wing in subsonic and supersonic flow at a high angle of attack are shown in Figure 9. The arrows represent the magnitude of the aerodynamic loading at specific wing locations considered in the aerodynamic analysis.

## 5.3 Carriage and Launch Methods

Areas that do not bear directly on the aerodynamic design of Pegasus are the carriage and launch characteristics. The carriage loads are critical to the design of the B-52 pylon adaptor as well as flight safety and mission viability. The launch characteristics are important not only for the safety of the launching aircraft but for the initial flight conditions of Pegasus. These characteristics can be measured experimentally, but the expense and delay in the design schedule are usually not practical for a commercial effort; therefore, an analytical approach was selected.

Carriage loads and launch characteristics require that Pegasus' aerodynamic loads be known in the flow field of the launching aircraft, a B-52 for the initial analysis. Previous work in the prediction of store separation from various aircraft (Ref. 13), including the B-52 (Ref. 14), provided the necessary capability. Previous validation of these methods (Ref. 15) on a number of different store separation problems was sufficient to give confidence in the predicted results.

Carriage loads were calculated using both the load prediction method in the store separation code, SUBSTR (Ref. 13), and the panel code SUBDL integrated into SUBSTR. In each case Pegasus was placed in the predicted nonuniform flow field associated with the B-52 at various flight conditions. Altitude, airspeed, and perturbations to the flight path caused by gusts were considered. Forces and moments on Pegasus were predicted, and the loads on the pylon attachment points were calculated and examined for problems. In every case, the predicted loads were within accepted safety limits.

Launch characteristics were calculated using SUBSTR with its six-degree-of-freedom trajectory simulation capability. For this analysis, Pegasus is launched from the B-52 with all controls inactive and neutral for the first five seconds; therefore, the initial flight trajectory while in the influence of the B-52 determines the position and attitude of Pegasus at ignition. The first three seconds of a normal launch are shown in Figure 10. Notice that Pegasus falls away from the B-52 with a slightly nose down attitude and small roll angle away from the fuselage. The predicted Pegasus trajectory is in good agreement with measured and predicted X-15 trajectories (Ref. 16); however, the pitch and roll angles associated with Pegasus are much less than those experienced by the X-15.

Another feature of the analytical launch prediction method is its ability to investigate non-standard launch characteristics. Though not planned, if Pegasus is dropped with controls locked in various fully deflected positions corresponding to pitch, yaw, or roll control, it is essential to identify a priori any emergency launches which could endanger the B-52 aircraft. A number of extreme launch conditions were simulated with SUBSTR. In every case, though the trajectory may have been erratic and uncontrollable, Pegasus cleared the B-52 and fell safely away from the aircraft.

#### 5.4 Other Methods

Based on the results presented above, the missile designer may begin to believe that all aerodynamics problems can be solved with one code or another. Before this happens, it is time to return to reality and examine an important area in which large uncertainties exist in analytical methods. That area is the calculation of static and dynamic stability derivatives.

The Missile DATCOM, MISL3, SUBDL and SUPDL codes have the capability of calculating important stability derivatives, but there has not been enough verification to build the confidence level for the results. Fortunately, the similarity between the X-15 and Pegasus provides a means to estimate the quality of the predicted stability derivatives. Static longitudinal and lateral derivatives are available from Missile DATCOM and MISL3 at specified flow conditions, and  $\alpha = 5^\circ$  was selected for the calculations between Mach 0.6 and 5.0. The results from the MADM code were in good agreement with these results between Mach 4 and 5; therefore, MADM was used for predictions to Mach 8. The predicted static longitudinal derivatives as a function of horizontal tail deflection angle and Mach number are shown in Figure 11 along with flight measurements on the X-15 from Reference 17. One difference in the moment curves between Pegasus and the X-15 is caused by the large movement of the center of gravity during first-stage burn and its effect on the derivatives at high Mach numbers. Similar results and comparisons for the static lateral characteristics are shown in Figure 12. In general, the static characteristics of Pegasus are very similar to those for the X-15 over the entire flight range of interest.

The SUBDL and SUPDL codes were used to check the above results at selected flow conditions at moderate Mach numbers. This higher level calculation verified the simpler methods.

The prediction of dynamic stability derivatives is more difficult, and there are few codes available for this task. As a consequence, the level of uncertainty is higher than for the static derivatives. A method based on supersonic linear theory is described in Reference 18, and it proved successful for the X-15. This approach was applied to Pegasus, and the predicted pitch damping results are shown in Figure 13 as the curve denoted Linear Theory. Flight test and wind tunnel measurements on the X-15 are shown in the same figure, and the general character of this derivative is very similar to the predictions for Pegasus. As a check on this simple approach, the code SUPDL was applied to a pitching Pegasus configuration, and the results are compared to the linear theory. The agreement between the methods is very good in the limited Mach number range of the code. Similar results were obtained for the yaw and roll damping derivatives on Pegasus.

#### 5.5 Computational Fluid Dynamics

As shown on Figure 3 and described above, a number of CFD codes were used for detailed flow simulations. Calculations have been

made with an Euler code, a parabolized Navier-Stokes code, two-dimensional and axisymmetric Navier-Stokes codes, and a three-dimensional Navier-Stokes code. A number of research CFD codes were used in cooperation with the NASA/Ames Research Center and the Numerical Aerodynamic Simulation facility. These involved the use of a parabolized Navier-Stokes code to predict fuselage pressure distributions, the use of an axisymmetric Navier-Stokes code to predict the possibility of rocket plume-induced separation near the tail control surfaces, and the use of a three-dimensional Navier-Stokes code to model the complete configuration at critical flight conditions to check details of the flow which may have been missed by the simpler methods. The CFD results have been used for the aerodynamic heating studies and design of the thermal protection system.

In this section, a number of different applications of CFD codes are described to illustrate the use of these advanced techniques in practical configuration design and analysis.

**Euler Solutions.** SWINT (Ref. 19) has been used for a number of different calculations during the Pegasus analysis. First, it was used to predict the dynamic pressure defect on the lee side of the configuration at supersonic speeds to assess rudder effectiveness for lateral stability analyses. This correction is included as part of the MISL3 code. Euler calculations were also used to predict detailed fuselage loads for the nose fairing design.

**Parabolized Navier-Stokes Solutions.** In the early design phase of Pegasus, a potential for first-stage rocket plume-induced separation of the flow near the aft end of the fuselage was identified. Since a separated flow region would occur in the vicinity of the control fins (Fig. 1), a significant loss in fin effectiveness could occur if the fins were immersed in this flow. A rapid CFD analysis was proposed to determine the possibility of flow separation in this region.

Considering the flight envelope shown in Figure 3, most of the flight occurs near an angle of attack less than  $5^\circ$ ; therefore, to further simplify the CFD analysis, the angle of attack is assumed zero, the wing and fins are neglected, and calculations are performed for the body only. These assumptions permit an axisymmetric analysis, which considerably reduces the required computational effort. Flow separation calculations were performed at three Mach numbers, 1.5, 5, and 8 corresponding to Mach numbers on the baseline mission profile.

A zonal calculation approach using three different computer codes was used for the supersonic analysis. First, an Euler blunt body code (Ref. 20) was used to compute the axisymmetric flow over a sphere to approximate the flow in the vicinity of the nose. These results are used as starting conditions for a parabolized Navier-Stokes (PNS) calculation using the UPS code (Ref. 21) from NASA/Ames Research Center. The PNS calculation produces a non-separated viscous solution in a very efficient manner since it uses a marching-type solution procedure. Turbulence in the fuselage boundary layer is modeled using the Baldwin-Lomax algebraic turbulence model (Ref. 22).

The grid used for the PNS calculations has  $100 \times 82$  points in the streamwise and body-normal directions, respectively. Sufficient grid points were used to insure adequate resolution of the fuselage boundary layer. At the left or incoming boundary, flow conditions obtained from the blunt body calculation are imposed, and freestream conditions are applied at the far field boundary which is located just beyond the nose bow shock. Each PNS calculation requires approximately fifteen minutes on the NAS Cray-2.

**Axisymmetric Navier-Stokes Solutions.** The results of the PNS calculation provide initial conditions for a full Navier-Stokes calculation in the region just upstream and downstream of the first stage rocket nozzle. These calculations were performed using the axisymmetric Navier-Stokes solver in the TURF code (Ref. 23) from NASA/Ames. Turbulence is modeled with the  $k-\epsilon$  equations in this code.

The grid used for the Navier-Stokes analysis of the base flow is shown in Figure 14. This grid has  $78 \times 100$  points in the streamwise and normal directions, respectively. The PNS results were applied at the left boundary, and the far field boundary was treated as

described above. A conical inviscid flow corresponding to the design rocket nozzle conditions was applied at the nozzle exit plane. The Navier-Stokes computations require approximately fifteen minutes on the NAS Cray-2.

Predicted Mach number contours at  $M_\infty = 5$  are shown in Figure 14. An oblique shock occurs due to the presence of the ramp at the rocket nozzle, and at higher Mach numbers (and altitudes), the spreading of the plume induces a second oblique shock which intersects the first shock, creating a lambda shock near the ramp. The pressure jump across the oblique shocks increases with Mach number. To determine if flow separation is present, streamlines are also shown in Figure 14. In all cases, the flow remains attached, even for the highest Mach number where the plume expansion is largest. These results are strictly valid only for the higher Mach number cases in the flight profile where the angle of attack is small; however, since the plume expands less at lower Mach numbers and altitude, it is likely that plume-induced flow separation is not a problem.

There were several interesting side benefits from the above CFD analysis. Surface heat transfer rates derived from these calculations provided a check on thermal calculations made for the design of Pegasus' thermal protection system. The predicted boundary layer thickness provided verification that adverse effects on control fin loading on the portion of the fins submerged in the boundary layer were not a problem. The boundary layer and Mach number profiles near the body also helped identify a possible heating problem on the control fin actuators.

**Three-Dimensional Navier-Stokes Solutions.** In early analyses of Pegasus, there was concern over possible deleterious effects from interaction between the shock waves produced by the wing and tail leading edges and the boundary layer on the body. The concern involved flow separation due to the shock wave/boundary layer interaction and increased heat transfer due to the high compression of the flow through the shock coming in contact with the body surface. Each of these conditions could affect the design of the thermal protection system. A CFD analysis using a complete three-dimensional model of Pegasus was proposed to examine the possibility of these adverse effects.

This analysis was carried out in two phases. The first phase involved a model of the fuselage and wing for two distinct flow conditions; (1)  $M_\infty = 1.2$ ,  $\alpha = 20^\circ$ , and (2)  $M_\infty = 5$ ,  $\alpha = 5^\circ$ . After successful completion of these computations, the second phase addressed the modeling of the complete configuration for calculations at the higher Mach number.

Development of the computational grid is a major part of any CFD study, and Pegasus is no exception. The Chimera composite-grid approach (Ref. 24) was chosen for the discretization process to achieve an accurate model of the entire configuration. The grid required for simulating the flow field around Pegasus was composed of two sections. The first section enclosed the body and wing, extending one grid cell beyond the trailing edge of the wing. The second section extended from the wing trailing edge to the base of the body. For the forward section, because of the blunt nose and the thick, round-edged wing, the grid was generated using the NASA/Ames code HYGRID (Ref. 25), a three-dimensional hyperbolic grid generator. For the aft section, because of the simpler, more cylindrical geometry, the grid was generated using a NEAR code, HYDAPT (Ref. 26), a two-dimensional hyperbolic grid generator. The two-dimensional grid generator was applied to compute grids in cross sections which were combined to create a fully three-dimensional grid.

The final grid is presented in Figure 15 where part of the grid on the surface of the body and wings is shown, along with the grid in the cross section at the trailing edge of the tail fins and in the plane of symmetry. Only 25% of the actual grid points are shown for clarity. Except for its final cross section just aft of the wing trailing edge, the grid on the forward part of the configuration was not restricted to planes normal to the axis of the body. The final cross section of the forward section is normal to the body in order to match more easily with the cross sections of the grid on the aft section. Note that a plane of symmetry was used to save computer time for longitudinal calculations. The forward grid contains  $92 \times 63 \times 51$  points and the aft grid contains  $54 \times 63 \times 51$  points, a total of

618,018 points. A very fine mesh was used next to the body surface to enhance the possibility of predicting the friction and heat transfer effects of the boundary layer.

The Chimera overset-grid scheme (Ref. 24) was used to allow treatment of the two part grid configuration. The approach allows multiple grids to be overlaid without requiring mesh boundaries to join in any special way. The two grids were designed so that the axial locations of the last two cross sections of the forward grid coincided with the first two sections of the aft grid.

The computation of the flow field was carried out using the code F3D (Ref. 27) from NASA/Ames. The code solves the compressible three-dimensional thin-layer Navier-Stokes equations, uses upwind spatial differencing in a streamwise direction, and is either first-order or second-order accurate in space. For the calculations described herein, the accuracy in time is first-order.

Numerical computations on the complete Pegasus configuration were carried out at  $M_\infty = 5$  and  $\alpha = 5^\circ$  for a Reynolds number of  $1.33 \times 10^6$ . The computations began by computing for the forward grid alone. After a converging solution was obtained, the aft grid was added and the solution continued. With the partially converged forward solution and uniform flow over the aft section as the initial condition, the solution advanced. A total of about 25 hours of CPU time on the Cray-2 computer was required for the calculations.

A typical outcome of a CFD computation is a large quantity of information that is difficult to assimilate using traditional methods. For example, results include surface stream lines, flow field velocity vectors, and surface pressure contours on the entire configuration; therefore, careful examination can reveal many interesting details about the flow around the vehicle. Flow field vectors and pressure contours are shown in Figure 16 at a station aft of the wing root chord leading edge to illustrate the flow in the region of the wing-fuselage fairing. These details show a separated region beneath the wing and the approximate position of the wing leading edge shock wave. It was an initial concern that the wing shock wave could impinge on the fuselage and fairing and cause heating problems. It appears from the computations that the wing shock wave never reaches the fuselage surface. Further examination of results aft of this station show vortices on top of the fairing behind the wing, and in the tail region, the vortex from the fairing seems to get "trapped" at the base of the rudder.

## 6. CONCLUSIONS

A major conclusion is an evaluation of the design capabilities of a number of the codes currently available to the missile design community. Though only a few of the available codes were used in this study, the experience illustrates the requirements for useful prediction methods at all levels of complexity.

In the preliminary design application, a number of codes are available which can provide moderately accurate results at a reasonable cost. The codes considered in this effort are generally available and easy to use, and for moderate flight conditions, there is good agreement in the results from different methods. At extreme flight conditions at high angles of attack, codes which include effects of nonlinearities are required, but as shown in this study, such codes are available.

As the level of complexity increases and as more detailed information is needed, engineering level codes are available, generally in the form of panel methods. The cost of these codes in both engineering time and computation time increases with the level of information produced, but the need for aerodynamic load distributions and vortex-induced effects make the extra effort justified. The use of these codes to check results from the preliminary design codes at selected flow conditions proved to be a valuable technique to increase confidence in the results from the simpler codes.

Finally, the use of CFD codes for practical application to design problems is becoming more feasible as the available codes are further developed. Euler codes are becoming available to even the smallest design group as costs for use decrease. These codes are



now available for missile design at a level equivalent to panel codes 10 to 15 years ago. Their use will only continue to increase as the codes become better and easier to use and computers run faster.

The use of Navier-Stokes codes for missile design is still in the preliminary or research stage. Their use is restricted to very special problems which cannot be solved in any other manner; for example, flow problems involving flow separation or other viscous phenomena. These codes are not yet available to many small missile design groups because of the difficulty using them and the high cost involved with solutions. The cost of maintaining a CFD capability is currently beyond many small organizations because of the dedication required to keep up with the rapid advances in computational knowledge. In spite of the current disadvantages, CFD will soon be a readily available analysis tool for missile designers.

With regard to Pegasus, initial test flights on the B-52 were made in early 1990 to check out the Pegasus systems and carriage loads. It was verified that actual carriage loads imposed on the B-52 pylon were well within the predicted levels.

## 7. EPILOGUE

On 5 April 1990, the first drop and flight of Pegasus was accomplished successfully. Pegasus cleared the B-52 safely as predicted, the aerodynamic portion of the mission profile was completed as planned, and most important, the first payload was placed into its prescribed orbit. Future computational efforts for Pegasus will involve comparisons of measured flight test data with predictions.

## 8. ACKNOWLEDGEMENTS

The authors gratefully acknowledge the Orbital Sciences Corporation for the sponsorship of the technical investigation reported herein. The personnel and facilities of the Numerical Aerodynamic Simulator (NAS) at the NASA/Ames Research Center are acknowledged for their assistance in obtaining the computational fluid dynamic results on Pegasus. Specifically, Dr. Joseph Steger and members of the Space Shuttle Flow Simulation Group were instrumental in the successful application of the three-dimensional Navier-Stokes code. Parts of the CFD effort and the preparation of this paper were funded by a NEAR IR&D program.

## 9. REFERENCES

1. Baker, W. B., Jr.: "Use of Semiempirical Aerodynamic Methods for Preliminary Design," In *Missile Aerodynamics Proceedings*, Nielsen Engineering & Research, 1989.
2. Lesieutre, D. J., Mendenhall, M. R., Nazario, S. M., and Hensch, M. J.: "Prediction of the Aerodynamic Characteristics of Cruciform Missiles Including Effects of Roll Angles and Control Deflections," NEAR-TR 360, August 1986.
3. Lesieutre, D. J., Dillenius, M. F. E., Mendenhall, M. R., and Torres, T. O.: "Aerodynamic Analysis Program MISL3 for Conventional Missiles With Cruciform Fin Sections," NEAR TR 404, December 1989.
4. Vukelich, S. R., et al: "MISSILE DATCOM, Volume I - Final Report," AFWAL-TR-86-3091, December 1988.
5. Vukelich, S. R. and Jenkins, J. E.: "Missile Datcom: Aerodynamic Prediction of Conventional Missiles Using Component Build-Up Techniques," AIAA 84-0388, January 1984.
6. Gentry, A. E., Smyth, D. N., and Oliver, W. R.: "The Mark IV Supersonic-Hypersonic Arbitrary-Body Program," AFFDL TR-73-159, Nov. 1973.
7. Williams, J. E., et al: "Missile Aerodynamic Design Method (MADM)," AFWAL-TR-87-3109, February 1988.
8. Lesieutre, D. J., Mendenhall, M. R., Nazario, S. M., and Hensch, M. J.: "Aerodynamic Characteristics of Cruciform Missiles at High Angles of Attack," AIAA 87-0212, January 1987.
9. Lesieutre, D. J., Mendenhall, M. R., and Dillenius, M. F. E.: "Prediction of Induced Roll on Conventional Missiles with Cruciform Fin Sections," AIAA 88-0529, January 1989.
10. Stoy, S. L. and Vukelich, S. R.: "Prediction of Aerodynamic Characteristics of Unconventional Missile Configurations Using Component Build-Up Techniques," AIAA 86-0489, January 1986.
11. Dillenius, M. F. E., Perkins, S. C., Jr., and Lesieutre, D. J.: "Modified NWCDM-NSTRN and Supersonic Store Separation Programs for Calculating NASTRAN Forces Acting on Missiles Attached to Supersonic Aircraft," NWC TP 6834, September 1987.
12. Covell, P. F.: "Supersonic Aerodynamic Characteristics of Canard, Tailless, and Aft-Tail Configurations for Two Wing Planforms," NASA TP 2434, 1985.
13. Dillenius, M. F. E., Goodwin, F. K., and Nielsen, J. N.: "Extension of the Method for Predicting Six-Degree-of-Freedom Store Separation Trajectories at Speeds up to the Critical Speed to Include a Fuselage with Noncircular Cross Section, Vol. I - Theoretical Methods and Comparisons with Experiment," AFFDL-TR-74-130, November 1974.
14. Goodwin, F. K. and Smith, C. A.: "Theoretical Separation Characteristics of Two Conceptual Solid Rocket Booster Parachute Test Units From the B-52 Aircraft," NEAR TR 114, August 1976.
15. Dillenius, M. F. E., Goodwin, F. K., and Nielsen, J. N.: "Analytical Prediction of Store Separation Characteristics from Subsonic Aircraft," J. Aircraft, Vol. 12, No. 10, October 1975, pp 812-818.
16. Matranga, G. J.: "Launch Characteristics of the X-15 Research Airplane as Determined in Flight," NASA TN D-723, February 1961.
17. Yancy, R. B.: "Flight Measurements of Stability and Control Derivatives of the X-15 Research Airplane to a Mach Number of 6.02 and an Angle of Attack of 25°," NASA TN D-2532, November 1964.
18. Walker, H. J. and Wolowicz, C. H.: "Theoretical Stability Derivatives for the X-15 Research Airplane at Supersonic and Hypersonic Speeds Including a Comparison with Wind-Tunnel Results," NASA TM X-287, August 1960.
19. Priolo, F. J. and Wardlaw, A. B., Jr.: "A Comparison of Inviscid Computational Methods for Supersonic Tactical Missiles," AIAA 87-0113, January 1987.
20. Hsieh, T. and Priolo, F. J.: "Generation of the Starting Plane Flowfield for Supersonic Flow Over a Spherically Capped Body," NSWC TR 84-484, 1984.
21. Lawrence, S. L., Tannehill, J. C. and Chausee, D. S.: "An Upwind Algorithm for the Parabolized Navier-Stokes Equations," AIAA 86-1117, 1986.
22. Baldwin, B. S. and Lomax, H.: "Thin Layer Approximation and Algebraic Model for Separated Turbulent Flows," AIAA 78-0257, January 1978.

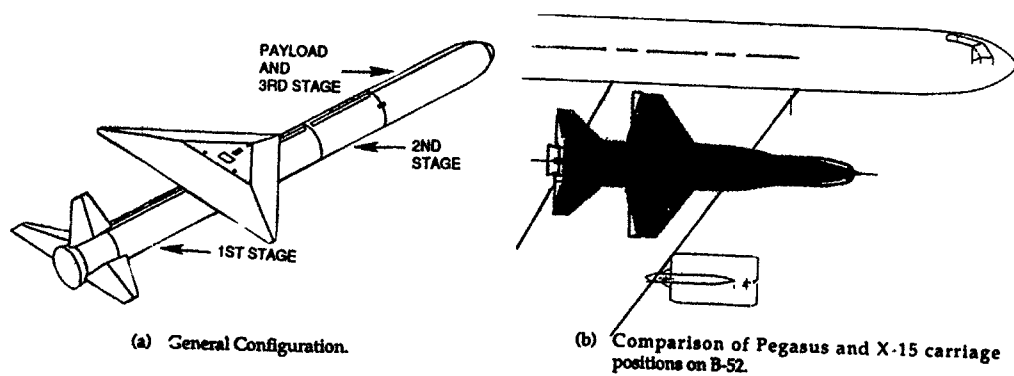


Figure 1.- Pegasus.

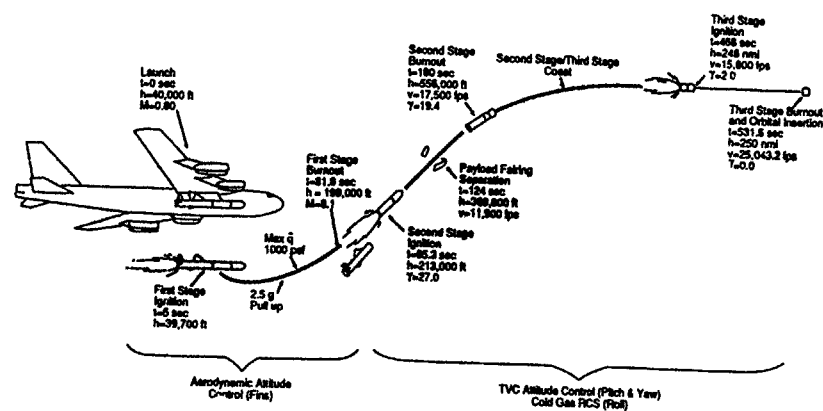


Figure 2.- Pegasus baseline mission profile.

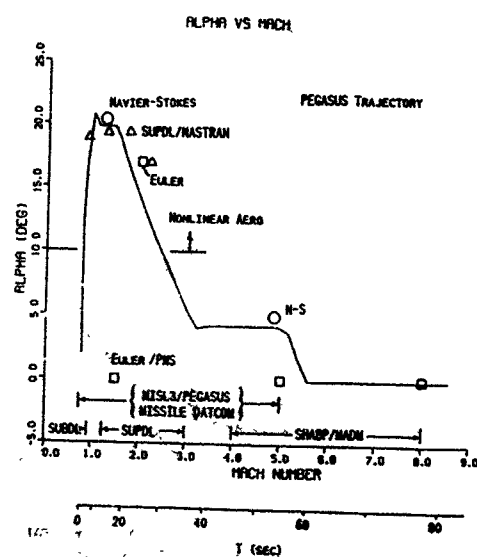


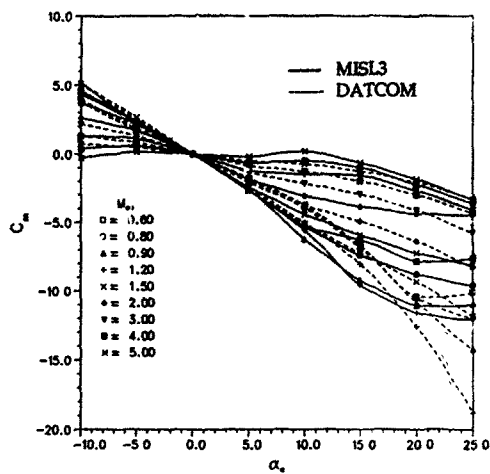
Figure 3.- Aerodynamic analyses flight envelope.

Trajectory Simulations	Longitudinal Matrix ( $M_\infty, \alpha, \delta$ )	Flow Conditions
		504
	Lateral Matrix ( $M_\infty, \alpha, \beta, \delta_A, \delta_R$ )	918
Wing/Fin Detail Design Loads:		4
Nose Distributed Loads		1
Plume-Induced Separation:		3
Wing Fairing Shock Interference.		2
B-52 Pylon Carriage Loads:		3
Separation Trajectory		4

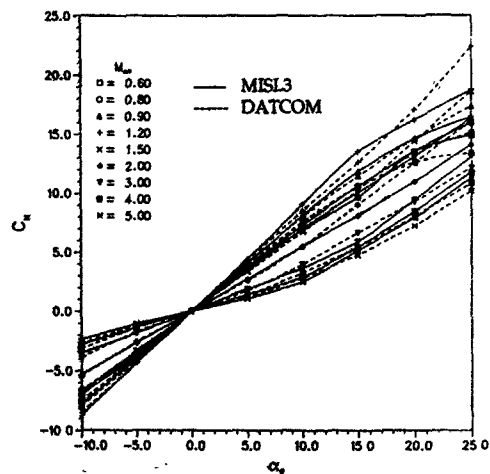
Figure 4.- Predicted aerodynamic requirements

Code	Developed By	Description
MISL3	NEAR (DOD/NASA)	Database/Theory
DATCOM	McDAG (AF)	Database/Theory
SUBDL	NEAR (Navy)	Panels/Viscous Effects
SUPDL	NEAR (NASA)	Panels/Viscous Effects
SHABP	McDAG (AF)	Shock Exp/Impact Theory
MADM	McDAG (AF)	Shock Exp/Impact Theory
SWINT	NSWC	Euler
UPS	NASA/AMES	Parabolized Navier-Stokes
ARC2D	NASA/AMES	Two-Dimensional N-S
TURF	NASA/AMES	Axisymmetric N-S
F3D	NASA/AMES	Three-Dimensional N-S

Figure 5- Prediction methods.



(b) Pitching-moment coefficient



(a) Normal-force coefficient

Figure 6- Comparison of MISL3 and Missile DATCOM longitudinal aerodynamic characteristics.

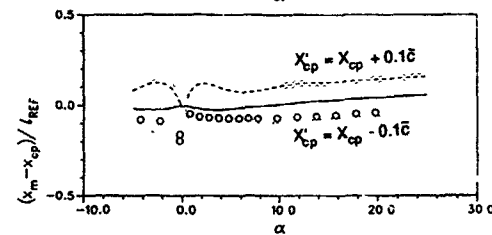
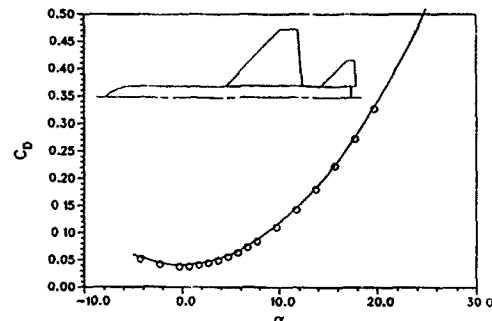
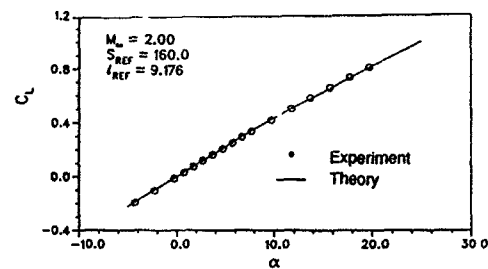


Figure 7- Measured and predicted longitudinal aerodynamic characteristics of a wing-body-tail configuration.

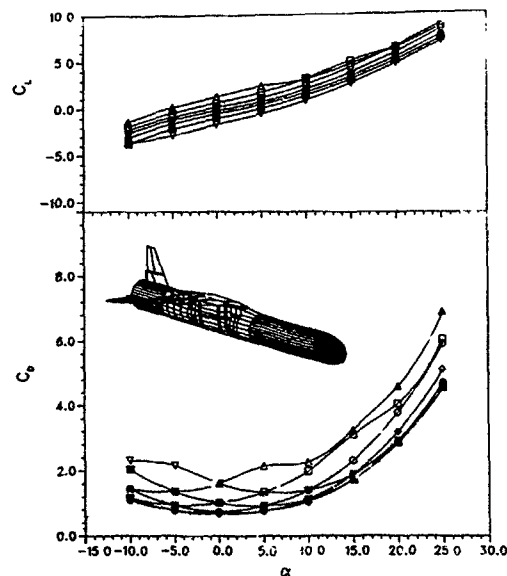


Figure 8- Predicted longitudinal aerodynamic characteristics from the MADM code.

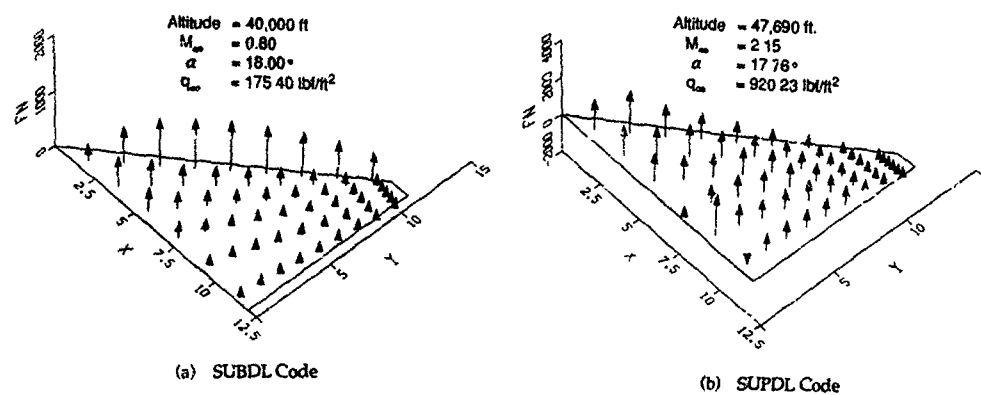


Figure 9.- Predicted aerodynamic loading distribution on the Pegasus wing.

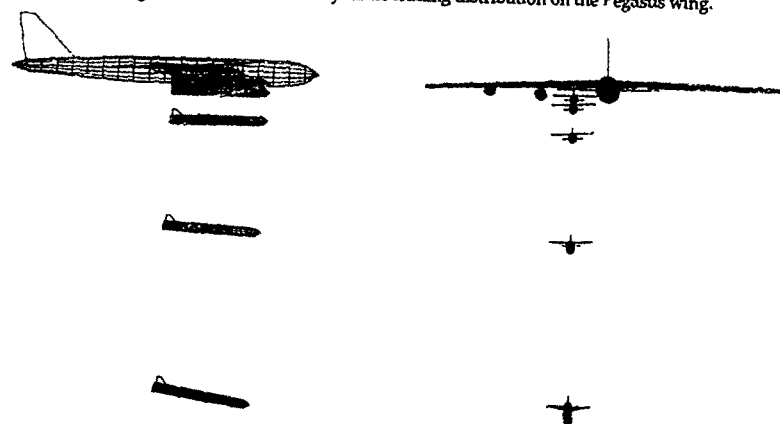
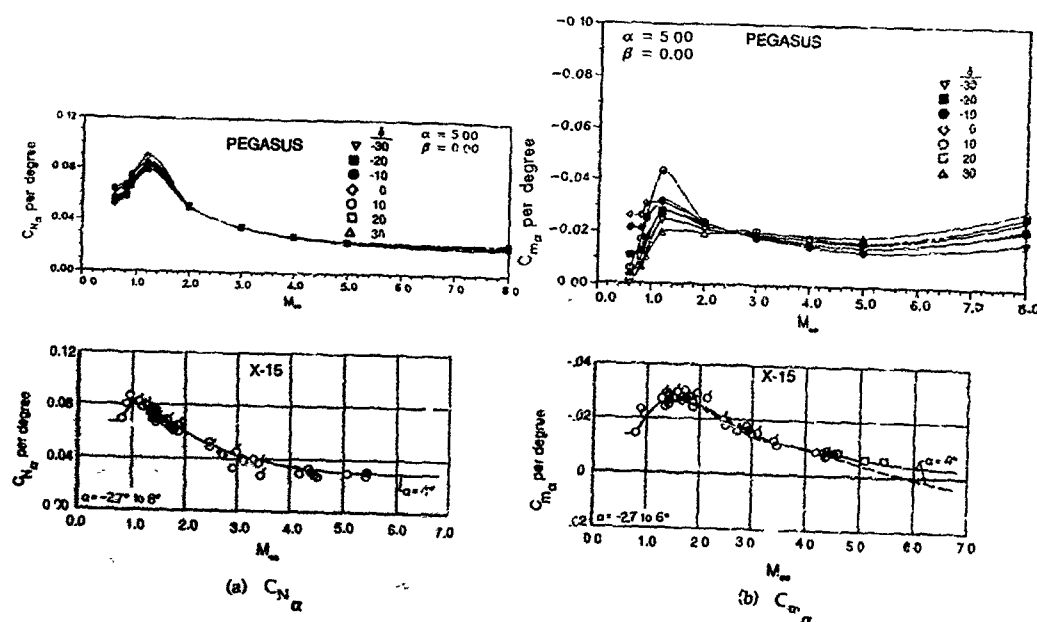
Figure 10.- Simulated Pegasus standard drop from the B-52, Program SUBSTR,  $M_{\infty} = 0.8$ ,  $t = 0, 0.5, 1.0, 2.0$ , and  $3.0$  seconds

Figure 11.- Comparison of Pegasus and X-15 longitudinal stability derivatives.

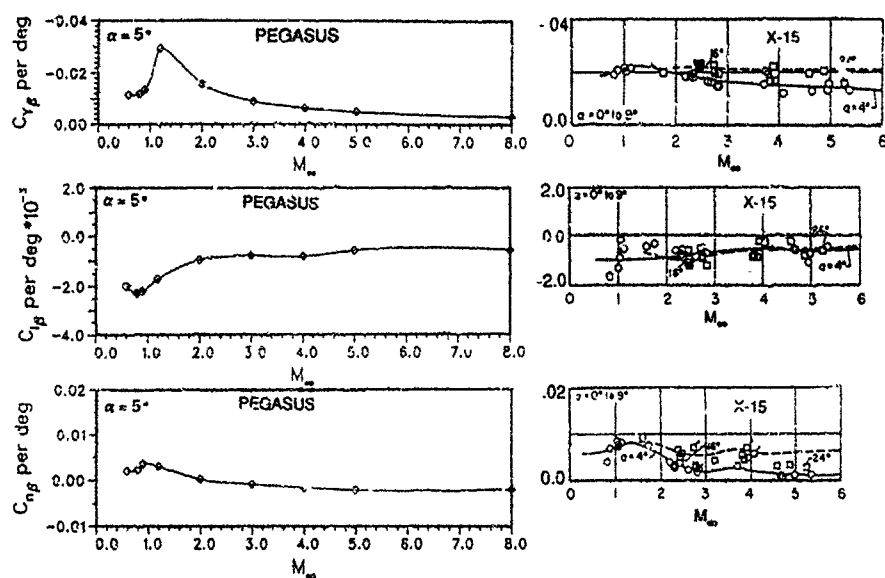


Figure 12.- Comparison of Pegasus and X-15 lateral stability derivatives.

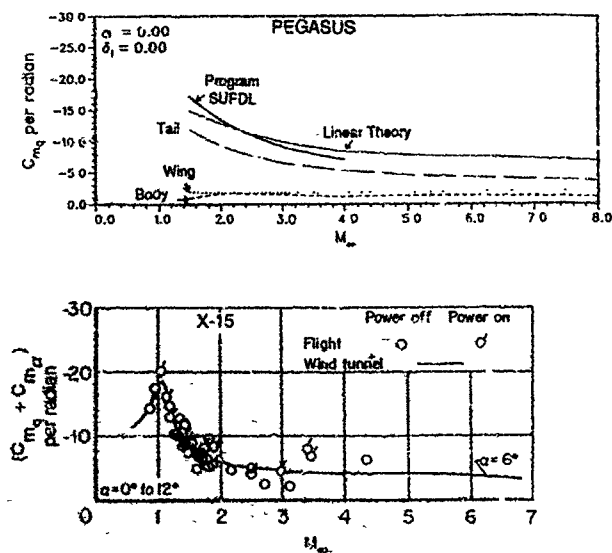


Figure 13.- Comparison of Pegasus and X-15 dynamic stability derivatives.

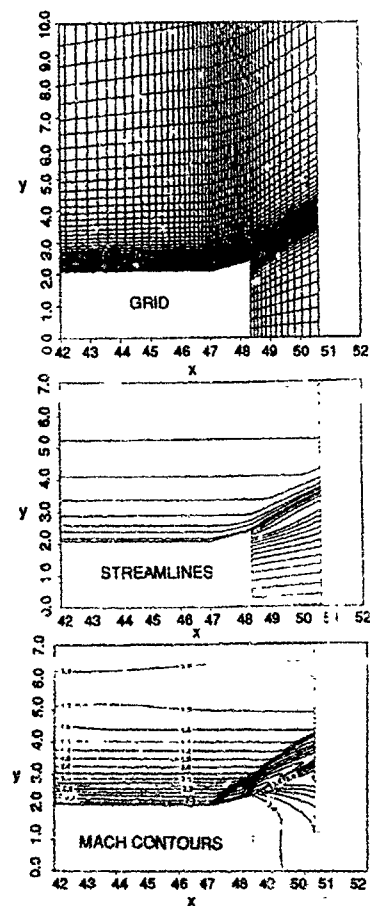


Figure 14.- Pegasus plume interference predictions,  $M_\infty = 5$ .

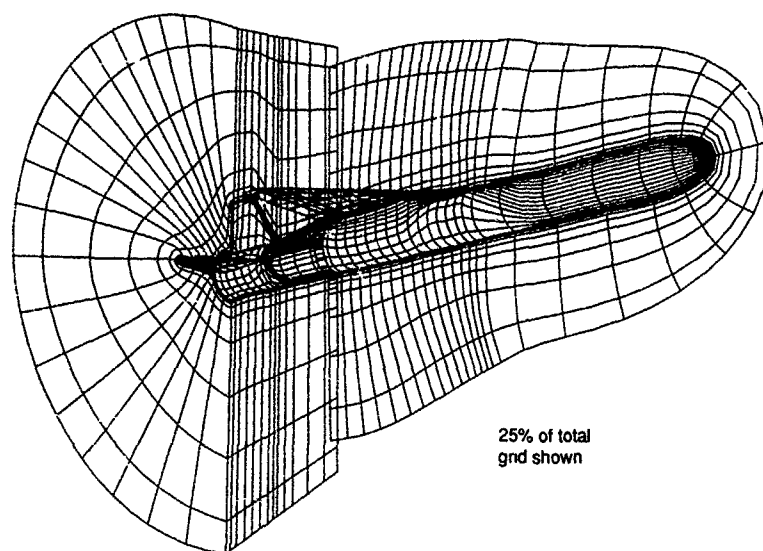


Figure 15.- Pegasus grid for three-dimensional Navier-Stokes calculations,  $M_{\infty} = 5$

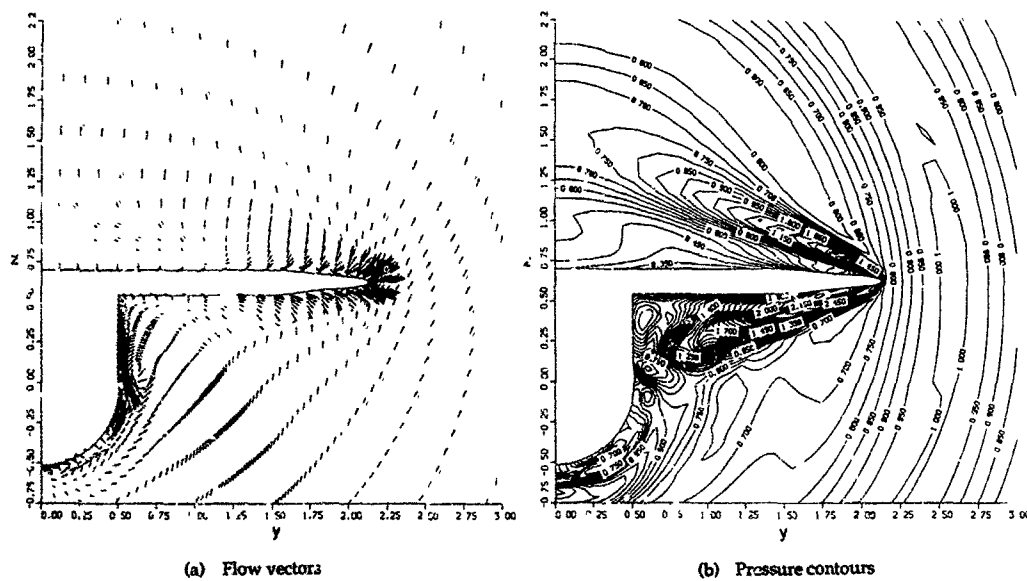


Figure 16.- Predicted flow characteristics in vicinity of Pegasus wing fillet,  $M_{\infty} = 5$ ,  $\alpha = 5^\circ$ .

# APPLICATION OF EULER AND NAVIER-STOKES CODES TO MISSILE TYPE BODIES WITH HIGH L/D RATIOS

by

D.J. Jones NAE, Ottawa, Canada

J. Evans DREV, Valcartier, Quebec, Canada

F. Priolo NSWC, Silver Spring, MD, United States

W. Sturek BRL, Aberdeen, United States

A. Wardlaw NSWC — White Oak, Applied Mathematics Branch (R44)  
Silver Spring, MD 20903-5000  
United States

## SUMMARY

Several Euler codes and a Parabolised Navier-Stokes code are used to predict normal forces, pitching moments and centres of pressure on long axisymmetric bodies which are cone cylinders or tangent ogive cylinders one of which has 3 fins. Only supersonic flow situations are considered so that downstream marching methods are valid. The Mach number range is from 2 to 5 and the incidence range is up to  $15^\circ$ .

## Nomenclature

b	body radius	r	radial distance
$C_m$	pitching moment	x	axial distance (also z)
$C_L$	lift coefficient	$X_{cp}$	centre of pressure from nose
$C_p$	pressure coeff	z	axial distance
D	cylinder diameter	$\alpha$	angle of incidence
L	length of body	$\beta_s, \beta_o$	separation parameters
$L_n$	length of nose	$\phi$	circumferential angle
M	Mach number	$\phi_s, \phi_o$	separation parameters
$M_{cr}$	critical Mach for clipping		

## 1.0 INTRODUCTION

The aim of this paper is to assess the accuracy of numerical predictions of surface pressures, normal forces and pitching moments about several bodies at moderate incidences (up to  $15^\circ$ ). Only one practical missile shape is considered and this is an axisymmetric cone cylinder with three fins. The other 4 bodies are ogive- and cone- cylinders of various nose lengths and total lengths. This is considered to be a good cross section of data suitable for testing present day CFD codes. All the data considered are for supersonic free stream Mach numbers from 2 to 5. It was decided as part of a more comprehensive exercise to concentrate on these simpler bodies for which data is readily available. Good prediction methods for these shapes can then be considered for more complicated geometries.

The complication of the flow field can be illustrated using the conical flow field shown in Fig 1 (taken from Ref 1 where a comprehensive description of the flowfield developments is given). Usually the primary crossflow separation just leeward of  $90^\circ$  is enhanced by a crossflow shock. This causes symmetrical (at moderate incidence) vortices to be formed just off the surface and a reverse flow from the leeward plane of symmetry near to the surface. This in turn can produce a secondary separation (perhaps with a shock) and a secondary vortex. In a similar way a third vortex may be formed in some cases. These phenomena can be correlated in some cases with the leeward pressure distribution as illustrated in Fig 2 (taken from measurements - see Ref 2).

Since the flowfield is so complex it is understandable that the numerical methods have difficulty in making a complete flowfield prediction. Our efforts here will not be to study the flowfield but rather to find methods of predicting normal force  $C_n$ , pitching moment  $C_m$  and centre of pressure  $X_{cp}$  as accurately as possible.

It was decided to limit the computations to Euler and Navier-Stokes codes since modern computer methods and computers can fairly conveniently be used in such cases. This is possible because of the supersonic freestream making downstream marching feasible.

A parabolised Navier-Stokes (PNS) code is used in the present study. At the start of the study it was uncertain how accurate these codes would be in predicting crossflow shocks and separation although they are designed to be capable of such predictions for moderate separation (Ref 3). It will be seen that PNS predictions are good at low incidence but some of the Euler codes with forced separation modelling are capable of better predictions at the higher incidences. It seems that the turbulence modelling in the Navier-Stokes code (Baldwin-Lomax) is not sufficiently accurate, probably because of length scales, for the higher incidences. A modification to the PNS code (described in Ref 4), which limited the turbulence model from having too large a length scale, was also attempted but did not show much improvement.

The Euler codes alone on a fine grid without any forced viscosity yield results which predict a strong crossflow shock at moderate incidences. This is unrealistic and so several methods for improving the situation have been attempted - particularly at the Naval Surface Warfare Center (see Refs 5 and 6 for example). Firstly, computing on a crude circumferential grid, which imparts more artificial viscosity into the flow, can be advantageous and shows some improvement over the fine grid results. One of the best methods seems to be to impart more circulation into the flow by the method termed 'clipping'. Here the crossflow velocities near the surface are slowed down in effect simulating the viscous layer. It will be seen that 'clipping' combined with a fairly coarse grid can give reasonable predictions. One of the reasons seems to be that the largest error in  $C_p$  occurs away from the windward and leeward planes of symmetry thus having little effect on the normal force and pitching moment. Although the above predictions are reasonable, the method will not in general accurately predict the off body flow field.

The first section will describe the 5 geometries used in this CFD validation process. Then the Navier-Stokes and Euler methods will be described and finally the results will be assessed.

## 2.0 WIND TUNNEL DATA.

**2.1 DFVLR DATA.** This is data obtained in the transonic and high speed wind tunnel facilities at DFVLR (see Ref 7). The data was taken with a view to improving available information for fuselage type bodies at high incidences so that this could be used, for example, for improving CFD codes. At these incidences separation is very dependent on Reynolds number and a series of tests were performed to study its effect on  $C_p$ . Several Mach numbers from 0.5 to 2.21 were run at incidences up to 90°. Pressure coefficients,  $C_p$ ,  $C_n$  and flow viz were obtained on the body which is shown in Fig 3. The body is a tangent ogive cylinder up to  $x/D=3$  and given by

$$\frac{x}{D} = 0.30984\left(\frac{x}{D}\right) - 0.039867\left(\frac{x}{D}\right)^2 - 0.002615\left(\frac{x}{D}\right)^3$$

The total length is 19 diameters. The present study will concentrate on the data obtained at  $M=2.21$  and incidences of 5, 10 and 15°. The Reynolds number based on diameter, which is 4cm., is  $3 \times 10^5$ .

**2.2 DREV DATA.** The long body anti-tank flechette shown in Fig 3 has a conical nose (7.5 deg half angle) followed by a cylindrical body and a finned aft end. This model together with several others was tested (see Ref 8) in the Defence Research Establishment Valcartier (Canada) 0.6m x 0.6m supersonic wind tunnel. Tests were carried out using different nose cones, fin shapes, cant angles and surface finishes. For each configuration, normal and axial forces as well as pitching and rolling moments were recorded at angles of incidence from -5 to 15 deg. and for Mach numbers from 1.75 to 4. Pressure data was not recorded.

The case selected here for computing is designated N3B3P8. The fins are located every 120 degrees with one at the leeward plane of symmetry. The Mach number is 3 and the incidences are 0, 5, 10 and 15 deg. The Reynolds number of the tests was  $8.1 \times 10^6$  per metre and the actual diameter of the body was 0.875 inches.

**2.3 NAE DATA.** A series of tests on bodies of revolution was carried out in the NAE 5X5ft High Speed Wind Tunnel in the 1960's. Sixteen bodies in all were tested at one subsonic (0.5) and two supersonic (2 and 3.5) Mach numbers. Each of the models consisted of a cylindrical aft body of length either 6 or 12 diameters (the diameter was 4 inches). The nose shapes were either conical or tangent ogives and were of 3 or 5 diameters in length. The models were swept up to 28° in the first phase of the tests (Ref 9) in which only balance measurements were taken. In the second phase (Ref 2) pressure measurements were made at approximately 3, 7, and 11° incidence and some flow viz was taken on the conical nose body with the longer aft body. Both balance and pressure integrated values are plotted. The models used for the current comparison are shown in Fig 3. The first one, designated 1001, is a conical nose of half angle 5.7° and the second is an ogive cylinder, designated 3001, with the ogive defined as

$$\frac{x}{L_n} = 1 - \left(1 - \frac{x}{L_n}\right)^n$$

where  $n=5/3$  and  $L_n$  is the nose length (5 diameters in this case). This body has a nose with a half angle of 9.5°.



2.4 BRL DATA FOR SEARS HAACK BODY. The forebody of this configuration (see Fig 3) is the Sears Haack body given by

$$r = 0.5 \left[ 1 - \left( \frac{x}{2.42} - 1 \right)^2 \right]^{0.75}$$

where the nose length is 2.42 calibres and the total length including the cylinder is close to 36 calibres (one calibre is 23.8mm).

Wind tunnel data in the form of total aerodynamic coefficients are available for this configuration (quoted in Ref 4). Data was taken at +2° and -2° incidence with several lengths of cylindrical aft bodies giving data at body lengths between 20 and 36. It will be seen that  $C_x$  and  $C_y$  differ depending on sign of incidence at the longer body length indicating difficulty measuring accurately on these very long bodies.

For this body it is assumed in the computations that the cylinder is of constant diameter rather than diminishing as shown in the figure; it is thought that this will not have significant effect.

### 3.0 COMPUTER CODES.

3.1 SWINT Computer Code. This is a space marching Euler code designed for computing supersonic flow about bodies with Nose, Inlet and Tail (see Ref 5). The body, together with the attached inlet (if any), must be a single valued function of circumferential angle  $\phi$ . In general leading edges must be sharp and 'sufficiently' supersonic, otherwise semi empirical methods are used. Fin thicknesses are ignored (only the slope is used in the computation) and they must be close to radial. The Euler equations are integrated step by step downstream using a MacCormack predictor-corrector scheme. On each step the shock location is determined by using characteristics and the Rankine Hugoniot relations. Slope discontinuities are handled by analysis to account for expansions or compressions. Smoothing is applied in some cases, either where the user requests it or if the pressure goes negative. This is done by applying a Schuman filter to the conserved variables and can be thought of as a form of artificial viscosity. The original code tried to simulate crossflow separation by prescribing the direction of the two body surface streamlines nearest to the experimentally determined separation line to be in the direction of the separation line. This works well in some cases but is unsatisfactory as a knowledge of the separation line is first needed. At higher incidences secondary separation may occur and will eventually cause instability although smoothing may help in some cases.

A later version of the code incorporates a separation modelling called 'clipping'. This works by limiting the crossflow velocities rather than rigidly prescribing streamline directions near the experimental separation line. The method, developed by Baltakis et al (Ref 6), limits crossflow Mach number with a more severe limitation near the body than further away, thus adding more circulation to the flow. After trials with several formulas the final form used in the program is

$$M_{\infty} = 0.145 \sqrt{\epsilon} (r/b)^3$$

This was found to be good for turbulent, high Reynolds number flows. Thus the crossflow velocity  $v$  is 'clipped' but without changing pressure, density, enthalpy or entropy. The total stagnation enthalpy is kept constant by redefining the axial velocity  $w$ . Baltakis shows [6] improved  $C_p$  distributions for the case of a tangent ogive cylinder at Mach numbers up to 4.5 with the improvement being more pronounced at lower Mach numbers. However  $C_x$  and  $C_y$  are not improved by any significant amount. The reason for this appears to be that substantial change to pressure occurs around  $\phi=90^\circ$ , which does not affect normal force and pitching moment very much, while on the leeward side  $\phi>120$  deg the differences are smaller. In the tangent ogive case shown in Ref 6 the normal force and pitching moment were predicted quite accurately even with no 'clipping' applied. In the case with fins, also shown in Ref 6,  $C_x$  and  $C_y$  were improved considerably using the 'clipping' option.

The current interest in this paper is to investigate the accuracy of SWINT with and without clipping. It will be seen that in most cases,  $C_x$ ,  $C_y$  and pressure distributions are improved considerably with the clipping option.

3.2 AEUS Computer Code. This is a method (see Ref 10) based on a Zonal Euler Solver. It is a second order Godunov method which is applied to the Riemann problem associated with each finite volume cell. Since the Godunov method is based on local analysis the method can handle more complicated geometries than the SWINT code mentioned above. It was found that SWINT lacked robustness in cases of complicated geometries and the artificial viscosity had to be increased to force a solution. Experience with a first order Godunov method was found to be more robust. However to obtain good accuracy in smooth flow regions it was found that a very fine mesh was needed. The second order method used here overcame the problems and produces accurate solutions for complicated geometries using efficient grids.

In the ZEUS code the clipping option mentioned above in the SWINT code is also available as an option. In our comparisons shown later we will be comparing both with and without clipping. Also in the ZEUS code there is an option for clustering grid points in the radial direction so as to get better definition near the body; some of these results will also be shown.

Another option in the ZEUS code is to activate the Salford Separation Model which is described in Ref 11. In this model an approximation to the separation line must be known in advance. On each point on either side of this line the pressure and density are axially advanced from an averaging of the values on each side in the crossflow plane. The velocity components at these cells are computed from the constraint of total enthalpy and the specification of the streamline directions on each side of the separation line. This requires 4 angles to be specified  $\phi_u, \phi_s, \beta_u, \beta_s$  where the first two define the upstream streamline directions, axially and crossflow, and are normally taken to be  $20^\circ$  and  $20^\circ$ . The latter two are for the downstream streamline normally taken to be  $5^\circ$  and  $20^\circ$ . The vortex sheet off the surface is then captured by the numerical scheme. The constants in the model were chosen from work on bodies at  $12$  to  $16^\circ$ . In the present paper the method is applied at  $7$  and  $11^\circ$  on the NAE bodies.

**3.3 PNS Computer Code.** The Parabolized Navier-Stokes code used here is the version developed by Schiff and Steger (Ref 3) and subsequently modified by Rai and Chaussee of NASA Ames Research Centre. This code is an approximately factored, fully implicit, thin layer code based on the Beam-Warming algorithm. The computations assume a fully turbulent boundary layer which is modelled using a Baldwin-Lomax algebraic turbulence model. The code accomplishes the computations by marching in the axial direction using a conical flow starting solution. The restrictions on the computations are supersonic outer flow and no flow separation in the axial direction (flow separation in the circumferential direction is allowed). A modification to the code (Ref 4) was included for some of the calculations to try to extend the range of applicability of the modelling. In this modification limits are imposed to keep the turbulence model from having too large a length scale. In general it was found that this did not give significant improvement.

#### 4.0 RESULTS

##### 4.1 DFVLR DATA

a) **SWINT Results.** SWINT was run on a  $36 \times 40$  mesh (40 radially). To observe the major differences in  $C_p$  with and without clipping it is best to observe the highest incidence case of  $15^\circ$ . (see Figs 4a and b). It can be seen that on the windward side,  $\phi < 45^\circ$  say, the experiment and theories are well matched and thus the windward contribution to lift is fairly accurate. However on the leeward side the result without clipping gives too high a pressure due to prediction of a strong shock at about  $120^\circ$  (for  $x/D = 8.22^\circ$  for instance). This leads to too low a value for local lift due to these differences on the leeward side - emphasized in Fig 4a by the shaded area. On the other hand the clipped result of Fig 4b shows a much flatter pressure distribution on the leeward side, and this is very close to the experimental data - the difference for  $x/D = 8.225$  is again highlighted on the figure. Now the local lift is much closer to experiment as confirmed in Fig 5b compared to Fig 5a.

b) **ZEUS Results.** A ZEUS result without clipping at  $\alpha = 10^\circ$  is shown on Fig 6 - this is shown to demonstrate the inaccuracy obtained without clipping. The ZEUS results with clipping on a  $72 \times 72$  mesh were very similar to those of SWINT ( $36 \times 40$ ) with clipping. Clustering of points nearer to the body helped to give second order improvement. The final result was very satisfactory and, for instance,  $X_{cp}$  was computed to half a calibre accuracy.

c) **PNS Results.** At  $\alpha = 5^\circ$  the PNS results are very good (see Fig 7) but at  $10^\circ$  the accuracy is quite poor. Looking at the pressure plots at  $10^\circ$  (Fig 8) it can be seen that the pressure appears generally to be too high on the leeward side at least prior to the experimental recompression at about  $150^\circ$  and this results in the lower lift predictions of Fig 7.

**Conclusions.** SWINT and ZEUS without clipping are clearly inadequate and should not be used in such calculations. The clipping option yields much better results which are accurate enough for design purposes on this sort of configuration. The PNS code does not appear to be sufficiently accurate except at  $5^\circ$  incidence.

##### 4.2 DFVLR FINCHETTE

a) **SWINT SEPARATION MODEL Results.** The results obtained using the SWINT separation model (see SWINT description above) are shown together with ZEUS results on Figures 9-11. The separation model was not used in the fin region. The code was used with a  $36 \times 40$  grid (every  $5^\circ$ ). It can be seen that  $C_p$  and  $C_m$  are not quite as accurate as the ZEUS results at least when  $\alpha$  is above  $10^\circ$ . Below  $7.5^\circ$  the results are in good agreement with experiment. In general all results for  $X_{cp}$  are within half a calibre of the experiment. It can be seen from Figure 10 that the local lift is similar to that of ZEUS. The effect of fin lift can be observed in this figure and its major contribution to total lift is clear. This is probably the reason for such a good agreement of  $C_p$  compared to experiment for this configuration as opposed to other cases studied in this paper. The pressure ratio plots (Figs 11a-11e) indicate that

separation modelling has already been used in the SWINT code as early as one calibre downstream. However with differences compensating on the leeward side and with being over such a small distance and area it does not affect total lift appreciably. On the windward side SWINT results match very well to those of ZEUS without clipping.

b) **ZEUS Results.** Also shown on Figures 9-11 are results obtained using ZEUS and ZEUS with clipping and clustering (designated C+C). The clustering in this case was applied in the fin region and biased points toward the body giving about 10 points on the widest part of the fin; this was achieved using  $r^{1.4}$  as a transformation. The fin thickness was taken to be zero. A 36X36 grid was used in two zones with 12 circumferential points between the windward plane of symmetry and the fin at 60 degs and 24 points between this fin and the leeward plane of symmetry (where there is also a fin). As can be observed the overall forces and moments appear to be equally accurate and very close to the experimental data. ZEUS(C+C) is clearly more accurate in centre of pressure prediction (Fig 9c) at 5° but this may be fortuitous as the numerator and denominator in the ratio are still relatively small. To be sure more computations would have to be done at the smaller angles of incidence. The pressure results are shown on Figs 11a-11e. The clipping becomes effective at  $x/D=3$  while clustering is effective only in the fin region ( $x/D>22$ ).

**Conclusions.** All the results appear to be reasonably good in this case with centre of pressure being accurate to within about half a calibre. Even the ZEUS results without clipping are surprisingly good when one considers the poor DFVLR result. The reason for this is possibly that the fins contribute a large amount to total forces and moments. ZEUS(C+C) is more accurate in predicting  $X_{cp}$  at 5° but this may be fortuitous (see above). In general any of the above methods could be used for design purposes in this finned body case.

#### 4.3 NAE BODIES 1001 and 3001.

a) **SWINT.** Results were computed on a 36X40 grid with clipping. In general the results were not as good as the similar DFVLR case covered above. In fact with the 1001 body (conical nose) at Mach 2 the local normal force was negative downstream of about 7 diameters. However at  $M=3.5$  the results matched the experiment fairly well as they also did for the 3001 body at both Mach 2 and 3.5. This seems to indicate that the stronger shock cases may be easier to compute - recall that the DFVLR body was a 7.5° nose half angle run at  $M=2.21$ . On Figs 12 and 13 are shown the comparisons of  $C_n$  and  $C_m$  at the 3 incidences. It can be seen that  $X_{cp}$  is predicted to within 1 calibre for the successful computations.

b) **PNS.** The PNS results are exceptionally good (see Figs 12 and 13) in all four of the low incidence cases  $\alpha=3^\circ$  with, for example,  $X_{cp}$  being accurate to half a calibre. Also the Mach 3.5 cases at  $\alpha=7^\circ$  are exceptionally good and should lead to a good design and prediction for these bodies. The only shortcoming is at Mach 2 at the 7° incidence; in this case the  $X_{cp}$  values are predicted close to one calibre upstream of the experimental value. As will be seen the other prediction methods suffer here also. Looking at the local normal force shown on Figs 14a) and b) it is seen that the absolute error in local lift is about the same whether the Mach number is 2 or 3.5. However in the case of Mach 2 the relative error will be bigger since the total lift is smaller. Total pitching moment will also be smaller - leading to a greater inaccuracy at Mach 2 compared to Mach 3.5.

c) **ZEUS.** This code was run on a 72X72 mesh and the computations were made with the regular code and also with the Salford Separation Model described earlier. One can clearly see the inaccuracy of the regular code at Mach 2 while at Mach 3.5 the prediction is only good at  $\alpha=11^\circ$ , the indication being that the stronger shock will produce better results. A second run on a 36X36 mesh produced quite reasonable results for this case (Figs 12 and 13) unlike the DFVLR configuration covered earlier in which a 36X40 SWINT result without clipping was quite poor and misleading in its predictions.

The separation model gives exceptionally good results for both angles of 7° and 11° at Mach 3.5. It is also very satisfactory at Mach 2 and  $\alpha=11^\circ$  but is not so good at Mach 2 and  $\alpha=7^\circ$ . The angles used in the separation model were based on experimental data at 12 and 16° so the inaccuracy at the lower incidence is probably due to this but with Mach 3.5 being more forgiving.

**Conclusions.** At the low incidence of 3° the PNS code is exceptionally good. Also at low incidence the 36X40 SWINT results with clipping are generally acceptable except that for configuration 1001 the code gave negative local lift over a large part of the cylinder putting the usefulness of this approach in doubt for these low incidence cases. The same problem was encountered at 7°. One can conclude, somewhat unsatisfactorily, that the code only works reasonably well as long as the local lift values remain positive.

For this configuration the regular ZEUS program on a 36X36 grid performed very well at 7° and 11° contrary to experience with the DFVLR configuration where a similar grid using SWINT produced poor results. The reason for this is not understood at this time.

The Salford Separation Model produced exceptionally good results at  $\alpha=11^\circ$ . It would be worth investigating model constants that were more suitable for lower incidence so that good predictions could also be made in these cases.

#### 4.4 SEARS HAACK BODY

a) PNS. The PNS results were obtained using a  $10^\circ$  half vertex angle and so tend to differ over the forebody from the ZEUS and SWINT results to be shown later. It can be seen (Fig 15a-15d) that excellent results are predicted using the Baldwin-Lomax model of this code, clearly showing that the boundary layer growth is being predicted accurately.

b) SWINT. This case made an interesting case study for SWINT calculations since initial results were so poor that several modifications were attempted to obtain improvement. Without clipping applied (Fig 16a) the results for  $C_x$  and  $C_m$  are clearly in error particularly as the pitching moment about the nose goes negative. Applying clipping, although not really designed for this low incidence application, does give some improvement (Fig 16b) but  $C_x$  is still only about 0.2 instead of being of order 1. Clearly the boundary layer growth is essential for obtaining further improvement. To this end a simple linear growth of  $0.00495(x-2.42)$  was applied to the body aft of the nose region ( $x=2.42$ ). This growth was first applied without clipping and gave some improvement as shown in Fig 16c. However a much improved solution was obtained by clipping and also allowing the simulated boundary layer growth as is shown in Fig 16d. This result indicates that a more sophisticated prediction of the boundary layer would be worth incorporating into the inviscid codes. Only the Mach 4 results were computed for this body.

c) ZEUS. The ZEUS results on a 72x72 grid without clipping (not shown) were quite similar to SWINT results although they did not show quite so much loss in lift. Results improved somewhat by allowing for boundary layer growth but pitching moment was still very low indicating insufficient accuracy in the boundary layer approximation (Fig 17).

Conclusions. Clearly the boundary growth has to be simulated for this very long body at small incidence. The PNS code automatically computes this with the Baldwin-Lomax model and is obviously accurate in its prediction.

#### 5. CONCLUSIONS.

a) Computationally efficient Euler and Navier-Stokes methods are available for predicting long body computations in supersonic flow.

b) The PNS code gives a good prediction for incidences up to  $5^\circ$  but it is not so accurate at higher values. It was the best method for the very long Sears-Haack body at  $\alpha=2^\circ$ .

c) At higher incidence and Mach number above 2 the SWINT or ZEUS results on a coarse grid with clipping are usually accurate to 1 calibre in centre of pressure prediction. At Mach 2 none of the methods seemed to be completely reliable. Extrapolation of coefficients from results at higher numbers may be more suitable. The Salford separation model, if the separation parameters can be standardised, looks like a promising technique.

d) The case of the long body with fins produced excellent results with the Euler codes modified for separation modelling.

#### REFERENCES.

1. Rainbird W.J. "Turbulent Boundary Layer Growth and Separation on a Yawed Cone" AIAA Journal Vol 6, No 12, Dec 1968.
2. Atraghji E.G. "Pressure Distribution over a Family of Inclined Long slender Bodies of Revolution at  $M=0.5$ , 2.0 and 3.5" National Research Council of Canada Report LTR-HA-5X5/0029, 1968
3. Schiff L.D. and Steger J.L. "Numerical Simulation of Steady Supersonic Viscous Flow" AIAA Journal Vol 18, no 12, Dec 1980.
4. Weinacht P., Guidos B.J., Sturek W.B., Hodes B.A. "PNS Computations for Spinning Shell at Moderate Angle of Attack and for Long L/D Finned Projectiles." AIAA Paper 85-0273, Jan, 1985.
5. Wardlaw A.B., Baltakis F.P., Solomon J.M. and Hackerman L.B. "An Inviscid Computational Method for Tactical Missile Configurations" Naval Surface Weapons Center Report NSWC/TR-81-457, Dec 1981.

6. Baltakis F.P., Wardlaw A.B. and Allen J.M. "Leeside Crossflow Modeling in Euler Space-Marching Computations" Naval Surface Weapons Center Report NSWC/TR-86-342, Nov 1986.

7. Hartmann K. "On the Influence of Reynolds Number on the Normal Forces of Slender Aircraft Bodies" DFVLR Report 251-76-A-20, 1976.

8. Evans J., Drouin G. and Cheers B. "Second Series of Wind Tunnel Tests of the Flechette Anti-Tank Penetrator - Trial FATWT-2" Defence Research Establishment (Canada) Report DREV Memorandum 2677/84. March 1984.

9. Atraghji E.G. "The Influence of Mach Number, Reynolds Number, Semi-nose Angle and Roll Rate on the Development of the Forces and Moments over a Series of Long Slender Bodies of Revolution at Incidence." National Research Council of Canada Report LTR-HA-5X5/0020, 1967.

10. Wardlaw A.B. and Davis S.F. "A Second Order Godunov Method for Tactical Missiles" Naval Surface Weapons Center Report NSWC TR 86-506, Dec 1986.

11. Kwong C.M. and Myring D.F. "Fusiform-Body Separated Flow Field Calculation using Euler and Boundary Layer Equations" Royal Aero Soc Conference on Prediction and Exploitation of Separated Flows. Paper No 27, April 1989.

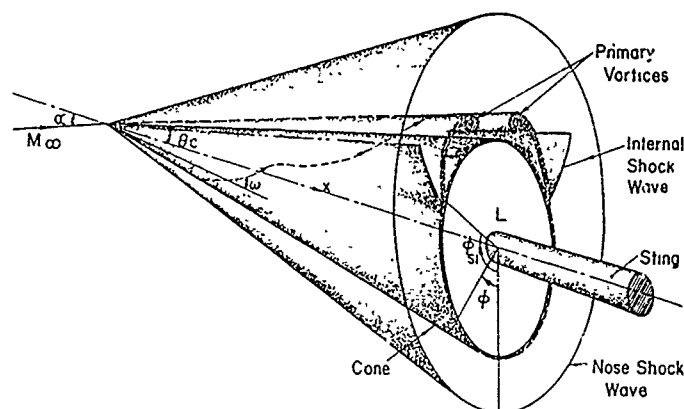


Fig 1. Sketch of Flow Past a Yawed Cone.

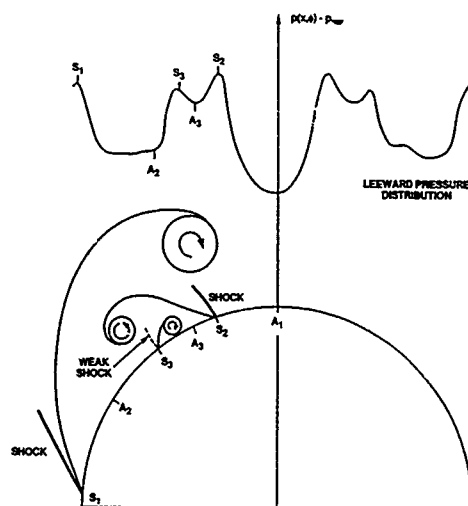


FIG. 2: AN INTERPRETATION OF THE CIRCUMFERENTIAL PRESSURE DISTRIBUTION ON A TANGENT OGIVE - CYLINDER

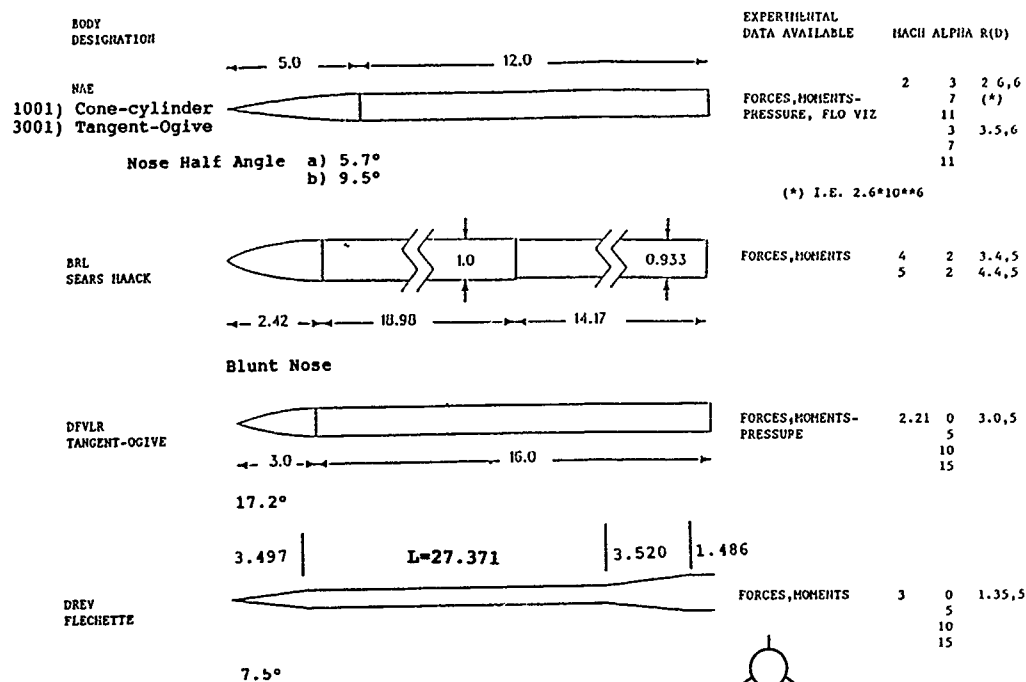
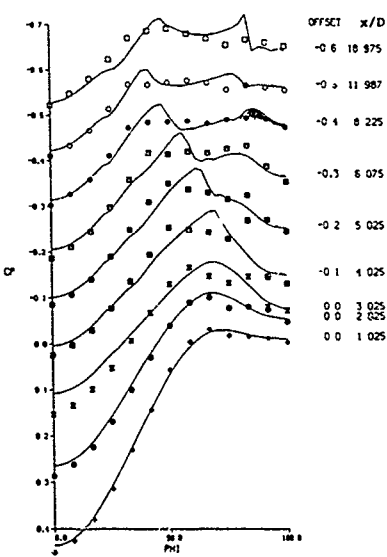
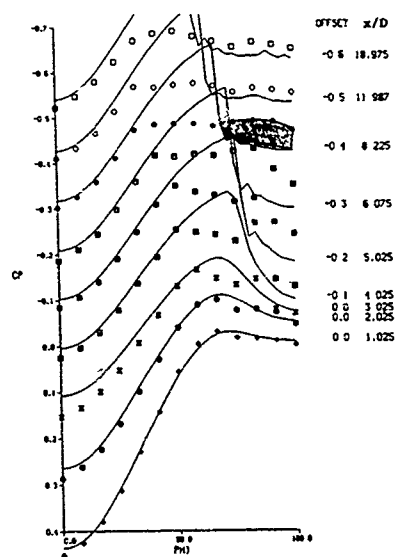


FIG. 3: CONFIGURATIONS USED IN THE CFD STUDY



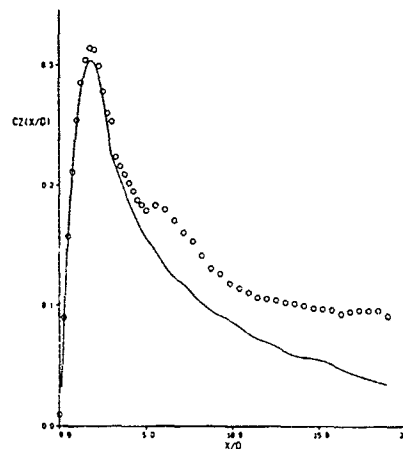


Fig 5a. Local Lift Coefficient versus  $x/D$ .  
DFVLR Body.  $M=2.21$ ,  $\alpha=15^\circ$ .  
SWINT without Clipping.

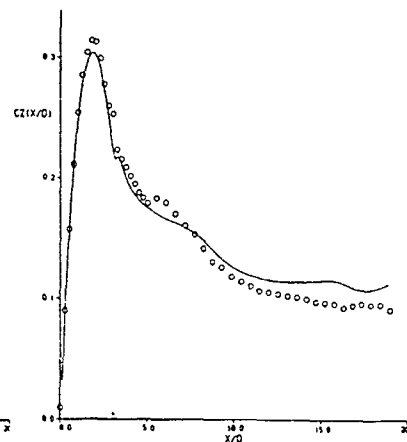


Fig 5b. Local Lift Coefficient versus  $x/D$ .  
DFVLR Body.  $M=2.21$ ,  $\alpha=15^\circ$ .  
SWINT with Clipping at  $x/D=3$ .

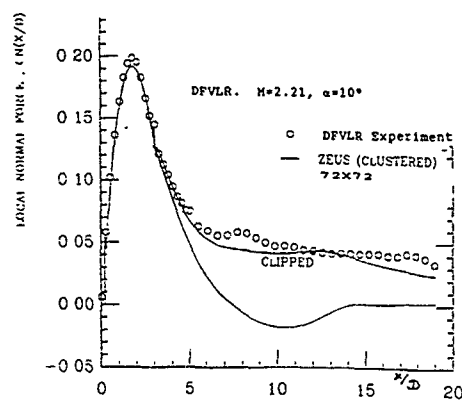


Fig 6. Local Lift Coefficient for DFVLR Body.  
ZEUS with and without Clipping.

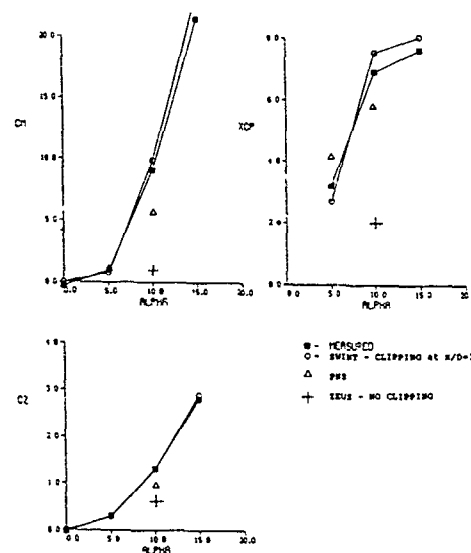


Fig 7. Total Coefficients and  $X_{cp}$  for DFVLR Body.

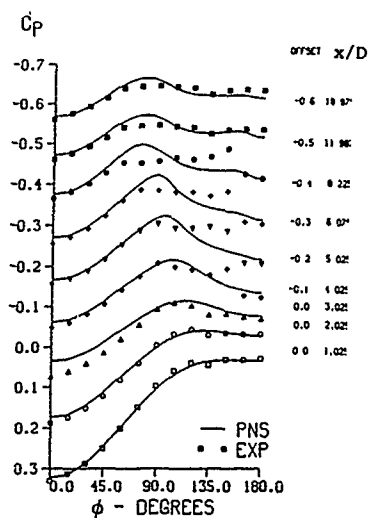


Fig 8. PNS Computations of  $C_p$  for DFVLR Body.  
 $M=2.21$ ,  $\alpha=10^\circ$

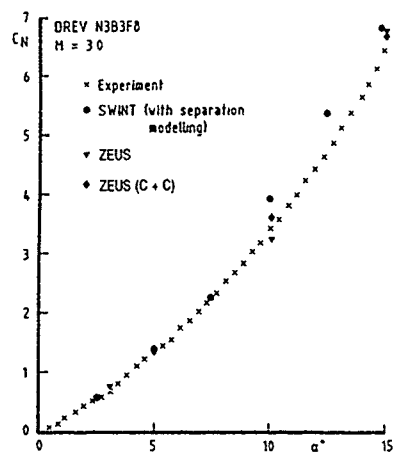
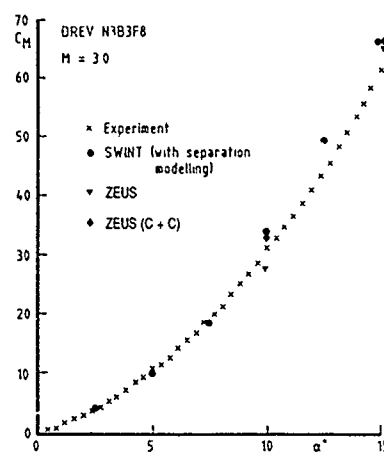
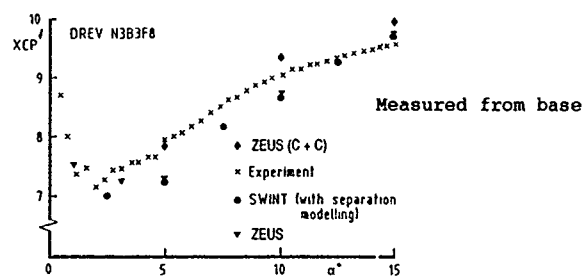
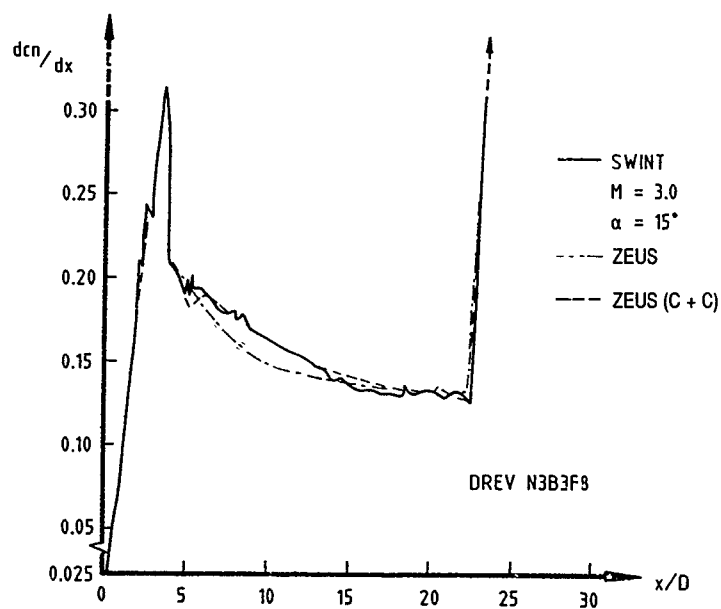
Fig 9a.  $C_N$  for the DREV FlechetteFig 9b.  $C_M$  for the DREV FlechetteFig 9c.  $X_{cp}$  for the DREV Flechette

Fig 10. Lift Curve Slope for the DREV Flechette



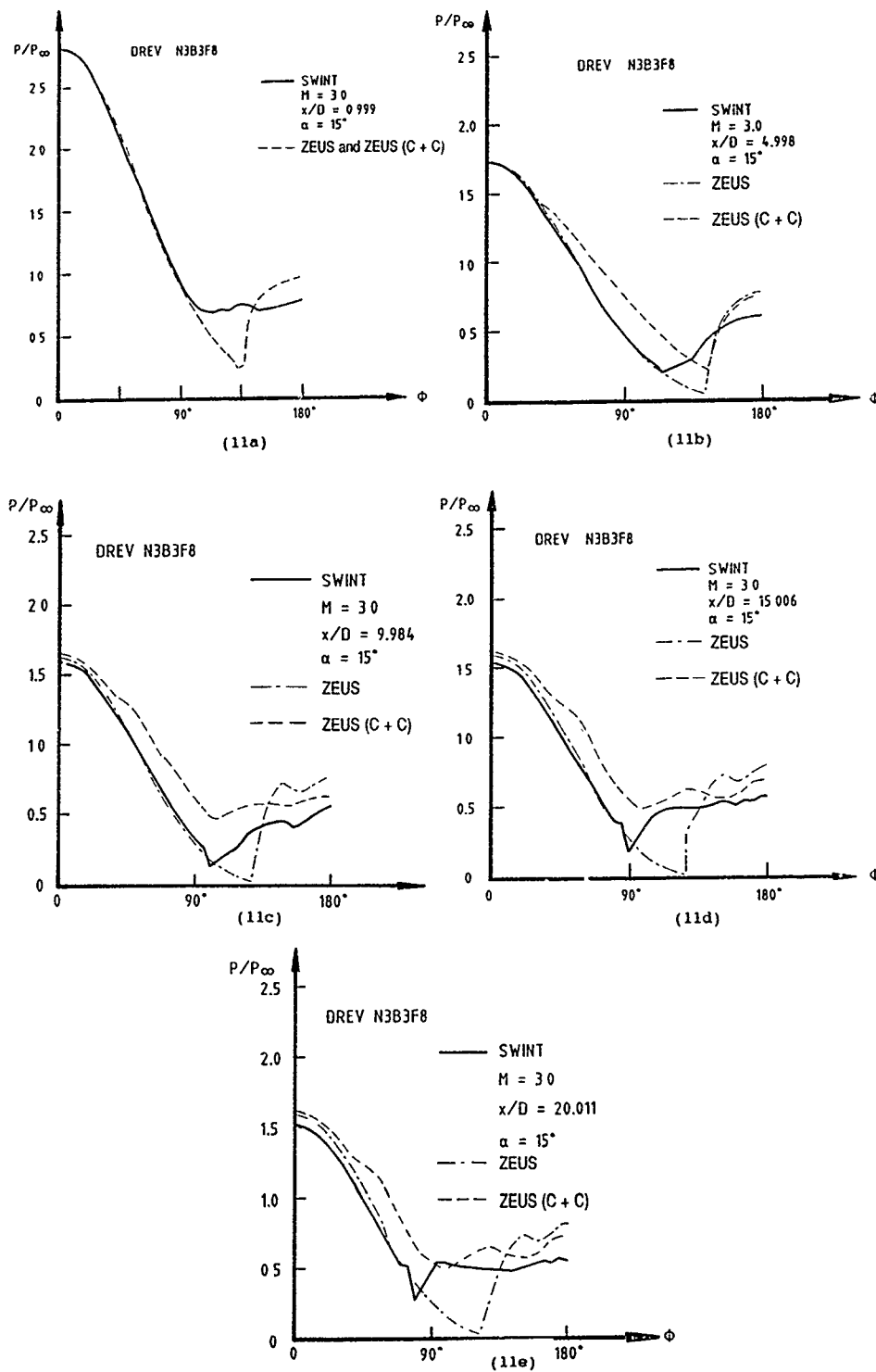
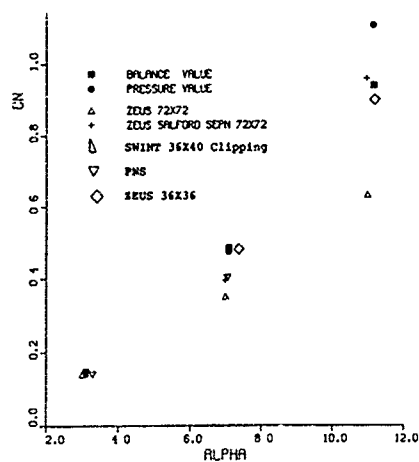
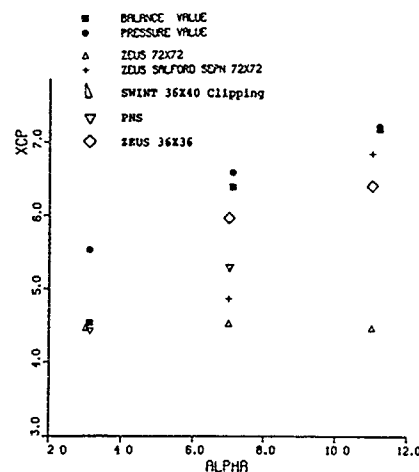
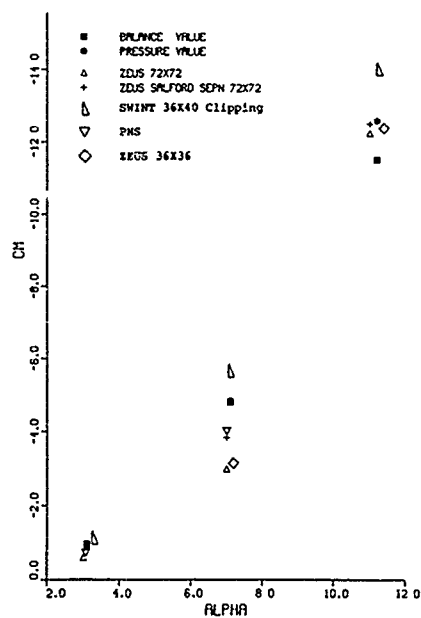
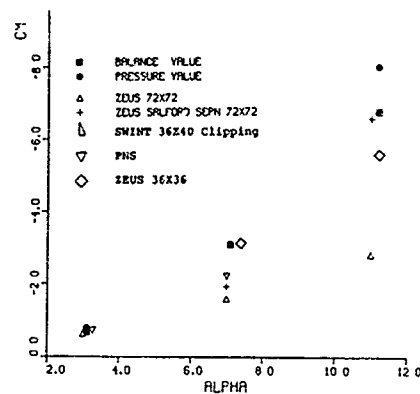
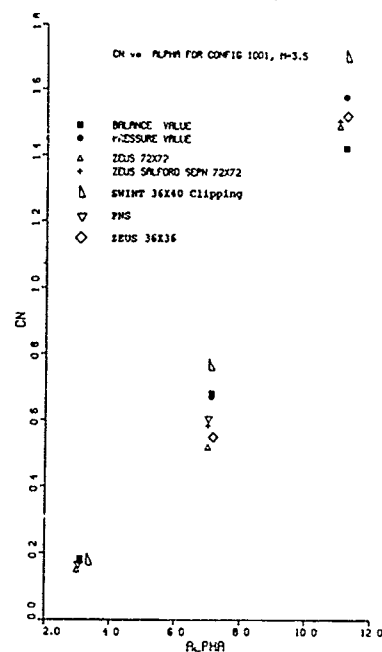
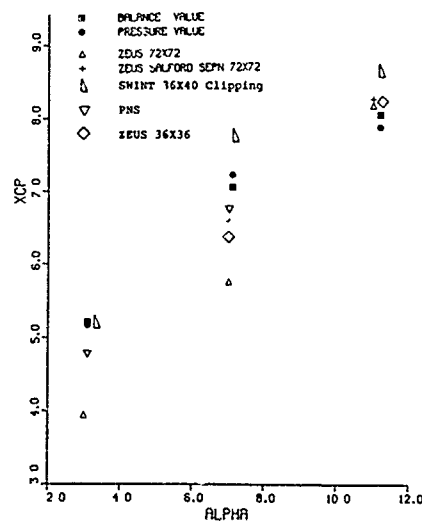
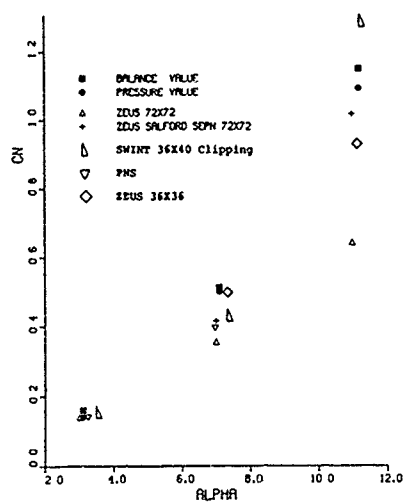
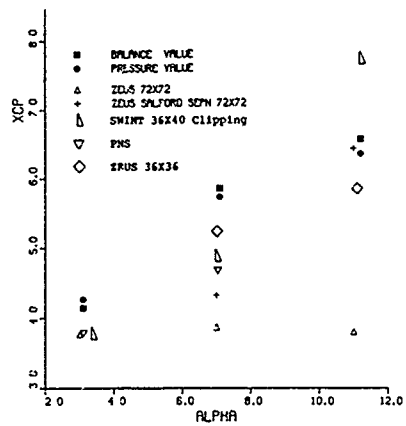
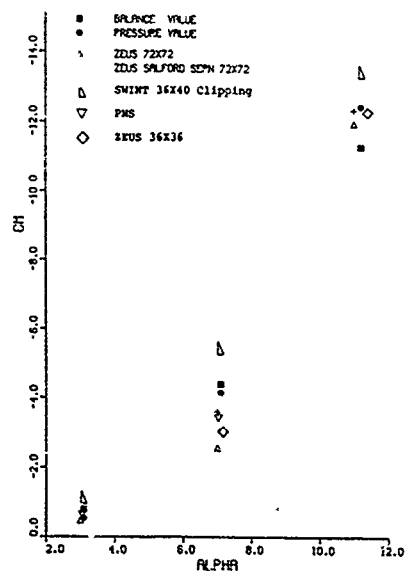
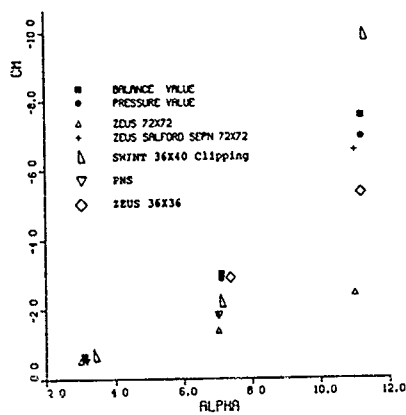
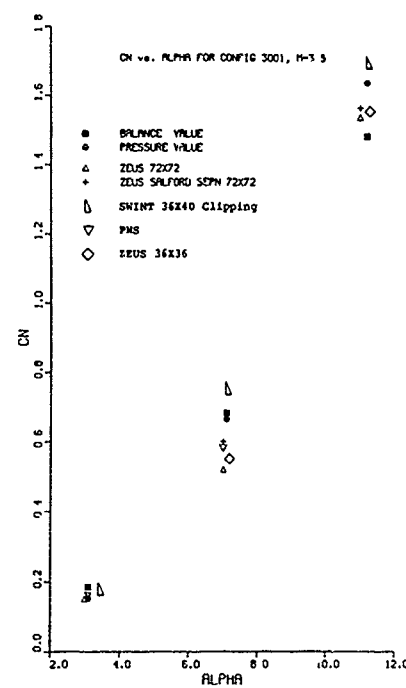
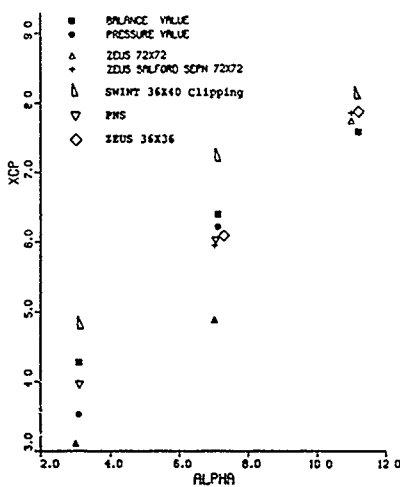


Fig 11a-11e. Pressure Distributions on the DREV Flechette at Various  $x/D$

Fig 12a.  $C_n$  vs.  $\alpha$  for Configuration 1001,  $M=2$ Fig 12c.  $X_{cp}$  vs.  $\alpha$  for Configuration 1001,  $M=2$ Fig 12e.  $C_n$  vs.  $\alpha$  for Configuration 1001,  $M=3.5$ Fig 12b.  $C_n$  vs.  $\alpha$  for Configuration 1001,  $M=2$ Fig 12d.  $C_n$  vs.  $\alpha$  for Configuration 1001,  $M=3.5$ Fig 12f.  $X_{cp}$  vs.  $\alpha$  for Configuration 1001,  $M=3.5$

Fig 13a.  $C_p$  vs.  $\alpha$  for Configuration 3001,  $M=2$ Fig 13c.  $X_{cp}$  vs.  $\alpha$  for Configuration 3001,  $M=2$ Fig 13e.  $C_p$  vs.  $\alpha$  for Configuration 3001,  $M=3.5$ Fig 13b.  $C_p$  vs.  $\alpha$  for Configuration 3001,  $M=2$ Fig 13d.  $C_p$  vs.  $\alpha$  for Configuration 3001,  $M=3.5$ Fig 13f.  $X_{cp}$  vs.  $\alpha$  for Configuration 3001,  $M=3.5$

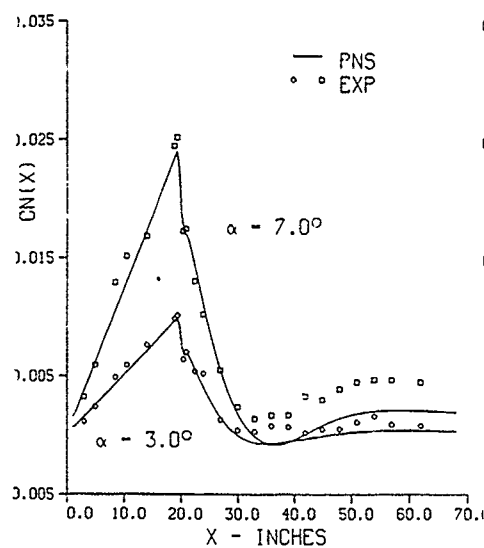


Fig 14a. PNS Code Applied to NAE Config 1001, M=2

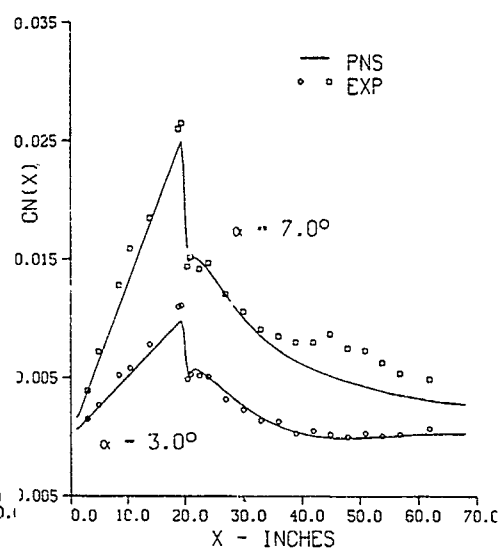
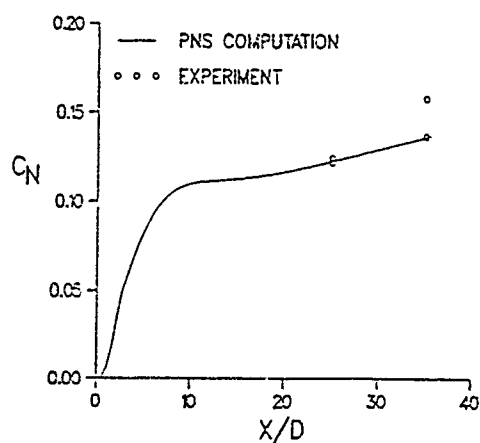
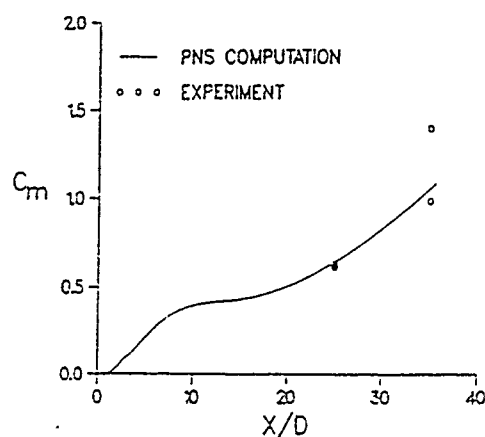
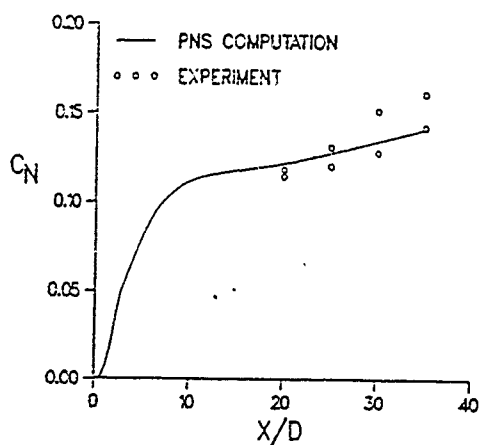
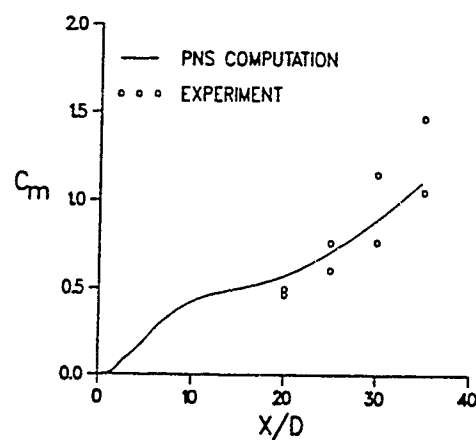


Fig 14b. PNS Code Applied to NAE Config 1001, M=3.5

Fig 15a. PNS Results for  $C_N$  for the Sears Haack Body, M=4Fig 15b. PNS Results for  $C_M$  for the Sears Haack Body, M=4Fig 15c. PNS Results for  $C_N$  for the Sears Haack Body, M=5Fig 15d. PNS Results for  $C_M$  for the Sears Haack Body, M=5

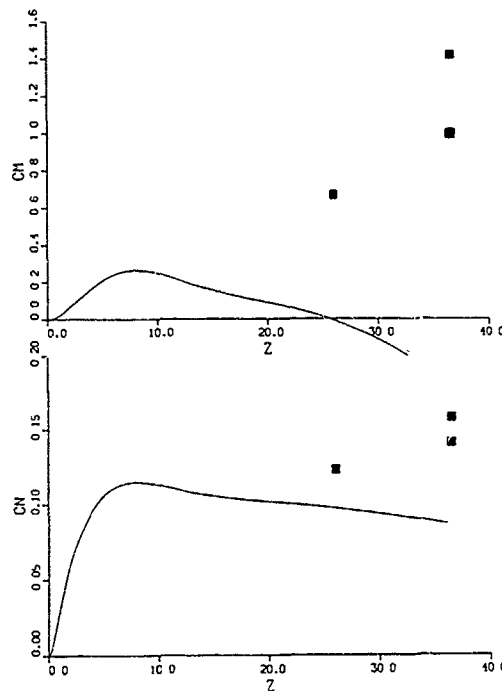


Fig 16a. SWINT(36X40) Applied to Sears Haack Body, No Clipping

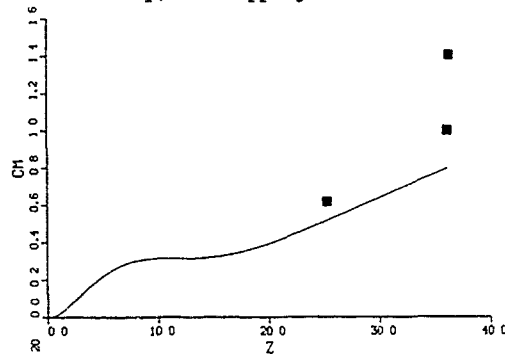


Fig 16c. SWINT(36X40) Applied to Sears Haack Body, No Clipping, Boundary Layer Simulation

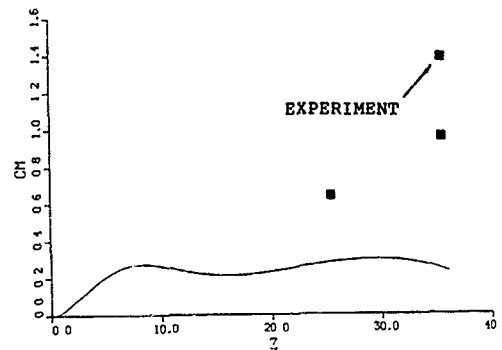


Fig 16b. SWINT(36X40) Applied to Sears Haack Body, Clipping at  $z=3$

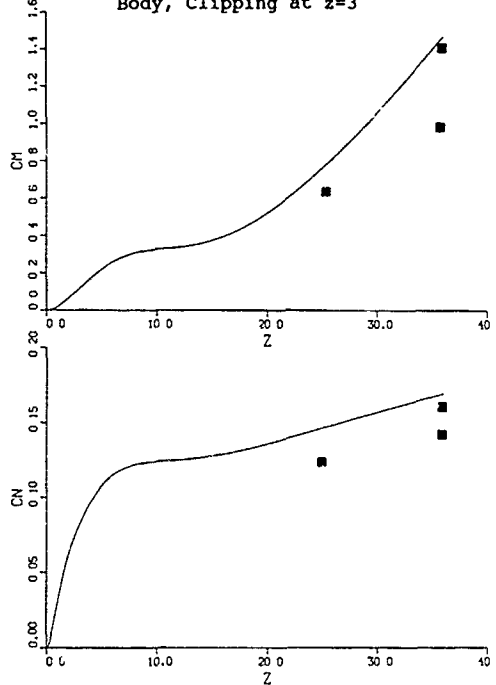


Fig 16d. SWINT(36X40) Applied to Sears Haack Body, Clipping at  $z=3$ , Boundary Layer Simulation

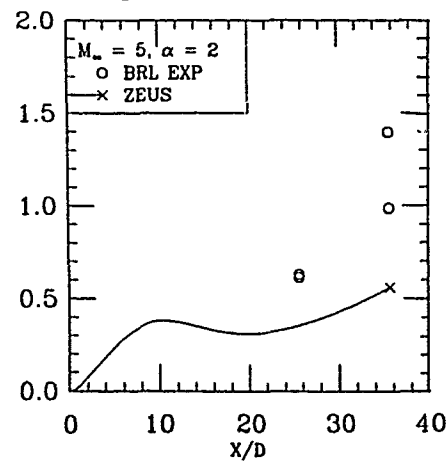
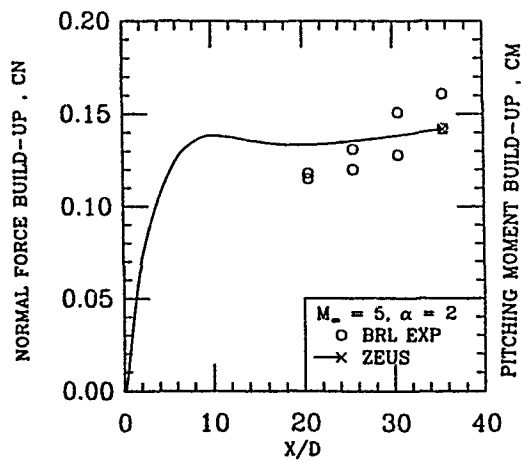


Fig 17. ZEUS Computations on Equivalent Body for Sears Haack Body

NUFA : A SEMI-EMPIRICAL METHOD FOR THE PREDICTION OF  
ISOLATED WEAPON AERODYNAMICS

by

S. McDougall, A. J. Press and P. S. Barratt,  
Aerodynamics and Vulnerability Research Dept.,  
Sowerby Research Centre,  
British Aerospace PLC,  
PO Box 5,  
Filton,  
Bristol BS12 7QW,  
UK

SUMMARY

The NUFA method was developed from the ABACUS program to provide estimates of weapon aerodynamic loads when immersed in non-uniform, as well as uniform, onset flows. Being semi-empirical in nature, the method is relatively simple and inexpensive to use. The body load prediction method within NUFA has recently undergone significant development to both the inviscid and viscous load contributions including the introduction of an initial square body capability. Results from each of these developments are presented. A feature of NUFA is the ability to provide estimates of body load distributions. This capability has been exploited to predict pitch damping derivatives. A comparison with experiment demonstrates a first application of NUFA to aerodynamic derivative prediction. The load distribution facility is further illustrated by predictions using a non-uniform flow as input. It is hoped that the flexibility of the body load prediction method has been demonstrated.

NOMENCLATURE

$C_{mq}$	Pitch damping moment coefficient, $M_q/qS(\omega D/V)D$
$C_N$	Normal force coefficient, $N/qS$
$C_Y$	Side force coefficient, $Y/qS$
$D$	Body maximum diameter (width)
$L$	Body length
$M$	Mach number
$M_q$	Damping moment
$N$	Normal force
$q$	Dynamic pressure
$r$	Corner radius
$r_b$	Radius of blunting
$Re_D$	Reynolds number based on body maximum diameter (width)
$S$	Reference area, $nD^2/4$
$V$	Freestream velocity
$W$	Body diameter (width)
$x$	Axial station
$X_{cp}$	Centre of pressure (positive aft of moment reference point)
$X_{ROT}$	Centre of rotation
$Y$	Side force
$z$	Vertical position of weapon centreline relative to wing mean chord plane/pylon base
$\alpha$	Aircraft/wing angle of incidence (degrees)
$\sigma$	Weapon total angle of incidence (degrees)
$\phi$	Roll angle (degrees)
$\omega$	Pitch rate (rad/s)

INTRODUCTION

The NUFA semi-empirical store load prediction method was developed from the ABACUS computer program (Ref.1) in order to provide a simple and inexpensive method of estimating weapon aerodynamic loads when immersed in a non-uniform onset flow. To date the method has almost exclusively been used for the calculation of store carriage and trajectory loads. The input to the method retains the simplicity of the ABACUS method, with knowledge of the weapon geometry and the surrounding flowfield being required. The flowfield, in general, is obtained from theoretical methods (eg. 3-D panel or Euler methods), although experimental flowfields have been utilised.

The NUFA method, having been originally based on the ABACUS computer program, has a similar approach to the prediction of weapon aerodynamic loads. The method was originally described by Bizon in Ref.2. NUFA uses a component build-up technique. The body and lifting surface loads are calculated in isolation. These are then summed with suitable interference terms to provide estimates of aerodynamic loads and moments. The most significant difference between the ABACUS and NUFA methods is in the prediction of body aerodynamic loads. NUFA uses a segmentation approach. The body may be divided into as many as a thousand segments (the number of segments being controlled by the user). The local flow at each segment is used to calculate a load distribution. This distribution is then summed to provide a total load. Using this approach, pitching moment is easily calculated using the moment arm for each segment. Use of the segmentation approach thus allows a non-uniform flow prediction capability to be incorporated.

Using Slender Body Theory for calculating the linear (inviscid) load on portions of the body which are either expanding or contracting, releases the method from the constraints imposed on ABACUS of, strictly speaking, being applicable to bodies with either sharp tangent-ogive or sharp or spherically blunted conical nose profiles. The body may in fact have a continuously varying profile. In this case the user provides the program with the definition of the body shape by inputting coefficients for a series of polynomials.

The requirement to predict the aerodynamics of weapons when immersed in a non-uniform flowfield necessitates the incorporation of

additional terms within the body load calculation technique. Principally these terms account for buoyancy and effective camber, however additional higher order terms may be included. These body load terms, which have been incorporated within NUFA, have been derived by Isaacs (Ref.3) and are associated with transverse and longitudinal velocity gradients in the flowfield within which the store is immersed.

It is the intention of this paper to provide an overview of current developments being applied within the NUFA semi-empirical store load prediction method. The techniques described are very recent and consequently most remain under development. All the techniques are concerned with the prediction of weapon body loads, as several research studies undertaken at the Sowerby Research Centre highlighted the need for an accurate but inexpensive body aerodynamic load prediction method.

Many weapons now necessitate the need for an accurate prediction of body aerodynamic loads. For instance, dispenser weapons may have their lifting surfaces stowed during carriage. In addition, these types of weapons tend to have bodies of non-circular cross-section, which generally provide a greater contribution to the overall load from the body than weapons of circular cross-section. To accommodate these trends within weapon design, a square body load prediction capability is currently being developed within the NUFA method. Whilst considering this development a strategy was devised which, when completed, will hopefully allow a relatively rapid modification of the body load prediction method for any specified cross-sectional shape.

In order to produce a program development strategy, critical features of the prediction method which require alteration when a new body cross-section load estimation capability is required have been identified. For each of these critical features a development tool has been or will be produced. The relevant tools have, however, all been identified. They are largely theoretical in nature, thus some experimental data is required for validation of any modification to the NUFA method, made as a result of using some of them. The purpose of their development is to provide a relatively quick method of enhancing the range of body cross-sections for which the semi-empirical method is able to provide accurate estimates of aerodynamic loads and moments, without recourse to a major wind tunnel test programme.

The body load for uniform onset flow cases is composed of a linear (inviscid) and a non-linear (viscous) term. It is typical for methods such as ABACUS and NUFA to use Slender Body Theory to calculate the linear load with a cross-flow drag calculation providing the non-linear term. Development of both of these techniques, within the NUFA method, has been undertaken at the Sowerby Research Centre. For a number of body geometries the application of standard Slender Body Theory within NUFA has been replaced by a new prediction technique which incorporates modifications to the standard form of the Slender Body Theory calculation. In addition, the cross-flow drag model has been significantly developed in order to enhance the capability of the method to estimate Reynolds number effects on body loads.

#### SCOPE OF PROGRAM AND ACCURACY LIMITS

The program, being originally based on the ABACUS prediction method, is largely constrained to the same geometric and onset flow limits. The lifting surface and interference terms are virtually identical and were detailed in Ref.1. Figure 1 (extracted from Ref.1) summarises the lifting surface and onset flow limitations of the method.

When developing the NUFA program the intention has been to retain the accuracy limits as applied to the ABACUS program i.e.  $\pm 5\%$  of body length for centre of pressure position and  $\pm 10\%$  of normal force.

#### A MODIFIED SLENDER BODY THEORY LOAD PREDICTION METHOD

Although application of the standard Slender Body Theory method can provide relatively accurate estimates of normal force, the distribution of force and consequently the prediction of pitching moment can be significantly in error. Thus, in order to improve the prediction of pitching moment due to the distribution of inviscid load, modifications to the Slender Body Theory calculation technique were incorporated within NUFA. These modifications were also necessary in order to aid validation of the NUFA method when predicting the distribution of normal and side force on bodies immersed in non-uniform onset flows.

To validate the inviscid calculation, comparisons are generally undertaken against predictions from theoretical methods (eg. 3-D panel methods). It is not possible to extract the various contributions to the inviscid load predicted by a 3-D panel or Euler method (eg. the buoyancy or effective camber terms) when modelling a weapon body immersed in a non-uniform onset flow. This inability to decompose the inviscid load makes the validation of the NUFA body load prediction method all the more difficult. By improving the accuracy of the Slender Body load calculation technique within NUFA, it was felt that at least one possible source of error for non-uniform flows could be removed. The inviscid load predicted by a panel method can be decomposed in part by devising certain special test cases which ensure that at least one of the inviscid terms are eliminated. These test cases have no physical significance to the prediction of weapon aerodynamic loads, other than that they allow the partial decomposition of the constituent parts of the load. By comparing the predictions from NUFA for these test cases with the output data from the 3-D panel method, factors were derived for the buoyancy, effective camber and higher order Slender Body Theory terms. Application of these factors has been found, in general, to provide an improvement in the calculation of the inviscid load distribution on bodies immersed in non-uniform onset flows.

The Slender Body Theory method was modified such that both the magnitude and position of the peak nose load were altered on tangent-ogive nose profiles. Similar modifications were incorporated for conical nose profiles. In addition, a carryover from the nose to the body was incorporated. Although the prediction of total normal force was unaltered by these modifications, the distribution of load was significantly

improved. These modifications provide a more accurate prediction of the inviscid load distribution on bodies with nose profiles which are either blunted or sharp, conical or tangent-ogives. For other nose profiles, standard Slender Body Theory is utilised. The modified Slender Body Theory method is currently limited to Mach numbers below 0.8, although it is intended to extend the method to Mach numbers up to 5.0. The load distribution on bodies with cross-sections varying from square ( $r/W=0.0$ ) to circular ( $r/W=0.5$ ) may be calculated.

Two examples of the improvement in the prediction of the nose load distribution are shown in Figures 2 and 3. The load distributions from both NUFA and a 3-D panel method are shown for a hemispherical nose (Figure 2) and a blunted tangent-ogive (Figure 3). Both configurations are of square cross-section with an incompressible onset flow at ten degrees of incidence. The panel densities for the nose geometries are shown in Figure 4. Assuming that the predictions from the 3-D panel method are nominally exact, then clearly the application of the modified Slender Body Theory method provides a significant improvement in the prediction of the load distribution in both cases. Of note is the accuracy of the prediction of the double peak in the load distribution on the blunted nose configuration (Figure 3).

#### PREDICTION OF THE PITCHING MOMENT ON BODIES OF SHORT NOSE LENGTH

Using either the basic or the modified application of Slender Body Theory, as described above, will, on its own, be unable to provide accurate predictions of the (inviscid) pitching moment for bodies of short nose length. Despite the fact that the new potential load calculation can provide relatively accurate predictions of the distribution of normal force, the accuracy of the pitching moment prediction decreases with decreasing nose length. In terms of pitching moments on the nose of the body due to the inviscid load distribution, the predictions may be in error by up to 50%. As nose length decreases the axial force distribution provides a significant contribution to the pitching moment. Of course, as the name implies, Slender Body Theory was never intended to be applied to bodies with bluff nose profiles.

In order to account for the effect of the axial force distribution, a factor has been derived for both blunted and sharp conical and tangent-ogive nose profiles. The effect of applying this correction is shown in Figure 5. Normal force and centre of pressure position due to the inviscid load distribution for the nose only are plotted against nose length. The predicted data from NUFA are compared with those from a 3-D panel method. Examples of the panel densities used for the nose geometries are shown in Figure 6. Results are presented for a corner rounding of 0.3, with onset flow of  $M=0.4$  at 2.5 degrees of incidence. The moment reference point is taken to be at the nose apex. The predicted normal force and pitching moment from the 3-D panel method are assumed, for the purposes of this comparison, to be nominally exact. The normal force predicted by NUFA is, as would be expected from the previous figures, accurate for all nose lengths presented. However, it can

clearly be seen that the predicted centre of pressure position, before the application of the factor, is too far forward, for the short nose lengths. The discrepancy decreases with increasing nose length. The maximum error occurs at the shortest nose length and is of the order of 50%. Application of the pitching moment factor results in a substantial improvement in the predicted centre of pressure position with no change in the total normal force. Although the data presented in Figure 5 was obtained at an angle of incidence of 2.5 degrees, the percentage error in pitching moment (without the application of the pitching moment factor) would be invariant with angle of incidence. Two and a half degrees of incidence was chosen only to demonstrate the need for a pitching moment factor, the incidence angle itself having no particular significance.

#### VISCOUS BODY LOAD PREDICTION METHOD

The accurate prediction of the viscous load generated by the body of a configuration can be extremely important, particularly in the high incidence regime within which modern weapons are required to operate. These viscous loads, which tend to dominate the overall body generated forces at high incidences, can be strongly dependent upon both Mach number, and particularly, Reynolds number, as well as other factors such as surface roughness and freestream turbulence.

A viscous body load prediction method has been developed within NUFA based upon the well known Crossflow Drag Analogy (which reduces the problem to predicting a crossflow drag coefficient). The method predicts a crossflow drag coefficient for each body segment, at which the flow conditions are known, accounting for the effects of both Reynolds number and Mach number. This method can be applied to any body of circular cross-section, at incidences up to 90 degrees, Mach numbers up to 5.0 and for any flow Reynolds number. The method basically determines a characteristic Reynolds number at each body segment, primarily as a function of freestream Reynolds number and local incidence. This characteristic Reynolds number, together with the local crossflow Mach number, is used to determine the crossflow drag coefficient at each body segment.

A comparison is presented in Figure 7 between experimental data (extracted from Ref.4) and predictions of the variation of normal force coefficient for a simple nose-cylinder body with Reynolds number at 30 degrees of incidence, at four Mach numbers. The NUFA method generally predicts the variation with Reynolds number well, showing the progression from subcritical (low Reynolds number) flow through the critical region to supercritical flow. The prediction of normal force coefficient with varying Mach number is of good quality, clearly demonstrating the reducing dependence of the viscous loads on Reynolds number, with increasing Mach number.

Predictions from NUFA are compared with experimental data from Ref.5 in Figures 8 to 11. Comparisons of normal force coefficient and centre of pressure position for a nose/cylinder body at a low subsonic Mach number are shown at four different Reynolds numbers. The two sets of experimental data are due to the use of two different wind



tunnel models - one painted and pressure tapped and the other unpainted and smooth. The normal force coefficients and centre of pressure position are very well predicted up to 40 degrees incidence. The predicted characteristics are well within the overall accuracy target. Above 40 to 50 degrees incidence the centre of pressure position tends to be predicted too far aft. The prediction of normal force coefficient at the lowest Reynolds number is excellent over the whole incidence range, with the method predicting well the sudden steepening of the curve at around 20 degrees incidence. At the two intermediate Reynolds numbers the normal force coefficient is somewhat overpredicted above 50 degrees.

The predictions of body loads and moments, obtained to date with the viscous model, over a range of test Reynolds and Mach numbers, have been encouraging. The method has provided good results for a range of configurations up to high incidence.

An example of a body-wing-tail configuration is shown in Figure 12. In this figure the longitudinal aerodynamics of the Sparrow III configuration are presented at three angles of incidence over a range of Mach numbers. The experimental data were extracted from Ref. 6. The NUFA predictions include the new viscous body load prediction method, however, the Mach number range is too high for the modified Slender Body Theory method to be utilised. The prediction of both normal force and centre of pressure position are within the accuracy limits of the method, except for the prediction of centre of pressure position at the highest incidence and Mach number. At this combination of conditions the centre of pressure is predicted to be too far forward. The contribution to the normal force from the body at these conditions is very significant. By modifying the distribution of load on the nose (reduction of the peak force and inclusion of a carryover onto the body), it is expected that the predicted centre of pressure position would be improved.

#### PREDICTION OF LOADS ON A BOATTAILLED BODY

In terms of body loads the accurate prediction of boattail loads is extremely important. The relatively long moment arm and the fact that the load on the boattail will form a couple with the nose load, means that the accuracy of pitching moment prediction is extremely sensitive to the boattail load.

In principle, for conical or tangent-ogive boattails, the new nose (linear) load prediction method could be utilised. A composite load distribution has been produced in Figure 13 to give some indication of the quality of the predictions which could be obtained from NUFA if the new inviscid load model was applied to boattails. The predicted load distribution is compared with that from a 3-D panel method. Clearly the NUFA predicted load distribution is far superior to that produced by Slender Body Theory (Figure 14). Both the magnitude and position of the peak loads are predicted well. The error in the position of the nose peak load as predicted by NUFA is simply due to the use of a linear interpolation method for extracting information from a fixed dataset. This could easily be cured by applying a curve fit to the data.

Application of the new inviscid load model to the boattail should result in an improvement in the predicted centre of pressure position. The NUFA method is, however, currently limited to using Slender Body Theory on boattails.

Use of the NUFA load distribution (new nose inviscid load model with Slender Body theory applied to the boattail), as it stands, would result in a significant underprediction in the total normal force and an additional nose-up pitching moment. Viscous effects are usually assumed to result in a reduction of the inviscid load on contracting body profiles. A simple correction to account for viscous effects (other than those modelled by the cross-flow drag method) has been incorporated. More sophisticated methods have been examined (eg. Refs. 7 to 12), however, they are all limited in the range of configurations to which they may be applied. A new method based on the load distribution predicted by the NUFA method is currently under consideration.

The effect of applying the simple boattail (inviscid) load correction is shown in Figure 15. There is a significant change in the normal force and centre of pressure position due to the inviscid load distribution when the correction is applied. The inclusion of a load due to the cross-flow drag calculation shows that an accurate prediction of both normal force and centre of pressure position can be achieved throughout the incidence range. Since at low incidence the NUFA predicted centre of pressure position tends towards the inviscid value, the need for the boattail load correction is obvious.

Comparisons with experimental data for the bomb body over a range of Mach numbers and angles of incidence are shown in Figure 16. Given that a simple correction has been applied to the boattail load distribution, the centre of pressure predictions are very good. The prediction of normal force is relatively accurate throughout the Mach number and incidence range presented, except at the highest incidence where, in general, NUFA underpredicts the normal force.

#### PREDICTION OF SQUARE BODY AERODYNAMICS

Provision of a prediction capability for bodies of square cross-section obviously involves development of most aspects of a component 'build up' method. Of concern here is the development of the body load prediction capability. The linear load calculation technique encompasses a square body prediction capability up to M0.8. This has been described above. A cross-flow drag model (due to Clarkson, Ref. 13) has been incorporated allowing the prediction of the non-linear aerodynamics. As with the linear aerodynamic model, the technique allows an arbitrary corner radius to be modelled.

In order to validate and aid development of square body aerodynamic load prediction methods within British Aerospace, two wind tunnel test programmes have been undertaken to date in order to establish an aerodynamic database for bodies of square cross-section. The testing has involved measuring isolated and installed forces and pressures on a series of bodies ranging in cross-section from circular to square. A range of body and lifting surface combinations have been tested. Individual lifting surfaces have

been instrumented, allowing lifting surface as well as total configuration loads and moments to be measured. Measurements have been taken over a range of incidences and roll angles. The store geometries are similar to those tested by Yechout et al. (Ref.14).

Data from these tests are presented together with predictions using the NUFA method in Figures 17 to 19. Figure 17 shows the effect of decreasing corner radius on the normal force and centre of pressure position of a body alone configuration. A consistent accuracy in the prediction of normal force is not achieved. For the non-zero corner roundings the accuracy is outside the acceptable limit for the prediction method. The normal force on the square body ( $r/W=0.0$ ) is shown in Figures 18 and 19. Of note in these figures is the poor prediction of yawing moment despite the relatively accurate prediction of side force.

It is evident from the comparisons presented in Figures 17 to 19, that the initial square body load prediction capability within NUFA requires further development. In particular, the method currently lacks both a true capability to model Reynolds number effects on bodies of non-circular cross-section and an interface with the new circular body cross-flow drag model.

#### TRANSITION STRIP MODELLING

The vast majority of data used for validation of weapon aerodynamic load prediction methods is obtained from wind tunnel tests. These tests, in general, rely on the use of transition strips in an attempt to model full scale phenomena. Use of a transition strip, particularly at low test Reynolds numbers, can have a significant effect upon the measured aerodynamic loads. If an attempt is made to model the configuration at the actual test Reynolds number using a prediction technique which does not account for the presence of the transition strip, then considerable errors may result.

A short study was conducted at the Sowerby Research Centre incorporating some preliminary ideas for simulating the effects of a circumferential transition band on the nose of a body of circular cross-section. Modifications were made to the existing NUFA Reynolds number dependent viscous load calculation. Some results from this study are shown in Figure 20. Experimental data were available from the square stores database created by British Aerospace. Using the actual test Reynolds number, which is well into the sub-critical range ( $0.2 \times 10^5$ , based on body maximum diameter), within the NUFA method, results in a substantial overprediction of the normal force. By incorporating an initial methodology for estimating transition strip effects, the prediction of normal force and centre of pressure position are substantially improved.

No claims as to the generality of the method are being made. This exercise simply indicates that the prediction of transition strip effects may be possible where wind tunnel tests are carried out at low Reynolds numbers.

#### AERODYNAMIC DERIVATIVE PREDICTION

Work has recently commenced to investigate the ability of the NUFA method to provide estimates of aerodynamic derivatives. Two methods of predicting pitch damping force and moment derivative coefficients have been investigated. One of the techniques is based on a method used in conjunction with the ABACUS program. This method uses an equation extracted from Ref.15. Prediction of the pitch damping moment coefficient is, using this method, dependent upon the distribution of pitching moment, the pitching moment curve slope, angle of incidence and the body centre of pressure position. Similarly the pitch damping force coefficient is dependent upon normal force terms and the body centre of pressure position. The alternative method requires a non-uniform flow prediction capability and, as such, is unsuited to a method such as ABACUS. A pitch rate is simulated in the prediction method by applying a linear variation in onset flow to the weapon model. By predicting the pitching moment and normal force using this method the derivative with respect to pitch rate may be derived. In principle this second method should be capable of providing predictions at any angle of incidence or Mach number (below 5.0) and allow any offset between the moment reference point and the centre of rotation of the weapon. Other aerodynamic derivatives may be predicted using either the equation or onset flow based method.

To date the NUFA prediction method has been applied to two test cases. The results are shown in Figures 21 and 22. For the configuration shown in Figure 21, identical results for pitch damping moment coefficient were achieved using both the equation and onset flow based techniques. The experimental data were extracted from Ref.16. The results are seen to be reasonably accurate throughout the Mach number range tested. The advantage of estimating damping derivatives from a method which accurately predicts the distribution of normal force is clearly seen when the results from NUFA are compared with those of ABACUS. Results for a body-tail configuration are shown in Figure 22, for two different centres of rotation. The comparison with experimental data (extracted from Ref.17) is very encouraging, with the prediction method accurately estimating the effect of shifting the centre of rotation. Further validation is required in order to provide confidence in the prediction method.

#### PREDICTION OF AERODYNAMIC LOADS IN NON-UNIFORM FLOW

The NUFA method was specifically developed from the ABACUS program to provide estimates of store loads when immersed in non-uniform onset flows.

For weapons installed on aircraft, the non-uniformity of the flow encountered may be such that additional load components due to gradients in the flowfield may be as large as the inviscid (Slender Body Theory) and viscous aerodynamic terms. It is therefore important to include components such as buoyancy and higher order terms.

Typical applications of the method are for the prediction of underwing and underfuselage carriage and trajectory loads. The method has been incorporated within a trajectory

suite. In this application a 'ghosted' flowfield is calculated by a 3-D panel method, the flowfield being calculated only once in order to reduce the overall cost of execution.

In order to indicate the quality of the predictions of load distribution from the NUFA method, comparison with predicted load distributions from a 3-D panel method are shown in Figures 23 and 24. Both comparisons are shown for an onset flow of twelve degrees of incidence at  $MO_{19}$ . The predicted load distributions shown in these figures are due to the inviscid aerodynamic terms only (ie. no cross-flow drag). For the purposes of comparison, the results from the panel method are assumed to be nominally exact for inviscid flow. The 3-D panel method was used to provide a flowfield for use with NUFA. The predicted normal force distribution shown in Figure 23 is for a store body under a three dimensional, constant section swept wing. The vertical locations of the store relative to the wing are shown in Figure 25. The NUFA predicted load distributions compare well with those of the panel method. Even at the lowest position the store experiences some disturbance from the wing since over the cylindrical portion of the body the inviscid load is non-zero.

The side force distributions shown in Figure 24 are for the wing-pylon-store body configuration shown in Figure 26. The store positions vary from installed to almost freestream. Again the comparison between the predicted load distributions from NUFA and the panel method are good over most of the store length. NUFA seems to underpredict the load aft of the peak nose load. This also appeared on the wing-store body case (not shown here) and requires further investigation, as does the discrepancy at the rear of the installed body. The NUFA predicted installed load is very good given the extremely high velocity gradients predicted by the panel method around the base of the pylon. The results clearly indicate that the NUFA semi-empirical method is capable of providing estimates of the load distribution on weapon bodies of a similar quality to that obtained by a 3-D panel method, when a 'ghosted' flowfield is utilised. The NUFA method may, however, be provided with a flowfield from any source, for example, experimental data.

#### CONCLUSIONS

The NUFA semi-empirical store load prediction method can provide accurate predictions of store body load distributions in both uniform and non-uniform onset flows. The method will provide estimates of aerodynamic loads up to Mach 5.0. NUFA utilises a combination of Slender Body Theory and a cross-flow drag prediction method.

The method is inexpensive to use in terms of computing, is simple and flexible, allowing bodies of arbitrary profile and axisymmetric cross-section to be modelled by utilising a polynomial input capability.

The accuracy of the inviscid load distribution has been improved by incorporating modifications to the standard Slender Body Theory prediction method. This modified method can provide a similar level of accuracy to that of a 3-D panel method for bodies of circular or square cross-section

with blunted or sharp, conical or tangent-ogive nose profiles. Although limited to subsonic Mach numbers, the method, when extended, will provide accurate inviscid load predictions at low cost for Mach numbers up to 5.0.

A relatively sophisticated cross-flow drag prediction method has been developed and incorporated within NUFA. The method is capable of providing estimates of the viscous load contribution on bodies of circular cross-section for Mach numbers between 0.0 and 5.0. The Reynolds number range of the method is unlimited. Comparisons with experimental data have shown that the method is able to estimate adequately the effects of varying Reynolds number.

The ability of the NUFA method to provide estimates of body load distributions has been clearly shown to enhance the prediction of the pitch damping moment coefficient on isolated weapon bodies. As a first application of the NUFA method to the prediction of aerodynamic derivatives, the results presented here are extremely promising.

An initial square body load prediction capability has been incorporated within NUFA. However, comparisons with experimental data indicate that the cross-flow drag prediction method requires further development. This will be part of the ongoing development of the NUFA method which will also include further investigation of the transition strip modelling and body boattail modelling capabilities.

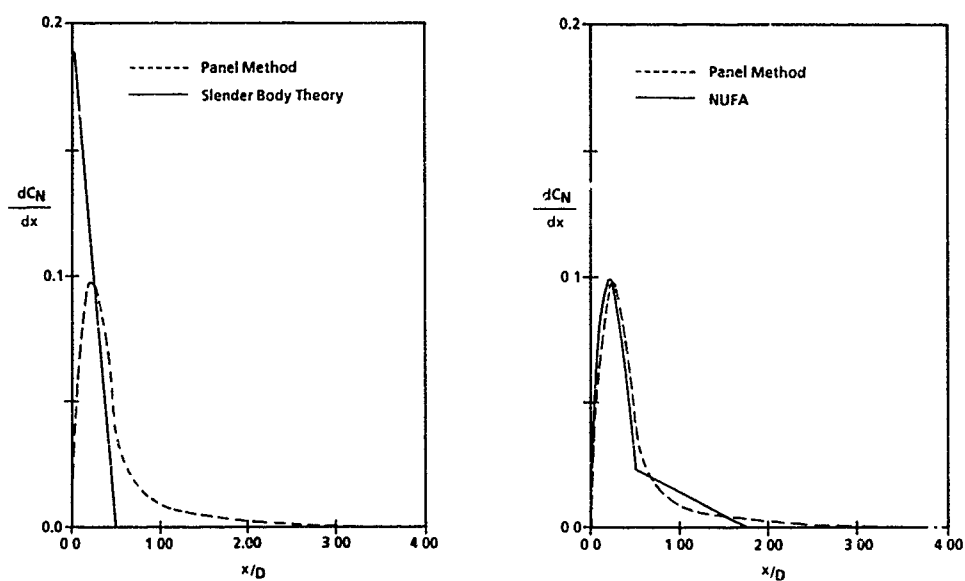
#### REFERENCES

1. Herring, P.G.C., 'A computer program which evaluates the longitudinal aerodynamic characteristics of typical weapon configurations'. AGARD-CP-336 Paper No. 26, Missile Aerodynamics. September 1982.
2. Bizon, S. A., 'NUFA - A technique for predicting characteristics of store configurations in a non-uniform flowfield'. AGARD-CP-389 Paper No. 14. October 1985.
3. Isaacs, D., 'Slender Body Theory analysis of the loading on axisymmetric bodies which are in motion through a non-uniform subcritical flow'. RAE Tech Memo Aero 1889. January 1981.
4. Polhamus, E. C., 'A review of some Reynolds Number effects related to bodies at high angle of attack'. NASA Contractor Report 3809. August 1984.
5. Champigny, P., 'Pressure and force measurements on a 3D ogive nose and cylindrical body at high angles of attack'. GATEUR No. 01/AG04. October 1983.
6. Monta, W. J., 'Supersonic aerodynamic characteristics of a Sparrow III type missile model with wing controls and comparison with existing tail-control results'. NASA Tech. Paper 1078. November 1977.

7. Engineering Sciences Data Unit. Item Number 87033.
8. Washington, W. D. and Pettis, W. Jr., 'Boattail effects on static stability at small angles of attack'. US Army Missile Command, Redstone Arsenal, Alabama, Report No. RD-TM-73-5. July 1968.
9. Moore, F. G., 'Body alone aerodynamics of guided and unguided projectiles at subsonic, transonic and supersonic Mach numbers'. Naval Weapons Laboratory Report No. NWL TR-2796. November 1972.
10. Nielsen, J. N., Goodwin, F. K., and Smith, C. A., 'Method for predicting tail control effects on conical afterbodies of submersibles'. Naval Coastal Systems Command Report No. NCSC TM 347-82. August 1982.
11. Darling, J. A., 'Handbook of blunt-body aerodynamics. Volume 1 - Static Stability'. NOLTR 73-225. December 1973.
12. Fidler, J. E., and Smith, C. A., 'Methods for predicting submersible hydrodynamic characteristics'. Naval Coastal Systems Command Report No. NCSC TM-238-78. July 1978.
13. Clarkson, C. D. S., 'A method for improving the load prediction capabilities of the SPARV/FIM computer program suite'. BAe, Military Aircraft Ltd., Report No. YAD 5189. February 1988.
14. Yechout, T. R., Zollars, G. J. and Daniel, D. C., 'Experimental aerodynamic characteristics of missiles with square cross-sections'. AIAA 19th Aerospace Sciences Meeting, St. Louis, Missouri. January 12-15, 1981. Paper AIAA-81-0144.
15. Bailey, R. H., 'The prediction of aerodynamic derivatives by the aerodynamic prediction program 'ABACUS''. BAe, Sowerby Research Centre, Report No. JS 10600. April 1986.
16. Whyte, R. H., 'Effects of boattail angle of aerodynamic characteristics of 175mm M437 projectile at supersonic Mach numbers'. Picatinny Arsenal Technical Memorandum 1646. September 1965.
17. Shantz, I. and Groves, R. T., 'Dynamics and static stability measurements of the basic Finner at supersonic speeds'. NAVORD Report 4516. September 1960.

LIFTING SURFACES	UP TO TWO SETS CRUCIFORM OR MONOPLANE IN LINE OR INDEXED SWEPT OR UPSWEPT (but L.E. not swept forward) STRAIGHT EDGES STREAMWISE TIPS 'LOW' ASPECT RATIO WING AND/OR 'TAIL' MAY BE DEFLECTED
INCIDENCE ANGLE	UP TO 90°
MACH NUMBER	UP TO M5.0
ROLL ANGLE	0° TO 360°

Fig.1 SUMMARY OF PROGRAM CAPABILITIES

Fig.2 PREDICTED INVISCID LOAD DISTRIBUTION ON A HEMISPHERICAL NOSE  
( $r/W = 0.0$ )

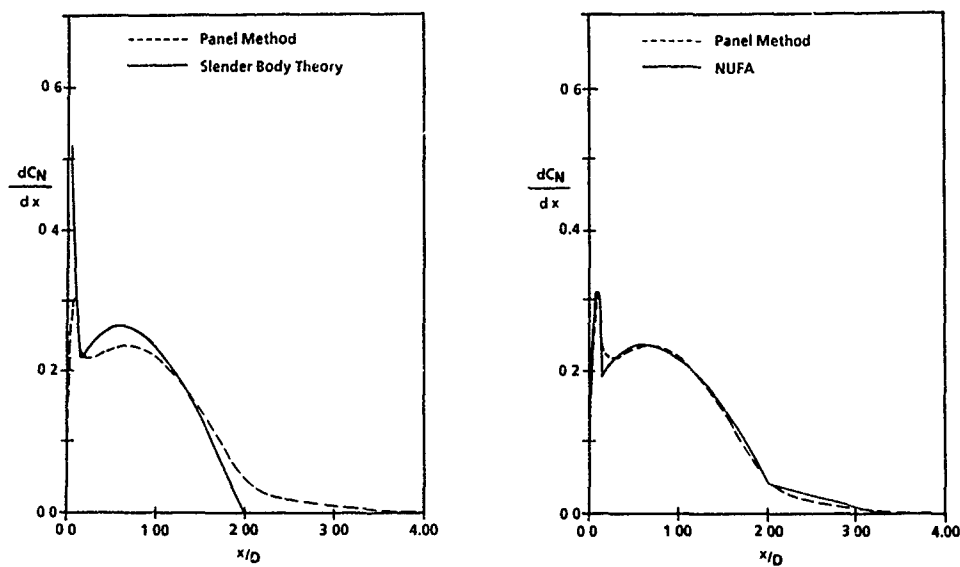


Fig.3 PREDICTED INVISCID LOAD DISTRIBUTION ON A 2 calibre, BLUNTED ( $r_b/W = 0.2$ ) TANGENT-OGIVE NOSE ( $r/W = 0.0$ )

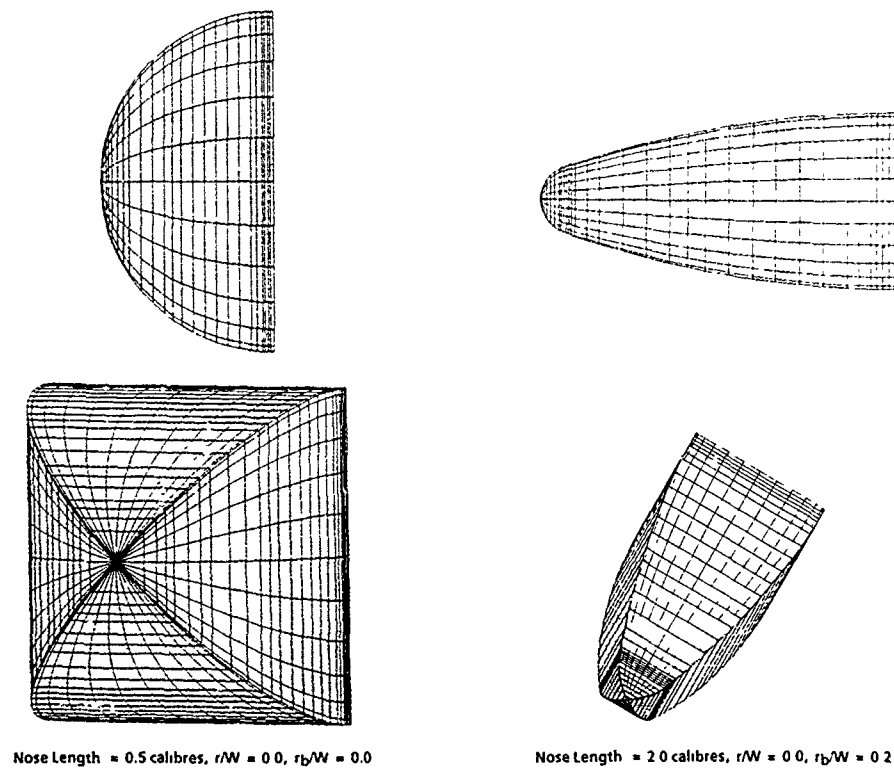


Fig.4 PANEL DENSITIES ON NOSE GEOMETRIES

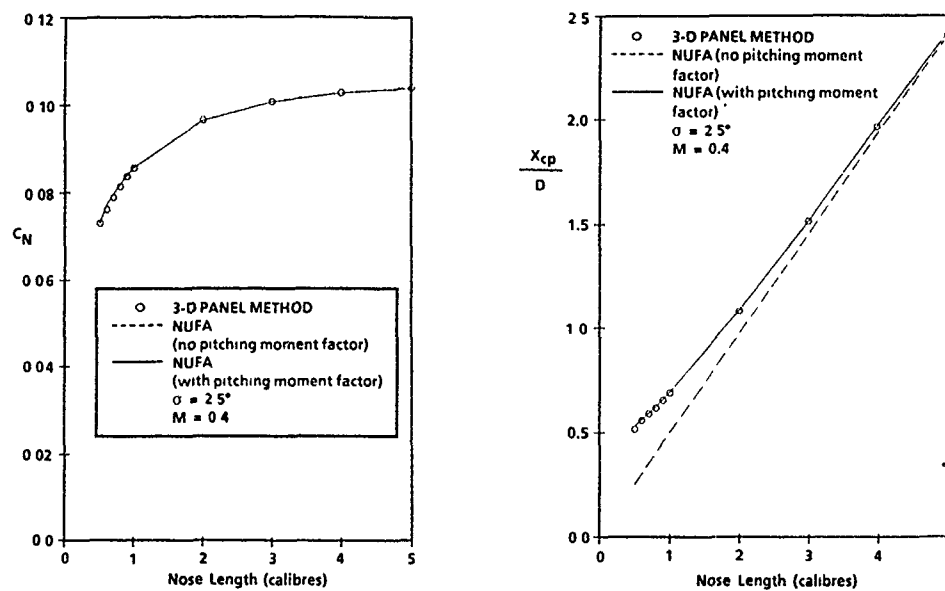


Fig.5 EFFECT OF SHORT NOSE PITCHING MOMENT FACTOR ON NORMAL FORCE AND CENTRE OF PRESSURE

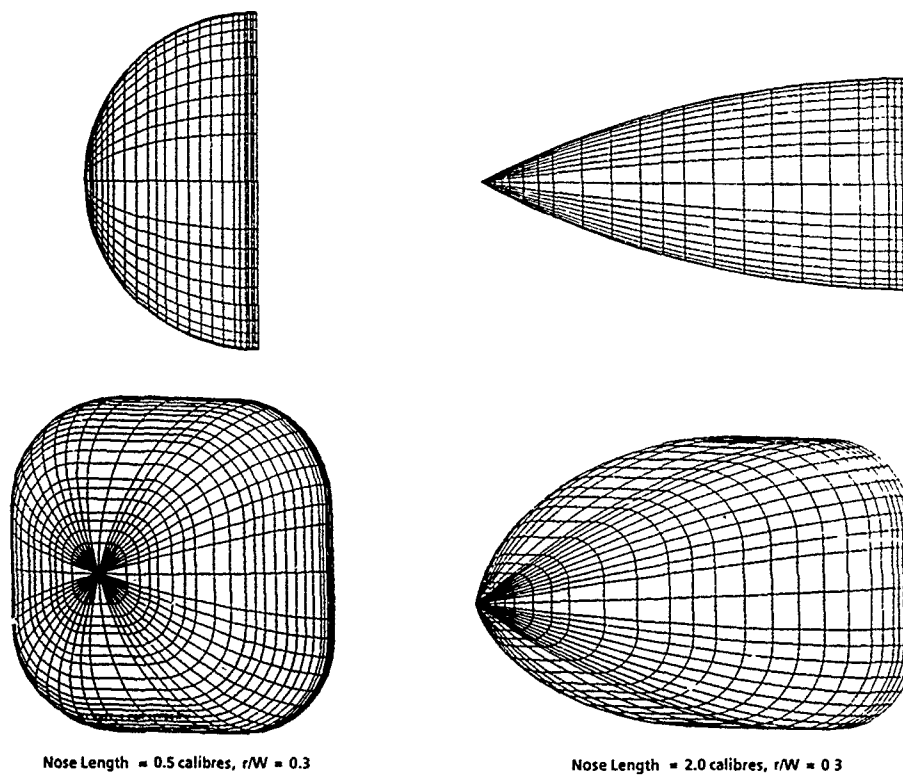


Fig.6 PANEL DENSITIES ON SAMPLE NOSE GEOMETRIES

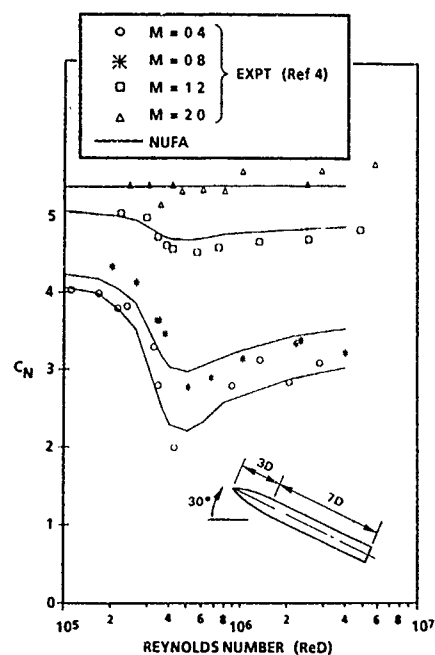


Fig.7 EFFECT OF REYNOLDS NUMBER AND MACH NUMBER ON NORMAL FORCE COEFFICIENT CHARACTERISTICS

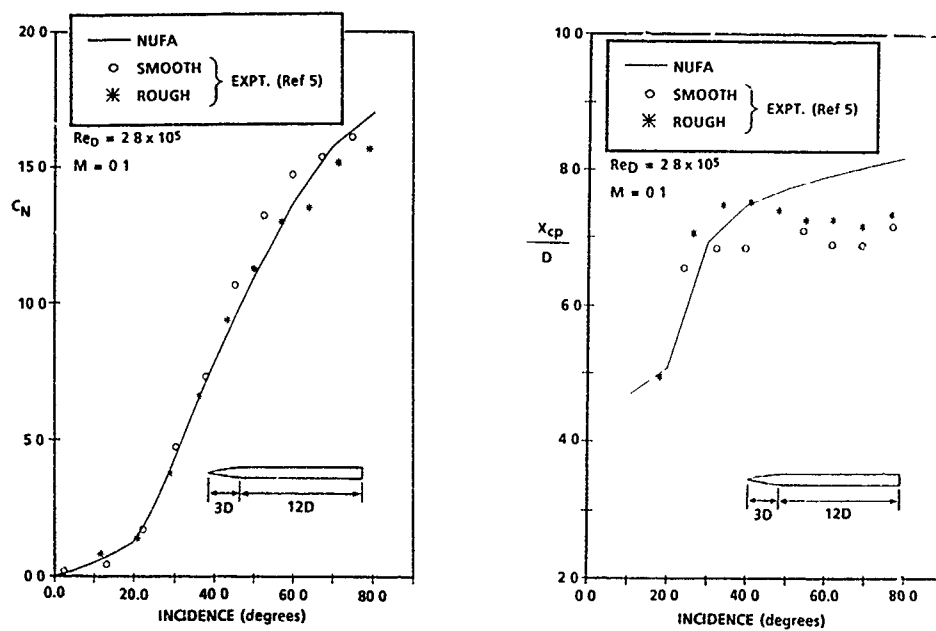


Fig.8 NORMAL FORCE AND CENTRE OF PRESSURE POSITION FOR AN ISOLATION BODY,  $Re_D = 2.8 \times 10^5$



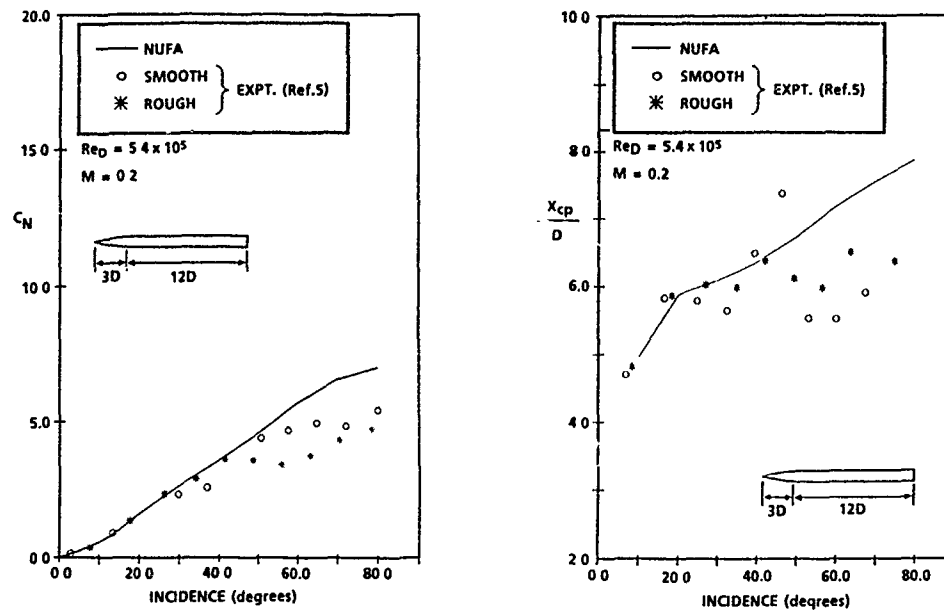


Fig.9 NORMAL FORCE AND CENTRE OF PRESSURE POSITION FOR AN ISOLATED BODY,  
 $Re_D = 5.4 \times 10^5$

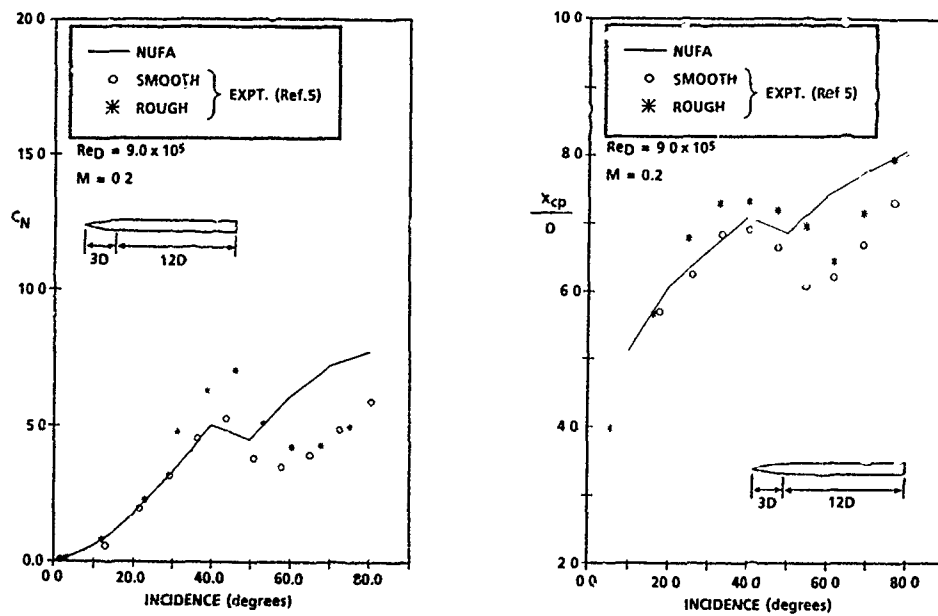


Fig.10 NORMAL FORCE AND CENTRE OF PRESSURE POSITION FOR AN ISOLATED BODY,  
 $Re_D = 9.0 \times 10^5$

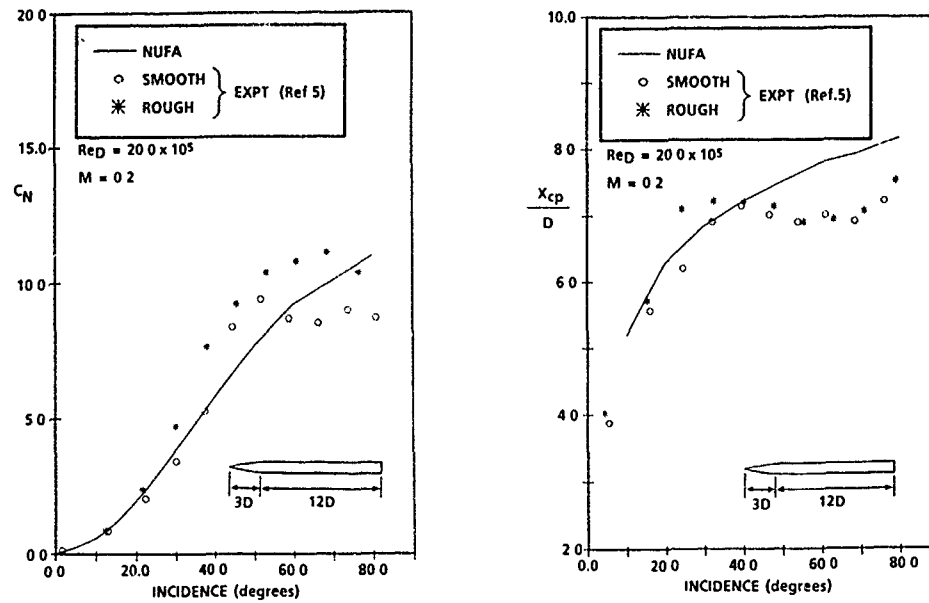


Fig. 11 NORMAL FORCE AND CENTRE OF PRESSURE POSITION FOR AN ISOLATED BODY,  
 $Re_D = 20.0 \times 10^5$

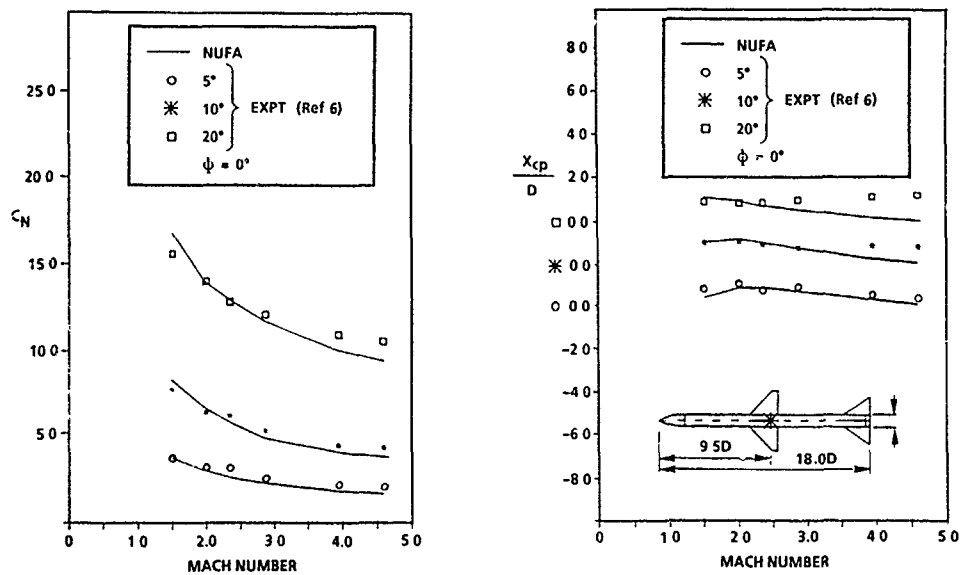


Fig. 12 NORMAL FORCE AND CENTRE OF PRESSURE POSITION FOR  
THE SPARROW III CONFIGURATION

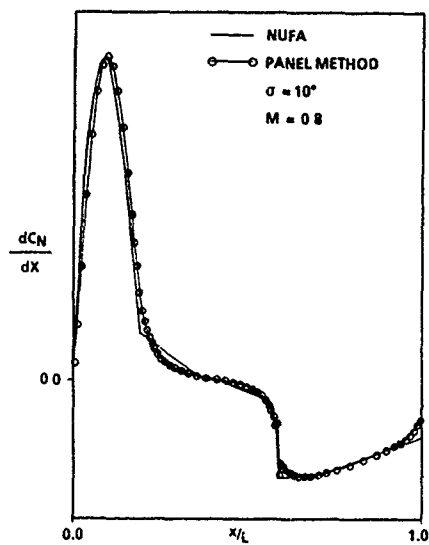


Fig. 13 DISTRIBUTION OF INVISCID LOAD ON A BOAT-TAILED BODY - COMPARISON OF RESULTS FOR NUFA AND A 3-D PANEL METHOD

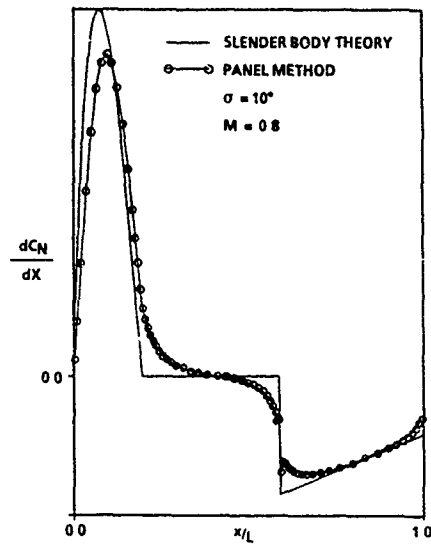


Fig. 14 DISTRIBUTION OF INVISCID LOAD ON A BOAT-TAILED BODY - COMPARISON OF RESULTS FROM SLENDER BODY THEORY AND A 3-D PANEL METHOD

- |   |   |  |                |
|---|---|--|----------------|
| + | PANEL METHOD                                  | *  | NUFA POTENTIAL |
| o | NUFA POTENTIAL                                | (with viscous correction to inviscid load) |                |
|   | (without viscous correction to inviscid load) | □  | NUFA TOTAL     |
|   |   | Δ  | EXPERIMENT     |

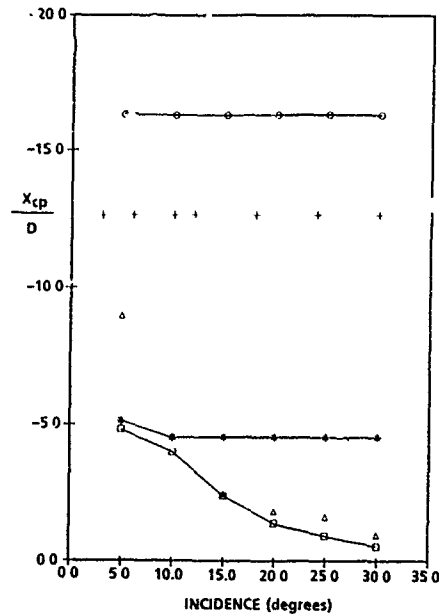
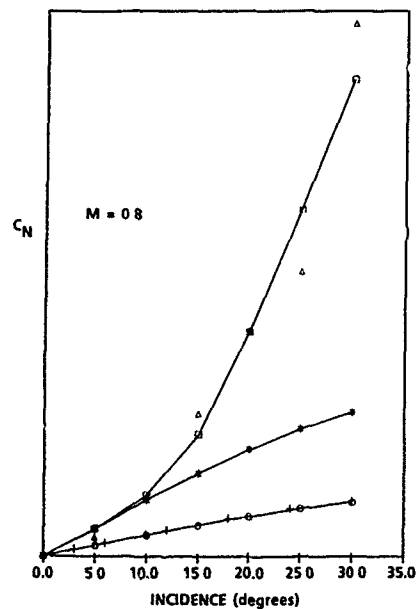


Fig. 15 NORMAL FORCE AND CENTRE OF PRESSURE POSITION FOR A BOAT-TAILED BODY,  $M=0.8$

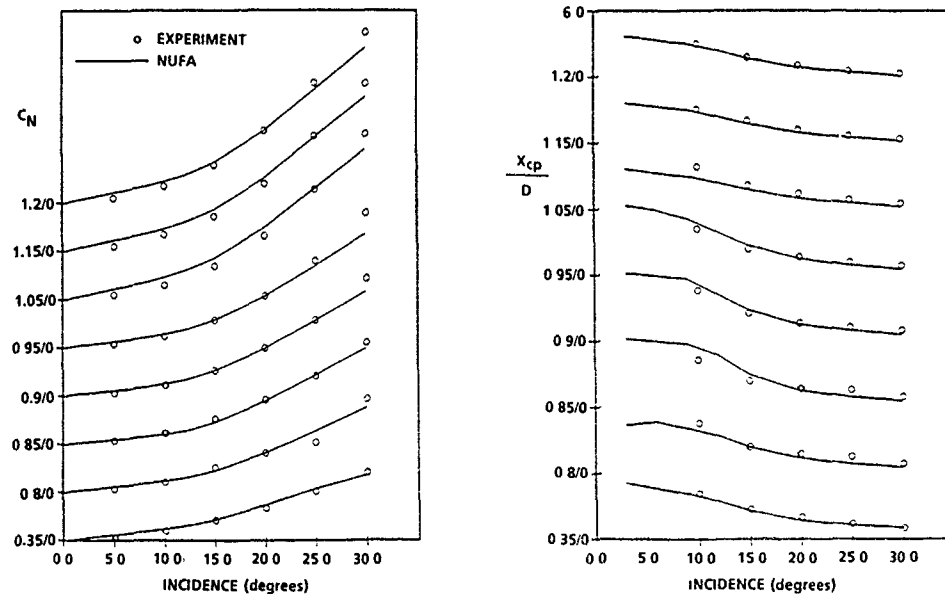


Fig. 16 EFFECT OF MACH NUMBER AND ANGLE OF INCIDENCE ON THE NORMAL FORCE AND CENTRE OF PRESSURE POSITION FOR A BOAT-TAILED BODY

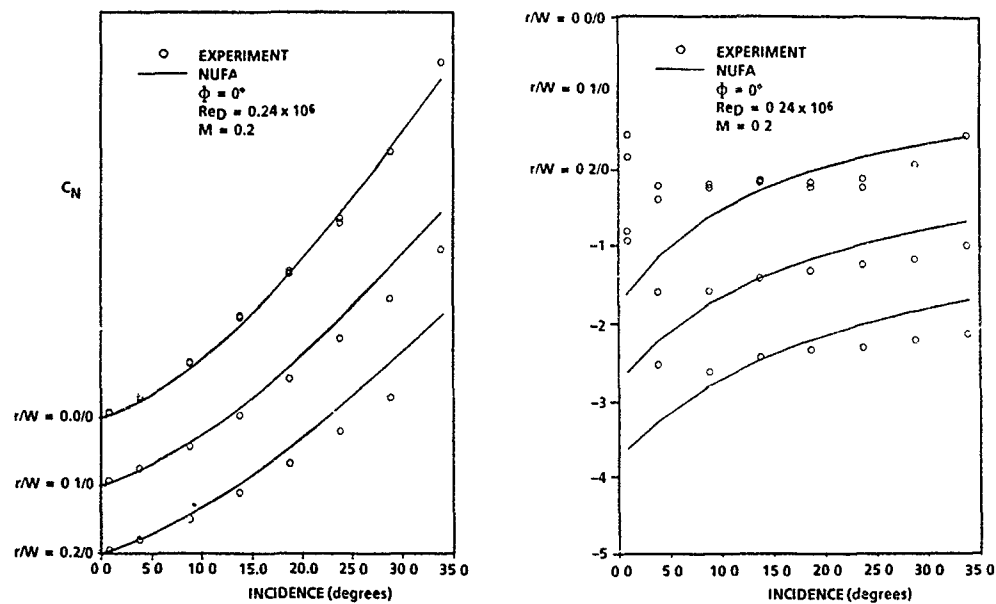


Fig. 17 EFFECT OF CORNER RADIUS ON THE NORMAL FORCE AND CENTRE OF PRESSURE POSITION OF AN ISOLATED BODY

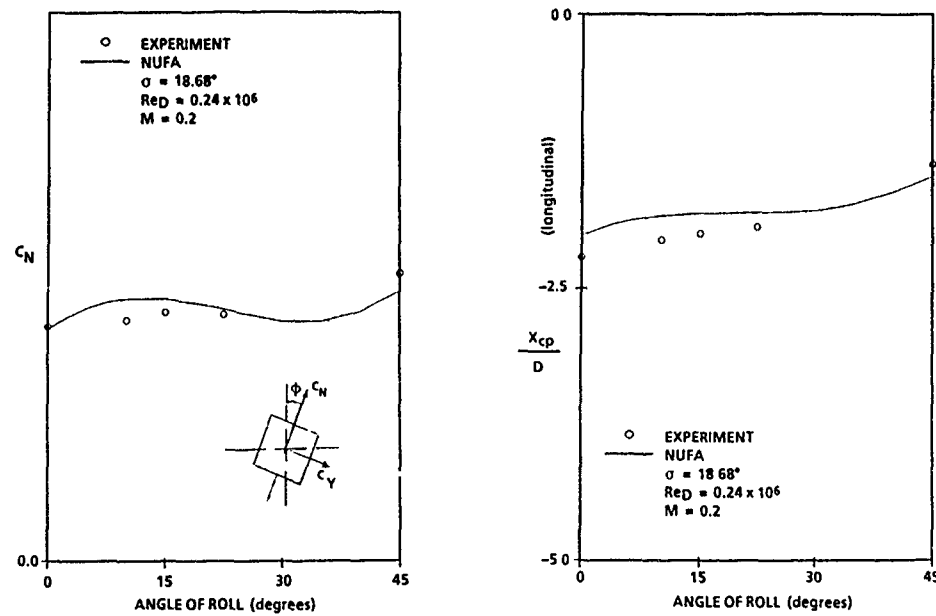


Fig. 18 EFFECT OF ROLL ANGLE ON THE LONGITUDINAL AERODYNAMIC CHARACTERISTICS OF A SQUARE BODY ( $r/W = 0.0$ )

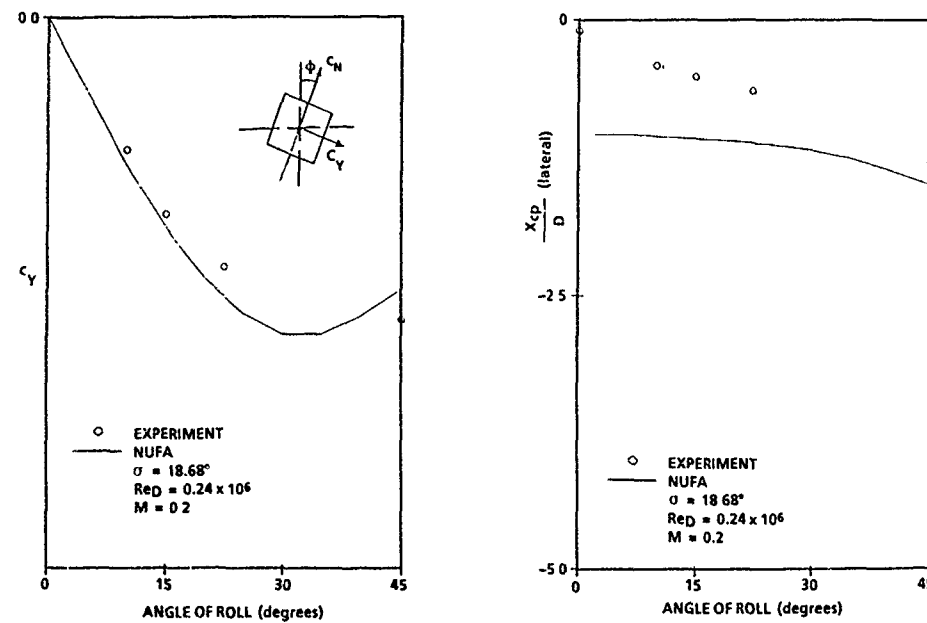


Fig. 19 EFFECT OF ROLL ANGLE ON THE LATERAL AERODYNAMIC CHARACTERISTICS OF A SQUARE BODY ( $r/W = 0.0$ )

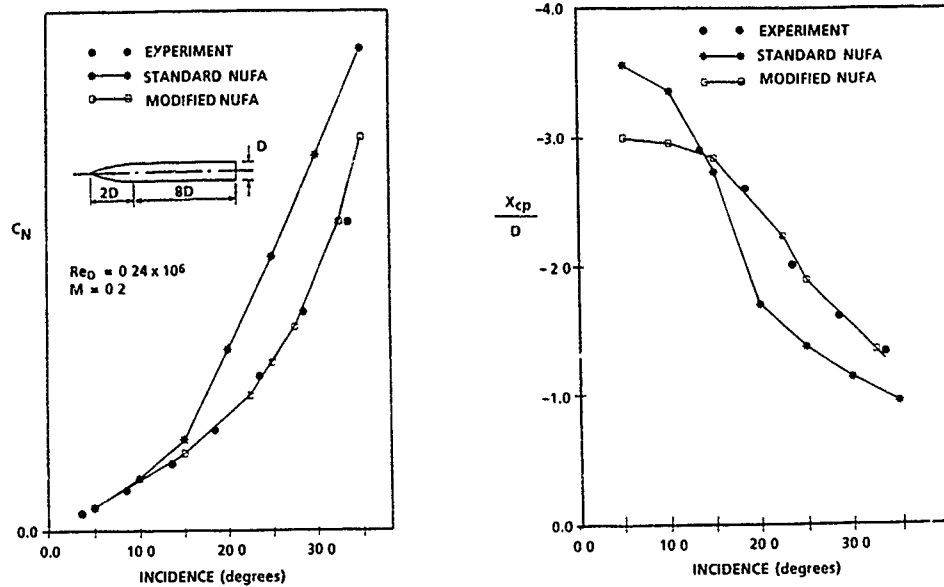


Fig.20 EFFECT OF INCLUDING A TRANSITION STRIP MODEL ON THE NORMAL FORCE AND CENTRE OF PRESSURE OF A WEAPON BODY ( $r/W = 0.5$ )

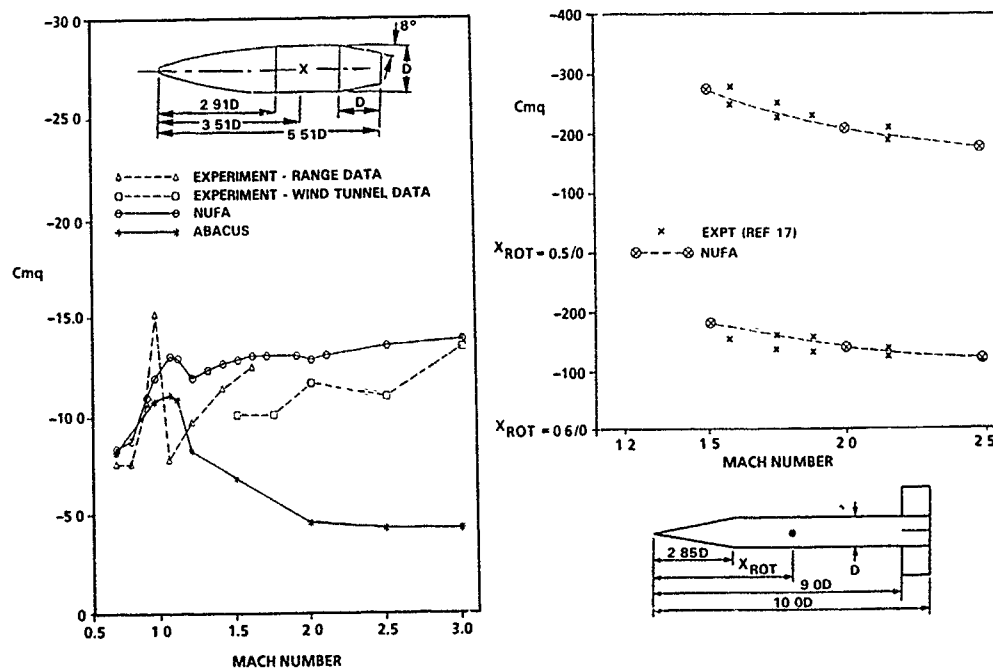


Fig.21 PREDICTION OF PITCH DAMPING MOMENT COEFFICIENT

Fig.22 PITCH DAMPING COEFFICIENT FOR A BOAT-TAIL CONFIGURATION

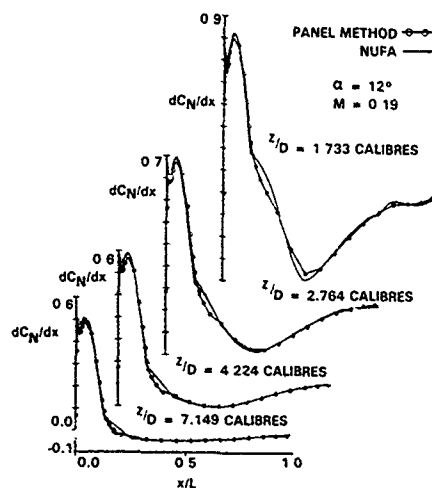


Fig.23 NORMAL FOR (INVISCID) DISTRIBUTIONS ON A WEAPON BODY UNDER A 3-D SWEEP WING

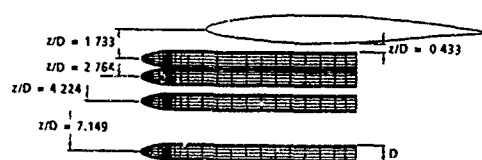


Fig.25 VERTICAL LOCATIONS OF WEAPON BODY UNDER A 3-D SWEEP WING

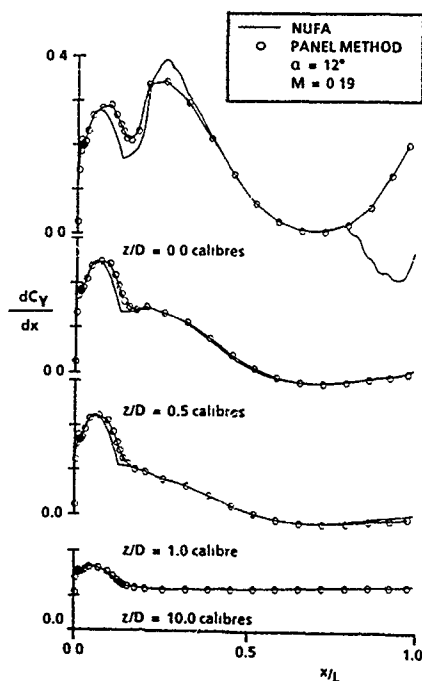


Fig.24 SIDE FORCE (INVISCID) DISTRIBUTIONS ON A WEAPON BODY UNDER A WING-PYLON CONFIGURATION

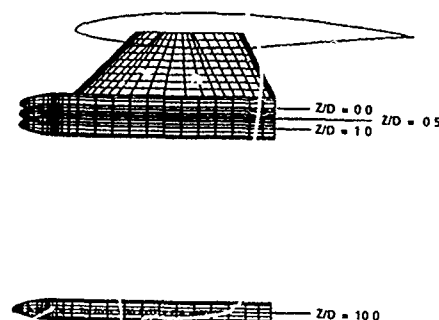


Fig.26 VERTICAL LOCATIONS OF WEAPON BODY UNDER THE WING-PYLON CONFIGURATION

## A SEMI-EMPIRICAL PREDICTION METHOD FOR MISSILE AERODYNAMICS

by

**K.-W. BOCK**  
Dornier Luftfahrt GmbH, BF20  
Postfach 1303  
D-7990 Friedrichshafen 1  
Federal Republic of Germany

### 1. SUMMARY

This paper describes the calculation procedure of the new semiempirical computer code AAVEX (aerodynamics of air vehicles, extended version) for the static aerodynamic coefficients of missiles with a body of revolution and up to three cross wings. The range of application is: Mach-number  $M \leq 4$ , angle of incidence  $i \leq 90^\circ$ , roll angle arbitrary, and all fins independently deflectable. An existing program for missiles at zero roll angle with wings in + position is extended with respect to the roll angle influence and an improved front to rear wing interference. Special emphasis is set on this extension because it is applicable to other zero roll angle codes and thus might be of general interest.

The whole procedure can be roughly divided into three different stages:

- calculation for wings in + position at zero roll angle,
- empirical modification of forces and moments for wings in arbitrary position, at given roll angle,
- calculation of front to rear wing interference.

Especially the second stage is based on a wide data base with systematically varied cross wings at a body of revolution.

Although the code is new and has still got a potential for improvement, the examples presented in this paper well agree with experiments.

### 2. INTRODUCTION

For the design and the simulation of missiles it is very important to determine the static aerodynamic coefficients and the most important dynamic derivatives quickly and at low cost without affecting the accuracy too much. As long as the roll angle is zero and the cross wings are in + position, there are many computer codes available which meet these demands. One of these is the Dornier program AAV (aerodynamics of air vehicles) which is applicable for Mach-numbers  $M \leq 4$  and angles of incidence  $i \leq 180^\circ$ .

For arbitrary roll angles this method uses a rough approximation which is not able to predict the roll angle and the corresponding cross-coupling effects as accurately as it is necessary for advanced, future air vehicles. So it was decided to develop an extended version of this code which fulfils the new requirements but keeps the advantages as there are: wide range of application, high accuracy for the zero roll case, and low

computation time and cost. With regard to the cost and the complexity of the three-dimensional flow it was obvious that only a semi-empirical procedure is adequate. There was a wide base of experimental data available for systematically varied cross wings on standard bodies. So it was promising to analyse these data and to develop a method to extend the zero roll angle results to arbitrary roll angle. This was the basis of the new code AAVEX which is presented below.

### 3. DESCRIPTION OF CALCULATION METHOD

#### 3.1 Range of Application

The AAVEX is a computer code for the static aerodynamic coefficients of missiles. It is applicable to the following

- geometry:
  - bodies of rotation; different noses and tails, frustum,
  - up to three cross wings; straight and cranked leading edges, different profiles, flaps,
  - all wing fins independently deflectable (comp. fig. 1).

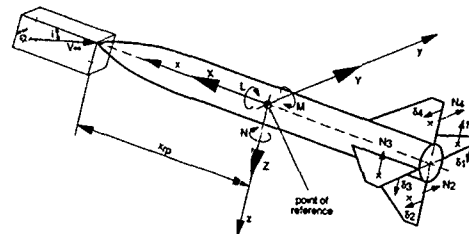


Fig.1: Coordinate System, Attitude Definition, Forces and Moments

The calculations are valid for the

- flight conditions (comp. fig. 1):
  - angle of incidence  $0^\circ \leq i \leq 90^\circ$
  - roll angle  $0^\circ \leq \phi \leq 360^\circ$
  - Mach-number  $0 \leq M \leq 4$
  - fin deflections  $10^\circ \leq \delta \leq 90^\circ$
  - Reynoldsnumber given explicitly or by flight altitude.

The method is able to predict the

- aerodynamic coefficients of (comp. fig. 1):
  - total forces  $X, Y, Z$  and moments  $L, M, N$
  - fin forces  $N_k$ , hinge moments  $M_k$  and root bending moments  $B_k$



Two postprocessing programs are available for

- trimmed aerodynamic coefficients
- dynamic derivatives including cross coupling effects.

### 3.2 General Procedure

The AAVEX is the computer code of a semi-empirical method. This means that theoretical relations are taken whenever available and updated with experimental and/or more precise theoretical results whenever possible and necessary. In cases where no theoretical formulas could be found, all kinds of experimental and theoretical data which were available and reliable have been used to create empirical relations by curve fitting and interpolation. It has been considered to be important that limiting cases are obeyed, e.g. that results at angles of incidence  $i = 0^\circ$  and  $i = 90^\circ$  etc. are correct. The main principle is to compose the forces and moments by summing up the contributions of all missile components. Thereby interactions between these components are regarded. This concerns the fin to fin, the wing to body, the body to wing, and the front to rear wing interference. The whole procedure can be roughly divided into three different stages:

- stage one:  
calculation of forces and moments for all wings in + position at zero roll angle; only symmetrical deflection of horizontal fins, front to rear wing interference neglected so far,
- stage two:  
modification of forces and moments for wings in arbitrary position at given roll angle; individual fin deflection, front to rear wing interference neglected so far,
- stage three:  
calculation of front to rear wing interference.

The following chapters give a survey of these stages with special emphasis on the last two.

### 3.3 Missile at Zero Roll Angle with Wings in + Position

On the basic stage of the AAVEX method the missile is examined at zero roll angle with all wings in + position. The front to rear wing interference is neglected while the body vortex influence on the wings is regarded. The calculation method at this stage is almost identical to that of the original AAV program which is described in the documentation by K.-W. Bock, H. Fuchs, H. Lehra [1].

In this case opposite fins of each cross wing are always examined together. The following terminology shall be used (comp. fig. 1):

- wing plane H: horizontal fins 1 and 3 together
- wing plane V: vertical fins 2 and 4 together

The equations below describe how the contri-

butions of the different missile components are superimposed to get the total force and moment coefficients in the missile fixed coordinate system (comp. fig. 1).

X-force coefficient: <sup>1)</sup>

$$-C_X \cdot S_{\text{ref}} = \sum_{l=1}^3 [(C_{TW1})_H + (C_{TW1})_V] \cdot S_{W1} + C_{TB} \cdot S_B \quad (1)$$

Z-force coefficient: <sup>1)</sup>

$$-C_Z \cdot S_{\text{ref}} = \sum_{l=1}^3 [C_{NW1} + C_{NB(W1)} + C_{NW1vtx}]_H \cdot S_{W1} + C_{NB} \cdot S_B \quad (2)$$

Pitching moment coefficient: <sup>1)</sup>

$$-C_m \cdot S_{\text{ref}} \cdot x_{\text{ref}} = \sum_{l=1}^3 [(C_{NW1} + C_{NW1vtx}) \cdot \Delta x_{W1} + C_{NB(W1)} \cdot \Delta x_{B(W1)}]_H \cdot S_{W1} + C_{mB} \cdot x_B \cdot S_B \quad (3)$$

The symbols herein are defined as follows:

H	index of wing plane H (fins 1 and 3 together)
V	index of wing plane V (fins 2 and 4 together)
l	wing number
$S_{\text{ref}, W1, B}$	reference area, exposed wing planform area, body cross section area
$x_{\text{ref}, B}$	missile reference length, body reference length
$C_{TW1}$	wing 1 tangential force coefficient
$C_{NW1}$	wing 1 normal force coefficient including body to wing interference (comp. equ.(3.4))
$C_{NW1vtx}$	body vortex influence on the wing normal force
$C_{NB}$	isolated body normal force coefficient
$C_{NB(W1)}$	additional body normal force due to wing 1 (comp. equ.(3.8))
$C_{mB}$	isolated body pitching moment
$\Delta x_{W1}$	rearward position of wing 1 point of pressure relative to given missile reference point

<sup>1)</sup> These equations are valid for cases without fin deflection. If there are fin deflections,  $C_{NW}$  has to be replaced by  $C_{NW} \cos \delta - C_{TW} \sin \delta$  and  $C_{TW}$  has to be replaced by  $C_{NW} \sin \delta + C_{TW} \cos \delta$ .

$\Delta x_B(W)$  rearward position of point of pressure of the additional body normal force due to wing 1

The different force and moment contributions in these equations are determined semiempirically by use of methods taken from various publications. The details will not be described here because the main topic of this paper is the procedure for the roll angle influence which is presented later. So only the most essential formulas for the zero roll angle case shall be mentioned. The wing normal force including the body to wing interference is determined by

$$C_{NW} = C_{NW}^{(a)} + C_{NW}^{(\delta)} + C_{NW}^{(n)} \quad (4)$$

with the "linear angle of attack part"

$$C_{NW}^{(a)} = C_{NWa} \cdot \sin \alpha \cdot \cos \delta \cdot |\cos(\alpha + \delta)| \cdot K_{W(B)}^* \quad (5)$$

the "linear deflection part"

$$C_{NW}^{(\delta)} = C_{NWa} \cdot \sin \delta \cdot \cos \alpha \cdot |\cos(\alpha + \delta)| \cdot K_{W(B)}^* \quad (6)$$

and the "nonlinear angle of attack and deflection part"

$$C_{NW}^{(n)} = C_{NWaa} \cdot \sin(\alpha + \delta) \cdot |\sin(\alpha + \delta)| \quad (7)$$

The additional normal force acting on the body due to the presence of the wing (wing to body carry-over) is determined by

$$C_{NB(W)} = C_{NB(W)}^{(a)} + C_{NB(W)}^{(\delta)} \quad (8)$$

with the "linear angle of attack part"

$$C_{NB(W)}^{(a)} = C_{NWa} \cdot \sin \alpha \cdot \cos \delta \cdot |\cos(\alpha + \delta)| \cdot K_{B(W)}^* \quad (9)$$

and the "linear deflection part"

$$C_{NB(W)}^{(\delta)} = C_{NWa} \cdot \sin \delta \cdot \cos \alpha \cdot |\cos(\alpha + \delta)| \cdot K_{B(W)}^* \quad (10)$$

The interference factors  $K^*$  (due to  $\alpha$ ) and  $K^*$  (due to  $\delta$ ) for the wing in the presence of the body ( $W(B)$ ) and for the wing to body carry-over ( $B(W)$ ) are empirically modified values of the original slender body theory factors.

Many details of the zero roll angle case procedure are taken from the DATCOM [2] and modified, supplemented and updated by help of further publications and experiments whenever useful and necessary. The other most frequently used reports shall be listed in alphabetical order without claiming completeness: W.B. Baker [3], P.T. Eaton [4], ESDU [5], L.H. Jorgenson [6], W.C. Pitts et al [7], B.F. Safel [8], and R.T. Schemensky [9].

### 3.4 Missile at Given Roll Angle with Wings in Arbitrary Position

#### 3.4.1 Without Fin Deflection

The AAVEX method is based on systematical experiments and additional calculations. The experiments are wind tunnel measurements of the fin normal force of widely varied test configurations. They all consist of a cruciform wing on a standard body with a 3 caliber ogive nose. Fig. 2 shows the configuration TC10.05.10 which is one of this series.

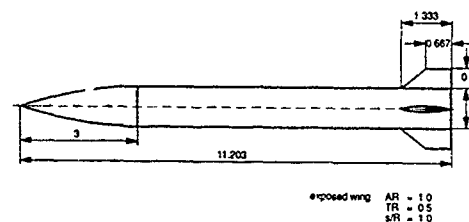


Fig. 2: Test Configuration TC 10.05.10

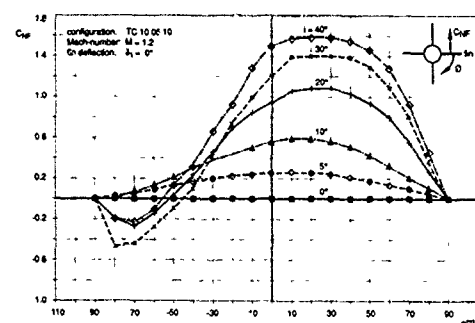


Fig. 3: Fin Normal Force Coefficient versus Roll Angle; Experiment, no Deflection

In fig. 3 the fin normal force of TC10.05.10 at the Mach-number  $M = 1.2$  is plotted versus the roll angle  $\phi$  for angles of incidence  $0^\circ \leq i \leq 40^\circ$ . The values refer to fin number 1 (comp. fig. 1) which is on top of the body for  $\phi = -90^\circ$ , on the right side for  $\phi = 0^\circ$ , and at the bottom for  $\phi = +90^\circ$ . The normal force variation is characteristic of body-cruciform wing configurations and well-known from many publications, e.g. by J.R. Spahr [10]. For low angles of incidence the fin normal force steadily decreases to zero when the fin is rotated (together with the other fins) from the horizontal to the top or to the bottom position. The reason is the decreasing "geometrical angle of attack" of this fin ( $\alpha = \arctan(\tan i \cdot \cos \phi)$ ). For medium angles of incidence the potential cross flow of winged circular cylinders results in an increased normal force on the windward side while it is decreased on the leeward side ([10]). For higher angles the body vortices and the dead water regions on the lee side might even convert the sign of the normal force. This behaviour observed in fig. 3 depends on the wing geometry, the forebody, and the Mach-number. Principally it is always similar.

Fig. 4 shows this general fin normal force variation with the roll angle for cases with and without fin deflection. For the moment only the non-deflection case shall be consi-

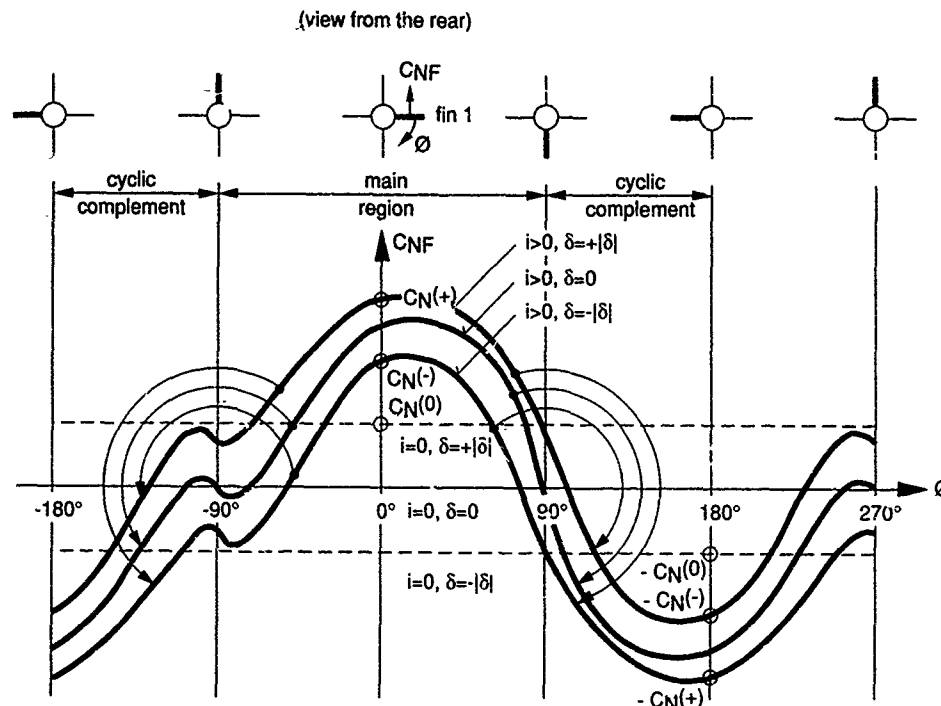


Fig.4: Principle of Normal Force versus Roll Angle with and without Fin Deflection

dered. Because of symmetry the  $C_N(\phi)$  function, which is periodical every  $360^\circ$ , can be supplemented by rotating the  $-90^\circ \leq \phi \leq 90^\circ$  section around the points  $\phi = -90^\circ$  or  $\phi = +90^\circ$ .

Many missile aerodynamic codes, like the original AAV, give good estimations of the  $C_N(\phi=0)$  value. So the idea was born to use this value and the zero conditions at  $\phi = \pm 90^\circ$  to approximate the whole periodical function  $C_N(\phi)$  by some kind of "shape function". For that all experiments available for the test configurations already mentioned were analysed in detail. It was found to be helpful to introduce the following shape function:

$$f(\phi) = C_N(\phi, \delta=0) / C_N(\phi=0, \delta=0) \quad (11)$$

This shape function is plotted in fig. 5 for the case already examined in fig. 3. It turned out that the fin normal force coefficient of a body-cross wing configuration can be approximated by

$$C_N(i, \phi, \delta=0) = C_N(i, \phi=0, \delta=0) \cdot f(\phi; i, M, AR, TR, s/R) \quad (12)$$

with the shape function  $f(\phi)$  depending on the parameters

- $i$  : angle of incidence,
- $M$  : Mach-number,
- $AR$  : exposed wing (opposite fins together) aspect ratio,
- $TR$  : exposed wing (opposite fins together) taper ratio;
- $s/R$  : exposed fin span to body radius.

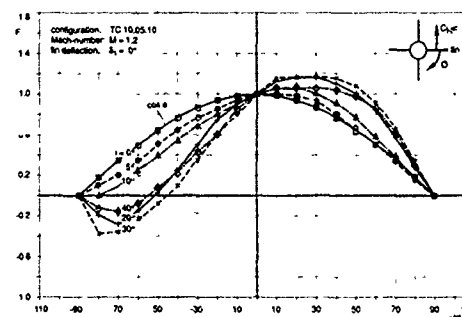


Fig.5: Fin I Normal Force Shape Function; Experiment, no Deflection

The forebody length influence on this function is significant only for very short forebodies. So it was neglected as well as the nose shape. The empirical formula for the shape function is based on experiments, supplemented by results of more sophisticated codes for the following parameter values.

- $\phi$  [°] =  $90, -80, \dots, 80, 90$
- $i$  [°] =  $0, 2, 5, 10, 15, \dots, 45$
- $M$  =  $0.6, 0.8, 0.9, 1.2, 1.5, 2.0, 3.0, 3.5, 4.5$
- $AR$  =  $0.25, 0.5, 1.0, 2.0, 4.0$
- $TR$  =  $0.0, 0.5, 1.0$
- $s/R$  =  $0.5, 1.0, 2.0, 4.0$

The range of interest for typical missiles is covered by this data base. For angles of incidence  $i > 45^\circ$  the shape function can be approximated by the  $i = 45^\circ$  value. The empirical formula is a 6th order Fourier series:

$$f(\phi'; i, M, AR, TR, s/R) = \sum_{k=1}^6 c_k(i, M, AR, TR, s/R) \cdot \sin(k\phi') \quad (13)$$

with

$$\phi' = \phi - \pi/2 \quad (14)$$

The Fourier coefficients  $c_k$  can be approximated as follows:

angle of incidence dependence,  
third order polynomial:

$$c_k(i; M, AR, TR, s/R) = \sum_{l=1}^4 c_{kl}(M, AR, TR, s/R) \cdot i^{l-1} \quad (15)$$

Mach-number dependence,  
third order polynomial:

$$c_{kl}(M; AR, TR, s/R) = \sum_{m=1}^4 c_{klm}(AR, TR, s/R) \cdot M^{m-1} \quad (16)$$

aspect and taper ratio dependence,  
second order twodimensional Taylor-approximation:

$$c_{klm}(AR, TR; s/R) = \sum_{n=1}^6 c_{klmn}(s/R) \cdot g_n(AR, TR) \quad (17)$$

with

$$\begin{aligned} g_1 &= 1 & ar &= \log AR \\ g_2 &= ar & tr &= TR - 0.5 \\ g_3 &= tr \\ g_4 &= ar^2 \\ g_5 &= tr^2 \\ g_6 &= ar \cdot tr \end{aligned}$$

span over body radius dependence,  
linear interpolation between:

$$\begin{aligned} c_k(s/R=0.5), c_k(s/R=1.0), \\ c_k(s/R=2.0), c_k(s/R=4.0). \end{aligned}$$

The coefficients  $c_{klmn}$  of equ.(17) are stored in the AAVEX code in DATA-statements for the span to body radius points of support  $s/R = 0.5, 1.0, 2.0, 4.0$ . Fig. 6 shows the shape function empirically approximated for the same case as in fig. 5 where the experimental values are presented.

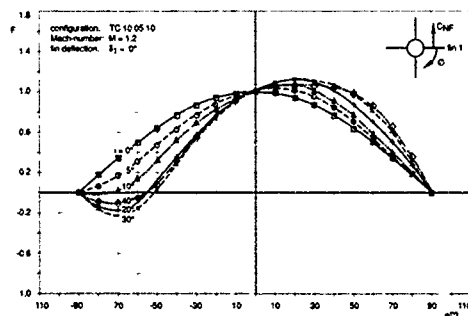


Fig. 6: Fin I Normal Force Shape Function; Empirical, no Deflection

For body tail configurations without fin deflection equ.(12) already gives the final results for the fin normal forces at arbitrary roll angles. In chapter 4.1 such an example can be found.

### 3.4.2 With Fin Deflection

If the fin under consideration is deflected, the roll angle influence becomes more complicated than in the non-deflection case described above. This can be seen in fig. 7 and fig. 8 which differ from fig. 3 only by a positive and a negative deflection ( $\delta = \pm 20^\circ$ ) of fin number 1 (other fins not deflected). The curves are shifted to higher ( $\delta > 0$ ) or lower ( $\delta < 0$ )  $C_N$  values. Due to the nonlinear lift characteristics of the fins and the complex interference this shifting depends on the angle of incidence and the roll angle. So the "shape function" of the non-deflection case cannot simply be applied.

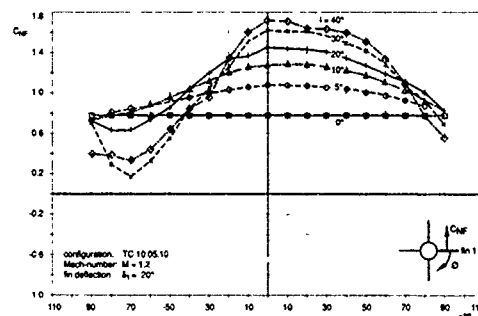


Fig. 7: Fin I Normal Force Coefficient versus Roll Angle; Experiment,  $\delta_1 = 20^\circ$  Deflection

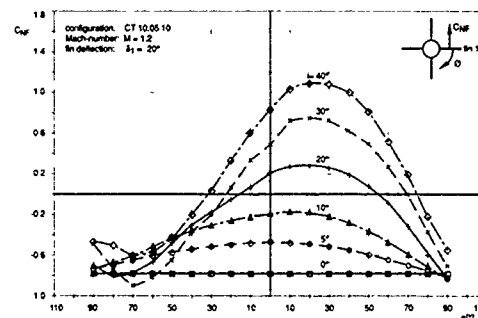


Fig. 8: Fin I Normal Force Coefficient versus Roll Angle; Experiment,  $\delta_1 = -20^\circ$  Deflection

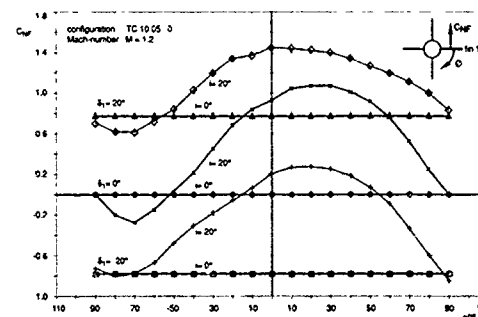


Fig. 9: Fin I Normal Force Coefficient versus Roll Angle; Experiment,  $\delta_1 = 0^\circ, \pm 20^\circ$  Deflection

Fig. 9 combines curves of fig. 3, 7 and 8 ( $i = 0^\circ, 20^\circ$ ;  $\delta = -20^\circ, 0^\circ, 20^\circ$ ) to show the characteristic influence of a fin deflection on the  $C_N(\phi)$ -curves. These curves are abstracted and used for the principle sketch

of fig. 4 which shall help to find a general approximation procedure. If the angle of incidence is  $i \neq 0$ , any positive ( $+|\delta|$ ) and the same negative ( $-|\delta|$ ) deflection in general cause different increments to the normal force. Only at  $\phi = \pm 90^\circ$  the fin efficiency is the same for positive and negative deflections. By analysing the available data base an "efficiency modification factor"  $h(i)$  was developed to give a simple approximation of the fin efficiency in top ( $i > 0$ ) or bottom ( $i < 0$ ) position:

$$C_N(i, \phi = \pm 90^\circ, \delta) = C_N(i=0, \delta) \cdot h(\pm i) \quad (18)$$

$h(i)$  was found by a least square approximation of the whole data base without respect to the special geometry and Mach-number. This will be improved in the future.

Using the conditions at  $\phi = 0$ , the "shape function" of equ.(12) and the "efficiency modification factor" of equ.(18) a new method has been developed to determine the general  $C_N(i, \phi, \delta)$ -function. First the following  $\phi = 0$  values are calculated by the zero-roll angle method described in chap. 3.3 with all wings in +position:

$$1. \quad C_N^{(0)} = C_{NF}(i=0; \delta = +|\delta|), \quad (19)$$

$$2. \quad C_N^{(+)} = C_{NF}(i; \phi=0, \delta = +|\delta|), \quad (20)$$

$$3. \quad C_N^{(-)} = C_{NF}(i; \phi=0, \delta = -|\delta|), \quad (21)$$

Knowing these values and using equ.(18) four points of the  $\delta > 0$ -curve can be determined in the interval  $-90^\circ \leq 270^\circ$  of fig. 6:

$$C_{NF}(i, \delta \geq 0) = \begin{cases} C_N^{(0)} \cdot h(-i); & \phi = -90^\circ \\ C_N^{(+)} & ; \quad \phi = 0^\circ \\ C_N^{(0)} \cdot h(+i); & \phi = 90^\circ \\ C_N^{(-)} & ; \quad \phi = 180^\circ \end{cases} \quad (22)$$

These points are connected by a periodic function that takes care of the shape, which must be similar to that for  $\delta=0$  ("shape function"  $f(\phi; i)$ ), and that includes the limiting cases  $i \neq 0, \delta=0$  (equ. (12)) and  $i=0, \phi \neq 0$  ( $C_N(\phi) = \text{const.}$ ). The result is:

$$C_{NF}(i, \phi, \delta \geq 0) = +C_N^{(0)} * g(i, \phi) + [(C_N^{(+)} - C_N^{(0)}) * \cos^2 \frac{1}{2} \phi + (C_N^{(-)} + C_N^{(0)}) * \sin^2 \frac{1}{2} \phi] * f(\phi; i)$$

$$C_{NF}(i, \phi, \delta \leq 0) = -C_N^{(0)} * g(i, \phi) + [(C_N^{(-)} + C_N^{(0)}) * \cos^2 \frac{1}{2} \phi + (C_N^{(+)} - C_N^{(0)}) * \sin^2 \frac{1}{2} \phi] * f(\phi; i)$$

(23)

with the abbreviation:

$$g(i, \phi) = \begin{cases} h(-i) * \sin^2 \phi + \cos^2 \phi; & \sin \phi \leq 0 \\ h(+i) * \sin^2 \phi + \cos^2 \phi; & \sin \phi \geq 0 \end{cases} \quad (24)$$

The limiting cases mentioned above can be easily verified.

The method needs three  $\phi=0$ -calculations to determine  $C_N^{(0)}, C_N^{(+)}$ , and  $C_N^{(-)}$  for each deflected fin.  $C_N^{(0)}$  is independent of  $\delta$  and so identical for all four fins.  $C_N^{(+)}$  and  $C_N^{(-)}$  depend on  $\delta$ . Thus they might be different for each fin because  $\delta$  might be different. These "basic normal force coefficients" are determined like in the original AAV for the missile at zero roll angle with all wings in + position and with and without symmetrical deflection of the horizontal fins.

Equ.(23) is a periodic function through points of support which are based on  $\phi = 0$ -cases for a cross wing on a body. So the "basic coefficients" have to include body vortex effects. For that an empirical body vortex pair is assumed starting at the body nose shoulder for the front wing and another pair starting at the front wing trailing edge position for the rear wing (fig. 10). For the calculation of the body vortex influence on the wing compare chap. 3.5.2 (same method).

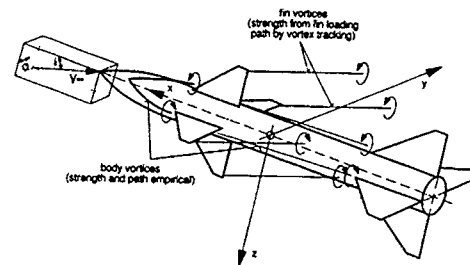


Fig.10: Vortex System for Body to Wing and Wing to Wing Interference

Summing up the body and wing components for the total force and moment coefficients in this more general  $\phi \neq 0, \delta \neq 0$ -case leads to equations different from eqs. (1 to 3). Due to the roll angle, unsymmetrical fin deflections, and cross coupling effects there might be a side force, a yawing moment, and a rolling moment in addition.

### 3.5 Front to Rear Wing Interference

The method described so far presumes isolated cross wings at a body of rotation. So the body vortex influence is included, but the front to rear wing interference still has to be determined. For that an approximation method was developed. It can be roughly divided into two steps:

- shedding of fin vortices at the front wing trailing edges (due to linear lift) and above trailing edges (due to nonlinear lift), tracking them together with empirical body vortices of variable strength to the rear wing position,
- calculation of front wing vortex influence on rear wing normal force.

### 3.5.1 Shedding and Tracking of Vortices between Wings

The body vortex influence on the rear wing is already included so far in "basic coefficients" of equ.(23)). Nevertheless they are still important for the path of vortices leaving the front wing. So body vortices are shedded along the midbody (between front and rear wing). The local strength is empirically deduced from the body loading after D. Jacob [11].

Then fin vortices are shed at the trailing edge position of the front wing. The total strength is calculated from the fin loading and divided into a linear (due to linear lift) and a nonlinear part (due to nonlinear lift). One "nonlinear vortex" with the nonlinear part of the vortex strength is shed above each fin trailing edge to simulate the rolled up leading edge vortex. The number of "linear vortices" per fin is given by program input. If multiple "linear vortices" are shed from each fin, they are assumed to be of equal strength and their properties are determined for elliptical loading. The method can be found in the book of J.N. Nielsen [12].

For the vortex tracking a twodimensional flow in each cross plane is assumed. At the location of each front wing vortex the velocity components  $v$  and  $w$  are calculated. For that the velocities induced by all other fin vortices, the body vortex pair, the image vortices inside the body, and by the body cross flow are calculated and summed up. These velocity components are used to determine the displacement of the fin vortices on their way downstream by integrating

$$dy/dx = v/V_\infty \text{ and } dz/dx = w/V_\infty \quad (25)$$

This method is described by J.N. Nielsen [12]. In the AAVEX the integration of equ. (25) is done by a Runge-Kutta method.

The twodimensional consideration of the cross flow becomes wrong with the angle of incidence increasing. But in this method it is guaranteed that for higher angles the body cross flow becomes more and more dominant over the vortex induced contributions, which become wrong. Due to that the front wing vortices more and more follow the streamlines without influence of other vortices for increasing angles.

### 3.5.2 Front Wing Vortex Influence on Rear Wing

To determine the interference on the rear wing, first for each rear wing an "equivalent induced angle of attack" is estimated by integrating the local fin load in the following way (e.g. for fin 1):

$$\begin{aligned} \tan(\Delta\alpha_{F1}) &= v_{F1}/V_\infty = \quad (26) \\ &= 1/(V_\infty \cdot C_{NaF1}) \cdot \\ &\quad \int_{F1} [v_{F1}(y) \cdot cc_{1Nr}(y) \\ &\quad + v_{F2}(y) \cdot cc_{1Nu}(y) \cdot e_{adj} \\ &\quad + v_{F3}(y) \cdot cc_{1Nl}(y) \cdot e_{opp} \\ &\quad + v_{F4}(y) \cdot cc_{1Nu}(y) \cdot e_{adj}] \cdot d(y/s) \end{aligned}$$

Analogous equations are used for the other fins. The expressions used herein are:

$v_{F1,2,3,4}(y)$	velocity component vertical to fins 1 to 4 induced by the front wing vortices and their images at the spanwise position $y$
$cc_{1Nr,1,u}(y)$	span loading coefficient for a cross wing fin: index $r$ : due to unit incidence on fin itself, index $u$ : due to unit incidence on adjacent fins, index $l$ : due to unit incidence on opposite fin
$e_{adj,opp}$	reduction factor due to reduced influence region in supersonic flow: index $adj$ : adjacent fin, index $opp$ : opposite fin
$C_{Na}$	coefficient of fin normal force slope at zero angle of incidence

This equation was developed for small angles of incidence and small induced angles using the slender body theory and the reverse flow theorem. It is described in detail by J.N. Nielsen et al. [13]. Integrating the root bending moment loading analogous to equ. (26) allows to approximate the "point of action" of the induced interference force.

To determine the induced normal force, equ. (4) is used twice for each fin: first with  $i = \alpha_F$  and secondly with  $i = \alpha_F + \Delta\alpha_F$ , where  $\alpha_F$  is the "geometrical angle of attack" and  $\Delta\alpha_F$  is the induced angle of attack of equ. (26). The difference gives

$$\begin{aligned} C_{NFint} &= C_{NF}(i=\alpha_F + \Delta\alpha_{fin}, \phi=0, \delta_F) \\ &\quad - C_{NF}(i=\alpha_F; \phi=0, \delta_F) \end{aligned} \quad (27)$$

This completes the final total force and moment coefficients of the missile.

#### 4. EXAMPLES

##### 4.1 Body-Tail Configuration

Fig. 11 shows the fin normal force coefficient of a body-cross wing configuration (referred to  $A_{ref} = \pi D^2/4$ ) versus the angle of incidence at different roll angles for the Mach-number  $M = 2.36$  in comparison with experiments of reference [14]. The roll angle varies between  $\phi = 0^\circ$  (fin 1 horizontal) and  $\phi = -90^\circ$  (fin 1 on top of body). The  $\phi \neq 0$  cases in the AAVEX are based on the  $\phi = 0$  curve. So the accuracy is limited by the zero roll accuracy. Even these values are difficult to predict, because they are influenced by the body vortex system which sensitively depends on the Reynolds-number and the experimental conditions. Nevertheless the results, especially the roll dependence is sufficiently correct.

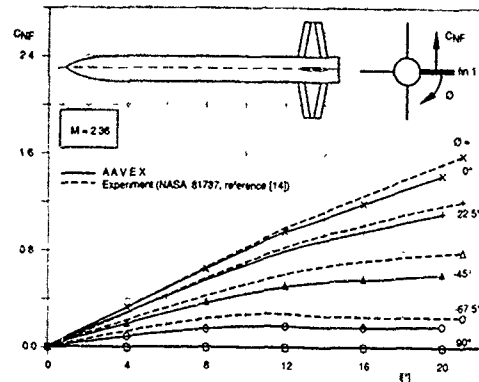


Fig.11: Fin 1 Normal Force Coefficient of a Body-Tail Configuration

##### 4.2 Body-Wing-Tail Configuration

Test calculations were made for the body-wing-tail configuration FRL218 of reference [15]. Its geometry is shown in fig. 12. In figs. 13 and 14 the pitching and rolling moment coefficients of this configuration are plotted versus the angle of incidence for roll angles  $0^\circ \leq \phi \leq 45^\circ$  and the Mach-number  $M = 2.5$ .  $C_m$  is the coefficient of the pitching moment in a "balance coordinate system" where the y-direction is horizontal and the x-direction is the body axis. Both coefficients are referred to  $l_{ref} = D$  and  $A_{ref} = \pi D^2/4$ .

Although there are considerable cross-flow effects and strong front to rear wing interferences, the roll influence on both moments is sufficiently predicted. The largest distance between the predicted and measured rearward point of pressure (not explicitly shown) is below  $D/3$ . The same good agreement was found for all other tests of this configuration presented in reference [15] between  $M = 0.7$  and 3.1.

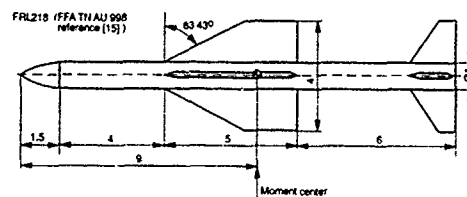


Fig.12: Body-Wing-Tail Configuration FRL 218 (reference [15])

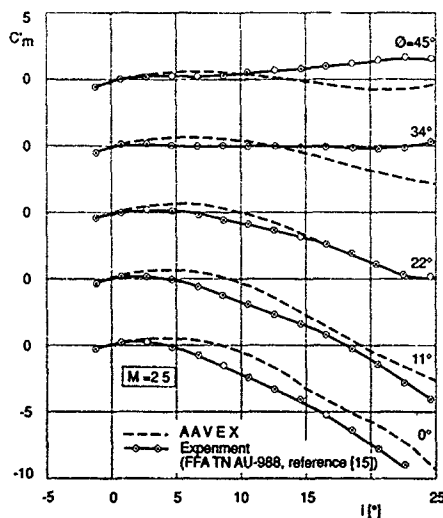


Fig.13: Pitching Moment of Body-Wing-Tail Configuration FRL 218 (reference [15])

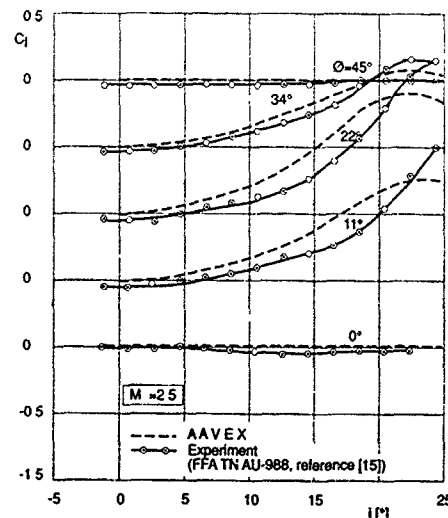


Fig.14: Rolling Moment of Body-Wing-Tail Configuration FRL 218 (reference [15])

#### 4.3 Body-Canard-Wing Configuration

The third example is the canard controlled missile of fig. 15. The experimental results at Mach-number  $M = 2.5$  are taken from reference [16]. Figs. 16 and 17 show the normal force and pitching moment coefficient versus the angle of incidence without fin deflection at zero roll angle. Both values are expressed in the body fixed coordinate system of fig. 1 and referred to  $A_{ref} = \pi D^2/4$  and  $l_{ref} = 0$  (moment only). The experimental values, which are available up to  $i = 18^\circ$ , are well predicted by the AAVEX. The dashed curves represent the AAVEX method without canard to wing interference. Obviously there is a downwash effect which reduces the rear wing normal force. Especially for the pitching moment this contribution must not be omitted.

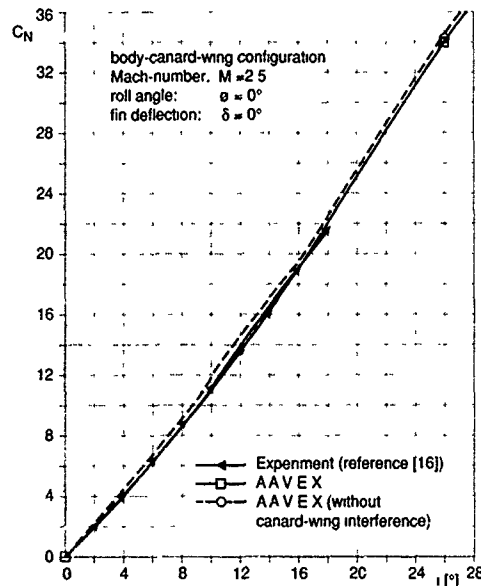


Fig. 16: Normal Force of Body-Canard-Wing Configuration;  $\phi = 0^\circ$ ,  $\delta = 0^\circ$

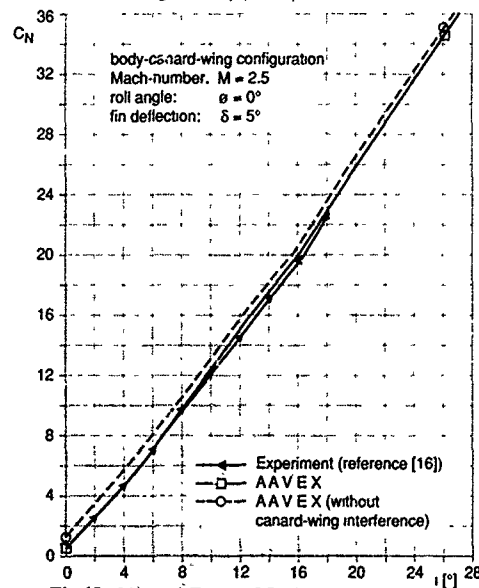


Fig. 18: Normal Force of Body-Canard-Wing Configuration;  $\phi = 0^\circ$ ,  $\delta = 5^\circ$

Canard Controlled Missile (NASA TP 2157, reference [16])

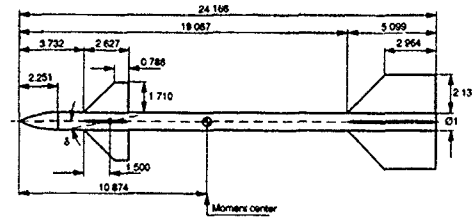


Fig. 15: Body-Canard-Wing Configuration (NASA TP 2157, reference [16])

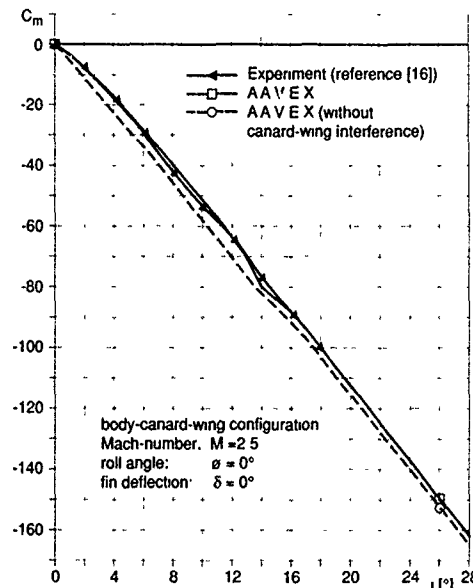


Fig. 17: Pitching Moment of Body-Canard-Wing Configuration;  $\phi = 0^\circ$ ,  $\delta = 0^\circ$

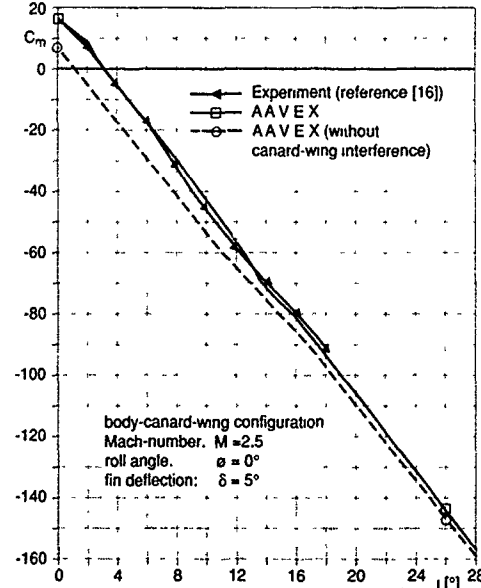


Fig. 19: Pitching Moment of Body-Canard-Wing Configuration;  $\phi = 0^\circ$ ,  $\delta = 5^\circ$



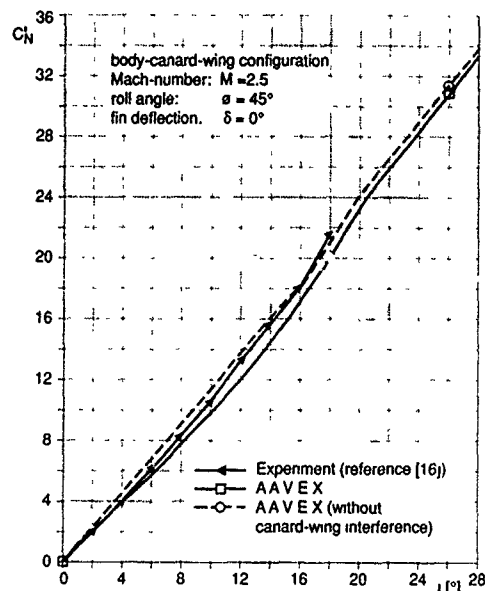


Fig. 20: Normal Force of Body-Canard-Wing Configuration;  $\phi = 45^\circ$ ,  $\delta = 0^\circ$

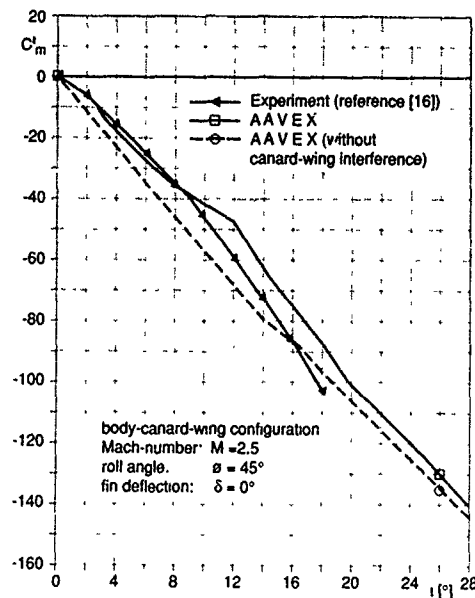


Fig. 21: Pitching Moment of Body-Canard-Wing Configuration;  $\phi = 45^\circ$ ,  $\delta = 0^\circ$

In figs. 18 and 19 the normal force and pitching moment coefficient are plotted for  $\delta = 28^\circ$  deflection of the two horizontal canard fins. It can be seen that about half of the canard deflection efficiency is the result of the canard to wing interference.

In figs. 21 and 22 the normal force and pitching moment coefficient (in the "balance coordinate system") are presented for  $\phi = 45^\circ$  without canard deflection. Now at angles of incidence  $i \geq 10^\circ$  the agreement between AAVEX and the experiment is not as good as for  $\phi = 0$  but still sufficient. The maximum pitching moment deviation corresponds to a point of pressure deviation of  $\Delta x_{cp} = 0/2$ . The front to rear wing interference seems to be overpredicted at medium angles of incidence, when the vortices of the lower canard fins (x-position!) pass the upper rear wing fins at a short distance. Further examinations concerning e.g. vortex dissipation and bursting are planned and might lead to an improvement.

##### 5. CONCLUSIONS

The new computer code AAVEX (aerodynamics of air vehicles, extended version) has been created for the aerodynamic forces and moments of cross wing missiles with all deflectable fins at arbitrary roll angles. For that the well-approved zero roll angle code AAV has been extended to include the correct roll angle influence. The following experiences of this development are of special interest:

- For the body to cross wing and the fin to fin interference a new empirical "shape function" has been developed from a wide systematical data base of experiments and calculations. This function allows to modify zero roll angle results of body-cross wing configurations for arbitrary roll angles. The fins might be deflected independently.

- The front to rear wing interference can be approximated by shedding leading and trailing edge vortices from the front wing, tracking them together with mid-body vortices to the rear wing, and calculating equivalent induced angles of attack for all rear wing fins.
- The results of all test calculations are sufficient although the computation time is short.
- The accuracy might decrease in cases with strong vortices passing fins at a short distance or when vortex dissipation and bursting is likely. This will be improved in the future.
- The method is applicable to most zero roll angle codes which thus can be extended to arbitrary roll angles.

##### 6. REFERENCE

- [1] K.-W. Bock, H. Fuchs, H. Lehra: The Missile Coefficient Program "AAV", Part I: Documentation. DORNIER-report BF 1/85 (1985)
- [2] DATCOM: USAF Stability and Control DATCOM. McDonnell Douglas Corporation, Douglas Aircraft Division (1972 and 1976)
- [3] W.B. Baker: An Aerodynamic Coefficient Prediction Technique for Slender Bodies with Low Aspect Ratio Fins at Mach Numbers from 0.6 to 3.0 and Angles of Attack from 0 to 180 Degrees. AEDC-TR-77-97 (1978)
- [4] P.T. Eaton: A Method for Predicting the Static Aerodynamic Characteristics of Low-Aspect-Ratio Configurations. Naval Ship Research & Dev. Center, Rep. 2216 (1966)

- [5] ESDU: Engineering Science Data Unit.  
ESDU, London
- [6] L.H. Jorgensen: Prediction of Static Aerodynamic Characteristics for Slender Bodies Alone and with Lifting Surfaces to Very High Angles of Attack.  
NASA TM X-73,123 (1973)
- [7] W.C. Pitts, J.N. Nielsen, G.E. Kaattari: Lift and Center of Pressure of Wing-Body-Tail Combinations at Subsonic, Transonic and Supersonic Speeds.  
NACA- TR-1307 (1957)
- [8] B.F. Saffel et al: A Method for Predicting the Static Characteristics of Typical Missile Configurations for Angles of Attack to 180°.  
Naval Ship Research a. Dev. Center, rep. 3645 (1971)
- [9] R.T. Schemensky: Development of an Empirically Based Computer Program to Predict the Aerodynamic Characteristics of Aircraft.  
Volume I: Empirical Methods.  
General Dynamics, AD-780 000 (1973)
- [10] J.R. Spahr: Contribution of the Wing Panels to the Forces and Moments of Supersonic Wing-Body Combinations at Combined Angles.  
NACA TN 4146 (1958)
- [11] O. Jacob: Untersuchungen zur Flugkörper-Wirbelinterferenz (Phase I).  
DORNIER-report 78/19 B (1978)
- [12] J.N. Nielsen: Missile Aerodynamics.  
Nielsen Engineering & Research, Inc., Mountain View, Ca, 1988
- [13] J.N. Nielsen, M.J. Hensch, C.A. Smith: A Preliminary Method for Calculating the Aerodynamic Characteristics of Cruciform Missiles to High Angles of Attack Including Effects of Roll Angle and Control Deflections.  
NRLAR TR 152, ONR-CR215-226-4F, Nov.1977
- [14] M. Lamb, C.D. Trescot: A Study of Panel Loads and Centres of Pressure of Three Different Cruciform Aft-Tail Control Surfaces of a Wingless Missile from Mach 1.60 to 3.70.  
NASA TM 81787 (1980)
- [15] S.E. Gudmundson, L. Torngren: Transonic and Supersonic Wind-Tunnel Tests on Slender Cruciform Wing-Body-Tail Configurations in Different Pitch and Roll Positions.  
FFA TN AU-988 (1975)
- [16] A.B. Blair, J.M. Allen, G. Hernandez: Effect of Tail Fin Span on Stability and Control Characteristics of a Canard Controlled Missile at Supersonic Mach-numbers.  
NASA TP 2157 (1983)

AERODYNAMIC CHARACTERISTICS OF CYLINDRICAL BODIES  
WITH POINTED AND TRUNCATED CONICAL NOSES

V. ATLI\*  
Istanbul Technical University  
Faculty of Aeronautics and Astronautics  
(ITU Uçak ve Uzay Bilimleri Fakültesi)  
80626 Maslak, Istanbul  
Turkey

1. SUMMARY

The aerodynamic characteristics of cylindrical bodies, with pointed and truncated conical noses, are investigated experimentally and theoretically, at a low Mach number, over the range of angle of attack from 0 to 20 deg. The Reynolds number, based on the maximum body diameter, is about  $4.1 \times 10^4$ . The surface-flow visualization is performed by applying the oil method. The balance measurements are made by using a sting-type strain-gage balance which is designed and constructed under the project T40 of FDP of AGARD. The results of the balance measurements are compared with the potential theory and the method of viscous crossflow analogy. It is observed that the method of viscous crossflow analogy is applicable to the cylindrical bodies with pointed and truncated conical noses even at high angles of attack, unlike the potential theory. The nose-cone angle and the bluntness are the parameters affecting the flowfield around and the aerodynamic characteristics of a pointed or truncated cone-cylinder body.

2. LIST OF SYMBOLS

A : axial force  
C<sub>A</sub> (or C<sub>AX</sub>) : axial force coefficient  
( $= \frac{A}{q_{\infty} S_r}$ )  
C<sub>D</sub> : drag coefficient ( $= \frac{D}{q_{\infty} S_r}$ )  
C<sub>DO</sub> : drag coefficient at  $\alpha=0$  deg  
C<sub>d</sub> : crossflow drag coefficient  
C<sub>dc</sub> : crossflow drag coefficient of circular cylinder section  
C<sub>L</sub> : lift coefficient ( $= \frac{L}{q_{\infty} S_r}$ )  
C<sub>M</sub> (or C<sub>MD</sub>) : pitching moment coefficient  
( $= \frac{M}{q_{\infty} S_r l_r}$ )  
C<sub>N</sub> (or C<sub>ND</sub>) : normal force coefficient  
( $= \frac{N}{q_{\infty} S_r}$ )  
CXCP : location of center of pressure in dimensionless form  
( $= x_{cp} / l$ )  
D : drag  
d : maximum body diameter  
(diameter of the main body)  
d<sub>n</sub> : diameter of cylinder corresponding to missile  
( $= S_p / l$ )

d<sub>t</sub> : body flat-nose diameter  
d<sub>t</sub>/d : nose bluntness ratio  
f(x) : normal force distribution  
l : total body length  
l<sub>n</sub> : nose length  
l<sub>r</sub> : reference length ( $= l$ )  
M : pitching moment  
M<sub>∞</sub> : freestream Mach number  
M<sub>c</sub> : crossflow Mach number  
( $= M_{\infty} \sin \alpha$ )  
N : normal force  
q<sub>∞</sub> : freestream dynamic pressure  
( $= \frac{1}{2} \rho V_{\infty}^2$ )  
R : local body radius  
Re : Reynolds number based on the maximum body diameter  
( $= \frac{V_{\infty} d}{\nu}$ )  
Re<sub>cds</sub> : crossflow Reynolds number  
based on d<sub>n</sub>, ( $= \frac{V_{\infty} \sin \alpha d_n}{\nu}$ )  
S : local cross sectional area  
( $= \pi R^2$ )  
S<sub>b</sub> : body base area  
S<sub>np</sub> : nose planform area  
S<sub>p</sub> : total body planform area  
( $= \int_0^l 2R dx$ )  
S<sub>np</sub>/S<sub>p</sub> : nose planform area ratio  
S<sub>r</sub> : reference area ( $= \frac{\pi d^2}{4}$ )  
S<sub>t</sub> : body flat-nose area  
V<sub>∞</sub> : freestream velocity  
W : body volume ( $= \int_0^l \pi R^2 dx$ )  
x : body axis (axial distance from body nose)  
x<sub>c</sub> : axial distance from body nose to centroid of body planform area  
x<sub>cp</sub> : axial distance from body nose to center of pressure (location of center of pressure)  
x<sub>m</sub> : pitching moment center (axial distance from body nose to pitching moment center)  
x<sub>cp</sub>/l : location of center of pressure in dimensionless form  
( $= CXCP = \frac{x_m}{l} - \frac{C_M}{C_N}$ )

\* Assoc. Prof., Ph.D., Member of AGARD FDP, Senior Member AIAA.

$\alpha$  : angle of attack  
 $\rho$  : density of air  
 $\nu$  : kinematic viscosity of air  
 $\eta$  : correction factor for influence of fineness ratio on  $c_{dc}$

$\theta$  : nose cone angle

### 3. INTRODUCTION

The flowfield around, and, consequently the aerodynamic characteristics of a missile depend on the geometrical shape of the missile as well as angle of attack, Mach number and Reynolds number. The flowfield around a missile starts to develop from its nose. Therefore, the entire flowfield around a missile is naturally under the influence of the geometry of the nose. Cylinders and cones are the major geometrical forms used widely in missile configurations as main body and nose respectively. The discontinuity in the slope of the body surface, between the conical nose and the cylindrical main body (the nose-main body junction), causes a circular flow separation at zero angle of attack [1]. This flow separation is modified with angle of attack and becomes more complex [1].

The experimental and theoretical techniques for missile aerodynamics are outlined in some of the recent publications [2-6] presenting many works. Atli [1] has shown that the geometrical complexity of a missile strongly affects the flowfield around it and its aerodynamic characteristics. However, systematic studies are necessary to investigate the effects of geometrical modifications such as the nose geometry. On the other hand, it is necessary to verify the applicability of some theoretical and empirical methods, such as the method of viscous crossflow analogy for the calculation of the aerodynamic characteristics of different configurations.

In the present work, the aerodynamic characteristics of four pointed and two truncated cone-cylinder bodies, are investigated experimentally and theoretically at a low Mach number, over the range of angle of attack from 0 to 20 deg. The Reynolds number, based on the maximum body diameter, is about  $4.1 \times 10^4$ . Surface-flow visualization is performed by applying the oil method at the angles of attack  $\alpha=0$  and 20 degs. Hence, the flow separations on the bodies are investigated qualitatively. Balance measurements are made, over the range of angle of attack  $0 \leq \alpha \leq 20$  deg. by using a sting-type strain-gage balance which is designed and constructed under the project T40 of FDP of AGARD. The results of the balance measurements are compared with the potential theory and the method of viscous crossflow analogy.

### 4. DESCRIPTION OF MODELS AND EXPERIMENTAL TECHNIQUE

The configurations of the models are presented in Fig.1. The first four models

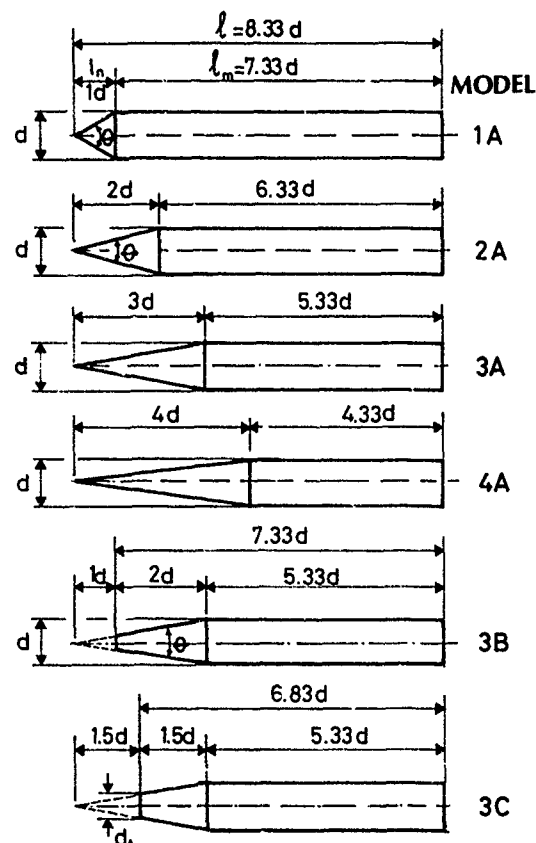


Fig.1 Models ( $d=30$  mm for flow visualization models,  $d=60$  mm for balance measurement models.)

(Models 1A, 2A, 3A, 4A) are pointed cone-cylinder bodies with the same fineness ratio,  $l/d=8.33$ , but with the different nose cone angles,  $\theta=53.1, 28.1, 18.9, 14.3$  deg. (with the different nose fineness ratio  $l_n/d=1, 2, 3, 4$ ) for the Models from 1A to 4A respectively. The last two models (Models 3B, 3C) are the truncated versions of Model 3A with the different nose bluntness ratio,  $d_1/d=0.33, 0.50$  for Models 3B and 3C respectively. The maximum diameter (the diameter of the cylindrical main body) of the flow visualization models,  $d$  is 30 mm. The dimensions of the models used for the balance measurements are twice of those used for the flow visualization. However, the configurations are the same for the balance measurements and the flow visualization tests. Some of the geometrical characteristics of the configurations are given in Tab.1.

The surface flow visualization tests are performed by applying the oil technique, in order to observe the flow separations on the bodies. These tests are conducted in an open-circuit wind tunnel with a test

Tab.1 Some of the geometrical characteristics of the configurations

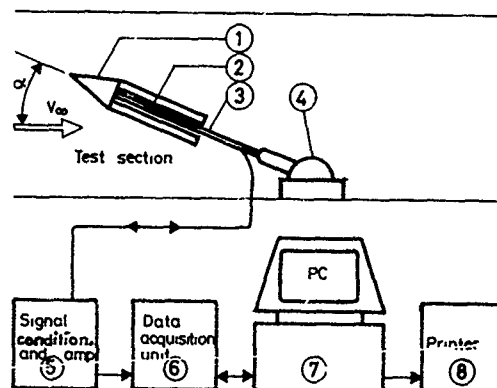
Model	Nose Type	Total fineness ratio $l/d$	Nose fineness ratio $l_n/d$	Nose planform area ratio $S_n/S_r$	Nose cone angle $\theta$ , deg.	Nose bluntness ratio $d_t/d$
1A	pointed cone	8.33	1	0.064	53.1	0
2A	pointed cone	8.33	2	0.136	28.1	0
3A	pointed cone	8.33	3	0.220	18.9	0
4A	pointed cone	8.33	4	0.316	14.3	0
3B	truncated cone	7.33	2	0.250	18.9	0.33
3C	truncated cone	6.88	15	0.174	18.9	0.50

section of  $50 \times 50 \times 200$  cm at the freestream velocity  $V_\infty = 20$  m/s and at the angles of attack  $\alpha = 0$  and  $20$  degs. The Reynolds number, based on the maximum body diameter, is  $Re_d = 41067$  ( $\approx 4.1 \times 10^4$ ). The photographs of the flow visualization are taken by a camera from one side during the tunnel run.

The aerodynamic force and moment measurements are made in a closed-circuit wind tunnel with a test section of  $80 \times 10 \times 162$  cm, over the range of angle of attack  $0 \leq \alpha \leq 20$  deg. The freestream velocity in these balance measurements,  $V_\infty$ , is  $10$  m/s which is the half of that in the flow visualization tests. However, the Reynolds number is the same as  $Re_d \approx 4.1 \times 10^4$  since the dimensions of the models used in the balance measurements are twice of those used in the flow visualization.

The instrumentation of the balance measurements is sketched in Fig.2. As seen from this figure, a sting-type, strain-gage balance, which is designed and constructed under the project T40 of FDP of AGARD, is employed with a data acquisition system. The data acquisition system consists of a six-component signal conditioner/amplifier (Measurements Group, System 2100), a multi-channel data acquisition unit (Validyne, Model DA380) and a personal computer (Goupil G40) and a line printer (Epson FX-1000). Although the balance has six components only three components (normal force  $N$ , axial force  $A$ , and pitching moment  $M$ ) are considered in the balance measurements. The calibration data of these components are plotted in Fig.3. The sensitivities of the balance components of  $A$ ,  $N$  and  $M$ , with no amplification and for a 1 Volt excitation, are  $0.179 \mu V/(grf \cdot V)$ ,  $0.186 \mu V/(grf \cdot V)$ ,  $0.046 \mu V/(grf \cdot cm \cdot V)$  respectively. The accuracies ( $\pm 2\sigma$ ) of the same components of the balance are  $\pm 2.1$  grf,  $\pm 1.8$  grf and  $\pm 18.4$  grf $\cdot$ cm respectively. The balance and the data acquisition system are operated with an excitation voltage  $E$  of  $\pm 2$  Volts and an amplification ratio of 4000.

A data acquisition and reduction program in "Basic" is developed and employed. In the data reduction, the aerodynamic force and



- ① : Model
- ② : 6-Component sting-type strain-gage balance
- ③ : Sting support
- ④ : Angle of attack mechanism
- ⑤ : Signal condition. and amplifier system (Measurements Group System 2100)
- ⑥ : Multi-channel data acquisition unit (Validyne, Model DA380)
- ⑦ : Personal computer (Goupil G40)
- ⑧ : Line-printer (Epson FX-1000)

Fig.2 Instrumentation of the balance measurements,

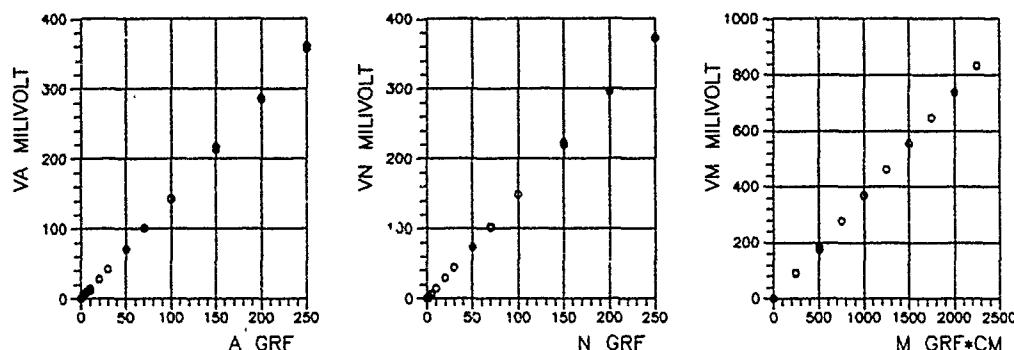


Figure-3 The calibration graphics of the balance

moment coefficients ( $C_A$ ,  $C_N$ ,  $C_M$ ) and the location of the center of pressure

$$(CXCP = \frac{x_{cp}}{l} = \frac{x_m}{l} - \frac{C_M}{C_N})$$

for the different angles of attack. Here, the pitching moment is referred to the nose tip point of the model. Then, the variations of  $C_N$ ,  $C_A$ ,  $C_M$  and  $x_{cp}/l$  with angle of attack  $\alpha$  are plotted. These plots are presented in Section 6 together with the theoretical results.

#### 5. THEORETICAL BASIS: THE METHOD BASED ON THE VISCOUS CROSSFLOW ANALOGY

At an angle of attack greater than a few degrees, the flow around a body of revolution, even of simple-type, separates from the lee-side of the body because of the effects of the viscosity and rolls up to form vortices in the leeward flowfield. This large-scale leeward flow separation produces a large increase in the normal force distribution reducing the lee-side pressure. The variations of the aerodynamic loads with the angle of attack become nonlinear.

Although the potential theory is sufficient at small angles of attack, it is necessary to consider the effects of the leeward flow separation at high angles of attack. For this purpose, some certain theoretical and empirical methods have already been developed [7]. Unfortunately, the theoretical methods have large computational requirements [7]. In the viscous crossflow analogy, which is an empirical method, an empirical term representing the viscous leeward flow separation is added to a term representing the potential theory for the normal force and pitching moment. This relatively simple method was originally proposed by Allen [8,9] and has successfully been applied to simple-type bodies of revolution in many studies [9-20]. This method has recently been applied to some complex bodies of revolution, by Atli [1]. The comparison of this method with the available experimental data has shown a good agreement not only for the simple-type bodies of revolution [14,16,19,20] but also for the complex ones [1], even at high angles of attack.

The method based on the viscous crossflow analogy is explained in Ref 1 in detail. In this method, the crossflow around an inclined slender body is treated independently from the axial flow, and the effects of the viscous leeward flow separation are considered by the viscous crossflow analogy. According to the viscous crossflow analogy, the crossflow around a slender body, moving at the velocity  $V_\infty$ , with the angle of attack  $\alpha$ , is similar to the two dimensional flow around a corresponding circular cylinder moving at the velocity  $V_\infty \sin \alpha$  [7,9,4,1]. Hence, the

normal force distribution on a body of revolution of a finite length  $l$ , moving at the velocity  $V_\infty$  and with the angle of attack  $\alpha$  may be expressed as

$$f(x) = q_\infty \left( \frac{dS}{dx} \right) \sin 2\alpha \cos^2 \frac{\alpha}{2} + 2\eta c_{dc}(x) R q_\infty \sin^2 \alpha \quad (1)$$

where the first term on the right hand side comes from the potential theory and the second term is the contribution of the viscous leeward flow separation. From Eqn.1 the normal force coefficient

$$C_N = N / (q_\infty S_r) = \int_0^l f(x) dx / (q_\infty S_r)$$

and the pitching moment coefficient about an arbitrary point on the body axis with an axial distance  $x_m$  from the nose

$$C_M = M / (q_\infty S_r l) = \int_0^l f(x) (x_m - x) dx / (q_\infty S_r l)$$

may be derived as

$$C_N = \left( \frac{S_b - S_t}{S_r} \right) \sin 2\alpha \cos^2 \frac{\alpha}{2} + C_d \frac{S_p}{S_r} \sin^2 \alpha \quad (2)$$

$$C_M = \left[ \frac{W - S_b(l - x_m) - S_r x_m}{S_r l} \right] \sin 2\alpha \cos^2 \frac{\alpha}{2} + C_d \frac{S_p}{S_r} \left( \frac{x_m - x_c}{l} \right) \sin^2 \alpha \quad (3)$$

where

$$C_d = \frac{\int_0^l \eta c_{dc}(x) 2R dx}{S_p} \quad (4)$$

$$x_c = \frac{\int_0^l \eta c_{dc} (x) 2R x dx}{S_p c_d} \quad (5)$$

Obviously, the first terms on the right hand sides of Eqns. 2 and 3 come from the potential theory, while the second terms represent the effects of the viscous leeward flow separation. For  $S_l=0$ , Eqns. 2 and 3 take the forms for the closed-nosed bodies [9,16-20]. Therefore, Eqns. 2 and 3 may be used for the closed-nosed as well as for the flat-nosed bodies of revolution. It is obvious that  $C_d$  and  $x_c$  should be evaluated first, in order to calculate  $C_N$  and  $C_M$  from Eqns. 2 and 3. For this purpose, the bodies may be tested at  $\alpha=90$  deg. in the wind tunnel, as has been done by Allen and Perkins [9]. But, these parameters may also be calculated by using the available sufficient experimental drag data on cylinders in two-dimensional flow [9]. The variation of  $c_{dc}$  with the crossflow Mach number and the crossflow Reynolds number and the variation of  $\eta$  with the length-diameter ratio of the cylinder are given in Refs. 18, 19, and 20, based on the experimental data. It is not easy to calculate  $C_d$  and  $x_c$  from Eqns. 4 and 5 by assuming that  $c_{dc}$  and  $\eta$  are functions of  $x$ . Therefore, Allen and Perkins [9] have assumed that the crossflow around a body of revolution of finite-length  $l$  moving at the velocity  $V_\infty$  and with the angle of attack  $\alpha$  is similar to the crossflow around a corresponding cylinder of finite-length  $l$  and of constant diameter  $d_s = S_p/l$  moving at the velocity  $V_\infty \sin \alpha$ . Thus, since  $c_{dc}$  and  $\eta$  are not functions of  $x$ , and Eqns. 4 and 5 become, respectively, as

$$C_d = \eta c_d \quad (6)$$

$$x_c = \frac{\int_0^l 2R x dx}{S_p} \quad (7)$$

where the value of  $c_{dc}$  corresponds to the crossflow Reynolds number

$$Re_{cd} = \frac{V_\infty \sin \alpha d_s}{\nu}$$

and the crossflow Mach number

$$M_c = M_\infty \sin \alpha$$

while the value of  $\eta$  corresponds to the ratio of  $l/d_s$ . The data given in the literature [18,19,20] for  $\eta$  is for subsonic conditions, but in practice it has been found that  $\eta$  should be set to unit in supersonic flow [7]. Hence,  $C_d$  may be calculated from Eq. 6 by using the experimental data given in the literature [18,19,20] for  $c_{dc}$  and  $\eta$  for the circular cylinder.

For rough engineering estimations, the axial force coefficient for slender bodies may be approximated as

$$C_A = C_{d0} \cos^2 \alpha \quad (8)$$

by assuming that the axial force is produced only by the axial flowfield that is similar to the flowfield in the  $\alpha=0$  deg. case [18,19]. Here,  $C_{d0}$  is the drag coefficient at  $\alpha=0$  deg.

After the determination of  $C_N$ ,  $C_A$  and  $C_M$ , the lift and drag coefficients and the position of the center of pressure may be obtained, respectively, by

$$C_L = C_N \cos \alpha - C_A \sin \alpha \quad (9)$$

$$C_D = C_N \sin \alpha + C_A \cos \alpha \quad (10)$$

$$\frac{x_{cp}}{l} = \frac{x_m}{l_r} - \frac{C_M}{C_N} \quad (11)$$

where  $x_{cp}$  shows the axial distance from the body nose to the center of pressure [19].

This method is applied to the configurations considered in the balance measurements. In this application, the values of  $C_{d0}$  obtained by the balance measurements are used to calculate  $C_A$  from Eqn. 8. The theoretical results are presented in Section 8, together with the balance measurements, for comparison.

## 6 RESULTS AND DISCUSSION

The surface flow visualization photographs for  $\alpha=0$  and 20 degs. are shown in Figs. 4 and 5, respectively for the pointed and truncated cone-cylinder bodies. The limiting streamlines and the separation lines on the bodies are observable from these photographs. Hence, these photographs give some qualitative results about the effects of the geometrical shape and the angle of attack on the flowfield.

As seen from the photographs for  $\alpha=0$  deg in Figs. 4 and 5, the gravity effect on the oil flow over the models during the flow visualization tests, makes it difficult to analyse these photographs, since the oil flow keeps a curved path near the aftward of the models due to this effect. However, the circular flow separations (hence the circular separation bubbles) around the nose-main body junction and around the truncated nose of the models are quite clear. The effects of the geometrical modifications considered here on these flow separations may also be analysed qualitatively from these photographs as follows. The circular separation and the circular separation bubble are quite significant around the nose-body junction on Model 1A. This flow separation becomes less significant when the nose cone angle,

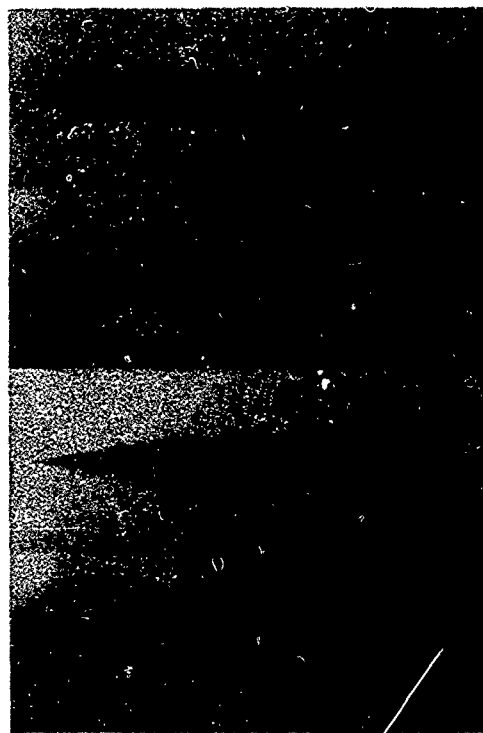


Fig. 4a Surface flow visualization photographs of the pointed cone-cylinder bodies for  $\alpha = 0^\circ$  deg.



Fig. 4b Surface flow visualization photographs of the pointed cone-cylinder bodies for  $\alpha = 20^\circ$  deg.

MODEL

1A

2A

3A

4A

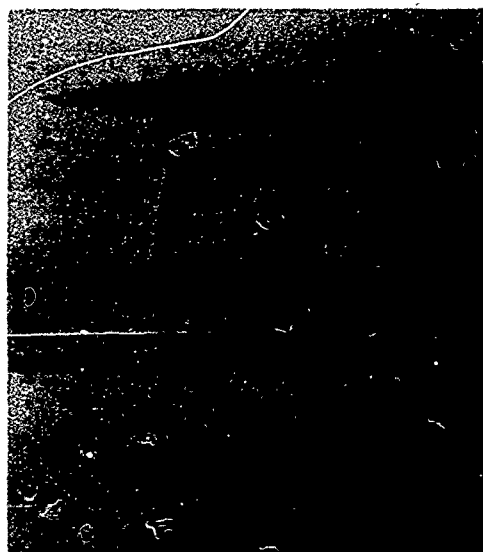


Fig. 5a Surface flow visualization photographs of the truncated cone-cylinder bodies for  $\alpha = 0^\circ$  deg.



Fig. 5b Surface flow visualization photographs of the truncated cone-cylinder bodies for  $\alpha = 20^\circ$  deg.

MODEL

3A

3B

3C



$\theta$ , decreases, so that it is not identified on Model 4A. Circular flow separations with the circular separation bubbles are also exist around the truncated conical noses. This separation becomes more significant when the nose bluntness,  $d_1/d$ , increases.

It is also interesting to see that the separation around the truncated nose of the model, reduce the significance of the separation around the nose-main body junction.

As seen from the photographs for  $\alpha=20$  deg. in Figs. 4 and 5, the leeward flow separation produced by the incidence, cooperates with the circular flow separations. On the leesides of the conical and cylindrical parts of the models, the primary separation lines are completely observable. The secondary separation lines on the cylindrical parts of the models are partly visible. On the lee-sides of the cylindrical parts of the models, just after the conical noses, (on the shoulders of the nose-main body junction) three dimensional complicated vortex formation exists as a result of the interactions between the flow separations caused by the incidence and the discontinuities in the slope of the body surface. It is not easy to sketch the full structure of this complex vortex formation from the present photographs taken from only one side, but it is observable that this vortex formation is quite sensitive to the nose cone angle,  $\theta$ . The complexity of this three dimensional vortex formation becomes more significant when the nose cone angle,  $\theta$ , increases. The leeward primary separation lines, on the cylindrical parts of the models, first make a curve near the nose (due to the vortex formation), and then lie along about the equatorial line of the body. The leeward separation lines, on the conical noses of the models, lie along the meridian lines. However, the locations of these separation lines move with the nose cone angle,  $\theta$ , so that when  $\theta$  decreases the separation line moves downward toward the equatorial line of the conical nose. For instance, the leeward separation line on the conical nose of Model 4A exist along about the equatorial line, although it is not observable on the

nose of Model 1A from the side-view. Obviously, this fact affects the vortex formation and the flow separation on the cylindrical parts of the bodies. The leeward separation lines on the truncated conical noses make a curve near the nose-tip due to the vortex formation on the nose-tip of the truncated conical noses. The vortex formation over the nose-tip of the truncated conical nose becomes larger when the nose bluntness,  $d_1/d$ , increases

The experimental and theoretical results for the variations of  $C_N$ ,  $C_M$ ,  $C_A$  and  $x_{cp}/l$  with  $\alpha$  are plotted in Figs. 8-9 and Figs 10-13 respectively for the pointed and truncated cone cylinder models. The observations obtained from these plots are as follows:

1) Unlike the potential theory, the method of viscous crossflow analogy is generally in agreement with the experimental results for the pointed and truncated cone-cylinder bodies even at high angles of attack.

The scatter in the experimental data for  $C_A$  is large, since the balance measurements are performed at a very low freestream velocity as 10 m/s so that the axial force to be measured has very small values.

There is a considerable discrepancy between the experimental results and the method of viscous crossflow analogy for the location of the center of pressure in the case of small angles of attack ( $\alpha < 10^\circ$  deg.). However Eqn. 11, used to obtain the location of the center of pressure from  $C_N$  and  $C_M$  loses its meaning in the case of small angles of attack since the values of both  $C_N$  and  $C_M$  go to zero. In the case of the small angles of attack, the accuracy of the balance tends to be poor for the same reason.

2) The variations of  $C_N$  and  $C_M$  with  $\alpha$  are nonlinear for all the pointed and truncated cone-cylinder models.  $C_A$  shows a

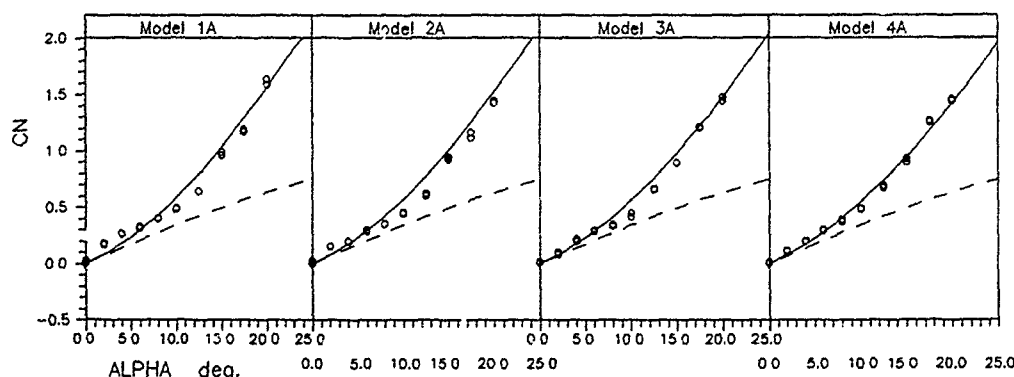
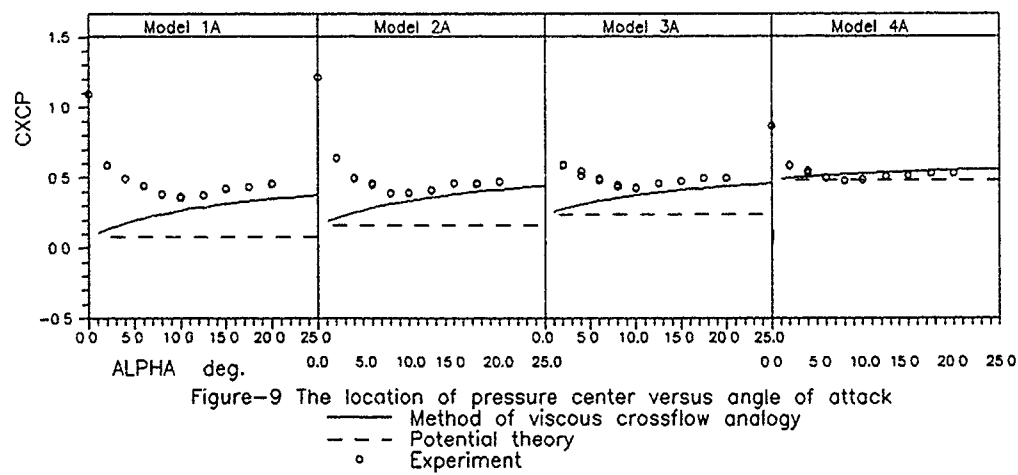
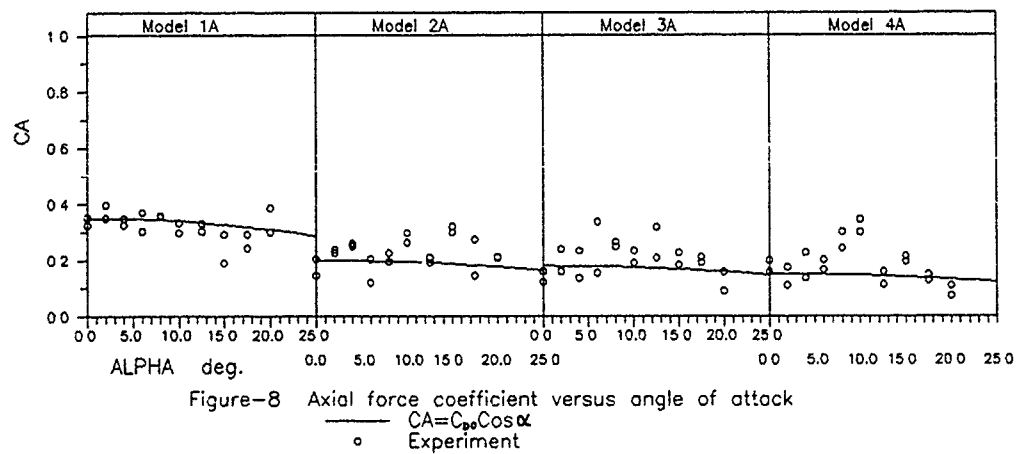
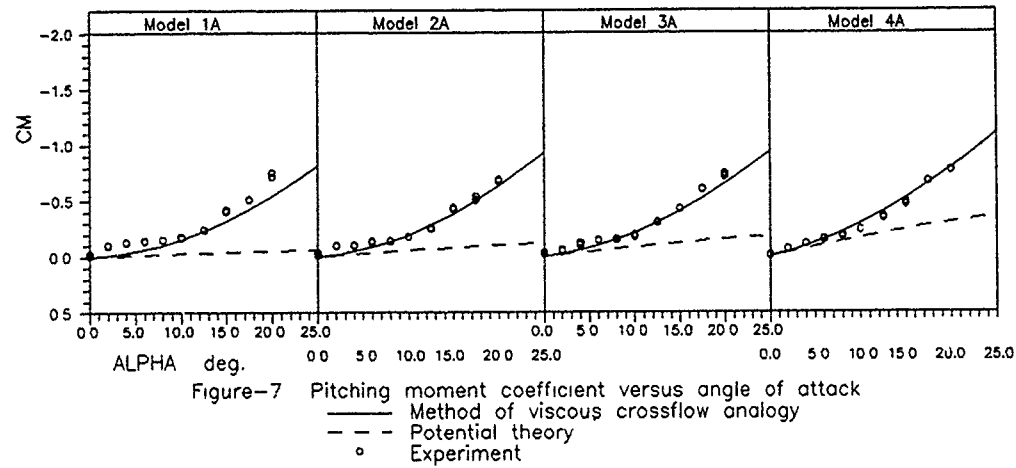


Figure-6 Normal force coefficient versus angle of attack  
 ——— Method of viscous crossflow analogy  
 - - - Potential theory  
 ° Experiment



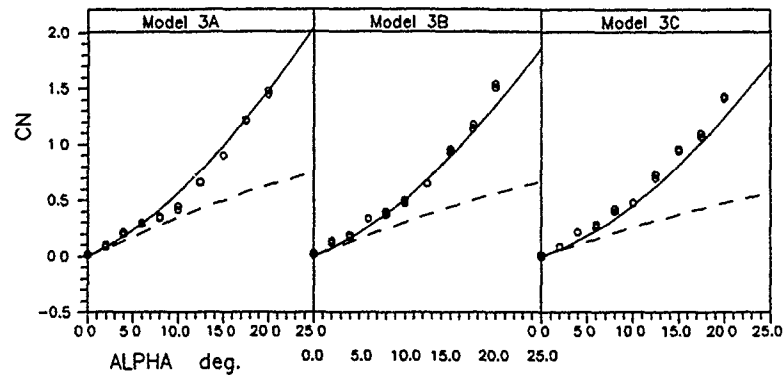


Figure-10 Normal force coefficient versus angle of attack  
 — Method of viscous crossflow analogy  
 - - Potential theory  
 ° Experiment

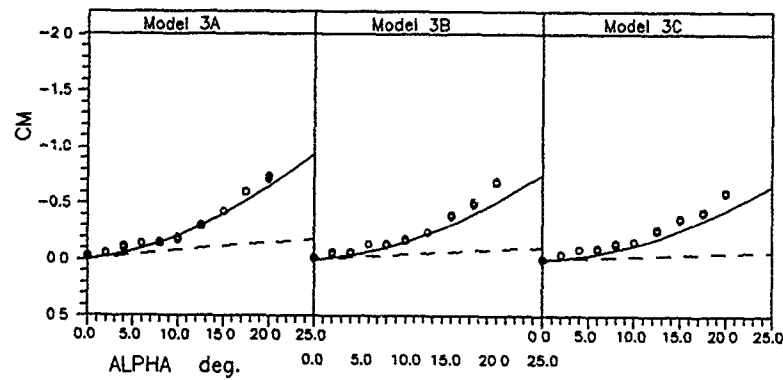


Figure-11 Pitching moment coefficient versus angle of attack  
 — Method of viscous crossflow analogy  
 - - Potential theory  
 ° Experiment

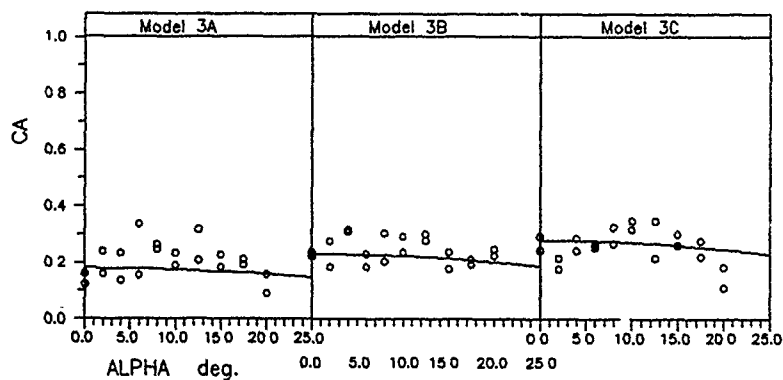


Figure-12 Axial force coefficient versus angle of attack  
 —  $CA = C_n \cos \alpha$   
 ° Experiment

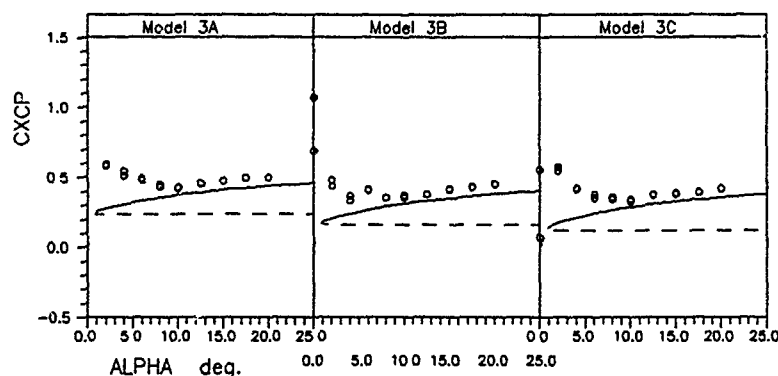


Figure-13 The location of pressure center versus angle of attack  
 — Method of viscous crossflow analogy  
 - - - Potential theory  
 ° Experiment

slight decrease with  $\alpha$  in the range of  $\alpha$  considered here. The center of pressure moves forward with  $\alpha$  in the range of small angles of attack ( $\alpha < 10$  deg.) and then slightly moves backward according to the experimental data.

3)  $C_A$  slightly decreases when the nose cone angle decreases for the pointed cone-cylinder models as seen from Fig. 8. For instance, for  $\alpha = 0$  deg.  $C_A$  (i.e.,  $C_{D0}$ )  $\approx$  0.35, 0.20, 0.19, 0.18 for Models 1A, 2A, 3A and 4A respectively.

The axial force of a cone-cylinder body is increased by truncating the conical nose. Hence,  $C_A$  increases with the nose

bluntness. For instance, for  $\alpha = 0$  deg.,  $C_A$  (i.e.,  $C_{D0}$ )  $\approx$  0.19, 0.22, 0.28 for Models 3A, 3B and 3C respectively.

4) The nose cone angle of a pointed cone-cylinder body affects not only the axial force but also the other aerodynamic characteristics such as the variations of  $C_N$  and  $C_M$  with  $\alpha$ . When the nose cone angle decreases (from model 1A to 4A), the increase of  $C_N$  with  $\alpha$  becomes slightly slower and the increase of  $-C_M$  (with respect to the nose tip point) becomes slightly faster as seen from Figs. 6 and 7 respectively. However, these facts are not clear in the present balance measurements as much as in the results of the method of viscous crossflow analogy. Therefore, more accurate balance measurements are necessary. Indeed, the first fact may be due to the decrease of planform area when the nose cone angle decreases and the second fact may be related with the movement of center of pressure backward (thus, may be related with the planform area distribution and the flow field) when the nose cone angle increases as would be seen from Fig. 9.

The aerodynamic characteristics, not only  $C_A$  but also  $C_N$  and  $C_M$  of a cone-cylinder body are affected by truncating the nose of the body. The increases of  $C_N$  and  $-C_M$  (with

respect to the nose tip point) with  $\alpha$  become slower by truncating the conical nose of a cone-cylinder body as seen from Figs. 10 and 11 respectively. However, these facts are not clear in the present balance measurements as much as in the results of the method of viscous crossflow analogy. Therefore, as indicated before, more accurate balance measurements are necessary. Indeed, the first fact may be due to the decrease of planform area when truncating the nose and the second fact may also be related with the movement of center of pressure forward (thus, may be related with the planform area distribution and the flowfield) when truncating the nose, as would be seen from Fig. 13.

5) According to the balance measurements, the center of pressure moves with  $\alpha$ , first forward in the range of small angles of attack ( $\alpha < 10$  deg.), then backward in the range of high angles of attack ( $\alpha > 10$  deg.) for all the models, as seen from Figs. 9 and 13. However, the method of viscous crossflow analogy indicates a backward movement of the center of pressure in all the range of angles of attack considered here. The agreement between the results of the balance measurements and the method of viscous crossflow analogy, for the location of the center of pressure, is rather good at high angles of attack ( $\alpha > 10$  deg.), unlike that at small angles of attack.

As seen from Fig. 9, when the nose cone angle,  $\theta$ , decreases (from model 1A to 4A), the center of pressure moves backward.

Fig. 13 indicates that the center of pressure of a cone-cylinder body moves forward by truncating the conical nose.

These facts are related with the normal force distribution and hence may be related with the planform area distribution and the flowfield. However, to analyse these facts in more detail, some pressure measurements on the models and some more flow visualization tests that show the top-views of the models are necessary.

## 7. CONCLUSIONS

The aerodynamic characteristics of cylindrical bodies with pointed and truncated conical noses are investigated experimentally and theoretically at the low Mach number in the range of angle of attack of  $0 \leq \alpha \leq 20$  deg. The Reynolds number, based on the maximum body diameter and the freestream conditions, is about  $4.1 \times 10^4$ .

Surface flow visualization is made by using the oil method at the angles of attack  $\alpha = 0$  and 20 degs. Balance measurements are performed and the potential theory and the method of viscous crossflow analogy are applied in order to obtain the variations of  $C_N$ ,  $C_M$ ,  $C_A$  and  $x_{cp}/l$  with  $\alpha$ , experimentally and theoretically, over the range of angle of attack  $0 \leq \alpha \leq 20$  deg. Comparison is made between the experimental and the theoretical results. The major conclusions are as follows:

1) At zero angle of attack, a circular separation (a circular separation bubble) exists around the nose-main body junction of a pointed cone-cylinder body. The nose cone angle is a parameter affecting on the scales of this circular separation bubble so that this circular separation bubble becomes smaller and finally disappears when the nose cone angle decreases.

If the nose is truncated, a circular separation bubble also exist around the blunt nose. The nose bluntness affects not only the scales of the separation around the blunt nose but also that around the nose-main body junction. When the nose bluntness increases, the nose separation becomes larger but the separation around the nose-main body junction becomes slightly smaller.

If the cone-cylinder body has an angle of attack, the leeward flow separation produced by the incidence interacts with the circular flow separations. Then, the flow field becomes more complex. Pairs of vortices exist over the upward-side of the truncated blunt noses and over the nose-main body junctions. The complexity of this three dimensional vortex formation becomes more significant when the nose cone angle and bluntness increase.

2) Unlike the potential theory, the method of viscous crossflow analogy is generally in agreement with the experimental results for the pointed and truncated cone-cylinder bodies even at high angles of attack.

3) The variations of normal force and pitching moment with angle of attack,  $\alpha$ , are nonlinear for the pointed and truncated cone-cylinder bodies. The axial force shows a slight decrease with  $\alpha$ . The center of pressure moves forward with  $\alpha$  in the range of small angles of attack ( $\alpha < 10$  deg.) and then slightly moves backward.

4) The axial force increases when the nose cone angle or the bluntness increases.

5) The nose cone angle and the nose

bluntness of a cone-cylinder body affect not only the axial force but also the other aerodynamic characteristics such as the normal force, pitching moment and the location of the center of pressure.

When the nose cone angle decreases, the increase of the normal force with  $\alpha$  becomes slightly slower although the increase of the pitching moment (with respect to the nose tip point), in the negative direction, becomes slightly faster.

The increases of the normal force and the pitching moment (with respect to the nose tip point), in the negative direction, with  $\alpha$ , become slower by truncating the conical nose of a cone-cylinder body. The nose bluntness increases these effects.

The center of pressure of a cone-cylinder body moves backward when the nose cone angle decreases and moves forward by truncating the conical nose.

These facts may be related with the variation and the distribution of the planform area of the body and the flowfield around it.

6) More experimental studies are necessary to analyse the problem in more detail.

## 8. ACKNOWLEDGEMENTS

The balance, used in this work, was designed and constructed under the project T40 of FDP of AGARD. The VKI of Belgium and ITU of Turkey participated in this project. This work was also supported by the DPT project of ITU. The author wishes to express his appreciation to FDP, AGARD, VKI, DPT and ITU for their supports.

## 9. REFERENCES

1. Atli, V., "Aerodynamics of Complex Bodies of Revolution", AIAA Journal, 26, 4, April 1988, pp 387-391.391
2. "High Angle of Attack Aerodynamics", AGARD CP 247, January 1979.979.
3. "Missile Aerodynamics", AGARD LS 98, February 1979.
4. "High Angle of Attack Aerodynamics", AGARD/VKI LS 121, March 1982.982.
5. Hemsch, M.J. and Nielsen, J.N., "Tactical Missile Aerodynamics", Vol.104, 04, Progress in Astronautics and Aeronautics, American Institute of Aeronautics and Astronautics Inc., New York USA (ISBN 0-930403-13-4), 1986.
6. "Special Course on Missile Aerodynamics", AGARD-R-754, April 1988.
7. Wardlaw, A.B., Jr., "High-Angle-of-Attack Missile Aerodynamics", in "Missile Aerodynamics", AGARD LS 98, 1979.

8. Allen, H.J., "Estimation of the Forces and Moments on Inclined Bodies of Revolution of High Fineness Ratio", NACA RM A9126, 1949.
9. Allen, H.J., and Perkins, E.W., "A Study of Effects of Viscosity on Flow Over Slender Inclined Bodies of Revolution", NACA Rept. 1048, 1951.
10. Perkins, E.W., and Kuehn, D.M., "Comparison of the Experimental Theoretical Distributions of Lift on a Slender Inclined Body of Revolution at  $M=2$ ", NACA TN-3715, 1956.
11. Perkins, E.W., and Jorgensen, L.H., "Comparison of Experimental and Theoretical Distributions (Including Reynolds Number Effect) on an Ogive-Cylinder Body at Mach Number 1.98", NACA TN-3716, 1956.
12. Jorgensen, L.H., "Inclined Bodies of Various Cross Sections at Supersonic Speeds", NASA MEMO 10-3-58A, 1958.
13. Jorgensen, L.H., and Perkins, L.W., "Investigation of Some Wake Vortex Characteristics of an Inclined Ogive-Cylinder Body at Mach Number 2", NACA Rept. 1371, 1958.
14. Jorgensen, L.H., and Treon, S.L., "Measured and Estimated Aerodynamic Characteristics for a Model of a Rocket Booster at Mach Numbers From 0.6 to 4 and at Angles of Attack From  $0^\circ$  to  $180^\circ$ ", NASA TM-X-580, 1961.
15. Saffel, B.F., Jr., Howard, M.L., and Brooks, B.N., Jr., "Method for Predicting the Static Aerodynamic Characteristics of Typical Missile Configurations for Angles of Attack to 180 Degrees", Naval Ship Research and Development Center, Rept. 3645, March 1971.
16. Jorgensen, L.H., "Prediction of Static Aerodynamic Characteristics for Space-Shuttle-Like and Other Bodies at Angles of Attack from  $0^\circ$  to  $180^\circ$ ", NASA TII-D-6996, 1973.
17. Jorgensen, L.H., "Estimation of Aerodynamics for Slender Bodies Alone and With Lifting Surfaces at  $\alpha$ 's From  $0^\circ$  to  $90^\circ$ ", AIAA Journal, Vol 11, March 1973, pp. 409-412.
18. Jorgensen, L.H., "A Method for Estimating Static Aerodynamic Characteristics for Slender Bodies of Circular and Noncircular Cross Section Alone and With Lifting Surfaces at Angles of Attack From  $0^\circ$  to  $90^\circ$ ", NASA TN-D-7228, 28, 1973.
19. Jorgensen, L.H., "Prediction of Static Aerodynamic Characteristics for Slender Bodies Alone and With Lifting Surfaces to Very High Angles of Attack", NASA TR-R-474, 1977.
20. Jorgensen, L.H., "Prediction of Aerodynamic Characteristics for Slender Bodies Alone and With Lifting Surfaces to High Angles of Attack", in "High Angles of Attack Aerodynamics", AGARD CP 247, 1979.

# Systematic Investigations of Body-Wing-Tail Interference at High Angles of Attack

K. Hartmann  
Deutsche Forschungsanstalt für Luft- und Raumfahrt e.V.  
Institut für Experimentelle Strömungsmechanik  
D-3400 Göttingen, Bunsenstr. 10, FRG

and

D. Nikolitsch  
Messerschmitt-Bölkow-Blohm GmbH  
Unternehmensbereich Verteidigungssysteme  
D-8000 München-Ottobrunn, FRG

## Abstract

Six component measurements were carried out on several combinations of an ogive-circular cylinder body without and with lifting surfaces having rectangular planform and sharp leading and trailing edges. These experiments were performed in the subsonic compressible speed range at various Reynolds numbers up to high angles of attack. For the same geometries the forces and moments were calculated and compared with the experimental results. It was the aim of this combined investigations to get a better understanding of the vortex flows over such body-wing-tail combinations and to generate a reliable data base for the validation and improvement of prediction methods and to obtain hints for a more accurate theoretical modelling of the flow fields.

## Nomenclature

$\alpha$	Angle of attack
A	Aspect ratio
$C_m = M/(q \cdot S \cdot D)$	Pitching moment coefficient; reference point is body nose tip
$C_N = Z/(q \cdot S)$	Normal force coefficient Orientation of all forces and moments see system of coordinates in Fig. 1a. Moments are positive if they form right hand screws looking in positive direction of x, y, z
D	Body diameter, reference length, 35 mm
M	Pitching moment, reference point is body nose tip
Ma	Mach number
Ma <sub>c</sub>	Cross-flow Mach number
N	Yawing moment, reference point is body nose tip
p	Freestream static pressure
$q = (1/2)\rho V^2$	Freestream dynamic pressure
Re	Reynolds number, based on body diameter
$S = (\pi D^2)/4$	Body cross-section, reference area
V	Freestream velocity
x, y, z	Cartesian coordinates, origin in body nose tip, see Fig. 1a
Y	Side force
Z	Normal force
$\alpha_{crit}$	Critical angle of attack, definition see Figs. 16a and 16b
$\phi$	Roll position of the lifting surfaces relative to the body, see Fig. 1a
$\phi$	Body roll angle about longitudinal axis, $\phi = 0^\circ$ , see Fig. 1a
$\rho$	Freestream density

## 1. Introduction

The 3-d flow fields around slender bodies without and with lifting surfaces can be very complex and are predominantly dependent on the geometry of the combinations, the angle of attack and the Mach and Reynolds number. The complexity of such flows causes great difficulties in the understanding of the underlying flow phenomena and their theoretical treatment. At higher angles of attack the flow separates from the body and lifting surfaces. Consequently, vortices are shed from the configurations in different ways and a variety of flow patterns on the leeside can occur. These flow structures produce large forces and moments in the pitch and yaw plane in a non-linear way.

In this connection the body alone is the most complicated component of a body-wing-tail combination because the positions of the separation lines are not fixed on it, as in the case of a sharp-edged wing. The flow separates from the body along lines which result from the interaction of the external flow with laminar or turbulent boundary layers. The state of the boundary layer prior to the separation has a striking influence on the aerodynamic loads which therefore depend considerably on the Reynolds number. Regarding the Reynolds number it is a problem to decide which kind of definition (characteristic length) describes best the transition and separation process of a 3-d boundary layer.

On the other hand the transition from an attached flow to a completely separated flow of a wing is reached already at low angles of attack especially if higher aspect ratios are involved.

Of great influence on the experimental results are the special test conditions of the wind tunnel consisting of flow unsteadiness (turbulence level and structure), model vibration (no ideally rigid model-support-system) and manufacturing imperfections especially on the body nose tip, on the wings and on their surfaces. The latter influence leads, at least in the case of a body, to a strong dependence of the forces and moments on body roll position ( $\phi$ ) and turbulence as shown for example by K. Hartmann [1].

In addition to the phenomena just described further problems are caused by the mutual interaction of the vortices arising from the body and the lifting surfaces of a body-wing-tail combination.

Starting from the background mentioned before a detailed test program has been established in order to investigate the complicated vortex flow fields over slender bodies in combination with lifting surfaces at high incidences and at various Reynolds numbers. Figure 1b comprises the tested configurations. The experimental results are considered as a contribution to the improvement of existing prediction codes. Such computational methods which can provide reliable results at low costs are a useful tool in applied aerodynamics.

## 2. Models

In order to restrict the number of geometrical parameters of the missile an ogive circular cylinder body of constant length was chosen as body alone. Cruciform lifting surfaces having rectangular planform areas were mounted on the body in a forward position as wing, at the body base as tail and simultaneously in the same locations as a complete body-wing-tail combination. The leading edges of the cruciform wing are positioned at a distance of  $4D$  behind the body nose tip. All lifting surfaces are rectangular panels with sharp leading and trailing edges. Their chord length is  $1D$  ( $D = 35$  mm, body diameter), see Figure 1b. The wing and tail panels are mounted on sleeves which are parts of the body. These sleeves can be rotated about the body longitudinal axis and fixed at any roll position ( $\phi$ ) relative to the body. All components of the models were made of steel to very close tolerances and with a high degree of surface finish. For surface flow visualizations the models were darkened first by browning and later by a black painting. Further informations were given by V. Kanagarajan and K. Hartmann [2,3,4,5].

## 3. Wind Tunnel and Test Set-Up

The measurements were carried out in the high speed wind tunnel (HKG = Hochgeschwindigkeits-Kanal Göttingen) of the DLR. A sketch of the wind tunnel (HKG) is given in Figure 2a. This tunnel is of the suck-down type and works between the atmosphere and a vacuum container with a capacity of  $10\,000\text{ m}^3$ . Atmospheric air flows through the dryer, the settling chamber, the test section inside a vacuum-proof plenum chamber, consisting of a subsonic open jet or, alternatively, a supersonic flexible Laval nozzle, the convergent-divergent adjustable diffuser and a butterfly valve into a vacuum vessel. The evacuation of the vessel is done either by vacuum pumps or by the suction pump of the DLR transonic wind tunnel. For the open-jet subsonic test section, which was used for the present experiments, the nozzle exit is of a square cross-section, measuring  $0.75\text{ m} \times 0.75\text{ m}$ , with a Mach number range from  $0.38$  to values approaching sonic speed. Depending on the selected Mach number, the large size vacuum container allows the wind tunnel to be operated for 40 to 60 sec. Figure 2b demonstrates how in this tunnel the Reynolds number varies with the Mach number. A detailed description of this tunnel was given by H. Ludwig and Th. Hottner [6,7].

The basic model support, Fig. 2c, allows a pitch range of  $-10^\circ$  to  $35^\circ$ . A cranked piece, Fig. 2d, was used in combination with the basic sting support to reach angles of attack up to  $70^\circ$  or somewhat more depending on the straight sting deflection. For the force and



moment measurements a strain gauge balance (TASK Corporation, USA) of an outer diameter of 75" was used. The electrical outputs of the balance were acquired by the electronic data acquisition system of the wind tunnel and processed on the main computer of the DLR.

#### 4. Test Program

Force and moment measurements were executed at three subsonic Mach numbers,  $Ma = 0.4, 0.6$  and  $0.8$ , at angles of attack ranging from  $-5^\circ$  up to about  $70^\circ$ . The accompanying Reynolds numbers, based on body diameter, are according to Fig. 2b,  $Re \cdot 10^{-4} = 0.28, 0.39$  and  $0.46$ .

It is known, for example from [1], that the flow asymmetry around the body alone and consequently the aerodynamic forces acting on it are, among other geometrical and aerodynamic parameters, dependent on the body roll orientation which is defined as roll angle  $\phi$  in Fig. 1a. In order to demonstrate the dependence on this roll angle  $\phi$  and to fix a body roll position of highly asymmetric flow structure on the leeside some additional tests were performed. To this end the body alone was rolled over  $360^\circ$  in steps of  $60^\circ$ . The starting roll position  $\phi = 0^\circ$  is arbitrary and was marked on the body. Great flow asymmetry was found at  $\phi = 60^\circ$ . At all tests the body was kept at this  $\phi = 60^\circ$  roll orientation. Under this condition the lifting surfaces were added to the body in order to get strong interference effects of the asymmetric body vortices on the wing and tail panels which were mainly intended to investigate. Measurements were made for the  $+$  ( $\varphi = 0^\circ$ ) and  $x$  ( $\varphi = 45^\circ$ ) position of the wings and tails.

In addition to the force and moment measurements some flow visualization experiments were conducted in the  $3\text{ m} \times 3\text{ m}$  low speed tunnel (NWG = Niedergeschwindigkeitswindkanal Göttingen) of the DLR using smoke and a laser light sheet. With the aid of this technique the leeside vortex structures were made visible for a subsequent quantitative image processing.

#### 5. Results

##### 5.1 Experiments

The complete data obtained in the course of all experiments are documented in several internal reports [2,3,4,5]. Due to space limitation a few significant cases were selected for the present publication. The data of the normal forces, pitching moments, side forces and yawing moments are given in this paper in form of their coefficients. In the figures the data points are connected by thin lines. As far as available the calculated results are, in most of the same figures, depicted by thick lines. All values of the Mach and Reynolds numbers in the legends of the figures are averages with a tolerance of less than 1% for the Mach number and less than 2% for the Reynolds number.

##### 5.1.1 Body Alone

In previous experiments the Reynolds number dependence of the forces acting on the present body was investigated up to a Reynolds number of  $5.7 \times 10^4$  in the incompressible speed range [5]. Figs. 3, 4, 5a and 5b provide informations about the Mach and Reynolds number dependence of the normal forces in the compressible speed range ( $Ma = 0.5$ ) and at Reynolds numbers which comprise the Reynolds numbers of the present investigation. These data were obtained for a body of revolution of higher length (18 D). Nevertheless, they can be used for the interpretation of the present results. The Reynolds number range of the present experiments is marked at the abscissa of Fig. 4. This suggests how strong the state of the boundary layer (turbulent, transitional, laminar), and consequently the type of separation, varies at a constant Reynolds number with increasing angle of attack. The effect of Mach number on the normal force coefficient is shown in Figs. 5a and 5b. As long as the cross-flow Mach number is small in comparison with the critical value of a circular cylinder in cross-flow the influence of the Reynolds number is predominant and leads to a strong change of the forces and moments in the transitional range. This strong change decreases with increasing cross-flow Mach number and vanishes finally.

It is shown in Figs. 7a to 7d how the forces and moments in the pitch and yaw plane depend on the body roll orientation  $\phi$ . Maximum side forces of different signs occur around  $50^\circ$  incidence and can achieve values up to 50% of the normal forces. The onset of side forces, as a consequence of flow asymmetry, starts at angles of attack greater than about  $15^\circ$ . Maximum side forces are correlated with the greatest variation of the normal forces. Similar results, as shown in Fig. 7 for  $Ma = 0.4$ , were also obtained for the other Mach numbers.

In addition to the parameters ( $Re, Ma, \phi$ ) described before, the measured forces and moments of the body alone can also depend essentially on the flow quality (turbulence etc.) in any test section. It is, therefore, a great problem for every experimentalist to obtain reliable data. The reader is asked to keep this always in mind when estimating the results of this presentation.

The measured forces and moments, as plotted in Figs. 8a to 8d, show a strong nonlinear characteristic with the angle of attack. In addition they depend on both Mach number and Reynolds number. Note that in the subsonic compressible speed range ( $Ma = 0.4, 0.6, 0.8$ ) the Reynolds number changes somewhat with the Mach number because this is conditioned by the wind tunnel, see Fig. 2b. It was shown in other investigations [8,9,19] that at small

angles of attack and at Reynolds numbers as given in Fig. 8 turbulent separation takes place because of great effective Reynolds numbers as a result of great effective reference lengths resulting in small values of the normal forces. With increasing angle of attack the influence of the body vortices becomes stronger and the limiting streamline as reference length of an effective Reynolds number ranging from the stagnation line up to the separation lines becomes shorter. Therefore, the effective Reynolds number becomes smaller and the separation passes into its critical mode (critical Reynolds number regime) accompanied by increasing normal forces. At Mach numbers greater than 0.4 the critical cross-flow Mach number is reached in the present case at  $\alpha \approx 45^\circ$  or  $\approx 32^\circ$ , respectively. This introduces additional effects, i.e. shock boundary layer interactions. Higher values of the normal forces were obtained at higher Mach numbers. The increase of the aerodynamic coefficient caused by the Mach number is greater at high incidences than at moderate ones where the change is mainly caused by the Reynolds number.

The accumulation of data points between  $\alpha = 30^\circ$  and  $40^\circ$  is caused by repeated measurements after changing the model support, see Fig. 2c and 2d, for measurements in the upper range of angles of attack.

The flow field around the body becomes asymmetric approximately at  $\alpha = 15^\circ$  which leads to the onset of side forces as can be seen in Figure 8. With increasing angle of attack the side forces grow, change their directions and reach maximum values at about  $40^\circ$  to  $50^\circ$  and  $60^\circ$  to  $70^\circ$ . The side forces decrease with increasing Mach number.

In addition some flow visualization experiments were carried out in the incompressible speed range in order to get a visual impression of vortex structures, which cause the side forces and moments. The trajectories of the shed vortices were extracted from the experiments and compared with calculations as shown in Figure 6.

### 5.1.2 Body-Tail and Body-Wing-Tail Combinations

In order to show the Mach number dependence of all forces and moments representative examples are selected from the complete data. These examples are plotted in Figs. 9a to 9d and 10a to 10d. It can be seen that differences among the normal forces and pitching moments occur mainly at high angles of attack and transonic Mach numbers ( $Ma = 0.8$ ). The side forces and yawing moments decrease with increasing Mach number, similar as described in 5.1.1. Their onset is independent of the Mach number.

All combinations have non-linear force and moment characteristics with respect to the angle of attack. These non-linearities are strongest for the +-position of the lifting surfaces, see Figs. 11a to 11d. They are weaker for the x-positions, see Fig. 12a to 12d. A nearly linear behaviour show the characteristics of the body-wing-tail combination in the x-position up to  $\alpha \approx 50^\circ$ , see Figs. 13a to 13d.

In the case of the body-wing-tail combinations the side forces and yawing moments are only weakly developed as Figs. 13c and 13d show. This is presumably caused by the far upstream located wing which strongly reduces the asymmetry of body vortices. In contrast to that the body-tail combinations show side forces and yawing moments which are of the same magnitude as for the body alone.

The trends of all normal force and pitching moment curves show an interesting common feature. A distinct decrease of the slopes of the characteristics can be observed at incidences of about  $10^\circ$ . This effect is especially evident in the case of the body-tail combination with 4D span. The measurements shown in Figures 9 to 13 clearly demonstrate that this phenomenon depends on the aspect ratio of the rectangular lifting surfaces, the roll orientation of the combination (+- or x-position), the Mach number and the local angle of attack of the lifting surfaces. It was attempted in section 5.2 of this paper to give an interpretation of this fact. The relating calculations seem to confirm this observation. But it must be kept in mind that downwash effects can contribute similar effects, particularly when a body-wing-tail combination is considered in x-position.

### 5.2 Calculation

The numerical technique used in this report for the computation of the aerodynamic coefficients of cruciform wing-body combinations for high angles of attack and for arbitrary roll angles in the subsonic speed range is based primarily on a component build-up technique of body and wing. This method is a very useful, fast and inexpensive tool for the prediction of the aerodynamic characteristics of slender body-tail and body-wing-tail combinations, and facilitates the design of such configurations. It has been applied before up to medium size angles of attack [11,12,13,14].

The measurements presented in this report were considered to be a valuable validation test for this prediction code. To check also the limits of the method calculations up to very high angles of attack were performed. The results presented in this report have been limited to  $Ma = 0.6$  cases. The configurations included in the tests (body alone, body + tail, body + wing + tail) represent rather challenging geometries with regard to theoretical treatment because of the long body and the relatively high aspect ratio wings.

The linear part of the body aerodynamics is treated with slender body theory or optionally with a 3-d method of source distributions on the body surface. The non-linear part of the body aerodynamics was simulated by a multi-vortex-model. This flow model works

with asymmetric vortex arrangements, so that 'out of plane' forces and moments can be estimated. The calculated normal forces of the body agree very well with the experimental data, see Figs. 7 and 11 to 13. A good agreement of the predictions with the measurements was obtained for the slopes of the normal force and pitching moment curves at  $\alpha = 0^\circ$ . Also the basic characteristic of the side forces for the body alone case is reproduced relatively well if one considers the complicated flow phenomena. The minimal disturbances fixing the directions of the side forces and yawing moments in the experiment cannot be simulated theoretically, for that reason the sign of the calculated characteristics was adapted to experiment. The vortex shedding is controlled by Strouhal number. The calculated vortex trajectories are compared in Fig. 6 with results of additional experiments as mentioned already in section 4.

The forces and moments of a cruciform wing are calculated by a non-linear vortex lattice method as described by D. Nikolitsch [9]. It was assumed that the free vortex sheets leave the cruciform wing inclined by a half of the local angle of attack. The influences of the body and the velocity field induced by the body vortices were taken into account by computing the downwash on the cruciform wings. Incidentally this approach is similar to the method of 'equivalent angle of attack'. Whereas the influence of the wing on the body is covered by the interference factor  $K_B(W)$  according to Nielsen [15], the Mach number effects are taken into account by the Prandtl-Glauert factor.

For all body-tail and body-wing-tail combinations the calculations reproduce the linear and non-linear parts of the normal forces and pitching moments relatively well at angles of attack up to about  $10^\circ$ . If the aspect ratio of the wing is small enough agreement with experiment is obtained up to angles of attack higher than  $10^\circ$ . A pronounced reduction of the normal force curve occurs for higher aspect ratio wing combinations at a certain angle of attack. This is obviously caused by the abrupt breakdown of the leeside structure of the wing flow. This effect is shifted to smaller angles of attack with increasing aspect ratio. It must also be kept in mind that due to the presence of the body the local angle of attack is increased, as shown in Fig. 14. Thereby the onset of flow breakdown is reached sooner. It is necessary to cover these effects in calculations, see the principal sketch in Fig. 15. As long as a fast prediction method for the wing alone characteristics up to  $90^\circ$  consistent with the component build-up technique is not available, an empirical data base has to be used. Since a systematical measurement for a special class of wings alone of different aspect ratio up to angles of attack of  $\alpha = 90^\circ$  exists (Esch [16]) an empirical correction of the prediction method with the aid of these data seemed to be possible as a preliminary extension. An equivalent angle of attack was calculated on the wing the aerodynamic values of which were determined by the procedures mentioned above if  $\alpha_{eq} < \alpha_{crit}$  (see Fig. 16a and 16b). For angles  $\alpha_{eq} > \alpha_{crit}$  the Esch data base was used to model the wing component in the component build-up procedure. As can be seen in Figs. 11a, 11d, 12a and 12d this method provides good agreement with experimental results up to very high angles of attack. Some calculations were performed without this empirical correction, see Figs. 13a and 13b, which show far higher discrepancies at high angles of attack.

## 6. Conclusions

For engineering purposes measurements of body, body-tail and body-wing-tail combinations were presented and compared with an analytical method which is based on the approach of coefficient synthesis. For the body alone the calculations provide reasonable results up to high angles of attack. The prediction of the characteristics of the body-tail and body-wing-tail combinations turned out to be more difficult at very high angles of attack due to the massive flow separation on the lifting surfaces. It is concluded that an improvement of the prediction method within the scope of a coefficient synthesis must comprise an enlarged empirical data base for wings and the development of theoretical flow models for the separated flow over arbitrary shaped wings. The Reynolds number influence for the body is to be taken into account, too.

## 7. References

- [1] K. Hartmann, "Experimental Investigation on an Ogive-nosed Body at High Incidence and Different Reynolds Numbers". Proceedings of the International Conference on Fluid Mechanics Beijing, China, July 1-4, 1987.
- [2] V. Kanagarajan, K. Hartmann, "Force Measurements on a Body-Tail Combination at Different Reynolds Numbers and Roll Angles up to Incidence of  $45^\circ$ ". DLR IB 222-85 A 38, 1985.
- [3] V. Kanagarajan, K. Hartmann, "Force Measurements on a Body-Wing-Tail Configuration (KaHa Model) at Mach Numbers of 0.4, 0.6 and 0.8 and Incidences up to  $30^\circ$ ". DLR IB 222-87 A 27, 1987.
- [4] V. Kanagarajan, K. Hartmann, "Force Measurements on a Body-Wing-Tail Configuration (KaHa Model) at Mach Numbers of 0.4, 0.6 and 0.8 and Incidences from  $30^\circ$  to  $65^\circ$ ". DLR IB 222-87 A 25, 1987.
- [5] V. Kanagarajan, K. Hartmann, "Force Measurements at Low Speeds on Body-Wing-Tail Combinations (KaHa Model) at High Reynolds Numbers and Incidences from  $-2^\circ$  to  $70^\circ$ ". DLR IB 222-89 A 13.

- [6] H. Ludwig, Th. Hottner, "Hochgeschwindigkeitskanal der Aerodynamischen Versuchsanstalt Göttingen". Z. Flugw. 7 (1959), Heft 10.
- [7] H. Ludwig, Th. Hottner, "Die Überschall-Meßstrecke (710 mm x 725 mm) des Hochgeschwindigkeitskanals der AVA". Z. Flugw. 11 (1963), Heft 4.
- [8] K. Hartmann, "Influence of the Reynolds Number on the Normal Forces of Slender Bodies of Revolution". NASA TM-76710, May 1982; and Z. Flugwiss. Weltraumforsch. 2 (1989), Heft 1, S. 22-35 (German original of preceding English version).
- [9] K. Hartmann, "Pressure and Force Distribution on an Ogive-Nosed Circular Cylinder at High Angles in an Incompressible Airstream". DLR IB 22-83 A 05.
- [10] H. Esch, "Der Einfluß der Reynoldszahl auf die Normalkraft-Charakteristik schlanker zylindrischer Rumpfe". DLR-FB 75-09 (1975).
- [11] D. Nikolitsch, "Normal Force and Pitching Moment Coefficient of Bodies and Wing-Body Combinations at Very High Angles of Attack". AIAA paper 78-63 (1978), AIAA 16th Aerospace Sciences Meeting, Huntsville, Alabama, Jan. 1978.
- [12] D. Nikolitsch, "Calculation of Pressure Distributions, Forces and Moments of Cruciform Wing-Body Combinations up to High Angles of Attack". AIAA paper 81-0398 (1981), AIAA 19th Aerospace Science Meeting, St. Louis, Missouri, Jan. 1981.
- [13] D. Nikolitsch, E. Waxweiler, "Berechnung der Rollmomentenbeiwerte von Flügel-Rumpf-Kombinationen bei hohen Anstellwinkeln im Unterschall". MBB Bericht TN-AE 12-5/81 (1981).
- [14] P. Hennig, E. Hartner, "Instationäre Beiwerte von Flugkörpern. Teil 4: Derivative der Längsstabilität von Flügel-Rumpf-Leitwerks-Anordnungen in Unter- und Überschallströmung". MBB Bericht UA-830-84 (1984).
- [15] W.C. Pitts, J.N. Nielsen, G.E. Kaattari, "Lift and Center of Pressure of Wing Body-Tail Combination at Subsonic, Transonic and Supersonic Speeds". NACA Report 1307 (1957).
- [16] H. Esch, "Normalkraft- und Kippmomentenmessung an schlanken Flugkörperflügeln im unteren Transschallbereich bei großen Anstellwinkeln". DFVLR IB 391-82-A-02.
- [17] J.E. Foley, "Results of a Study of Mach Number and Reynolds Number on the Cross Flow Drag Characteristics of Ogive-Cylinder and Ogive-Cylinder-Frustum-Cylinders at Angles of Attack to 30 Degrees". NASA CR-61356, October 1971.
- [18] E. Stanewsky, "Reynolds number effects in transonic flow". AGARDograph No. 303, 1988.

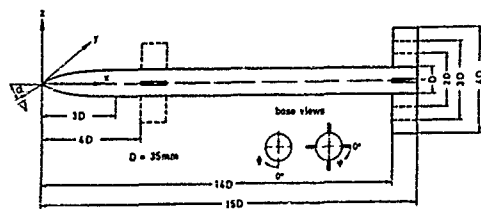


Figure 1a: Geometrical details of the various model configurations

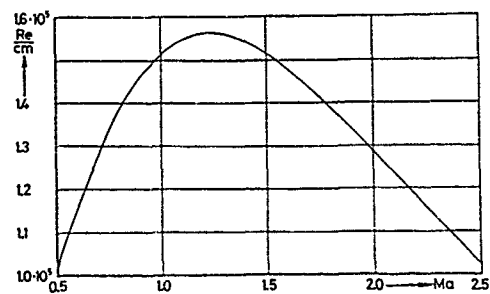


Figure 2b: Reynolds number per cm as function of the Mach number for the high speed wind tunnel (HKG) of the DLR

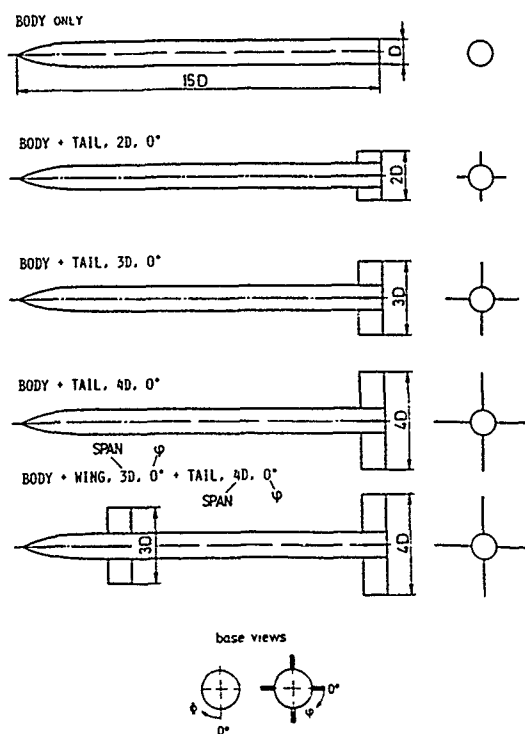


Figure 1b: Tested configurations

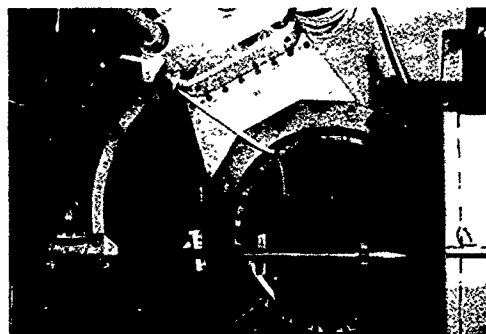


Figure 2c: Model support for the lower incidence range  $\alpha = -10^\circ$  to  $35^\circ$ . Model in the free jet test section inside the plenum chamber

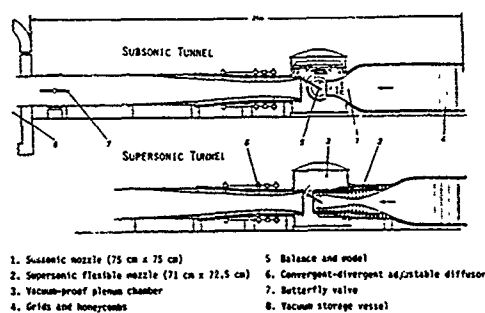


Figure 2a: High speed tunnel (HKG) of the DLR

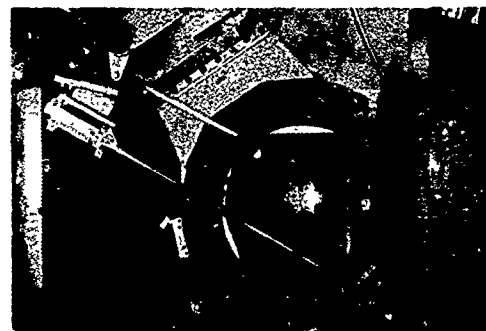


Figure 2d: Model support for the upper incidence range,  $\alpha = 30^\circ$  to  $70^\circ$

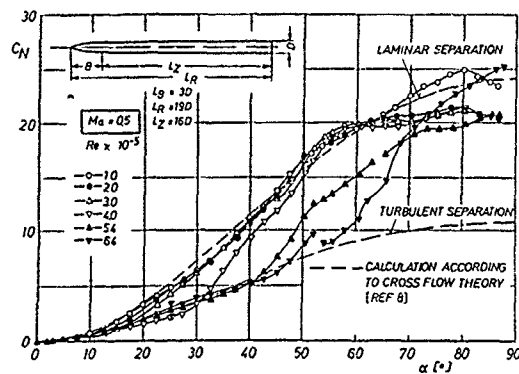


Figure 3: Normal force coefficient dependent on angle of attack and Reynolds number [8]

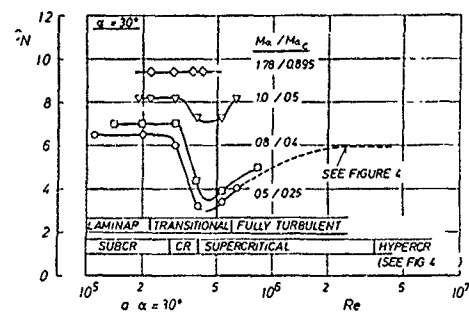


Figure 5a: Effect of Mach number on normal force coefficient for an ogive-cylinder body, figure prepared by Stanewsky [18]

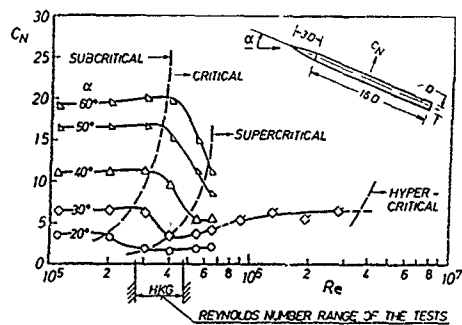


Figure 4: Effect of angle of attack on normal force coefficient for a slender body.  $Ma = 0.5$   
Data of Hartmann [8] and Folly ( $\alpha = 30^\circ$  only) [17]  
Figure prepared by Stanewsky [18]

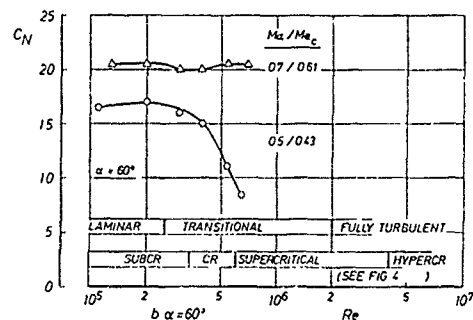


Figure 5b: Effect of Mach number on normal force coefficient for an ogive-cylinder body, figure prepared by Stanewsky [18]

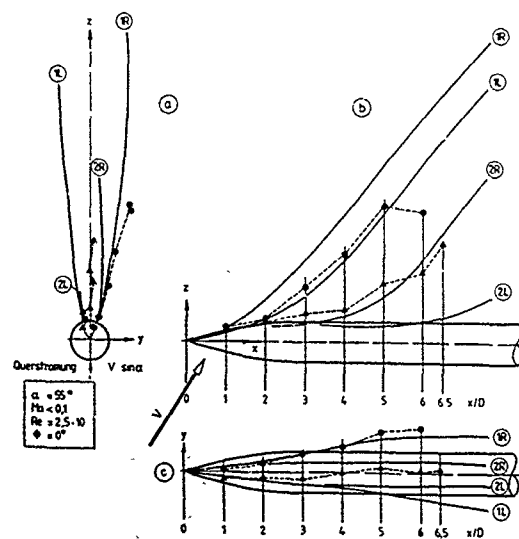


Figure 6: Vortex positions in different planes (a, b, c)  
--- Experiment  
— Calculation

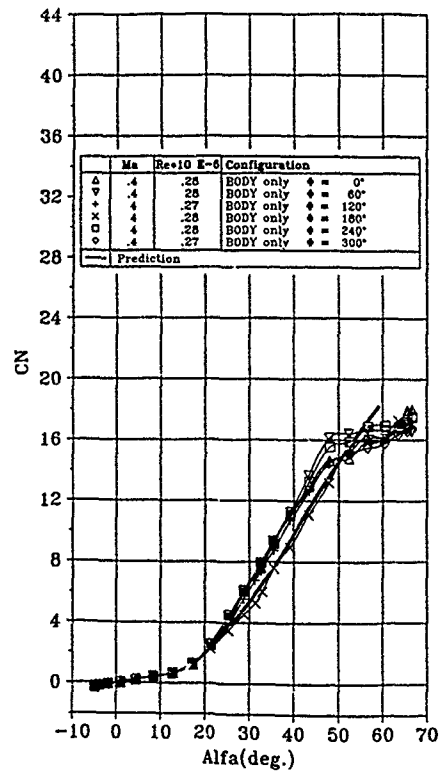


Figure 7a: Normal force coefficient versus angle of attack for different body roll positions  $\Phi$ , (definition of  $\Phi$  see Fig. 1a)

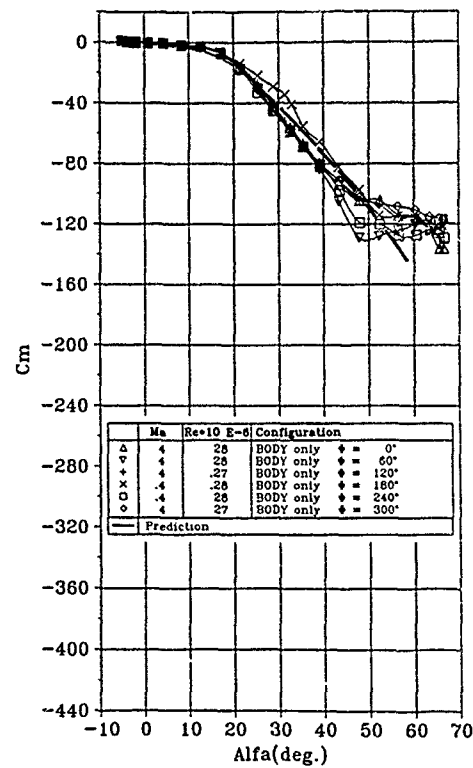


Figure 7b: Pitching moment coefficient versus angle of attack for different body roll positions  $\Phi$

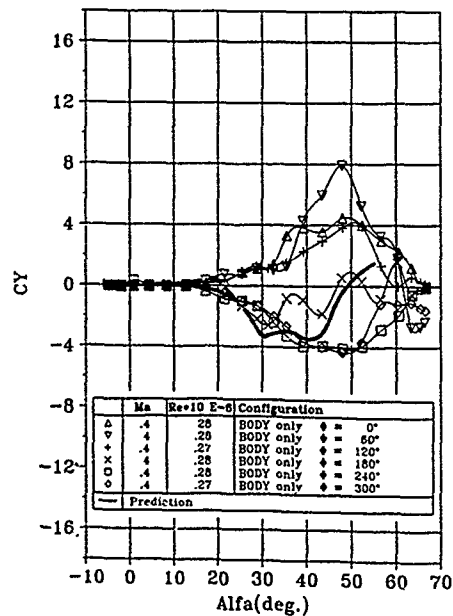


Figure 7c: Side force coefficient versus angle of attack for different body roll positions  $\Phi$

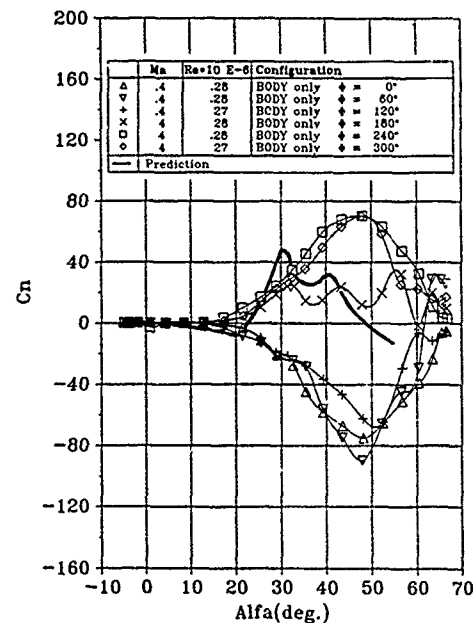


Figure 7d: Yawing moment coefficient versus angle of attack for different body roll positions  $\Phi$

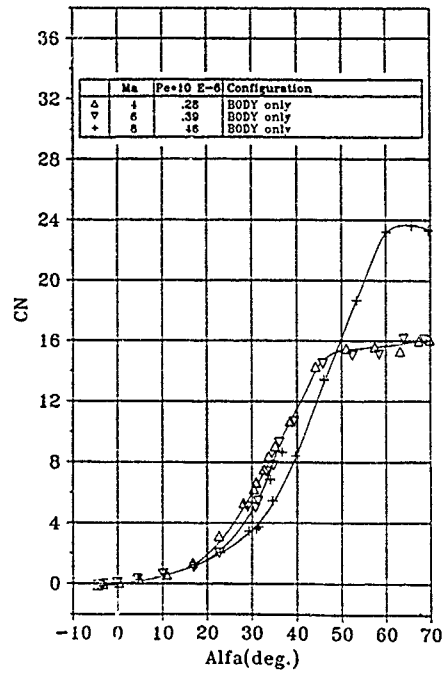


Figure 8a: Normal force coefficient versus angle of attack

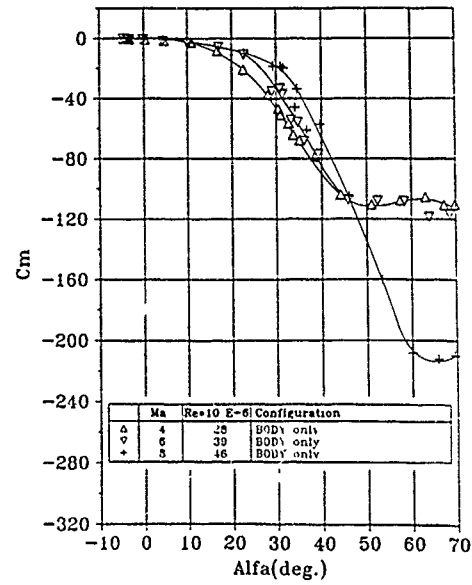


Figure 8b: Pitching moment coefficient versus angle of attack

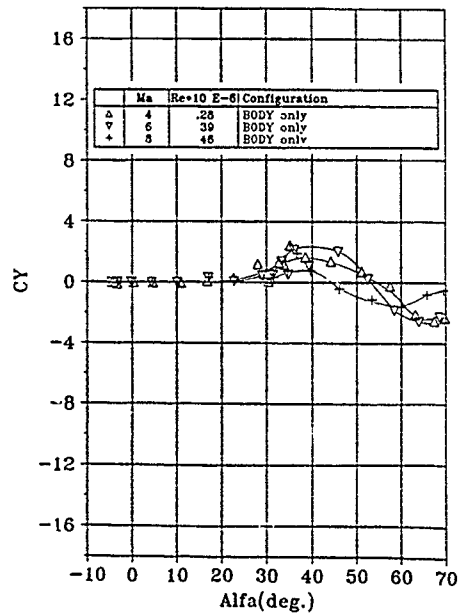


Figure 8c: Side force coefficient versus angle of attack

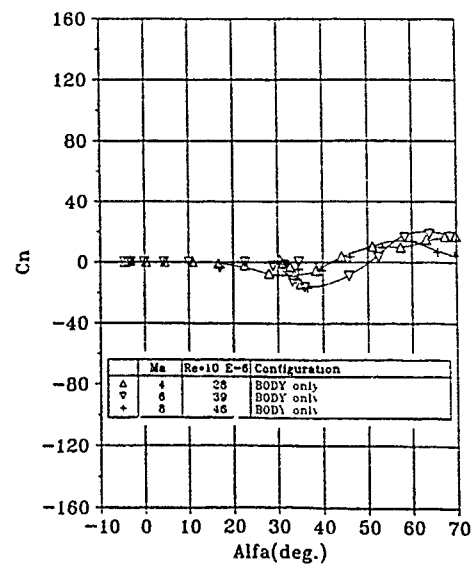


Figure 8d: Yawing moment coefficient versus angle of attack



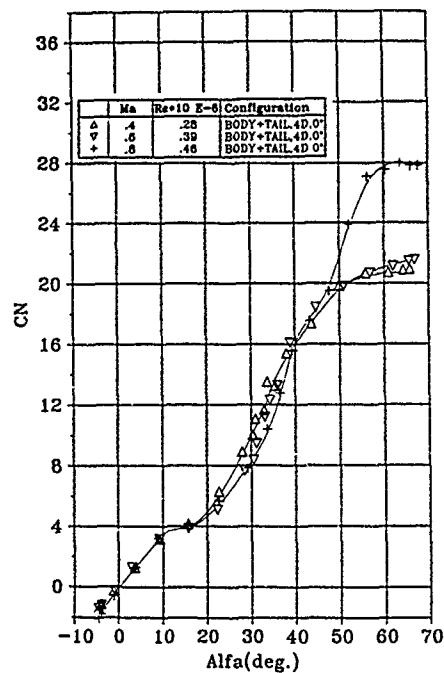


Figure 9a: Normal force coefficient versus angle of attack. All lifting surfaces in + position

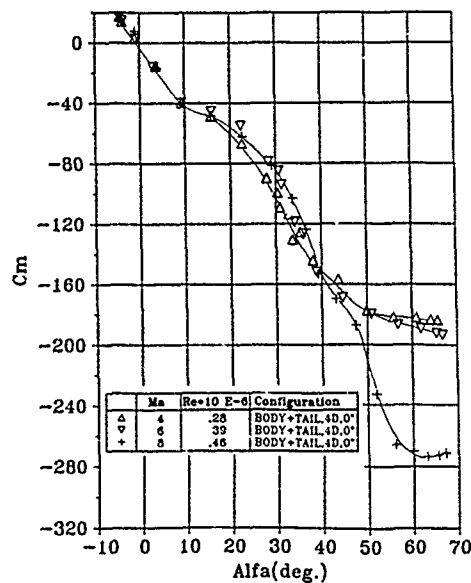


Figure 9b: Pitching moment coefficient versus angle of attack. All lifting surfaces in + position

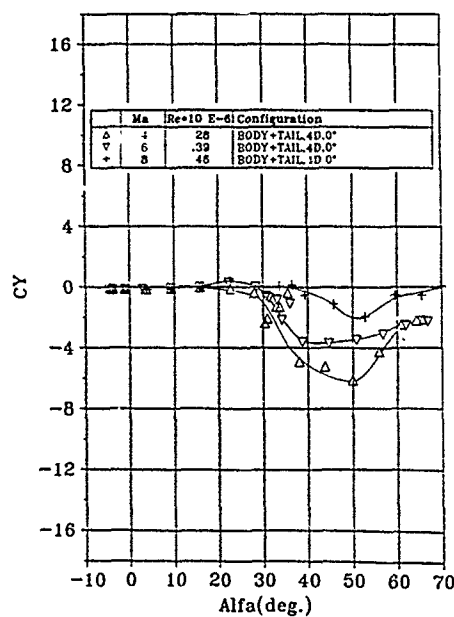


Figure 9c: Side force coefficient versus angle of attack. All lifting surfaces in + position

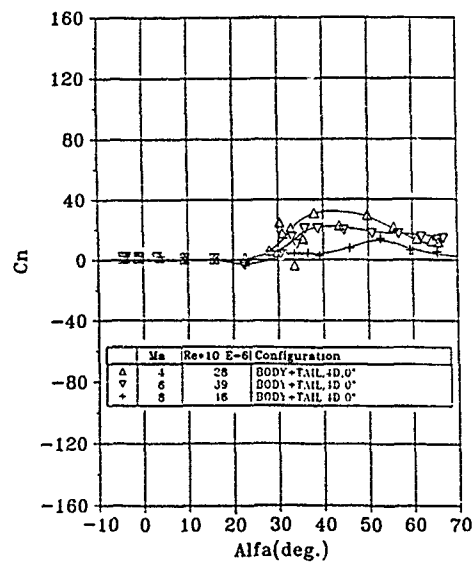


Figure 9d: Yawing moment coefficient versus angle of attack. All lifting surfaces in + position

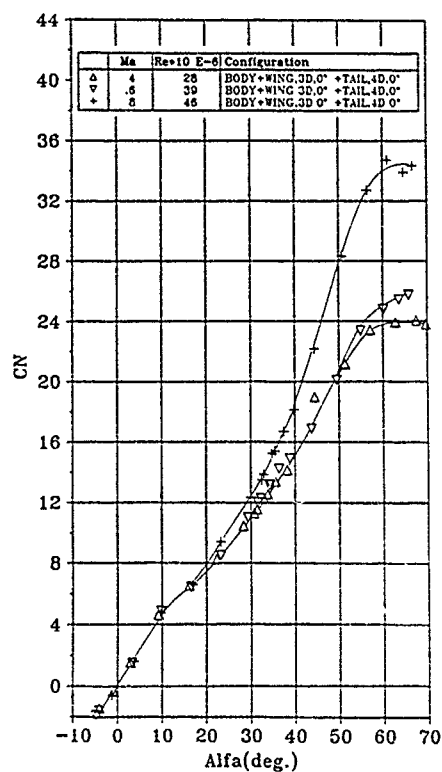


Figure 10a: Normal force coefficient versus angle of attack. All lifting surfaces in + position

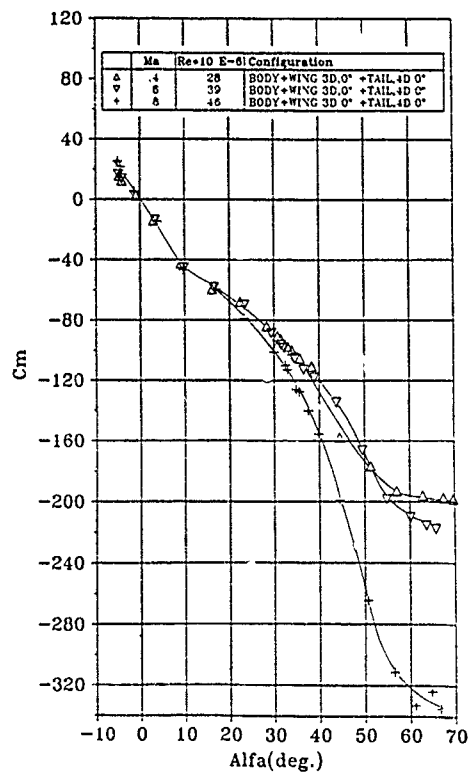


Figure 10b: Pitching moment coefficient versus angle of attack. All lifting surfaces in + position

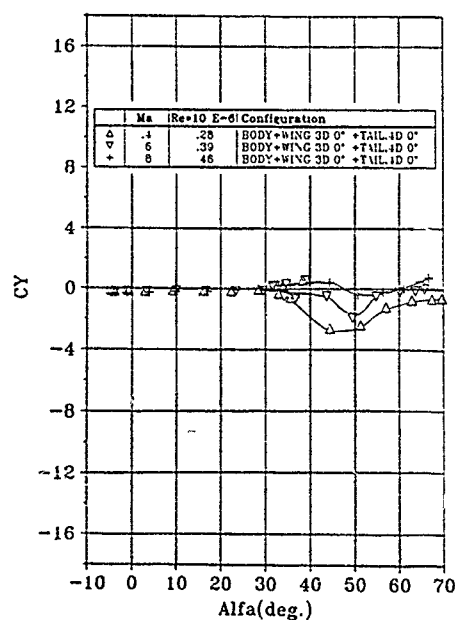


Figure 10c: Side force coefficient versus angle of attack. All lifting surfaces in + position

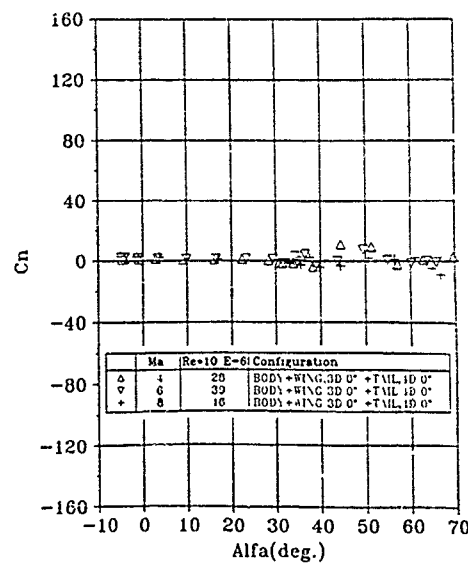


Figure 10d: Yawing moment coefficient versus angle of attack. All lifting surfaces in + position

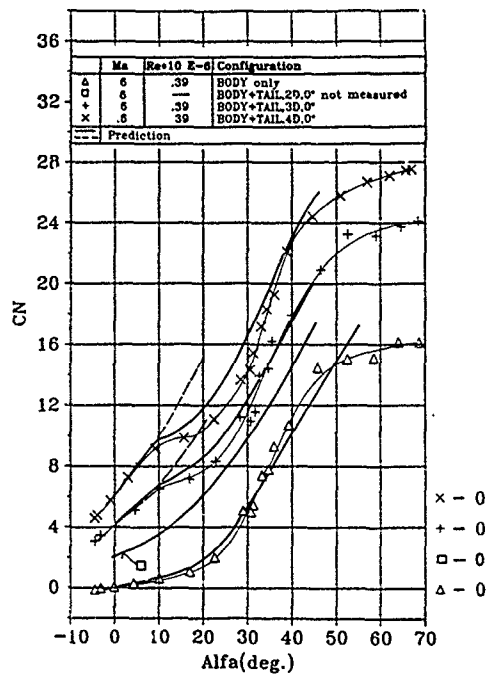


Figure 11a: Normal force coefficient versus angle of attack. All lifting surfaces in + position. Calculation with (—) and without (---) corrections beyond  $\alpha_{crit}$ .

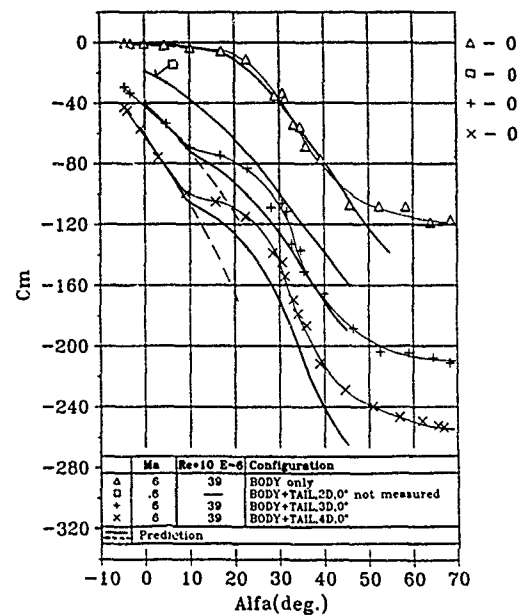


Figure 11b: Pitching moment coefficient versus angle of attack. All lifting surfaces in + position. Calculation with (—) and without (---) corrections beyond  $\alpha_{crit}$ .

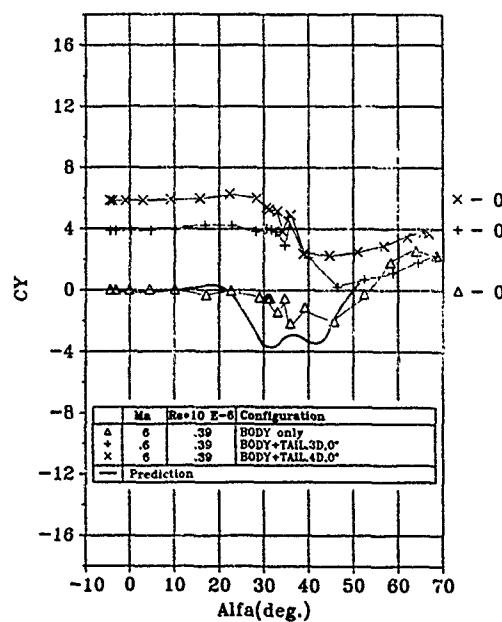


Figure 11c: Side force coefficient versus angle of attack. All lifting surfaces in + position.

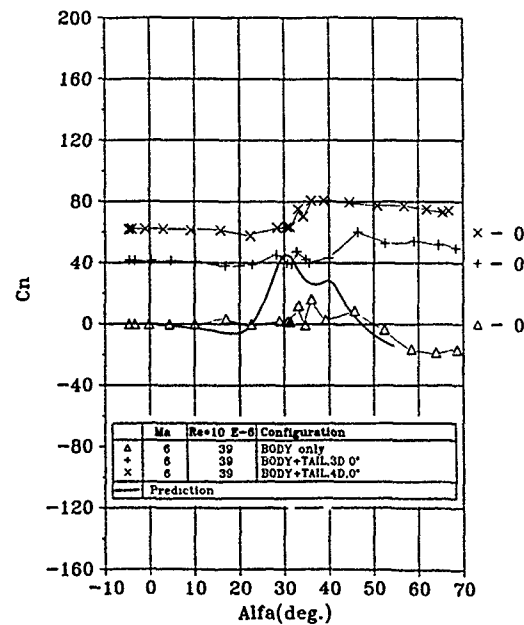


Figure 11d: Yawing moment coefficient versus angle of attack. All lifting surfaces in + position.

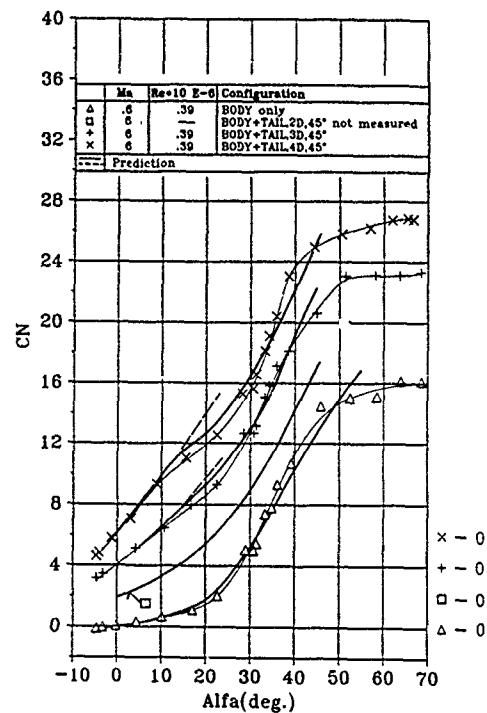


Figure 12a: Normal force coefficient versus angle of attack. All lifting surfaces in  $\times$  position. Calculation with (—) and without (---) corrections beyond  $\alpha_{crit}$ .

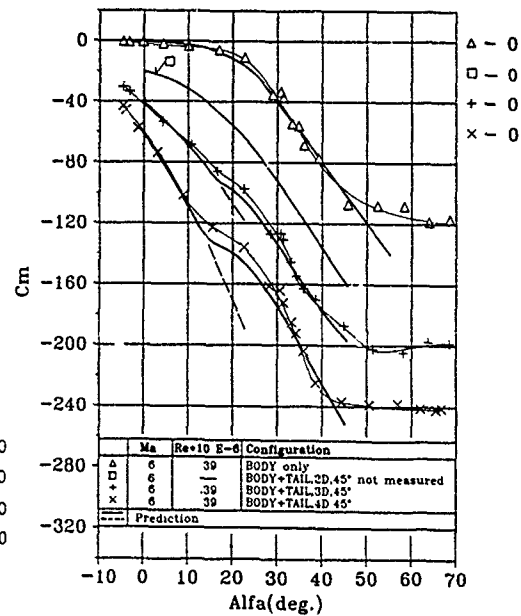


Figure 12b: Pitching moment coefficient versus angle of attack. All lifting surfaces in  $\times$  position. Calculation with (—) and without (---) corrections beyond  $\alpha_{crit}$ .

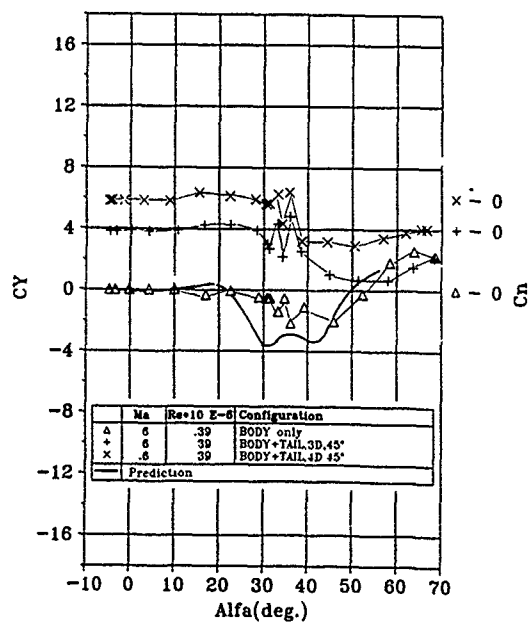


Figure 12c: Side force coefficient versus angle of attack. All lifting surfaces in  $\times$  position.

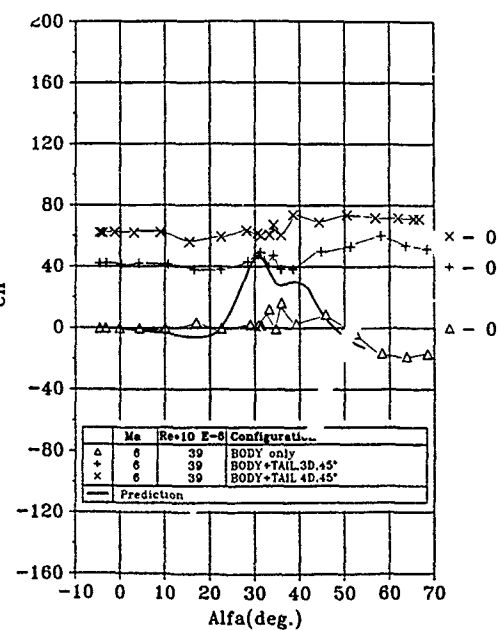


Figure 12d: Yawing moment coefficient versus angle of attack. All lifting surfaces in  $\times$  position.

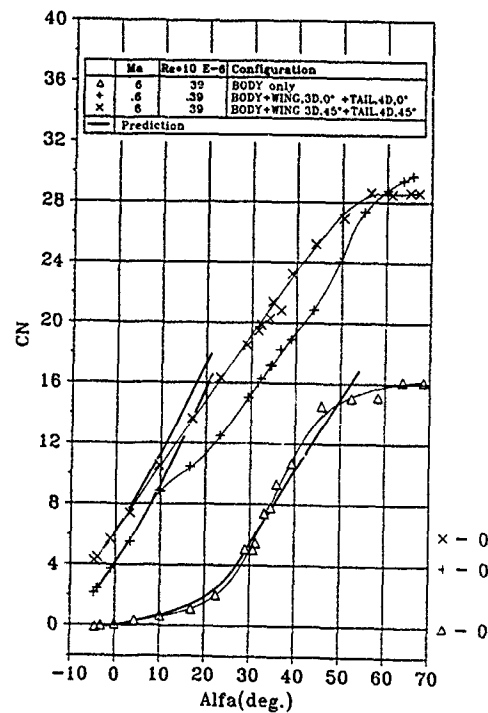


Figure 13a: Normal force coefficient versus angle of attack. All lifting surfaces either in + or x position

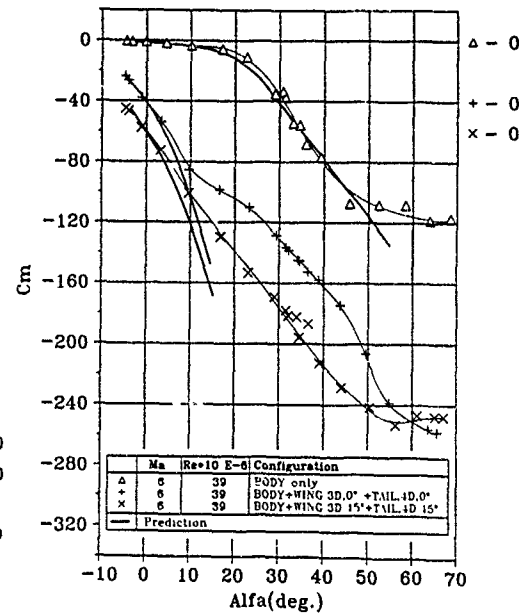


Figure 13b: Pitching moment coefficient versus angle of attack. All lifting surfaces either in + or x position

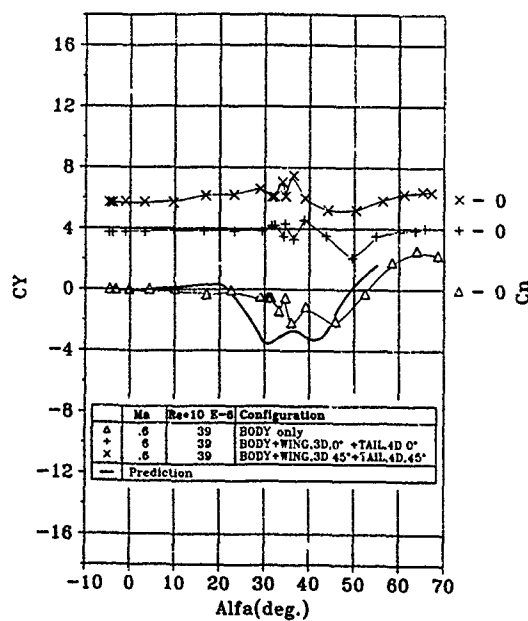


Figure 13c: Side force coefficient versus angle of attack. All lifting surfaces either in + or x position

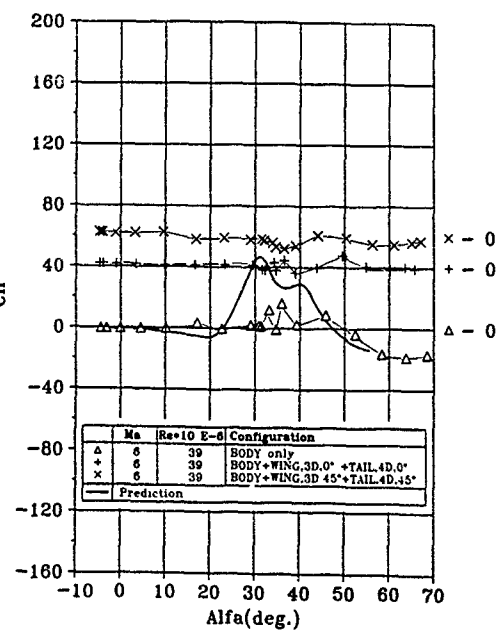


Figure 13d: Yawing moment coefficient versus angle of attack. All lifting surfaces either in + or x position

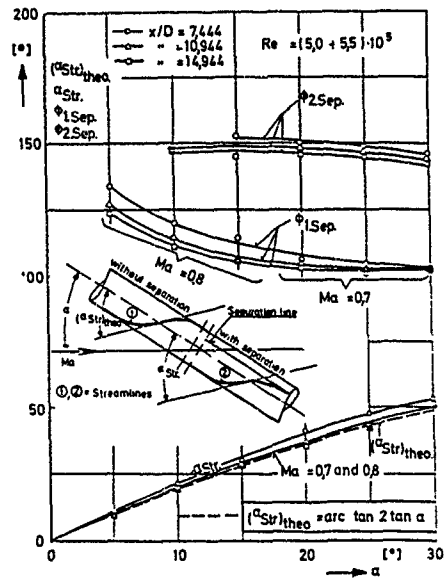


Figure 14: Separation lines and limiting streamlines on the body alone derived from oil flow pictures

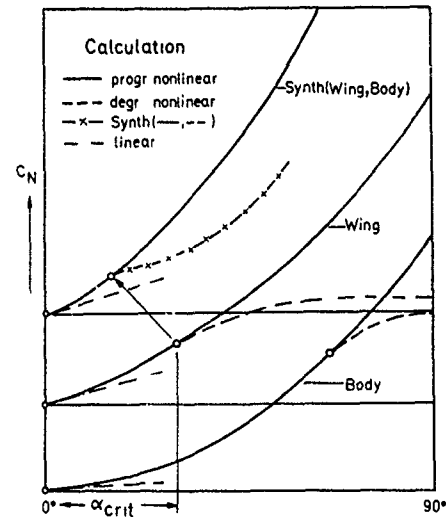


Figure 15: Principal sketch of component build up method used in predictions of Figs. 11 to 13

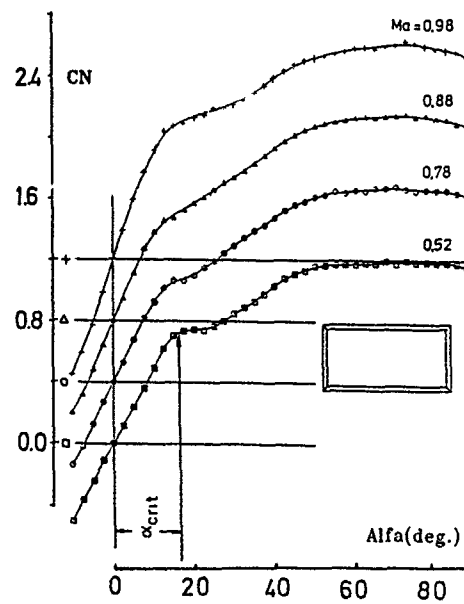


Figure 16a: Normal force characteristics of a rectangular wing with sharp edges and an aspect ratio  $A = 2$ . Data taken from H. Esch [16]

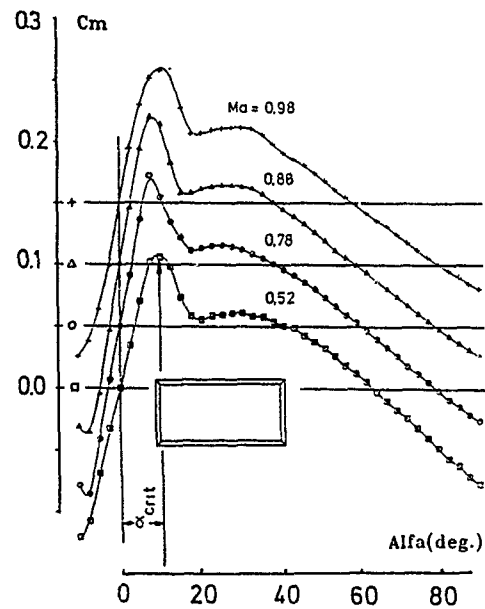


Figure 16b: Pitching moment characteristics of a rectangular wing with sharp edges and an aspect ratio  $A = 2$ . Data taken from H. Esch [16]  
Moment reference point = centre of wing  $a:ca$

# SUPERSONIC VORTEX FLOWS AROUND A MISSILE BODY BASIC EXPERIMENT AND EULER NUMERICAL COMPUTATION

by

Jérôme LORDON, Jean-Christophe FARE  
AEROSPATIALE, Division Engins Tactiques, Châtillon-sous-Bagneux, FRANCE

and

Didier PAGAN  
ONERA, Châtillon-sous-Bagneux, FRANCE

## ABSTRACT

At high or moderate angles of attack, boundary layers separate and vortices develop on the leeward side of tactical missile bodies. The purpose of this paper is to validate a numerical approach simulating these supersonic separated flows. In this iterative "Coupling Technique", the inviscid flow is computed by means of an Euler solver in which separation is forced by a parietal treatment. The location of the separation line is given by a boundary layer calculation based on a three-dimensional field method. A detailed experimental study was performed to provide a wide range of comparisons with computations over an ogive-cylinder configuration at Mach 2. Experiments are first described, then computational results are presented for different angles of attack. Calculations over a body-tail configuration finally evaluate the vortical flow interaction with wings.

## 1. INTRODUCTION

The resolution of the averaged Navier-Stokes equations to compute flows over missiles and planes is a tremendous task. If interesting results have already been presented [1] [2], both numerical and theoretical studies are still needed to get precise, effective and predictable tools. Furthermore, the problem of turbulence modelling is still largely open. Now, Euler codes can be very useful for many complex industrial problems and, thanks to calibration and validation, can be used in the development phase of a project. The present study is related to the prediction of separated flows over smooth bodies with an Euler code.

The nonlinearity of supersonic flows around missiles is a well known phenomenon, produced by shocks and vortices. Shocks are solutions of the Euler equations and Euler solutions often exhibit vortices. These vortices can be generated by sharp edges like leading edges or by curved shocks on the leeward side of smooth bodies. Once created near the body surface, vortex sheets develop into the flow field.

For missiles with large lifting surfaces, the main part of the nonlinear phenomena is created by wings and is rather well predicted by Euler codes [3], though the origin of the entropy creation remains an open problem. For smooth slender bodies, the agreement between experiments and calculations is often poor. We have already presented a local treatment which enhances the Euler results [4]. The study showed a great influence of the separation line used as a datum on the results (normal force, center of pressure, ...) but improvements in the field and force predictions were obtained. The lack of detailed experimental studies and the defect of empirical formula for the separation line position prevented us from setting up a prediction method. The new experiments realized by ONERA in 1989 now allow us to define and validate a "coupling method" for computing supersonic flows over smooth bodies, where a boundary layer code is used to determine the separation line from the Euler results. This method is also interesting to evaluate the interactions between body vortices and lifting surfaces.

## 2. BASIC EXPERIMENT

### 2.1 EXPERIMENTAL SET-UP AND TEST CONDITIONS

The first part of this study provides a set of experimental results, including surface pressure measurements, surface flow visualizations and flow field surveys, in order to constitute test cases for the validation of numerical calculations. Experiments have been performed on a 9 caliber ogive-cylinder body equipped with a 3 caliber circular ogive, in the ONERA S5Ch wind tunnel test facility (Fig. 1). The incidence values range from 0° to 20°. The test section of the S5Ch wind-tunnel is 300x300 mm<sup>2</sup>. The characteristics of the incoming free-stream have been fixed as follows.

- Mach number  $M_0 = 2$
- Stagnation pressure  $P_{t0} = 0.05$  MPa
- Stagnation temperature  $T_{t0} = 330$  K.

The diameter of the model is  $D = 30$  mm, which leads to a Reynolds number  $Re_D = 0.16 \cdot 10^6$ . The model is equipped with 17 pressure taps equally distributed along a meridian line. As shown in Fig. 2, the model was sting-mounted and could be rotated around its pitch and roll axes.

Visualizations and measurements have been completed in two cases: natural transition and transition triggered by means of a 5 mm large carborandum strip located 30 mm from the apex. For natural transition, acenaphthene coating visualization enabled us to verify that the boundary layer remained laminar all over the body at  $\alpha = 0^\circ$ . Except when it is especially mentioned, results presented in the experimental part are related to the laminar boundary layer case.

The external flow has been investigated by a five-hole pressure probe allowing to obtain the local Mach number  $M$ , the stagnation pressure  $P_1$  and the velocity vector (deduced with the assumption of a constant stagnation temperature, which is a good approximation for this value of incoming free-stream Mach number).

## 2.2 VISUALIZATION OF THE SKIN-FRICTION LINES PATTERN

Surface oil flow visualizations realized at  $\alpha = 5^\circ, 10^\circ, 15^\circ$  and  $20^\circ$  angle of attack, are presented in Fig. 3 a-d. These figures allow us to determine the conjectural skin-friction patterns given in Fig. 4 a-d, where top and side views are presented.

Skin-friction line patterns are topologically equivalent at  $\alpha = 5^\circ$  and  $10^\circ$ , and can be described as follows. All the lines start at the model apex. An attachment line  $A_1$  is present in the lower side of the symmetry plane. Primary separation occurs along  $S_1$ . An attachment line  $A_2$  is visible in the upper side of the symmetry plane. The boundary layer separates again along  $S_2$ . Between  $S_2$  and  $S_1$  a third attachment line  $A_3$  must exist. The latter is not visible on the visualizations because the velocity is very low after the secondary separation, so that friction forces are not large enough to drive the oil. The line  $S_1$ , as all skin-friction lines, starts at the apex, but it can be observed that the other lines do not join  $S_1$  before  $X/D = 4$  ( $\alpha = 5^\circ$ ) or  $X/D = 3$  ( $\alpha = 10^\circ$ ). The transverse flow organization of Fig. 5 which includes 2 vortices is consistent with the skin-friction pattern.

For higher angles of attack ( $\alpha = 15^\circ$  and  $20^\circ$ ), the primary separation line  $S_1$  is clearly visible from the apex. The singular lines  $A_1, A_2, S_2$  and  $A_3$  are also present, but between  $S_2$  and  $A_3$ , there are two other separation lines  $S_3$  and  $S_4$ . Different external flow topologies are compatible with these patterns. One of them, using  $S_1$  and  $S_2$  and deduced from the velocity field determined in a transverse plane (§ 2.3), is given in Fig. 6. In this sketch, there are three vortices and a saddle point embedded in the transverse flow field.

The location of the separation line  $S_1$  has been carefully determined and plotted in Fig. 7 for the laminar and turbulent boundary layer cases. We observe that the origin of  $S_1$  comes up to the body nose tip when incidence is increased, and reaches it at  $\alpha = 20^\circ$ . In the laminar case, lines determined at  $\alpha = 10^\circ, 15^\circ$  and  $20^\circ$  are close one to the other. In the turbulent case at  $5^\circ$  angle of attack, the flow is fully attached, as turbulence tends to stabilize the boundary layer; moreover, at  $10^\circ, 15^\circ$  and  $20^\circ$  incidence, separation line locations are similar to those respectively obtained at  $5^\circ, 10^\circ$  and  $15^\circ$  in the laminar case.

## 2.3 MEASUREMENTS REALIZED AT $\alpha = 20^\circ$ INCIDENCE

The surface pressure distribution has been determined by rotating the model around its roll axis. This technique allows to realize a great deal of measurements with few pressure taps. Results obtained at  $20^\circ$  angle of attack are plotted in Fig. 8 together with the separation line  $S_1$ .

Measurements realized with the five-hole pressure probe in the plane  $X/D = 5$  are presented in Fig. 9. In Fig. 9a the transverse velocity vector plots are given together with the pseudo-streamlines computed with the experimental 2D velocity field. The iso-Mach number map is presented in Fig. 9b and the iso-stagnation pressure map is plotted in Fig. 9c. The vector plot and the pseudo-streamlines reveal the location of the primary and secondary vortices. On the iso-Mach number pattern, high values of  $M$  (near 3) are reached in the area located between the primary vortex, the symmetry plane and the body. The lowest values of  $M$  are obtained near the separation sheet coming from  $S_1$  and in the secondary vortex area.

The iso-stagnation pressure map shows high dissipation levels in the sheet issued from  $S_1$ , the primary vortex core and the secondary vortex. In these regions,  $P_1/P_{10}$  reaches values as low as 0.2.

## 3. CALCULATION

### 3.1 THE NUMERICAL METHOD

#### 3.1.1 DESCRIPTION OF THE METHOD

The coupling technique presented here aims at improving the existing numerical calculation of vortical flows with an Euler solver. It consists in the generation of a vortex sheet into the flow thanks to a local treatment on the body surface (see §3.1.2). Therefore, the separation line location must be accurately known. We proceed in 2 steps :

- first, we need to validate the implementation of the separation treatment and evaluate how results evolve when separation is forced. To do this, we use the experimental line measured at ONERA and thus focalize on the improvements relevant to the numerical treatment itself;
- once the concept is validated, we are able to perform direct calculations using an iterating method, schematized in Fig. 10. A first Euler calculation (including no parietal treatment) supplies data for a boundary layer computation. Then, the interpretation of the resulting skin-friction pattern gives a first location for the separation line. This line can afterwards be used as a datum for a second calculation loop. The process is said to converge when two successive iterations lead to very close separation line positions.



### 3.1.2 EULER CODE AND PARIETAL SEPARATION TREATMENT

The Euler code FLU3C used for this study has been developed by ONERA and AEROSPATIALE [5]. It solves the 3D unsteady Euler equations for an inviscid gas with a finite volume approach. The flux-vector upwind splitting technique introduced by Van Leer [6] allows to compute flows with strong discontinuities. The second order in time and space is obtained via a MUSCL approach. A TVD correction on the slope calculations reduces the scheme to first order spatially near the extrema. A CFL condition limits the time step of the explicit scheme. For steady solutions, a local time step is used. For supersonic calculations, a pseudo-marching technique has been developed. It consists in iterating in time plane by plane, using only the upstream information. CPU time is thus dramatically lowered. The frontal shock is captured and the grid, defined before the calculation, is not adapted. Thanks to its precision and robustness, FLU3C has been used for several years at AEROSPATIALE to compute flows around missiles, shuttles, supersonic planes, as well as for jet calculations and unsteady studies [7].

By locally rotating the velocity vector at the body surface during the Euler calculation, we can create a vortex sheet which develops into the flow field. The aim is to make the velocity vector parallel to a given separation line. Therefore, in each calculation plane and at every iteration, for the two grid points surrounding the theoretical separation location, the flow variables are modified as follows :

Let  $\Psi$  be the ratio  $T \cdot U / |U|$  where  $T$  is the unit vector tangent to the fuselage in the plane orthogonal to its axis at the separation point. The separation line being known, we have  $\Psi = \Psi_s = T \cdot D / |D|$  where  $D$  is a vector tangent to the separation line. If the separation point is between grid points  $k$  and  $k+1$ ,  $\Psi$  is modified at these 2 points by interpolating according to the polar angle  $\phi$  :

$$\Psi_k = \Psi_{k-1} + (\phi_k - \phi_{k-1}) (\Psi_s - \Psi_{k-1}) / (\phi_s - \phi_{k-1}) ; \quad \Psi_{k+1} = \Psi_{k+2} + (\phi_{k+1} - \phi_{k+2}) (\Psi_s - \Psi_{k+2}) / (\phi_s - \phi_{k+2})$$

To avoid oscillations, entropy, pressure and total enthalpy values at points  $k$  and  $k+1$  are determined by an interpolation between values at points  $k-1$  and  $k+2$  and data belonging to the upstream plane. A relaxation technique is also used. The speed vector modulus  $|U|$  is then deduced from the energy equation.

### 3.1.3 BOUNDARY LAYER CODE

The code 3C3D, developed at ONERA-CERT/DERAT, solves the three-dimensional boundary layer equations, in which the external pressure field is a datum of the problem [8] [9]. Though parabolic, due to the diffusion terms, the boundary layer equations system becomes hyperbolic when only the first order partial derivative terms are taken into account. This implies the existence of influence and dependence domains, in relation with the characteristic surfaces. The streamlines are characteristic lines as well as the lines normal to the wall. Starting from initial flow direction, integration is performed by x-marching, the transverse derivatives being computed according to influence-dependence rules. The code uses a first-order but fully implicit discretization scheme and a mixing length turbulence model, though the implementation of new turbulence models is in progress. Several longitudinal and transversal transition criteria are available [10].

After each Euler computation, an automatic interface generates a curvilinear mesh - defined by its metric coefficients at the nodes - in which the boundary and initial conditions are given (geometrical shape, external pressure distribution calculated by the Euler code FLU3C, upstream characteristics). In each cell of the mesh, the continuity and momentum equations are discretized and integrated along characteristic lines so that the dependence rules are automatically satisfied. In practice, the momentum equations are written along the projection of the streamlines on the surfaces parallel to the wall, which simplifies the interpolation problems.

Compared with the integral method used up to now [4], this field method presents the advantage of allowing computation in a wider area of the flow (especially in separated regions). However, an important part of the calculation domain remains most of the time inaccessible to calculation, since streamlines are discarded when the boundary layer becomes too thick or the streamline deviation too large.

## 3.2 RESULTS

We compare computations and experiments to analyze the influence of the separation treatment in the Euler code. First of all, we use the experimental separation line measured at ONERA facilities as a datum, and thus validate the coupling method. We are then able to carry out calculations on a missile body without using any external data. Finally, calculations made on a body-tail configuration provide a practical engineering case showing the influence of vortex interaction on tails. Calculations were performed for  $\alpha = 5^\circ, 10^\circ$  and  $15^\circ$ , since the abandoned part of the body becomes too wide for higher angles of attack to allow a safe determination of the separation line location.

### 3.2.1 CALCULATION USING EXPERIMENTAL SEPARATION LINES

All the computations presented below over the ogive-cylinder body deal with laminar boundary layers calculations. Figure 11 presents 3 skin-friction patterns relative to calculations made at a 15 degrees angle of attack with the coupling method described above :

- 1 - using no separation treatment,
- 2 - using the laminar experimental line,
- 3 - using the laminar experimental line with a 15 degrees shift towards the leeside.

In such plots, the separation line is seen as a singular line to which several skin-friction lines converge from both sides of the flow or the locus where lines issuing from the windside are abandoned. Here, the computed separation line is close to the experimental one only in the third case. Other comparisons made at various angles of attack on iso-values in the crossflow planes lead us to conclude that the separation treatment within the Euler code FLU3C induces a constant shift of about 15 degrees between the separation line used as an input datum and the line found with a boundary layer calculation. This statement has not been well explained yet. From now on, we shall use a systematic shift of 15 degrees on the separation line before calculating with FLU3C.

Figures 12 and 13 present comparisons between experimental values and Euler calculations on iso-total-pressure and isobar lines in 2 crossflow planes at 15 degrees incidence. Two calculations are presented, one using no separation treatment, the other using the modified experimental line. The same color scales are used for the 2 planes. Total pressure plots prove that the general shape of the separated flow as well as the height of the vortex are better predicted when the separation is forced. The level of pressure is also nearer to the experimental value, though great discrepancies remain in the vortex core, most probably due to the viscous nature of the vortex not correctly described by our perfect fluid model.

Figure 14 shows the same comparisons on the local force coefficient at  $\alpha = 10^\circ$  and  $15^\circ$ . Experimental values were obtained via the integration of the measured pressure values (as few empirical data were available near the apex, the experimental results suffer from a crude interpolation in this area of the body). The separation treatment tends to lower the pressure values on the leeside so that the normal force increases and the center of pressure moves off the apex.

Global coefficients for each incidence computed are indicated thereafter. In each case the error on the center of pressure abscissa is reduced to less than 0.4 diameters and the normal force is predicted with less than 8% error, which is suitable for practical applications.

CN : Coefficient of the force normal to the body      Subscript "c" means Calculated value  
XCp : Center of pressure abscissa of the body      Subscript "e" means Experimental value.  
D : Body diameter

Separation	CNc	$\frac{CNc-CNe}{CNe}$	$\frac{XCpc}{D}$	$\frac{XCpc-XCpe}{D}$
Free	0.255	-10 %	1.80	-0.70
Expe line	0.276	- 2 %	2.17	-0.33

Mach = 2 -  $\alpha = 5^\circ$

Separation	CNc	$\frac{CNc-CNe}{CNe}$	$\frac{XCpc}{D}$	$\frac{XCpc-XCpe}{D}$
Free	0.60	-19 %	2.13	-1.10
Expe line	0.72	- 3 %	2.95	-0.27

Mach = 2 -  $\alpha = 10^\circ$

Separation	CNc	$\frac{CNc-CNe}{CNe}$	$\frac{XCpc}{D}$	$\frac{XCpc-XCpe}{D}$
Free	1.43	- 7 %	3.48	- 0.31
Expe line	1.67	+8 %	3.91	+0.12

Mach = 2 -  $\alpha = 15^\circ$

We have shown the benefit of the application of a separation treatment when the line used is the experimental one. We will now analyze the results given by the coupling method itself, starting with an Euler computation using no separation treatment at all.

### 3.2.2 COUPLING EULER CODE / BOUNDARY LAYER CODE

Whilst making calculations using the coupling method described herein, we note that the location of the separation line seems to converge after only two or three calculation loops. Results presented below are limited to the standard Euler calculation (involving no treatment of separation) and the first two coupling iterations (called "Coupling #1" and "Coupling #2"). Figure 15 presents the parietal streamlines given by the boundary layer code at 10 degrees incidence for these three cases. The "Coupling #2" case improves the skin-friction pattern near the origin of the separated sheet. The patterns show a swift convergence of the separation line location near the experimental line. A "Coupling #3" calculation corroborates that statement.

In Fig. 17 are shown the parietal pressure coefficient plots versus the roll angle corresponding to these three successive Euler calculations, in the crossflow plane  $X = 7D$  and at  $\alpha = 10^\circ$ . Despite a few oscillations on both sides of the separation line, the coupling calculation results follow the experimental contour much better than the first Euler calculation ones, especially near the leeside of the body. As expected, the separation has few effects on the parietal pressure on the windside.

As for local forces coefficients (see Fig. 16), the coupling method also provides closer results to the experiments. The global coefficients indicated below show the improvements given at all angles of attack when using this method.

Separation	CNc	CNc-CNe CNe	XCpc D	XCpc-XCpe D
Free	0.255	-10 %	1.80	-0.70
Coupling #1	0.260	- 8 %	1.93	-0.57
Coupling #2	0.275	- 2 %	2.20	-0.30

Mach = 2 -  $\alpha = 5^\circ$ 

Separation	CNc	CNc-CNe CNe	XCpc D	XCpc-XCpe D
Free	0.60	-19 %	2.13	-1.10
Coupling #1	0.72	- 3 %	2.94	-0.27
Coupling #2	0.76	+ 1 %	3.12	-0.10

Mach = 2 -  $\alpha = 10^\circ$ 

Separation	CNc	CNc-CNe CNe	XCpc D	XCpc-XCpe D
Free	1.43	- 7 %	3.48	-0.31
Coupling #1	1.53	- 1 %	3.59	-0.20
Coupling #2	1.58	+2 %	3.68	-0.11

Mach = 2 -  $\alpha = 15^\circ$ 

Figure 19 shows a comparison between experiments and a "Coupling #2" calculation ( $\alpha = 15^\circ$ ) for total pressure in several crossflow planes. Figure 20 presents a visualization of parietal pressures and skin-friction lines both with and without separation treatment.

The calculations presented above on an ogive-cylinder configuration as a validation of the coupling technique enable us to emphasize upon the interest of adding a separation treatment to our Euler code to predict flows around smooth bodies. We will now discuss the results obtained over a more practical body-tail configuration.

### 3.2.3 VORTICAL INTERACTION WITH FINS

Up to now, calculations have been carried out on smooth slender body configurations, upon which the coupling technique is of great use. However, fins located at the end of a missile body may also be influenced by the vortex sheet. In such a case, it is known that the height and location of the sheet have a strong effect over the wing lift. We shall now try to evaluate this influence.

The configuration used to study vortex interaction is the following :  
3D parabolic ogive + 12D cylinder + tail (see Fig. 18)

Measurements were performed at ONERA facilities at Mach 2 for several values of angle of attack ( $\alpha$ ) and roll angle ( $\phi$ ) values. The diameter-based Reynolds number was  $Re_D = 1.13 \cdot 10^6$ . In computations and experiments, transition is forced and fixed at  $X/D = 0.2$ . Calculations were made for  $\phi = 0^\circ$  (+ position) at  $\alpha = 10^\circ$  and  $15^\circ$  and for  $\phi = 45^\circ$  (x position) at  $\alpha = 10^\circ$ .

The coefficient of the force normal to the wing and the center of pressure abscissa on the wing calculated with the Euler code FLU3C, firstly without separation treatment and secondly after convergence of the coupling process (Coupling #2), have been compared to experimental values.

Incidence	Separation	CNc	CNc-CNe CNe	XCpc D	XCpc-XCpe D
10°	Free	0.563	+15 %	0.555	+0.01
	Coupling	0.525	+ 7 %	0.557	+0.01
15°	Free	0.733	+10 %	0.558	+0.01
	Coupling	0.715	+ 7 %	0.558	+0.01

 $\phi = 0^\circ$  - Horizontal wing

Separation	CNc	CNc-CNe CNe	XCpc D	XCpc-XCpe D
Free	0.39%	+64 %	0.55	- 0.02
Coupling	0.261	+ 8 %	0.60	+0.03

 $\phi = 45^\circ$  - Leeward wing -  $\alpha = 10^\circ$

Separation	CNc	$\frac{CNc-CNe}{CNe}$	$\frac{XCpc}{D}$	$\frac{XCpc-XCpe}{D}$
Free	0.420	+8%	0.55	+0.01
Coupling	0.405	+4%	0.56	+0.01

$Q = 45^\circ$  - Windside wing -  $\alpha = 10^\circ$

As already observed in previous calculations [4], the lift on the wing depends strongly on the separation line location, which determines the locus of the vortex core and the direction of the stream around the wing. When the tail is near the vortex ( $\phi = 45^\circ$ ), the values of CN are more accurately predicted when separation is forced. The influence decreases when the tail goes away from the vortex. For the wind side tail, very few influence of the vortex is noticed.

#### 4. CONCLUSION

After this study on the simulation of separated supersonic flows, we can draw the main following conclusions :

- even if not fully satisfactory from a theoretical point of view (shift in the input separation line, § 3.2.1), the "Coupling Technique" yields important improvements of the Euler results and is of great interest for practical engineering applications,
- the "Coupling Technique" ameliorates vortical interaction with fins as well as smooth body calculations,
- the location of the separation line is a critical datum, especially when evaluating the vortical interaction on wings and calculating hinge moments,
- there is a need for further experiments with other inflow conditions providing more experimental information about the position of the vortex sheet on a missile body for additional validations,
- with experimental and calculated separation lines, a data base could be realized to lower the number of iterations required.

At a time when Navier-Stokes solvers are still unable to compute all engineering configurations with a reasonable cost and when standard Euler results prove not precise enough, the coupling method may be very helpful. However, the boundary layer code involved should be able to compute all over the body, even at high incidences, in order to get precise separation lines ; a second order method, presently in progress at ONERA/CERT, could achieve this purpose. A parabolized Navier-Stokes method is also being developed at AEROSPATIALE and could present both the cost-effectiveness of the Euler codes and the global solution (viscid/inviscid) of the Navier-Stokes methods in one single run.

#### ACKNOWLEDGEMENTS

This study has been carried out with the support of the Direction des Recherches Etudes et Techniques (DRET)

We thank MM. J. Cousteix and R. Houdeville from ONERA/CERT for their helpful support related to the boundary layer code 3C3D.

#### REFERENCES

- [1] L.B. Schiff, R.M. Cummings, R.L. Sorenson, Y.M. Rizk : Numerical Simulation of High Incidence Flow over the F-18 Fuselage Forebody. AIAA paper 89-0339.
- [2] D. Degani, L.B. Schiff : Numerical Simulation of the Effect of Spatial Disturbances on Vortex Asymmetry. AIAA paper 89-0340.
- [3] R. Wood, S. Bauer, J. Byrd, B. McGrath, G. Wesselmann : Influence of Wing Geometry on Leading-Edge Vortices and Vortex-Induced Aerodynamics at Supersonic Speeds. AIAA paper 89-0085.
- [4] P. Guillen, J. Lordon : Numerical Simulation of Separated Supersonic Flows around Tactical Missile Bodies AGARD paper 88-CP-437.
- [5] M. Borrel, J.L. Montagné, J. Diet, Ph. Guillen, J. Lordon : Méthode de Calcul d'Ecoulements autour de Missiles Tactiques à l'aide d'un Schéma Décentré. La Recherche Aéronautique 1988-2.
- [6] J.L. Thomas, B. Van Leer, R.W. Walters : Implicit Flux-Split Schemes for the Euler Equations. AIAA paper 85-1680.
- [7] M. Dormieux, C. Mahe : Calcul Tridimensionnel de l'Interaction d'un Jet Latéral avec un Ecoulement Supersonique Externe. AGARD paper 88-CP-437.
- [8] C. Gleyzes, R. Houdeville, C. Mazin, J. Cousteix : Calculations of the Ercofac Case T1 performed at ONERA/CERT, Toulouse (FRANCE). Ercofac Workshop, March 1990.
- [9] R. Houdeville, C. Mazin : Calcul de Couche Limite Tridimensionnelle par une Méthode de Caractéristiques, Rapport final DRET, Mars 1990.
- [10] D. Arnal, M. Habiballah, E. Coustols : Théorie de l'Instabilité Laminaire et Critères de Transition en Ecoulements Bi et Tridimensionnel. La Recherche Aéronautique 1984-2.



Fig. 1 - MODEL AND FIVE-HOLE PROBE TRAVERSE SYSTEM IN S5CH WIND TUNNEL.

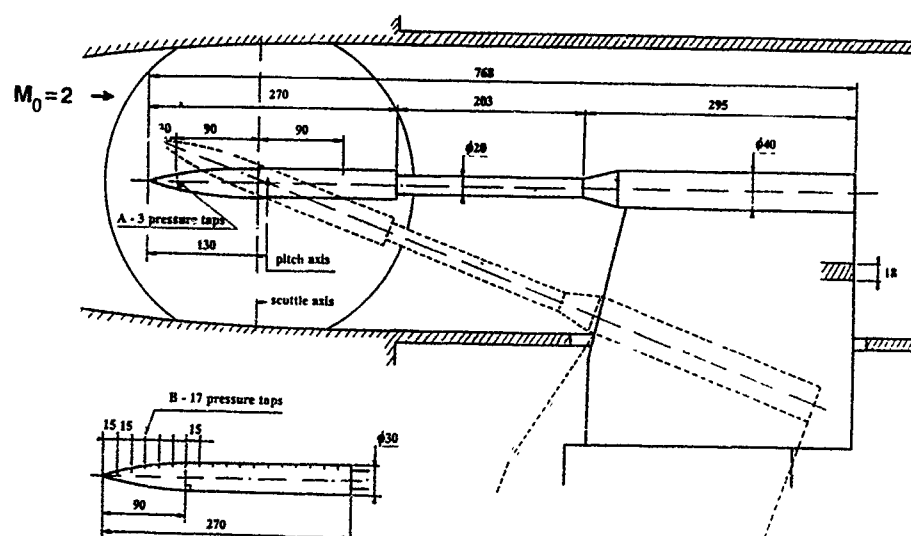


Fig. 2 - MODEL DEFINITION AND SETUP MAIN DIMENSIONS

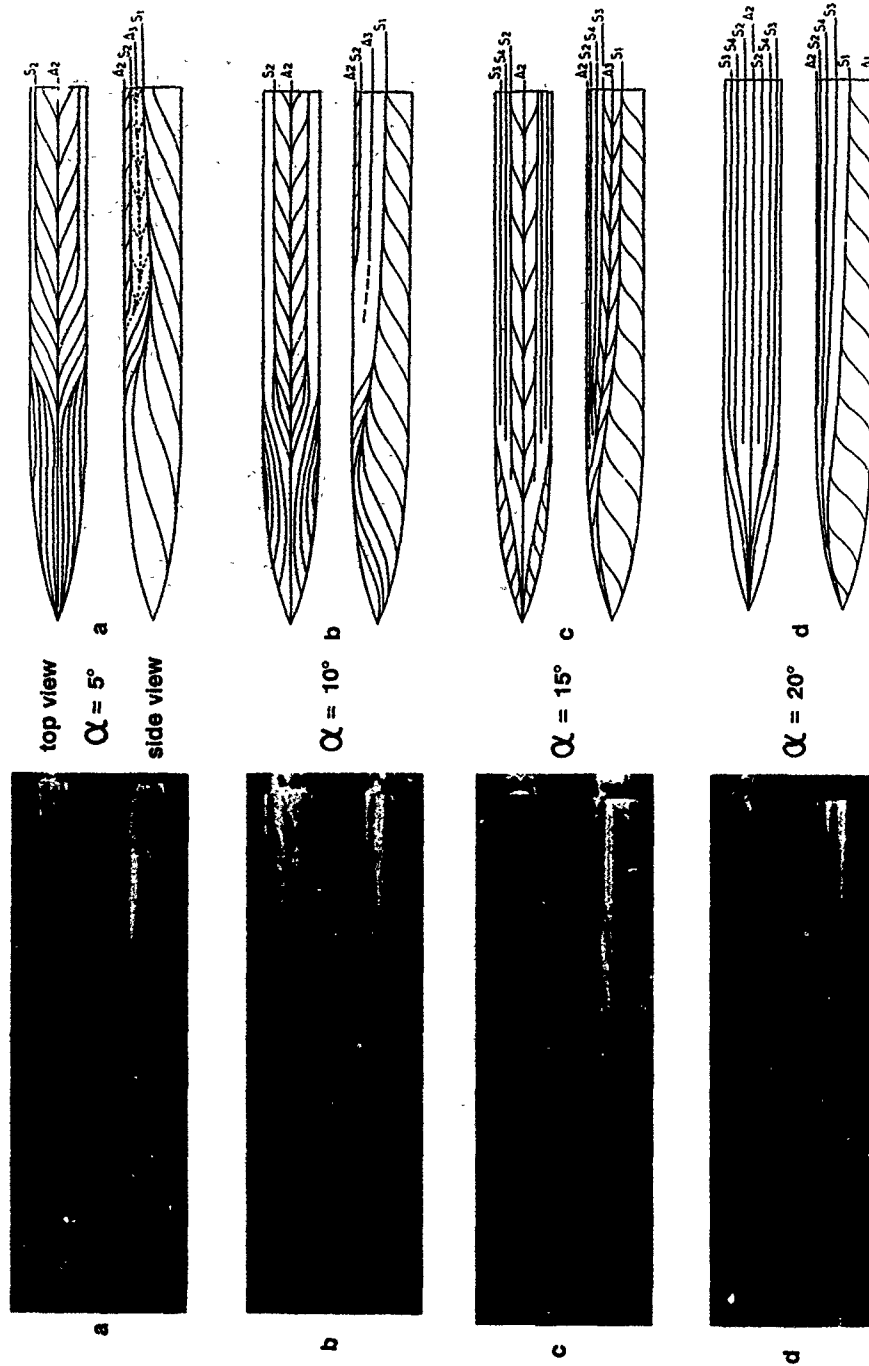


Fig. 3 - SKIN FRICTION PATTERN : OIL FLOW VISUALIZATIONS

Fig. 4 - SKIN FRICTION PATTERN : INTERPRETATIONS

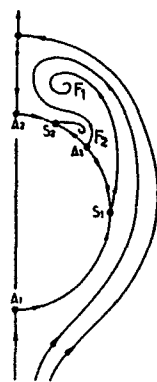


Fig. 5 - CROSS FLOW ORGANIZATION

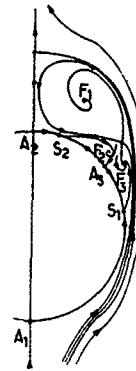


Fig. 6 - CROSS FLOW ORGANIZATION

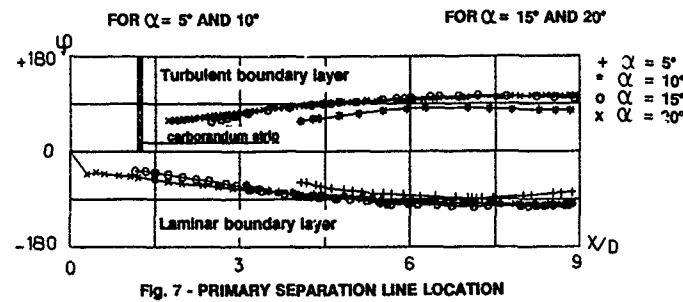
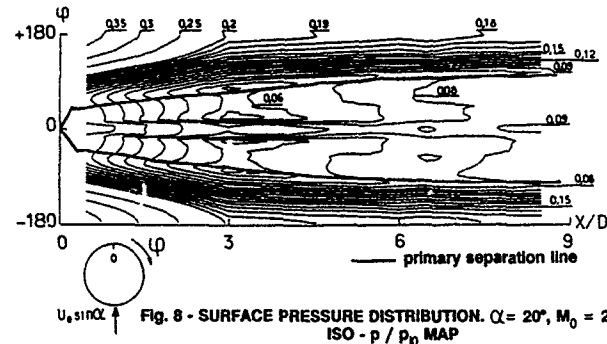
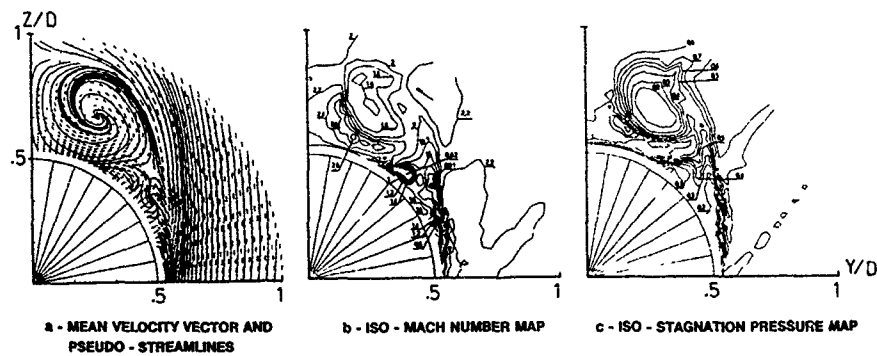


Fig. 7 - PRIMARY SEPARATION LINE LOCATION

Fig. 8 - SURFACE PRESSURE DISTRIBUTION.  $\alpha = 20^\circ$ ,  $M_0 = 2$ .  
ISO -  $p / p_0$  MAPFig. 9 - FIVE - HOLE PROBE MEASUREMENTS IN THE  $X/D = 5$  CROSSFLOW PLANE.  $\alpha = 20^\circ$ ,  $M_0 = 2$

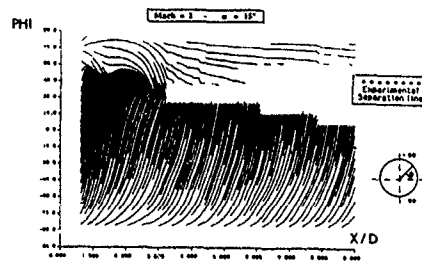


Fig 11-a: COMPUTED SKIN-FRICTION LINES ON THE BODY  
NO TREATMENT OF SEPARATION

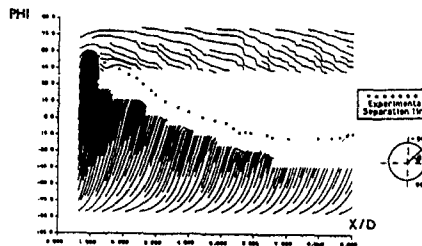


Fig 11-b: COMPUTED SKIN-FRICTION LINES ON THE BODY  
SEPARATION LINE = EXPERIMENTAL LINE

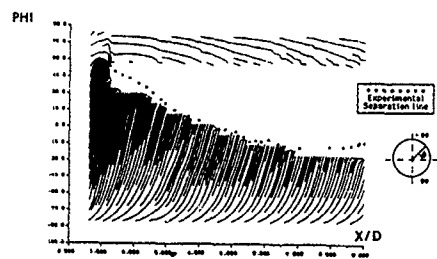


Fig 11-c: COMPUTED SKIN-FRICTION LINES ON THE BODY  
SEPARATION LINE = EXPERIMENTAL LINE + 15°

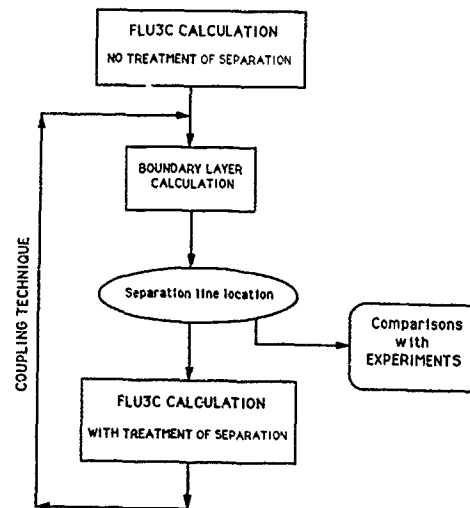
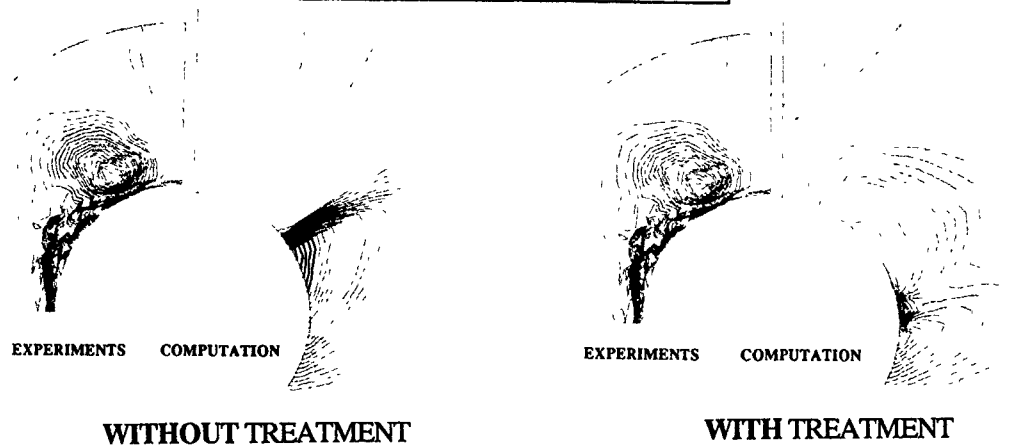


Fig. 10 : COUPLING TECHNIQUE

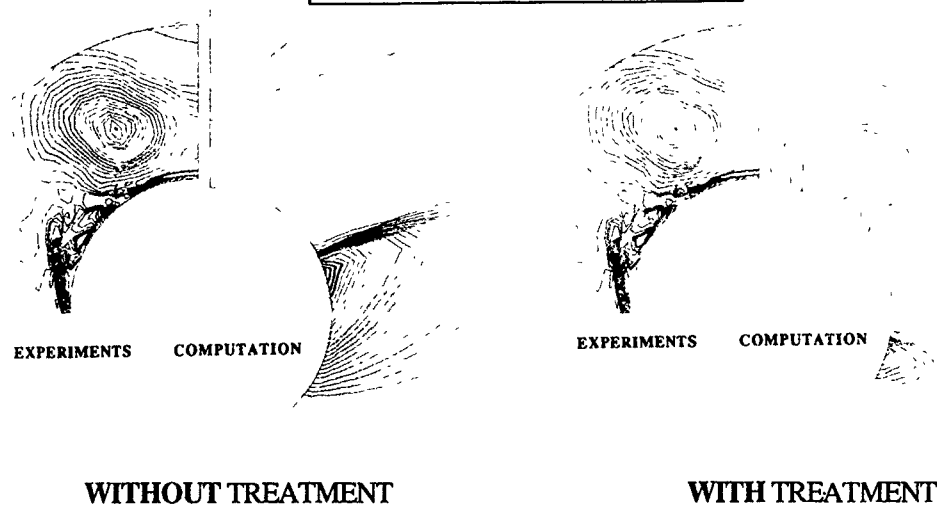


Mach = 2   -    $\alpha = 15^\circ$    -   X/D = 6



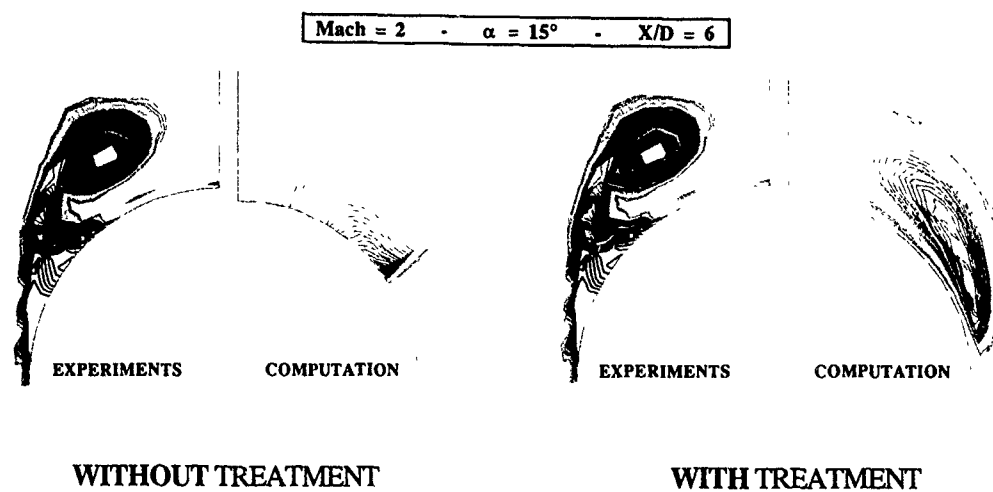
a)  $\frac{X}{D} = 6$

Mach = 2   -    $\alpha = 15^\circ$    -   X/D = 8

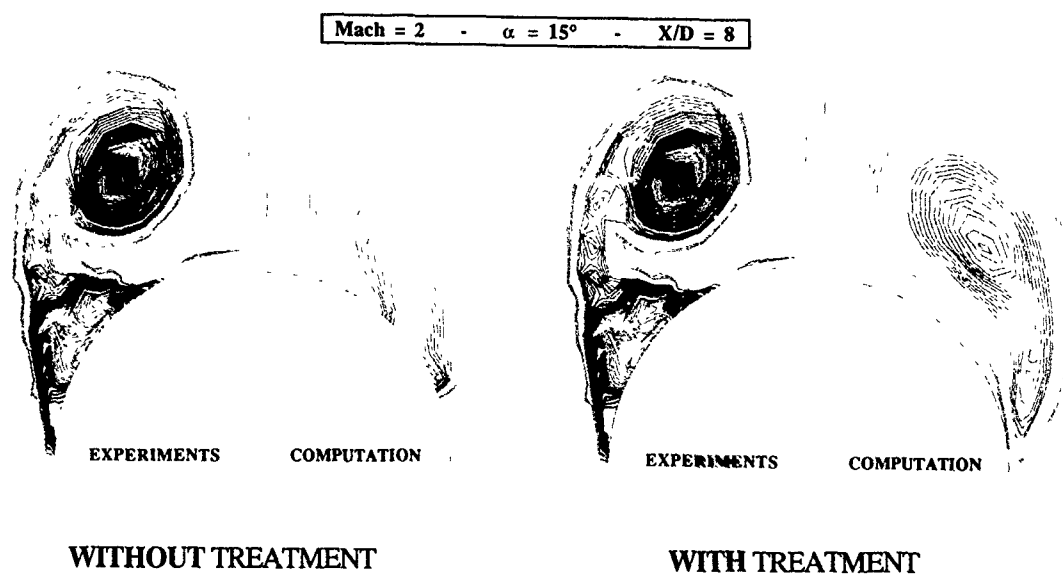


b)  $\frac{X}{D} = 8$

Fig. 12 : COMPUTED AND EXPERIMENTAL PRESSURE CONTOURS

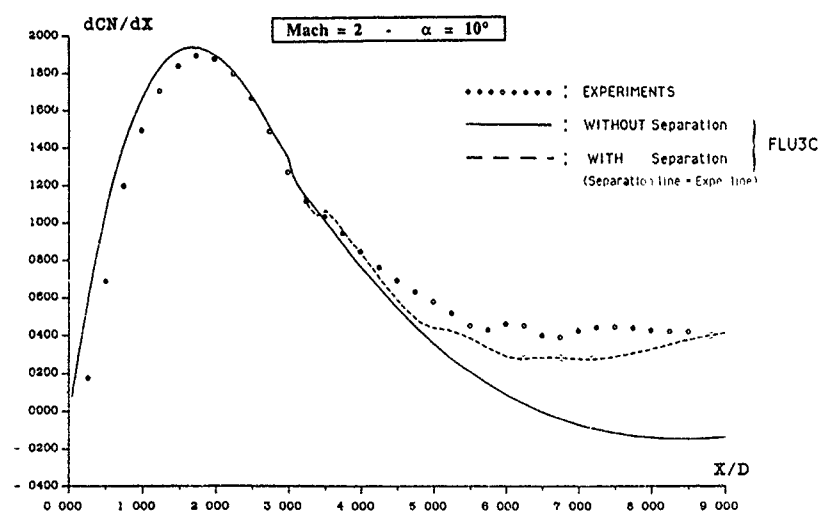


a)  $\frac{X}{D} = 6$

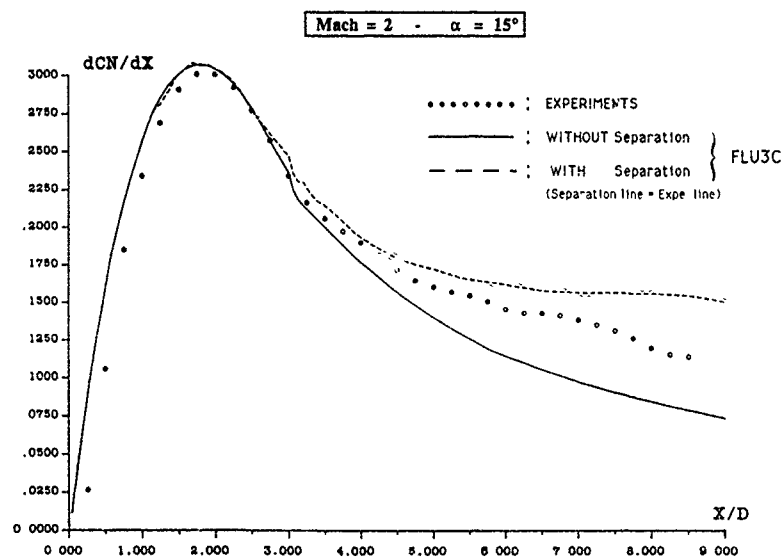


b)  $\frac{X}{D} = 8$

Fig. 13 : COMPUTED AND EXPERIMENTAL TOTAL PRESSURE CONTOURS



a)  $\alpha = 10^\circ$



b)  $\alpha = 15^\circ$

Fig. 14 : COMPUTED AND EXPERIMENTAL LOCAL NORMAL FORCES

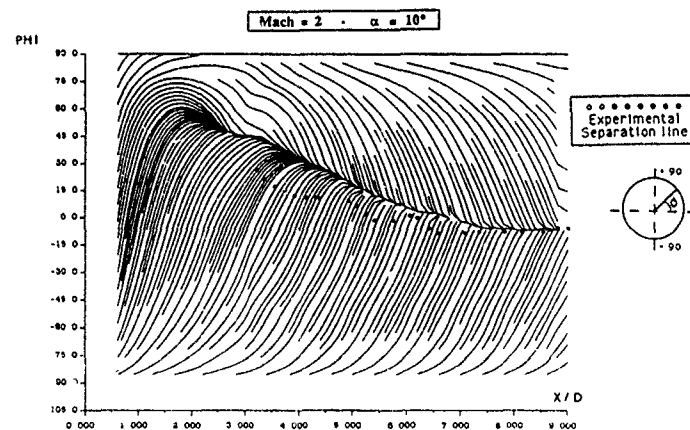


Fig 15-a : COMPUTED SKIN-FRICTION LINES ON THE BODY  
NO TREATMENT OF SEPARATION

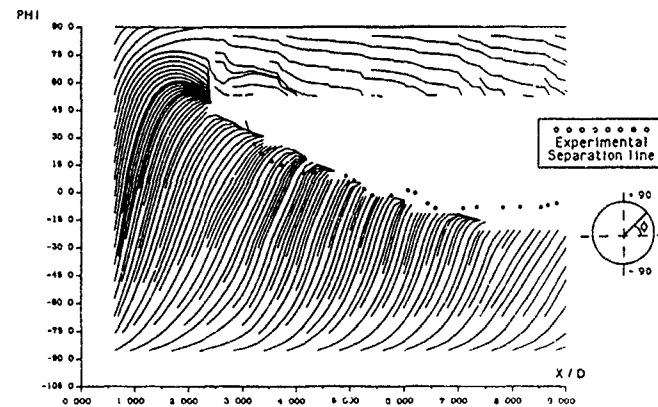


Fig 15-b : COMPUTED SKIN-FRICTION LINES ON THE BODY  
COUPLING #1

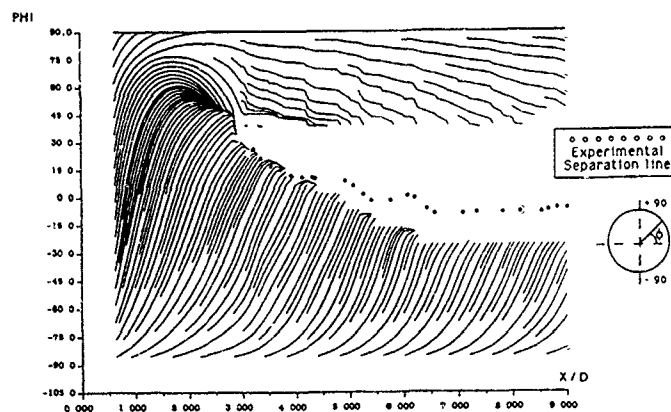


Fig 15-c : COMPUTED SKIN-FRICTION LINES ON THE BODY  
COUPLING #2

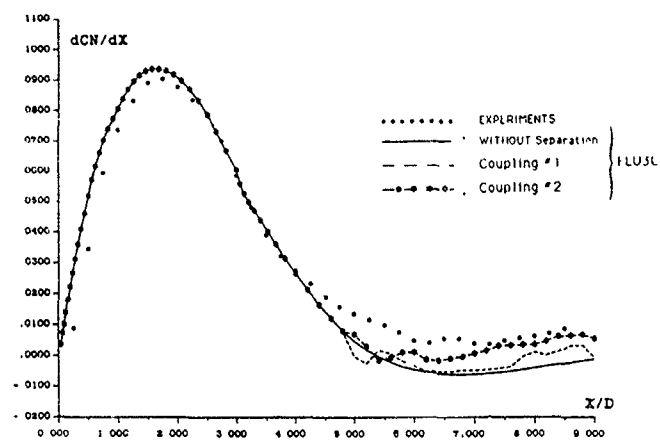
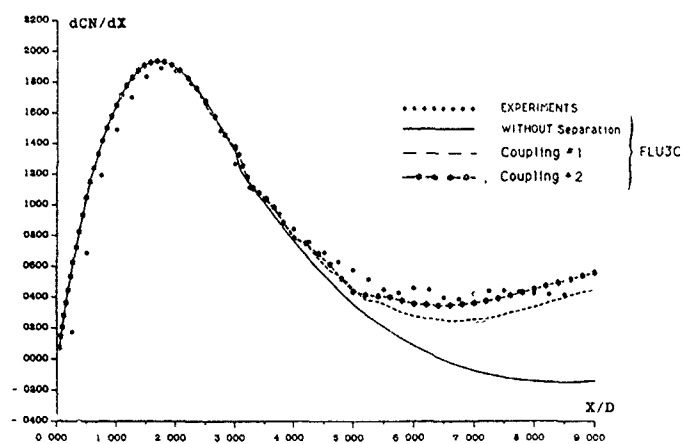
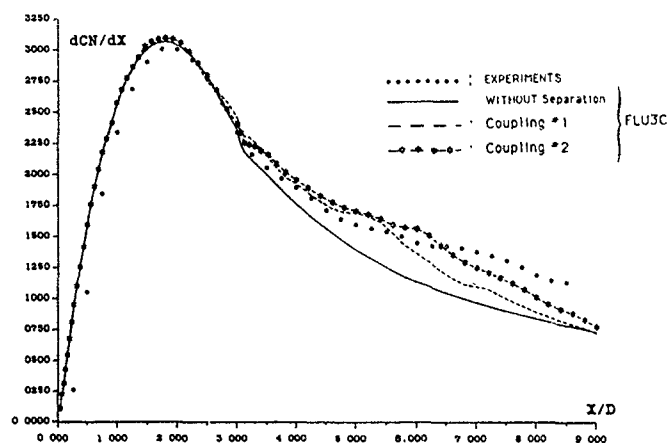
a)  $\alpha = 5^\circ$ b)  $\alpha = 10^\circ$ c)  $\alpha = 15^\circ$ 

Fig. 16 : COMPUTED AND EXPERIMENTAL LOCAL NORMAL FORCES

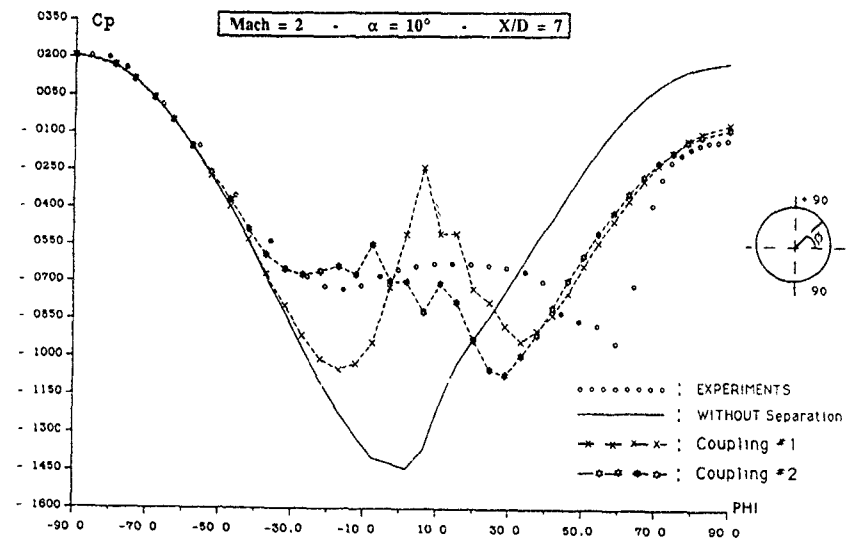


Fig. 17 : COMPUTED AND EXPERIMENTAL PARIETAL PRESSURE COEFFICIENTS

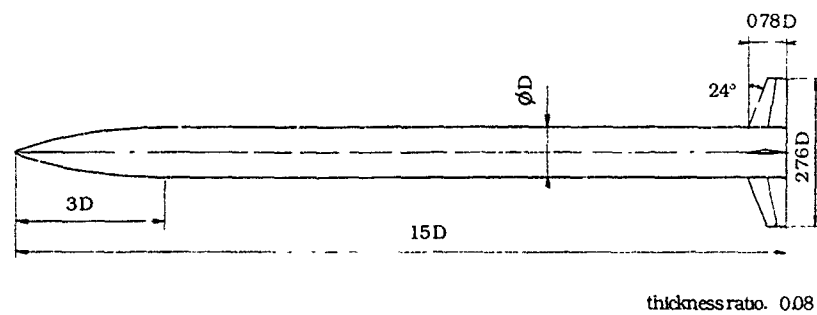


Fig. 18 : BODY-TAIL CONFIGURATION

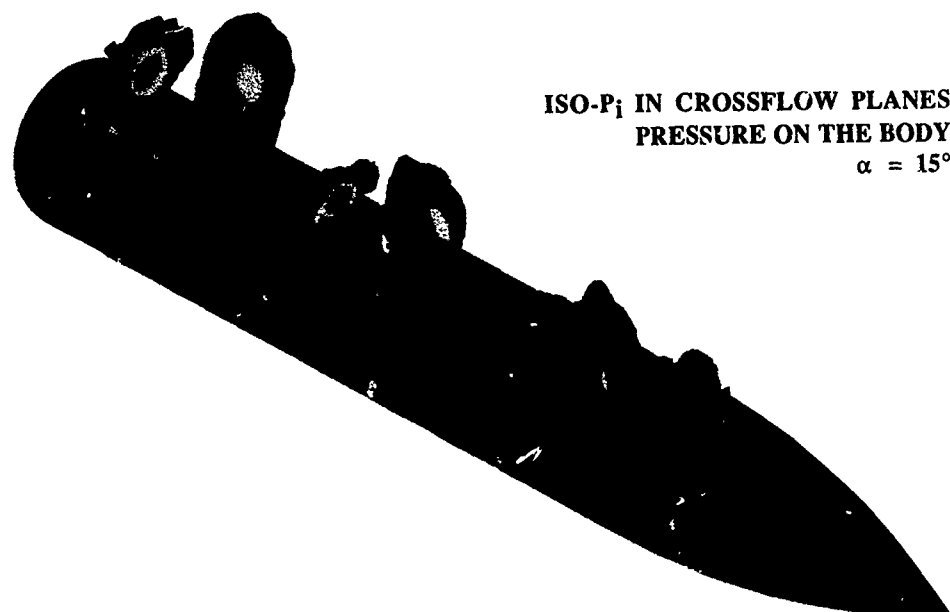


Fig. 19 : COMPARISON EXPERIMENTS / CALCULATION

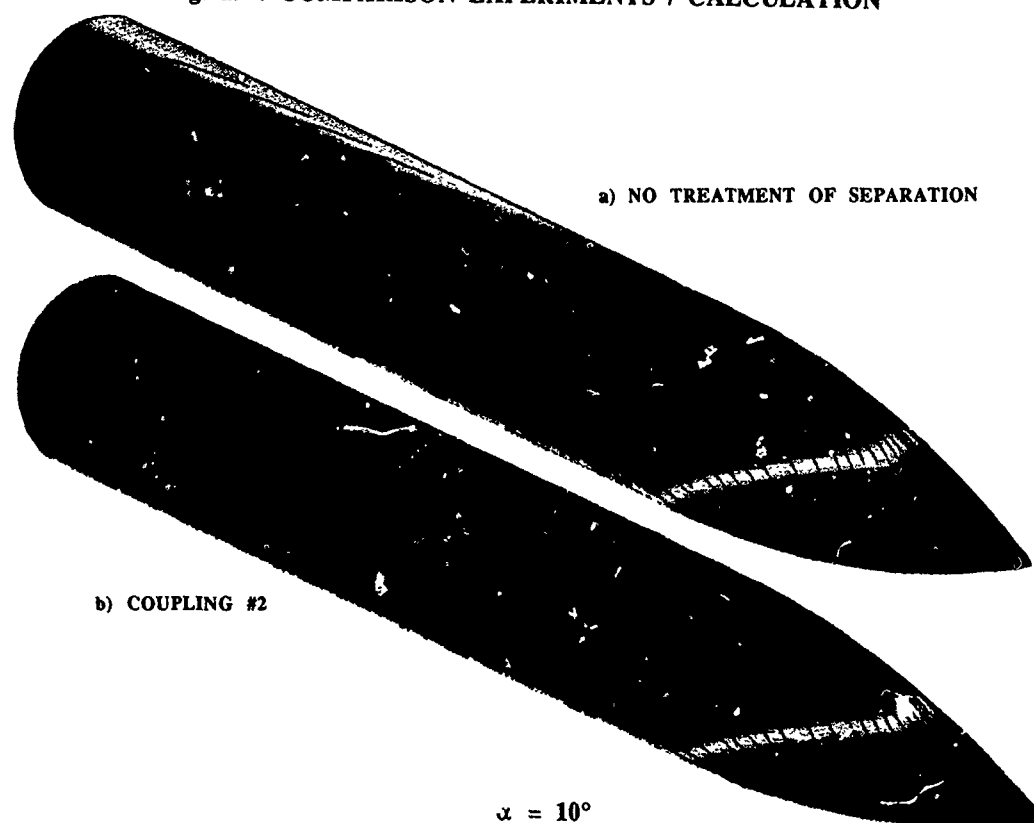


Fig. 20 : CALCULATED PRESSURE AND SKIN-FRICTION LINES

# ASYMMETRIC SUPERSONIC FLOW AROUND CONES WITH NONCIRCULAR SECTIONS

Osama A. Kandil

Professor, Department of Mechanical Engineering and Mechanics

Tin-Chee Wong

Graduate Research Assistant, Same Department

Old Dominion University, Norfolk, VA 23529, USA

C. H. Liu

Group Leader, Theoretical Flow Physics Branch

NASA Langley Research Center, Hampton, VA 23665, USA

## 1. Summary

The unsteady, compressible, single and double thin-layer, Navier-Stokes equations are used to solve for steady and unsteady, asymmetric, supersonic flow around pointed bodies with noncircular sections at high incidence and zero side slip. The equations are solved by using an implicit, upwind, flux-difference splitting finite-volume scheme. Since the flow is locally conical, the solutions are presented on a cross-flow plane at the axial station of unity. The grid is generated by using a modified Joukowski transformation. The computational applications cover noncircular sections with elliptic and diamond shapes. Unsteady asymmetric vortex shedding has been captured at large angles of attack. It is shown that for the same flow conditions and same cross-section fineness ratio, the diamond-section cones develop less flow asymmetry than the elliptic-section cones. Passive control of flow asymmetry has been also demonstrated computationally.

## 2. Preface

Very recently, the problem of asymmetric vortex flow about slender bodies and wings in the high-angle-of-attack range has received considerable attention by researchers in the numerical-simulation area<sup>1-5</sup> and by researchers in the experimental-study area<sup>6-12</sup>. The problem is of vital importance to the dynamic stability and controllability of missiles and fighter aircraft. When flow asymmetry develops, it produces side forces, asymmetric lifting forces and corresponding yawing, rolling and pitching moments that might be larger than those available by the control system of the vehicle.

The onset of flow asymmetry occurs when the relative incidence (ratio of angle of attack to nose semi-apex angle) of pointed forebodies exceeds certain critical values. At these critical values of relative incidence, flow asymmetry develops due to natural and/or forced disturbances. The origin of natural disturbances may be a transient side slip, an acoustic disturbance, or likewise disturbance of short duration. The origin of forced disturbances is geometric perturbations due to imperfections in the nose geometric symmetry or likewise disturbances of permanent nature. In addition to the relative incidence as one of the determinable parameters for the onset of flow asymmetry, the freestream Mach number, Reynolds number and shape of the body-cross sectional area are important determinable parameters.

In an attempt to simulate asymmetric vortex flow around an ogive-cylinder body at an angle of attack of 40°, a

Mach number of 0.2 and a Reynolds number of 200,000, Degani and Schiff<sup>1</sup> used the unsteady, thin-layer, Navier-Stokes equations along with an implicit scheme which is second-order accurate in time. The scheme uses central-differencing in the cross-flow plane and upwind flux-vector splitting in the streamwise direction. By introducing a forced asymmetric disturbance near the body nose in the form of a small surface jet, asymmetric flow solution was obtained. When the jet was turned off, the flow asymmetry dissipated and the flow recovered its symmetry.

In a later paper by Degani<sup>4</sup>, the same computational scheme was used to solve for the flow around the same ogive-cylinder body over a wide range of angle of attack;  $\alpha = 20^\circ - 80^\circ$ . His numerical experiments focused on investigation of the origin of vortex asymmetry. Based on his results, he suggested that the flowfield around slender bodies could be divided into three main groups depending on the angle of attack range. This range might change by  $\pm 10^\circ$ , depending on the flow conditions. In the range  $0^\circ < \alpha < 30^\circ$ , the flow was symmetric and introduction of small disturbances near the nose had a small effect on the flow symmetry. In the second range,  $30^\circ < \alpha < 60^\circ$ , the flow became steady asymmetric upon introduction of a space-fixed forced disturbance near the nose. The level of asymmetry was a function of the location and size of the forced disturbance, and for large size disturbances, the asymmetry became unsteady with very high frequency. However, when the disturbance was removed the flow recovered its symmetric shape. He attributed the origin of asymmetry to a convective-type-instability mechanism. In the very high range,  $60^\circ < \alpha < 80^\circ$ , the flow became unsteady with vortex shedding upon introduction of a small transient disturbance with short duration. He attributed the origin of flow unsteadiness and vortex shedding to an absolute-type-instability mechanism. In that range of angle of attack, he also showed that the convective-type-instability mechanism was possible upon introduction of a space-fixed disturbance near the nose. Although this investigation revealed good tentative conclusions, there are several remaining questions to be addressed, which are related to the scheme dissipative effects, particularly in the cross-flow planes, and the grid fineness and its resolution of the disturbance growth.

The present authors<sup>3</sup> used the unsteady, thin-layer, Navier-Stokes equations along with two different implicit schemes to simulate asymmetric vortex flows around cones with different cross-section shapes. The numerical investigation was focused on a 5°-semiapex angle circular cone. A local, conical flow was assumed. The



first implicit scheme was an upwind, flux-difference splitting, finite-volume scheme and the second one was a central-difference, finite-volume scheme. Keeping the Mach number and Reynolds number constants at 1.8 and  $10^5$ , respectively, the angle of attack was varied from  $10^\circ$  to  $30^\circ$ . At  $\alpha = 10^\circ$ , a steady symmetric solution was obtained and the results of the two schemes were in excellent agreement. At  $\alpha = 20^\circ$  and irrespective of the type or level of the disturbance, a steady asymmetric solution was obtained and the results of the two schemes were in excellent agreement. Two types of flow disturbances were used; a random round-off error or a random truncation-error disturbance and a controlled transient side-slip disturbance with short duration. For the controlled transient side-slip disturbance the solution was unique, and for the uncontrolled random disturbance the solution was also unique with the exception of having the same asymmetry changing sides on the cone. At  $\alpha = 30^\circ$ , an unsteady asymmetric solution with vortex shedding was obtained, and the vortex shedding was perfectly periodic. Next, the angle of attack was kept fixed at  $20^\circ$  and the Mach number was increased from 1.8 to 3.0. The solutions showed that the asymmetry become weaker as the Mach number is increased. The flow recovered its symmetry when the Mach number reached 3.0. Selected solutions of steady and unsteady asymmetric flows have been also presented for cones with elliptic and diamond cross-sectional areas. Passive control of the flow asymmetry has been tentatively demonstrated by using a fin on the leeward side of the body along the plane of geometric symmetry.

Sicilari<sup>5</sup> used the unsteady, Navier-Stokes equations with a multigrid, central-difference, finite-volume scheme to solve for steady asymmetric conical flows around cones with elliptic, diamond and biparabolic sections. He addressed steady-flow problems similar to those of the present authors in reference<sup>3</sup>. He considered the flow around circular cones with semi-apex angles of  $5^\circ$ ,  $6^\circ$ ,  $7^\circ$  and  $8^\circ$  at an angle of attack of  $20^\circ$  and a Reynolds number of  $10^5$ . Varying the Mach number from 1.4 to 3.0 with a step of 0.4, he showed that the flow recovered its symmetry as the Mach number increased. The higher the semi-apex angle was, the lower the Mach number was, for the flow to recover its symmetry. Fixing the Mach number at 1.8, the angle of attack at  $20^\circ$ , the Reynolds number at  $10^5$  and the semi-apex angle at  $5^\circ$ , he decreased the cross-section fineness ratio (ratio of width to length) for different cross-sectional shapes. He showed that the flow recovered its symmetry at a fineness ratio of 0.4 for the elliptic-section cone, at 0.6 for the biparabolic-section cone and at 0.6 for the diamond-section cone.

Experimental research efforts have also been directed to control asymmetric flows for eliminating or attenuating the asymmetric forces and the resulting moments by using either passive-control<sup>13-15</sup> or active control<sup>16-18</sup> methods. Passive control methods include the use of a vertical fin on the leeward side along the plane of geometric symmetry<sup>13</sup>, the use of fixed or movable forebody strakes<sup>14,17</sup>, or the use of a rotatable forebody tip having variable cross section; from a circular shape at its base to an elliptic shape at its tip<sup>15</sup>. Active control methods primarily include the use of blowing ports

with various blowing rates and directions on the forebody surface<sup>16,17</sup>. Computational simulations have also been used to study the effectiveness of both passive<sup>3</sup> and active control methods<sup>18</sup>.

In this paper, we focus on the steady and unsteady asymmetric conical-flow prediction and control for flows around cones with diamond and elliptic cross sections. The unsteady, compressible, single and double thin-layer, Navier-Stokes equations are used along with an implicit, upwind, flux-difference splitting, finite-volume solver.

### 3. Formulation

#### 3.1 Governing Equations

The three-dimensional compressible viscous flow around the body is governed by the conservative form of the dimensionless, unsteady, compressible, double thin-layer Navier-Stokes equations. In terms of time-independent body-conformed coordinates  $\xi^1$ ,  $\xi^2$  and  $\xi^3$ , the equations are given

$$\frac{\partial \bar{Q}}{\partial t} + \frac{\partial \bar{E}_s}{\partial \xi^s} - \frac{\partial (\bar{E}_v)_2}{\partial \xi^2} - \frac{\partial (\bar{E}_v)_3}{\partial \xi^3} = 0, s = 1, 2, 3 \quad (1)$$

where

$$\bar{Q} = \frac{\bar{q}}{J} = \frac{1}{J} [\rho, \rho u_1, \rho u_2, \rho u_3, \rho e]^t \quad (2)$$

$\bar{E}_m \equiv$  inviscid flux

$$\begin{aligned} &= \frac{1}{J} [\partial_k \xi^m \bar{E}_k]^t \\ &= \frac{1}{J} [\rho U_m, \rho u_1 U_m + \partial_1 \xi^m p, \rho u_2 U_m \\ &\quad + \partial_2 \xi^m p, \rho u_3 U_m + \partial_3 \xi^m p, (\rho e + p) U_m]^t, \\ &\quad m = 1, 2, 3 \end{aligned} \quad (3)$$

$(\bar{E}_v)_2 \equiv$  viscous and heat-conduction flux in  $\xi^2$  direction

$$\begin{aligned} &= \frac{1}{J} [0, \partial_k \xi^2 \tau_{k1}, \partial_k \xi^2 \tau_{k2}, \partial_k \xi^2 \tau_{k3}, \\ &\quad \partial_k \xi^2 (u_n \tau_{kn} - q_k)]^t \end{aligned} \quad (4)$$

$(\bar{E}_v)_3 \equiv$  viscous and heat-conduction flux in  $\xi^3$  direction

$$\begin{aligned} &= \frac{1}{J} [0, \partial_k \xi^3 \tau_{k1}, \partial_k \xi^3 \tau_{k2}, \partial_k \xi^3 \tau_{k3}, \\ &\quad \partial_k \xi^3 (u_n \tau_{kn} - q_k)]^t \end{aligned} \quad (5)$$

$$U_m = \partial_k \xi^m u_k \quad (6)$$

The first element of the three momentum elements of Eq. (5) is given by

$$\partial_k \xi^3 \tau_{k1} \equiv \frac{M_\infty \mu}{P_e} \left( \psi \partial_1 \xi^3 + \phi \frac{\partial u_1}{\partial \xi^3} \right) \quad (7)$$

where

$$\phi = \partial_k \xi^3 \partial_k \xi^3 \quad \psi = \frac{1}{3} \partial_k \xi^3 \frac{\partial u_k}{\partial \xi^3} \quad (8)$$

The second and third elements of the momentum elements are obtained by replacing the subscript 1, everywhere in Eq. (7), with 2 and 3, respectively. The last element of Eq. (5) is given by

$$\partial_k \xi^3 (u_n \gamma_{kn} - q_k) = \frac{M_\infty \mu}{Re} \left\{ \psi W + \phi \left[ \frac{1}{2} \frac{\partial}{\partial \xi^3} (u_1^2 + u_2^2 + u_3^2) + \frac{1}{(\gamma - 1) Pr} \frac{\partial (a^2)}{\partial \xi^3} \right] \right\} \quad (9)$$

where

$$W = \partial_n \xi^3 u_n \quad (10)$$

For Eq. (4), in the case of double thin-layer Navier-Stokes equations, the elements are given by equations similar to Eqs. (7)-(10) with the exception of replacing  $\xi^3$  by  $\xi^2$ . The double thin-layer, Navier-Stokes equations are used only for the passive control of flow asymmetry since the existence of the fin creates a second thin layer which is perpendicular to the cone thin layer. The reference parameters for the dimensionless form of the equations are  $L$ ,  $a_\infty$ ,  $L/a_\infty$ ,  $\rho_\infty$  and  $\mu_\infty$  for the length, velocity, time, density and molecular viscosity, respectively. The Reynolds number is defined as  $Re = \rho_\infty V_\infty L / \mu_\infty$ , and the pressure,  $p$ , is related to the total energy per unit mass and density by the gas equation

$$p = (\gamma - 1) \rho \left[ e - \frac{1}{2} (u_1^2 + u_2^2 + u_3^2) \right] \quad (11)$$

The viscosity is calculated from the Sutherland law

$$\mu = T^{3/2} \left( \frac{1 + C}{T + C} \right), \quad C = 0.4317 \quad (12)$$

and the Prandtl number  $Pr = 0.72$ .

In Eqs. (1)-(10), the indicial notation is used for convenience. Hence, the subscripts  $k$  and  $n$  are summation indices, the superscript or subscript  $s$  is a summation index and the superscript  $m$  is a free index. The range of  $k$ ,  $n$ ,  $s$  and  $m$  is 1-3, and  $\partial_k \equiv \frac{\partial}{\partial \xi_k}$ .

### 3.2 Boundary and Initial Conditions

Boundary conditions are explicitly implemented. They include inflow-outflow conditions and solid-boundary conditions. At the plane of geometric symmetry, periodic conditions are used for symmetric or asymmetric flow applications on the whole computational domain (right and left domains). At the far-field inflow boundaries, freestream conditions are specified, while at the far-field outflow boundaries first-order extrapolation from the interior points is used. On the solid boundary, the no-slip and no-penetration conditions are enforced;  $u_1 = u_2 = u_3 = 0$  and the normal pressure gradient is set equal to zero. For the temperature, the adiabatic boundary condition is enforced on the solid boundary. The initial conditions correspond to the uniform flow with  $u_1 = u_2 = u_3 = 0$  on the solid boundary.

For the passive control applications using a vertical fin in the leeward plane of geometric symmetry, solid-boundary conditions are enforced on both sides of the fin.

### 4. Highlights of the Computational Scheme

The computational scheme used to solve the governing equations is an implicit, upwind, flux-difference splitting, finite-volume scheme. It employs the flux-difference splitting scheme of Roe. The Jacobians matrices of the inviscid fluxes,  $A_s = \frac{\partial f_s}{\partial q}$ ;  $s = 1-3$ , are split into backward and forward fluxes according to the signs of the eigenvalues of the inviscid Jacobian matrices. Flux limiters are used to eliminate oscillations in the shock region. The viscous and heat-flux terms are centrally differenced. The resulting difference equation is solved using approximate factorization in the  $\xi^1$ ,  $\xi^2$  and  $\xi^3$  directions. The computational scheme is coded in the well known computer program "CFL3D".

Since the applications in this paper cover conical flows only, the three-dimensional scheme is used to solve for locally conical flows. This is achieved by forcing the conserved components of the flow vector field to be equal at two planes of  $x = 0.95$  and  $1.0$ .

### 5. Computational Applications

#### 5.1 Effect of Minimum Grid Spacing on the Asymmetric Solution

This numerical test has been carried out to ensure that the asymmetric flow solution is unique irrespective of the size of minimum grid spacing normal to the cone surface at its solid boundary,  $\Delta \xi^2$ . For this purpose, the supersonic flow around a  $5^\circ$ -semiapex circular cone at  $20^\circ$  angle of attack is considered. The freestream Mach number and Reynolds number are 1.8 and  $10^5$ , respectively. A grid of  $161 \times 81$  points in the circumferential and normal directions is generated by using a modified Joukowski transformation with a geometric series for the grid clustering. The minimum grid spacing at the solid boundary was varied in this test, while the maximum radius of the computational domain is kept at  $21 r$ , where  $r$  is the radius of the circular cone at the axial station of unity.

Three cases have been computed using  $\Delta \xi^2 = 10^{-3}$ ,  $10^{-4}$  and  $10^{-6}$ . Figure 1 shows the results of this case. In this figure, we show the logarithmic residual versus the number of iterations, the total-pressure-loss contours and the surface pressure versus the azimuthal angle  $\theta$ , which is measured from the leeward plane of geometric symmetry. The residual error figures show that the error reaches machine zero ( $10^{-10} - 10^{-11}$ ) in about 2,500 iterations for the first two cases and in 7,500 for the third case. Afterwards, the machine round-off error is acting as a random disturbance to the flow, and the residual error grows. The solutions are symmetric during these iterations. Then, the residual error drops down to  $10^{-13}$ ,  $10^{-10}$  and  $10^{-12}$  for the three cases, respectively, and steady asymmetric stable solutions are obtained. The solutions of the first and third cases are exactly the same, while the solution of the second case is an exact mirror image of these cases. Since the source of disturbance is a random one, it is perfectly acceptable that the solutions could be mirror images of each other.

## 5.2 Asymmetric Solutions for Diamond-Section Cones

In this section and the next one, we consider asymmetric solutions around diamond and elliptic section cones with different fineness ratio. A grid of  $161 \times 81$  points is used with a minimum spacing of  $10^{-4}$  at the solid boundary. Figure 2 shows a blow-up of these grids for the diamond and elliptic section cones. The cone angle of attack is  $25^\circ$ , the Mach number is 1.5 and the Reynolds number is  $10^5$ .

Figure 3 shows the solution for a diamond-section cone with fineness ratio of 0.8. The residual-error curve shows that the source of disturbance is a random truncation error and that the asymmetric solution is obtained after 5,000 iterations. The lift coefficient curve shows that a small increase in the lift develops after the asymmetric solution is obtained. The cross-flow velocity directions and total-pressure-loss contours show the primary vortices and secondary vortices beneath them. The surface pressure curve shows the strong asymmetry effect in the ranges of  $\theta$  of  $(0-90^\circ)$  and  $(270-360)$ .

Next, the diamond-section fineness ratio has been reduced to 0.6 keeping all the other flow conditions fixed, Fig. 4. The flow asymmetry took larger number of iterations to evolve; 12,500 iterations. The solution shows that the asymmetry is weak.

## 5.3 Asymmetric Solutions for Elliptic-Section Cones

Figure 5 shows the solution for an elliptic-section cone with fineness ratio of 0.8. The residual-error curve shows that the solution produces a symmetric flow through the first 5,000 time steps. Afterwards, the solution shows a transient unsteady flow response for 2,500 time steps which are followed by an unsteady, perfectly-periodic, vortex-shedding solution. The lift coefficient curve shows the same solution as that of the residual-error curve. This case is carried out using time-accurate stepping with  $\Delta t = 10^{-3}$ .

In Fig. 5, we also show snapshots of the total-pressure-loss contours and surface-pressure coefficients at the time steps of 12,000; 12,500; 13,000; 13,500; 14,000 and 14,500. We also show snapshots of the cross flow velocity at 12,000; 12,500 and 13,000. The solutions at  $n = 12,000$  and 14,500 are mirror images of each other which confirms that the solution is periodic. The period of oscillation is  $5,000 \times 10^{-3} = 5$  which corresponds to a shedding frequency of 1.257. At  $n = 12,000$ , the total-pressure-loss contour shows that the right-side vortex is stretched having two vortices; one is at the top and the second one is below it. In addition, a secondary vortex is seen at the surface. The left-side vortex has expanded to the right with two vortices beneath it. At  $n = 12,500$ , the top vortex on the right side has been almost shed while the one below it is expanding. At  $n = 13,000$ , the top vortex on the right side has been shed and convected with the flow while the vortex below it is expanding to the left. As times passes, the vortex on the left side is stretching upwards and the vortex on the right side is expanding to the left, as seen from the snapshots at 13,000; 13,500; 14,000. At  $n = 14,500$ , the vortices on the left

side and right side become mirror images of those on the right side and left side, respectively, at  $n = 12,000$ .

Figure 6 shows the solution for an elliptic-section cone with a fineness ratio of 0.6. It is seen that the asymmetric solution is steady and that the symmetry is strong. It is much stronger than that of the diamond-section cone for the same flow conditions and same section fineness ratio, see Fig. 4.

## 5.4 Passive Control of Flow Asymmetry for a Diamond-Section Cone

In Figure 7, we show the results of passive control of flow asymmetry for a diamond-section cone of fineness ratio of 0.8. This is the flow case considered previously in Fig. 3. The control of flow asymmetry has been achieved by inserting a fin in the leeward plane of geometric symmetry with a fin height,  $h$ , equal to 0.75 the local width of the section. Here, the double thin-layer Navier-Stokes equations have been used to obtain the solution. The jump of the residual error curve at the 5000 iteration step is due to switching the solver from a single thin-layer, Navier-Stokes equations to a double thin-layer, Navier-Stokes equations.

## 5.5 Passive Control of Flow Asymmetry for An Elliptic-Section Cone

Figures 8 and 9 show the results of passive control of flow asymmetry for an elliptic-section cone of fineness ratio of 0.6. This is the flow case considered previously in Fig. 5. Two fin heights of 0.75 and 1.0 the local minor axis have been considered. Figure 8 shows that with  $h = 1.5a$  ( $= 0.75$  local minor axis), the flow asymmetry is still persistent almost at the same strength as that of Fig. 5. Since the fin height is shorter than the height of the free-shear layer on the right side, the disturbance is communicated between the right and left sides. In Fig. 9, we show that when  $h$  is increased to  $2a$  ( $= 1.0$  local minor axis), the flow recovered its symmetry.

One should note that the elliptic-section cones require taller fences than those required by the diamond-section cones with the same fineness ratio and same flow conditions in order to obtain symmetric flows.

## 6. Concluding Remarks

This paper presents steady and unsteady asymmetric supersonic solutions for locally conical flows around cones with diamond and elliptic cross sections. The unsteady, compressible, single or double thin-layer, Navier-Stokes equations have been used along with an implicit, upwind, flux-difference splitting, finite-volume scheme. Several issues related to the asymmetric flow solutions have been addressed. It has been shown that a unique asymmetric flow solution is obtained irrespective of the size of the minimum grid spacing at the solid boundary. The asymmetry could reverse sides due to the random nature of the disturbance. It has been also shown that for the same flow conditions and same section fineness ratio, diamond-section cones with sharp edges have less flow asymmetry than those of the elliptic-section cones.

Moreover, it has been shown that passive control of flow asymmetry of diamond-section cones requires fence

heights that are not necessarily equal to the local section width. On the other hand, passive control of flow asymmetry of circular<sup>3</sup> and elliptic-section cones require fences with heights that are, at least, equal to the local section width. Again, we have also shown that unsteady periodic asymmetric flow with vortex shedding has been predicted.

#### 7. Acknowledgement

This research work is supported by the NASA Langley Research Center under grant No. NAS1-18584-71.

#### 8. References

1. Degani, D. and Schiff, L. B., "Numerical Simulation of the Effect of Spatial Disturbance on Vortex Asymmetry," AIAA Paper 89-0340, January 1989.
2. Kandil, O. A., Weng, T. C. and Liu, C. H., "Navier-Stokes Computations of Symmetric and Asymmetric Vortex Shedding Around Slender Bodies," AIAA-89-3397-CP, August 1989, pp. 433-443.
3. Kandil, O. A., Wong, T. C. and Liu, C. H., "Prediction of Steady and Unsteady Asymmetric Flows Around Cones," AIAA 90-0598, January 1990.
4. Degani, D., "Numerical Investigation of the Origin of Vortex Asymmetry," AIAA 90-0593, January 1990.
5. Siclari, M. J., "Asymmetric Separated Flows at Supersonic Speeds," AIAA 90-0595, January 1990.
6. Peake, D. J., Fisher, D. F. and McRae, D. S., "Flight, Wind Tunnel and Numerical Experiments with a Slender Cone at Incidence," *AIAA Journal*, Vol. 20, No. 10, October 1979, pp. 1338-1345.
7. Lamont, P. J., "Pressures Around an Inclined Ogive Cylinder with Laminar, Transitional, or Turbulent Separation," *AIAA Journal*, Vol. 20, No. 11, November 1980, pp. 1492-1499.
8. Lamont, P. J., "The Complex Asymmetric Flow Over a 3.5D Ogive Nose and Cylindrical Afterbody at High Angles of Attack," AIAA Paper 82-0053, January 1982.
9. Yanta, W. J. and Wardlaw, Jr., "The Secondary Separated Region on a Body at High Angles-of-Attack," AIAA Paper 82-0343, January 1982.
10. Keener, E. R. and Chapman, G. R., "Similarity in Vortex Asymmetries Over Slender Bodies and Wings," *AIAA Journal*, Vol. 15, No. 9, September 1977, pp. 1370-1372.
11. Rediniotis, O., Stapountzis, H. and Telinois, D. P., "Vortex Shedding Over Nonparallel Edges," VPI&SU Engineering Report, VPI-E-88-39, December 1988.
12. Zilliac, G., Degani, D. and Tobak, "Asymmetric Vortices on a Slender Body of Revolution," AIAA 90-0388, January 1990.
13. Stahl, W., "Suppression of Asymmetry of Vortex Flow Behind a Circular Cone at High Incidence," AIAA 89-3372-CP, August 1989, pp. 231-236.
14. Ng, T. T., "On Leading Edge Vortex and Its Control," AIAA 89-3346-CP, August 1989, pp. 1-15.
15. Moskovitz, C., Hall, R. and DeJarnette, "Experimental Investigation of a New Device to Control the Asymmetric Flowfield on Forebodies at Large Angles of Attack," AIAA 90-0069, January 1990.
16. Skow, A. M. and Peake, D. J., "Control of the Forebody Vortex Orientation by Asymmetric Air Injection, (Part B) — Details of the Flow Structure," AGARD-LS-121, High Angle-of-Attack Aerodynamics, August 1982, pp. 10.1-10.22.
17. Ng, T. T., "Aerodynamic Control of NASP-Type Vehicles Through Vortex Manipulation," AIAA 90-0594, January 1990.
18. Tavella, D. A., Schiff, L. B. and Cummings, R. M., "Pneumatic Vortical Flow Control at High Angles of Attack," AIAA 90-0098, January 1990.

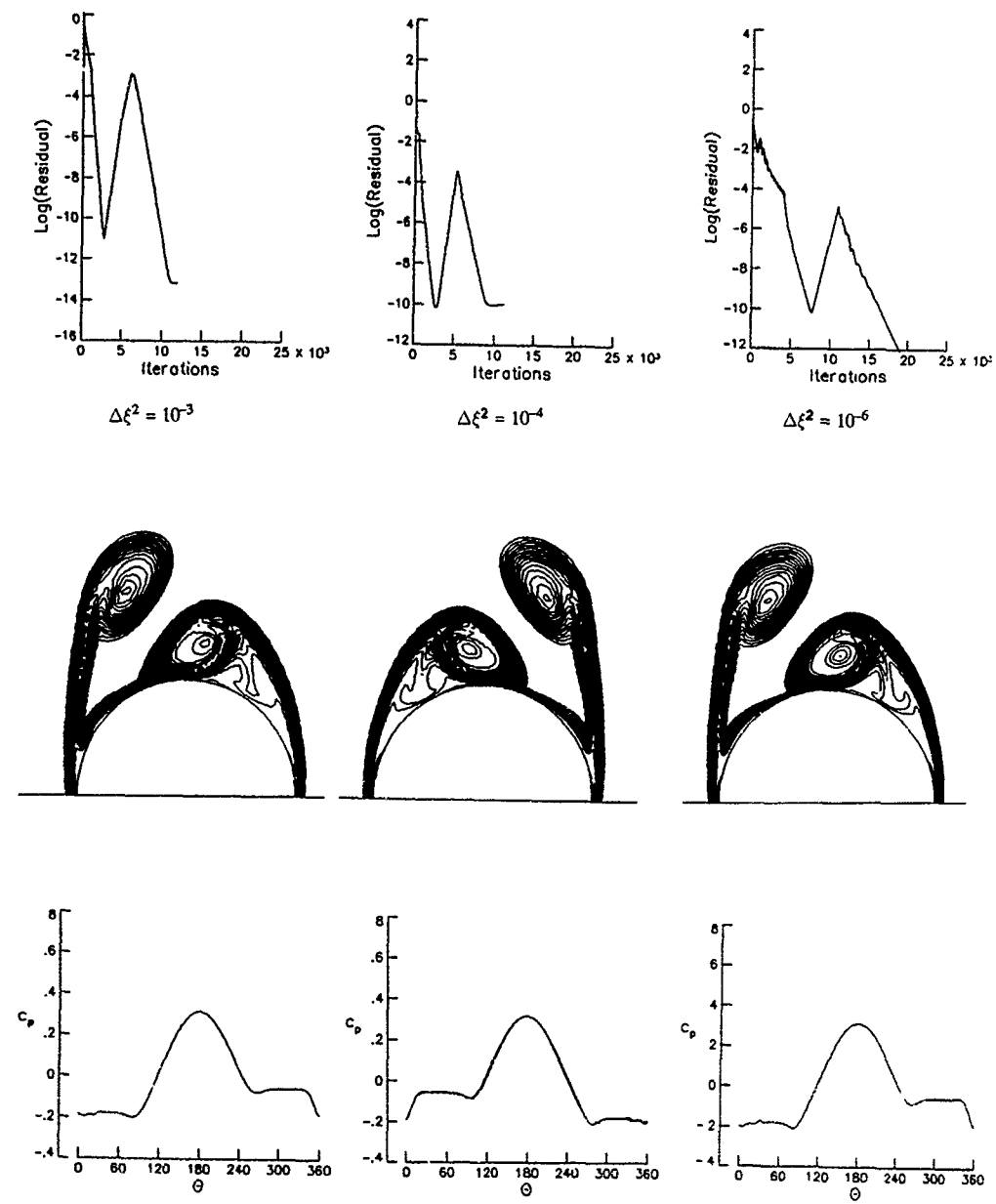


Figure 1. Effect of the minimum space on the asymmetric solution,  $\alpha = 20^\circ$ ,  $M_\infty = 1.8$ ,  $Re = 10^5$ ;  $\Delta\xi_{min}^2 = 10^{-3}$ ,  $10^{-4}$  and  $10^{-6}$ .

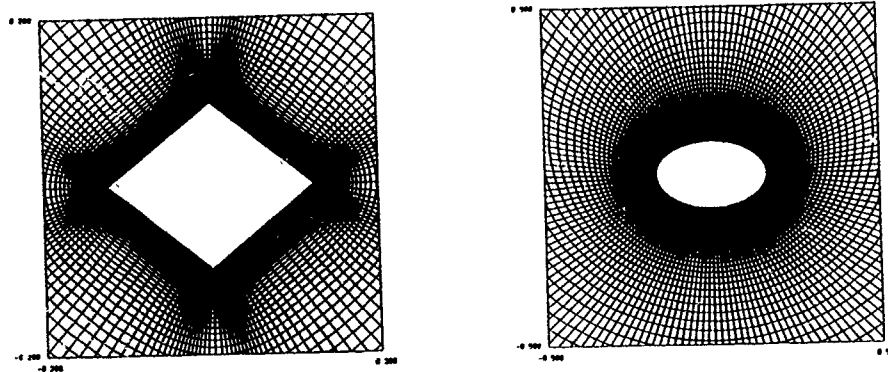


Figure 2. Typical grids for a diamond and an elliptic section,  $161 \times 81$ ,  $\Delta \epsilon_{\min}^2 = 10^{-4}$ .

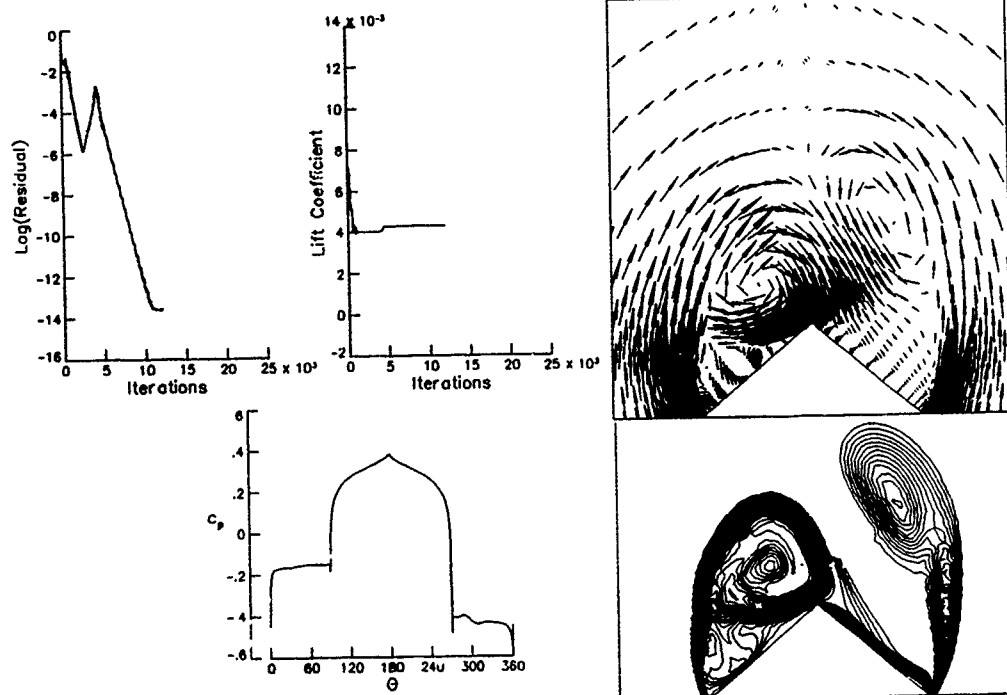


Figure 3. Steady asymmetric flow solution for a cone with diamond section,  $\alpha = 25^\circ$ ,  $M_\infty = 1.5$ ,  $Re = 10^5$ ,  $f_t = 0.8$ .

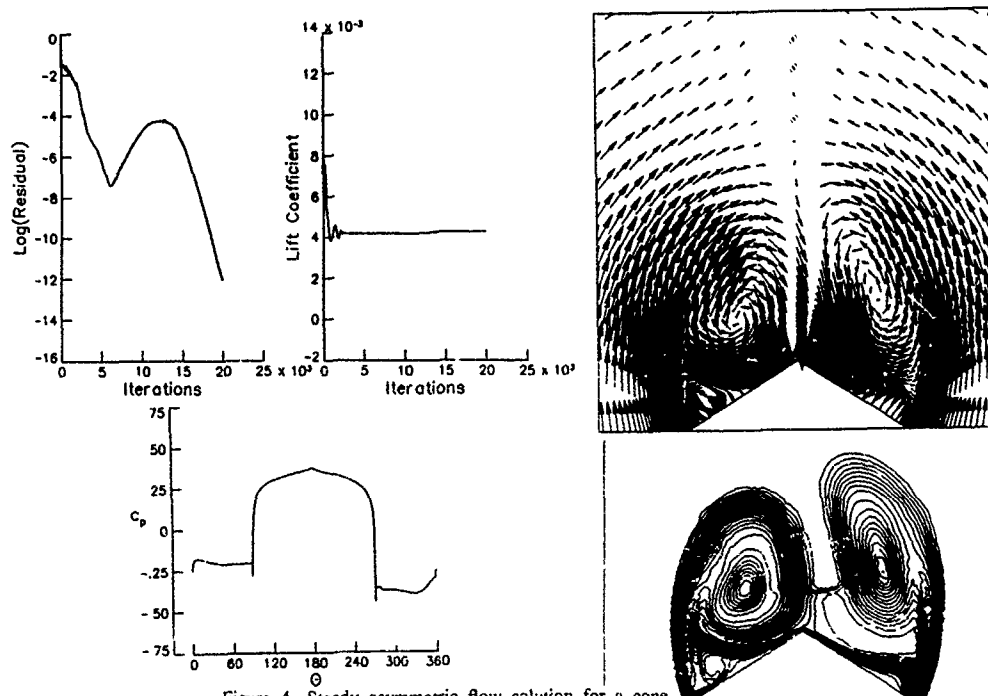
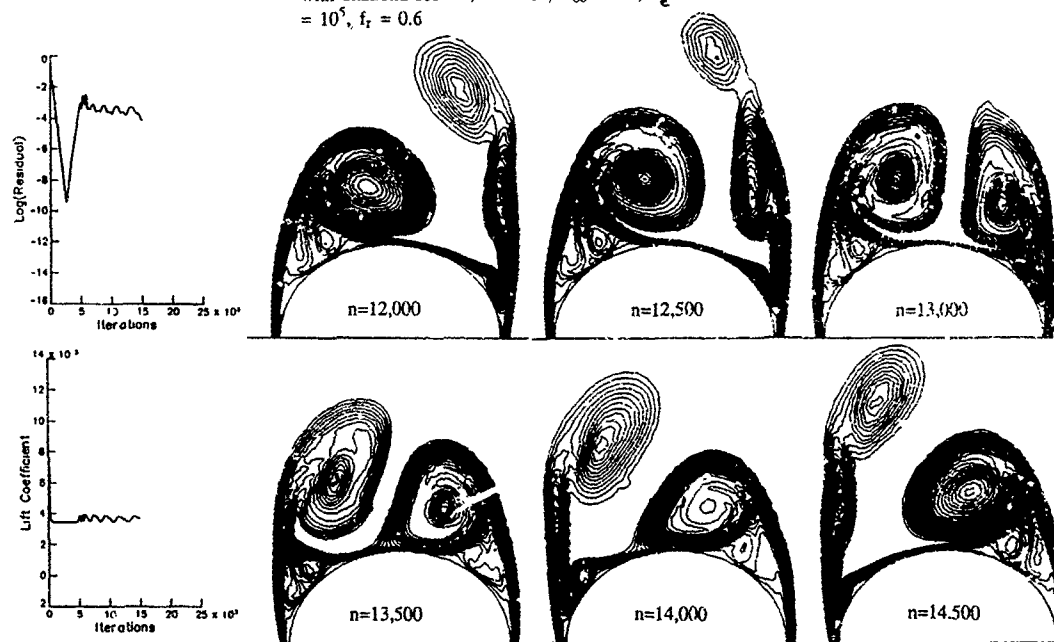


Figure 4 Steady asymmetric flow solution for a core with diamond section,  $\alpha = 25^\circ$ ,  $M_\infty = 1.5$ ,  $P_e = 10^5$ ,  $f_r = 0.6$



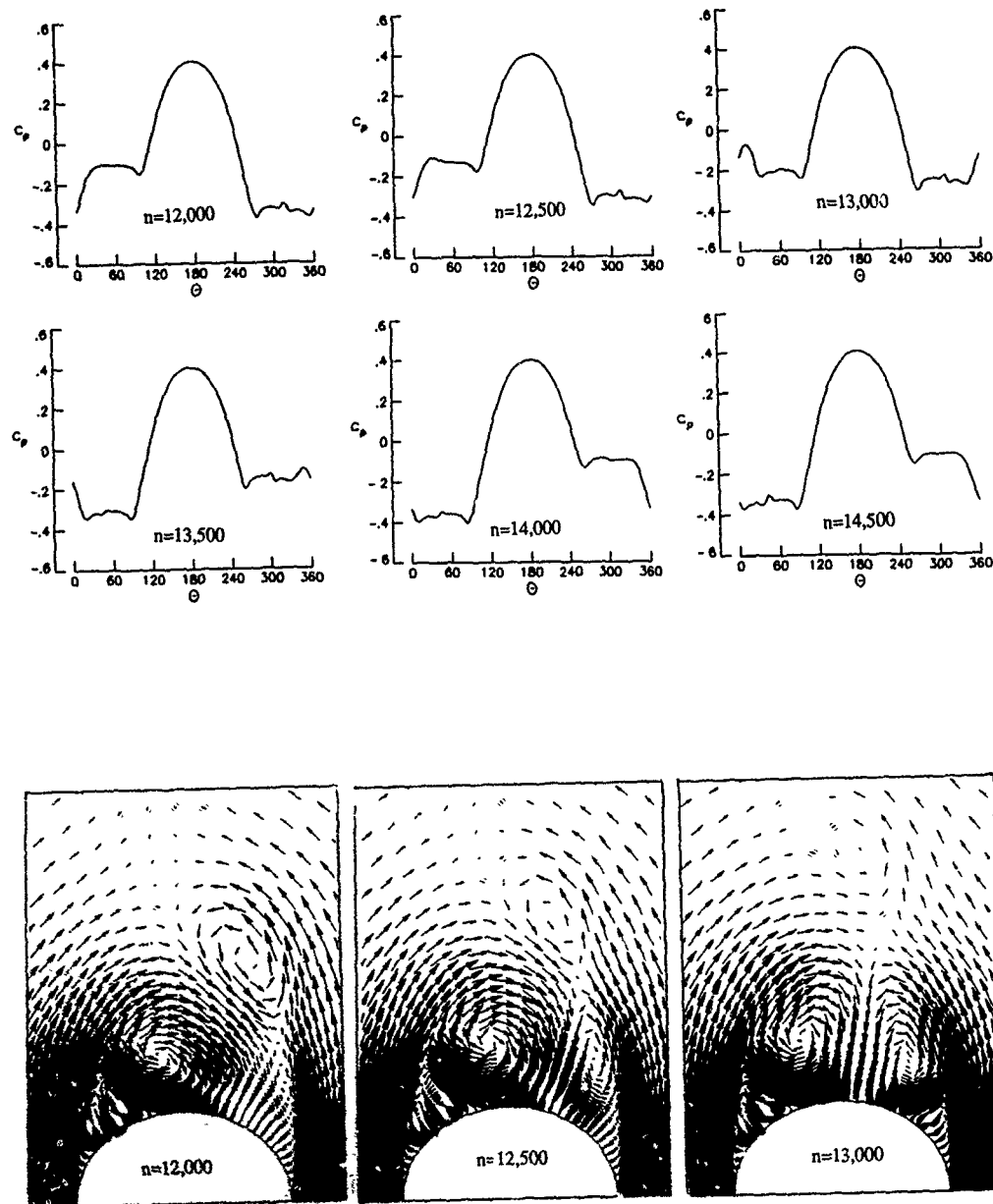


Figure 5. Unsteady vortex shedding solution for a cone with elliptic section,  $\alpha = 25^\circ$ ,  $M_\infty = 1.5$ ,  $R_e = 10^5$ ,  $f_t = 0.8$ ,  $\Delta t = 10^{-3}$ .



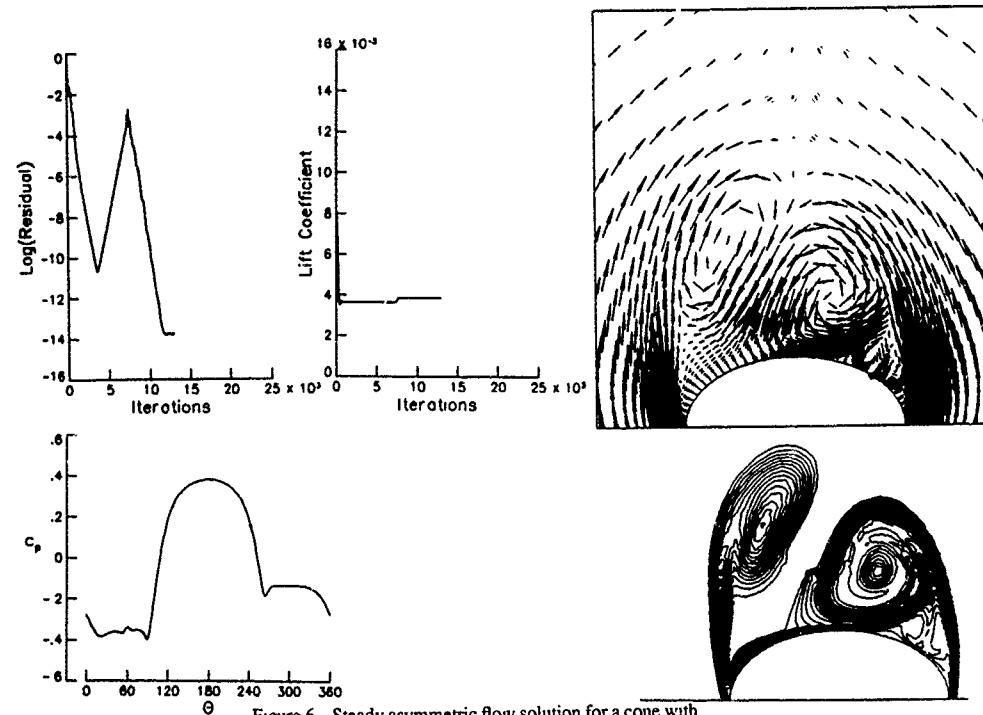


Figure 6 Steady asymmetric flow solution for a cone with elliptic section,  $\alpha = 25^\circ$ ,  $M_\infty = 1.5$ ,  $R_e = 10^5$ ,  $f_t = 0.6$ .

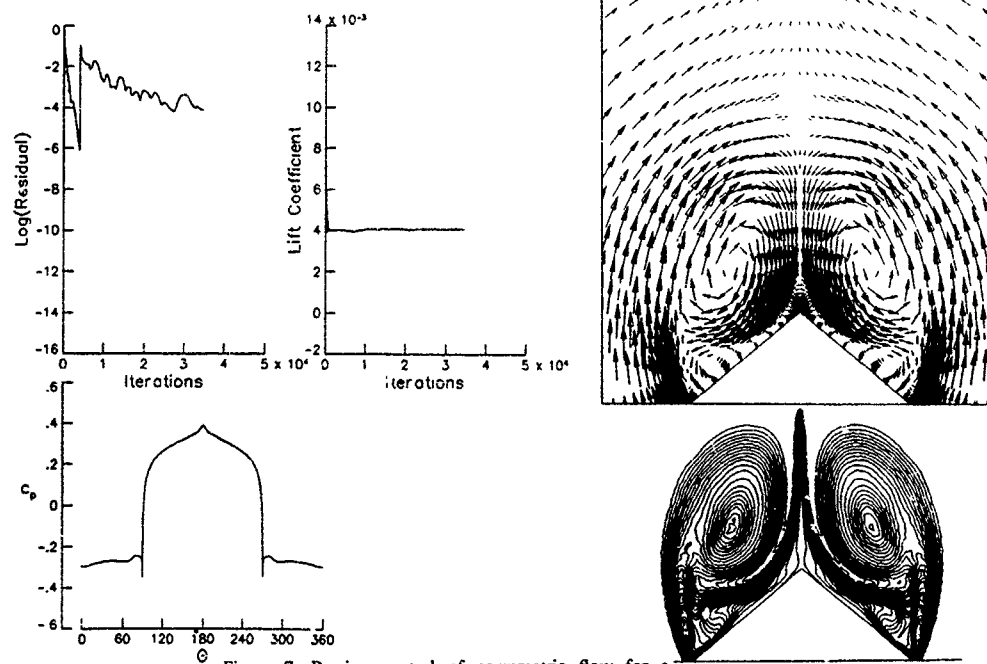


Figure 7. Passive control of asymmetric flow for a diamond-section cone using a vertical fin in the leeward geometric plane of symmetry,  $\alpha = 25^\circ$ ,  $M_\infty = 1.5$ ,  $R_e = 10^5$ ,  $f_t = 0.8$ ,  $h = 1.5a$  ( $a \equiv$  one half the minor axis).

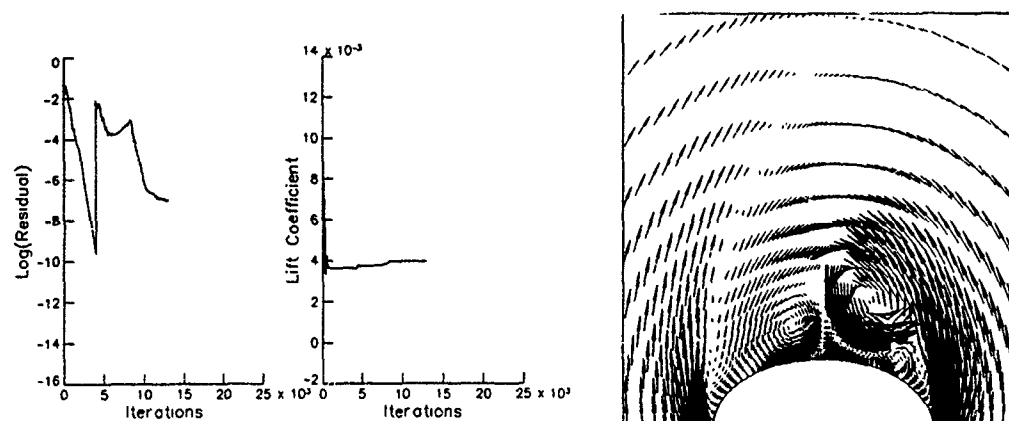


Figure 8. Passive control of asymmetric flow for an elliptic-section cone using a vertical fin in the leeward geometric plane of symmetry,  $\alpha = 25^\circ$ ,  $M_\infty = 1.5$ ,  $Re = 10^5$ ,  $f_r = 0.6$ ,  $h = 1.5a$ .

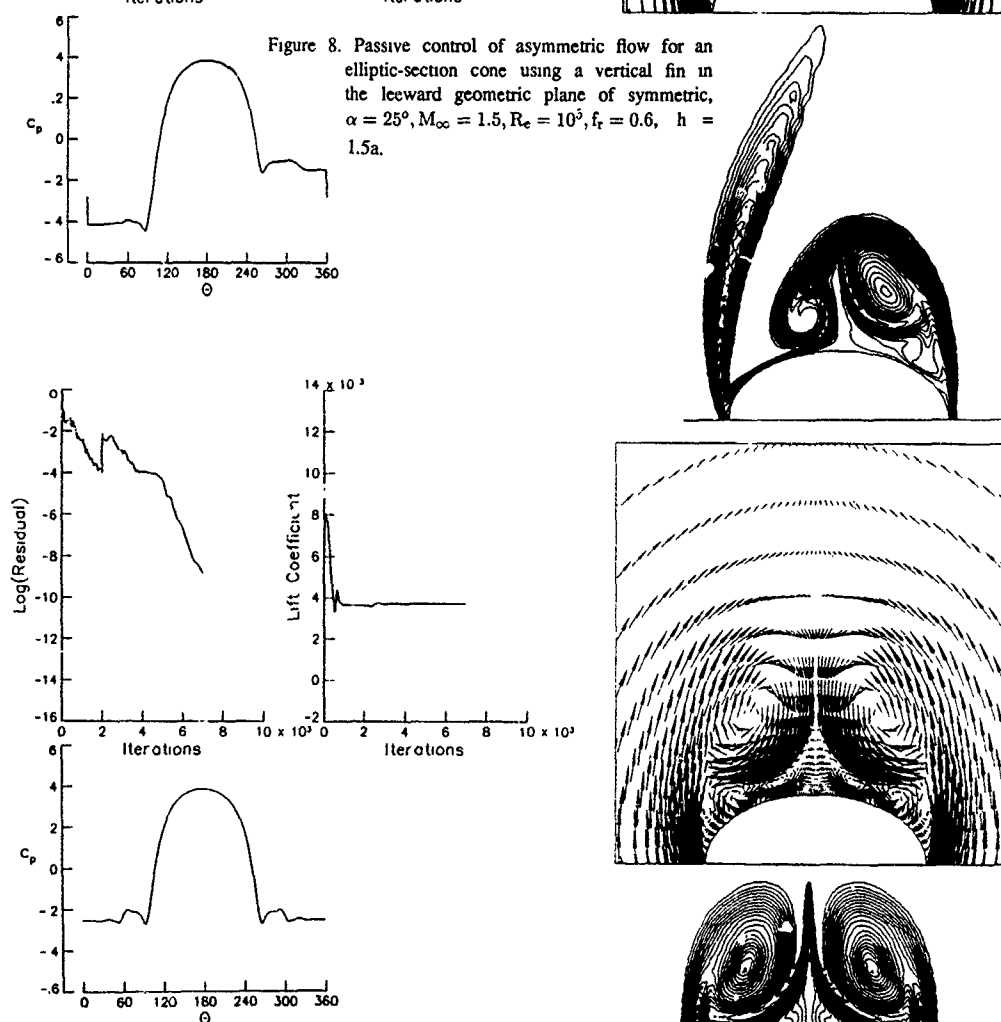


Figure 9. Passive control of asymmetric flow for an elliptic-section cone using a vertical fin in the leeward geometric plane of symmetry,  $\alpha = 25^\circ$ ,  $M_\infty = 1.5$ ,  $Re = 10^5$ ,  $f_r = 0.6$ ,  $h = 2a$ .

COMPARAISON DE DIFFERENTES METHODES DE CALCUL  
APPLIQUEES A UN FUSELAGE DE SECTION LENTICULAIRE

par

P. D'ESPINEY

Office National d'Etudes et de Recherches Aéronautiques  
Boite Postale N° 72 - 92322 Chatillon CEDEX  
FRANCE

RESUME

Un corps de section non circulaire, représentatif de formes non conventionnelles de missiles, a fait l'objet de mesures dans les souffleries de l'ONERA pour des nombres de Mach compris entre 0,4 et 4,5, jusqu'à 20° d'incidence et 10° de dérapage. La banque de données constituée comporte essentiellement des mesures de pression pariétale et quelques mesures dans le champ à Mach 2 à 10° et 20° d'incidence.

Le but de cet article est de présenter, en incidence pure, des comparaisons calcul-expérience effectuées avec différents codes de calcul : SHABP (méthode semi-empirique), ECOPAN, HISSS (méthodes de singularités) et FLU3C (méthode EULER).

Après un bref rappel des particularités des codes de calcul, les avantages et inconvénients, des points de vue de la précision et du temps de calcul, sont ensuite dégagés.

ABSTRACT

Measurements on a non-circular body were made in the ONERA wind tunnels. This model, representative of non-conventional missile shapes, was studied for Mach numbers from 0.4 to 4.5, angles of attack up to 20° and sideslip angles up to 10°. The data base mainly consists of wall static pressure measurements but also of flowfield measurements at Mach number 2 for angles of attack 10° and 20°.

The present paper reports comparisons between calculations and experiments obtained with different codes : SHABP (a semi-empirical prediction method), ECOPAN, HISSS (panel methods) and FLU3C (Euler method).

After a brief survey of the codes, their advantages and drawbacks in terms of accuracy and cost-time are shown.

1. INTRODUCTION

L'estimation des caractéristiques aérodynamiques globales d'un missile de forme classique est relativement aisée, grâce en particulier aux codes semi-empiriques. En revanche, la définition de formes nouvelles, telles que celles relatives aux missiles futurs, avec des fuselages de section non circulaire, nécessite l'utilisation de codes de calcul plus sophistiqués [1].

Dans ce cadre, et avec l'appui des Services Officiels français, l'ONERA s'est chargé de constituer une banque de données expérimentales (pressions pariétales, champ des vecteurs vitesse) sur un fuselage de section quasi-lenticulaire afin d'évaluer différents codes de calcul, aussi bien au niveau des efforts globaux, qu'au niveau des phénomènes locaux.

La configuration retenue (figure 1) présente les particularités suivantes : d'une part une section non circulaire avec deux arêtes latérales fixant le décollement en incidence pure, d'autre part un rétreint sur sa partie arrière. Elle constitue en cela un cas-test difficile pour des méthodes de calcul en fluide parfait.

Les mesures effectuées jusqu'à des incidences de 20° ou des dérapages de 10°, pour différents nombres de Mach subsoniques et supersoniques, ont ainsi permis d'éprouver plusieurs types de méthodes. Celles retenues dans cette étude comparative peuvent être classées en :

- méthode semi-empirique :

• le code SHABP, développé à la Douglas Aircraft Company, regroupant des méthodes approchées ou empiriques adaptées au calcul de géométries variées en supersonique élevé et en hypersonique ;

- méthodes de singularités :

■ code ECOPAN, développé à l'ONERA pour les écoulements subsoniques, utilisant des singularités d'ordre faible de type source-doublet ;

■ code HISSS, développé par MBB pour les écoulements sub-supersoniques, utilisant une double distribution surfacique de singularités d'ordre élevé (sources à variation linéaire et doublets à variation quadratique) associée à une double condition aux limites (externe et interne) ;

- méthode EULER

■ code FLU3C, développé à l'ONERA, utilisant une formulation conservatrice de type volumes finis avec un schéma explicite décentré, précis au second ordre.

Après une brève description des différentes méthodes de calcul retenues, cet article présente des comparaisons calcul-expérience en incidence pure, portant sur les coefficients globaux, les répartitions des charges et les structures de l'écoulement tourbillonnaire.

## 2. MAQUETTES ET CONDITIONS D'ESSAI

Deux maquettes, représentatives de la même configuration illustrée par le maillage de calcul de la figure 1, ont été utilisées pour les mesures aérodynamiques.

- La première maquette, de longueur 1200 mm, a servi aux mesures des pressions pariétales dans les souffleries S2MA et S3MA. Elle est équipée de 227 prises de pression réparties selon 21 sections sur l'extrados. Les essais ont été effectués pour des nombres de Mach allant de 0,4 à 4,5, jusqu'à 20° d'incidence et 10° de dérapage. Les nombres de Reynolds de soufflerie, adimensionnés suivant la longueur de la maquette, varient de 13 à 21 millions pour ces différentes conditions d'essai.

- La seconde maquette, plus petite (360 mm), a servi à des mesures du champ aérodynamique dans deux sections, la première se situant environ au milieu du corps ( $X/L = 0,571$ ) et la seconde à l'arrière au niveau du rétroint ( $X/L = 0,915$ ). Les sondages de l'écoulement, réalisés dans la soufflerie S5 de Chalais-Meudon avec une sonde à 5 trous (de 1,5 mm de diamètre), ont permis d'obtenir entre autres les cartes de pression génératrice et les champs de vitesse, pour  $Mach = 2$ ,  $\alpha = 10^\circ$  et  $20^\circ$ . Le nombre de Reynolds est d'environ 2 millions et la transition de la couche limite, naturelle ou forcée au nez du fuselage, n'a pas modifié les résultats d'essai.

## 3. CARACTERISTIQUES DES CODES DE CALCUL UTILISES

### 3.1. SHABP

Le code SHABP a été développé à la Douglas Aircraft Company dans les années 68-73 [2] pour traiter, avec un faible temps de calcul, des formes complexes en supersonique élevé et en hypersonique. Il regroupe un ensemble de méthodes de calcul approchées et empiriques simples (voir tableau n°1 de la référence 2), certaines d'entre elles tenant compte des effets visqueux, de gaz réels... etc. Le choix d'une ou plusieurs méthodes pour le calcul d'une configuration dépend à la fois de la complexité de la géométrie et des conditions de vol (Mach-incidence).

Deux maillages de la géométrie du corps doivent être utilisés lorsque l'on veut tenir compte des effets visqueux. Le premier est un maillage surfacique assez fin, adapté aux méthodes non visqueuses. Le second est un maillage très grossier sur lequel des calculs du type "couche limite de plaque plane" sont effectués. Les maillages sont définis par sous-ensembles, sur lesquels une méthode de calcul est choisie.

En général, moyennant un choix judicieux de celle-ci, SHABP estime assez correctement les coefficients globaux mais se prête mal à l'étude des phénomènes locaux. En effet, pour la plupart des méthodes de SHABP, les valeurs du  $K_p$  sont calculées de façon très simple ( $K_p$  n'est fonction que de la vitesse de l'écoulement amont et de l'angle que la facette fait avec celle-ci). Elles ne peuvent donc être utilisées qu'à des nombres de Mach élevés. Pour des nombres de Mach plus faibles, compris approximativement entre 2 et 4, il est nécessaire de prendre en compte les influences mutuelles de l'écoulement entre facettes voisines. Le code SHABP dispose de méthodes le faisant de façon rudimentaire : l'influence est limitée à la facette amont appartenant à la même ligne de courant que la facette de calcul. Celles-ci sont actuellement en cours de validation à l'ONERA et nous nous sommes restreints au calcul en hypersonique ( $Mach = 4,5$ ). Deux méthodes, non visqueuses, ont été choisies d'après l'expérience des utilisateurs [3,4] :

- cône tangent empirique pour l'intrados (zone d'impact),
- méthode ACN pour l'extrados (zone d'ombre).

### 3.2. Les codes de singularités

Les méthodes de singularités utilisent une formulation intégrale obtenue par application de la troisième identité de Green à l'équation de LAPLACE en subsonique et à l'équation des ondes en supersonique.

La discrétisation de l'équation intégrale conduit à la résolution d'un système linéaire où les inconnues (les distributions de singularités), sont réparties uniquement sur la surface de l'obstacle. Ces méthodes numériques sont attractives pour les études des configurations complexes car elles ne nécessitent qu'un maillage de surface de l'obstacle. Toutefois, les hypothèses sur l'écoulement sont assez restrictives : écoulements non décollés et irrotationnels, sauf dans les sillages, et hypothèse des petites perturbations en compressible.

Deux codes de singularités sont utilisés :

- Le premier, ECOPAN, développé à l'ONERA par KIRRMANN en 1980, est limité au régime subsonique. Il utilise des singularités d'ordre faible (source-doublet à densité constante sur chacune des facettes). Les corps épais sont traités avec des conditions aux limites de type DIRICHLET intérieur et avec une répartition de la densité de source préimposée sur la surface du corps. Cette condition, appelée aussi condition aux limites de MORINO, permet d'obtenir la tangence de la vitesse pour l'écoulement extérieur à partir des conditions imposées sur le potentiel à l'intérieur du fuselage. Pour ce faire, les densités de sources sont imposées avec la valeur  $\sigma = -\vec{V} \cdot \vec{n}$  sur toutes les facettes du fuselage et les densités des doublets sont calculées à partir de la résolution du système linéaire résultant de l'écriture des conditions aux limites sur le potentiel. Le champ des vitesses de l'écoulement physique, à l'extérieur, se déduit soit directement des valeurs locales des gradients des doublets ( $\vec{V} = \text{grad } \phi + \vec{V}_\infty + \sigma \vec{n}$ ), soit de la sommation des vitesses induites par toutes les distributions de singularités réparties sur l'obstacle.

Dans le cas des écoulements subsoniques, le code ECOPAN dispose d'une correction de compressibilité appelée règle de Goëthert n° 1. Elle se traduit par le calcul préalable de l'écoulement autour d'un corps transformé par l'affinité :  $x' = x$ ,  $y' = y \sqrt{1-M^2}$ ,  $z' = z \sqrt{1-M^2}$ . L'écoulement sur la surface réelle du corps s'obtient par application de la transformation inverse au champ de vitesse calculé.

Les coefficients de pression, obtenus par l'équation de l'énergie, ne sont fonction que de la vitesse locale de l'écoulement et de la valeur du nombre de Mach à l'infini amont (relation isentropique). Les coefficients globaux s'obtiennent par intégration de la répartition des pressions sur les facettes.

Orienté vers l'étude de configurations réalistes (interactions nacelle-voilure, avions complets), ECOPAN a fait l'objet de travaux sur des sillages figés, en particulier sur la détermination des intensités de doublets sur ces nappes (condition de Kutta-Joukowski) ainsi que sur la mise en équilibre de celles-ci. Deux options sont disponibles pour la détermination de la valeur initiale des intensités de doublets : la continuité de la densité du doublet avec celle calculée sur le corps ou l'égalité des pressions de part et d'autre de la nappe. Pour satisfaire l'une ou l'autre de ces conditions un processus itératif est utilisé.

- Le second code, HISSS, développé par FOMASIER à MBB en 1984 [5], traite à la fois les écoulements subsoniques et supersoniques.

Pour pallier les défauts rencontrés avec les codes de singularités en supersonique, HISSS utilise des singularités d'ordre élevé (variation quadratique de doublets et variation linéaire de sources sur chaque facette) permettant ainsi d'assurer la continuité de la solution sur tout le corps. Ceci est particulièrement important lorsqu'on cherche à traiter des configurations complexes. En supersonique, du fait de la nature de l'équation à traiter (équation des ondes) deux problèmes, liés à la propagation des ondes dans tout l'espace, peuvent conduire à une dégradation des résultats. Ils proviennent :

- des ondes virtuelles qui se forment à l'intérieur des corps épais et qui en se réfléchissant sur les parois intérieures et entre elles viennent perturber la solution extérieure ;

- du non évanouissement à distance des perturbations dues aux discontinuités d'intensité de singularités entre des facettes voisines.

Si le second problème est résolu par l'ordre élevé de l'intensité des singularités, le premier l'est par l'utilisation dans ce code d'une répartition mixte (source - doublet) sur la surface du corps, dont les intensités sont obtenues par une double condition aux limites (potentiel de perturbation nul à l'intérieur si  $= 0$ , et vitesse totale extérieure tangentielle à la paroi  $\vec{V} \cdot \vec{n} = 0$ ).

L'application conjointe de ces deux conditions aux limites permet dans le code HISSS de supprimer les ondes virtuelles se propageant à l'intérieur des obstacles.

Les conditions aux limites signalées ci-dessus sont les plus utilisées pour les corps épais, mais beaucoup d'autres options sont disponibles dans le code.

La prise en compte de la compressibilité dans HISSS peut s'effectuer comme dans ECOPAN, mais aussi par la règle de Goëthert n° 2 : cette dernière, mieux adaptée pour les calculs en supersonique, consiste à exprimer la condition de glissement sur la surface réelle du corps.

Dans la version 1987, disponible à l'ONERA, il n'y a pas de possibilité d'équilibrage des nappes de sillage et la densité du doublet est obtenue par continuité avec les densités de doublets calculées sur les corps. Contrairement à ECOPAN, ces densités sont déterminées directement par la résolution du système linéaire.

Des exemples concernant l'application de ce code à plusieurs types de configurations (avions et missiles) peuvent être trouvés dans les références [6,7,8].

### 3.3. FLU3C

Le code FLU3C, développé à l'ONERA par BORREL et MONTAGNE, résout les équations d'EULER instationnaires [9].

Suivant les idées de VAN LEER, ces auteurs ont mis au point un schéma explicite décentré, précis au second ordre, de type MUSCL, qui, par sa robustesse et sa précision, est adapté au calcul des écoulements présentant de fortes discontinuités.

Par ailleurs, une procédure numérique de "marche en espace" a été développée dans les zones purement supersoniques, ce qui rend ce code très performant pour des applications industrielles [10, 11, 12].

La discrétisation des équations d'EULER est réalisée suivant une formulation conservative du type volumes finis et les conditions aux limites peuvent être traitées par flux ou par relations de compatibilité.

### 3.4. Maillages

Le maillage surfacique de la demi-configuration, servant de base aux trois codes SHABP, ECOPAN et HISSS, est constitué de 798 facettes (figure 1). Les points de contrôle, au centre des facettes, coïncident avec les prises de pression de la maquette.

Le maillage volumique (figure 2) utilisé avec le code FLU3C, est obtenu plan par plan avec le mailleur GRAPE [13]. Il comporte environ 54000 points, ce qui correspond à un maillage surfacique deux fois plus fin que celui présenté précédemment, et est bien adapté au calcul de "marche en espace".

## 4. CONFRONTATIONS CALCUL - EXPERIENCE

### 4.1. Comparaisons à Mach = 0

La comparaison des pressions pariétales à 2° d'incidence (figure 3), calculées avec les deux codes de singularités, montre que ces codes donnent approximativement les mêmes résultats sur la majeure partie du fuselage. Toutefois, des différences entre ECOPAN et HISSS sont mises en évidence au nez du fuselage, au voisinage des arêtes et au rétreint (figure 4), pour 5° d'incidence. Ces écarts proviennent d'une part des différences intrinsèques aux codes et d'autre part du choix dans la modélisation des sillages de culot. Ces derniers, bien que choisis de forme géométrique identique pour ECOPAN et HISSS portent des intensités de doublets déterminées par des conditions de calcul différentes (condition de nappe solide pour ECOPAN et continuité de l'intensité du doublet avec celle du corps pour HISSS).

Par rapport aux valeurs des coefficients de pression de l'essai, mesurées à Mach 0,4 et pour laquelle cette comparaison est licite compte tenu de l'effet négligeable de la compressibilité, ECOPAN et HISSS fournissent des résultats satisfaisants.

La répartition du coefficient de force normale locale (figure 5), obtenue par intégration des pressions (mesurées et calculées), illustre clairement l'ordre de grandeur des différences calcul-expérience. Celles-ci sont visibles dès le quart avant du fuselage et deviennent particulièrement importantes au voisinage du culot, compromettant alors une bonne estimation de la stabilité de ce corps. La prise en compte des détails de l'écoulement au culot, notamment de l'existence du dard, se révèle une tâche hasardeuse avec le concept de nappe de doublets. Par contre, une tentative pour prendre en compte les décollements latéraux a permis une amélioration de la répartition des coefficients de force normale à cette incidence de 5°. Pour cela, une modélisation par nappe figée (figure 5) a été testée dans les codes HISSS et ECOPAN, en tenant compte des travaux déjà effectués sur ce même fuselage avec le code HISSS [8].

Une nappe inclinée de 5° par rapport au plan horizontal est connectée à l'arête latérale du fuselage en aval du maître-couple de celui-ci. La nappe est représentée par des distributions de doublets, dont l'intensité, constante dans la direction de l'axe du fuselage, est obtenue par continuité avec les valeurs des doublets sur l'arête du corps. Dans le code HISSS, la valeur de cette intensité est obtenue directement par la résolution du système linéaire, tandis qu'avec ECOPAN un processus itératif est nécessaire. Ce dernier n'a pas convergé et des pics irréalistes sont apparus au niveau des arêtes latérales du fuselage. Cette modélisation n'a donc pu être effectuée qu'avec le code HISSS.

L'évolution des coefficients de force normale et de moment de tangage avec l'incidence (figure 6), très fortement non linéaire, ne peut être estimée par les codes de singularités sans une prise en compte réaliste des décollements latéraux et des nappes de sillage, pour chacune des incidences.

L'amélioration apportée par le sillage latéral dans HISSS, décrite précédemment, se retrouve au niveau des coefficients globaux, mais reste très insuffisante pour les incidences supérieures à 2°.

Une bonne évolution du coefficient de force axiale CA en fonction de l'incidence est obtenue avec ECOPAN et HISSS (figure 7). La surestimation du CA par le code HISSS provient du rétreint, comme cela est mis en évidence dans la répartition du CA local. La non prise en compte de couches limites peut expliquer cette surestimation, par contre le doute subsiste lorsqu'on compare les pressions sur le rétreint entre ECOPAN et HISSS : des dépressions moins intenses sont calculées par ECOPAN sur le rétreint.

#### 4.2. Comparaisons à Mach 2

Sur la figure 8, on présente à faible incidence, la répartition des coefficients de pression pour les codes HISSS, FLU3C et l'essai. Un bon accord calcul-expérience est obtenu pour ces deux codes, avec toutefois une très légère surestimation des dépressions sur le rétreint du fuselage.

Comme en subsonique, à 5° d'incidence les décollements sur les arêtes latérales existent déjà en amont du maître couple du fuselage. La modélisation des décollements latéraux, utilisée précédemment dans le code HISSS, est insuffisante et seules les répartitions de pression en amont du maître couple sont obtenues correctement par HISSS (figure 9).

Une illustration plus globale des résultats calculés avec les codes HISSS et FLU3C est donnée par la répartition des charges en fonction de l'abscisse réduite, (figure 10). On peut constater le bon accord entre HISSS et l'essai à 2° d'incidence. À 5°, des différences apparaissent dès 40% de la longueur du fuselage et s'aggravent encore lorsque l'incidence croît.

Par contre, le code FLU3C estime très correctement le  $C_{x\text{ local}}$  même aux incidences élevées ( $\alpha = 20^\circ$ ). Ce bon accord provient de la captation des décollements sur les arêtes latérales du corps et d'un bon positionnement des tourbillons marginaux associés à ces décollements.

Les évolutions du coefficient de force normale et du centre de poussée (figure 11) avec l'incidence mettent en évidence l'effet fortement non linéaire sur le  $C_{x\text{ des tourbillons marginaux}}$ , ainsi qu'un recul du centre de poussée avec l'incidence. Cet effet est pris correctement en compte par FLU3C. À 20° par exemple, ce code estime le  $C_{x\text{ et la position du centre de poussée}}$  à moins de 2% près et ceci avec un faible temps de calcul.

Le code HISSS estime assez bien la pente à l'origine du  $C_{x\text{ et le centre de poussée}}$  à 2° d'incidence (-7% L). Ce dernier a plutôt tendance à avancer vers le nez du fuselage lorsqu'on garde fixe la position du sillage latéral, introduit dans la modélisation. Seul un calcul avec un équilibrage du sillage permettrait d'obtenir en principe une tendance opposée, conforme à l'expérience (recul du centre de poussée).

Le coefficient de force axiale est légèrement surestimé par les deux codes (figure 12).

En ce qui concerne les grandeurs aérodynamiques dans le champ, nous présentons maintenant quelques comparaisons entre FLU3C et l'expérience.

Sur la figure 13 sont tracées les lignes iso-Mach dans le plan de symétrie pour Mach = 2 et 20° d'incidence. La position du choc issu du nez du fuselage calculée par FLU3C est en bon accord avec la visualisation faite par striescopie.

Les répartitions des coefficients de pression, à la paroi ainsi que dans deux sections transversales, sont données sur les figures 14 et 15, pour 10 et 20° d'incidence.

À 10° d'incidence (figure 14) les résultats d'essai montrent clairement la trace des tourbillons principaux. Sur la section amont, le tourbillon est très proche de la paroi et son noyau n'est pas clairement visible sur les répartitions des pressions. Par contre sur la section aval, la zone de dépression qui caractérise le cœur du tourbillon est nettement détachée de la paroi du fuselage. Les résultats obtenus par FLU3C sont qualitativement corrects mais les dépressions associées aux tourbillons s'étalent jusqu'à la paroi du corps dans les deux sections et ont des valeurs sensiblement moins élevées que celles de l'essai. Ainsi par exemple, dans la section aval, les coefficients de pression calculés dans les noyaux des tourbillons sont compris entre -0,1 et -0,15 contre -0,2 et -0,25 pour les valeurs mesurées.

À 20° d'incidence (figure 15) les noyaux des tourbillons principaux se sont clairement détachés de la paroi du corps, même sur la section amont. Comme à 10°, les estimations par FLU3C sont qualitativement correctes.

Si on analyse de plus près le champ aérodynamique dans la section amont, à 10° d'incidence (figure 16), on constate des différences importantes sur le champ des vitesses entre FLU3C et l'expérience. Cette dernière met en évidence deux couples de tourbillons près de la paroi du fuselage et tournant dans le même sens. Le tourbillon le plus proche du plan de symétrie vertical est caractéristique de cette incidence et disparaît à 20° d'incidence, laissant alors place à une amorce de tourbillon contrarotatif placé au voisinage de l'arête. Sur les coefficients de pression pariétale on décelle l'effet induit du tourbillon proche du plan de symétrie vertical, qui se traduit par une chute du  $K_p$ . Le code FLU3C estime correctement les coefficients de pression pariétale dans cette section sauf naturellement les effets, très localisés, induits par ces tourbillons.

Dans la section plus à l'aval du corps, on n'observe plus qu'un seul couple de tourbillons, de forte intensité, aussi bien à 10° qu'à 20° d'incidence. L'augmentation de l'incidence se traduit seulement par un accroissement de l'intensité du tourbillon principal et d'un déplacement de son centre (vers le plan vertical et éloignement de la paroi). L'existence d'un tourbillon contrarotatif secondaire, au voisinage de l'arête, associé au tourbillon principal, ne ressort pas clairement des mesures effectuées sur ce fuselage. À 20° d'incidence, la figure 17 montre que la position du tourbillon principal est bien estimée par le calcul. Les coefficients de pression sont en excellent accord avec l'essai sauf naturellement au voisinage de l'arête latérale où l'essai révèle un plateau de  $K_p$  constant associé à un décollement.

Les comparaisons relatives aux rapports des pressions génératrices locales à celle de l'écoulement amont, (fig. 18), montrent que :

- dans la section aval les pertes de pression sont presque correctement estimées par FLU3C (70% pour le calcul, 80% pour l'essai) bien que les lignes iso- $\pi$  ne soient que qualitativement restituées,
- dans la section amont, le calcul ne reproduit pas fidèlement les phénomènes expérimentaux et, en particulier, la trace des tourbillons précédemment cités ; une perte plus importante de  $\pi$  est trouvée au coeur du tourbillon situé près de l'arête (80% contre 60% pour l'autre tourbillon).

#### 4.3. Comparaisons à Mach = 4.5

Le calcul de l'écoulement à Mach 4,5 par le code HISSS n'est plus réaliste, pour deux raisons :

- les hypothèses de linéarisation ne sont plus justifiées à haut Mach ;
- le nez du fuselage a un angle d'ouverture supérieur à l'angle de Mach infini amont et ne peut plus être traité comme une surface solide.

Les comparaisons des  $K_p$  calculés par les deux codes, FLU3C et SHABP, avec l'essai (figure 19) sont tout à fait satisfaisantes à l'intrados du fuselage. À l'extrados, elles le sont un peu moins et seule l'allure des zones iso- $K_p$  est assez bien reproduite par FLU3C. Comparativement aux résultats présentés en subsonique (Mach 0,4) et en supersonique (Mach 2), les répartitions de pression pariétale sont assez plates, en particulier sans pic de dépression au niveau des arêtes (figure 20). C'est pourquoi le code SHABP, qui ne dispose d'aucune modélisation des décollements, permet une bonne estimation globale des coefficients de pression sur ce fuselage, en dépit des modèles très simples qu'il utilise.

Les variations du coefficient de force normale et du centre de poussée en fonction de l'incidence sont bien estimées jusqu'à  $15^\circ$  (figure 21). Il en est de même pour les répartitions des charges (figure 22).

De même, le coefficient de force axiale à incidence nulle est bien estimé par les deux codes (figure 23), bien que SHABP surévalue ce coefficient lorsque l'incidence croît.

On peut remarquer, par rapport à Mach 0,4 et 2, un changement de comportement dans l'évolution du  $C_x$  avec l'incidence. Le code FLU3C estime encore correctement cette évolution jusqu'à  $15^\circ$  d'incidence.

#### 4.4. Effet du nombre de Mach

Pour résumer les résultats à faible incidence qui viennent d'être exposés, on présente figure 24 les évolutions du gradient de portance et du centre de poussée en fonction du nombre de Mach.

En incompressible, les codes HISSS et ECOPAN (sans sillage latéral) fournissent à 10% près les mêmes résultats. L'évolution du gradient de portance avec le Mach est trop rapide pour ECOPAN, trop lente pour HISSS. Cette différence provient d'un choix différent dans la prise en compte de l'effet de compressibilité (règle de Gœthert n° 1 pour ECOPAN, règle de Gœthert n° 2 pour HISSS). Il n'y a pas de critère général permettant d'adopter l'une ou l'autre de ces corrections de compressibilité. Nous avons adopté la règle de Gœthert n° 2 pour HISSS, car elle permet d'obtenir une meilleure évolution globale des coefficients aérodynamiques en subsonique et en supersonique.

Lorsqu'on inclut le sillage latéral dans HISSS, l'estimation du gradient de portance est nettement améliorée, mais l'amélioration est encore plus remarquable pour la stabilité.

Le code FLU3C est en très bon accord avec l'essai aussi bien pour la portance (5%) que pour la stabilité (5%).

Le code SHABP fournit, par contre, un résultat très moyen à faible incidence sur le gradient du coefficient de force normale (19%), alors que la stabilité est bien calculée (5%).

#### 5. CONCLUSION

Plusieurs codes de calcul en fluide parfait ont été utilisés pour estimer les caractéristiques aérodynamiques longitudinales d'un corps à section quasi lenticulaire.

L'aérodynamique de ce corps, qui présente des décollements même aux faibles incidences, est de ce fait un cas test particulièrement difficile pour les codes de calcul.

Lorsqu'on compare en incompressible les codes de singularités, on constate qu'ils donnent sensiblement les mêmes répartitions de coefficient de pression ; les principales différences étant observées au nez, sur les arêtes latérales et au niveau du rétreint. Les écarts sur les coefficients aérodynamiques globaux peuvent atteindre 10% et sont attribués à l'ordre des singularités et aux choix des modélisations du culot. Par ailleurs, une première prise en compte du décollement sur les arêtes latérales de ce corps, a permis une nette amélioration de l'estimation de sa stabilité. Celle-ci n'a pu aboutir qu'avec le code HISSS, plus robuste qu'ECOPAN.



En supersonique, HISSS est un des rares codes de singularités permettant le calcul de configurations complexes, mais, comme en incompressible, il est limité à 2° d'incidence sur ce corps.

Les temps de calcul obtenus avec la version 1987 de HISSS, seule disponible à l'ONERA, sont nettement supérieurs à ceux obtenus avec ECOPAN. Ainsi, pour un maillage de 798 facettes, le code ECOPAN prend 296 sec (CPU) sur le CRAY-XMP de l'ONERA, tandis que HISSS prend 1800 sec (en subsonique et en supersonique). FLU3C, utilisé seulement en supersonique, réussit à capter les décollements issus des arêtes vives et à positionner à peu près correctement les tourbillons principaux dus à ces décollements. Bien que les phénomènes aérodynamiques locaux dus à la viscosité ne puissent être pris en compte en EULER, ce code calcule des répartitions de pression en très bon accord avec l'essai hors des régions concernées par les effets visqueux. Les estimations des coefficients aérodynamiques globaux sont très bonnes.

L'utilisation de la méthode de marche en espace, possible avec cette configuration pour les nombres de Mach calculés, réduit notablement le temps de calcul, soit environ 612 sec CPU sur CRAY2 pour 54000 points de maillage.

En haut supersonique, les effets des décollements sont moindres et le code semi-empirique SHABP qui ne dispose d'aucune modélisation des décollements, fournit les coefficients aérodynamiques avec une bonne précision et moyennant des temps de calcul très faibles, de l'ordre de 10 sec sur une station de travail BULL DFX 5000.

#### REFERENCES

- [1] P. CHAMPIGNY  
"Prévision de la stabilité des missiles"  
AGARD - CP - 431, 1988.
- [2] GENTRY A.E. and AL  
"The Mark IV Supersonic Hypersonic Arbitrary Body Program". Volumes I, II, III.  
Douglas Aircraft Company.  
Report AFFDL-TR 73-159.
- [3] M. LECUYER  
"Prévision des coefficients aérodynamiques de véhicules hypersoniques par les codes HABP et SHABP; comparaisons avec l'expérience".  
AAAF - Poitiers (1987).
- [4] J.E. GREGOIRE and R.J. KRIEGER  
Aerodynamic Prediction for Advanced Arbitrary Shaped Missile Concepts.  
AIAA - 80-0256 (1980).
- [5] L. FOMASIER  
"HISSS. A Higher Order Subsonic/Supersonic Singularity Method for Calculating Linearized Potential Flow".  
AIAA 84-1646 (1984).
- [6] L. FOMASIER  
"Linearized Potential Flow Analysis of Complex Aircraft Configurations by HISSS, a Higher-order Panel Method".  
AIAA 85-281, 1985.
- [7] S. HEISS, L. FOMASIER  
"Analysis of a Fighter Type Aircraft configuration with the HISSS Panel Method at Subsonic and Supersonic Speeds", Z. Flugwiss und Weltraumforsch, Vol. 12, 1988, pp 224-232.
- [8] L. FOMASIER, P. d'ESPINEY  
"Prediction of Stability Derivatives for Missiles Using the HISSS Panel Code".  
AGARD - CP - 431, 1988.
- [9] M. BORREL, J.L. MONTAGNE  
"Numerical Study of a non centered scheme with Applications to Aerodynamics".  
AIAA 85 - 1497 - CP (1985).
- [10] M. DORMIEUX et C. MAHE  
"Calcul tridimensionnels de l'interaction d'un jet latéral avec un écoulement supersonique externe".  
AGARD - CP - 437 Vol. 1, 1988.
- [11] P. GUILLEN, and J. LORDON,  
"Numerical simulation of separated supersonic flows around tactical missiles"  
AGARD - CP - 437 vol. 1, 1988.
- [12] M. BORREL, J.L. MONTAGNE, J. DIET, J. LORDON  
"Méthode de calcul d'écoulements autour de missiles tactiques à l'aide d'un schéma décentré".  
La Recherche Aérospatiale 1988.
- [13] J.L. STEGER, R.L. SORENSON  
"Automatic Mesh Point Clustering Near a Boundary in Grid Generation with Elliptical Partial Differential Equation".  
J. Comp. Phys. Vol. 33, p. 405-410 (1979).

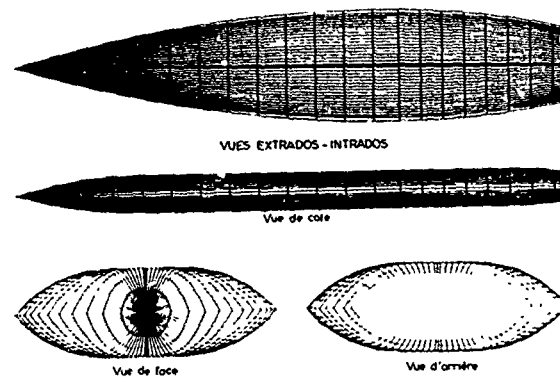


Fig. 1 - Maillage surfacique du fuselage (798 facettes - demi configuration).

Maillage volumique pour le corps a section lenticulaire - FLU3C

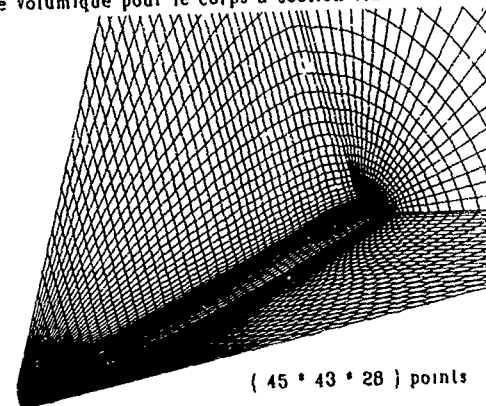


Fig. 2 - Maillage volumique pour FLU3C (54180 points de grille - demi configuration)

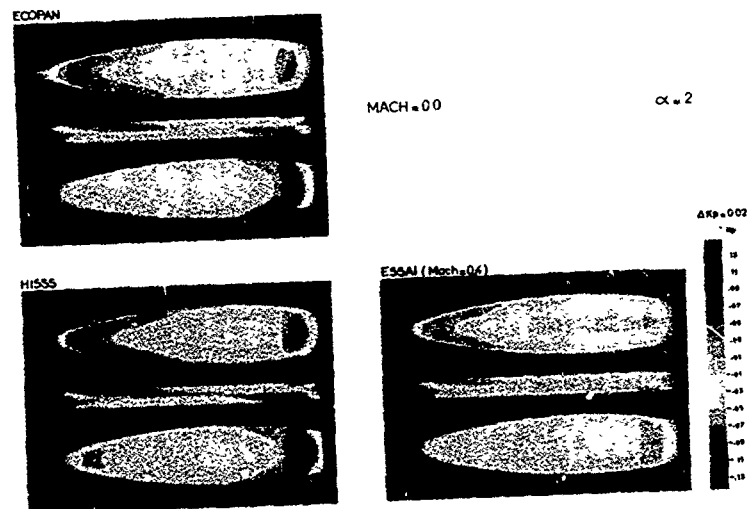


Fig. 3 - Répartitions de pression pariétale à Mach = 0 et  $\alpha = 2^\circ$  (ECOPAN - HISSS - essai).

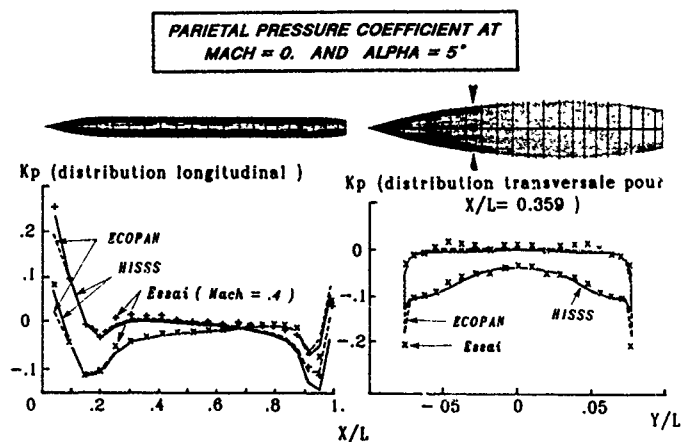


Fig. 4 - Répartitions longitudinale et dans une section transversale ( $X/L = 0.359$ ) des pressions pour Mach = 0 et  $\alpha = 5^\circ$  (ECOPAN - HISSS - essai).

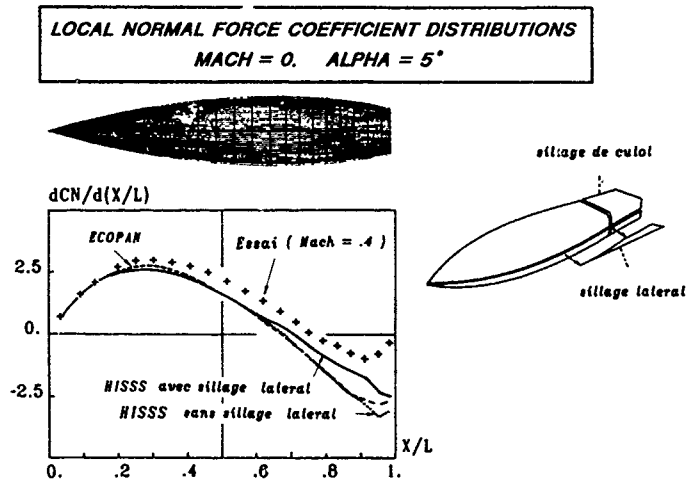


Fig. 5 - Répartitions du coefficient de force normale locale pour Mach = 0 et  $\alpha = 5^\circ$  (ECOPAN - HISSS - essai).

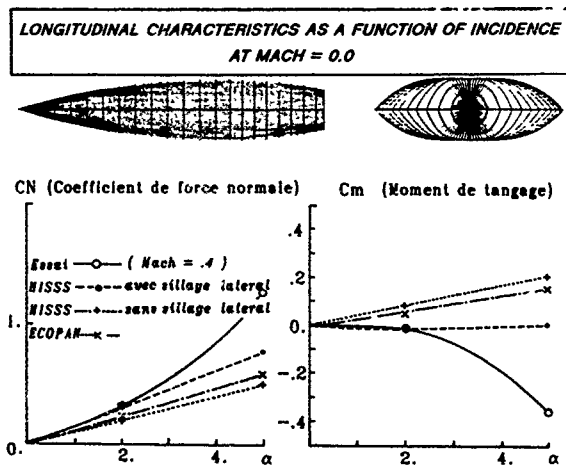


Fig. 6 - Caractéristiques longitudinales en fonction de l'incidence à Mach = 0 (ECOPAN - HISSS - essai).

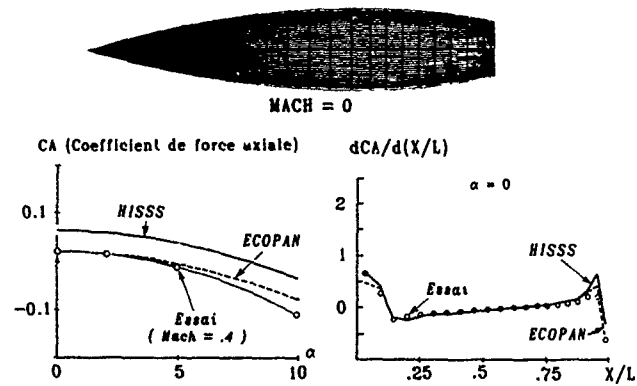


Fig. 7 - Coefficient de force axiale en fonction de l'incidence pour Mach = 0 et répartitions de force axiale locale pour Mach = 0,  $\alpha = 0^\circ$  (ECOPAN - HISSS - essai).

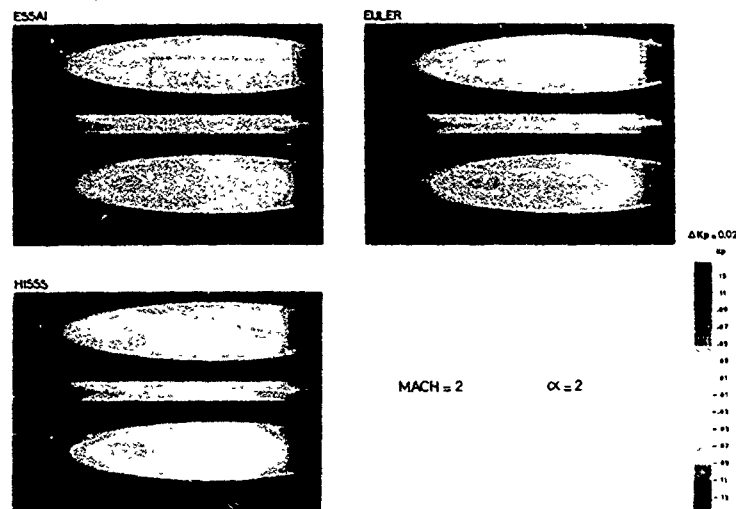


Fig. 8 - Répartitions de pression pariétale à Mach = 2 et  $\alpha = 2^\circ$  (HISSS - FLU3C - essai).

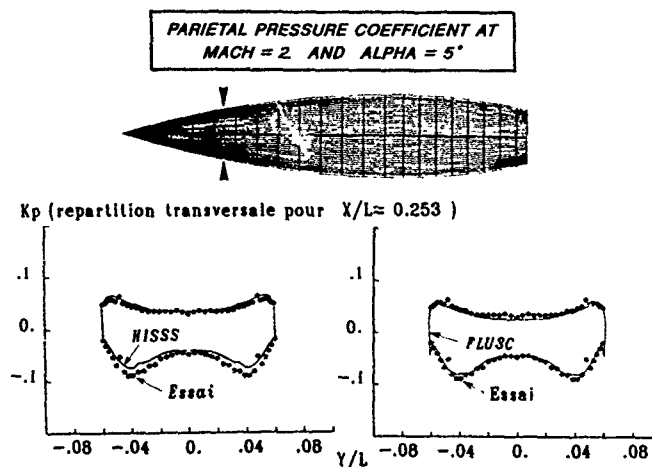


Fig. 9 - Répartitions de pression dans une section transversale ( $X/L = 0.253$ ) à Mach = 2,  $\alpha = 5^\circ$  (HISSS - FLU3C - essai).

LOCAL NORMAL FORCE COEFFICIENT DISTRIBUTIONS  
MACH = 2

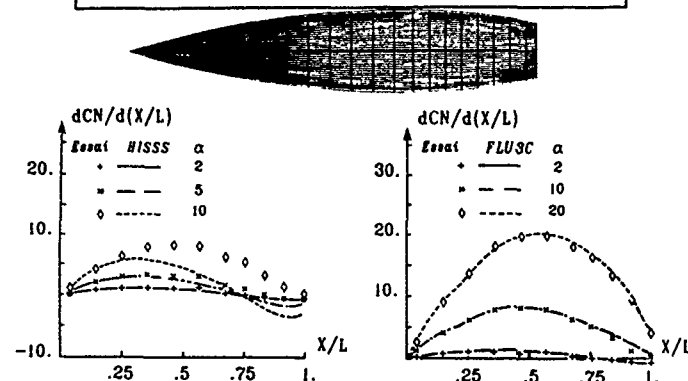


Fig. 10 - Répartitions du coefficient de force normale locale pour Mach = 2 à plusieurs incidences (HISSS - FLU3C - essai).

LONGITUDINAL CHARACTERISTICS AS A FUNCTION OF INCIDENCE  
AT MACH = 2.0

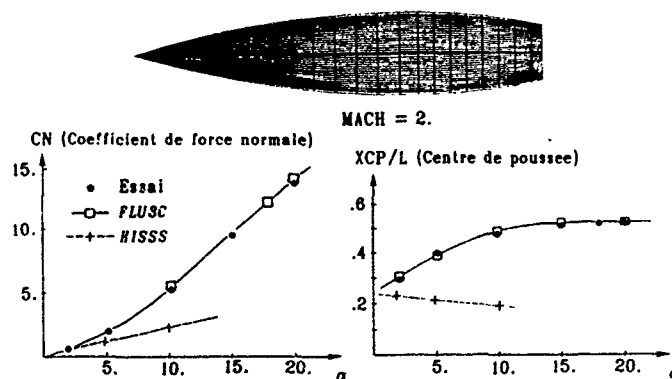


Fig. 11 - Caractéristiques longitudinales en fonction de l'incidence à Mach = 2 (HISSS - FLU3C - essai).

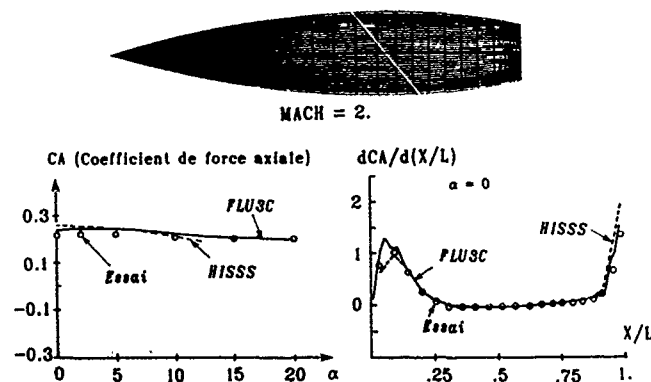


Fig. 12 - Coefficient de force axiale en fonction de l'incidence pour Mach 2 et répartition de force axiale locale pour Mach = 2,  $\alpha = 0^\circ$  (HISSS, FLU3C - essai).

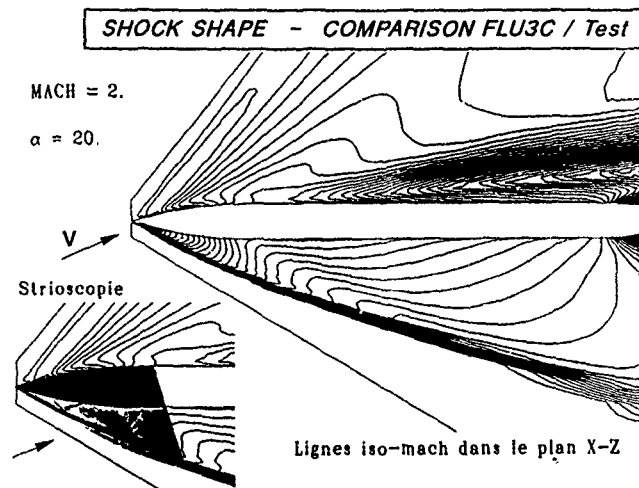


Fig. 13 - Comparaison de la position du choc au nez du fuselage calculée par FLU3C avec une visualisation faite par strioscopie - Mach 2,  $\alpha = 20^\circ$ .

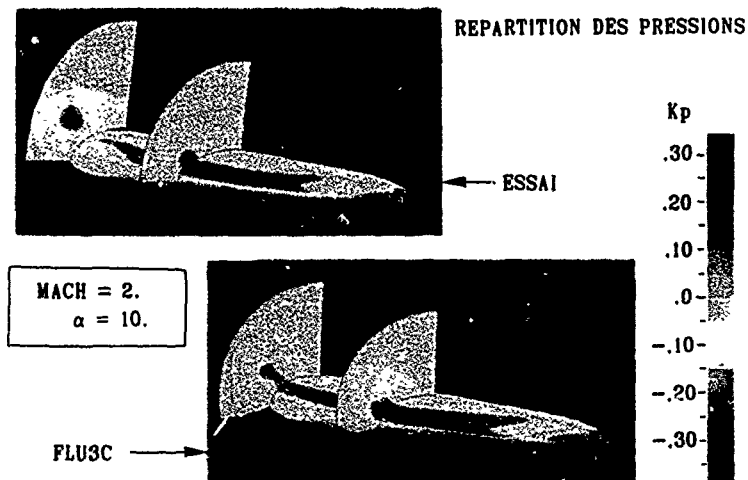


Fig. 14 - Répartitions de pression pariétale dans le champ pour Mach = 2 et  $\alpha = 10^\circ$  (FLU3C - essai).

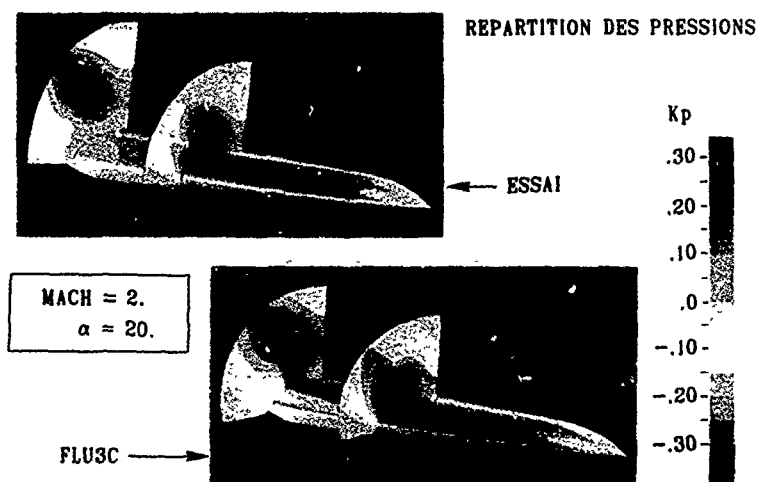


Fig. 15 - Répartitions de pression pariétale et dans le champ pour Mach = 2 et  $\alpha = 20^\circ$  (FLU3C - essai).

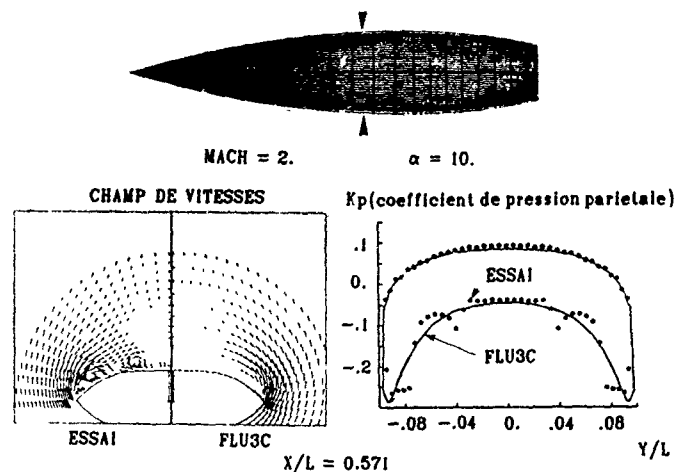


Fig. 16 - Champ des vitesses et répartitions de pression pariétale dans la section  $X/L = 0.571$  pour Mach = 2 et  $\alpha = 10^\circ$  (FLU3C - essai).

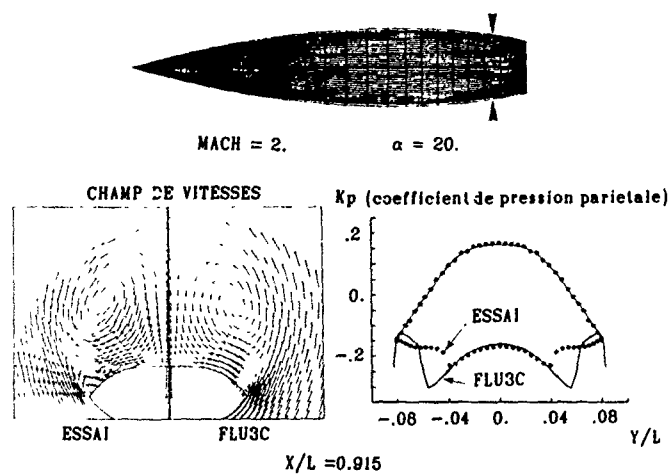


Fig. 17 - Champ des vitesses et répartitions de pression pariétale dans la section  $X/L = 0.915$  pour Mach = 2,  $\alpha = 20^\circ$  (FLU3C - essai).

COMPUTED AND EXPERIMENTAL TOTAL PRESSURE CONTOURS  
IN CROSSFLOW PLANES

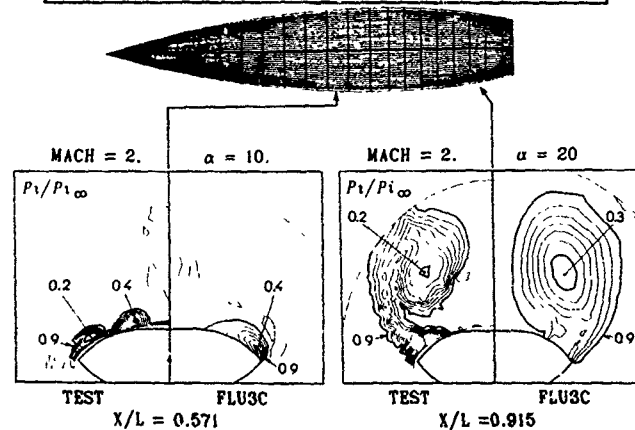


Fig. 18 - Répartitions de pression d'arrêt dans la section  $X/L = 0.571$  pour Mach = 2,  $\alpha = 10^\circ$  et dans la section  $X/L = 0.915$  pour Mach = 2,  $\alpha = 20^\circ$  (FLU3C - essai).

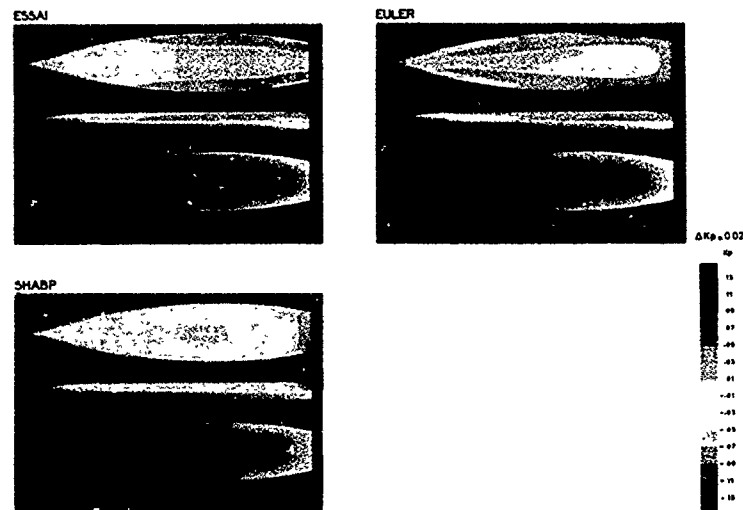


Fig. 19 - Répartitions de pression pariétale à Mach = 4,5 et  $\alpha = 10^\circ$  (SHABP - FLU3C - essai).

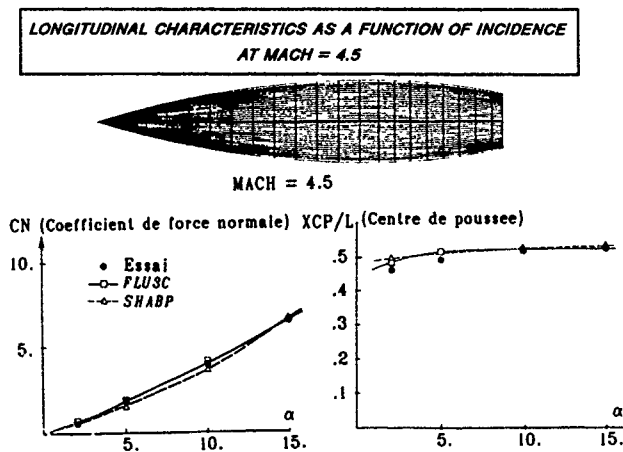


Fig. 20 - Répartitions de pression dans une section transversale ( $X/L = 0,571$ ) à Mach = 4,5 et  $\alpha = 10^\circ$  (SHABP - FLU3C - essai).

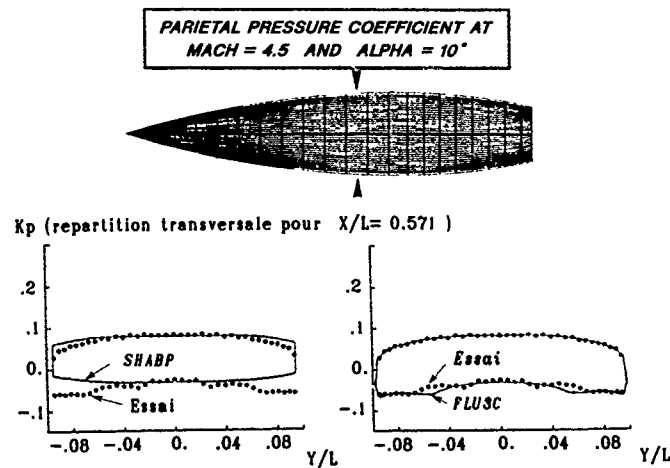


Fig. 21 - Répartitions du coefficient de force normale locale pour Mach = 4,5 à plusieurs incidences (SHABP - FLU3C - essai).



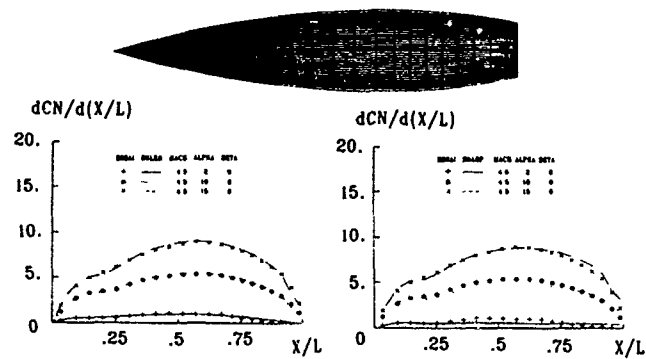


Fig. 22 - Caractéristiques longitudinales en fonction de l'incidence à Mach = 4,5 (SHABP - HISSS - FLU3C).

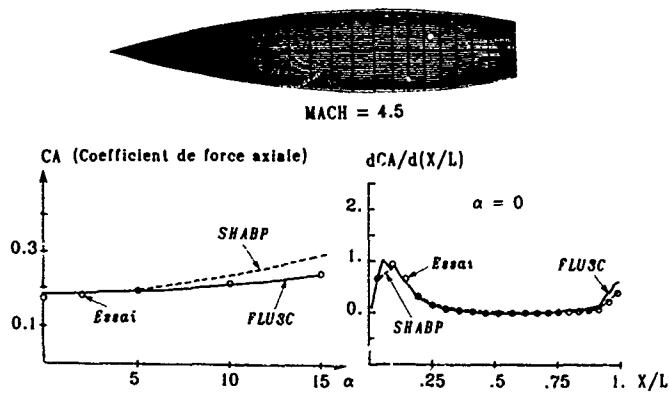


Fig. 23 - Coefficient de force axiale en fonction de l'incidence pour Mach = 4,5 et répartitions de force axiale locale pour Mach = 4,5,  $\alpha = 10^\circ$  (SHABP - FLU3C - essai).

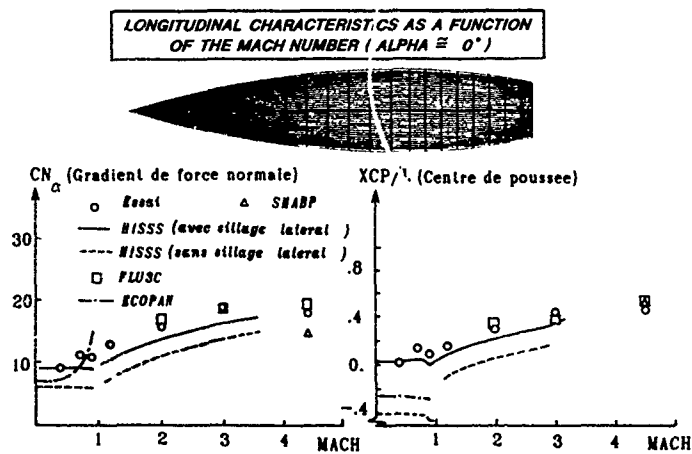


Fig. 24 - Caractéristiques longitudinales en fonction du nombre de Mach au voisinage de l'incidence nulle (ECOPAN - HISSS - FLU3C - SHABP - essai).

# **THREE DIMENSIONAL FLOW CALCULATIONS FOR A PROJECTILE WITH STANDARD AND DOME BASES**

Jubaraj Sahu  
Charles J. Nietubicz  
Launch and Flight Division  
U.S. Army Ballistic Research Laboratory  
Aberdeen Proving Ground, Maryland 21005-5066, U.S.A.

## **1. SUMMARY**

Test firings of the 155mm XM825 artillery projectile have shown that its flight performance was affected by configurational changes to the base cavity. This was an unexpected result and a clear understanding of why these changes affected the flight behavior did not exist. A computational study has been made for the two different base cavity configurations which were flight tested. Flowfield computations have been performed at  $0.8 < M < 1.5$  and  $\alpha = 4.0^\circ$  using a recently developed 3D Navier-Stokes code. The computed results show the qualitative features of the base region flow field for the two base cavities. The base changes are found to alter the recirculation patterns in the wake which in turn affect the expansion at the base corner. These changes in the flow structure contribute to small changes in the base pressure. Aerodynamic force and moment coefficients have been obtained from the computed pressures and are presented as a function of Mach number. Computed results show small differences in normal force and pitching moment coefficients similar to that found in the range data.

## **2. LIST OF SYMBOLS**

a	speed of sound
$c_p$	specific heat at constant pressure
$C_p$	pressure coefficient
D	projectile diameter
e	total energy per unit volume
$\hat{F}, \hat{G}, \hat{H}$	flux vectors in transformed coordinates
J	jacobian
M	Mach number
Pr	Prandtl number
$Pr_t$	turbulent Prandtl number
$\hat{q}$	vector of dependent variables
R	body radius
$\hat{S}$	vector containing viscous terms
t	time
T	temperature
u, v, w	axial, circumferential, and normal velocity components of the Navier-Stokes equations
U, V, W	Contravariant velocities of the transformed Navier-Stokes equations
x, y, z	physical Cartesian coordinates

## **Greek Symbols**

$\alpha$	Angle of attack
----------	-----------------

$\gamma$	ratio of specific heats
$\kappa$	molecular and turbulent thermal conductivity
$\mu$	molecular and turbulent viscosity
$\xi, \eta, \zeta$	transformed coordinates
$\rho$	density
$\phi$	circumferential angle

## **Subscripts**

$\infty$	free stream conditions
----------	------------------------

## **3. INTRODUCTION**

The ability to compute the base region flow field for projectile configurations using Navier-Stokes computational techniques has been developed over the past few years<sup>1,2,3</sup>. This capability is very important for determining aerodynamic coefficient data including the total aerodynamic drag. The majority of base flow calculations to date have modeled the base region as a flat solid surface. Many of the actual configurations have some form of base cavity. General opinion has been that the inclusion of a base cavity or modifications to the interior cavity of a projectile base would have little or no effect on the overall flight performance parameters.

The M825 projectile under certain conditions is expected to be aeroballistically similar to its parent configuration the M483A1. The M825 has an aluminum/steel base which is configured as a flat cavity (standard). A recent Product Improvement Program (PIP), undertaken to reduce the production costs and improve shell integrity, resulted in the design of a new base configuration. This new PIP configuration has an all steel base and contains a dome cavity. A series of aeroballistic tests<sup>4</sup> were conducted in the Transonic Range Facility of the US Army Ballistic Research Laboratory (BRL), to determine any difference in the aeroballistics which may occur between the standard and dome base configurations. As a result of these tests, differences in aerodynamic performance were found to exist between the two rounds. The most significant changes in the aerodynamic data were in the lift and static moment coefficients. The drag was found to differ by a few percent with the dome configuration having the lower drag at low transonic speeds.

A computational study was undertaken to determine the ability of the present Navier-Stokes codes to predict these differences and to further understand the

fluid dynamic behavior which can account for such small changes. The use of Navier-Stokes codes can provide a detailed description of the flow field associated with the M825 configuration as well as the integrated aerodynamic coefficients. The initial results for the zero degree angle of attack case have been reported by Sahu et al.<sup>5</sup>. This was accomplished using an axisymmetric base flow code and the results showed the same effect as the range data, that is, a small reduction in the total aerodynamic drag at low transonic speeds ( $M < 0.95$ ) for the dome base configuration. The trend reversed at high transonic speeds ( $M > 0.98$ ). This paper describes an extension of that work into three dimensions.

Numerical computations have been performed using a 3D zonal, implicit Navier-Stokes code. The Mach number range was  $0.8 < M < 1.5$  for an angle of attack,  $\alpha = 4.0^\circ$ . Results presented include the qualitative features of the base region flow field for the two base cavities. Aerodynamic force and moment coefficients have been obtained from the computed solutions and are presented as a function of Mach number. Computed results show small differences in normal force and pitching moment coefficients similar to that found in the range data.

#### 4. GOVERNING EQUATIONS AND SOLUTION TECHNIQUE

The complete set of time-dependent thin-layer Navier-Stokes equations is solved numerically to obtain a solution to this problem. The numerical technique used is an implicit finite difference scheme. Although time-dependent calculations are made, the transient flow is not of primary interest at the present time. The steady flow, which is the desired result, is obtained in a time asymptotic fashion.

##### 4.1 GOVERNING EQUATIONS

The complete set of three dimensional, time dependent, generalized geometry, thin-layer, Navier-Stokes equations for general spatial coordinates  $\xi, \eta, \zeta$  can be written as<sup>6</sup>:

$$\partial_\tau \hat{q} + \partial_\xi \hat{F} + \partial_\eta \hat{G} + \partial_\zeta \hat{H} = Re^{-1} \partial_\zeta \hat{S} \quad (1)$$

where

$$\begin{aligned} \xi &= \xi(x, y, z, t) && \text{longitudinal coordinate} \\ \eta &= \eta(x, y, z, t) && \text{circumferential coordinate} \\ \zeta &= \zeta(x, y, z, t) && \text{nearly normal coordinate} \\ \tau &= t && \text{time} \end{aligned}$$

and

$$\begin{aligned} \hat{q} &= \frac{1}{J} \begin{bmatrix} \rho \\ \rho u \\ \rho v \\ \rho w \\ e \end{bmatrix} & \hat{F} &= \frac{1}{J} \begin{bmatrix} \rho U \\ \rho u U + \xi_x p \\ \rho v U + \xi_y p \\ \rho w U + \xi_z p \\ (e + p)U - \xi_t p \end{bmatrix} \\ \hat{G} &= \frac{1}{J} \begin{bmatrix} \rho V \\ \rho u V + \eta_x p \\ \rho v V + \eta_y p \\ \rho w V + \eta_z p \\ (e + p)V - \eta_t p \end{bmatrix} & \hat{H} &= \frac{1}{J} \begin{bmatrix} \rho W \\ \rho u W + \zeta_x p \\ \rho v W + \zeta_y p \\ \rho w W + \zeta_z p \\ (e + p)W - \zeta_t p \end{bmatrix} \end{aligned} \quad (2)$$

and where

$$\hat{S} = \frac{1}{J} \begin{bmatrix} 0 \\ \mu(\zeta_x^2 + \zeta_y^2 + \zeta_z^2)u_\zeta + \frac{\mu}{3}(\zeta_x u_\zeta + \zeta_y v_\zeta + \zeta_z w_\zeta)\zeta_x \\ \mu(\zeta_x^2 + \zeta_y^2 + \zeta_z^2)v_\zeta + \frac{\mu}{3}(\zeta_x u_\zeta + \zeta_y v_\zeta + \zeta_z w_\zeta)\zeta_y \\ \mu(\zeta_x^2 + \zeta_y^2 + \zeta_z^2)w_\zeta + \frac{\mu}{3}(\zeta_x u_\zeta + \zeta_y v_\zeta + \zeta_z w_\zeta)\zeta_z \\ \{(\zeta_x^2 + \zeta_y^2 + \zeta_z^2)\frac{\mu}{2}(u^2 + v^2 + w^2)\zeta \\ + \frac{\kappa a_\infty^2}{Pr(\gamma - 1)}\} \\ + \frac{\mu}{3}(\zeta_x u + \zeta_y v + \zeta_z w)(\zeta_x u_\zeta + \zeta_y v_\zeta + \zeta_z w_\zeta) \end{bmatrix} \quad (3)$$

In equation (1), the thin-layer approximation is used and the viscous terms involving velocity gradients in both the longitudinal and circumferential directions are neglected. The viscous terms are retained, however, for velocity gradients in a direction nearly normal to the surface where large flowfield gradients exist. These viscous terms in  $\zeta$  are collected into the vector  $\hat{S}$ .

For this computation, the diffusion coefficients  $\mu$  and  $\kappa$  contain molecular and turbulent parts. The turbulent contributions are supplied through an algebraic eddy-viscosity hypothesis which has been developed by Baldwin and Lomax.<sup>7</sup>

The velocities in the  $\xi, \eta$ , and  $\zeta$  coordinate directions can be written

$$\begin{aligned} U &= \xi_t + u\xi_x + v\xi_y + w\xi_z \\ V &= \eta_t + u\eta_x + v\eta_y + w\eta_z \\ W &= \zeta_t + u\zeta_x + v\zeta_y + w\zeta_z \end{aligned}$$

which represent the contravariant velocity components.

The Cartesian velocity components ( $u, v, w$ ) are retained as the dependent variables and are nondimensionalized with respect to  $a_\infty$  (the free stream speed of sound). The local pressure is determined using the relation

$$p = (\gamma - 1)[e - 0.5\rho(u^2 + v^2 + w^2)] \quad (4)$$

where  $\gamma$  is the ratio of specific heats. Density ( $\rho$ ) is referenced to  $\rho_\infty$  and the total energy ( $e$ ) to  $\rho_\infty a_\infty^2$ . The transport coefficients are also nondimensionalized with respect to the corresponding free stream variables. Thus the Prandtl number which appears in  $\hat{S}$  is defined as  $Pr = c_{p\infty} \mu_\infty / \kappa_\infty$ .

In differencing these equations it is often advantageous to difference about a known base solution denoted by subscript 0 as

$$\begin{aligned} \delta_\tau(\hat{Q} - \hat{Q}_0) + \delta_\xi(\hat{F} - \hat{F}_0) + \delta_\eta(\hat{G} - \hat{G}_0) \\ + \delta_\zeta(\hat{H} - \hat{H}_0) - Re^{-1}\delta_\zeta(\hat{S} - \hat{S}_0) \\ = -\partial_\tau \hat{Q}_0 - \partial_\xi \hat{F}_0 - \partial_\eta \hat{G}_0 - \partial_\zeta \hat{H}_0 + Re^{-1}\partial_\zeta \hat{S}_0 \end{aligned} \quad (5)$$

where  $\delta$  indicates a general difference operator, and  $\partial$  is the differential operator. If the base state can be properly chosen, the differenced quantities can have smaller and smoother variation and therefore less differencing error.

#### 4.2 NUMERICAL TECHNIQUE

The implicit approximately factored scheme for the thin layer Navier Stokes equations that uses central differencing in the  $\eta$  and  $\zeta$  directions and upwinding in  $\xi$  is written in the form

$$\begin{aligned} & \left[ I + h\delta_\xi^b(\hat{A}^+)^n + h\delta_\zeta \hat{C}^n - hRe^{-1}\delta_\zeta J^{-1}\hat{M}^n J - D_1|_\zeta \right] \\ & \times \left[ I + h\delta_\xi^f(\hat{A}^-)^n + h\delta_\eta \hat{B}^n - D_1|_\eta \right] \Delta \hat{Q}^n = \\ & - \Delta t \{ \delta_\xi^b[(\hat{F}^+)^n - \hat{F}_\infty^+] + \delta_\xi^f[(\hat{F}^-)^n - \hat{F}_\infty^-] + \delta_\eta(\hat{G}^n - \hat{G}_\infty) \\ & + \delta_\zeta(\hat{H}^n - \hat{H}_\infty) - Re^{-1}\delta_\zeta(\hat{S}^n - \hat{S}_\infty) \} - D_e(\hat{Q}^n - \hat{Q}_\infty) \end{aligned}$$

where  $h = \Delta t$  or  $(\Delta t)/2$  and the free stream base solution is used. Here  $\delta$  is typically a three point second order accurate central difference operator,  $\delta$  is a midpoint operator used with the viscous terms, and the operators  $\delta_\xi^b$  and  $\delta_\xi^f$  are backward and forward three-point difference operators. The flux  $\hat{F}$  has been eigensplit and the matrices  $\hat{A}$ ,  $\hat{B}$ ,  $\hat{C}$ , and  $\hat{M}$  result from local linearization of the fluxes about the previous time level. Here  $J$  denotes the Jacobian of the coordinate transformation. Dissipation operators,  $D_e$  and  $D_1$ , are used in the central space differencing directions.

The smoothing terms used in the present study are of the form:

$$D_e|_\eta = (\Delta t)J^{-1}[\epsilon_2\delta_\eta(B)\beta\delta + \epsilon_4\delta\frac{\rho(B)}{1+\beta}\delta^3]|_\eta J$$

$$D_1|_\eta = (\Delta t)J^{-1}[\epsilon_2\delta_\eta(B)\beta\delta + 2.5\epsilon_4\delta\eta(B)\delta]|_\eta J$$

where  $\beta = \frac{|B|^2 p}{(1+\delta^2)p}$  and where  $\rho(B)$  is the true spectral radius of  $B$ . The idea here is that the fourth difference will be tuned down near shocks, that is, as  $\beta$  gets large the weight on the fourth difference drops down while the second difference tunes up.

For simplicity, all the boundary conditions have been imposed explicitly. On the body surface, the no-slip boundary condition is used and the wall temperature is specified. Free stream boundary conditions are used at the computational outer boundary. A symmetry boundary condition is imposed at the circumferential edges of the grid while a simple extrapolation is used at the downstream boundary. The flowfield is initially set to free stream conditions everywhere and then advanced in time until a steady state solution is obtained. Atmospheric flight conditions were used.

#### 4.3 COMPOSITE GRID SCHEME

In the present work, a simple composite grid scheme<sup>8</sup> has been used where a large single grid is split into a number of smaller grids so that computations can be performed on each of these grids separately. These grids use the available core memory one grid at a time, while the remaining grids are stored on an external disk storage device such as the solid state disk device (SSD) of the Cray X-MP/48 computer. The Cray-2 has a large incore memory to fit the large single grid. However, for accurate geometric modeling of complex projectile configurations which include blunt noses, sharp corners and base cavities, it is also desirable to split the large data base into a few smaller zones on Cray-2 as well.

The use of a composite grid scheme requires special care in storing and fetching the interface boundary data, i.e., the communication between the various zones. In the present scheme, there is a one to one mapping of the grid points at the interface boundaries and thus, no interpolations are required. Details of the data storage, data transfer and other pertinent information such as metric and differencing accuracy at the interfaces can be found in Reference 8 and 9. This scheme has been successfully used by Sahu<sup>9</sup> to compute three dimensional transonic flow over two projectiles. The computed results clearly showed the transonic critical aerodynamic behavior in pitching moment coefficient observed in free flights. The present work is a further application of this technique to a more complicated projectile with base cavities.

#### 5. MODEL GEOMETRY AND COMPUTATIONAL GRID

The external configuration of the M825, excluding the base, is similar to the M483A1 shown in Figure 1. The features of this projectile which have not been modeled exactly are the meplat on the fuze and the rotating band near the base. The rotating band was eliminated for simplicity and the meplat was modeled as a hemisphere cap. The computational model is shown in Figure 2 and consists of a 2.84 caliber nose, a 2.7 caliber cylindrical section, and a 0.26 caliber 8° boattail. The ogive contour as well as the undercut on the cylindrical section were matched.

The current problem of interest is the effect of the different base geometries on the overall projectile aerodynamics. Figure 3 shows the standard and dome base configurations. The standard base is a combination of aluminum and steel and contains a base cavity which is characterized as a flat surface. The PIP configuration is an all steel base and is characterized as a dome surface. The cavity volume is also significantly larger for the dome configuration.

The solution technique requires the discretization of the entire flow region of interest into a suitable computational grid. The grid outer boundary has been placed at 2.5 body lengths upstream and surrounding the projectile. The downstream boundary was placed at 2 body lengths. Since the calculations are in the subsonic/transonic regime the computational boundaries must extend out beyond the influence of the body. This ensures that the boundary conditions specified in the flow code are satisfied.

Figure 4 and Figure 5 show the grids generated for the standard base and dome base configurations, respectively. Each of these grids consists of 225 points in the streamwise direction and 50 points in the normal direction. This is broken down into two sections: a body region and a base region. The surface points for each region are selected using an interactive design program. Each grid section is then computed separately using a hyperbolic grid generation program<sup>10</sup>. Longitudinally, there are 106 points along the projectile surface and 60 points in the base region downstream of the base corner. The normal distribution of points in base region consists of 50 points along the base cavity. An expanded three dimensional view of the base grid is shown in Figure 6. This grid has 33 points in the circumferential direction. The generally flat sections on the standard base enabled a grid to be routinely generated. However, due to the extreme concavity the grid for the dome base (Figure 7) required an increase in the smoothing values used by the hyperbolic grid generator, as well as the addition of a grid averaging technique.

## 6. RESULTS

Numerical computations have been made for both the standard and the dome base configurations for a range of Mach numbers from  $M = 0.80$  to  $1.5$  and at  $4$  degrees angle of attack. Computed results obtained at zero degree angle of attack are also included for comparison purposes.

A few qualitative results are presented next. Figure 8 and Figure 9 show the velocity vectors in the base region for both base configurations at  $M_\infty = 0.98$  and  $\alpha = 0.0^\circ$ . The recirculatory flow in the base region is evident and as expected, is symmetric. As shown in Figure 8, the recirculation region for the standard base extends to about one and a half caliber downstream of the base corner. The back flow, upon reaching the cavity follows the contour of the cavity and leaves the cavity pushing the flow upwards. The shear layer leaving the base corner is displaced upwards weakening the expansion at the base. Figure 9 for the dome configuration shows a weak secondary bubble inside the cavity in addition to the primary bubble. The flow again follows the contour of the cavity and, upon leaving the dome cavity, is almost parallel to the streamwise direction. This flow, thus, has less effect on the free shear layer and doesn't weaken the expansion at the base corner as much compared to the standard base. The net effect is that the size of the primary bubble for the dome base is slightly smaller than that for the standard base. The reattachment point is therefore closer to the base and results in lower base pressure or higher base drag at this Mach number<sup>5</sup>. Figure 10 and Figure 11 show the velocity vectors in the base region for the base configurations at  $M_\infty = 0.98$  and  $\alpha = 4.0^\circ$  for both windside (bottom half) and leeside (top half). Again the recirculatory flow in the base region is evident and as expected, the flow in the wake is asymmetric. As shown in these figures, the separation bubbles on windside and leeside in the wake differ in size and shape (the one on windside being more thin and elongated). In addition, a number of secondary separation bubbles can be seen to form inside the cavity for both base configurations. These changes in the flow structure contribute to small changes in the base pressure and thus, to the aerodynamic forces and

moments.

Figure 12 and Figure 13 show the Mach number contours in the base region for both base configurations at  $M_\infty = 0.98$  and  $\alpha = 0.0^\circ$ . These figures show the flow expansion at the ogive corner, boattail corner and the base corner. One can also see a shock wave on the cylinder portion of the projectile as well as a recompression shock system which exists downstream of the base corner. The flow field is symmetric for this condition. As angle of attack is increased to  $4$  degrees, the flow field becomes asymmetric (see Figure 14 and Figure 15). A small asymmetry can be observed in the location of the shock wave on the cylinder. The windside shock is further aft compared to the corresponding one on the leeside. The asymmetry can be clearly seen in the wake flow and its associated shock system. As can be seen in these figures, the wake flow field changes for the different base configurations.

The entire flowfield over the projectile including the base region is computed. Therefore, the computed results include any upstream influence the base region flow may have on the boattail flowfield. Surface pressures including the base pressure and the viscous stresses are known from the computed flow field and can be integrated to give the aerodynamic forces and moments. Figure 16 shows the computed base pressure distribution for the dome base configuration at  $M_\infty = 1.1$  and  $\alpha = 4.0^\circ$  for windside and leeside. As seen in this figure, the pressure on the windside ( $Z/D = -0.5$ ) is higher than the pressure on leeside. Since this pressure acts normal to the inside surface of the cavity, it produces a downward force (see Figure 17). Figure 17 shows the normal force coefficient for the dome base as a function of Mach number. The dotted line represents the normal force coefficient,  $C_N$  for the dome base projectile where the base region is excluded in the force and moment calculations. The solid line is for the entire projectile including the contribution from the base region. As mentioned earlier, the base region produces a negative contribution and thus, the normal force is reduced somewhat for high transonic Mach numbers ( $M > 0.90$ ). The reverse is true for low transonic speeds ( $M < 0.85$ ). Figure 18 shows the normal force coefficient comparison for both base configurations as a function of Mach number. The dotted line represents the dome base result whereas the solid line shows the result for the standard base. As seen in this figure, the dome base has a higher normal force coefficient at transonic speeds compared to the standard base. The difference is small, of the order of a few percent, at higher transonic speeds ( $M > 0.90$ ) and gets as large as 10-12 % at low transonic speeds ( $M < 0.90$ ).

An aerodynamic coefficient which is of primary concern is the pitching moment coefficient,  $C_{m_a}$ . Figure 19 shows the  $C_{m_a}$  comparison for both base configurations. The computed  $C_{m_a}$  is also compared with the range data<sup>4</sup> for both base configurations. Here  $C_{m_a}$  is referenced to the center of gravity of the projectile. The computed result clearly shows a sharp rise in  $C_{m_a}$  between  $M = 0.80$  to  $0.88$  which is followed by a sharp drop as Mach number is increased to  $M = 0.95$ . As the Mach number is increased further  $C_{m_a}$  rises gradually again which is unlike the behavior of other projectiles such as the M549<sup>9</sup>. This critical behavior in  $C_{m_a}$  observed in



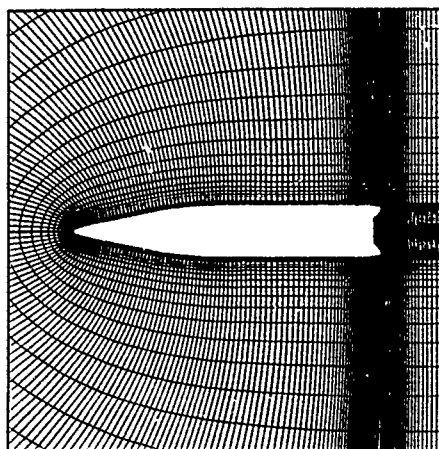


Figure 4. Computational grid for the standard base.

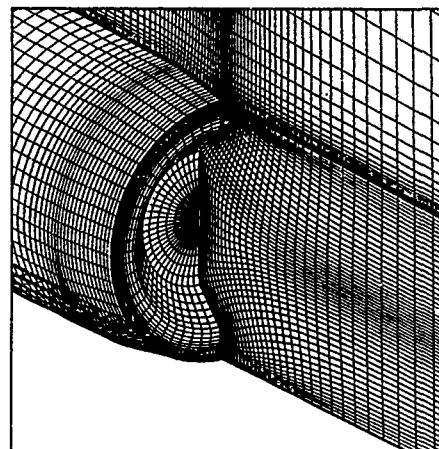


Figure 6. Base region grid for the standard base

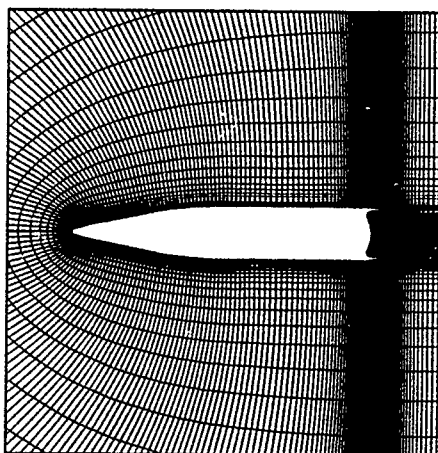


Figure 5. Computational grid for the dome base.

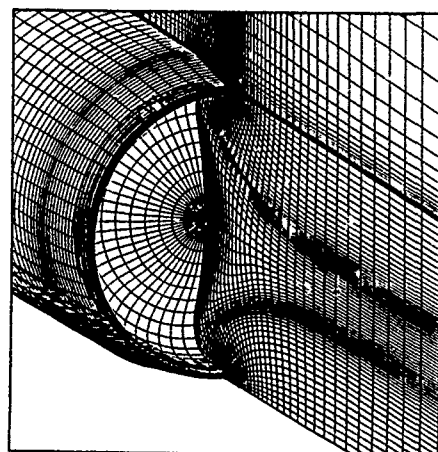


Figure 7. Base region grid for the dome base.

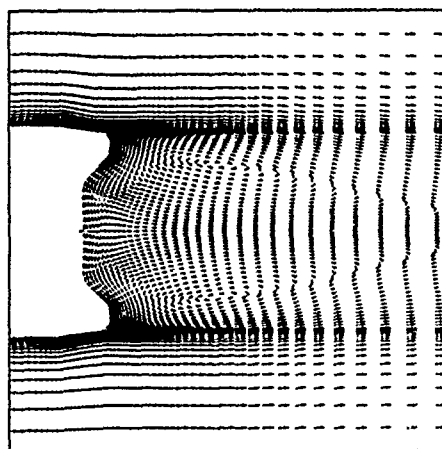


Figure 8. Velocity vectors in the base region,  $M_\infty=0.98$ ,  $\alpha = 0.0^\circ$ , (standard base).

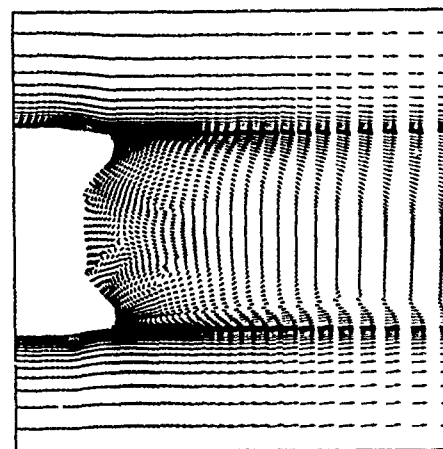


Figure 10. Velocity vectors in the base region,  $M_\infty=0.98$ ,  $\alpha = 4.0^\circ$ , (standard base).

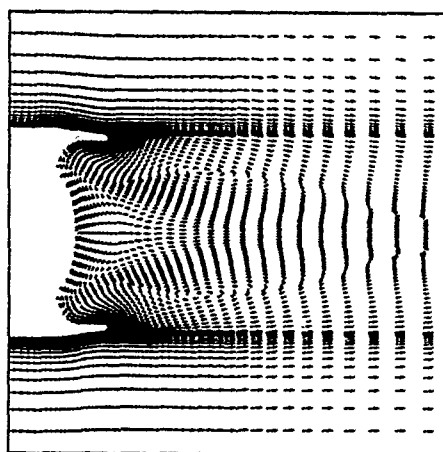


Figure 9. Velocity vectors in the base region,  $M_\infty=0.98$ ,  $\alpha = 0.0^\circ$ , (dome base).

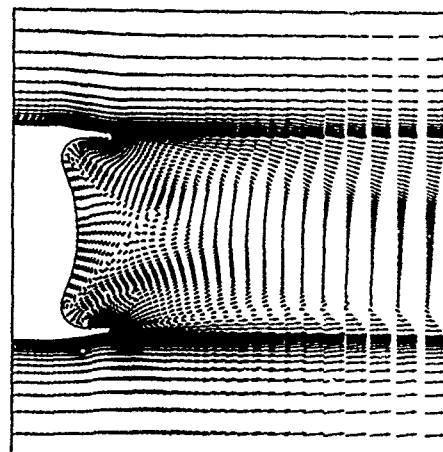


Figure 11. Velocity vectors in the base region,  $M_\infty=0.98$ ,  $\alpha = 4.0^\circ$ , (dome base).



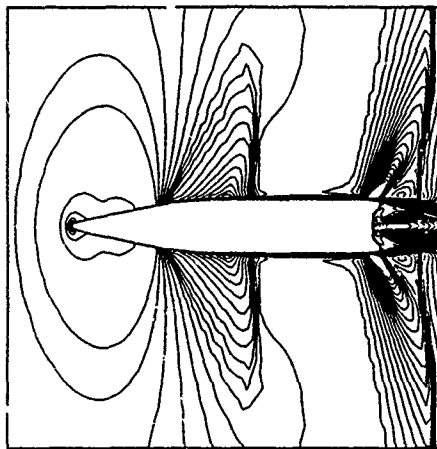


Figure 12. Mach number contours,  $M_{\infty}=0.98$ ,  $\alpha = 0.0^\circ$ , (standard base).

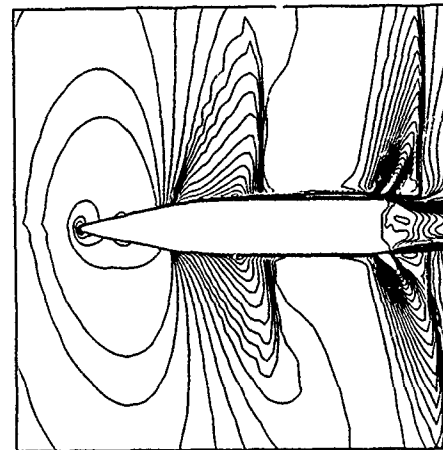


Figure 14. Mach number contours,  $M_{\infty}=0.98$ ,  $\alpha = 4.0^\circ$ , (standard base).

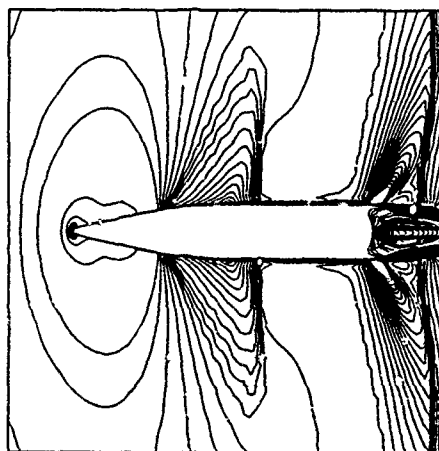


Figure 13. Mach number contours,  $M_{\infty}=0.98$ ,  $\alpha = 0.0^\circ$ , (dome base).

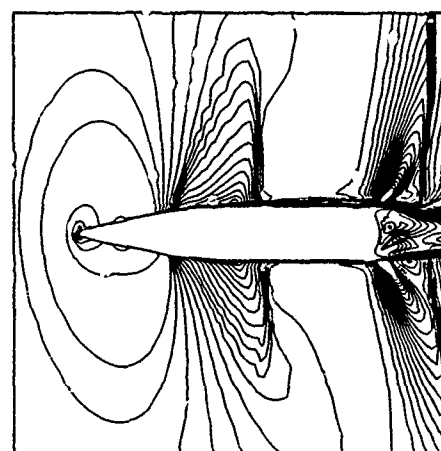


Figure 15. Mach number contours,  $M_{\infty}=0.98$ ,  $\alpha = 4.0^\circ$ , (dome base).

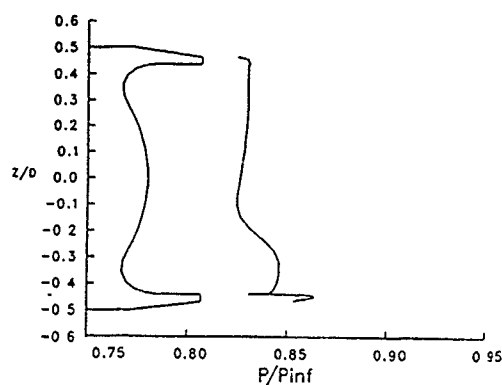


Figure 16. Base pressure distribution for the dome base,  $M_\infty=1.1$ ,  $\alpha = 4.0^\circ$ .

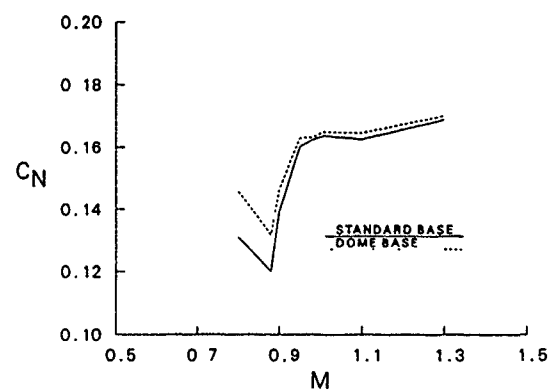


Figure 18. Normal force coefficient,  $C_N$  vs Mach number (standard base and dome base).

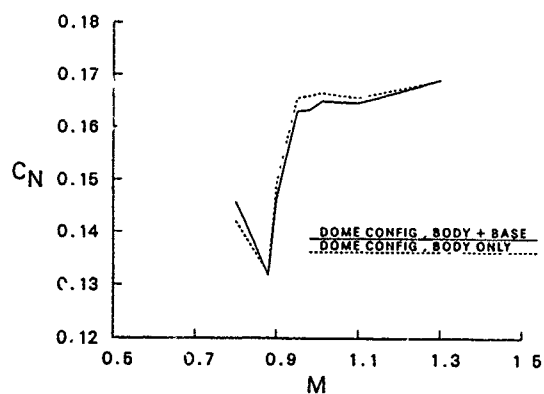


Figure 17. Normal force coefficient,  $C_N$  vs Mach number (dome base).

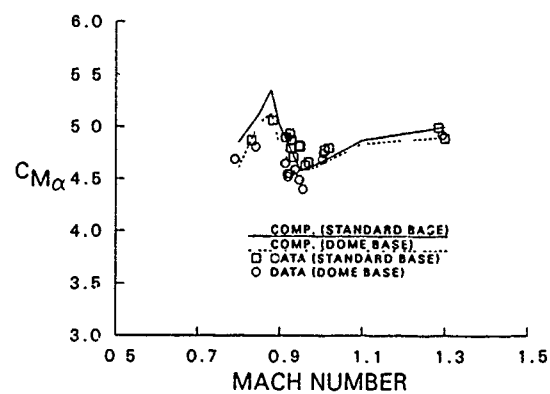


Figure 19. Pitching moment coefficient,  $C_{m_\alpha}$  vs Mach number (standard base and dome base).

# **NAVIER-STOKES PREDICTIONS OF STATIC AND DYNAMIC AERODYNAMIC DERIVATIVES FOR HIGH L/D FINNED PROJECTILES**

Paul Weinacht  
Walter B. Sturek  
Launch and Flight Division  
U.S. Army Ballistic Research Laboratory  
Aberdeen Proving Ground, Maryland 21005-5066

## **1. SUMMARY**

The current research effort has examined several aspects of the aerodynamics of finned projectiles. These are (1) static aerodynamics at angle of attack, (2) aerodynamics in pure rolling motion, and (3) aerodynamics in steady coning motion. In each case, three-dimensional viscous flow field computations have been performed over a range of supersonic Mach numbers using the parabolized Navier-Stokes technique of Schiff and Steger. The computational approach has been applied to two high L/D finned projectiles. From the flow field predictions at constant angle of attack, determination of the normal force, pitching moment, and side moment coefficients has been made. Computation of the flow field about the projectile in rolling motion has allowed the determination of the roll producing and roll damping moment coefficients, and the equilibrium spin rate. Finally, the predictions of the flow field about the projectile in steady coning motion has allowed prediction of the pitch-damping aerodynamic coefficients. Where possible, comparisons have been made between computational results and results obtained from range firings.

## **2. LIST OF SYMBOLS**

$a_\infty$	freestream speed of sound
$C_l$	net roll moment coefficient
$C_{l_0}$	roll producing moment coefficient
$C_{l_p}$	roll damping moment coefficient
$C_m$	pitching moment coefficient
$C_{m_\alpha}$	slope of the pitching moment coefficient with angle of attack
$C_{m_\alpha} + C_{m_\delta}$	pitch damping moment coefficient
$C_n$	side moment coefficient
$C_{n_\alpha}$	slope of the side moment coefficient with angle of attack
$\hat{C}_{n_\alpha}$	fluctuating part of side moment slope
$\tilde{C}_{n_\alpha}$	non-fluctuating part of side moment slope
$\hat{C}_{n_\delta}$	slope of the side moment coefficient with coning rate
$C_{n_{p\omega}}$	Magnus moment coefficient
$C_{N_\alpha}$	slope of the normal force coefficient with angle of attack
$C_{N_\alpha} + C_{N_\delta}$	pitch damping force coefficient
$C_{Y_\delta}$	slope of the side force coefficient with coning rate
$C_{Y_{p\omega}}$	Magnus force coefficient
$D$	projectile diameter
$e$	total energy per unit volume
$\hat{E}, \hat{F}, \hat{G}$	flux vectors in transformed coordinates

$\hat{H}$	source term in Navier-Stokes eqs.
$J$	Jacobian
$l$	characteristic length, typically $D$
$M_\infty$	freestream Mach number
$p$	pressure, as used in N-S eqs
$\dot{p}$	spin rate, as used roll equations
$p_\infty$	freestream static pressure
$Re$	Reynolds number, $a_\infty \rho_\infty D / \mu_\infty$
$s$	distance downrange
$s_{cg}$	center of gravity shift, calibers
$\vec{S}$	viscous flux vector
$S_{ref}$	reference area of projectile, $\pi D^2 / 4$
$t$	time
$u, v, w$	velocity components in x, y, z directions
$V$	freestream velocity
$x, y, z$	Cartesian coordinates w.r.t. body
$x_{cg}$	axial location of body center of gravity

Note. Force coefficients are scaled,  $F / \frac{1}{2} \rho_\infty a_\infty^2 M_\infty^2 S_{ref}$ ,  
Moment coefficients are scaled,  $M / \frac{1}{2} \rho_\infty a_\infty^2 M_\infty^2 D S_{ref}$

## **Greek Symbols**

$\alpha, \beta$	vertical and horizontal components of angle of attack in non-rolling coordinates
$\alpha_t$	total angle of attack, $\sqrt{\alpha^2 + \beta^2}$
$\gamma$	ratio of specific heats, in N-S eqs
$\gamma$	cosine of the angle of attack, as used in aerodynamic force and moment eqs.
$\delta$	sine of the angle of attack
$\mu, \mu_t$	laminar and turbulent viscosity
$\xi, \eta, \zeta$	transformed coordinates in N-S eqs.
$\xi$	complex angle of attack
$\rho$	density
$\rho_\infty$	freestream density
$\phi$	coning rate of projectile
$\frac{\phi D}{V}$	nondimensional coning rate
$\Omega_c$	angular rate of rotating coordinate frame

## **Superscripts**

$()$	rate of change with respect to time
$()'$	rate of change with respect to space
$()$	referenced to non-rolling coordinate frame

## **3. INTRODUCTION**

The Computational Aerodynamics Branch, Launch and Flight Division has been actively developing the capability to predict the aerodynamics of US Army projectiles using Computational Fluid Dynamics (CFD) tech-

niques. Currently under development is the capability to predict the supersonic aerodynamics of finned projectiles such as kinetic energy (KE) penetrators.

The current research effort has examined several aspects of the aerodynamics of KE projectiles. These are (1) static aerodynamics at angle of attack, (2) aerodynamics in pure rolling motion, and (3) aerodynamics in steady coning motion. In each case, three-dimensional viscous flow field computations have been performed over a range of supersonic Mach numbers using the parabolized Navier-Stokes technique of Schiff and Steger<sup>1</sup>. In this paper, results obtained by applying the computational approach to two finned high L/D KE projectiles, the M829 and the M735, are presented. Schematics of these projectiles are shown in Figures 1 and 2.

By examining the three motions described above, several important aerodynamic parameters can be determined. From the flow field predictions at constant angle of attack, determination of the normal force and pitching moment coefficients has been made. These predictions allow the static aerodynamic stability of the projectile to be assessed. Computation of the flow field about the projectile in rolling motion has allowed the determination of the roll producing and roll damping moment coefficients. These aerodynamic coefficients can then be used to predict the roll history of the projectile, including the steady-state spin rate. Finally, the predictions of the flow field about the projectile in steady coning motion has allowed prediction of the pitch-damping moment coefficient. This coefficient is essential in predicting the rate of decrease of the projectile's yaw during flight. Where possible, comparisons have been made between computational results and results obtained from range firings<sup>2</sup>.

In the next several sections, the computational technique is briefly described, and the results obtained by examining the three types of projectile motion are presented.

#### 4. COMPUTATIONAL APPROACH

Computation of the viscous flow field about the finned projectile configurations was accomplished by solving the thin-layer Navier-Stokes equations using a parabolized Navier-Stokes technique. Flow field predictions about the projectile in rolling or coning motion are performed using a rotating coordinate frame which rotates at the roll rate or coning rate of the projectile. The fluid flow relative to the rotating coordinate frame does not vary with time, allowing the steady (non-time varying) Navier-Stokes equations to be applied. The solution of the steady Navier-Stokes equations can be performed at a reasonable computational cost. In order to implement the rotating coordinate frame, the governing equations have been modified to include the effect of centrifugal and Coriolis forces. The steady thin-layer Navier-Stokes equations are shown below.

$$\frac{\partial \hat{E}}{\partial \xi} + \frac{\partial \hat{F}}{\partial \eta} + \frac{\partial \hat{G}}{\partial \zeta} + \hat{H} = \frac{1}{Re} \frac{\partial \hat{S}}{\partial \zeta} \quad (1)$$

Here,  $\hat{E}$ ,  $\hat{F}$ , and  $\hat{G}$  are the inviscid flux vectors,  $\hat{S}$  is the viscous flux vector, and  $\hat{H}$  is the source term containing the Coriolis and centrifugal force terms which result

from the rotating coordinate frame. Each of these matrices are functions of the dependent variables represented by the vector  $q(\rho, \rho u, \rho v, \rho w, e)$ , where  $\rho$  and  $e$  are the density and the total energy per unit volume, and  $u$ ,  $v$ , and  $w$ , are the velocity components in  $x$ ,  $y$ , and  $z$  directions. The flux terms are shown below.

$$\begin{aligned} \hat{E} &= \frac{1}{\gamma} \begin{bmatrix} \rho U \\ \rho u U + \xi_x p \\ \rho v U \\ \rho w U \\ (e + p)U \end{bmatrix} & \hat{F} &= \frac{1}{\gamma} \begin{bmatrix} \rho V \\ \rho u V + \eta_x p \\ \rho v V + \eta_y p \\ \rho w V + \eta_z p \\ (e + p)V \end{bmatrix} \\ \hat{G} &= \frac{1}{\gamma} \begin{bmatrix} \rho W \\ \rho u W + \zeta_x p \\ \rho v W + \zeta_y p \\ \rho w W + \zeta_z p \\ (e + p)W \end{bmatrix} & \hat{H} &= \frac{1}{\gamma} \begin{bmatrix} 0 \\ H_2 \\ H_3 \\ H_4 \\ H_5 \end{bmatrix} \\ \hat{S} &= \frac{1}{\gamma} \begin{bmatrix} 0 \\ m_1 \frac{\partial u}{\partial \zeta} + m_2 \zeta_x \\ m_1 \frac{\partial v}{\partial \zeta} + m_2 \zeta_y \\ m_1 \frac{\partial w}{\partial \zeta} + m_2 \zeta_z \\ m_3 \end{bmatrix} \end{aligned} \quad (2)$$

where

$$\begin{aligned} H_2 &= -2\Omega_c \sin \alpha_t \rho v - \rho \Omega_c^2 \sin^2 \alpha_t (x - x_{cg}) \\ &\quad + \rho \Omega_c^2 z \sin \alpha_t \cos \alpha_t \\ H_3 &= 2\Omega_c \sin \alpha_t \rho u - 2\Omega_c \cos \alpha_t \rho w - \rho \Omega_c^2 y \\ H_4 &= 2\Omega_c \cos \alpha_t \rho v + \rho \Omega_c^2 \sin \alpha_t \cos \alpha_t (x - x_{cg}) \\ &\quad - \rho \Omega_c^2 z \cos^2 \alpha_t \\ H_5 &= (-\Omega_c^2 \sin^2 \alpha_t (x - x_{cg}) + \Omega_c^2 z \sin \alpha_t \cos \alpha_t) \rho u \\ &\quad - (\Omega_c^2 y \sin^2 \alpha_t + \Omega_c^2 z \cos^2 \alpha_t) \rho v \\ &\quad + (\Omega_c^2 \sin \alpha_t \cos \alpha_t (x - x_{cg}) - \Omega_c^2 z \cos^2 \alpha_t) \rho w \end{aligned} \quad (3)$$

$$\begin{aligned} U &= u \xi_x \\ V &= u \eta_x + v \eta_y + w \eta_z \\ W &= u \zeta_x + v \zeta_y + w \zeta_z \end{aligned} \quad (4)$$

$$\begin{aligned} m_1 &= (\mu + \mu_t)(\zeta_x^2 + \zeta_y^2 + \zeta_z^2) \\ m_2 &= \frac{1}{3}(\mu + \mu_t)(\zeta_x \frac{\partial u}{\partial \zeta} + \zeta_y \frac{\partial v}{\partial \zeta} + \zeta_z \frac{\partial w}{\partial \zeta}) \\ m_3 &= \frac{1}{(\gamma - 1)} \left( \frac{\mu}{Pr} + \frac{\mu_t}{Pr_t} \right) (\zeta_x^2 + \zeta_y^2 + \zeta_z^2) \frac{\partial a^2}{\partial \zeta} \\ &\quad + \frac{1}{2} m_1 \frac{\partial q^2}{\partial \zeta} + m_2 (u \zeta_x + v \zeta_y + w \zeta_z) \\ a^2 &= \frac{\gamma p}{\rho}, \quad q^2 = u^2 + v^2 + w^2 \end{aligned} \quad (5)$$

$$\begin{aligned} \xi_x &= \frac{1}{x_\xi} \\ \eta_x &= J(z_\xi y_\eta - y_\xi z_\eta) & \eta_y &= J(x_\xi z_\eta) & \eta_z &= J(-x_\xi y_\eta) \\ \zeta_x &= J(y_\xi z_\eta - z_\xi y_\eta) & \zeta_y &= J(-x_\xi z_\eta) & \zeta_z &= J(x_\xi y_\eta) \\ J &= 1/(x_\xi(y_\eta z_\eta - y_\xi z_\eta)) \end{aligned} \quad (6)$$

The computations at angle of attack do not employ the rotating coordinate frame ( $\Omega_c = 0$ ) and the

source term is not required. The flow field predictions for the projectile in pure rolling motion are performed at zero angle of attack and the coordinate frame rotates at the spin rate of the projectile,  $p$ ; ( $\alpha_t = 0, \Omega_c = p$ ). Computations for the projectile in steady coning motion are performed at a non-zero angle of attack with the coordinate frame rotating at the coning rate of the projectile,  $\phi$ ; ( $\alpha_t \neq 0, \Omega_c = \phi$ ).

The pressure,  $p$ , which appears in the flux terms, can be related to the dependent variables by applying the ideal gas law.

$$p = (\gamma - 1) \left[ e - \frac{\rho}{2} q^2 \right] \quad (7)$$

The turbulent viscosity,  $\mu_t$ , which appears in the viscous matrices was computed using the Baldwin-Lomax turbulence model<sup>3</sup>.

The thin-layer equations are solved using the Parabolized Navier-Stokes technique of Schiff and Steger<sup>1</sup>. Following the approach of Schiff and Steger, the governing equations, which have been modified here to include the Coriolis and centrifugal force terms, are solved using a conservative, approximately factored, implicit finite-difference numerical algorithm as formulated by Beam and Warming<sup>4</sup>.

Following the approach of Schiff and Steger, the equations are first linearized and placed in delta form, where the equations are solved for the difference in the dependent variables rather than the variable itself. This set of equations is then factorized using the approach of Beam and Warming. The following set of equations is obtained.

$$\left[ \tilde{A}_i^j + (1 - \alpha) \Delta \xi \left( \delta_{ij} \tilde{B}^j + \tilde{D}^j \right) \right] \Delta \tilde{q}^* = RHS \quad (8)$$

$$\left[ \tilde{A}^j + (1 - \alpha) \Delta \xi \left( \delta_{ij} \tilde{C}^j - \frac{1}{Re} \left( \tilde{\delta}_i \tilde{M}^j \right) \right) \right] \Delta \tilde{q}^j = \tilde{A}_i^j \Delta \tilde{q}^* \quad (9)$$

$$\begin{aligned} RHS = & -(\tilde{A}_i^j - \tilde{A}_i^{j-1}) \tilde{q}^j + \alpha (\tilde{E}_i^j - \tilde{E}_i^{j-1}) \\ & - [(\xi_x/J)^{j+1} \tilde{E}_p^j - (\xi_x/J)^j \tilde{E}_p^{j-1}] - (1 - \alpha) \Delta \xi \{ \\ & \delta_{ij} [\eta_x^{j+1} (E/J)^j + \eta_y^{j+1} (F/J)^j + \eta_z^{j+1} (G/J)^j] \\ & + \delta_{ij} [\zeta_x^{j+1} (E/J)^j + \zeta_y^{j+1} (F/J)^j + \zeta_z^{j+1} (G/J)^j] \\ & + \tilde{H}^j - \frac{1}{Re} \tilde{\delta}_i \tilde{S}^j \} \end{aligned} \quad (10)$$

The form of the equations, as well as the notation, is similar to that used by Schiff and Steger. Here,  $\tilde{A}$ ,  $\tilde{B}$ ,  $\tilde{C}$ , and  $\tilde{M}$  are the Jacobian matrices of the flux vectors  $\tilde{E}$ ,  $\tilde{F}$ ,  $\tilde{G}$ , and  $\tilde{S}$ . Further details on the definitions of these matrices can be found in Reference 1. The important difference here is the addition of the matrices  $\tilde{D}$  and  $\tilde{H}$  due to the rotating coordinate system. Although the Jacobian matrix,  $\tilde{D}$ , can be included in either the circumferential inversion or in the normal inversion, including this term in the circumferential inversion simplifies slightly the implementation of the shock fitting boundary conditions.

The computations presented here were performed using a shock fitting procedure reported by Rai and

Chaussee<sup>5</sup>. This procedure solves the five Rankine-Hugoniot jump conditions, two geometric shock-propagation conditions, and one compatibility equation to determine the values of the five dependent variables immediately behind the shock, as well as the position of the shock. By including the implicit part of the source term due to the rotating coordinate frame in the circumferential inversion, the shock fitting procedure of Rai and Chaussee can be used without modification, as long as the correct free-stream conditions are specified as shown below.

$$\begin{aligned} \rho &= \rho_\infty \\ \rho u &= \rho_\infty M_\infty a_\infty \cos \alpha_t + \rho_\infty y \Omega_c \sin \alpha_t \\ \rho v &= \rho_\infty \Omega_c (z \cos \alpha_t - (x - x_{cg}) \sin \alpha_t) \\ \rho w &= \rho_\infty M_\infty a_\infty \sin \alpha_t - \rho_\infty y \Omega_c \cos \alpha_t \\ e &= p_\infty / (\gamma - 1) + \frac{1}{2} \rho_\infty \{ (M_\infty a_\infty \cos \alpha_t + y \Omega_c \sin \alpha_t)^2 \\ &+ (\Omega_c (z \cos \alpha_t - (x - x_{cg}) \sin \alpha_t))^2 \\ &+ (M_\infty a_\infty \sin \alpha_t - y \Omega_c \cos \alpha_t)^2 \} \end{aligned} \quad (11)$$

The computational results presented here were obtained using a grid which consisted of 60 points between the body and the shock. In the circumferential direction, gridding was performed over the entire body (360 degrees), except for the computations in pure rolling motion, where symmetry allows the computations performed over a 60 degree sector. The full plane computations employed 72 circumferential points on the forebody and 300 points on the finned portion of the body. Algebraic grid generation approaches were applied on the forebody. The grid over the finned part of the body was generated using an elliptic grid generation scheme presented by Rai and Chaussee<sup>6</sup>.

The computations were performed on a Cray-2 supercomputer. Full plane solutions required one and a half to two hours of CPU time. The roll calculation required about 20 percent of the full plane run times because the symmetry.

## 5. RESULTS

The computational technique has been applied to examine several aspects of the aerodynamics of KE projectiles. These are (1) the static aerodynamics at angle of attack, (2) aerodynamics in pure rolling motion, and (3) aerodynamics in steady coning motion. Each of these topics are examined in the following three sections.

### 5.1 Static Aerodynamics at Angle of Attack

In this section, the results of computations performed with the projectile held at a fixed angle of attack (angle of inclination with respect to the freestream velocity) are presented. Aerodynamic coefficient predictions have been made for the pitching moment, normal force, and side force and moment. The computations discussed below were performed at two degrees angle of attack and over a range of Mach numbers ( $M = 3.0$  to 5.5) for free-flight (sea-level) atmospheric conditions. Representative results are shown for the M829 and M735 projectiles.

Figure 3 shows the computed pitching moment coefficient as a function of Mach number for the M829. Both the computed results and the results obtained from

the range firings are shown. The computed results and the range results show the same variation with Mach number, though the computation over-predicts the pitching moment coefficient by about eight percent. This difference is greater than the estimated error in the range data, which is about two percent for most of the rounds shown here. The differences in the two results is most likely due to the effect of the sabot grooves which cover a large part of the cylindrical portion of the body. The grooves increase the thickness of the boundary layer and, thus, may decrease the lift of the fins. The grooves are currently not modeled in the computations. Results obtained for the M735 show similar behavior, as shown in Figure 4.

The computed normal force coefficient as a function of Mach number for the M735 is shown in Figure 5. Also shown is data obtained from range firings. The normal force coefficient from the range firings is determined from the swerving motion of the projectile (motion of the center of gravity). This motion tends to be small for this class of projectiles due to their high mass. Hence, the range data for this coefficient is often not well determined according to the criteria proposed by Murphy<sup>7</sup>. The computational predictions are within the scatter of the range data.

A finned projectile can develop a side moment in the absence of spin when pitched up at angle of attack. A finned projectile with symmetrically arranged fins and symmetrical fin cross-sections can develop a side moment which varies periodically according to the orientation of the fins with respect to the pitch-plane. Of course, when the orientation of the fins is symmetrically arranged about the pitch-plane, the side moment will be zero. For a projectile with an even number of fins, this will occur when one set of fins is aligned with the pitch-plane or when one set of fins is aligned normal to the pitch-plane. For the typical flight profile of US Army kinetic energy projectiles, this side moment due to roll orientation will not have a significant effect because it is usually small and the periodic nature of the side moment is "integrated out" since the projectile typically spins at roll rates which are above the pitching frequency.

If the finned projectile has fins which have cross-sections which are not symmetric with respect to the axis of symmetry of the projectile, (i.e. if the fins are canted or if the fins have leading and/or trailing edge bevels) the projectile can develop an additional component of side moment. The asymmetric fin cross-section will produce a lift force on each of the fins. This lift force when integrated over each of the fins will produce a roll producing moment which will cause the projectile to roll. At zero angle of attack, the lift produced by each fin will be equal in magnitude and the integrated effect of the lift force will produce a couple about the axis of symmetry of the projectile. Thus, no net side force or moment is generated. At a non-zero angle of attack, the lift on each of the fins may not be identical because each of the fins is exposed to a different flow upstream of the leading edge. In particular, some of the fins may be in the wake created by the projectile body.

The variation of the side moment coefficient as a function of roll angle at Mach 4 is shown in Figure 6. The computational results are shown at roll angle increments of six degrees. A sine curve was fit through the

data using a least squares procedure. The sine curve had the following form,

$$C_{n_s} = \bar{C}_{n_s} + \hat{C}_{n_s} \sin 6(\phi + \phi_0) \quad (12)$$

The coefficient,  $\bar{C}_{n_s}$ , represents the non-fluctuating component (with respect to roll angle), while the coefficient,  $\hat{C}_{n_s}$ , represents the amplitude of the fluctuating component. A phase angle,  $\phi_0$ , was also included. The phase angle was  $\pm 2$  degrees across the Mach number regime. Figure 6 demonstrates that the computed side moment coefficient exhibits a sinusoidal variation with roll angle, as evidenced by the quality of the least squares fit. Similar variation was seen at each of the Mach numbers examined.

Figure 7 shows the variation of the non-fluctuating and fluctuating components of the side moment coefficient with Mach number. The non-fluctuating component shows a peak at about Mach 3.5 and drops rapidly with increasing Mach number. The non-fluctuating component of the side moment is seen to be greater than the fluctuating component across the Mach number regime.

## 5.2 Aerodynamics in Pure Rolling Motion

Aero-ballisticians describe the spin history of the projectile in terms of the following ordinary differential equation<sup>7</sup>:

$$I \frac{dp}{dt} = \frac{1}{2} \rho_{\infty} a_{\infty}^2 M_{\infty}^2 D S_{ref} C_l \quad (13)$$

where  $p$  is the spin rate,  $t$  is time,  $I$  is the axial moment of inertia,  $C_l$  is the net aerodynamic roll moment coefficient acting on the projectile, and  $\rho_{\infty}$ ,  $a_{\infty}$ ,  $M_{\infty}$ ,  $D$ , and  $S_{ref}$  are, respectively, the reference density, speed of sound, Mach number, diameter, and area.

The net aerodynamic roll moment is composed of two components, the roll producing moment and the roll damping moment. The roll producing moment, which induces spin on the projectile, results from the aerodynamic loads produced by either the machined asymmetries in the fin geometry or by the fin cant, while the roll damping contribution consists of pressure and viscous forces that oppose the spin. The relationship of these contributions to the net aerodynamic roll moment is expressed below in non-dimensional form,

$$C_l = C_{l_p} + C_{l_r} \frac{pD}{V} \quad (14)$$

where  $C_{l_p}$  is the roll producing moment coefficient,  $C_{l_r}$  is the roll damping moment coefficient and  $\frac{pD}{V}$  is the non-dimensional spin rate. The roll damping coefficient will differ in sign with the roll producing moment coefficient and will be negative if the direction of positive roll moment is in the direction of positive spin.

In the computational frame work, where the projectile is flying at constant velocity, Equation 14 shows that the roll producing moment can be obtained by computing the net aerodynamic roll moment at zero spin rate. Likewise, the roll damping moment is obtained by computing the net aerodynamic roll moment on the projectile at a fixed spin rate, subtracting the roll producing moment from it and dividing by the spin rate. The

equilibrium spin rate, which occurs when the net aerodynamic roll moment is zero, is obtained by dividing the roll producing moment by the roll damping moment.

Predictions of these aerodynamic parameters have been obtained for the M829 kinetic energy projectile and comparisons made with data obtained from range firings. In order to determine these aerodynamic parameters, computations were performed over a range of Mach numbers ( $M = 3.0$  to  $5.5$ ) and non-dimensional spin rates ( $pD/V = 0$  to  $.015$ ) for free-flight (sea-level) atmospheric conditions. Roll histories also were obtained by solving the roll equation using the computed aerodynamic roll moment coefficients and were compared with the range measurements. The steady-state spin rate and the roll producing and roll damping moment coefficients were also determined from the range measurements. The comparison between range and computed values of these parameters is made in the next several figures.

Figure 8 shows the comparison of the steady-state spin rate as a function of Mach number. The computed results are bracketed by the range data, demonstrating that the predictions of the steady-state spin rate are within the accuracy of measurements.

Comparisons of the roll producing and roll damping moment coefficients are shown in Figures 9 and 10. The computed results for both coefficients lie somewhat above the range data. At Mach 5.25, the range values of the roll producing moment coefficient are 4 to 35 percent below the computed result, while the range values of the roll damping moment coefficient are 10 to 38 percent below the computed value. The result that both coefficients show similar comparisons between range and computed values is a reflection of the fact that the steady-state spin rate is approximately the ratio of the roll producing moment coefficient to the roll damping moment coefficient. As was shown in Figure 8, this ratio is accurately predicted.

Some of the variability in the range values of roll producing and roll damping moment coefficient can be traced to the measurement of the spin rate at the two measurement stations. For example, it can be shown that a  $\pm 10$  percent variation in the roll rate at the first measurement location will result in about a  $\pm 20$  percent variation in the roll producing or roll damping moment coefficients. Improvements in the determination of the roll coefficients can be made by adding additional measurement stations.

Using the computed roll producing and roll damping moment coefficients, spin histories of the projectile were determined by solving the roll equation (Equation 13). Spin trajectories were obtained for four launch Mach numbers; 3.5, 4.0, 4.65, and 5.25; corresponding closely to the four groups of launch Mach numbers used in the range firings. A representative trajectory (Launch Mach = 5.25) is shown in Figure 11. The computed spin history falls within the range of the range data at both of the measurement locations. The computed trajectories show that at the second measurement station, the projectile is within 3 percent of the steady-state spin rate.

### 5.3 Aerodynamics in Steady Coning Motion

Gun tube launched kinetic energy (KE) projectiles typically fly with some degree of pitching motion caused by launch disturbances such as the whipping motion of the gun tube, inbore balloting of the projectile, and the sabot discard process. The pitching motion of the projectile decreases or damps as the projectile travels downrange due to the aerodynamic properties of the projectile body. For finned KE projectiles, the rate at which the pitching motion is damped is a function of the pitch damping aerodynamic coefficient and the body's transverse moment of inertia.

The ability to accurately predict the pitch-damping aerodynamic coefficient of KE projectiles is of significant importance to the projectile designer because the terminal ballistic performance of these projectiles is sensitive to the pitching motion at the target. Small levels of pitching motion may result in significant degradation of the penetrator's terminal ballistic performance. If the penetrator and the target are closely matched, this degradation of penetrator performance can result in the inability of the penetrator to defeat the target.

By applying linear flight mechanics theory such as that developed by Murphy<sup>7</sup>, it can be shown that aerodynamic side force and moment coefficients acting on a projectile in steady coning motion can be related to the pitch damping force and moment coefficients. Steady coning motion is defined as the motion performed by a missile flying at a constant angle with respect to the free stream velocity vector (angle of attack) and undergoing a rotation at a constant angular velocity about a line parallel to the freestream velocity vector and coincident with the projectile center of gravity. This is shown schematically in Figure 12. Coning motion is, in fact, a specific combination of two orthogonal planar pitching motions, plus a spinning motion. It is significant that the combination of these unsteady or time-dependent motions (pitching and spinning) produces a steady coning motion. The use of steady coning motion to determine the pitch damping aerodynamic coefficients provides an interesting approach for determining the aerodynamics which are normally associated with unsteady or time-dependent motions.

Previously, Tobak, Schiff, and Peterson<sup>8</sup> examined the aerodynamics of bodies of revolution in coning motion and proposed that the non-linear aerodynamic forces and moments acting on a body performing large amplitude non-planar motions could be composed of four characteristic motions, (1) steady angle of attack, (2) pitching motion, (3) rolling motion, and (4) coning motion. Typically, the linear aerodynamic force and moment formulation considers only forces and moments due to the first three motions, and assumes that a non-planar motion can be described by the vector sum of two independent planar motions. The addition of coning motion allows for coupling between planar motions in the non-linear formulation. Their nonlinear theory also confirms the linear theory result that the side force and moment due to coning motion is related to the linear pitch damping coefficients.

To provide additional validation for the theory, Schiff and Tobak<sup>9</sup> performed wind tunnel experiments on a conical body undergoing separate or combined spin-

ning and coning motions. Their results showed that, at low angles of attack, the slopes of the side force and moment with angle of attack normalized by the coning rate were in good agreement with predictions of the damping-in-pitch force and moment coefficients obtained using linearized theory. They also demonstrated that the Magnus force and moment (variation of side force and moment with spin rate and angle of attack) was negligible, thus the linear pitch damping coefficients could be determined from the side force and moment due to coning alone.

As part of the development, Schiff<sup>10</sup> computed the supersonic inviscid flow about a conical body undergoing coning motion. To compute the flow around the body in coning motion, Schiff made use of a rotating coordinate frame. Within the rotating coordinate frame the flow was steady, thus the steady Euler equations could be solved. The governing equations were modified to include the centrifugal and Coriolis force terms. His computed results compared well with experimental results and with estimates of pitch-damping coefficients using a linear theory. Later studies by Agarwal and Rakich<sup>11</sup> and Lin<sup>12</sup> also employed rotating coordinate frames to compute the supersonic viscous flow about conical bodies in coning motion.

### 5.3.1 Relation between Coning and Pitching Motions

As was discussed previously, steady coning motion is defined as the motion performed by a missile flying at a constant angle with respect to the free stream velocity vector (angle of attack) and undergoing a rotation at a constant angular velocity about a line parallel to the freestream velocity vector and coincident with the projectile center of gravity. This is shown schematically in Figure 12. With respect to a non-rolling coordinate frame, the vertical and horizontal components of the angle of attack,  $\alpha$  and  $\beta$ , vary in a periodic fashion as the projectile rotates about the free-stream velocity vector. This is shown in Figure 13. The total angle of attack,  $\alpha_t = \sqrt{\alpha^2 + \beta^2}$  is constant, however.

Both of these components of the angle of attack when plotted as a function of time are seen to be sinusoidal, constant amplitude, pitching motions which are out of phase with each other by one quarter of a cycle, as shown in Figure 14. This demonstrates that coning motion is composed of a specific combination of two orthogonal planar pitching motions.

In addition to the pitching motion, the projectile body will undergo a rotation with respect to the non-rolling coordinate system, which by definition, is a spinning motion. The change in the orientation of a set of axes fixed to the body as the body performs the coning motion is also shown in Figure 13. The spin rate,  $p$ , is proportional to the coning rate,  $\dot{\phi}$ , as shown below.

$$p = \gamma \dot{\phi} = \cos(\alpha_t) \dot{\phi} \quad (15)$$

Thus, coning motion is a combination of two orthogonal planar pitching motions, plus a spinning motion. These are the three motions shown schematically in Figure 14.

The combination of the two pitching motions and the spinning motion when viewed by an observer fixed

to any part of the projectile body produces a motion which does not vary with time. The same can be said for an observer in the flow field external to the body whose position is fixed with respect to the body. Thus, the coning motion and the flow field produced by the coning motion are steady (or non-time varying) phenomenon. This allows steady flow modeling techniques to be applied to determine the flow field produced by this motion. The governing equations must be modified, however, because the coordinate system is rotating as discussed previously.

It is significant that the combination of these unsteady or time-dependent motions (pitching and spinning) produces a steady motion (coning). The use of steady coning motion to determine the pitch damping aerodynamic coefficients provides an interesting approach for determining the aerodynamics which are normally associated with unsteady or time-dependent motions.

### 5.3.2 Relation between Side Moment due to Coning and Pitch Damping Moment

The moment expansion for a finned kinetic energy penetrator in the non-rolling coordinate frame is shown below. This moment expansion is a variant of the expansion discussed by Murphy for symmetric missiles<sup>7</sup>. The difference is that the expression here includes a side moment due to angle of attack,  $C_{n_s}$ . The moment formulation uses complex variables to separate the moment components,  $\tilde{C}_m$  and  $\tilde{C}_n$  which produce rotations in the vertical and horizontal planes.

$$\tilde{C}_m + i\tilde{C}_n = \left[ \left( \frac{p}{V} \right) C_{n_{ps}} + C_{n_s} - iC_{m_s} \right] \tilde{\xi} - \frac{i}{\gamma} [C_{m_s} + \gamma C_{m_s}] \tilde{\xi}' \quad (16)$$

In the moment formulation, the pitching moment coefficient,  $C_{m_s}$ , and pitch damping moment coefficient,  $C_{m_s} + C_{m_s}$ , produce moments proportional to the complex angle of attack,  $\tilde{\xi}$ , and angular rate,  $\tilde{\xi}'$ , respectively. The Magnus moment coefficient,  $C_{n_{ps}}$ , accounts for a side moment due to flow asymmetries from a combination of spin and angle of attack. The side moment due to angle of attack,  $C_{n_s}$ , is retained to account for a side moment variation with angle of attack which is caused by the beveled fins.

The moment expansion presented above has been developed for rotationally symmetric missiles. Murphy<sup>7</sup> has shown that the form of the linear force and moment expansion for a symmetric finned missile with three or more fins should have the same form as for a body of revolution. Effects of the orientation of the fins with respect to the pitch-plane are believed to be small for kinetic energy projectiles. Furthermore, these projectiles typically roll at spin rates which are greater than the pitching frequency. Effects of roll orientation are averaged out since the frequency of the effects of roll orientation is much greater than the pitching frequency.

In order to develop the relation between the side moment due to coning motion and the pitch damping moment coefficient, it is convenient to resolve the moment components in non-rolling coordinates into moment components which cause rotations in and out of the plane of the angle of attack. This relation is shown below. Here,  $C_m$  is the in-plane moment (the moment



which causes rotation of the body in the plane of the attack of attack), and  $C_n$  is the side moment (the moment that causes rotations of the body out of the angle of attack plane). Also shown are relations for the complex angle of attack, angular rate, and spin rate. These relations, valid for steady coning motion, have been simplified from the general case of arbitrary motion<sup>13</sup>

$$\begin{aligned} C_m + iC_n &= ie^{-i\gamma\phi t}(\bar{C}_m + i\bar{C}_n) \\ \bar{\xi} &= \delta e^{i\gamma\phi t} \\ \bar{\xi}' &\equiv \frac{d\bar{\xi}}{d(\frac{\phi}{V})} = i\delta\gamma\frac{\phi}{V}e^{i\gamma\phi t} \\ p &= \gamma\phi \end{aligned} \quad (17)$$

The moment formulation in the aerodynamic coordinate frame is shown below.

$$\begin{aligned} C_m + iC_n &= C_{m_0}\delta + i\left\{\left(\frac{\gamma\phi}{V}\right)C_{n_{ps}}\delta + C_{n_0}\delta\right. \\ &\quad \left.+ \delta\left(\frac{\phi}{V}\right)[C_{m_0} + \gamma C_{m_0}]\right\} \end{aligned} \quad (18)$$

As expected, the resulting expression for the in-plane and side moments is independent of time. The in-plane moment results only from the pitching moment, while the total side moment consists of contributions from the side moment due to angle of attack, Magnus moment and pitch damping moment.

The side moment due to coning normalized by the coning rate can be written as follows;

$$\frac{C_n - C_{n_0}\delta}{\frac{\phi}{V}} = \delta(\gamma C_{n_{ps}} + [C_{m_0} + \gamma C_{m_0}]) \quad (19)$$

The notation can be simplified by noting that the left hand side of Equation 19 is simply the variation of side moment with coning rate, valid for linear variations of side moment with coning rate.

$$C_{n_0} \equiv \frac{\partial C_n}{\partial(\frac{\phi}{V})} = \frac{C_n - C_{n_0}\delta}{\frac{\phi}{V}} = \delta(\gamma C_{n_{ps}} + [C_{m_0} + \gamma C_{m_0}]) \quad (20)$$

This relation is similar to that presented by Schiff and Tobak<sup>9</sup> for bodies of revolution. However, for the case of the finned projectile with side moments due to the beveling, computations at two separate coning rates (which may include zero coning rate) are required to determine the variation of side moment due to coning. For bodies of revolution, a single computation at a non-zero coning rate is sufficient, since the side moment at zero coning rate is zero.

The relationship between the variation of the side moment with coning rate,  $C_{n_0}$ , the pitch damping coefficient,  $[C_{m_0} + \gamma C_{m_0}]$ , and the Magnus moment coefficient,  $C_{n_{ps}}$ , is shown in Equation 20. At the present time, determination of the Magnus moment coefficient for finned projectiles using three-dimensional Euler or Navier-Stokes approaches has not been performed. This would involve an unsteady time-accurate calculation which would be very expensive. However, the Magnus moment coefficient is typically much smaller than the pitch

damping coefficient for many projectiles. In the case of finned projectiles similar to those examined in this study, this has been confirmed by applying simple inviscid theories to estimate the Magnus moment and pitch damping coefficients<sup>14</sup>. Additional confirmation can be found from ballistic range testing of kinetic energy projectiles. The Magnus moment coefficient can be quite difficult to measure due in part to its small magnitude in relation to the other aerodynamic coefficients and due to the low spin rates that these projectiles experience in flight.

For the case of pitch damping moment coefficient much larger than the Magnus coefficient, Equation 20 can be rewritten, as shown below. Because this expression is valid in the linear aerodynamics regime (small angles of attack), the cosine of the angle of attack,  $\gamma$ , has been dropped.

$$[C_{m_0} + C_{m_0}] \approx \frac{C_{n_0}}{\delta} \quad (21)$$

A similar expression relating side force due to coning to the pitch damping force and Magnus force can be developed using the same approach as discussed above. The Magnus contribution to the force relationship can also be ignored allowing the side force due to coning to be related directly to the pitch damping force.

### 5.3.3 Results

Computations have been performed to determine the aerodynamics of kinetic energy projectiles in steady coning motion. Results have been obtained for two finned kinetic energy projectiles; the M735 and the M829. The computations have been performed over a range of Mach numbers ( $M = 3.0$  to  $5.5$ ), coning rates ( $\phi D/V = 0$  to  $.010$ ), and angles of attack for free-flight (sea-level) atmospheric conditions. The variation of the side moment with coning rate normalized by the angle of attack has been used to determine the pitch damping coefficients for these finned projectiles. Comparisons are made with data obtained from range firings<sup>2</sup>.

The computed variation of the side moment coefficient with coning rate at Mach 4 and two degrees angle of attack for the M735 is shown in Figure 15. The variation of the side moment coefficient with coning rate is seen to be linear across the range of coning rates examined here. This range of coning rates is representative of the pitching frequencies experienced by this projectile in flight. At Mach 4, the non-dimensional pitching frequency of the projectile is 0.004. The results also show a small non-zero side moment coefficient at zero coning rate. As was discussed previously, this side moment is due to bevels on the fins. The existence of this side moment at zero coning rate requires that computations be performed for at least two coning rates in order to evaluate the variation of the side moment coefficient with coning rate,  $C_{n_0}$ .

Figure 16 shows the slope of the side moment coefficient with coning rate as a function of  $\delta$  (the sine of the angle of attack), at Mach 4 for the M735. The dashed line displayed on this figure is representative of a linear variation of  $C_{n_0}$  with the sine of the angle of attack,  $\delta$ , across the range of angles of attack examined. The computed results show that at small angles of attack,  $C_{n_0}$

varies linearly with  $\delta$ , but departs from a linear variation as the angle of attack increases.

Figure 17 shows the development of  $\frac{C_{n\dot{\delta}}}{\delta}$  over the M735 kinetic energy projectile at Mach 4 and two degrees angle of attack. This figure shows that the fins contribute most of the side moment due to coning (and hence, the pitch damping) with a smaller contribution from the nose.

The computed variation of  $\frac{C_{n\dot{\delta}}}{\delta}$  with Mach number for the M735 is shown in Figure 18. The computed results are compared with range measurements of the pitch damping moment coefficient. The agreement between computation and range measurement supports the contention that the coning computations allow a reasonable determination of the pitch damping moment coefficient.

Similar computations were performed for the M829 kinetic energy projectile. Figure 19 shows the computed variation of  $\frac{C_{n\dot{\delta}}}{\delta}$  with Mach number for the M829. Again, the computed results are compared with range measurements of the pitch damping moment coefficient. The range data has considerable scatter because the range firings produced rounds with very low yaw (less than one degree average yaw). Thus, the rate at which the yaw decreased in flight was difficult to determine. The computational results are within the scatter of the range data. Both the computations and the range results show the order of magnitude increase in the coefficient compared with the predictions shown for the M735. This increase is primarily due to the larger length-to-diameter ratio of the M829 ( $L/D=23$ ) compared with the M735 ( $L/D=14$ ).

The predicted variation of the damping force as a function of Mach number is shown in Figure 20. This coefficient appears in the swerve equation (the equation which describes in-flight motion of the projectile center of gravity). For finned projectiles, the fluctuating part of the swerving motion is composed of contributions from the lift and pitch damping forces. Despite the large magnitude of the pitch damping force coefficient, the swerving motion is dominated by the contribution from the lift force. Because the pitch damping force contributes very little to the projectile motion, it is very poorly determined from range firings, thus no experimental data is shown. This coefficient is, however, important for determining the change in the pitch damping moment coefficient due to changes in center of gravity location. Thus, this result is significant.

One situation where changes in the center of gravity location are often encountered is in aerodynamic range testing of kinetic energy projectiles. Because of restrictions on firing kinetic energy projectiles with heavy metal penetrators through aerodynamic test ranges, surrogate projectiles are often used. Externally, these projectiles appear the same as the war round, though internally the heavy metal core has been replaced with a core of a different composition, typically steel. Replacing the penetrator core can result in a shift in the center of gravity. In the case of the M829, this shift is greater than a quarter of a caliber.

In steady coning motion, the projectile rotates about

its center of gravity (CG). Flow field computations were performed to determine the effect of CG location on the side force and moment due to coning (and hence on the pitch damping force and moment coefficients). The CG position was moved fore and aft of the baseline CG position by 1 and 2 body diameters. These results are shown in Table 1 for Mach numbers of 3, 4, and 5.

Predictions of the variation of the side force and moment due to coning with center of gravity location can be made using the center of gravity translation relations presented by Murphy<sup>7</sup>. The relations, presented by Murphy for the individual aerodynamic coefficients, are combined to obtain relations for the coefficients of interest here. These are shown below. The coefficients represented with a "p" represent the predicted value for a CG shift of  $s_{cg}$  body diameters. The aerodynamic coefficients on the right side of these expressions represent the values for the baseline configuration.

$$\dot{C}_{N_p} + \gamma \dot{C}_{N_{\delta}} + \gamma \dot{C}_{Y_{p\delta}} = C_{N_p} + \gamma C_{N_{\delta}} + \gamma C_{Y_{p\delta}} + s_{cg} C_{N_{\delta}} \quad (22)$$

$$\dot{C}_{m_p} + \gamma \dot{C}_{m_{\delta}} + \gamma \dot{C}_{n_{p\delta}} = C_{m_p} + \gamma C_{m_{\delta}} + \gamma C_{n_{p\delta}} - s_{cg} (C_{N_p} + \gamma C_{N_{\delta}} + \gamma C_{Y_{p\delta}}) + s_{cg} C_{m_{\delta}} - s_{cg}^2 C_{N_{\delta}}$$

By applying equation 20, the above relations are reduced to the following.

$$\dot{C}_{Y_{\delta}}/\delta = C_{Y_{\delta}}/\delta + s_{cg} C_{N_{\delta}} \quad (23)$$

$$\dot{C}_{n_{\delta}}/\delta = C_{n_{\delta}}/\delta - s_{cg} (C_{Y_{\delta}}/\delta) + s_{cg} C_{m_{\delta}} - s_{cg}^2 C_{N_{\delta}}$$

In deriving these relations, the Magnus force and moment coefficients are retained for consistency, though their effect is thought to be small.

Using these relations and the aerodynamic coefficient predictions for the baseline configuration, predictions of the side force and moment variation due to coning for varying CG position were obtained. These results are also shown in Table 1. The differences between the direct computation of the side moment coefficient at the various CG locations and the values obtained from the CG translation relations is less than 0.2 %, and provides additional validation of the computational approach. The side moment (and hence the pitch damping) varies by more than  $\pm 35$  % for a center of gravity shift of  $\pm 2$  calibers. Changing the CG position is one possible approach for increasing or decreasing the pitch damping of these projectiles.

## 6. CONCLUSIONS

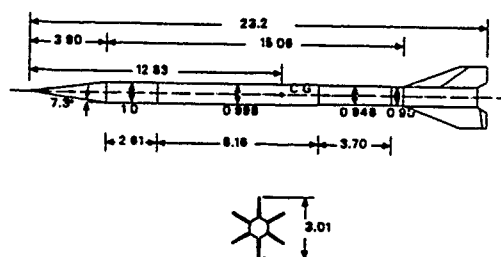
Several aspects of the aerodynamics of kinetic energy penetrators have been investigated by examining three types of flight motion. These are (1) static aerodynamics at angle of attack, (2) aerodynamics in pure rolling motion, and (3) aerodynamics in steady coning motion. The aerodynamic coefficients derived from the computed three-dimensional viscous flow field predictions were seen to be in reasonable agreement with the results obtained from range firings. The computational predictions have also revealed the existence of a side moment which is not currently considered in the range testing. In some cases, it appears that the computed results provide a more consistent set of data than do the range results.

## References

1. Schiff, L.B., and Steger, J.L., "Numerical Simulation of Steady Supersonic Viscous Flow," AIAA Journal, Vol 18, No. 12, December 1980, pp. 1421-1430.
2. Brandon, F.J., "Private Communication," U.S. Army Ballistic Research Laboratory, Aberdeen Proving Ground, Maryland
3. Baldwin, B.S., and Lomax, H., "Thin Layer Approximation and Algebraic Model for Separated Turbulent Flows," AIAA Paper 78-257, 16th Aerospace Sciences Meeting, January, 1978.
4. Beam, R., and Warming, R.F., "An Implicit Factored Scheme for the Compressible Navier-Stokes Equations," AIAA Journal, Vol. 16, No. 4, 1978, pp 85-129.
5. Rai, M.M., and Chaussee, D.S., "New Implicit Boundary Procedure: Theory and Applications," AIAA Paper 83-0123, Reno, Nevada, January 1983
6. Rai, M.M., and Chaussee, D.S., "Calculation of Viscous Supersonic Flows over Finned Bodies," AIAA Paper 83-1667, Danvers, MA, July 1983.
7. Murphy, C.H., "Free Flight Motion of Symmetric Missiles," U.S. Army Ballistic Research Laboratory, Aberdeen Proving Ground, Maryland, Report No 1216, July 1963. (AD A442757)
8. Tobak, M., Schiff, L.B., and Peterson, V.L., "Aerodynamics of Bodies of Revolution in Coning Motion," AIAA Journal, Vol. 7, No. 1, January 1969, pp. 95-99.
9. Schiff, L.B., and Tobak, M., "Results from a New Wind-Tunnel Apparatus for Studying Coning and Spinning Motions of Bodies of Revolution," AIAA Journal, Vol 8, No. 11, November 1970, pp. 1953-1957.
10. Schiff, L.B., "Nonlinear Aerodynamics of Bodies in Coning Motion," AIAA Journal, Vol 10, No. 11, November 1972, pp. 1517-1522.
11. Agarwal R., and Rakich, J.V., "Computation of Supersonic Laminar Viscous Flow Past a Pointed Cone at Angle of Attack in Spinning and Coning Motion," AIAA Paper 78-1211, AIAA 11th Fluid and Plasma Dynamics Conference, Seattle, WA, July 1978
12. Lin, T.C., "A Numerical Study of the Aerodynamics of a Reentry Vehicle in Steady Coning Motion," AIAA Paper 78-1358, AIAA Atmospheric Flight Mechanics Conference, Palo Alto, CA, August 1978.
13. Levy, L.L., and Tobak, M., "Nonlinear Aerodynamics of Bodies of Revolution in Free Flight," AIAA Journal, Vol. 8, No. 12, December 1970, pp. 2168-2171.
14. Devan, L., "Nonaxisymmetric Body, Supersonic, Inviscid Dynamic Derivative Prediction," AIAA Paper 89-2195-CP, AIAA 7th Applied Aerodynamics Conference, Seattle, WA, August 1989.

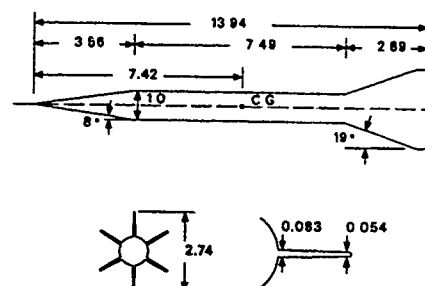
Table 1. CG Translation - Comparison of Results Using CG Translation Equations and Direct Computation

MACH NUMBER	$s_{cg}$	COMPUTED		TRANSFORMED	
		$C_{Y_s}/b$	$C_{N_s}/b$	$C_{Y_s}/b$	$C_{N_s}/b$
3.0	-2.0	224.37	-1550.1	224.61	-1551.2
	-1.0	241.89	-1853.2	242.01	-1853.9
	+1.0	276.93	-2564.6	276.81	-2563.7
	+2.0	294.45	-2972.8	294.21	-2970.8
4.0	-2.0	179.59	-1373.4	179.85	-1374.9
	-1.0	195.32	-1615.7	195.45	-1616.6
	+1.0	226.78	-2194.7	226.65	-2193.6
	+2.0	242.52	-2531.5	242.25	-2528.9
5.0	-2.0	192.75	-2080.6	192.46	-2077.8
	-1.0	178.75	-1812.7	178.62	-1811.5
	+1.0	150.78	-1361.1	150.92	-1362.0
	+2.0	136.80	-1177.2	137.08	-1178.8



ALL DIMENSIONS IN CALIBERS (ONE CALIBER = 27.08 mm)

Figure 1. Schematic of M829 projectile



ALL DIMENSIONS IN CALIBERS (ONE CALIBER = 36.2 mm)

Figure 2. Schematic of M735 projectile

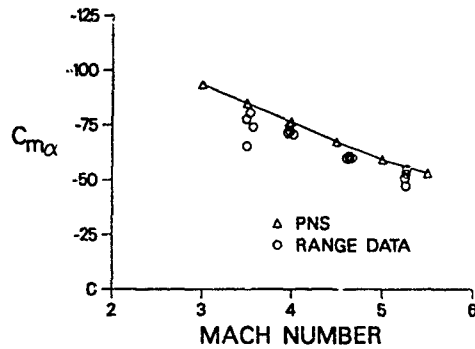


Figure 3. Pitching moment coefficient as a function of Mach number, M829

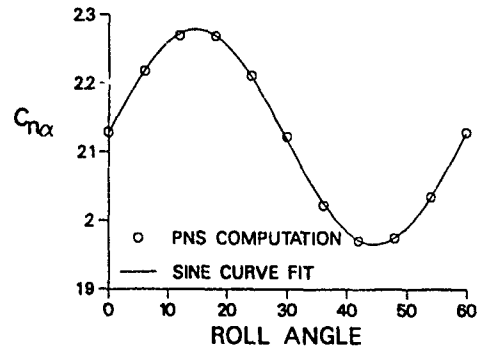


Figure 6. Side moment coefficient as a function of roll angle, M829, Mach 4

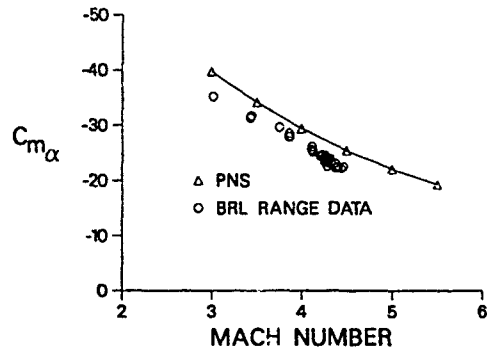


Figure 4. Pitching moment coefficient as a function of Mach number, M735

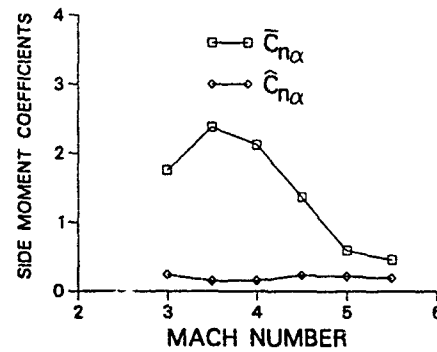


Figure 7. Fluctuating and non-fluctuating component of side moment coefficient as a function of Mach number, M829

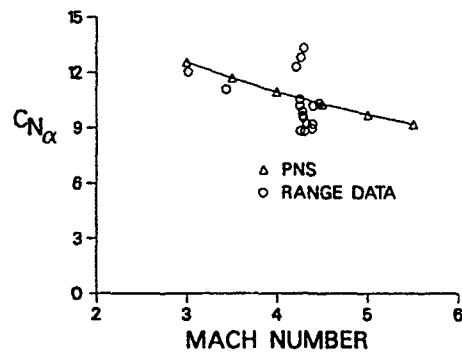


Figure 5. Normal force coefficient as a function of Mach number, M735

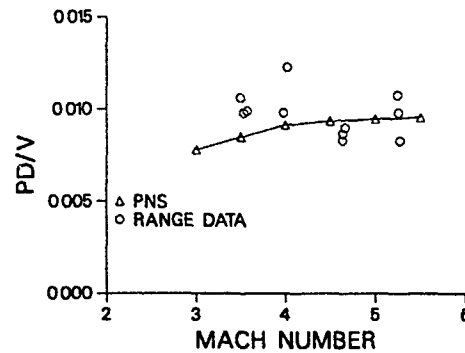


Figure 8. Comparison of computed Mach number variation of equilibrium spin rate with range data, M829

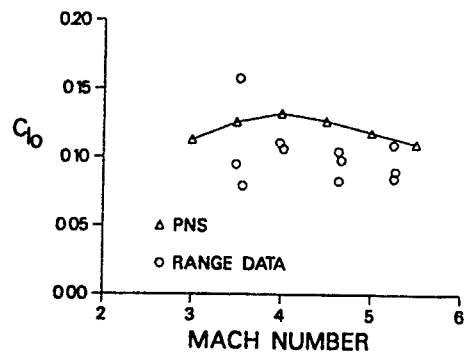


Figure 9 Comparison of computed Mach number variation of roll producing moment coefficient with range data, M829

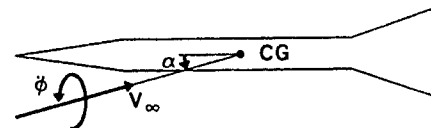


Figure 12 Schematic of coning motion

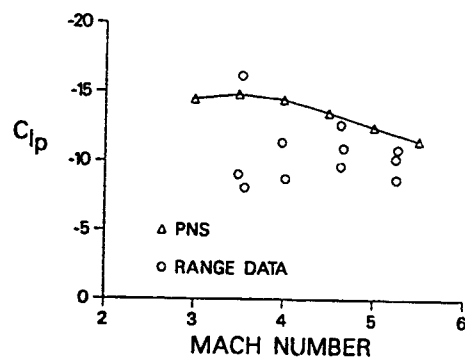


Figure 10. Comparison of computed Mach number variation of roll damping moment coefficient with range data, M829

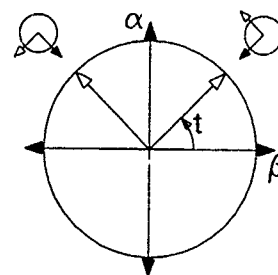


Figure 13. Coning motion with respect to non-rolling coordinates

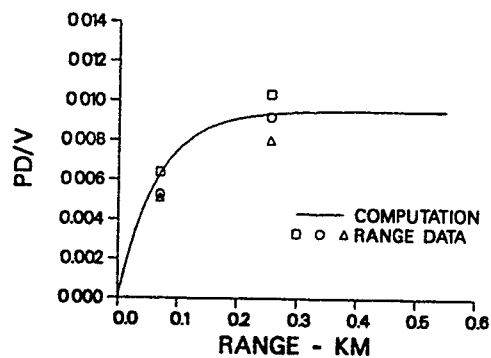


Figure 11. Comparison computed roll history with range data - Launch Mach number = 5.25, M829

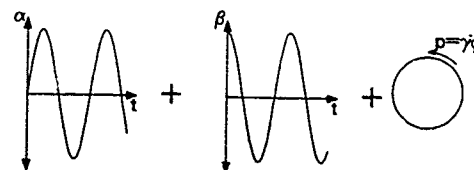


Figure 14 Components of coning motion

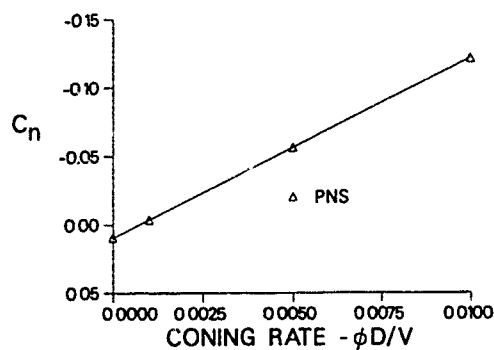


Figure 15. Variation of side moment coefficient with coning rate, M735, Mach 4,  $\alpha = 2^\circ$

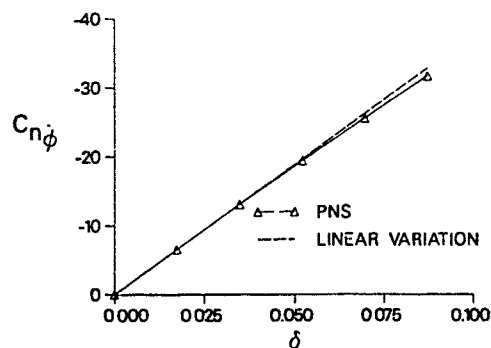


Figure 16. Variation of the slope of the side moment coefficient due to coning,  $C_{n\phi}$ , as a function of the sine of the angle of attack,  $\delta$

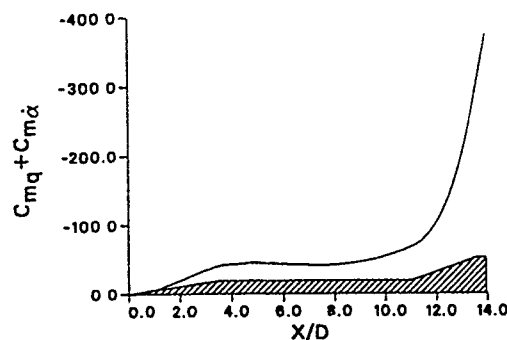


Figure 17. Development of normalized side moment slope due to coning,  $\frac{C_{n\phi}}{\delta}$ , over M735 projectile, Mach 4

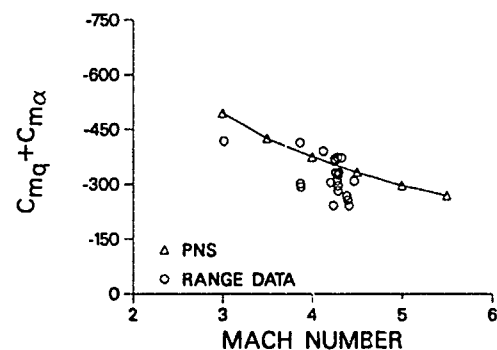


Figure 18. Mach number variation of computed normalized side moment slope due to coning compared with range measurement of pitch damping, M735

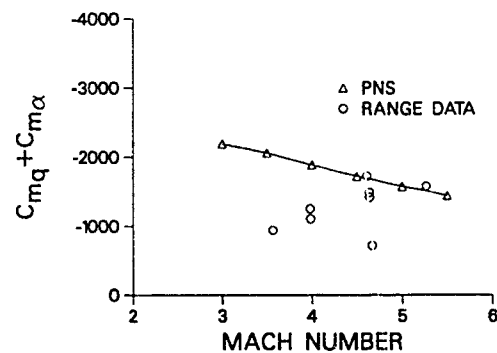


Figure 19. Mach number variation of computed normalized side moment slope due to coning compared with range measurement of pitch damping, M829

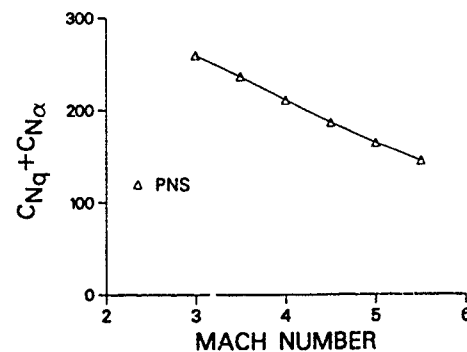


Figure 20. Mach number variation of pitch damping force coefficient as determined from side force due to coning, M829

## OVERVIEW OF PROPULSION CONCEPTS FOR TACTICAL MISSILES

FREDRICK C ZARLINGO  
Head, Airbreathing Propulsion Branch (Code 3276)  
Naval Weapons Center  
China Lake, CA 93555-6001  
United States of America

### 1. SUMMARY

Several propulsion concepts lend themselves to application in tactical missiles; many of them can improve missile system performance by means of longer range, high speed, or both. Tactical missile propulsion systems generally fall into one of two categories: rockets that carry all their fuel and oxidizer and airbreathing engines that have to carry only their fuel since their oxidizer is obtained from the surrounding air. Tactical missiles have typically been propelled by conventional solid propellant powered rockets or, occasionally, liquid propellant powered rockets. However, newly emerging requirements and needs are placing more emphasis on sustained high speed and longer ranges, as well as reduced cost and improved reliability and safety. In addition, there is more emphasis on launcher (aircraft or ground based) survivability. Survivability can be enhanced by longer ranges or reduced visibility. These needs can be implemented either singly or in combination by using selected propulsion systems. Pulse rockets, ramjets (both liquid fueled and solid fueled), turbojets, and air-turbo-rockets (or turbo-ramjets) possess the potential of long range and high speeds. This paper provides an overview of the various propulsion concepts considered applicable to tactical missiles and describes and discusses the merits of each.

### 2. NOMENCLATURE

ALVRJ	Advanced Low Volume Ramjet
ASALM	Advanced Strategic Air Launched Missile
ATR	air-turbo-rocket
CTPB	carboxyl-terminated polybutadiene
DR	ducted rocket
GORJE	Generic Ordnance Ramjet Engine
HTPB	hydroxyl-terminated polybutadiene
Isp	specific impulse (pounds force (thrust) per pounds mass per seconds of fuel)
LFRJ	liquid fuel ramjet
SFRJ	solid fuel ramjet

### 3. INTRODUCTION

Tactical missiles have to be capable of delivering the payload to the target in a reliable manner even after long-term storage at potentially unfavorable temperatures (e.g., -65°F to +140°F), and after having been subjected to adverse environmental conditions (e.g., rain, snow, dust, vibration, etc.). Singly, these conditions can be very severe and detrimental to a

missile system operation; usually, however, they are combined in either series or parallel. These conditions make the selection of the propulsion system for tactical missiles critical. Simplicity is generally consistent with reliability and this has generally led to the selection of the solid propellant powered rocket motor (solid rocket) as the propulsion system of choice (other systems have been used, though). However, newly emerging requirements are placing even more demands upon new as well as existing tactical missile systems. Increased costs have dictated many of these requirements; consequently, more emphasis is being placed upon increasing the system effectiveness (and usefulness). Also, versatility may be a future requirement, as the cost of maintaining the inventory of missiles becomes more of a problem. Regardless, effectiveness and reliability will remain the most critical requirements for new propulsion systems.

The various propulsion systems applicable to tactical missiles are described in this paper. In addition, the merits of each are discussed, and a generalized logic that is typically used in the selection of a propulsion system is presented.

### 4. DESCRIPTION

#### 4.1 Rocket Propulsion

Of the propulsion systems applicable to tactical missiles (rocket or airbreathing), the rocket is considered the simplest and, as a result, is typically selected for use in tactical missiles. There are two categories of rockets, depending on the propellant type; i.e., solid or liquid. Both are discussed below.

In the rocket, the fuel and oxidizer, which are carried aboard the missile, are combusted in a common chamber. This results in a simple system, especially in the case of the all-boost solid rocket (Figure 1), which is perhaps the simplest system. An all-boost solid rocket does not contain any tankage for the fuel and oxidizer, other than the combustion chamber. However, the fuel and oxidizer are in intimate contact; hence, an energy source such as an igniter can initiate combustion. It does have the limitation that whatever versatility that is desired must be built into the design (for example, the thrust profile is usually designed into the grain design). It is not easy to add a variable flow control system to the solid rocket to achieve variable thrust since the throttle system would have to control the hot, usually >4000°F, combustion products.

Several thrust profiles (Figure 2) can be achieved with a solid rocket. These are usually accomplished

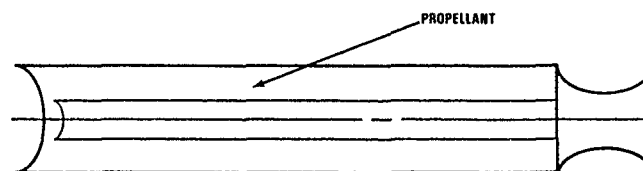


FIGURE 1. All-Boost Solid Rocket With Center Perforation Radial Burner.

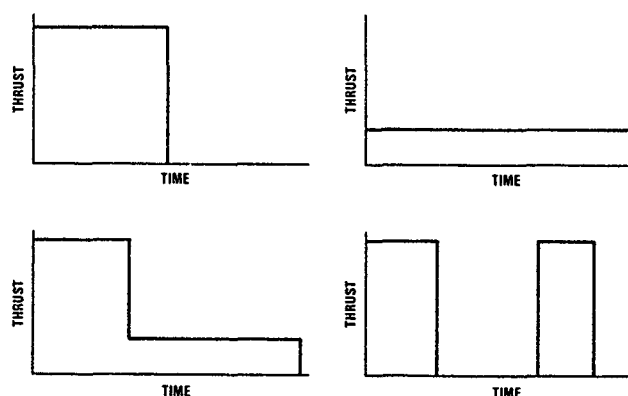


FIGURE 2. Typical Pressure or Thrust-Time Profile.

through the choice of propellant grain type and ultimately shape. For example, if an all-boost, short burn time thrust profile is desired, the center burn grain such as that shown in Figure 1 would probably be selected. However, if a long burn time at low thrust level is desired, an end burning grain similar to that shown in Figure 3 would probably be selected.

The other types of thrust profiles, boost-sustain or pulse, are generally achieved with an increased degree of complexity in the grain and ultimately in the motor design. Such thrust can be accomplished by locating the boost and sustain (or pulse) in separate chambers either through a barrier between the grains or by actually introducing an additional end dome in the motor case design (Figure 4). Alternatively, it is possible to overcast the boost propellant on the sustain propellant grain (Figure 5). This requires careful integration of the propellant grains; the propellants must be compatible; they must have adequate and acceptable physical properties; and, above all, the bond between them must be of highest quality to achieve as uniform a grain as possible and prevent the introduction of any unplanned or unnecessary burning surfaces on the grains which could be catastrophic. A limited boost-sustain thrust profile

can be achieved with a single grain design that is much more complex than that required for an all-boost-thrust profile.

Some degree of tailoring can be achieved with the grain design. For example, a progressive or regressive thrust-time profile can be attained by the proper selection of the specific grain design, and this aspect must be considered. With the proper choice of the internal shape or perforation on the internal burning grain, one can achieve a nearly neutral, increasing, or decreasing shape of the thrust-time profile. Of the two general grain port configurations, a circular shape will result in a progressive design, whereas a star shape can be selected to achieve the desired profile, within limitations. However, the propellant must have adequate physical properties to accommodate any nonuniform stresses or strains which may be introduced as a result of the shape.

In addition to the two general grain port configurations noted above, these can be integrated into a single grain. For example, one could combine a circular port section with a conical shaped section into a single grain called a conocyl and attain a degree of flexibility from the circular port grain. However,



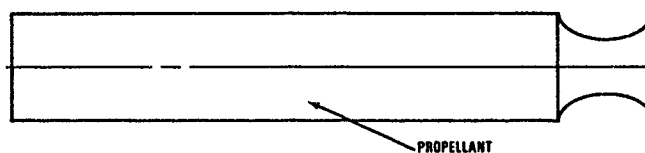


FIGURE 3. All-Boost Solid Rocket With End Burner.

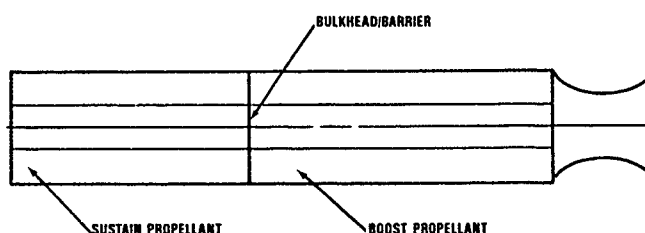


FIGURE 4. Boost-Sustain or Pulse Motor.

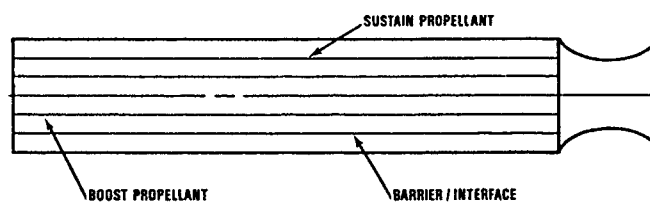


FIGURE 5. Boost-Sustain or Pulse Motor (Alternative).

internal case insulation would have to be increased to protect the motor case from the hot combustion products as the aft (conical) end of the grain burns away and exposes the case wall.

The propellant grains may be extruded or cast to the desired shape. Several types of rocket propellant are used to make propellant grains. The selection of propellant type may be dictated by the manufacturing technique (or vice versa). Extrusion may require a propellant similar to the older double-base propellant, while a cast grain will usually use a composite propellant. (These are general statements and not absolute, as there can be cast double-base or extruded composite propellants.) Double-base propellants were in common use in the 1940s through 1960s; they are still in use, but are not usually the propellant of choice today. Double-base propellants usually contain nitrocellulose and nitroglycerin.

In more common use today are composite, castable propellants, which can use any of several binders such as CTPB or HTPB. An older composite propel-

lant binder was polyurethane. Generally the oxidizer of choice is ammonium perchlorate. The binder also acts as the fuel, and a metal additive (e.g., aluminum) is included as additional fuel to increase the impulse resulting from the propellant. Some metal may also be used as a combustion stabilizer. However, the introduction of metal into the propellant also introduces metal oxides into the exhaust, and these are usually visible as smoke.

Liquid propellant rockets (liquid rockets) (Figure 6) are more complex than solid rockets; they require separate tanks to contain the fuel and oxidizer and a separate combustion chamber, as well as plumbing between the tanks and the combustion chamber. In addition, they may also require some form of valving for fuel control and a tank pressurization/pumping system. They do have the merit that they may readily be throttled and can be shut down as desired. Liquid rocket systems are generally volumetrically less efficient than the solid rocket and may be heavier.

A typical tactical liquid propellant oxidizer is red fuming nitric acid (or nitrogen tetroxide) while a typical fuel could be monomethyl hydrazine (or unsymmetrical dimethylhydrazine). Both of these can be gelled, which improves safety characteristics but makes them harder to pump. Also metal additives can be added to the fuel to enhance its performance. Because of their complexity, liquid rockets are generally not used for tactical missiles unless there is a need for their merits, usually throttling

#### 4.2 Airbreathing Propulsion

Of the alternate propulsion systems types, airbreathing ramjets have been the mainstay of the long range high speed propulsion concepts. There are three basic types (Figure 7) liquid fuel ramjet, solid fuel ramjet, and the ducted rocket. The three ramjet concepts are similar in that they require a booster to get them up to operational speed and they require a fuel system, a combustion chamber to burn the fuel with the air, and an air induction system to capture the

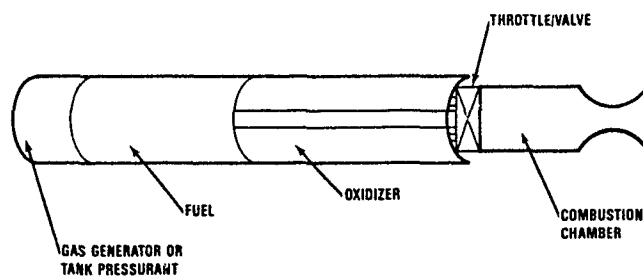


FIGURE 6. Liquid Fueled Rocket.

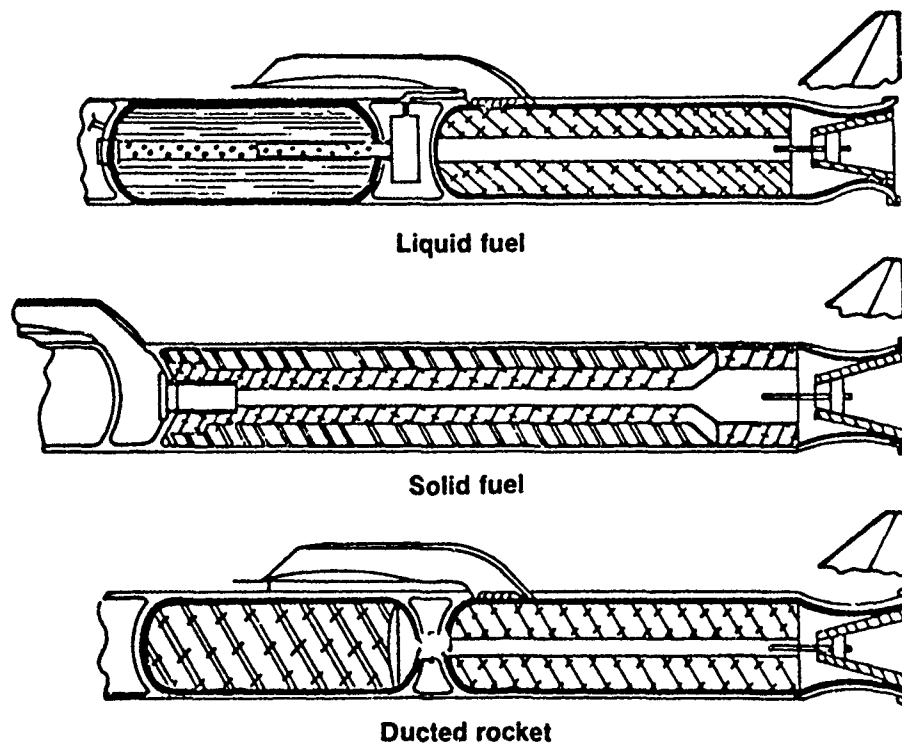


FIGURE 7. Types of Ramjets.

air and provide it to the combustion chamber. The DR is similar in packaging to the LFRJ and is the solid analog of the LFRJ; both use a separate combustion chamber for combustion of the "fuel" with the air. The fuel tank in the LFRJ is replaced by a gas generator in the DR. In the SFRJ the booster chamber is the fuel gas generation chamber and is also the ramjet combustion chamber. The DR differs from the other two in that the DR "fuel" is fuel-rich effluent from the gas generator propellant, which contains oxidizer, and is self-sustaining in the same manner as a solid rocket. The fuels in the LFRJ and SFRJ do not contain any oxidizer and are not self-sustaining. The LFRJ and SFRJ burn a fuel or a fuel vapor mixture with the air in the combustion chamber, while the DR burns the exhaust products from its gas generator with the air.

As noted above, ramjets usually must be boosted up to operational speeds. These boosters are typically solid rockets. The ramjets may be packaged in either of two configurations, nonintegral booster or integral booster (Figure 8). The nonintegral type would necessitate the incorporation of a separate, perhaps separable, booster to accelerate the ramjet system to operational velocities. It may be configured with the booster in a tandem manner (as in Talos) or podded

manner (as in BOMARC). It may be satisfactory for some applications. In this approach, the booster may be separated from the missile after boost is completed. A variation on the nonintegral type is the parallel approach used on the GORJE system (Figure 9), where the booster case was located forward of the ramjet combustor in the missile; and the fuel tank was located forward of the booster motor. It had an annular ramjet combustor formed by the rocket motor blast tube and the missile external airframe.

The integral type, in which the booster chamber is also used as the ramjet combustion chamber, is more volumetrically efficient and is the most modern, but it requires the most attention to overall system and subsystem (e.g., booster and ramjet) integration. The integral type requires a dual nozzle system: an ejectable nozzle (although nozzleless booster motors can be built) to maintain the high booster pressure and a larger nozzle for ramjet operation, as well as a set of port covers to seal the ramjet combustion chamber at the air entrance during booster operation. During operation (Figure 10), the booster propellant burns; the ramjet accelerates to operational speeds; then the nozzle is ejected, the port cover(s) "open," and ram air is introduced into the combustor along with the fuel where they are mixed and

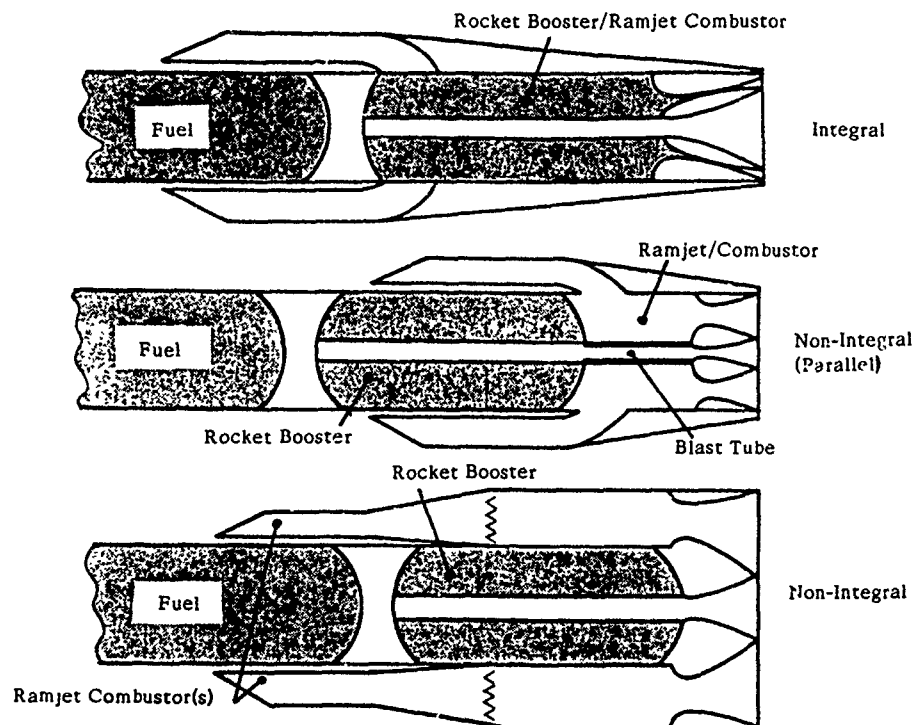


FIGURE 8. Boost Rocket/Ramjet Sustain Engine Arrangements.

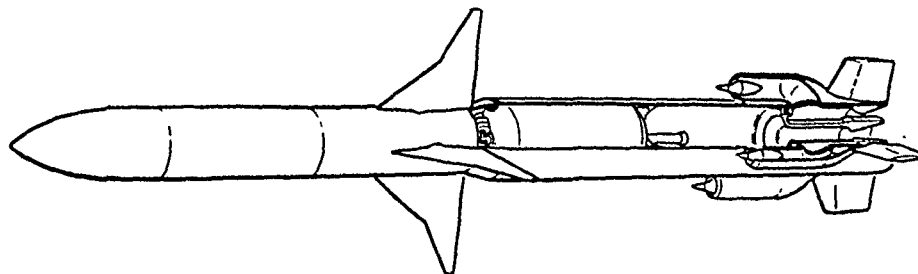


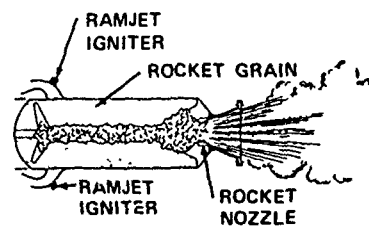
FIGURE 9. GORJE.

burned. This configuration is typical of that found in the ALVRJ (Figure 11) and ASALM flight vehicles. Close attention must be paid, in these systems, to port cover integrity to avoid a booster leak. Another problem is the integrity of the common booster case/ramjet combustor insulation. Not only must there be a good bond between the booster propellant and the insulation, but the insulation must be adequate to survive high temperature associated with the long-duration ramjet burn and high speed flight.

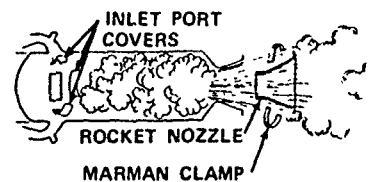
The five systems discussed above were all LFRJs, which are the most mature ramjets although the history of the DR and the SFRJ is quite long. Both the BOMARC and Talos were 1950s generation ramjets while the ALVRJ, GORJE and ASALM were late 1960s and 1970s generation systems. In addition, many other LFRJ engines were built, and many were flight tested. The early ramjets used bare wall or ceramic coated combustors. As a result, the systems operated at lower equivalence ratios (higher air-to-fuel ratios) and subsequently lower combustion temperatures than is usual of today's ramjets. Operation at lower equivalence ratios requires a larger propulsion system to achieve the same thrust level. The use of ablative liners in the combustion chambers has allowed operation at higher equivalence ratios (and thus higher combustion temperatures) with consequently smaller propulsion systems. The LFRJ commonly has five major subsystems: an air induction system (inlet), a fuel tank and expulsion system, a fuel control system, a combustor, and a booster. Of these, the fuel management system (fuel tank and control system) is unique to the LFRJ and is perhaps its most complex part; certainly, it is usually the most expensive. The tank may or may not incorporate a bladder to contain the fuel. It has one, the bladder may be used as part of a positive expulsion system (pressure-fed) to expel the fuel from the tank to the fuel control system and ultimately to the combustor. Alternatively, some systems use a turbopump to pump the fuel from the tank to the fuel control system. The turbopump can be an integral part of the fuel control system, but not necessarily. A bladder may be desired regardless of the fuel expulsion/pump system.

The fuel control system is considered the brains of the LFRJ system. It is not only a fuel flow controller,

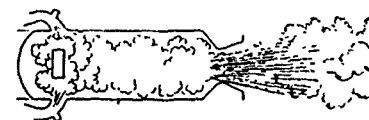
but also a combustor pressure regulator and a missile speed controller. The degree of complexity of the fuel control system is dependent upon the needs of the missile system and ultimately upon the mission. Older systems are analog, and use analog signals from the various system sensors (inlet and combustor



A. ROCKET OPERATION



B. ROCKET TO RAMJET TRANSITION



C. RAMJET OPERATION

FIGURE 10. Operating Sequence of Integral Rocket Ramjet.

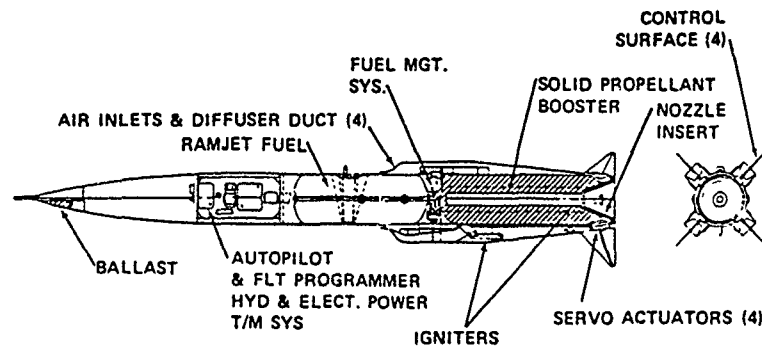


FIGURE 11. ALVRJ.

pressure, air data (pitot type), and fuel flow meters) Newer systems are digital and use digital data directly rather than converting it to analog signals. This has resulted in reduced fuel controller size, as well as reduced cost. Other alternative fuel control systems are the pneumatic and electronic systems which also have the potential of reducing the cost and size of the fuel control system. Recently, extensive progress has resulted in simplifying the fuel control systems and reducing their volume, weight and cost.

As noted above, the DR is similar in packaging to the LFRJ with the fuel tank replaced by the gas generator. There are two types of DR systems: fixed flow and variable flow. The former is the older and more commonly known, but it does possess operational limits. It suffers from wide excursions in combustor operating equivalence ratio as wide altitude and Mach number variations are encountered. To minimize these excursions, active variable flow throttle systems are included to control the fuel flow (hot combustion products gas) into the chamber. A variation of the active throttle system is the use of an unchoked gas generator which passively controls the fuel generation rate in response to the pressure in the combustion chamber. To be effective, both throttle approaches prefer the use of a gas generator "fuel" with a high burn rate sensitivity to pressure in order to attain maximum throttling. A major concern with the unchoked gas generator system is that while the fuel generation rate is decreased based upon the combustion pressure, as the pressure gets lower and lower as a result of wide altitude excursions, the resultant gas generator pressure may become too low for stable burning. Although low pressures could be obtained in the gas generator of the valve throttled system, the pressures would still be higher than in the unchoked approach.

Also as noted earlier, the DR gas generator "fuel" contains oxidizer, is self-sustaining, and, therefore, is more like a propellant than a fuel. It is, however, a very fuel-rich propellant and provides the fuel to burn with the ingested air. It also possesses all the same problems encountered in a propellant (e.g.,

burning rate sensitivity over the operating temperature range). Early DR gas generator propellants contained magnesium as the fuel to provide hot particles for burning with the air. More recently, progress has been made in incorporating all-hydrocarbon fuels and other higher performing metals in the gas generator propellant. Even so, the presence of the oxidizer in the gas generator fuel does limit the performance potential of the DR as compared to the all-fuel LFRJ.

The SFRJ can be perhaps the simplest of the ramjet systems; however, it is the most difficult to analyze and understand. The ramjet fuel and booster propellant are contained and burned sequentially in a common combustion chamber; the booster propellant is ignited and burned in the chamber; as it burns out and the pressure decays, ram air is introduced into the combustion chamber near the head end of the chamber, and fuel is generated and burned in the chamber for ramjet operation. Integration of the two grains into the common chamber is a critical design feature.

There are two basic types of SFRJ combustors (Figure 12): the center dump, coaxial nonbypass concept and the side dump nonbypass concept. In the center dump concept flame is held by the rearward facing step formed by the head end of the combustor and the air inlet, while in the side dump, the flame is held by the entire combustor head end and locally around the air inlet dumps. The size of the steps is a function of the fuel formulation and the combustor operating conditions (air inlet temperature and velocity). The center dump concept is by far the most mature, but suffers from limited mixing of the fuel and air.

Either of these concepts may incorporate bypass air as part of the design approach. In the bypass concept, shown in Figure 12 as center dump bypass, part of the air is bypassed around the fuel grain and dumped into the combustor just aft of the fuel grain; thus, less air traverses the fuel grain post. Because the air velocities in the fuel grain are reduced, bypass air offers the advantage of improved mixing of the fuel and air and increased fuel loading. This approach also offers the highest system performance.

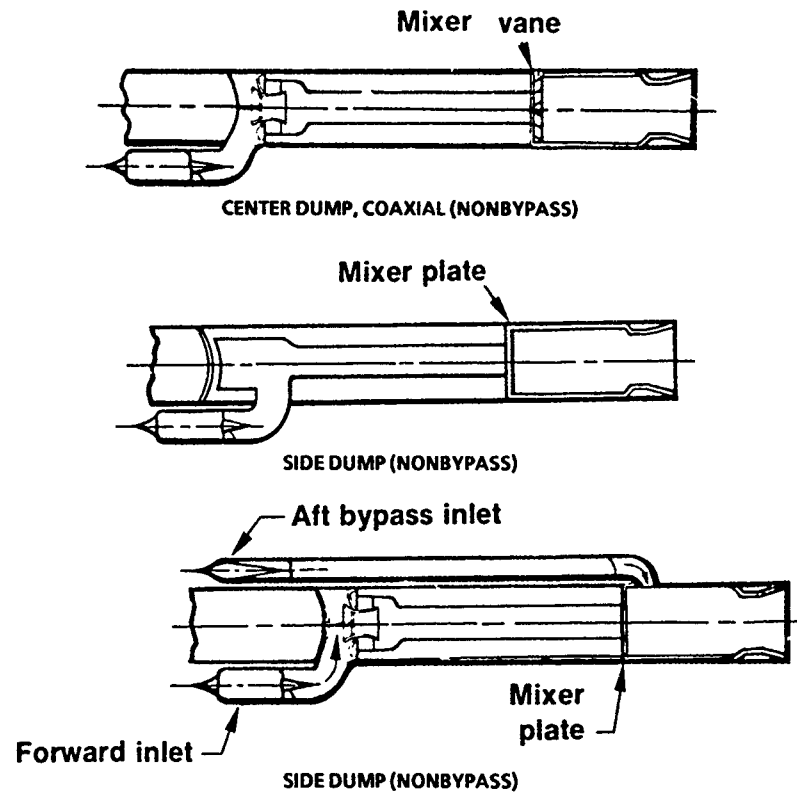


FIGURE 12. SFRJ Combustor Configurations.

Packaging the booster and fuel in a common combustion chamber is a detriment, because the inlets must be located very far forward on the missile, perhaps even covering part of the payload (warhead). The effect of the inlets on warhead effectiveness has not been adequately explored. The common chamber also results in the propulsion system weighing more than an LFRJ of comparable size.

The SFRJ has an inherent throttle capability which maintains its operation nearer on-design than would otherwise be the case. The SFRJ seldom operates on-design. The throttle capability is more of a compensation device than an active throttle and operates as a function of the air flowing through the fuel grain post. This capability can be used to advantage for an active throttle if desired or necessary. The SFRJ must be designed with the total mission in mind in the same manner as the solid propellant rocket.

The fuel for the SFRJ usually does not contain any oxidizer and typically is an all-hydrocarbon formulation. It may, however, contain metals for improved performance in much the same manner as a solid rocket. It is necessary for the fuel to be compatible with the booster propellant since they are packaged

together in the common chamber. It thus is desirable for both to contain many of the same ingredients, especially any ingredient that may migrate between the two.

The nonramjet airbreathing propulsion systems—the turbojet (Figure 13), the air-turborocket (ATR) (Figure 14), and the turbooramjet—produce static thrust and generally do not require separate boosters to accelerate them to operational speeds. They contain rotating machinery, which allows them to compress the incoming air even at zero velocity, while a ramjet relies upon the system velocity to compress (ram) the air into the engine. The compressor is driven by the turbine in the combustor. Both may have an afterburner to augment the propulsion system thrust temporarily. The turbojet is generally considered a lower speed (subsonic) propulsion system for aircraft and, more recently, cruise missiles. Low-cost tactical (ordnance quality) turbojet engines which require less duration capability have been built, and significant progress is being made in the development of high speed tactical turbojet engines having the capability of sustaining the high temperatures resulting from high-speed (supersonic) flight.

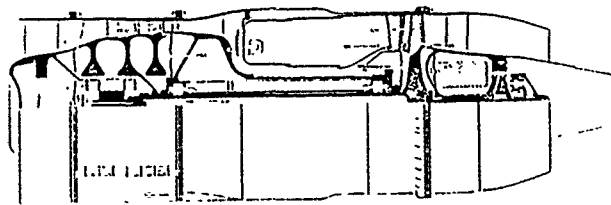


FIGURE 13. Turbojet.

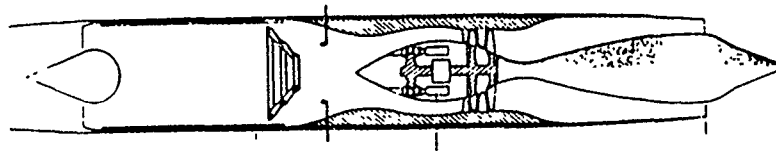


FIGURE 14. Air-turborocket.

The liquid fueled turbojet propulsion system, as well as a liquid fueled ATR and LFRJ, can incorporate fuel in nonconventional tankage geometries. This allows fuel integration into the missile airframe with more flexibility (and more complexity), but may be more overall volumetrically efficient from a system viewpoint. Still, as in the LFRJ, fuel management and control can be a major contributor to the system complexity.

The ATR is a combination of the turbojet and the ramjet and may have the complexities and merits of both. The ATR functions as a turbojet at low speed and relies upon the compressor to provide high pressure air for operation. As the speed increases to supersonic velocities, providing more energy to the incoming air, the engine transitions to operation more typical of a ramjet, and relies less upon the air compressor for high pressure air (besides the air temperature is becoming quite high for sustained compressor operations and is greater than required for efficient propulsion system operation). Also, the afterburner operation becomes more like ramjet combustor operation.

The ATR may be liquid fueled, or it may be powered by a fuel-rich solid propellant gas generator. The fuel is used to drive the turbine, which is subsequently combusted with the air in the combustor. When the ATR is liquid powered, it may have the airframe integration advantage of the liquid powered systems; but when it is powered by the solid propellant gas generator, its packaging may be as difficult as or even more than that of any of the airbreathing propulsion systems. In the solid system the effluent from the gas generator is the fuel. Ducting fuel-rich hot gasses from the gas generator to the ATR turbine and combustor becomes a requirement.

Should mission needs include attaining operational velocities more rapidly than possible on engine thrust, both the turbojet and the ATR can be integrated with a separate booster. The addition of a separate booster renders these systems less volume and weight efficient and thus reduces their performance potential.

## 5 PERFORMANCE

The turbojet delivers the highest level of propulsion system performance (Isp) of all the airbreathing propulsion systems. Typically a turbojet has the potential of delivering Isp in excess of 2000 seconds and frequently in excess of 3000 seconds. This high Isp makes the turbojet very attractive for long range, relatively low speed tactical missiles. With the attainment of higher speed capability turbojets, this operational speed regime will be enhanced.

The highest performing and most versatile of the ramjets is the LFRJ. Typically, an all-hydrocarbon LFRJ has the performance potential of delivering an Isp in excess of 1200 seconds. If metallized slurry fuels are incorporated in the system, this performance potential and consequently mission performance can be greatly enhanced. The use of a fuel control system allows the LFRJ to operate near its maximum performance potential or to throttle up or down as mission needs dictate. System performance can be further enhanced through the use of variable geometry inlets and nozzles. This enhancement, with its associated complexity and cost, is currently not considered attractive for tactical systems; the performance-cost benefit is not sufficiently great or warranted.

The closest solid propellant analog to the LFRJ is the DR. Unfortunately, it is also the lowest performer of the three ramjet systems because of its need to carry some oxidizer in the gas generator fuel. Typically, a DR can deliver an Isp of about 700-800 seconds. In the fixed flow system, the Isp is usually degraded from this level as the system is required to operate off-design; as a result, the overall system performance and mission versatility are degraded. A variable for DR provides the capability, at some cost and complexity, for enhanced mission performance. Even so, its performance capability is below that attainable with an LFRJ of nearly equal complexity. However, it is a solid fuel system.

The SFRJ performance generally lies between that of the LFRJ and the DR. An SFRJ typically has a performance potential in excess of 1000 seconds, a little lower than that of the LFRJ. Of the two SFRJ concepts, the side dump has a higher performance potential because it is more volumetrically efficient; the plenum upstream of the combustor in the center dump is eliminated in the side dump, and this void volume can be reallocated to fuel and booster propellant (to the extent possible). In addition, the side dump is a higher performer than the center dump, but not as well characterized or understood.

Bypass air increases the mission performance potential and, to a limited extent, the performance of the SFRJ. Addition of an active throttle to the SFRJ can enhance the performance of the SFRJ by up to 20 percent under the right conditions.

The SFRJ fuel usually does not contain any oxidizer, but it can, should it be required to improve the fuel's merits. Usually, inclusion of oxidizer in the fuel will reduce performance (Isp). Improved SFRJ system performance can be achieved by using metal-loaded fuels. Grain design can also greatly affect the overall performance of the SFRJ; and, as noted earlier, the fuel and propellant must be compatible, not only chemically, but also physically, if the fuel and propellant are to be integrated into a common unit (as opposed to tandem packaging).

The performance level of the ATR is comparable to that of the DR, which is still about three times that of the typical solid rocket. Its biggest advantage is its capability of static thrust, which obviates the need for a booster if relatively slow acceleration to operating velocities can be tolerated by the mission requirements.

At the low end of the performance spectrum lies the solid rocket; however, in some missions, such as one of relatively short range that may require high thrust-to-weight ratios, the solid rocket may be the preferred propulsion approach. The pulse motor and, to some extent, the boost-sustain thrust profiles can be used to advantage to extend the range potential of the solid rocket; but, as in the case of the boost-sustain motor, average specific impulse for the motor would be reduced to that which would be encountered with a boost-sustain motor. The liquid rocket generally has a greater Isp potential than the solid

rocket, however, its volumetric efficiency is less than that of the solid rocket.

The operating envelope of the various systems is illustrated in Figures 15 and 16. The specific envelope may be enhanced or degraded by the specific system design. A typical velocity histogram for some of the systems is shown in Figure 17, along with the history of a typical solid rocket.

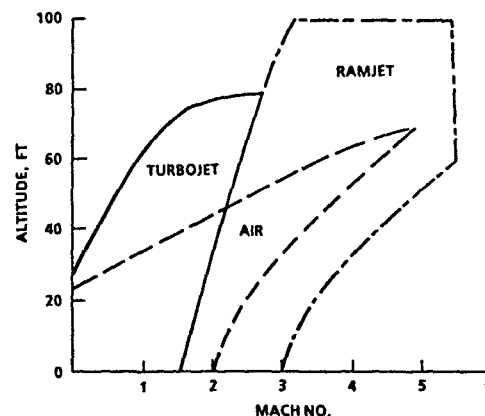


FIGURE 15. Operating Envelopes.

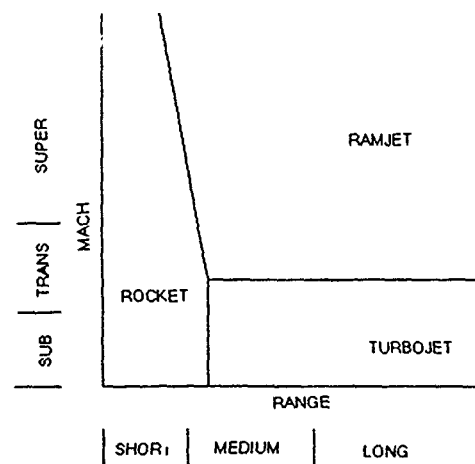


FIGURE 16. Applicator Envelopes.



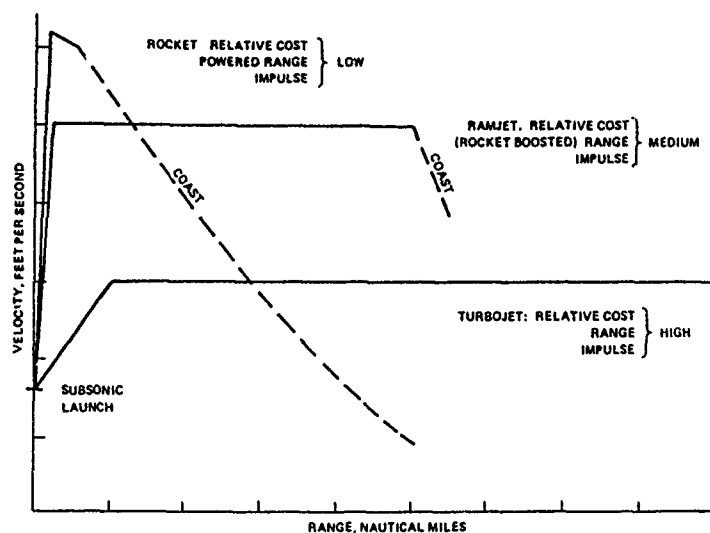


FIGURE 17. Typical Velocity Histograms.

## 6 COST

Cost of the various propulsion systems is relative and very much a function of the mission. Even so, the propulsion system cost is typically less than 20% of the missile cost. The cost of the various propulsion systems is discussed in general terms, with qualifiers as warranted.

The turbojet, LFRJ, and ATR are perhaps the most expensive of the tactical propulsion systems, while the solid rocket is the least expensive. The ATR and the LFRJ may be comparable from a cost viewpoint, since the ATR possesses some expensive rotating machinery but may not necessarily require a booster, which is required for the LFRJ. The liquid rocket is generally comparable in complexity and thus cost to these systems. The SFRJ and the simple, fixed-flow DR are perhaps the least expensive of the airbreathing propulsion systems.

To some degree the cost of the liquid fueled systems can be reduced by using less complex fuel control systems; however, the remainder of its fuel management system remains a potentially expensive item. The degree of complexity and thus the cost of the fuel management system are very much functions of the mission needs. Significant improvements are being made by designing systems with digital and pneumatic fuel control systems.

The SFRJ, like the conventional solid rocket, is perhaps operationally the simplest and through this simplicity achieves its low cost. Packaging the SFRJ fuel grain in a common chamber with the booster propellant grain simplifies the SFRJ case manufacture, but the SFRJ does require multiple casting

operations to fabricate the fuel and propellant grains. The cost of the SFRJ can increase if the added complexity of an active throttle is implemented.

The DR requires multiple chambers, one for the generator and one for the booster-combustor chamber. Addition of an active throttle to the DR in the variable flow system significantly adds to the cost of the system, even though it enhances the mission versatility of the DR. The cost of a pulse solid rocket is probably comparable to that of a simple ducted rocket.

The SFRJ, as well as the DR and any other solid system, is going to be more expensive to develop when one considers the cost per data point. Liquid fueled systems are most attractive from this aspect.

## 7. RELIABILITY AND MAINTAINABILITY

Reliability and maintainability of the different candidate propulsion systems are difficult to assess. Subjectively, the simpler, the more reliable. This approach favors the conventional solid rocket, the SFRJ or the fixed flow DR. On these systems there is little to check out after assembly and little to malfunction. All three possess this characteristic of the solid rocket. However, development can lead to turbojets, liquid rockets, and LFRJs which can be reliable and require little maintenance during their lifetime. A large data base is being gathered on the reliability and maintainability of the turbojet systems.

## 8. CONCLUSION

For most conventional tactical missiles the solid rocket, by virtue of its simplicity and cost, is the propulsion system of choice. A pulse motor can extend the performance potential, specifically the range, or the solid rocket

Airbreathing propulsion will provide the energy necessary for future high speed, long range tactical missiles. For lower speed systems, turbojets appear to be the best candidate propulsion system. As the speed needs increase, ramjets become more attractive with the LFRJ providing the highest performance of the ramjet systems. In between these extremes lie the capabilities and applicability of the ATR, SFRJ, and DR.

Turbojets deliver the highest performance of the airbreathing propulsion systems but currently suffer from the limitation of materials and designs that can withstand the temperatures resulting from sustained, high speed flight. They are the propulsion system of choice for long duration, moderate speed (high subsonic) flight.

The LFRJ, which possesses the capability of versatility for mission optimization and as well as high performance, makes it the first choice for long duration high speed (supersonic) flight over a wide operating regime.

The DR appears best suited to shorter range tactical missiles. Such missiles have smaller airbreathing propulsion systems which have higher thrust capability (a result of oxidizer in its gas generator fuel) than a ramjet usually possesses and which still are not oversized for the longer duration portion of the mission.

The SFRJ performance capability is between that attainable with an LFRJ and a DR. SFRJs are more attractive for tactical missiles which require performance near that of the LFRJ but not the versatility of an LFRJ. The SFRJ can be the simplest ramjet in operation but the most difficult to analyze and apply to tactical missiles. It must be designed as part of the system and must be designed to operate over the total mission. While the SFRJ possesses an inherent throttle capability, it is more for compensation for off-nominal conditions (the SFRJ rarely operates on-design). As with the solid rocket, the performance capability of the SFRJ must be designed into the system. The SFRJ does not lend itself to extensive adaptation after design development.

The ATR is a relative newcomer to the field of airbreathing propulsion for high speed tactical missiles, and, as such, its technology base is the least mature. It possesses the capability of static thrust and delivers moderately good performance. But a major disadvantage is its complexity, which is a result of its marriage to two systems, the turbojet and the ramjet. The ATR appears to have multimission capability (static thrust for acceleration from zero and for low speed flight and durability for sustained high speed

flight). It may be more useful for larger size missile systems that require higher speed with moderate acceleration capability (to operating speed).

In summary, use:

Turbojet for long duration moderate speed flight

LFRJ for the maximum long duration high speed flight

SFRJ, DR, ATR for other missions as applicable

Solid rocket for most conventional tactical missiles requiring short range

Above all, use the simplest system capable of performing the mission

PREVISION DES COEFFICIENTS AERODYNAMIQUES  
DE MISSILES MUNIS DE PRISES D'AIR

par

P. CHAMPIGNY - D. BAUDIN

Office National d'Etudes et de Recherches Aérospatiales (ONERA)  
B.P. N° 72 - 92322 CHATILLON CEDEX (France)

et

P. GONIDEK

Laboratoire de Recherches Balistiques et Aérodynamiques  
BP n° 914 - 27207 VERNON CEDEX (France)

RESUME

Pour les nouvelles générations de missiles devant voler plus loin et plus vite, la propulsion aérobie (par turboréacteur ou statoréacteur) constitue un moyen de propulsion très intéressant, mais au prix d'une augmentation de la complexité du missile, en particulier avec la présence de prises d'air.

Dans ce contexte, une étude paramétrique expérimentale a été effectuée à la soufflerie C4 du Laboratoire de Recherches Balistiques et Aérodynamiques (LRBA) afin d'analyser l'influence des prises d'air sur la portance et le centre de poussée du fuselage.

L'objet de cette communication est de présenter quelques résultats obtenus au cours de cette étude, ainsi que la modélisation qui a été développée à l'ONERA pour étendre les capacités du code MISSILE au cas des missiles aérobie.

ABSTRACT

One of the most promising systems for the propulsion of high performance (velocity, range) missiles of the next generation is the airbreathing propulsion concept (turbojet or ramjet), but it leads to complex configuration with air-intakes.

That is why parametric experimental studies were conducted in the LRBA ("Laboratoire de Recherches Balistiques et Aérodynamiques) C4 wind-tunnel in order to evaluate air-intake influence on body lift and center of pressure.

The purpose of this paper is to present some of the results obtained during this study as well as the prediction method included in the MISSILE code for airbreathing missiles calculations.

1. INTRODUCTION

Dans le cadre de la prévision des coefficients aérodynamiques d'un missile, de nombreuses études expérimentales ont été menées à l'ONERA pour aboutir à un code de calcul dit "MISSILE" (figure 1). Jusqu'à maintenant, ce code de prédiction ne concernait que les missiles à fuselages de révolution munis d'une ou deux séries de voilures. Il utilise des méthodes semi-empiriques, simples à mettre en oeuvre et très rapides, basées sur des théories simples ou sur des banques de données (figure 2).

Pour les nouvelles générations de missiles devant voler plus vite et plus loin, il est intéressant d'envisager une propulsion de type aérobie (turboréacteur ou statoréacteur) mais au prix d'une augmentation de la complexité du missile, en particulier avec la présence de prises d'air.

Ainsi, les prises d'air qui vont être placées dans le champ aérodynamique du fuselage, devront fournir le débit nécessaire avec une efficacité suffisante pendant tout le vol, quelles que soient les manoeuvres effectuées, et ces prises d'air auront également beaucoup d'influence sur l'aérodynamique externe du missile [1].

Dans ce contexte, et avec le support des Services Officiels français, une banque de données expérimentales a été constituée à la Soufflerie C4 du Laboratoire de Recherches Balistiques et Aérodynamiques (LRBA) afin de quantifier l'influence des prises d'air sur la portance et la stabilité des missiles.

L'objet de cette communication est de présenter quelques résultats obtenus au cours de cette étude, ainsi que la modélisation qui a été entreprise à l'ONERA pour étendre les capacités du code MISSILE au cas des missiles aérobie.

2. NOTATIONS

AR : allongement des prises d'air,  $= (s-D)/l$   
CN : coefficient de force normale  
CN<sub>s</sub> : gradient de force normale  
CN<sub>s</sub> : coefficient lié à la portance tourbillonnaire

23-2

D : diamètre du fuselage  
k : coefficient lié à la portance tourbillonnaire  
K<sub>t</sub> : coefficient lié au gradient de force normale  
l : longueur de la prise d'air  
M : nombre de Mach  
s : envergure des prises d'air  
S<sub>ref</sub> : surface de référence,  $= \frac{\pi D^2}{4}$   
S<sub>planform</sub> : surface en plan des prises d'air,  $= s \cdot D \cdot l$   
X<sub>cp</sub> : position du centre de poussée  
 $\alpha$  : angle d'incidence  
 $\beta$  : facteur de compressibilité  $= \sqrt{M^2 - 1}$   
 $\gamma$  : inclinaison des prises d'air/plan horizontal (cas des configurations à 2 prises d'air)  
 $\phi$  : position en roulis des configurations à 4 prises d'air

#### Indice

N.L. : relatif à la portance tourbillonnaire (ou terme non linéaire)

### 3. ETUDE EXPERIMENTALE

#### 3.1. Configurations étudiées

Le choix de la configuration des prises d'air est un compromis difficile entre diverses contraintes : aérodynamiques, opérationnelles et technologiques.

On peut ainsi envisager divers positionnements de la prise d'air par rapport au fuselage :

- prise d'air frontale
- prise d'air nasale
- prises d'air latérales
- ou même des prises d'air plus intégrées au fuselage comme sur certains concepts futuristes de missiles aérobies hypersoniques de très longue portée.

Pour cette étude paramétrique expérimentale, seules des configurations classiques à prises d'air latérales ont été considérées.

Les principaux paramètres analysés au cours des essais sont (figure 3) :

- le type de prises d'air : bidimensionnelle ou de révolution ;
- leur nombre : 2, 3 ou 4 ;
- leur inclinaison par rapport au plan horizontal dans le cas des configurations à deux prises d'air :  $\gamma = 0, 22,5^\circ$  ou  $45^\circ$  ;
- leur longueur : 5 ou 9 calibres
- leur envergure :  $s/D = 1,68$  à  $2,44$ , ce qui correspond à des taux de motorisation  $A1/S_{ref}$  de 0,30 à 0,60.

#### 3.2. Moyens expérimentaux

Compte tenu du caractère paramétrique de cette étude expérimentale, les essais ont été effectués dans une soufflerie de recherche du LRBA (Soufflerie C4) dont les dimensions de la veine d'expérience sont 0,4m x 0,4m.

Les conditions d'essais retenues ont permis de couvrir une large gamme de nombres de Mach (0,7 à 4,3) et d'incidences (jusqu'à  $15^\circ$ ).

La maquette, de diamètre 22 mm, est constituée d'un fuselage avec ogive parabolique pointue, sur lequel viennent se monter les différentes configurations de prises d'air (figure 4).

Les mesures effectuées à l'aide d'une balance dynamométrique sont relatives aux coefficients aérodynamiques globaux et plus particulièrement à la portance et la stabilité.

#### 4. ANALYSE DES RESULTATS

A partir de la banque de données expérimentales constituée à l'issue des essais, une modélisation des différents coefficients aérodynamiques (portance et stabilité) a été entreprise.

C'est sur la base de cette modélisation que vont être présentés les résultats, ce qui a l'avantage d'offrir une vue synthétique de l'influence des différents paramètres considérés, et d'éviter au lecteur d'être submergé par un trop grand nombre de courbes de résultats expérimentaux.

##### 4.1. Principe de la modélisation

Les méthodes de prédiction des coefficients aérodynamiques des missiles reposent généralement sur une décomposition par éléments : fuselage, ailes, gouvernes...

Ainsi, pour un ensemble fuselage + prises d'air, on peut aussi dissocier les effets des prises d'air du fuselage, soit :

$$C_{N \text{ P.A.}} = C_{N \text{ fus + PA}} - C_{N \text{ fus}} \quad (1)$$

$$X_{cp \text{ P.A.}} = \frac{(C_{N \text{ fus + PA}} X_{cp}) - (C_{N \text{ fus}} X_{cp})}{C_{N \text{ P.A.}}} \quad (2)$$

Les coefficients aérodynamiques associés aux prises d'air (en présence du fuselage) sont alors modélisés par analogie avec ceux d'un fuselage, suivant une expression composée d'un terme "linéaire" auquel on ajoute un terme non linéaire soit :

$$C_N(\alpha) = C_{N_0} \frac{\sin 2\alpha}{2} + C_{N_{\alpha_0}} \sin^2 \alpha \frac{S_{\text{planform}}}{S_{\text{ref}}} \quad (3)$$

De même le coefficient de moment de tangage peut être calculé en associant aux deux termes de portance précités un centre de poussée au voisinage de l'incidence nulle  $(X_{cp})_{\alpha=0}$  et un centre de poussée relatif aux efforts non linéaires  $(X_{cp})_{\alpha>0}$ .

##### 4.2. Gradient de force normale et centre de poussée à $\alpha=0$

La prise d'air constitue un élément portant de faible allongement dont la variation du gradient de force normale en fonction de l'envergure se comporte comme celle relative à une aile mince de faible allongement (figure 5).

On note cependant, qu'à envergure donnée, une prise d'air a un gradient de force normale beaucoup plus élevé qu'une aile mince, effet dû à l'épaisseur très importante de la prise d'air.

A partir de l'analyse de l'ensemble des résultats expérimentaux, on montre que la loi d'évolution du  $C_{N_0}$  en fonction de l'envergure est de la forme :

$$C_{N_0} = K_1 [(s/D - 1) \cos \gamma]^{1.6} \quad (4)$$

où

-  $(s/D - 1) \cos \gamma$  représente l'envergure effective de la prise d'air, en projection sur le plan horizontal,

- et  $K_1$  traduit l'effet du type de prise d'air et du nombre de Mach (figure 6).

A ce propos, on remarque que c'est la configuration à 2 prises d'air bidimensionnelles qui donne le plus fort gradient de force normale. Il est en particulier plus élevé que pour 4 prises d'air, ce qui est assez étonnant. Par contre les prises d'air de révolution apportent un peu moins de portance, ce qui est plus prévisible compte tenu de leur forme.

Quand le nombre de Mach croît, ou quand la longueur de la prise d'air diminue, la portance diminue, et on observe qu'à l'extrémité du domaine exploré, qui correspond aux grands nombres de Mach, le gradient de force normale est pratiquement indépendant du type de prise d'air.

La position du centre de poussée au voisinage de l'incidence nulle dépend assez peu du type de prise d'air, et est située très près de l'origine de celles-ci, ce qui est conforme à la théorie des ailes droites très élancées, figure 7.

Quand le nombre de Mach augmente, on s'écarte évidemment de cette théorie, et le centre de poussée recule jusqu'à environ 30 à 40% de la longueur de la prise d'air.

#### 4.3. Portance tourbillonnaire

A partir des résultats expérimentaux, il est possible de calculer la portance tourbillonnaire (contribution non linéaire à la portance globale) à partir de la relation (3), et du coefficient  $C_{N.L.}$  déterminé précédemment soit :

$$C_{N.L.} = C_N(\alpha) - C_{N.L.} \frac{\sin 2\alpha}{2}$$

expérience

On suppose alors que cette portance tourbillonnaire évolue en fonction de l'incidence selon une loi de la forme :

$$C_{N.L.} = C_{N.L.} \sin^k \alpha \frac{S_{planform}}{S_{ref}} \quad (5)$$

ce qui est assez bien vérifié expérimentalement (figure 8).

Ensuite, en effectuant un lissage des points expérimentaux par une méthode des moindres carrés, on a déduit les coefficients  $C_{N.L.}$  et  $k$  de la relation (5).

Le coefficient  $k$ , qui traduit le degré de non-linéarité des courbes de portance, dépend essentiellement de la configuration de prise d'air et assez peu du nombre de Mach (figure 9). Sa valeur est comprise entre 1,5 et 2,5, ce qui est assez proche de la valeur donnée par la théorie de l'écoulement transversal pour un fuselage de section circulaire ( $k = 2$ ).

L'intensité de la portance tourbillonnaire, quantifiée ici par le coefficient  $C_{N.L.}$ , dépend peu du type de prise d'air ou de leur nombre (figures 10 et 11). Par contre, elle peut passer d'un rapport de 1 à 10 suivant le nombre de Mach ou l'allongement de la prise d'air.

D'après la base de données établie ici, le coefficient  $C_{N.L.}$  est une fonction du produit  $\beta AR$ , et on constate, comme pour une aile de faible allongement, que la portance tourbillonnaire diminue quand le nombre de Mach augmente.

Par ailleurs, pour les configurations à quatre prises d'air, la position en roulis  $\theta = 45^\circ$  est la plus défavorable. Cet effet peut être attribué aux deux prises d'air d'extrados qui détruisent la portance tourbillonnaire propre au fuselage.

Le centre de poussée associé à cette portance tourbillonnaire est situé, en moyenne, un peu plus en arrière que le centre de surface de la prise d'air (50% l), et varie dans une plage assez importante (de 40% à 100% l) suivant la configuration de prise d'air et le nombre de Mach (figures 12 et 13).

#### 4.4. Application de la méthode de prédiction

La contribution des prises d'air à la portance et au moment de tangage du fuselage a donc été quantifiée au cours de cette étude paramétrique, pour une large gamme de nombres de Mach, et pour une grande diversité de configurations.

L'analyse de la banque de données a permis de mettre au point une modélisation simple, directement utilisable dans un code de prédiction, comme celui développé à l'ONERA, le code "MISSILE".

La figure 14 montre un exemple de prédictions du coefficient de force normale et de la position du centre de poussée. La précision obtenue par ce type de méthode est satisfaisante sur toute la plage d'incidence.

Il faut cependant souligner que les prises d'air considérées ici sont de section constante jusqu'au culot du fuselage, alors que dans la réalité celles-ci se terminent généralement par des rétreints, afin de minimiser la traînée du missile. L'influence de ces rétreints reste cependant très modérée comme cela avait été montré dans la référence [1], figure 15, et les résultats présentés ici peuvent être utilisés pour des applications industrielles avec une bonne précision.

#### 5. PERSPECTIVES

Pour assurer le pilotage d'un missile, il faut évidemment disposer de surfaces de contrôle, dites gouvernes, qui pour un missile aérodynamique sont placées à l'arrière. Plus précisément, elles seront montées sur les carénages prolongeant les prises d'air, qui sont très utiles pour loger les dispositifs de commande des gouvernes.

Une difficulté apparaît alors pour estimer les portances et efficacités de ces gouvernes, qui sont placées sur un fuselage de section non-circulaire.

Dans la référence [1], deux méthodes avaient été présentées pour calculer les interactions fuselage-prises d'air-gouvernes aux faibles incidences (figure 16).

La première repose sur la théorie des corps élancés, appliquée à une aile montée sur un fuselage de diamètre fictif égal à l'envergure des prises d'air.

La deuxième méthode qui peut être envisagée, consiste à faire correspondre à la section réelle du fuselage, une section circulaire, à l'aide d'une transformation conforme. Il est alors possible de calculer les incidences locales au niveau de la gouverne, et donc le coefficient d'interaction du fuselage sur l'aile.

Cette deuxième méthode, beaucoup plus lourde, est cependant très utile pour des architectures de prises d'air et gouvernes très complexes.

Un exemple d'application de la première méthode est donné figure 17, où on observe que l'accord calcul-expérience est très satisfaisant, en particulier en supersonique.

En incidence, ce type d'analogie entre un fuselage muni de prises d'air et un fuselage circulaire n'est plus possible, compte tenu du système tourbillonnaire très complexe généré par l'ogive et les prises d'air (figure 18).

C'est pourquoi une nouvelle base de données a été constituée au LRBA afin de mesurer la portance de voilures montées sur un ensemble fuselage + prises d'air.

Les résultats ne sont pas encore totalement exploités, et feront l'objet d'une prochaine communication.

#### REFERENCES

- [1] P. CHAMPIGNY  
Problèmes liés à l'aérodynamique externe des missiles aérobie  
AGARD CP 336 - Septembre 1982.
- [2] G. LARUELLE  
Prises d'air de missiles  
VKI Lecture Series on Intake Aerodynamics -1988.

### PROGRAMME MISSILE

CN - CY - Cl - Cm - Cn ( Cmq - Ctp )


	Géométrie :	fuselage de révolution 1 ou 2 séries de voilures cruciformes prises d'air latérales (en cours)
	Méthodes :	bases de données théories simples concept d'incidence équivalente
	Conditions de vol	nombre de MACH = 0 à 4,0 incidence = 0 à 40° roulis : quelconque braquages de gouvernes : quelconques

Figure 1 : Caractéristiques du code "MISSILE" de l'ONERA

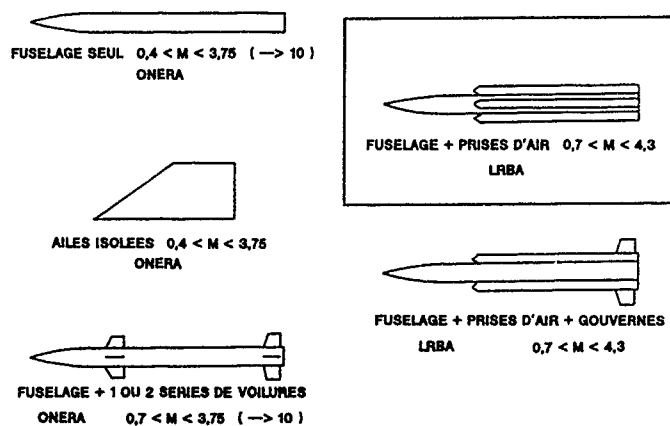


Figure 2 : Bases de données utilisées dans "MISSILE"

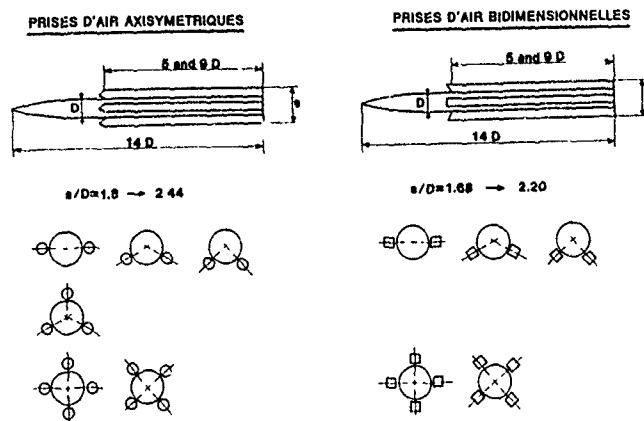


Figure 3 : Configurations étudiées



SOUFFLERIE C4 DU LRBA

VEINE : 0,4 m X 0,4 m

NOMBRE DE MACH : 0,7  $\rightarrow$  4,3

INCIDENCE : 0°  $\rightarrow$  15°

NOMBRE DE REYNOLDS :  $0,6 \cdot 10^6 / D$

Figure 4 : Maquette dans la soufflerie C4 du LRBA

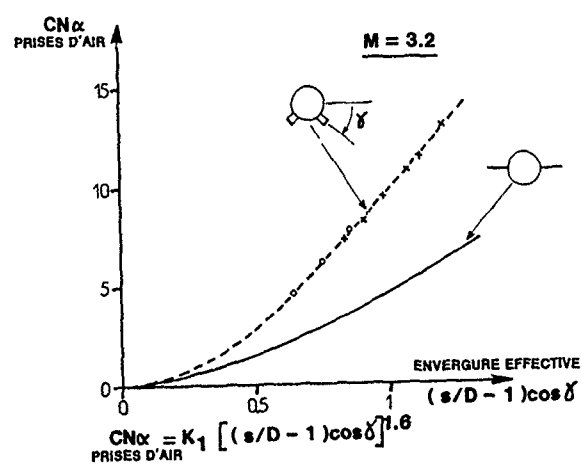


Figure 5 : Comparaison prises d'air-ailes nageoires



$$CN_{\alpha} = K_1 \left[ \left( \frac{s}{D} - 1 \right) \cos \delta \right]^{1.6}$$

PRISES D'AIR

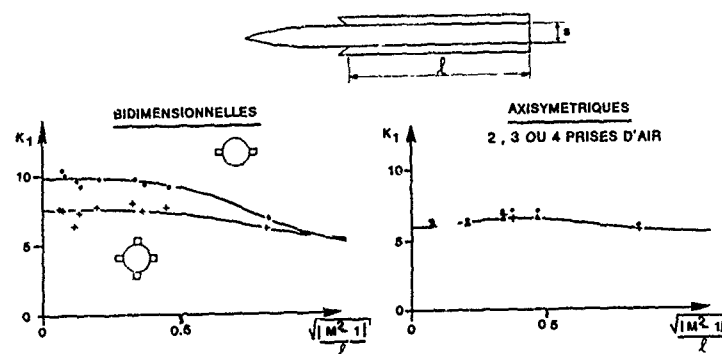


Figure 6 : Gradient de force normale

$$\alpha \approx 0^\circ$$

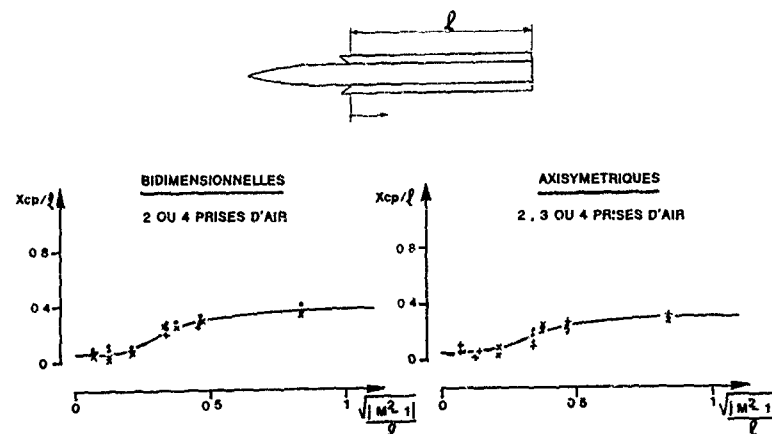


Figure 7 : Position du centre de poussée

$$CN_{NL} = CN_{\alpha\alpha} \sin^k \alpha \frac{S_{planform}}{S_{ref}}$$

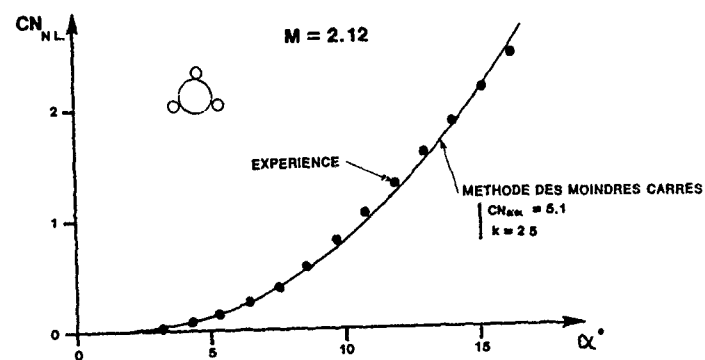


Figure 8 : Evolution de la portance tourbillonnaire avec l'incidence

$$CN_{NL} = CN_{\alpha\alpha} \sin^k \alpha \frac{S_{planform}}{S_{ref}}$$

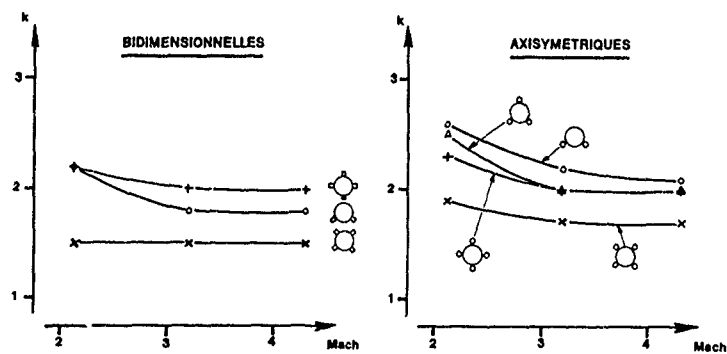


Figure 9 : Degré de non-linéarité de la portance tourbillonnaire

$$CN_{NL} = CN_{\alpha\alpha} \sin^k \alpha \frac{S_{planform}}{S_{ref}}$$

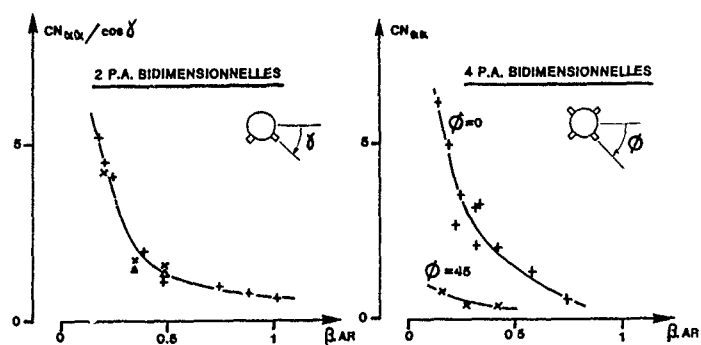


Figure 10 : Intensité de la portance tourbillonnaire (prises d'air bidimensionnelles)

$$CN_{NL} = CN_{\alpha\alpha} \sin^k \alpha \frac{S_{planform}}{S_{ref}}$$

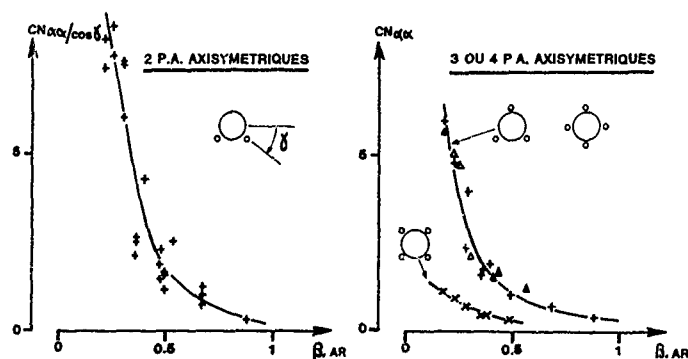


Figure 11 : Intensité de la portance tourbillonnaire (prises d'air axisymétriques)

$$CN_{N.L.} \rightarrow (X_{cp}/\ell)_{N.L.}$$

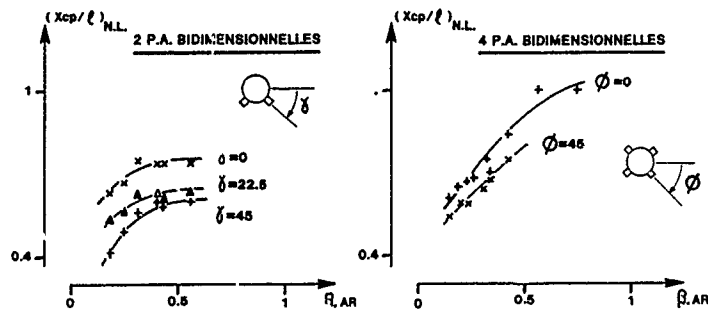


Figure 12 : Position du centre de poussée des efforts tourbillonnaires (prises d'air bidimensionnelles)

$$CN_{N.L.} \rightarrow (X_{cp}/\ell)_{N.L.}$$

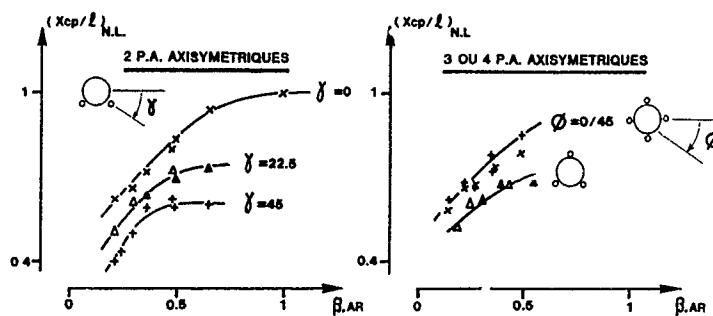


Figure 13 : Position du centre de poussée des efforts tourbillonnaires (prises d'air axisymétriques)

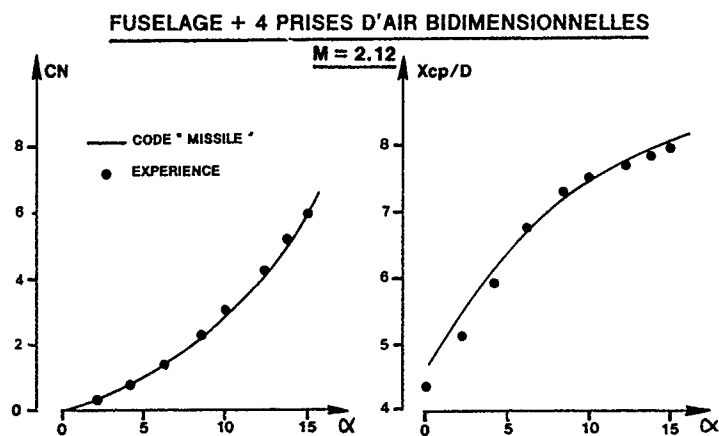
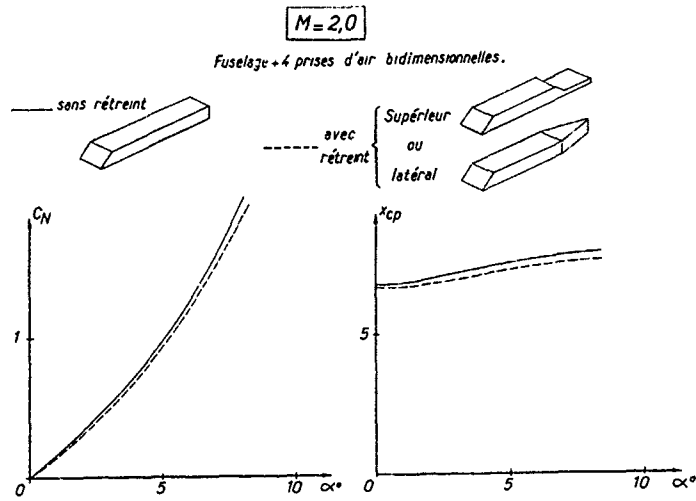
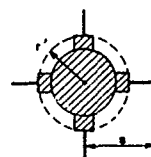


Figure 14 : Comparaison code "MISSILE" - expérience



$$\alpha \approx 0^\circ$$

## METHODE 1 :



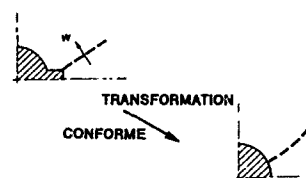
FUSELAGE CIRCULAIRE EQUIVALENT

$$\rightarrow r^2$$

THEORIE DES CORPS ELANCES

$$\rightarrow K_w, K_b = f(r^2/s)$$

## METHODE 2 :



$$\rightarrow w(y)$$

$$\rightarrow K_w$$

Figure 16 : Principe de calcul des interactions fuselage/prises d'air - gouvernes

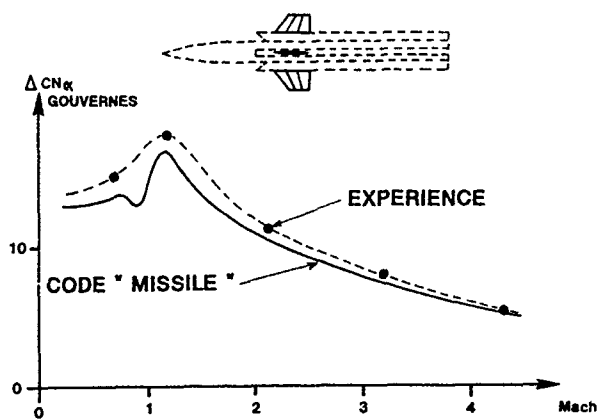


Figure 17 : Comparaison code "MISSILE" - expérience

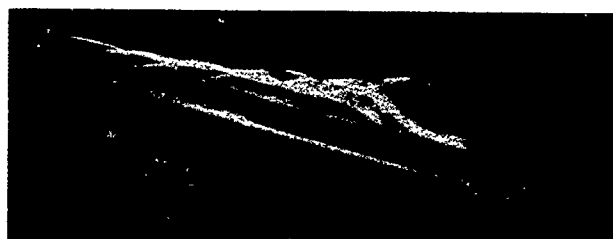


Figure 18 : Visualisation au tunnel hydrodynamique de l'écoulement tourbillonnaire sur un ensemble fuselage + prises d'air.

# COMPUTATION OF AXISYMMETRIC BASE FLOW WITH DIFFERENT TURBULENCE MODELS

by

F. MAGAGNATO  
Aerodynamics Department, BF 30  
Dornier Luftfahrt GmbH,  
Postfach 1303  
D-7990 Friedrichshafen 1  
Federal Republic of Germany

## Summary

The flow past axisymmetrical missile afterbodies with base is calculated using a finite-volume technique. The compressible Reynolds-averaged Navier-Stokes equations are solved with different turbulence models for the approximation of the Reynolds-stresses. Two algebraic eddy-viscosity models, which have been adjusted for the use in free shear layers, as well as the well known K-ε low-Reynolds-number turbulence model are used. Calculations were done on a conical afterbody with and without a centred propulsive jet. The results are found in good agreement with the experiments although some discrepancies occur in critical flow regions. The algebraic turbulence models have been extended to allow a meaningful application in those regions where the performance formerly has been poor.

## 1. Introduction

The compressible Reynolds-averaged Navier-Stokes-equations are solved with a finite-volume approach using a Runge-Kutta-type integration in time. The code is block-structured and uses the multigrid strategy to speed up convergence.

For the approximation of the Reynolds-stresses three different eddy-viscosity turbulence models were considered in the code. Firstly the Baldwin/Lomax model [1] which is an algebraic eddy-viscosity model based on the assumption that the turbulence is in local equilibrium. It is a modification of the Cebeci/Smith model [2] which was derived for boundary-layer flows. It relates the eddy viscosity to the mean flow by algebraic expressions distinguishing between an inner and an outer layer.

The recently proposed algebraic turbulence model from Martinelli/Yakhot [3] was investigated in the code due to its analytically derived parameters from the Renormalisation Group Theory.

Additionally to the algebraic models a K-ε two-equation model was considered. The low-Reynolds-number version proposed by Lam/Bremhorst [4] was chosen which needs no wall functions to account for the wall proximity effects.

Calculations were performed on a conical afterbody with and without a centred propulsive jet. In addition to these testcases three turbulence models on an afterbody with solid plume simulator were compared.

## 2. Governing Equations

In order to deal with turbulent flow situations with large separated regions only the Reynolds-averaged Navier-Stokes equations seems to be appropriate to predict this properly. The compressible, time-dependent Navier-Stokes-equations in integral form can be written as:

For mass conservation.

$$\iiint_V \frac{\partial \rho}{\partial t} dV + \iint_S \rho \vec{v} \cdot \vec{n} dS = 0$$

For momentum conservation.

$$\begin{aligned} \iiint_V \frac{\partial (\rho \vec{v})}{\partial t} dV + \iint_S \rho \vec{v} (\vec{v} \cdot \vec{n}) dS + \iint_S p \vec{n} dS - \\ \iint_S \vec{n} \cdot \vec{T} dS = 0 \end{aligned} \quad (II.1)$$

For energy conservation:

$$\begin{aligned} \iiint_V \frac{\partial (\rho E)}{\partial t} dV + \iint_S \rho E (\vec{v} \cdot \vec{n}) dS + \iint_S p (\vec{v} \cdot \vec{n}) dS - \\ \iint_S \vec{v} \cdot (\vec{n} \cdot \vec{q}) dS + \iint_S \vec{n} \cdot \vec{q} dS = 0 \end{aligned}$$

This is a system of hyperbolic equations with respect to time where E represents the total specific energy (summation of inner and kinetic energy) and  $\vec{q}$  being the energy flux vector.

It is assumed that the energy flux vector expresses only molecular energy transport which can be described by Fourier's law.

$$\vec{q} = -k \text{ grad } T$$

There k is the thermal conductivity which is determined on the assumption of constant Prandtl number according to:

$$Pr = \frac{c_p \mu}{k}$$

$\vec{T}$  in equation (II.1) is the "viscous stress tensor" which is described later on.

For an ideal gas the total specific energy writes:

$$E = e + p/2 v^2 = p/(\chi-1) + p/2 v^2$$

and the total specific enthalpy:

$$pH = E + p$$

Here  $e$  represents the inner energy,  $H$  is the total enthalpy and  $X$  stands for the ratio of the specific heats. In the numerical method the total energy is normalised by the free-stream total enthalpy:

$$\bar{E} = e - \rho H_\infty$$

This special treatment results in a subtraction of the continuity equation multiplied by the total enthalpy  $H_\infty$  from the energy equation. Later on the left hand side  $\bar{E}$  of the above equation is called  $E$ .

For Newton-type fluids the assumption is made, that the stress tensor  $\bar{T}$  (II.2) is continual varying with the deformation velocity tensor  $\bar{D}$  (Stokes hypothesis).

$$\bar{T} = 2\mu\bar{D} - \frac{2}{3}\mu\nabla \cdot (\nabla \bar{E}) \quad (\text{II.2})$$

The deformation velocity tensor  $\bar{D}$  is given by

$$\bar{D} = \begin{bmatrix} u_x & 1/2(u_y+v_x) & 1/2(u_z+w_x) \\ 1/2(u_y+v_x) & v_y & 1/2(v_y+w_y) \\ 1/2(u_z+w_x) & 1/2(v_y+w_y) & w_z \end{bmatrix}$$

$\mu$  being the total viscosity (laminar + turbulent) and  $\bar{E}$  being the unit-tensor. Furthermore the dependency of the laminar viscosity  $\mu_l$  from the pressure is neglected so that the Sutherland formulation can be used.

$$\mu_l = \frac{c\sqrt{T}}{1 + \frac{d}{T}}$$

with  $c$  and  $d$  being fluid specific constants which for air are given by:

$$c = 1.46 \cdot 10^{-4} \text{ [1/K]}$$

$$d = 112 \text{ [K]}$$

### 3. Turbulence Modelling

Since full direct simulation of the turbulent structure for large Reynolds-number is not feasible today with the available super computers. The turbulence effects have to be modelled by physical models. The task for turbulence modelling is to calculate the turbulent stresses appearing in the Reynolds-averaged equations. The simplest approach follows the eddy-viscosity concept according to Boussinesq [5]. This concept relates the turbulent stresses by a single scalar parameter  $\mu_t$  multiplied with the rate of strain tensor in the mean flow.

$$-\rho \overline{v_i v_j} = \mu_t \partial_{ij} \quad (\text{III.1})$$

The Baldwin/Lomax and the Martinelli/Yakhot model calculate the eddy-viscosity  $\mu_t$  algebraically from mean flow quantities whereas the K- $\epsilon$ -type models employs two differential equations for calculating the eddy-viscosity.

Baldwin/Lomax introduced a two layer concept based on the idea of Cebeci/Smith deviding the flow into an inner and an outer layer.

For the inner layer they assumed:

$$\mu_t = \rho l^2 |\omega| \quad (\text{III.2})$$

with

$$l = ky[1 - e^{-y^*/A^*}]$$

$y$  = normal distance from the wall

$$y^* = \frac{\sqrt{\rho_w \tau_w} y}{\mu_w}$$

$$|\omega| = \sqrt{\left(\frac{\partial u}{\partial y} - \frac{\partial v}{\partial x}\right)^2}$$

with the constants  $k = 0.4$  and  $A^* = 26$  according to van Driest.

For the outer layer:

$$\mu_t = k C_{cp} F_{wake} F_{kleb}(y) \quad (\text{III.3})$$

with

$$F_{wake} = \min \left[ y_{max} F_{max} \frac{C_{wk} y_{max} U_{diff}^2}{F_{max}} \right]$$

where  $y_{max}$  and  $F_{max}$  are determined by the maximum of the following function.

$$F(y) = y |\omega| [1 - e^{-y^*/A^*}]$$

This function generates for boundary layer flows a pronounced maximum. The normal distance to this point ( $y_{max}$ ) replaces the displacement thickness in the formulation of Cebeci/Smith. The Klebanoff-factor is given by:

$$F_{kleb}(y) = \frac{1}{[1 + 5.5 \left( \frac{C_{kleb} y}{y_{max}} \right)^2]}$$

and  $U_{diff}$  is the maximum of the velocity in the wall layer. The other constants are given below:

$$K = 0.0168 \text{ (Klauser)}$$

$$C_{cp} = 1.6, \quad C_{wk} = 0.25, \quad C_{kleb} = 0.3$$

The switching between the inner and the outer model is performed where for the first time the values of  $\mu$  became equal.

The algebraic turbulence model of Martinelli/Yakhot is based on the Renormalization Group Theory [6]. Although free from uncertainties related to the determination of modelling constants, they still require the specification of a length-scale which leads to a restriction in the generality of the model. The eddy-viscosity is obtained from the following relation.

$$\mu = \mu_l [1 + H \left( \frac{a}{\mu_l} \epsilon \Lambda_f^4 - C_0 \right)]^{1/3} \quad (\text{III.4})$$

where  $H(x)$  is the Heaviside function defined by  $H(x) = x$  for  $x \geq 0$  and  $H(x) = 0$  otherwise,  $\Lambda_f$  the wave vector corresponding to the integral scale of the turbulence in the inertial range, and  $\mu = \mu_l + \mu_t$  is the total viscosity (laminar plus turbulent). The constants  $a = .120$  and  $C_0 = .75$  were derived in [6]. The mean dissipation rate  $\epsilon$  and the wave vector  $\Lambda_f$  must be determined before using equation (III.4) to compute the eddy-viscosity.

The integral scale of turbulence  $L_f = \pi \Lambda_f^2$ , corresponding to the top of the inertial range, is postulated to be proportional to the distance from the wall  $y$  ( $L_f = \chi y$ , where  $\chi$  is the Von Karman constant).

In the outer region, it is plausible to take the integral scale in the order of the boundary layer thickness  $\delta$ . Following the idea of Stock/Haase [7] the boundary layer thickness  $\delta$  is determined by

$$\delta = 1.548 y_{\max}$$

where  $y_{\max}$  is the wall distance where the function

$$F(y) = y|w| [1 - e^{-y^*/A^*}]$$

has its maximum.

With this assumption equation (III.4) can be cast in the following form:

$$\mu = \mu_1 [1 + H(\frac{a}{\mu_1} e(\frac{1}{y} + \frac{1}{\gamma\delta}) - C_c)]^{1/3} \quad \text{[III.5]}$$

where  $a = .0192$  or  $a = .0256$ , depending whether the Von Karman constant is taken to be equal to the value predicted by the RNG theory ( $\kappa = .372$ ) or to the standard value ( $\kappa = .4$ ). The value of the parameter  $\gamma = 0.225$  has been chosen in order to recover the constant predicted by the RNG-theory for the outer part of the boundary layer. More precisely the value of  $\gamma$  has been chosen in such a way that  $\gamma a^{1/4} \delta \rightarrow .084 \delta$  as  $y \rightarrow \delta$ . Also equilibrium (Production = Dissipation) is assumed from which follows:

$$\epsilon = P_k = \mu_t \epsilon = \mu_t (\frac{\partial u_i}{\partial x_j} + \frac{\partial u_j}{\partial x_i} - \frac{2}{3} \delta_{ij} \frac{\partial u_k}{\partial x_k}) \frac{\partial u_i}{\partial x_j}$$

The turbulent eddy-viscosity  $\mu_t$  is then obtained by solving the cubic equation (III.5) at every point in the computational domain.

The K- $\epsilon$  model of Lam/Bremhorst can be written as:

$$\frac{\partial(Pk)}{\partial t} + \frac{\partial}{\partial x_i} (\rho u_i k - \mu_k \frac{\partial k}{\partial x_i}) = P_k - \rho \epsilon \quad \text{(III.6)}$$

$$\frac{\partial(\rho \epsilon)}{\partial t} + \frac{\partial}{\partial x_i} (\rho u_i \epsilon - \mu_\epsilon \frac{\partial \epsilon}{\partial x_i}) =$$

$$\frac{c_1 f_1 \epsilon}{k} P_k - \frac{c_2 f_2 \epsilon^2 \rho}{k}$$

$$P_k = \frac{\mu_t}{\mu} [\tau_{xx} \frac{\partial u}{\partial x} + \tau_{xy} (\frac{\partial u}{\partial y} + \frac{\partial v}{\partial x}) + \tau_{yy} \frac{\partial v}{\partial y}] - \frac{2}{3} \rho k (\frac{\partial u}{\partial x} + \frac{\partial v}{\partial y})$$

$$f_\mu = [1 - \exp(-0.0165 R_y)]^2 (1 + \frac{20.5}{R_T})$$

$$f_1 = 1 + (\frac{0.05}{f_\mu})^2$$

$$f_2 = 1 - \exp(-R_T^2)$$

$$R_y = \frac{\rho k^{0.5} y}{\mu_1} \quad R_T = \frac{\rho k^2}{\mu_1 \epsilon}$$

$$\begin{aligned} \mu &= \mu_1 + \mu_t & c_1 &= 1.14 \\ \mu_k &= \mu_1 + \lambda_k \mu_t & c_2 &= 1.92 \\ \mu_\epsilon &= \mu_1 + \lambda_\epsilon \mu_t & c_3 &= 0.0115 \\ \lambda_k &= 1.0 & c_4 &= 0.5 + 1.0 \\ \lambda_\epsilon &= 0.77 & c_\mu &= 0.09 \end{aligned}$$

with this the eddy-viscosity is calculated as:

$$\mu_t = \mu_1 c_\mu f_\mu R_t$$

#### 4. Results

Three testcases have been investigated. Two of them are axisymmetrical bodies with a conical boattail and the third case is an afterbody with solid plume simulator.

The first testcase was measured at the ISL [8] with a freestream Machnumber of  $Ma = 0.35$  without jet. The second testcase was measured at the ONERA [9] with a freestream Machnumber of  $Ma = 0.85$  and a jet Machnumber of  $Ma_j = 2.9$ . The ratio of the static pressure of the jet to the freestream pressure was 1.16.

Figure 1 shows the shape of the afterbody and the computational mesh used in the calculation. The mesh consists of approximately 4000 points.

In order to use the simple algebraic models on block-structured grids, we were faced with the problem of how to calculate the turbulent stresses in those blocks which do not have a boundary-layer type flow as for example in the wake of blunt bodies. Because the algebraic models calculate the characteristic length and velocity scale based on the normal distance to the wall, this is not appropriate for those blocks considered here. Therefore empirical distribution laws were considered as a possibility to describe the turbulence transport into these blocks. Because the production of turbulence energy in local equilibrium flows correlates with the vorticity this was taken as a weighting function to distribute the eddy-viscosity in that area, according to

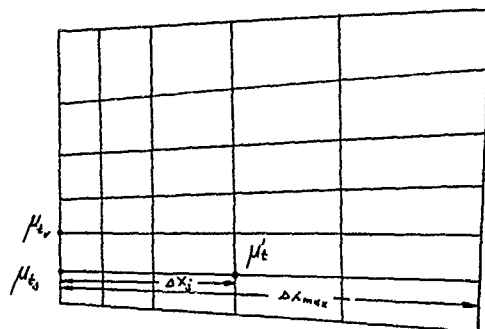
$$\mu_t^i = \mu_{t_v} \left( \frac{|w|}{|w_v|} \right)^\alpha \quad \text{(IV.1)}$$

where  $\mu_{t_v}$  is the max. eddy-viscosity along the upstream block face and  $|w_v|$  the local vorticity at that point.  $\alpha$  is determined by numerical experiments as  $\alpha = 0.2$ . In addition to the weighting the eddy-viscosity is smoothed by an exponential damping factor in order to ensure steadiness on the block faces.

$$\mu_t = \mu_t^i - (\mu_t^i - \mu_{t_j}) \exp(-\frac{\Delta x_j}{\Delta x_{\max}})$$

where  $\mu_{t_j}$  is the eddy-viscosity on the upstream blockface at the same  $j$ -station as  $\mu_t^i$  calculated with (IV.1). And  $\Delta x_j$  is the normal distance from the location of  $\mu_t^i$  to the location of  $\mu_{t_j}$ . And lastly  $\Delta x_{\max}$  is the length of the block in streamwise direction.





A typical result of this highly empirical procedure is shown in figure 2.

The velocity vector field in the wake of testcase 1 is shown on figure 3. The calculated flow field is qualitatively the same as in the experiment conducted by Berner [8]. Although the center of the vortex is not on the same point the centerline velocity distribution for this testcase is in surprisingly good agreement with the experiment for this simple empirical approximation. No differences between both turbulence models (figure 4) are found in predicting the centerline velocity distribution.

Figure 5 shows the pressure distribution at the base for both models. Only two points were measured by Berner indicating a constant value of the pressure. This behavior is represented very well by the calculation.

The next calculation was performed for an afterbody with centred jet. The freestream Machnumber was  $Ma = 0.85$  and the Reynoldsnumber 12.5 million per meter. The static pressure ratio of the jet was 1.16 and the jet Machnumber 2.9. A typical velocity vector field for this testcase is shown on figure 6. The velocity vector field at the base shows no large discrepancies between both algebraic models, so only one flow field is presented here. The length of the separation bubble (s) is correctly predicted by the calculation (figure 7) but the predicted reattachment point ( $R_C$ ) differs slightly from the experiment ( $R_E$ ).

A very good pressure distribution is found in applying the Baldwin/Lomax model, whereas the Martinelli/Yakhot model fails to predict the pressure on the conical part of the body accurately (figure 8). This is due to the overprediction of the turbulent shear stress in the adverse pressure region. Consequently the pressure at the base is also overpredicted by the Martinelli/Yakhot model. Comparing the pressure level at the base with the ONERA-experiment (fig. 9) a good agreement is found for the Baldwin/Lomax model. At the nozzle lip the pressure distribution shows a large peak. It is not clear if this peak is physical in nature or caused by the poor mesh resolution in that region.

Figures 10 and 11 show the turbulent shear stress  $u'v'$  at different stations at the wake. The stress very near the base at  $x/D = 0.2$  is well represented by the empirical approach described below but deviates more and more for stations downstream of the wake, e.g. at  $x/D = 0.4$ . Unfortunately no experimental data are available inside the jet.

A mesh used previously is shown in fig. 9. This c-type mesh had to be used before the blockstructured code became available. Obviously this mesh is highly sheared at the boattail corner. This seems to introduce very large discretisation errors in that region making the results on that mesh questionable. However this flow field was also calculated with the K-e model. The velocity vector field at the base shows a totally different flow field compared to the previously shown figures. One can recognize that the flow separates on the boattail and consequently the center of the primary separation bubble is displaced in radial direction (figure 13). The secondary vortices at the nozzle lip could have been produced by the quasi-laminar flow in that region. This quasi-laminar flow was due to the fact that a laminar K and e profile was given in the jet exit plane (no experimental data were given there).

Figure 14 shows the pressure distribution along the afterbody for the K-e model and a calculation conducted by Wagner [10] with a different computational scheme. In [10] a McCormack predictor-corrector scheme with the Baldwin/Lomax model was used.

The pressure distribution of the K-e model fail to predict the pressure on the boattail and causes the flow to separate on the boattail.

Although the mesh used by Wagner was very coarse, the agreement with the experiment was acceptable.

The pressure distribution at the base for the Baldwin/Lomax model, the K-e model and a laminar calculation are shown in figure 15. Here the Baldwin/Lomax model exhibits the best agreement with the experiment. The K-e model and the laminar calculation shows the same trend. So this underlines that the flow in the region of the nozzle lip is quasi-laminar in the calculation with the K-e model.

In addition to the previously shown testcases we compared the turbulence models on an afterbody with solid plume simulator. The freestream Machnumber for this flow was  $Ma = 0.64$  and the Reynoldsnumber was 11.4 million per meter.

In order to compare only the turbulence models free from uncertainties resulting from different meshes or different numerical schemes the same mesh and numerical scheme for each calculation was used.

Because the original algebraic turbulence models overpredicts the turbulent shear stress in the separated region the separation bubble is flattened (figure 17) and the pressure recovery is much higher than given in the experiment conducted by Benek [11] (figure 18).

A small modification of the algebraic models corrects this overprediction of the turbulent shear stress considerably. These algebraic models use the maximum of the function

$$F(y) = y |u| [1 - e^{-y^*/A^*}] \quad (IV.2)$$

to determine the boundary layer thickness  $\delta$ . In slightly separated flow fields the normal distance to the wall  $y$  is not appropriate to calculate the characteristic length scale for the eddy-viscosity. But if the normal distance is taken to the upper bubble edge this length scale is in better agreement with the physics. Therefore  $y$  in separated regions (IV.2) should be replaced by  $y_s = |y - y_{p1}|$ . This treatment results in a separation bubble being in closer agreement with the experimental findings.

With this modification the results of the algebraic models are as good as those calculated with the K- $\epsilon$  model (figures 17 and 18).

##### 5. Conclusion

Different turbulence models are investigated and the algebraic models have been extended to flow regions where a direct application of these models gave poor agreement with the experiment.

A very simple empirical distribution law for the wake of blunt bodies has shown good agreement with the experiment for the considered testcases.

A highly sheared mesh seems to falsify the calculation considerably even if the K- $\epsilon$  model is used.

A comparison between algebraic turbulence models and the K- $\epsilon$  model shows that the algebraic model can predict well slightly separated flows if a different length scale in the separation bubble is chosen.

Additional tests are necessary to verify if these modifications to the algebraic models are reasonable and appropriate for 3D-flows.

However there are strong indications that only the K- $\epsilon$  model or higher turbulence models will be capable to handle with highly complex and three-dimensional flow fields. Therefore further efforts will be directed to these models.

##### 6. References

- [1] Baldwin, B.S., Lomax, H.: Thin layer approximation and algebraic model for separated turbulent flows. AIAA-paper 78-257, 1978
- [2] Cebeci, T. and Smith, A.M.O.: Analysis of turbulent boundary layers. Applied Mathematics and Mechanics, Academic Press, 1974
- [3] Martinelli, L. and Yakhot, V.: RNG-Based turbulence transport approximations with applications to transonic flows. AIAA-paper 89-1950
- [4] Lam, C.K.G. and Bremhorst, K.: A modified form of the K- $\epsilon$  model for predicting wall turbulence. Journal of Fluids Engineering, 1981, Vol. 103
- [5] Coussinesq, J.: Théorie de l'écoulement tourbillonnant et tumultueux des liquides dans le lits rectilignes à grande section Tome I - II, Gautier-Villars, Paris 1897
- [6] Yakhot, V. and Orszag, S.A.: Renormalization group analysis of turbulence. I. Basic theory. Journal of Scientific Computing, Vol. 1, 1986
- [7] Stock, H.W. and Haase, W.: The determination of turbulent length scales in algebraic turbulence models for attached and slightly separated flows using Navier-Stokes methods. AIAA 19th Fluid Dynamics, Plasma Dynamics and Laser Conference, Honolulu, 1987
- [8] Berner, C.: Simultaneous 3D LDV measurements in the wake of bluff bodies. 3rd International Symposium on Application for Laser Anemometry to Fluid Mechanics, Lisbon, 1986 ISL Report - CO 224/86
- [9] Lacau, R.G., Desnoyer, D. and Delery, J.: Analyse au velocimetre laser de l'écoulement en aval d'arriere-corps de missiles. Symposium AGARD sur l'Aérodynamique des Missiles, Trondheim, 1982
- [10] Wagner, B.: Calculation of turbulent flow about missile afterbodies containing an exhaust jet. AIAA 17th Fluid Dynamics, Plasmadynamics & Laser Conference, 1984, Snowmass, Col.
- [11] Benek, J.A.: Separated and nonseparated turbulent flows about axisymmetric nozzle afterbodies, Part II AEDC-TR-79-22

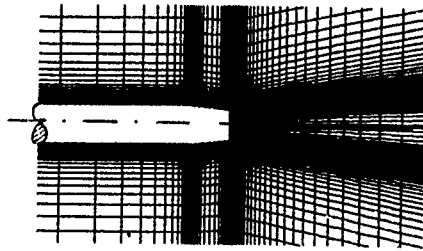


Fig. 1 : Computational mesh for testcase 1 and 2

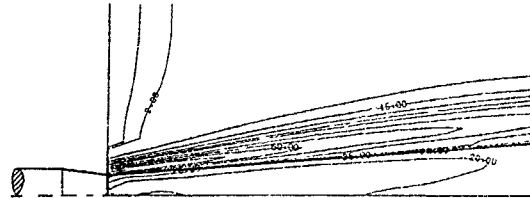


Fig. 2 : eddy viscosity (normalized) in the wake region

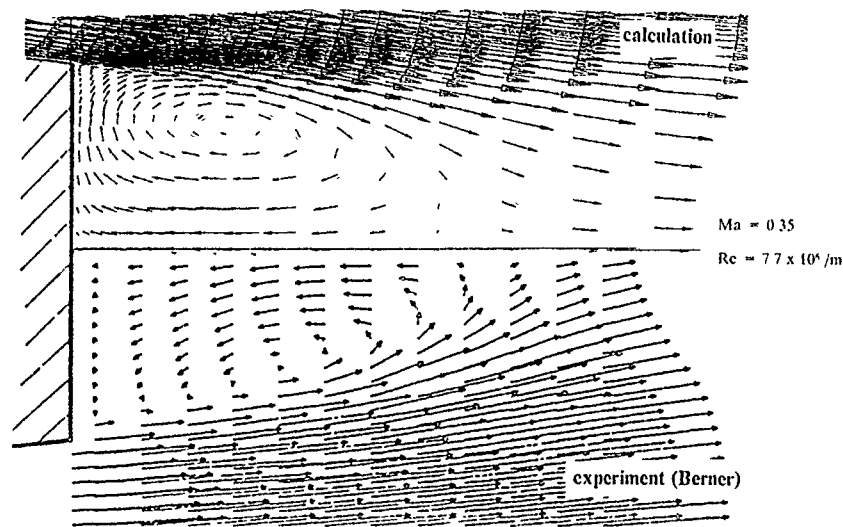


Fig. 3 : Velocity vectorfield in the wake of testcase 1

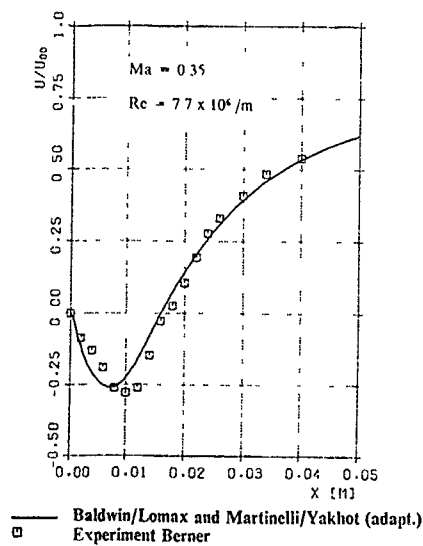


Fig. 4 : Centerline velocity distribution for testcase 1

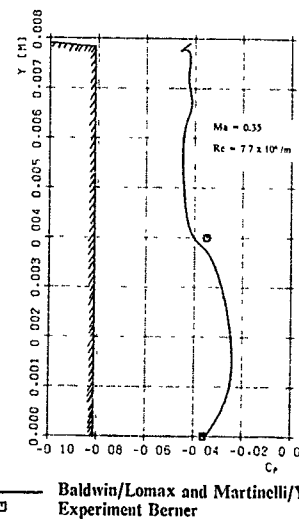


Fig. 5 : Pressure distribution at the base of testcase 1

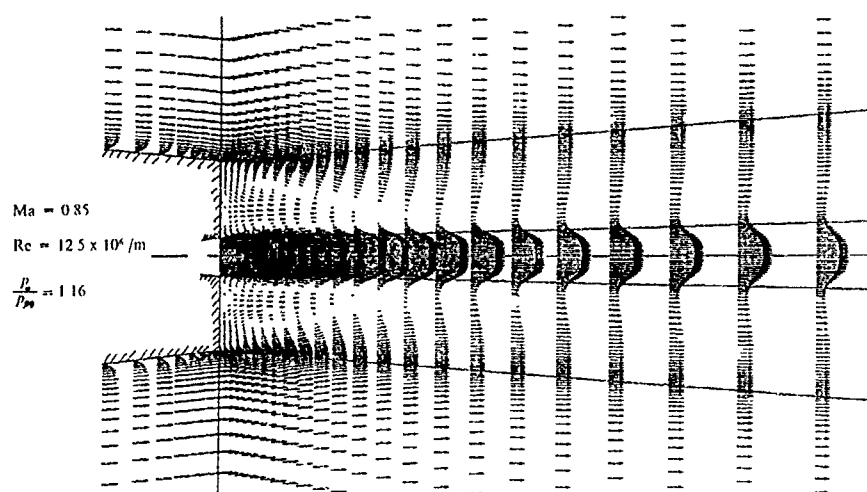


Fig. 6 : Velocity vector field for testcase 2

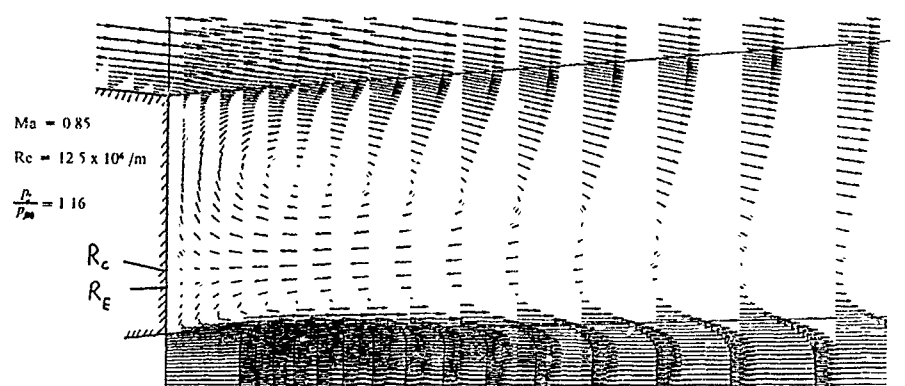


Fig. 7 : Velocity vector field at the base for testcase 2

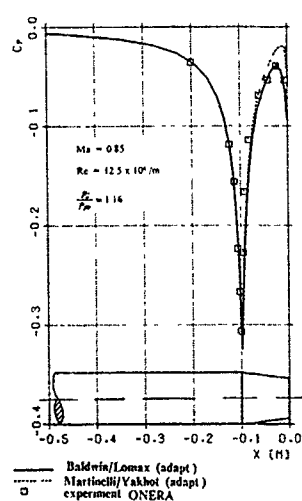


Fig. 8 : Pressure distribution along afterbody of testcase 2

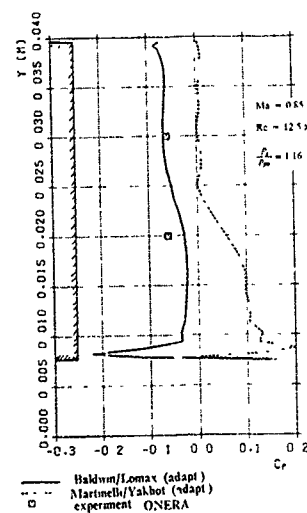
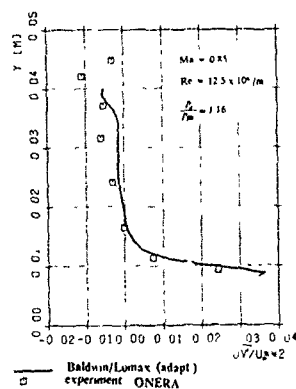
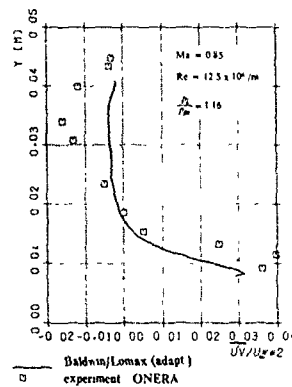
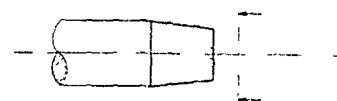
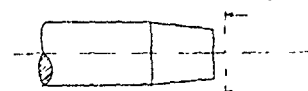


Fig. 9 : Pressure distribution at the base of testcase 2

Fig. 10 : Turbulent shear stress at  $x/D = 0.2$  of testcase 2Fig. 11 : Turbulent shear stress at  $x/D = 0.4$  of testcase 2

$Ma = 0.85$   
 $Re = 12.5 \times 10^6 / m$   
 $\frac{p_t}{p_0} = 1.16$

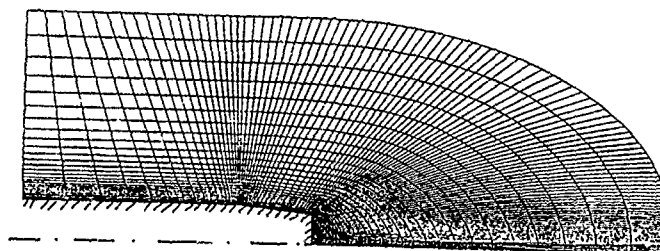
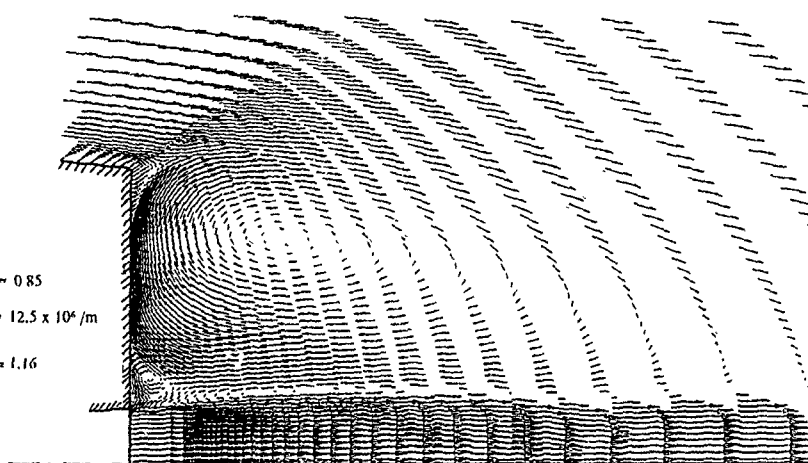


Fig. 12 : Unblocked mesh for testcase 2

$Ma = 0.85$   
 $Re = 12.5 \times 10^6 / m$   
 $\frac{p_t}{p_0} = 1.16$

Fig. 13 : Velocity vector field at the base for testcase 2 ( $k-\epsilon$ -model)

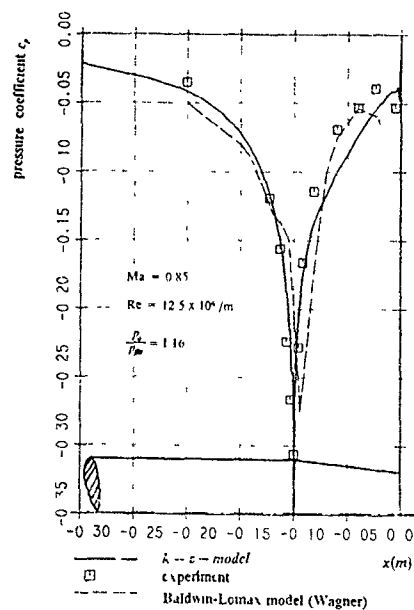


Fig. 14 : Pressure distribution along afterbody of testcase 2

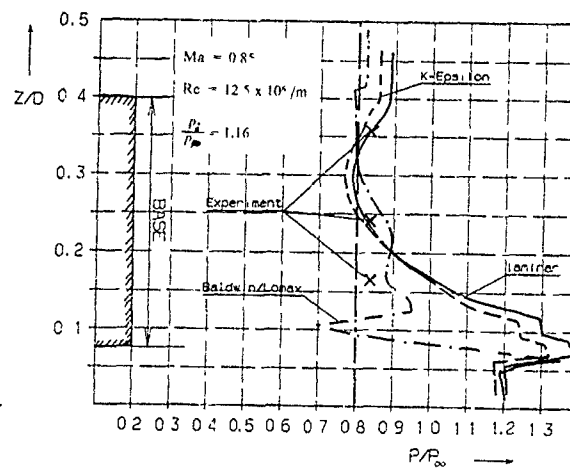


Fig. 15 : Pressure distribution at the base of testcase 2

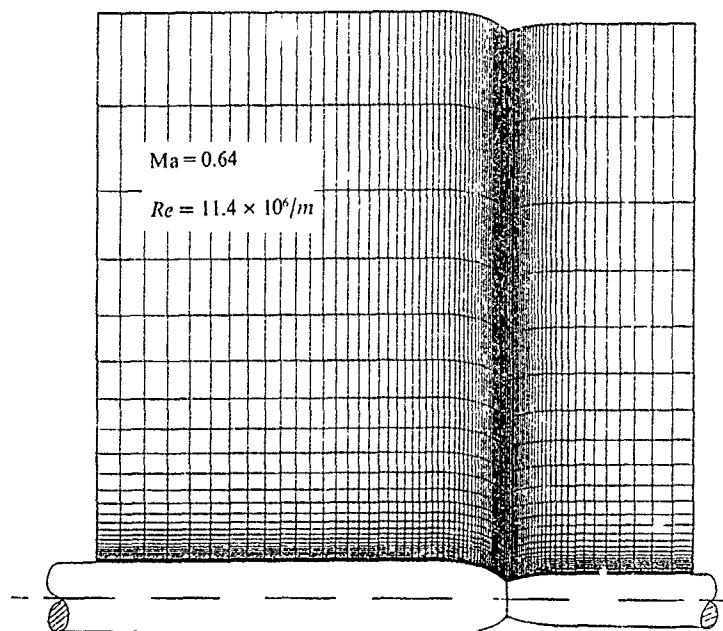


Fig. 16 : Computational mesh for testcase 3

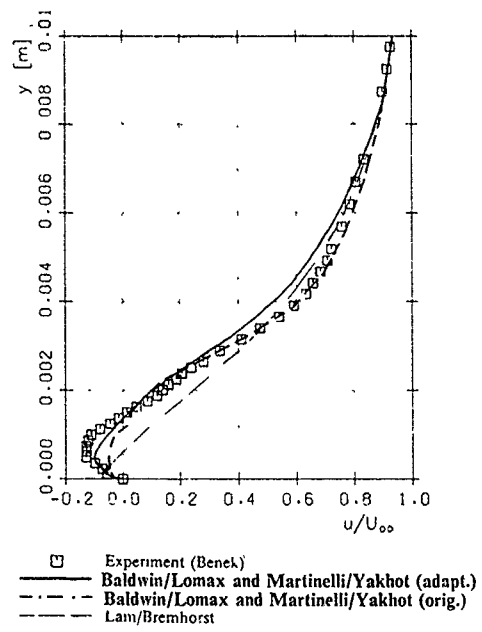
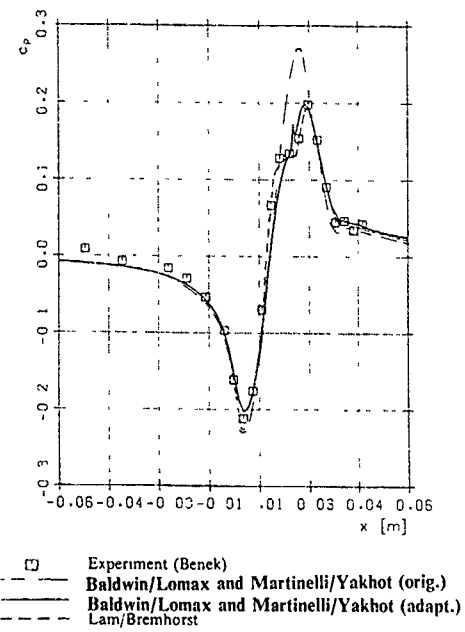
Fig. 17 : Velocity-profile at the separation bubble ( $x = 0.02m$ )

Fig. 18 : Pressure distribution along afterbody of test case 3

## RESULTS OF GARTEUR ACTION GROUP AG09 ON "FLOW PAST MISSILE AFTERBODIES"

by

J. DELERY

ONERA - 92320 CHATILLON - France

and

B. WAGNER

Dornier Luftfahrt - 7990 Friedrichshafen - W. Germany

SUMMARY

Accurate prediction of the aerodynamic behavior of missiles is still hampered by the lack of knowledge of afterbody flow, the influence of which increases with the complexity of the geometrical configuration. In a recent past, the AGARD Working Group 08 made a rather thorough review of afterbody flow studies by examining both the experimental and the theoretical sides of the question. However, the large majority of calculations were relative to aircraft afterbodies. Thus, due to the lack of reliable information on the aerodynamics of missile afterbodies, the GARTEUR Group of Responsables for Aerodynamics decided in 1986 the creation of an Action Group (AG09) on this subject. In the course of its activity, the AG has executed the following tasks: constitution of a comprehensive data base on base pressure results containing 158 test cases, testing of 12 semi-empirical or multi-component methods by comparison with the data base, constitution of a data base made of 6 well documented experiments including LDV measurements to test Euler and Navier-Stokes calculation, execution of Navier-Stokes calculations and confrontation of their results with the data base.

RESUME

La prévision précise du comportement aérodynamique des missiles est encore compromise par le manque de connaissances sur les écoulements d'arrière-corps dont l'influence augmente avec la complexité de la géométrie. Dans un passé récent, Le Groupe de Travail 08 de l'AGARD (WG08) a procédé à une revue très complète des études sur les arrière-corps en considérant à la fois les aspects théoriques et expérimentaux de la question. Toutefois, la grande majorité des calculs concernait les arrière-corps d'avion. Aussi, en raison du manque d'informations certaines sur l'aérodynamique des arrière-corps de missile, le Groupe des Responsables de l'Aérodynamique du GARTEUR a décidé, en 1986, la création d'un Groupe d'Action (AG09) sur ce sujet. Au cours de ses activités, l'AG 09 a exécuté les tâches suivantes: constitution d'une banque de données sur des mesures de pression de culot contenant 158 cas test, évaluation de 12 méthodes de prévision semi-empiriques et du type multi-composant par confrontation avec cette banque de données, rassemblement de 6 expériences très documentées et comprenant des mesures de champ par vélocimétrie laser en vue d'évaluer les codes Euler et Navier-Stokes, exécution de calculs Navier-Stokes et comparaison de leurs résultats avec la banque de données.

1 - INTRODUCTION

Accurate prediction of the aerodynamic behavior of missiles is still hampered by the lack of knowledge of afterbody flow, the influence of which increases with the complexity of the geometric configurations: simple unpowered afterbody, afterbody with one propulsive jet, multi-nozzle arrangement, existence of control surfaces, etc... In the first cases, uncertainties are associated with the drag coefficient and the heat transfer on the base region; in the latter, they affect the lift and the stability characteristics of the missile.

As is well known, the base region of a powered missile is a region of complex interactions between the hot propulsive jet and the "cold" external stream. Such interactions involve aerothermal processes and, in some circumstances, chemical reactions, these phenomena depending on many parameters; among them: the flight altitude, the afterbody geometry, the missile velocity, the nozzle expansion ratio, the ejected gas temperature and composition, etc... Base flows are also of special importance for unpowered projectiles since then the base drag can represent up to 50% of the total projectile drag at transonic or moderately



high Mach numbers.

Due to the great practical importance of afterbody flow and more particularly of base flows, in the past a great deal of effort has been devoted to the study of these flows by many organizations and research institutes [1,2]. Thus a relatively large amount of experimental results has been obtained and published. On the other hand, predictive methods have been developed, ranging from purely empirical methods to advanced numerical simulations based on the solution of the full time averaged Navier-Stokes equations.

Within international organization such as AGARD, researchers have brought together their work on afterbody flow problems in order to establish the state of the art of afterbody design methods and to make an evaluation of available predictive methods. In a recent past, the AGARD Working Group 08 made a rather thorough review of afterbody flow studies by examining both the experimental and the theoretical sides of the question [3]. In particular, special attention has been paid to existing prediction methods which were discussed and compared to experiment on a set of selected test cases. These methods included solutions of the Euler and Navier-Stokes equations, multi-component methods and inviscid-viscous interactive methods. However, the majority of test cases and calculations were relative to aircraft afterbodies so that no readily useful conclusions could be drawn for missile applications.

Thus, due to the lack of complete and reliable information on the aerodynamics of missile afterbodies, the GARTEUR Group of Responsables for Aerodynamics decided in 1986 the creation of a GARTEUR Action Group on the subject: "Flow Past Missile Afterbodies". This action would help to concentrate otherwise separated efforts, with a view to obtaining a large amount of results on a single objective acceptable to all the participants. It seemed necessary to closely associate theoreticians and experimentalists on such a complex issue which cannot be handled by purely numerical means but still requires some physical modelling.

## 2 - ACTION GROUP OBJECTIVES AND MEMBERSHIP

As concerns predictive methods, the existing and published data have been used to develop *empirical* and *semi-empirical* methods. An example of such methods is that incorporated in the British Aerospace DG Zero Incidence Drag Program (see below). Also collection of completely empirical correlations are frequently used, like those contained in the Engineering Sciences Data Unit (ESDU) data sheets [4].

On the other hand, several theoretical models based on a *multi-component* type approach have been proposed both in the USA and in Europe. Most of them are derived from the Chapman-Korst model and they allow a more rational prediction of the most important base flow features; e.g., the base pressure, the temperature level in the dead-air region, etc... However, except for a few models, these methods are restricted to axisymmetric configurations.

The multi-component models have given rise to computer codes, the computation cost of which is also very cheap. For this reason, these codes are widely used to evaluate missile afterbody characteristics at the preliminary design stage. Indeed, with such models it is in principle possible to represent the influence of many parameters (afterbody and nozzle geometries, jet temperature level, jet thermodynamic and chemical properties) the representation of which by empirical or semi-empirical methods would be extremely difficult, if not impossible. However, in spite of their great usefulness, the range of validity of existing multi-component methods is limited (and frequently ill known) in terms of jet Mach number and external stream Mach number for example. Also their accuracy can be questionable when they are applied to flow situations far from the limited domain in which they have been assessed. There is thus scope for improving these multi-component methods, in particular increasing their range of applicability.

In addition, the multi-component methods (like the semi-empirical methods) rely on some extent of empiricism. For this reason, their application can become uncertain if the flow is very complicated. For example, with such methods it is nearly impossible to represent the effect of angle of incidence, the influence of control surfaces or the complex chemical phenomena likely to occur in the base flow region. Also, although in principle possible, representation of jet temperature effect is subject to caution. Thus, to be able to treat those situations met in reality, it appears necessary to develop more advanced models based on the solution of local equations, such as the *time averaged Navier-Stokes equations*.

During the past twenty years, remarkable progress has been made in the domain of *numerical simulation* of flows. Thus, two-dimensional axisymmetrical computations are routinely performed and three-dimensional models are beginning to be applied. Application of this very promising approach allows for a more faithful and more detailed description of the flow past an afterbody and offers the possibility of treating three-dimensional configurations without difficulty (in principle, though there may be practical difficulties). However, the solution of local equations, according to what can be called a global approach,

raises new problems. For instance, the influence on the solution of the numerical viscosity or the artificial viscosity introduced to stabilize the computation in high gradient regions is not always clearly established. Also, present Navier-Stokes base-flow calculations are using extremely simple turbulence models, the validity of which is highly questionable in such complex situations. Thus, assessment of these calculations requires thorough and careful comparisons with well documented experiments providing information on the local mean and turbulent properties of the flow field.

In the above mentioned perspective, the objectives of the Action Group were:

- i) To review the well documented existing experimental results on missile afterbody flows in order to constitute a data base as complete as possible.
- ii) To compare the results of the semi-empirical and multi-component methods to the data base.
- iii) To select a small number of well documented and carefully made experiments, including field measurements, in order to test numerical simulation.
- iv) To analyse in depth the comparison between numerical simulation and experimental results in order to reach clear conclusions and to formulate recommendations for future work.

The GARTEUR Action Group (AG09) was constituted in 1986 with the following membership:

- Aérospatiale, Division Engins Tactiques, Châtillon, France
- British Aerospace, Sowerby Research Centre, Bristol, U.K.
- DLR, Institut für Entwurfsaerodynamik, Braunschweig, W. Germany
- Dornier Luftfahrt GmbH, Friedrichshafen, W. Germany
- ISL (French-German Research Institute, Saint- Louis, France
- MATRA DEFENSE, Velizy-Villacoublay, France
- MBB, Verteidigungssysteme, Munich, W. Germany
- ONERA, Direction de l'Aérodynamique, Châtillon, France

### 3 - DATA BASE COLLECTION FOR TESTING SEMI-EMPIRICAL AND MULTI-COMPONENT METHODS

In order to properly evaluate semi-empirical and multi-component methods, a large number of test cases have been collected by a thorough processing of the published data. Most of the results thus collected consist of measurements of the base pressure obtained for a great variety of situations. Attention has been concentrated on axisymmetric configurations, since nearly all the tested methods apply only to such situations. A total number of 158 test cases has been compiled by the Action Group. Information necessary to execute calculations - including afterbody geometry and aerodynamic conditions - and also measured base pressure values will be provided in the AG final report. Most of these data have been obtained in wind tunnel experiments. They cover a wide range of parameters including:

- External flow Mach number  $M_\infty$ .
- Jet exit Mach number  $M_j$ .
- Nozzle Pressure Ratio (NPR)  $\frac{P_{tj}}{P_\infty}$ .
- Ratio of stagnation temperatures:  $\frac{T_{tj}}{T_\infty}$ .
- Jet ratio of specific heats  $\gamma_j$ .
- Afterbody angle  $\beta_E \div \beta_F$  being positive for a flare and negative for a boattail.
- Nozzle divergence angle  $\beta_j$ .

- Afterbody reduced length  $\frac{L}{D_{\max}}$ , where  $D_{\max}$  is the afterbody maximum diameter (calibre).
- Reduced nozzle diameter  $\frac{D_j}{D_{\max}}$ .

Table I gives an overview of the range of parameters covered by the data collection,  $N_{\text{cases}}$  being the number of test cases for the values of the parameters. In fact, each case represents several results giving the base pressure evolution with one of the parameters (origin of data can be found in [5]).

TABLE I - RANGE OF PARAMETERS COVERED BY THE DATA BASE

AFTERBODY WITHOUT JET

$M_{\infty}$	$\beta_E^\circ$	$\frac{L}{D_{\max}}$	N cases
0.22 → 0.95	0 (cylindrical)		8
0.22 → 0.92	-2 → -10 (boattail)		17
0.8 - 0.85 - 0.9	6 (flare)		3
0.95 - 1.0 - 1.05	0		3
0.95	- 6	0.5 - 1.0	2
0.95	- 6	0.5 - 1.0	2
0.95	6	1	1
1.10 → 3.27	0		8
1.98 - 2.01 - 3.27	0 → - 10	0.5 - 1.0	4

AFTERBODY WITH JET

$M_{\infty}$	$M_j$	$\beta_E^\circ$	$\beta_j^\circ$	$\frac{D_j}{D_{\max}}$	$\frac{T_{tj}}{T_{t\infty}} (*)$	$\frac{P_{tj}}{P_{\infty}}$	N cases
0.8 - 0.9	~ 1	0	0	0.248 - 0.351	1 - 2.3 - 3.1	0 → 11	18
0.8 - 0.9	2.9	0	2.5	0.15	~ 1	0 → 2.7	3
0.8 - 0.9	2.9	- 6	2.5	0.15	~ 1	0 → 2.7	6
0.8 - 0.9	2.9	6	2.5	0.15	~ 1	0 → 2.7	3
~ 1	~ 1	0	0	0.248 - 0.351	- 2.7 - 4	0 → 11	6
0.95	1.5 → 2.9	0	2.5 → 5	0.111 → 0.333	~ 1	0 → 17	7
0.95	2.9	- 6	2.5	0.15	~ 1	0 → 2.7	2
0.95	2.9	6	2.5	0.15	~ 1	0 → 2.7	1

## AFTERBODY WITH JET

$M_\infty$	$M_j$	$\beta_E^\circ$	$\beta_j^\circ$	$\frac{D_j}{D_{max}}$	$\frac{T_{tj}}{T_\infty} (*)$	$\frac{p_{tj}}{p_\infty}$	N cases
1.1 → 2.41	~ 1	0	0	0.111 → 0.75	~ 1	1.2 → 2420	17
1.91	~ 1	- 5.63	0	0.375	~ 1	1.2 → 16.6	1
1.4 → 2.01	2 → 4.27	0	0	0.2 → 0.6	~ 1	2.6 → 240	10
2.0	2.0	0	0	0.645	1.2 - 2.5 - 3	4 → 16	4**
1.1 → 3.27	1 → 3.29	0	5 → 23.3	0.111 → 0.8	~ 1	1 → 391	36
1.6 → 2.0	2.8 → 4.27	0	15 - 18	0.5	3.37	60 → 200	4**
1.58	2.65	0	22	0.435	7.41	21.6 → 43	1**
1.4 - 1.91	1.0 → 2.7	5.63	0	0.2 → 0.375	4 ~ 1	1 → 38	3
1.6 → 3.27	1.78 → 3.2	-5 → -10	5 → 22	0.1 → 0.6	~ 1	11 → 99	15
1.2 → 1.97	2.7 → 3.38	3.28 → 10	17 - 20	0.575 - 0.8	~ 1	20 → 157	4

\* The external stagnation temperature  $T_\infty$  has been assumed equal to 300 K.

\*\* These cases include both temperature and  $\gamma_j$  effects.

#### 4 - PRESENTATION OF SEMI-EMPIRICAL AND MULTI-COMPONENT METHODS

##### 4.1 - INTRODUCTORY REMARKS

One of the problems often faced by the aerodynamicist when trying to assess the base drag characteristics of a new missile design is that, in the very early stages of the design process, very little information about the propulsion system may be available. In most cases, the only information which is known in the feasibility and initial design stages is the geometry of the afterbody, the thrust of the motor and possibly the jet exit diameter. It is at this point in the design process that the semi-empirical methods tend to be used. Such methods require a minimum of input data, are very simple and quick to use and, perhaps most importantly, provide results at minimum cost.

As the design proceeds, more information about the motor becomes available: the jet pressure ratio and nozzle geometry for example. Such information enables the multi-component methods to be used. These methods tend to be more time-consuming to implement, require more input information and are more expensive to use than the simpler semi-empirical methods. The multi-component methods do, however, attempt to represent as accurately as possible the real processes that exist. In contrast, the semi-empirical methods rely much more on simple correlations of existing experimental data which thus tends to limit their range of applicability or accuracy. On the other hand, they are able to provide results quickly and at minimum expense.

##### 4.2 - SEMI-EMPIRICAL METHODS

###### 4.2.1 - BAE Drag Program

This code was developed by the Sowerby Research Center over a period of several years under contract to the UK Ministry of Defence. The code provides estimates of the total zero incidence drag of typical weapon (missile and projectile) configurations, so the base and afterbody drag methods which have been assessed are a small part of the total calculation procedure [6]. The base drag data used by the code are in the form of graphical and carpet plots constructed and extrapolated / interpolated from various experimental results. The data are initially obtained in a form very similar to that adopted by the ESDU data sheets. Polynomial expressions are then fitted to the data plots, these polynomials then being used by the code. One of the major weaknesses of the code is the poor representation of the jet-on base drag characteristics.

#### 4.2.2 - Modified Brazzel and Henderson Method

**Subsonic External Flow.** The Brazzel and Henderson [7] empirical supersonic method has been extended to subsonic external flow by Glasgow et al. [8]. On the basis of experimental data it was found that the base pressure is a weak function of the afterbody geometry, represented by the base to maximum area ratio  $A_B / A_{max}$ , and of the jet to freestream momentum ratio  $R_{mf}$  defined as:

$$R_{mf} = \frac{\gamma_j p_j M_j^2 A_j}{\gamma_\infty p_\infty M_\infty^2 A_{max}}$$

In the above expression, j designates quantities relative to the nozzle exit plane and  $\infty$  designates quantities in the uniform incoming external flow.

The correlation is divided into two parts. The first part is a correlation of the annular base pressure for cylindrical afterbodies as a function of  $R_{mf}$ . The second part of the correlation relates annular base pressures for cylindrical afterbodies to annular base pressure for non-cylindrical (boattail) afterbodies as a function of  $A_B / A_{max}$ .

A fair estimate of the jet-off case is obtained by setting  $R_{mf} = 0$ , this procedure being justified because the base pressure ratio  $p_B / p_\infty$  is only a weak function of  $R_{mf}$  and  $A_B / A_{max}$ .

**Supersonic External Flow.** In this case, the base pressure ratio  $p_B / p_\infty$  is given as a function of  $R_{mf}$ ,  $A_B / A_{max}$  and in addition of:

- The ratio of the jet exit static temperature  $T_j$  to the nozzle throat temperature  $T_{th}$ .
- The distance to the base of the nozzle exit plane normalized by the afterbody maximum diameter:  $X_j / D_{max}$ , this parameter allowing for the effect of a nozzle protruding from the afterbody base.

In the supersonic case, applying the correlation to the jet-off case by setting  $R_{mf} = 0$  will generally lead to poor results.

#### 4.2.3 - Riedel Method

This method, which is based on the modified Brazzel-Henderson method, attempts to introduce some improvements in the following way by:

- Basing the correlation of experimental data on missile - type afterbodies in contrast to the correlation of Glasgow et al. which essentially applies to combat aircraft (fighter - type) afterbodies.
- Taking into account the Mach number of the external flow.
- Inclusion of a correlation for jet-off cases, both for subsonic and supersonic external flow.
- Making allowance of the nozzle divergence angle  $\beta_j$  (nozzle exit angle) as a parameter for supersonic flow.

For subsonic external flow, for both the jet-off and jet-on cases, the correlation is based on experimental data concerning missile afterbodies obtained by Tanner [9,10]. In the supersonic case, the jet-off correlation uses the Compton [11] and Esch [12] experimental results, and the jet-on correlation the Bromm and O'Donnel experimental data [13].

#### 4.2.4 - Tanner Program

The method of this semi - empirical code has been developed by Tanner in several steps over some years and has been programmed at MBB in close connection with Tanner's progress. An overview of the empirical and theoretical basis is given in detail by Tanner [14].

**Subsonic External Flow Without Jet.** For a cylindrical afterbody, the base pressure coefficient  $C_{pB}$  is given as a function of the upstream Mach number  $M_\infty$  derived from a correlations of measurements performed by Tanner and Hassbargen [15] and by Tanner [16]. In the case of an afterbody with a boattail, the  $C_{pB}$  corresponding to the cylindrical afterbody is multiplied by a factor involving the boattail angle  $\beta_e$  and the ratio  $D_B / D_{max}$ .

**Supersonic External Flow Without Jet.** The base pressure is computed by using the well known Oswatitsch formula linking the drag of a body to the rise in entropy produced by this body [17]. In the present

application, this formula leads to a relation between the afterbody drag and the increase in entropy across the shock at the reattachment point and in the viscous wake coming from the reattachment of the shear layer which originates at the base shoulder. By making a suitable assumption on the velocity distribution through the wake, it is possible to obtain an equation for the Mach number  $M_2$  at the edge of the wake. As soon as  $M_2$  is evaluated, the base pressure can be determined from oblique shock equations.

*Supersonic External Flow With Jet.* This part of the method consists of a collection of empirical equations derived from the experimental data of Agrell and White [18]. The different formulae allow to take account of the different parameters:  $M_\infty$ ,  $M_j$ ,  $\beta_E$ ,  $\beta_j$ ,  $D_j / D_{max}$ ,  $P_{tj} / P_\infty$ .

The Tanner code also includes formulae to compute the base pressure at transonic and hypersonic Mach numbers and to represent the effect of incidence.

#### 4.3 - MULTI-COMPONENT METHODS

##### 4.3.1 - The Basic Flow Model

The theoretical scheme utilized by the various multi-component methods is derived from the well known model proposed by Korst to compute the turbulent supersonic reattachment behind a step [19]. As shown in Fig. 1, the basic situation is that of an incoming supersonic flow separating at a base shoulder S and reattaching further downstream at point R, either on a rectilinear wall or on a cylindrical sting. The model includes a possible mass injection at low velocity performed through the base (base-bleed).

Following the Korst multi-component approach, the flow field is divided into four main domains which are represented by simplified theoretical models and then patched together in such a way that some compatibility conditions are satisfied. These domains are:

- i) The outer inviscid flow bounded by the isobaric boundary (f) along which the pressure is equal to the base pressure  $p_B$ . This part of the flow satisfies the Euler equations.
- ii) The initial boundary-layer which separates at S where it undergoes a rapid pressure change through an expansion fan or a shock, depending on the situation. Here, an approximate method assuming that the viscous terms (including turbulent stresses) do not act during such a rapid process is employed.
- iii) The turbulent mixing zone developing from the separation point S along the isobaric boundary (f). The velocity distribution across this mixing layer is represented by the following classical relationship:

$$(1) \quad \frac{u}{u_{eB}} \equiv \varphi = \frac{1}{2} (1 + \operatorname{erf} \eta) \quad \text{with: } \operatorname{erf} \eta = \frac{2}{\sqrt{\pi}} \int_0^\eta e^{-\eta^2} d\eta$$

and where  $u_{eB}$  is the velocity at the mixing layer outer edge and  $\eta = \sigma (Y/X)$  is a similarity variable,  $\sigma$  being the turbulent mixing parameter which characterizes the mixing layer spreading rate. The stagnation enthalpy profile  $h_g / h_{tB}$  can be readily deduced from the velocity profile if the turbulent Prandtl number is assumed equal to unity.

- iv) The reattachment region where the mixing zone impinges on the reattachment wall. Simultaneously, the outer non viscous flow undergoes a deflection through an angle  $\psi$  in order to become parallel to this wall. A compatibility condition, or *reattachment criterion*, must be satisfied by the flow in the reattachment region. Briefly speaking, this condition states that the mixing layer must have an energy level sufficient to allow it to negotiate the adverse pressure gradient at reattachment. In fact, the multi-component models considered by the Action Group differ mainly by the nature of the condition adopted in the reattachment region.

The method developed by Addy formerly used the *Escape Criterion* proposed by Korst in its original model. This criterion states that the stagnation pressure  $p_{t1}$  on the *stagnation streamline* - i.e., the streamline of the mixing zone which stagnates at the reattachment point R - must be equal to the pressure level  $p_2$  reached by the outer flow downstream of the reattachment region. As will be seen below, the Korst criterion was latter modified by Addy to obtain better agreement with experiment for missile applications in the jet-on condition.

In order to remedy some deficiencies of the Korst original criterion, Carrière and Sirieix [20] proposed an *Angular Reattachment Criterion*. This criterion postulates that the deflexion  $\psi$  undergone by the outer non viscous flow during reattachment must satisfy a well defined law of the form:

$$(2) \quad \psi = \Psi \left( M_{eB}, \gamma, \frac{h_B}{h_{t_{eB}}}, R, \bar{q}_B \right)$$

where  $\Psi$  is a function of the listed parameters ( $R$  is a factor representing the axisymmetric effect and  $\bar{q}_B$  is the mass flux injected per unit span in the dead-air region).

Determination of the mixing layer properties and application of the compatibility condition at reattachment require a knowledge of the base pressure  $p_B$  and of the dead-air temperature  $T_B$  (or enthalpy  $h_B$ ). Thus, the problem has two main unknowns, namely:  $p_B$ ,  $T_B$  ( $h_B$ ). These quantities are determined by writing global balance equations for mass and energy applied to a control volume encompassing the dead-air region.

#### 4.3.2 - Base Flow Models for Supersonic External Flow

*Missile in the Jet-Off Condition.* In order to apply the supersonic reattachment theory to a missile in the jet-off situation, or to a simple projectile, it is most often assumed that the flow separating at the base shoulder  $S$  reattaches on a fictitious sting which represents the viscous wake in the wake neck region. As shown in Fig. 2, the radius  $r^*$  of this sting can be provided by a purely empirical law (for example the correlation proposed by Chapman [21], see Fig. 2a). This kind of model is close to that proposed by Mueller [22].

However, this way of finding  $r^*$  appears as very unsatisfactory, especially when mass injection is performed at the base. Thus, in order to improve the situation the following methods have been proposed. In a further version of Mueller's theory, Roache [23] determines the value of  $r^*$  according to a criterion which consists in adopting for the radius  $r^*$  that makes the base pressure  $p_B$  a maximum. In the ONERA model (code ONERA2 [24]),  $r^*$  is computed by assuming that the mass flow through the near-wake at station  $R$  is equal to the mass flow streaming above the stagnation streamline plus a term  $q_E$  representing the extrainment effect taking place during the reattachment process. This problem is completely "closed" by assuming that the streamwise velocity profile in the wake at the reattachment station  $R$  is a universal function given by an empirical correlation.

*Missile in the Jet-On Condition.* The flow structure downstream of the base of an afterbody equipped with a propulsive nozzle is extremely complex and the multi-component models at our disposal to treat that kind of problem rely on a rough approximation of the real phenomena. The models that have been considered constitute an extension of methods developed for two-dimensional reattachment on a wall. In fact, all these models are based on the following scheme (see Fig. 3):

- i) The dead-air region is roughly limited by the curvilinear triangle  $S_E R_T S_J$  defined by the annular base and the isobaric boundaries ( $f_E$ ) and ( $f_J$ ) along which the pressure is equal to the base pressure  $p_B$ .
- ii) The viscous phenomena are superimposed on a perfect fluid structure entirely determined if the base pressure  $p_B$  is known.

The two boundaries ( $f_E$ ) and ( $f_J$ ) usually meet at the inviscid confluence point  $R_T$ . Downstream of  $R_T$ , the two inviscid streams have a common boundary ( $\Sigma$ ) - a slip line - on which both flows must have the same pressure  $p_2$  and same direction  $\varphi_2$ . The basic assumption of all the models is that everything happens as if each flow

- namely the external flow (E) and the flow issuing from the nozzle (J) - were reattaching on a wall representing the common confluence direction ( $\Sigma$ ). Thus, knowledge of the downstream pressure  $p_2$  and the initial direction  $\varphi_2$  of the slip line ( $\Sigma$ ) allows application - to each flow - of one of the reattachment criteria mentioned above.

Uniqueness of solution - i.e., the proper values of  $p_B$  and  $T_B$  (or  $h_B$ ) - is ensured by satisfying two overall balance equations for mass and energy applied to a control volume encompassing the dead-air region. The solution is most often found by iterating on  $p_B$  and  $T_B$  (or  $h_B$ ) until these two equations are simultaneously satisfied. The various multi-component methods closely follow the above general model. However, they differ on some points which are now emphasized.

#### The Addy Flow Model [25].

The inviscid streams are computed by the Method of Characteristics and the pressure downstream of reattachment -  $p_2$  - is computed by assuming oblique shock recompression. As in the simplified Korst model, the initial boundary-layers are neglected. The two balance equations for mass and energy are considered, so the model can solve the thermal problem. In order to remedy a deficiency of the original Korst reattachment criterion, a modification of this criterion is introduced which consists of assuming that the stagnation pressure on the limiting streamline is only a fraction of the downstream pressure  $p_2$ . Thus one writes:

$$(3) \quad \frac{p_{t1}}{p_B} = k \frac{p_2}{p_B}$$

In the above equation,  $k$  is an empirical factor function of the ratio  $\bar{r} = r_j / r_E$  of radii at  $S_j$  and  $S_E$  [26]. The original Korst Escape Criterion is recovered by letting  $k = 1$ .

The Addy code produces a message when plume induced separation on the afterbody is likely to occur, the risk of separation being detected by using Zukoski's criterion [27].

#### *The ONERA Flow Model (Code ONERA1) [24]*

The inviscid streams are computed by the Method of Characteristics. The initial direction -  $\phi_2$  - of the slip line ( $\Sigma$ ) starting from the confluence point is determined by assuming simple wave compression at  $R_T$ . The influence of the initial boundary-layers present at  $S_E$  and  $S_j$  is taken into account, their effect on the velocity distribution being represented by the virtual origin concept [28]. At  $R_T$ , the Angular Reattachment Criterion - formula 2 - is applied to the external flow and the jet. The reattachment angles  $\psi_E$  and  $\psi_j$  are defined as the angles between ( $\Sigma$ ) and the tangents to ( $f_E$ ) and ( $f_j$ ) at  $R_T$  respectively. The model also solves the thermal problem, both  $p_B$  and  $T_B$  being computed. Cases with plume induced separation on the fuselage can also be computed by using nearly the same procedure. The difference is that now the base pressure  $p_B$  is given by a separation criterion, the unknown being the location of the separation point. The criterion used is derived from the Chapman Free Interaction theory [29]. The criterion of Zukoski can also be used.

#### *The Dornier Flow Model [30]*

The method developed by Dornier is close to the ONERA model. However, in the present application of the Angular Reattachment Criterion to the two-mixing layers confluence problem, an iterative procedure is included to adjust the reattachment direction  $\phi_2$  for achieving equal reattachment pressure in both shear layers (this condition is not satisfied in the ONERA application of the Angular Reattachment Criterion). The pressure rise up to the reattachment point  $R$  is given by assuming an isentropic recompression on the stagnation streamline from  $p_B$  to  $p_R$ . Thus, in the Dornier method the reattachment direction is no longer that of the confluent inviscid flows downstream of  $R_T$ . Instead, the pressure is the same in the two reattaching mixing layers, which seems more satisfactory from a physical point of view. The initial boundary-layers at the separation points are taken into account by introducing the virtual origin concept for the two mixing layers and by using the equivalent bleed concept [31]. Plume induced separation can also be computed, a modified version of Zukoski's criterion accounting for incipient separation being introduced [32].

#### *The Moulden Flow Model [33]*

This method is based on a flow model which predicts the development of the boundary-layer along the body and then solves for the confluence of the resulting external shear layer with the jet exhaust plume (internal shear layer) behind the dead-air region. The calculation procedure begins by making an initial estimate of the angle through which the external flow is deflected at the base. The resulting pressure change is thus known and the shape of the exhaust plume which expands to the base pressure is determined by the Method of Characteristics. At the confluence point, the external and internal (jet) flows are matched so that the downstream flow direction is compatible for both flows. The "reattachment" pressure is obtained as an empirical function of the pressure rise required at the confluence point. A mass flow balance equation is used to calculate the mass flows entrained and returned near the confluence point and the difference evaluated. The angle of deflection of the external shear layer is then iterated until this difference becomes small (to within a specified tolerance).

#### 4.3.3 - Base Flow Models for Subsonic External Flow

*Missile in the Jet-Off Condition.* The model developed by Aérospatiale and ONERA (code ONERA/AS1 [24]) to treat the base flow problem for a subsonic external stream is derived from Vanwagenen's theory which originally applied to a cylindrical afterbody placed in an incompressible flow [34]. The adopted representation is shown in Fig. 4. Its key components are:

- i) The discriminating streamsurface ( $\psi_j$ ) originating from the base shoulder  $S$  and reaching the axis at the physical reattachment point  $R$ .
- ii) The displacement surface ( $\psi^*$ ) on which the outer inviscid flow streams.
- iii) The streamsurface ( $\psi_E$ ) belonging to the perfect fluid flow which passes through the edge  $E$  of the viscous wake at the reattachment station.



The basic principle of the method consists of an inviscid-viscous interactive calculation with coupling conditions written on the displacement surface ( $\psi^*$ ) constructed in an approximate way by applying global conservation laws for mass and momentum to adequate control volumes, like those represented in Fig. 4.

The procedure for determining the base pressure  $p_b$  is as follows. For a given value of the separation bubble length  $L = BR$ , an inviscid-viscous interactive calculation is iterated until convergence. Then, the correct value of  $L$  is determined by satisfying a "closure" relation similar to the Korst Escape Criterion. Thus, one has to perform an outer iteration loop on  $L$  until this criterion is satisfied. In the present version of the method, the outer non viscous flow is computed by a method of singularities, compressibility being taken into account by the Prandtl-Glauert rule.

*Missile in the Jet-On Condition.* In principle, the model developed by Aérospatiale and ONERA (code ONERA/AS2 [24]) to treat this situation, is only valid for an afterbody equipped with a nozzle, the diameter of which is small compared to the base diameter. Also, the nozzle pressure ratio must be not too far from adaptation conditions. Under such circumstances, it is legitimate to consider that the jet acts as a perturbing agency consisting of: a) - An obstacle effect, similar to a sting which would represent the propulsive jet. b) - A suction effect resulting from the strong entrainment occurring along the boundary of the high speed jet (see Fig. 5). In fact, this second effect is by far the most important. In these conditions, the main features of the model are:

i) The jet is replaced by a cylindrical sting, the radius of which is equal to the radius of the nozzle exit section. This very simple model gives an acceptable representation of reality if the jet is not too far from adaptation conditions.

ii) The suction effect is assumed to be uniformly distributed over the length  $L_j$  of the sting comprised between the base and the point  $R_j$  where the outer flow reattaches on the sting. Furthermore, one assumes that the suction velocity is normal to the sting surface; i.e., perpendicular to the longitudinal axis  $OX$ . The mass flow rate sucked off from the dead-air region by the jet entrainment effect is written in the form:

$$q_j = (2\pi r_j L_j) C_{Ej} \rho_{0j} u_{0j}$$

where  $\rho_{0j}$  and  $u_{0j}$  are relative to the perfect fluid flow of Mach number  $M_{0j}$  in the nozzle exit plane,  $C_{Ej}$  being a coefficient that represents globally the jet entrainment effect. The solution procedure is the same as in the jet-off case.

#### 4.4 - VALIDATION OF SEMI-EMPIRICAL AND MULTI-COMPONENT METHODS

##### 4.4.1 - Statistics of Computed Cases

Table II summarizes the various situations which can be computed with the codes tested by the Action Group and Table III gives the number of test cases computed for each basic configuration:

TABLE II - CAPABILITY OF THE TESTED MODELS

	Without Jet	With Jet
Subsonic External Flow	BAe Drag Program Brazzel-Henderson ONERA/AS1 Riedel Tanner	Brazzel-Henderson ONERA/AS2 Riedel Tanner
Transonic External Flow	BAe Drag Program Riedel Tanner	
Supersonic External Flow	BAe Drag program Brazzel-Henderson Moulden Mueller ONERA2 Riedel Tanner	Addy Brazzel-henderson Dornier Moulden ONERA1 Riedel Tanner

TABLE III - NUMBER OF CASES COMPUTED FOR EACH BASIC CONFIGURATION

	Without Jet	With Jet
Subsonic External Flow	14	21
Transonic Flow	14	0
Supersonic Flow	6	95

A total number of 448 calculations has been executed, most test cases having been computed with several codes. Table III shows that no case corresponding to transonic external flow in the jet-on condition could be computed, even with semi-empirical methods. On the other hand, a great quantity of calculations has been performed for supersonic cases with jet. Most of these calculations have been executed with the Addy code and the Moulden code which were run by several contributors. However, in this statistics we have considered only one code application for each test case.

#### 4.4.2 - Discussion of Typical Results

Due to the large amount of results obtained by the Action Group, we will present here a very limited number of comparisons between models and experiment, chosen among the most representative.

*Afterbody Without Jet for Subsonic and Transonic External Flow.* The subsonic and transonic external flow cases are presented together since in most applications these cases were treated simultaneously by the different models.

Variation of the base pressure coefficient  $C_{pB}$  with the external flow Mach number  $M_\infty$  for a cylindrical afterbody is shown in Fig. 6a. Experimental results are in the range  $0.42 \leq M_\infty \leq 1.14$ . Four codes have been run: BAe Drag Program, ONERA/AS2, Riedel and Tanner. The ONERA/AS2 is unable to give results in the transonic range itself, since the external inviscid flow of the coupling algorithm is computed by a method of singularities. Most results are acceptable in the subsonic range; i.e., for  $M_\infty \leq 0.95$ . However, the Riedel result shows an unexpected rise of  $C_{pB}$  in the lower subsonic range. Results are rather deceiving in the transonic domain, all models underpredicting largely the sharp decrease in base pressure occurring near  $M_\infty = 1$ . In this case, close to sonic conditions, the best prediction is given by Tanner's method. The second example, shown in Fig. 6b, corresponds to an afterbody with a boattail of angle  $\beta_E = -6^\circ$  and a length  $L = 0.5 D_{max}$ . In this case, no method is able to correctly predict the rise in base drag taking place near  $M_\infty = 1$ . Calculations made for other test cases - not presented here - show similar deficiencies of the models tested by the Action Group. However, before drawing definitive conclusions, one must be aware of the difficulty to make reliable base pressure measurement in transonic wind tunnels, so that most experimental results in this range should be considered with some suspicion.

*Afterbody Without Jet for Supersonic External Flow.* This case could be considered as the easiest since there exists a large number of reliable experimental data giving the base pressure in supersonic flow. Thus, Fig. 7a shows the classical evolution of the base pressure ratio  $p_B / p_\infty$  with the Mach number  $M_\infty$ . The Mueller and ONERA2 multi-component methods are in very good agreement with experiment. This is not a surprise, since these methods have been more or less "tuned" to agree with this basic curve. Riedel's code also works very well. The Tanner model leads here to a poor prediction. It is clear that the Brazzel-Henderson model is not adequate to treat supersonic base flows in the jet-off situation. Similar conclusions can be drawn from results presented in Fig. 7b which shows the evolution of the base pressure with boattail angle at  $M_\infty = 2.01$ . However, in the following application where the boattail length is shorter ( $L / D_{max} = 0.5$  instead of 1), the Tanner model gives a good prediction (see Fig. 7c).

It seems clear that multi-component methods are superior and safer to predict base pressure for a non powered projectile at supersonic velocity.

*Afterbody With Jet for Subsonic External Flow.* There exist few test cases for this situation. Here, we have considered three cases corresponding to fixed values of the external flow Mach number  $M_\infty$  and jet exit Mach number  $M_j$  and to different afterbody angles, namely:  $0$  (cylindrical),  $-6^\circ$  (boattail),  $+6^\circ$  (flare). Results are shown in Figs. 8a to 8c which give the evolution of the base pressure coefficient  $C_{pB}$  with the nozzle expansion ratio  $P_{t_j} / P_{t_\infty}$ . For these cases, the ONERA/AS2 code is in close agreement with experiment. This can be explained by the fact that the nozzle diameter is small compared to the afterbody maximum diameter ( $D_j / D_{max} = 0.15$ ) and that the jet is practically adapted. Thus, which satisfies the basic hypotheses of the Aérospatiale/ONERA model (see §4.3.3 above). For larger nozzles far from adaptation conditions, agreement is not so good. The Riedel model also gives good results for the cylindrical afterbody and the

afterbody with flare. The prediction is less satisfactory when there is a boattail. The Brazzel-Henderson model leads to an increase in  $C_{pB}$  with the nozzle expansion ratio, which is in contradiction with experiment.

*Afterbody With Jet for Supersonic External Flow.* Due to the great number of calculations performed for this situation and the scatter of the results, it is difficult to draw clear conclusions. A very limited number of test cases is discussed here, their choice having been made with a certain degree of arbitrariness.

The first example, shown in Fig. 9, concerns a cylindrical afterbody placed in a flow of Mach number  $M_\infty = 2$ . The nozzle is nearly sonic and its diameter is such that  $D_j / D_{max} = 0.6$ . In this case, 5 methods have been tested. The Addy model has been run with the corrected reattachment criterion (see formula 3 above) and with the initial version (obtained by setting  $k = 1$ ). All the methods - except that of Riedel - give here a very acceptable prediction of base pressure. However, the situation is not so satisfactory for the three following applications which also concern a cylindrical afterbody at  $M_\infty = 2$ . This afterbody is equipped with a conical nozzle of angle  $\beta_j = 5$  giving an exit Mach number  $M_j = 2$ . Three different values of the nozzle exit diameter are considered. When  $D_j / D_{max} = 0.8$ , all the methods applied in this case give a relatively good prediction, as shown in Fig. 10a. But, for most of them the quality of the results tends to deteriorate when the nozzle exit diameter is reduced as can be seen in Figs. 10b ( $D_j / D_{max} = 0.6$ ) and 10c ( $D_j / D_{max} = 0.4$ ). Here, the best performance is achieved by the Addy model incorporating the correction factor. The Dornier and ONERA1 codes also work relatively well. Results given by other methods are more erratic.

The two other applications are relative to afterbodies equipped with a conical nozzle having a large divergence angle. In the case presented in Fig. 11a - for which  $\beta_j = 22^\circ$  and  $D_j / D_{max} = 0.435$  - the five tested codes give a relatively good prediction, except that of Brazzel and Henderson. On the other hand, for the case presented in Fig. 11b - where  $\beta_j = 20^\circ$  and  $D_j / D_{max} = 0.2$  - the best prediction is given by the Brazzel-Henderson model, the other models leading to poor results. The ONERA1 model was unable to predict these cases, the Mach number downstream of the confluence point  $R_f$  being subsonic.

The last selected applications are relative to afterbody flows with plume induced separation on the fuselage. The cylindrical afterbody is equipped with a nozzle having a divergence angle  $\beta_j = 9.1^\circ$ , an exit diameter such that  $D_j / D_{max} = 0.8$  and giving a flow of Mach number  $M_j = 1.69$ . In the application shown in Fig. 12a, the external flow Mach number is equal to 2. Six methods are confronted with experiment. The three multi-component methods (Addy, Moulden, ONERA1) give acceptable results as concerns the prediction of the base pressure. However, there is a large discrepancy on the value of the nozzle expansion ratio corresponding to incipient separation at the base shoulder: the Addy code gives a limit value  $p_{t_j} / p_{t_\infty} \approx 12$ , whereas the ONERA1 code gives  $p_{t_j} / p_{t_\infty} \approx 18$ . Semi-empirical methods work poorly in this case. In the second example, shown in Fig. 12b, the external Mach number is equal to 1.65. The Moulden and ONERA1 codes still give good results. Surprisingly, the Addy model gives a poor prediction of base pressure for the lowest values of the nozzle expansion ratio where there is no separation on the body.

## 5 - DATA BASE COLLECTION FOR TESTING EULER AND NAVIER STOKES CALCULATIONS

### 5.1 - INTRODUCTORY REMARKS

The aim of this activity was to collect data on a limited number of well documented and carefully made experiments, including detailed analysis of the flow past typical afterbodies. The selection of the test cases was made by taking into account the following criteria:

- Only axisymmetric afterbodies with or without propulsion will be considered.
- Incoming flows (external plus jet) properties should be provided, including boundary-layer profiles.
- In addition to static pressure distributions on the afterbody, flow field measurements giving the mean velocity components and the Reynolds tensor components should be included.

After examination of several possible test cases, it was decided to retain only six test cases described in Table IV. The selected cases concern results obtained in the subsonic regime. No well documented and accurate data were available for the transonic and supersonic regimes, presently. Neither results concerning the effect of the jet nature or total temperature were found.

TABLE IV - SUMMARY OF TEST CASES FOR EULER AND NAVIER-STOKES CALCULATIONS

Test case	Origin	Afterbody geometry	$M_{\infty}$	Jet	Angle of attack	Measurements on the body in the flow
1A	ISL	$\beta = 0^\circ$	0.35	off	$0^\circ$	$P_{stat}$ , B-L $\vec{V}$ , $\bar{R}$
1B	ISL	$\beta = -6^\circ$ $\frac{L}{D_{max}} = 1$	0.35	off	$0^\circ$	$P_{stat}$ , B-L $\vec{V}$ , $\bar{R}$
2B	AS/ONERA	$\beta = 0^\circ$	0.85	on	$0^\circ$	$P_{stat}$ , B-L $\vec{V}$ , $\bar{R}$
2B	AS/ONERA	$\beta = 6^\circ$ $\frac{L}{D_{max}} = 1$	0.85	on	$0^\circ$	$P_{stat}$ , B-L $\vec{V}$ , $\bar{R}$
2C	AS/ONERA	$\beta = +6^\circ$ $\frac{L}{D_{max}} = 1$	0.85	on	$0^\circ$	$P_{stat}$ , B-L $\vec{V}$ , $\bar{R}$
3	ISL	$\beta = 6^\circ$ $\frac{L}{D_{max}} = 1$	0.54	off	$5^\circ$	$P_{stat}$ , B-L $\vec{V}$ , $\bar{R}$

$P_{stat}$ : surface pressure measurements,

B-L : incoming boundary-layer profile provided,

$\vec{V}$ ,  $\bar{R}$  : mean velocity vector and Reynolds tensor measurements.

The data bank consists in profiles of flow mean and turbulent properties and in tracings of contour lines of these quantities.

Results relative to the effect of angle of incidence have been obtained in experiments executed by ISL in the framework of the Action Group activity

## 5.2 - PRESENTATION OF SOME TYPICAL RESULTS

There is no place here to give much detail about this data bank which contains a considerable amount of information. We have selected a limited number of results to give an idea of the quality of the measurements and of the general structure of the investigated flows.

Test cases 1A and 1B have been investigated in a ISL blow down type wind tunnel. As shown in Fig. 13, the experimental arrangement comprises an axisymmetric nozzle of 0,21 m in length and of 0,1 m in diameter. Afterbody models are mounted at the extremity of a sting, of diameter 0,020 m, located in the test section and supported in the settling chamber by three shaped struts. The end of the sting is held in the test section by three wires of 0,3 mm in diameter adjustable by strap mounts. This system allows the models to be aligned in the flow direction (angle of attack and slide slip angle equal to zero) and leaves the flow in the test section undisturbed. The general flow conditions were as follows:

$P_{t_{\infty}}$	$M_{\infty}$	$Re_D$	$\alpha$
$10^5$ Pa	0.35	$1.54 \cdot 10^6$	0

$Re_D$ : Reynolds number computed with the model caliber.

At each measurement point, the flow field properties were calculated from 4096 individual samples of the instantaneous velocity components  $u$  and  $v$  obtained by means of a 2-D, two-colour LDV system [35].

The mean velocity vector field for the cylindrical afterbody (test case 1A) is represented in Fig. 14. This plot shows the vast recirculating zone existing just downstream of the base. The figure shows a good symmetry of the configuration, the reverse flow stagnation point being located right in the center of the base. From this vector field it was possible to determine the mean flow streamlines shown in Fig. 15, where the results obtained for the conical boattail have also been represented for purpose of comparison. One notes a noticeable reduction in the size of the near wake, when  $\beta = -6^\circ$ . Some results relative to the turbulence properties of the flow are represented in Figs. 16a and 16b by means of contour representations of the turbulent kinetic energy and of the Reynolds shear stress. One sees that the maximum turbulence levels are reached in the shear layer originating at the base shoulder at a location slightly upstream of the rear stagnation point.

Test cases 2A, 2B and 2C, which correspond to an afterbody in the jet-on situation, were studied in the ONERA S3Ch transonic wind tunnel [36]. Models are mounted with zero angle of attack and zero yaw on a sting, of diameter  $D = 0.1$  m, supported by a horizontal shaped strut located in the settling chamber and by three shaped wires caught at the collector walls (see Fig. 17). The jet is produced by a contoured supersonic nozzle of diameter  $D_j = 0.15$  m. The general test conditions were as follows:

#### External Flow

$P_{t\infty}$	$T_{t\infty}$	$M_\infty$	$Re_D$	$\alpha$
$10^5$ Pa	288 K	0.85	$1.25 \cdot 10^6$	$0^\circ$

#### Nozzle Flow

$P_{tj}$	$T_{tj}$	$M_j$	$\gamma_j$
$22.83 \cdot 10^5$ Pa	300 K	2.9	1.4

The flow field properties were calculated for each point based on 2000 individual samples of  $(u,v)$  obtained by means of a 2-D two color LDV system.

The mean velocity vector field for the cylindrical afterbody is shown in Fig. 18. A recirculating zone forms downstream of the base, its closure point being located at approximately 1.25 caliber from the base. The structure of the mean base flow is best visualized by the tracings of streamlines shown in Fig. 19. Considering first the cylindrical afterbody (see Fig. 19a), one can first distinguish a region where the streamlines are closed curves. This recirculating bubble is bounded by a *discriminating streamline* ( $j$ ) originating at the separation point  $S_F$ , located at the base shoulder, and ending at the stagnation point  $R$  located on the base between  $S_F$  and the nozzle exit  $S_j$ . Another line to be remarked is the streamline ( $s$ ) which delimits the reversed flow region. This streamline ( $s$ ) passes through point  $S$  where its tangent is vertical. The streamlines flowing between the wall and ( $s$ ) are first turned back towards the base; then, they are rapidly bent in the downstream direction by the strong entrainment effect of the supersonic jet. The mean flow streamlines for the afterbody with boattail (test case 2B) and with flare (test case 2C) are shown in Figs. 19b and 19c. One sees that the reverse flow region is much reduced when there is a boattail due to the tendency of the external flow to converge towards the axis. On the other hand, the presence of a flare leads to a considerable extension of the separated bubble.

The spatial distribution of the turbulence kinetic energy for the cylindrical afterbody is visualized in Fig. 20a by a tracing of the lines of constant values for  $k / U_\infty^2$ . In the external shear layer, originating at  $S_F$ , the maximum of  $k$  occurs just above the limit point  $S$ . In the jet mixing layer, the turbulence levels are between three and four times higher than in the outer flow shear layer. This increase in the levels results from a more intense turbulence production because of higher strain rates. The spatial distributions of the Reynolds shear stress given in Fig. 20b show similar tendencies.

The study of the afterbody at an angle of attack  $\alpha = 5^\circ$  (test case 3) was conducted in the ISL blow down type wind tunnel, the open test section being here a square in cross section measuring  $0.13 \times 0.13$  m<sup>2</sup>. As for test cases 2a to 2c, the afterbody model is mounted at the end of a sting supported in the settling chamber and held in the test section. Here, the sting is set at an angle  $\alpha = 5^\circ$  with respect to the test section axis (see Fig. 21). Great care was taken to align the model in the flow direction so that the sideslip angle be equal to zero. The flow field properties were measured with a 3-D, three color LDV system. Results are expressed in the reference system X,Y,Z as shown in Fig. 20 [37].

Clear representation of 3-D results is a difficult task [38]. Some insight into the complex flow organization can be gained by the tracings of Fig. 22 which show the *projected* mean velocity vector field in X - Y planes located at different spanwise locations Z. By a trajectographic method, it is possible to construct the *lines of force* of this vector field which are drawn on the same figures.

tracings reveal the existence in the selected planes of singular points of the focus and saddle types. Also, the vector field contains separation lines, the particularity of which is to go through a singular point. These features are typical of three dimensional separated flows [39]. Similar results relative to transverse  $Y - X$  planes located at different  $X$  locations are shown in Fig. 23.

Turbulent properties of the base flow are given in the next figure which shows contours of the turbulent kinetic energy  $k / U_\infty^2$  (Fig. 24a) and of the Reynolds shear stress component  $u'v' / U_\infty^2$  (Fig. 24b) for six transverse planes  $Z - Y$ . The Action Group Report will contain the complete set of data concerning this flow as also a physical interpretation of the results.

## 6 - VALIDATION OF EULER AND NAVIER-STOKES CALCULATIONS

### 6.1 - INTRODUCTORY REMARKS

First it must be mentioned that this activity has not yet been completed. Only preliminary Navier-Stokes results are available from different investigators and some Euler solutions have been performed as a preparatory step for achieving good Navier-Stokes solutions. Therefore, only a few figures concerning preliminary results will be shown here. Even the rough method descriptions must be understood as preliminary, these methods being still subject to some changes until the work will be finished.

Especially, it is planned to carry out some exercises on mesh refinement or mesh adaptation, running different codes in the same computational mesh and using different types of turbulence models within the same numerical scheme and the same grid. Hopefully, these very important exercises can be concluded within the lifetime of the Action Group.

### 6.2 - SURVEY OF THE COMPUTATIONAL METHODS USED FOR SOLVING THE NAVIER-STOKES EQUATIONS

Numerical contributions solving the Navier-Stokes equations will be provided by British Aerospace, Dornier, ISL and MATRA. The computational methods used by these investigators can be roughly characterized as follows.

*British Aerospace.* The steady averaged Navier-Stokes equations are solved by an iterative upwind finite difference scheme equivalent to a finite volume approximation since similar integrations are carried out over the complete surface of each computational cell. An iterative pressure correction technique is used in order to fulfill the continuity equation. The method is based on the semi implicit method of Spalding and Patankar. The  $[k, \epsilon]$  transport equation turbulence model is used in the code and the log-law is implemented for the velocity profile close to the walls in order to avoid very fine mesh resolutions there. The method is capable of treating the chemical reactions in the plume by adding the reaction and species conservation equations to the code. Further improvement are under development.

*Dornier.* A cell centered finite volume algorithm is used in block structured meshes. The time integration is performed by explicit Runge-Kutta type methods or, alternately, solutions can also be gained iteratively with an implicit L-U factorised scheme. Both approaches allow for a speed up by a multigrid scheme and the explicit scheme is also accelerated by local time steps and implicit residual averaging. The  $[k, \epsilon]$  turbulence model is implemented including a low Reynolds number damping model which permits fine mesh resolution near the wall, thus avoiding the use of a law of the wall. Also, the famous Baldwin-Lomax model can be used in a formulation well tuned for applying it safely across block boundaries and in complicated flow regions.

*ISL.* The code solves the vorticity transport equation and, in parallel, the Poisson equation for the stream function by an implicit finite difference integration method. The values of the variables in the flow field are provided at the nodes of the grid lines. The turbulent shear stress is modeled by classical mixing length models.

*MATRA.* The code solves the unsteady flow equations by a finite volume discretisation with the unknowns at the nodes and the time integration is performed by an explicit one-step Lax-Wendroff scheme. Multi-Block meshes are used and for the turbulence description the Baldwin-Lomax model is adopted. For low Mach numbers an artificial compressibility version is available.

### 6.3 - NAVIER-STOKES RESULTS

In Fig. 25 some results of Czichowsky, ISL, for the mean flow streamlines and the lines of constant vorticity corresponding to three values of the Reynolds number are shown. These results are relative to a

boattailed axisymmetric afterbody without jet in incompressible flow. The length of the recirculating bubble behind the base is displayed in Fig. 26 as function of Reynolds number for three different boattail angles, the boattailed part having a length of half caliber. Although these cases are not directly related to the test cases discussed above, it is quite interesting to recognise how the bubble length appears to reach an asymptotic value with increasing Reynolds number. This confirms from a theoretical point of view the well known fact that the base flow pattern is only slightly dependent on Reynolds number in the technically most important higher Reynolds number range.

Some recent results from Magagnato, Dornier, for Test Case 2B are displayed in Figs. 27 and 28. Compared to the Dornier calculations presented in [3] an essentially refined block structured mesh is used with good resolution of both shear layers at the free stream as well as at the jet boundary of the separated region. Also a different numerical scheme is used which is described in Section 6.2 above. For the present calculation, the formulation of the Baldwin-Lomax turbulence model has been thoroughly adjusted for the use in both free shear layers. More details are discussed in the paper of Magagnato within this conference [40].

Surprisingly, the flow pattern shown in Fig. 27 is not very much changed compared to [3] in spite of the definite improvement of the numerical treatment. The measured closure position C of the recirculation region is well represented in both calculations. On the other hand, the discrepancy between the measured reattachment position R at the base and the calculated point (point of vanishing tangential velocity at the base in Fig. 27) is not reduced compared to [3]. The only explanation at hand for this discrepancy may be that the shear layer at the jet boundary originated from the highly accelerated nozzle boundary-layer is perhaps initially laminar as also supposed in [3], while it is assumed to be turbulent in the calculation. This could be the reason for the fact that the substantial improvement of mesh resolution and turbulence model representation at the jet boundary does not produce the expected improvement effects.

Fig. 28 presents the pressure distribution on the afterbody for the same case where the pressure coefficient  $C_p$  is plotted versus the distance from the base (Fig. 28a) and the base pressure versus radius (Fig. 28 b). Now the surface pressure distribution is improved at the body-boattail junction ( $X = -0.1$  m) due to the better mesh resolution compared to [3]. The base pressure level is close to the experimental value as already observed in [3].

Some very preliminary Navier-Stokes calculations performed at British Aerospace are presented in Figs. 29a and 29b. The computed configurations correspond to Test Cases 1A and 1B. The upper half of each figure shows the computed velocity plot, the lower half the ISL experimental result. There is a general agreement between calculation and experiment, however the computed bubble length is here more important than the experimental one.

Examples of Navier-Stokes calculations performed at MATRA are presented in Fig. 30 which show tracings of velocity fields. The first example (see Fig. 30a) corresponds to Test Case 1B. The second calculation (see Fig. 30b) corresponds to Test Case 2B (boattailed afterbody with jet). This result is very encouraging the computed flow field reproducing faithfully the essential features of the measured field.

## 7 - CONCLUSION

Base flow phenomena can play an important role in the aerodynamic performance of a missile or a projectile. Furthermore, the base region can be the seat of complex aerothermal processes, involving possible after burning of the gas emitted by the propulsive jet, which are at the origin of large heat fluxes on the rear part of the missile. Due to the great practical importance of base flows, the GARTEUR Group of Responsables for Aerodynamics decided in 1986 the creation of an Action Group (AG09) on this subject with the title "Flow Past Missile Afterbodies". The task of this AG was to establish the state of the art in the matter of base flow prediction by making an in depth assessment of existing calculation methods by means of thorough comparisons with experimental results. The membership of this Action Group, which is close to the completion of its task, is as follows: Aérospatiale - Châtillon, British Aerospace - Bristol, DLR - Braunschweig, Dornier - Friedrichshafen, ISL - Saint-Louis, MATRA, MBB - Munich, ONERA

In this perspective, the AG collected 158 test cases covering both jet off and jet on situations and flight Mach number in the subsonic, transonic and supersonic ranges. This data bank was used to test a total of 12 semi-empirical and multi-component methods by executing 448 calculations which allowed a clear definition of the domain of applicability of these methods. Thus it appears that in this field, the situation is far from being satisfactory, the executed calculations showing large discrepancies not only between predictions and experiment but also between methods. In fact, semi-empirical methods are of poor quality outside the range of parameters for which they have been established. On the other hand, multi-component methods are superior to treat complex configurations involving a large number of parameters, for example afterbodies in the jet on situations. However, even in the case of a supersonic external flow - for which multi-component models seem well founded - no method actually works very well, especially when the size of the dead-air region at the base is large. Semi-empirical and multi-component methods are unable to predict base flow in the

transonic range, experiment in this field being also very difficult. Furthermore, application of these methods is restricted to axisymmetric configurations, their extension to 3D flows being extremely difficult and hazardous.

A data base consisting of 6 well documented experiments, including very detailed field measurements by 2D and 3D LDV techniques, was constituted to test more advanced computational methods based on the solution of the time averaged Navier-Stokes equations. Two experiments are relative to subsonic flow in the jet off situation, three to subsonic flow in the jet on situation, the last case being a particularly well documented 3D case in which an unpowered afterbody is set at an incidence of 5° in a subsonic stream. Four different Navier-Stokes codes, incorporating algebraic or transport equation turbulence models, have been investigated by the contributors. This activity, which has not yet been completed at the time of the present meeting, constitutes a very instructive exercise since it is in measure to lead to clear conclusions concerning both the numerical problems and the modelling difficulties met in the Navier-Stokes approach.

#### AKNOWLEDGMENT

This presentation is the result of the cooperative work of the authors' colleagues, participants to the GARTEUR Action Group 09: G. Berner and B. Jaeggy, ISL, M. Brédif and V. Deschamps, MATRA, P. Hennig, MBB, P.G.C. Herring and D. P. Hills, British Aerospace, R.G. Lacau and J. Diet, Aérospatiale, F. Magagnato, Dornier, Ph. Reijasse, GNERA and H. Riedel, DLR.

#### REFERENCES

- [1] Détery, J. et Sirieix, M. "Base Flow Behind Missiles". AGARD LS-98 on *Missile Aerodynamics* (1979)
- [2] Détery, J. et Lacau, R.-G. "Prediction of Base-Flows". AGARD Report N°. 754 *Special Course on Missile Aerodynamics* (1988)
- [3] Report of the Working Group 08 on *Aerodynamics of Aircraft Afterbody*. AGARD Advisory Report N°. 226 (1986)
- [4] E.S.D.U. (Engineering Sciences Data Unit) N° 79022, *Bodies of Revolution* (Oct. 1979)
- [5] Report of the GARTEUR Action Group 09 on *Flow Past Missile Afterbodies* (to be published)
- [6] Herring, P. G. C. "The Zero Incidence Drag of Weapon Configurations". A data handbook. BAe Dynamics Report S7 20139 (1978)
- [7] Brazzel, G. E. and Henderson, J. H. "An Empirical Technique for Estimating Power-on Base Drag of Bodies of Revolution with a Single Jet Exhaust" AGARD CP N° 10 (1966)
- [8] Glasgow, E. R., Santman, D. M. and Miller, L. D. "Experimental and Analytical Determination of Integrated Airframe Nozzle Performance". Technical Report AFFDL-TR-72-101, Vol. 1 (1972)
- [9] Tanner, M. "Empirische Formeln zur Bestimmung des Basisdruckes von Flugkörpern bei Unterschallgeschwindigkeit" DFVLR-FB 84-23 (1984)
- [10] Tanner, M. "Basisdruckmessungen an einem Flugkörper mit kleiner Versperrung bei Unterschall- und Transschallgeschwindigkeit". ZFW, Vol. 5, pp 112-119 (1981)
- [11] Compton III, W. B. "Effects on Base Drag of Recessing the Bases of Conical Afterbodies at Subsonic and Transonic Speeds". NASA TN D-4821 (1968)
- [12] Esch, H. "Messung des Widerstands kegliger Hecks im Ueberschall". DFVLR-IB 351-77/6 (1977)
- [13] Bromm, A.F. and O'Donnel, R. M. "Investigation at Supersonic Speeds of the Effect of Jet Mach Number and Divergence Angle of the Nozzle upon the Pressure of the Base Annulus of a Body of Revolution". NACA RM L54116 (1954)
- [14] Tanner, M. "Theoretical Prediction of Base Pressure for Steady Base Flow". *Progress in Aerospace Sciences*, Vol. 14, pp. 177-225 (1973)(Tanner). Teil I und II. Diplomarbeit FH München (1987)



- [15] Tanner, M. and Hassbargen, D. "Heckwiderstands- und Basisdruckmessungen an einem Flugkörperrumpf bei Anstellwinkeln bis  $\alpha = 25^\circ$  im Unterschall und Transschallbereich. Tabelle mit Ergebnissen". DFVLR-Bericht N° IB 251-77 A 05 (1978)
- [16] Tanner, M. "Heckwiderstands- und Basisdruckmessungen bei Anstellwinkeln bis  $25^\circ$  im Unterschall- und Transschallbereich". DFVLR-Bericht N° IB 251-77 A 47 (1978)
- [17] Oswatitsch, K. "Der Luftwiderstand als Integral des Entropiestromes". Nachr. Akad. Wiss. Göttingen, Math. Phys. Kl., pp. 88-90 (1945)
- [18] Agrell, J. and White, R. A. "An Experimental Investigation of Supersonic Axisymmetric Flow over Boattails Containing a Centred Propulsive Jet". FFA Tech. Note AU 913 (1974)
- [19] Korst, H. H. "A Theory for Base Pressure in Two-Dimensional Flow and Comparison with Experiment". J. Appl. Mech., N° 23, pp. 593-600 (1956)
- [20] Carrière, P. and Sirieix, M. "Facteurs d'influence du recollement d'un écoulement supersonique". 10th International Congress of Applied Mechanics, Stresa, Italy (1960)
- [21] Chapman, D. R. "An Analysis of Base Pressure at Supersonic Velocity and Comparison with Experiments". NACA Report N° 1051 (1951)
- [22] Mueller, T. J. "Determination of the Turbulent Base Pressure in Supersonic Axisymmetric Flow". Journal of Aircraft, Vol. 5, N° 1, pp. 101-107 (1967)
- [23] Roache, P. J. "Base Drag Calculations in Supersonic Turbulent Axisymmetric Flows". Journal of Spacecraft and Rockets, Vol. 10, N° 4, pp. 285-297 (1973)
- [24] Reijasse, P., Benay, R., Détery, J. and Lacau, R. G. "Prévision des écoulements au culot de missiles ou de projectiles par des méthodes multi-composant". La Recherche Aérospatiale, N° 1989-4 (1989)
- [25] Addy, A. L. "Analysis of the Axisymmetric Base Pressure and Base Temperature Problem with Supersonic Interacting Freestream Nozzle Flows Based on the Flow Model of Korst et al. - Parts I, II and III". US Army Missile Command RD-TR-69-12 (1969)
- [26] Addy, A. L. "Experimental-Theoretical Correlation of Supersonic Jet-on Base Pressure for Cylindrical Afterbodies". Journal of Aircraft, Vol. 7, N° 5, pp. 474-478 (1970)
- [27] Zukoski, E. E. "Turbulent Boundary-Layer Separation in Front of a Forward Facing Step". AIAA Journal, Vol. 5, N° 10, pp. 1746-1753 (1967)
- [28] Kirk, F. N. "An Approximate Theory of Base Pressure in Two-Dimensional Flow at Supersonic Speeds". RAE TN Aero 2377 (1959)
- [29] Chapman, D. R., Kuehn, D. M. and Larson, H. K. "Investigation of Separated Flow in Supersonic and Subsonic Streams with Emphasis on the Effect of Transition". NACA TN-3869 (1957)
- [30] Wagner, B. "Jet-Afterbody Interference on Missile in Supersonic Flow". AGARD CP N° 307 (1981)
- [31] Carrière, P. "Effet d'une injection fluide dans l'eau morte sur les conditions de recollement d'un écoulement plan supersonique". Compte-rendus de l'Académie des Sciences de Paris, t. 521, pp. 2877-2879 (1960)
- [32] Wagner, B. "Estimation of Angle of Attack Effect by Component Analysis and Axisymmetric Navier-Stokes Solutions for Missile Afterbodies with Jet". Proc. of the Symposium on Rocket/Plume Fluid Dynamic Interactions, The University of Texas at Austin, Vol. 3 (1983)
- [33] Wu, J. M., Moulden, T. H. and Uchiyama, N. "Aerodynamic Performance of Missile Configurations at Transonic Speeds Including the Effects of a Jet Plume". US Army Missile Command TR-RD076-23 (1976)
- [34] Vanwagenen Jr., R. G. "A Study of Axially Symmetric Subsonic Base-Flow". Ph. D. Dissertation, University of Washington (1968)
- [35] Berner, C., Petitdemange, V. and Dupéroux, J.P. "Mesures de vélocimétrie laser dans le sillage proche d'arrière-corps à symétrie de révolution". ISL- Report R 114/87 (1987)

- [36] Lacau, R. G., Desnoyer, D. and Détery, J. "Analyse au vélocimètre laser de l'écoulement en aval d'arrière-corps de missiles". AGARD CP-336 (1982)
- [37] Berner, C., Petitdemange, V. and Dupéroux, J. P. "Mesures simultanées des trois composantes du vecteur vitesse dans le sillage d'arrière-corps à symétrie de révolution en incidence". ISL Report to be published
- [38] Berner, C. "Measurements and Interpretation of 3-D High Speed Flows". Proceedings of the 3rd International Conference on Laser Anemometry, Advances and Applications, Swansea, United-Kingdom (196.)
- [39] Legendre, R. "Lignes de courant d'un écoulement permanent. Décollement et séparation". La Recherche Aérospatiale, N° 1977-6 (1977)
- [40] Magagnato, -. "Computation of Axisymmetric Base Flow with Different Turbulence Models". To be presented at the AGARD/FDP Symposium on "Missile Aerodynamics", Friedrichshafen, W. Germany, 23-26 April 1990

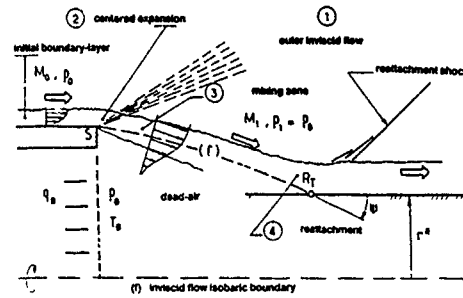


Fig. 1 - The Chapman-Korsv basic model for reattachment behind a base

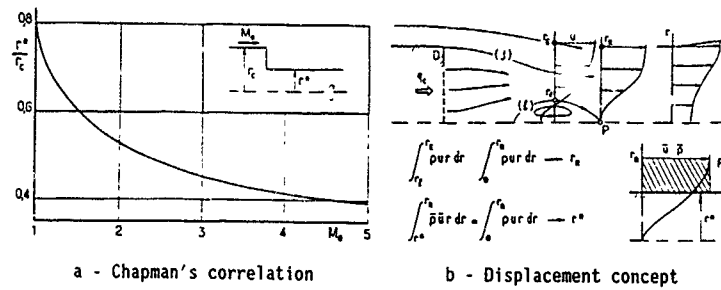


Fig. 2 - Determination of the fictitious sting radius

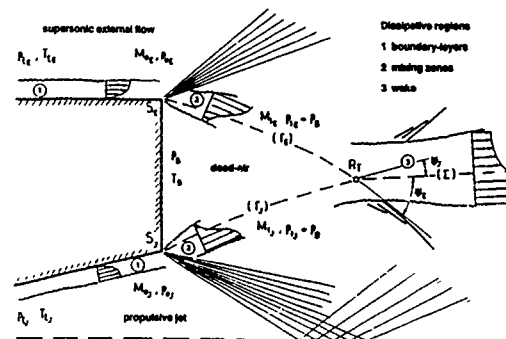


Fig. 3 - Flow model for base flow in jet-on condition

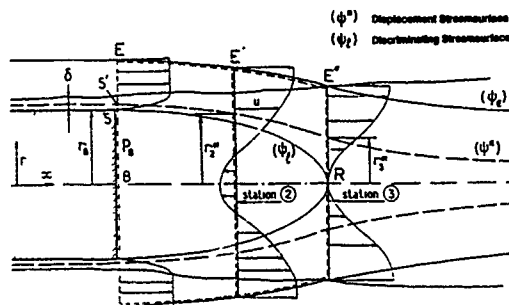


Fig. 4 - Flow model for subsonic base flow in jet-off condition

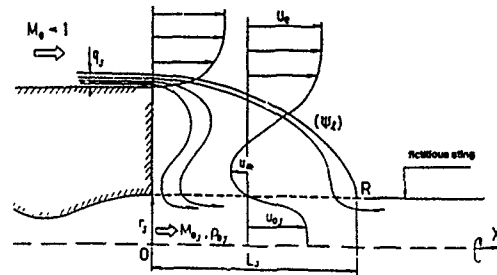


Fig. 5 - Flow model for subsonic base flow in jet-on condition

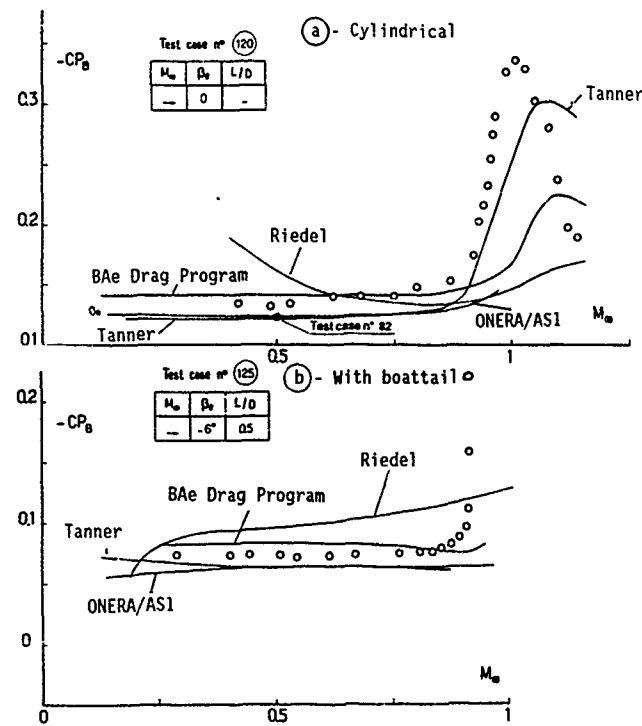
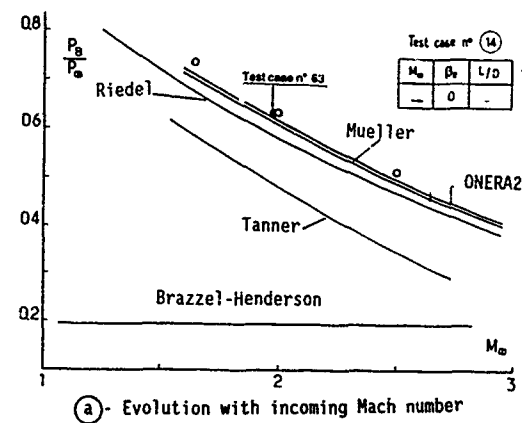


Fig. 6 - Test of semi-empirical and multi-component methods Subsonic-transonic external flow without jet



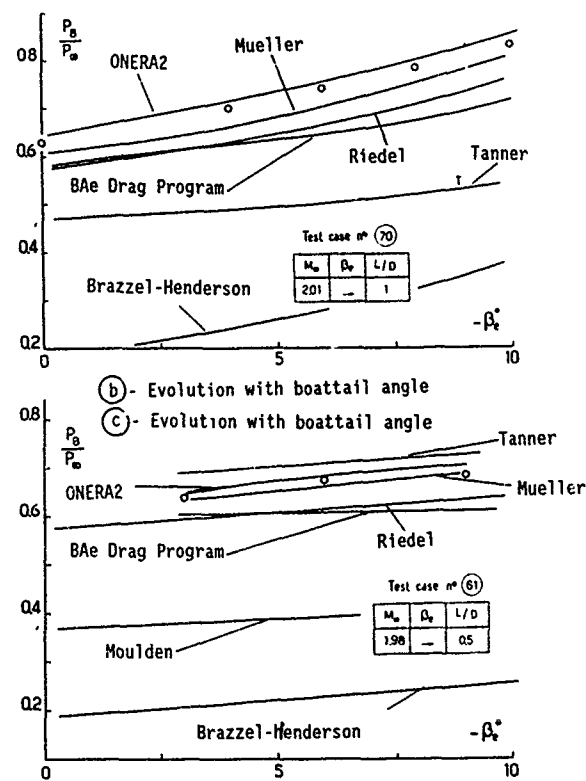
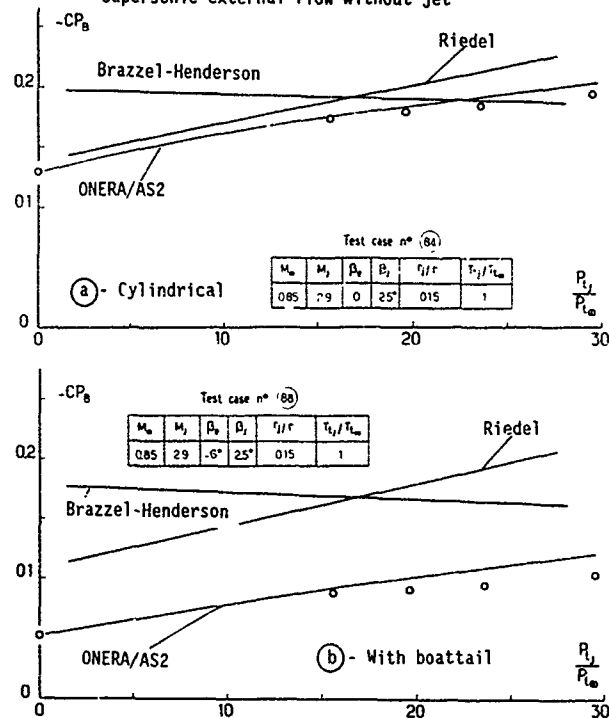


Fig. 7 - Test of semi-empirical and multi-component methods  
Supersonic external flow without jet



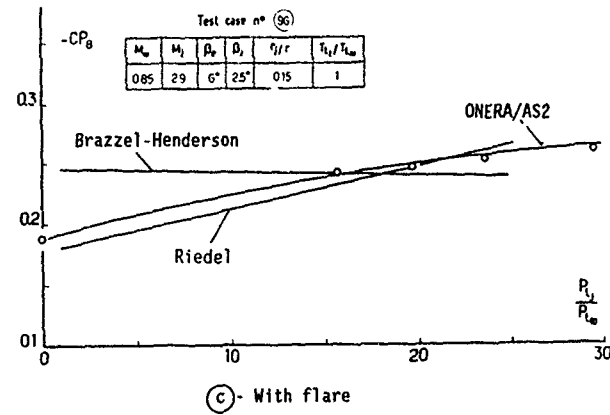


Fig. 8 - Test of semi-empirical and multi-component methods  
Subsonic external flow with jet

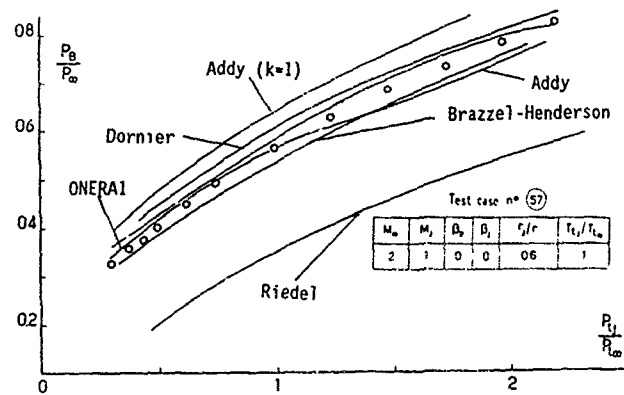
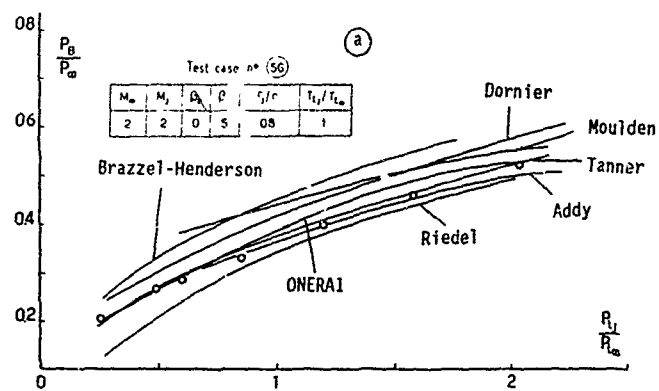


Fig. 9 - Test of semi-empirical and multi-component methods  
Supersonic external flow with jet



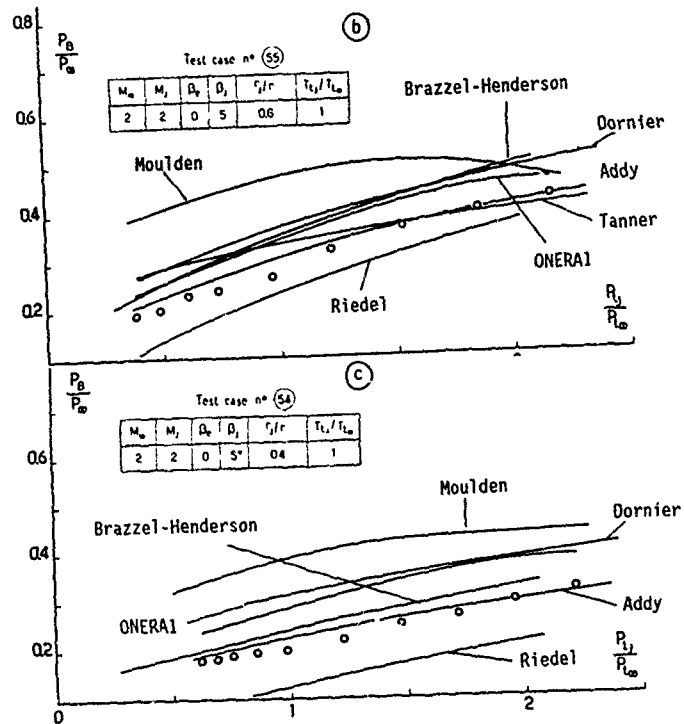


Fig. 10 - Test of semi-empirical and multi-component methods  
Supersonic external flow with jet

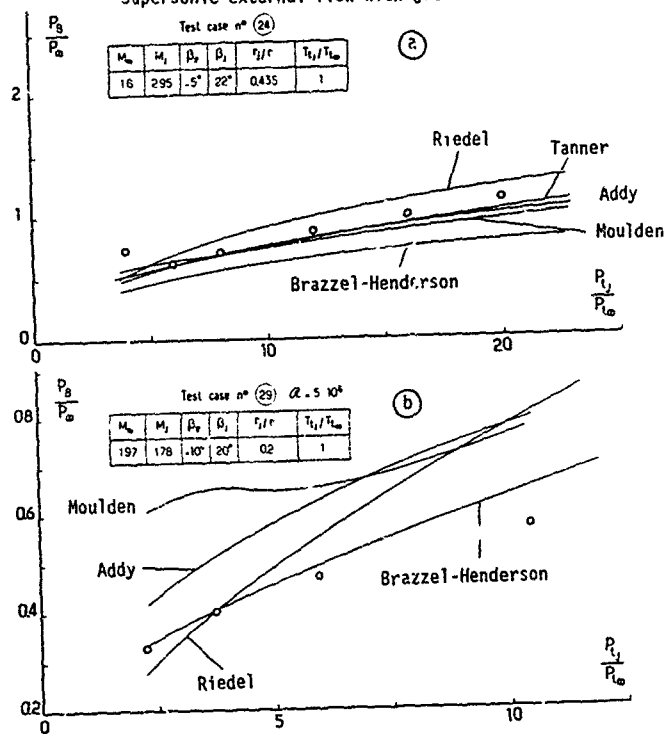


Fig. 11 - Test of semi-empirical and multi-component methods  
Supersonic external flow with jet

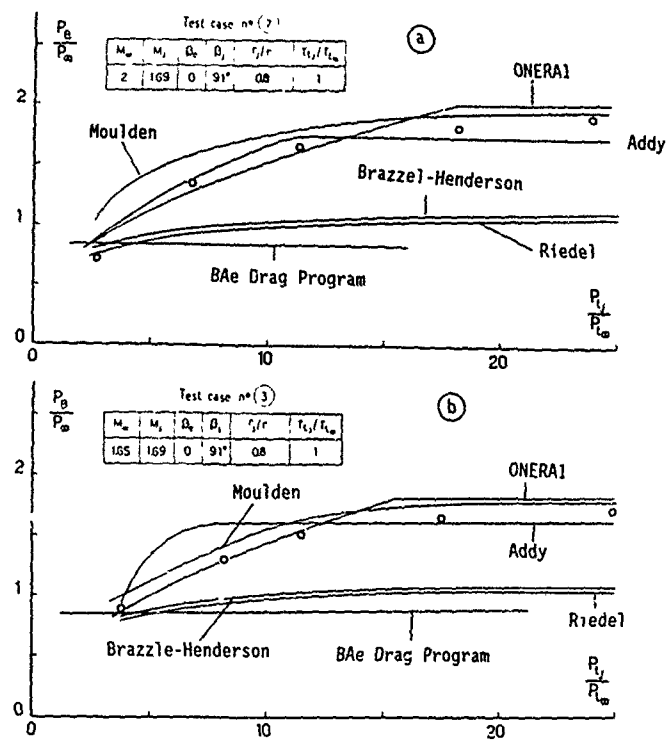


Fig. 12 - Test of semi-empirical and multi-component methods  
Supersonic flow with plume induced separation

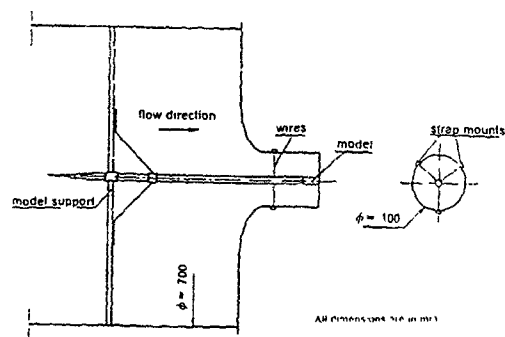


Fig. 13 - Subsonic base flow without jet. Model installation  
in the ISL wind tunnel



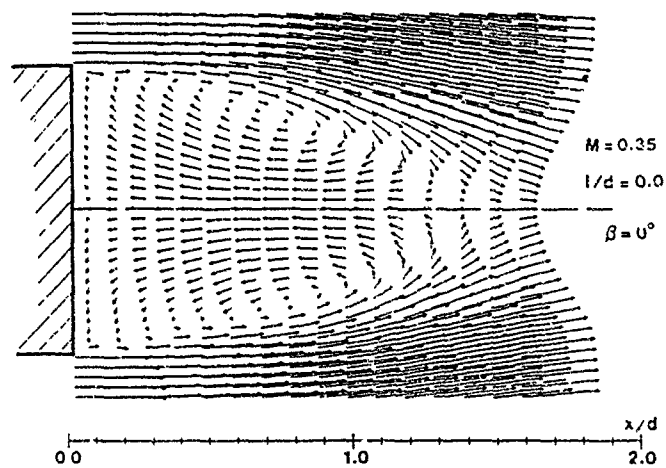


Fig. 14 - Subsonic base flow without jet (ISL results)  
Mean velocity vector field - Test case 1A

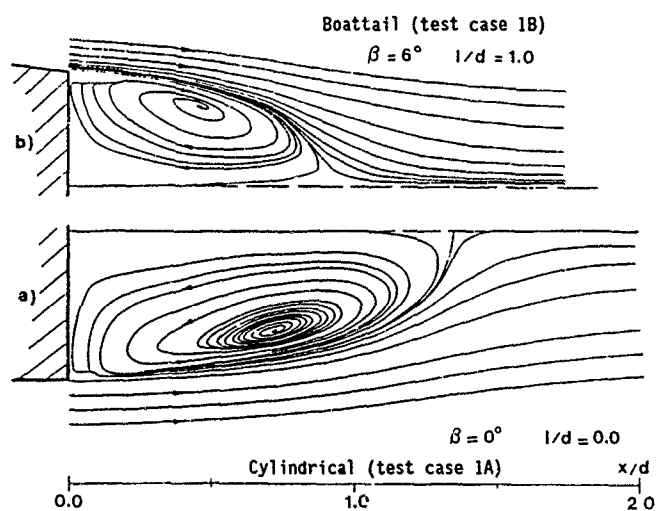


Fig. 15 - Subsonic base flow without jet (ISL results)  
Meanflow streamlines

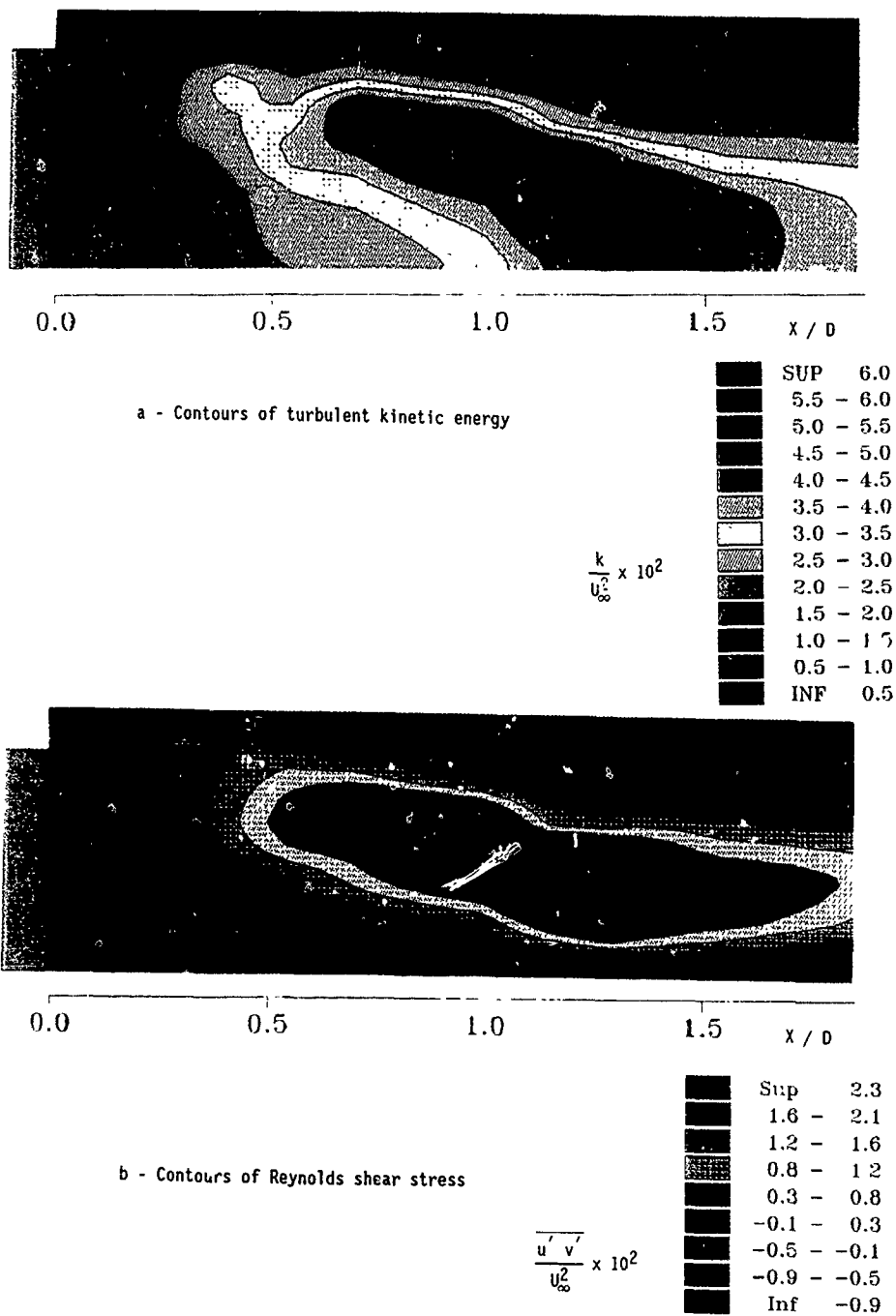


Fig 16 - Subsonic base flow without jet (ISL results)  
Turbulent properties - Test case 1A

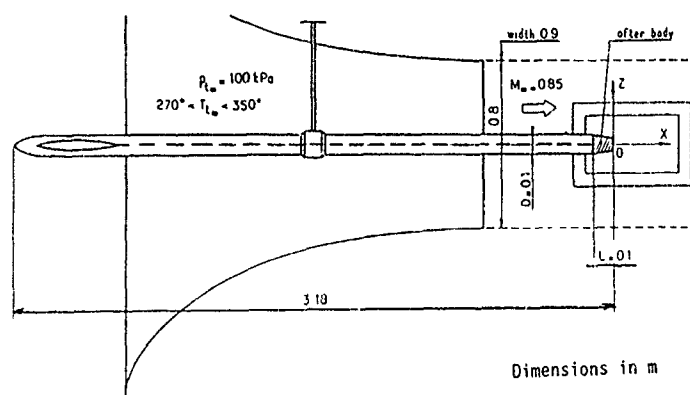


Fig. 17 - Subsonic base flow with jet - Model installation in the ONERA wind tunnel

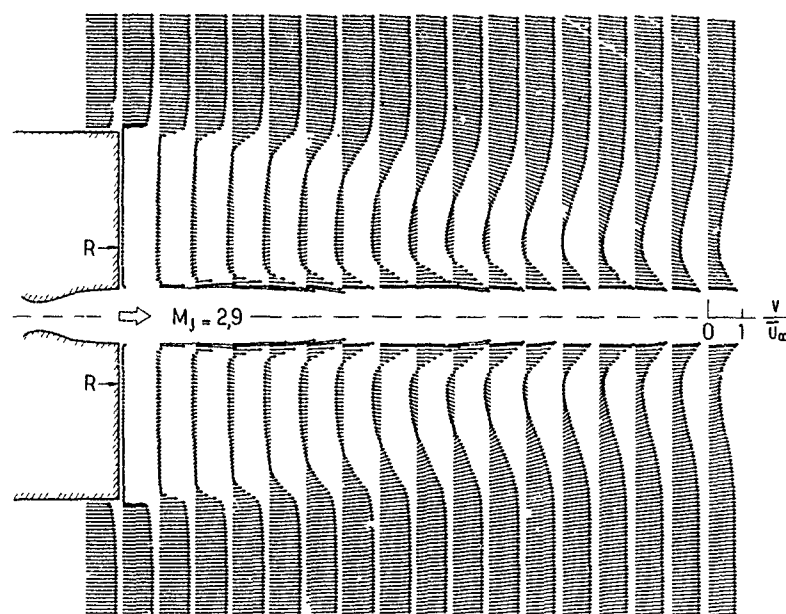
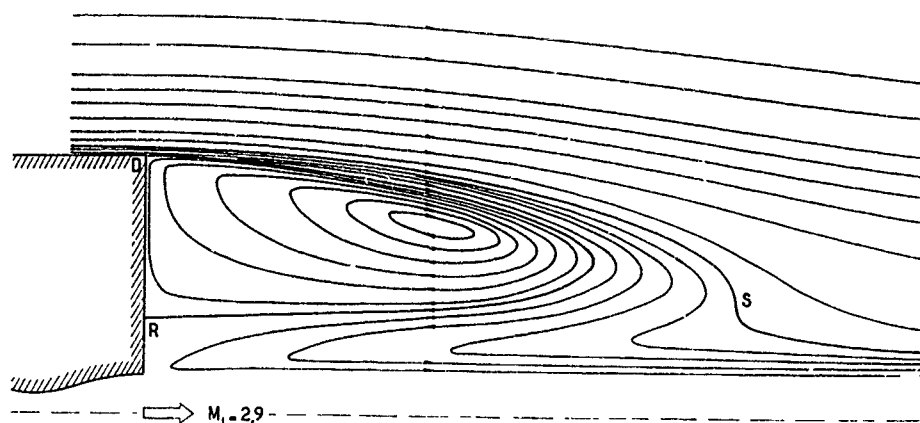
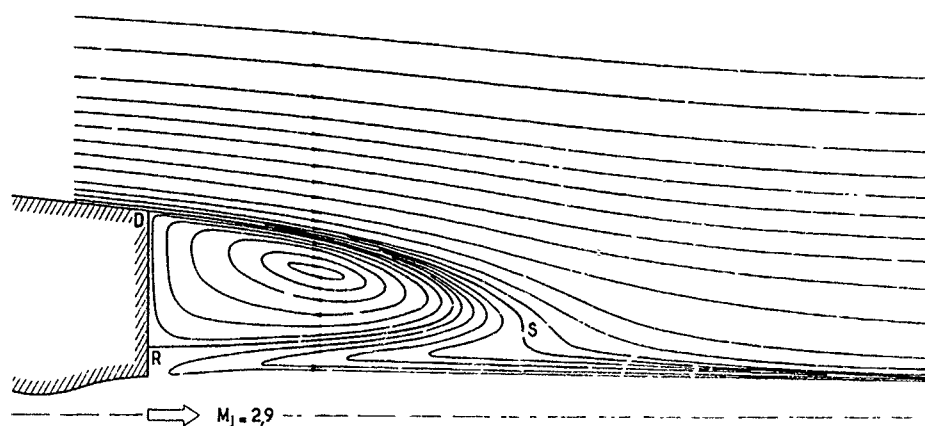


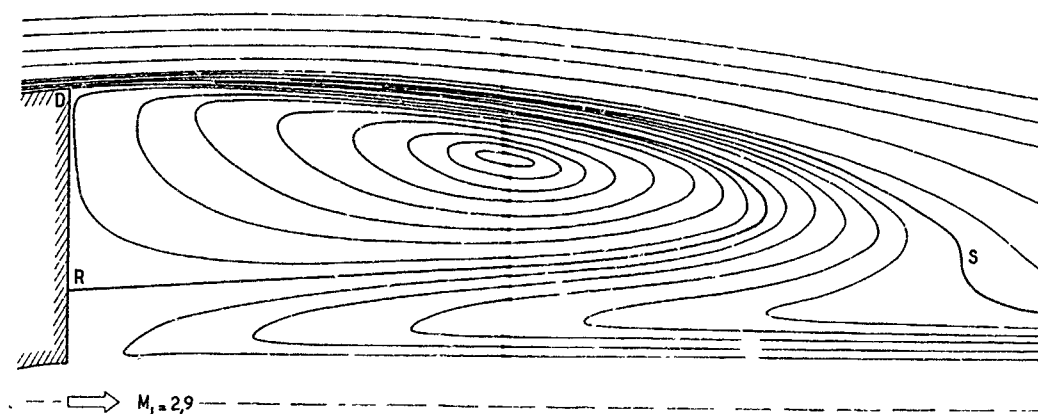
Fig. 18 - Subsonic base flow with jet (ONERA/AS results)  
Mean velocity vector field - Test case 2A



a - Cylindrical afterbody (test case 2A)



b - afterbody with boattail (test case 2B)



c - afterbody with flare (test case 2C)

Fig. 19 - Subsonic base flow with jet (ONERA/AS results)  
Mean flow streamlines

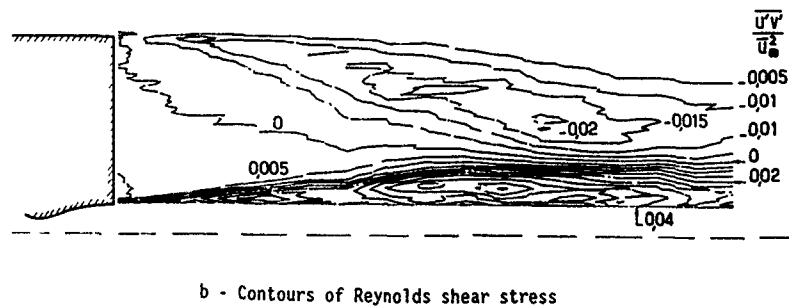
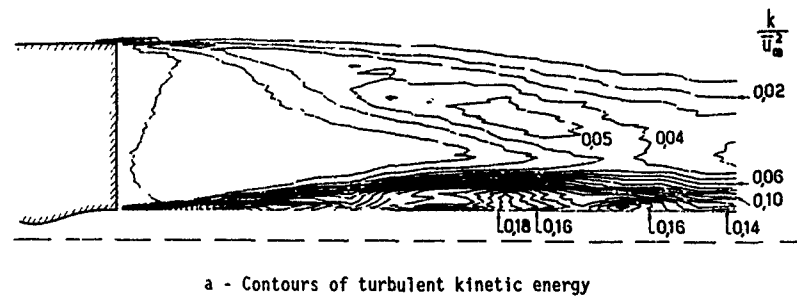


Fig. 20 - Subsonic base flow with jet (ONERA/AS results)  
Turbulent properties - Test case 2A

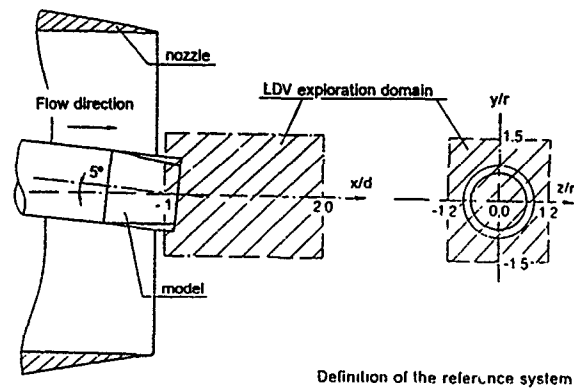


Fig. 21 - Subsonic base flow without jet at incidence  
Model installation in the ISL wind tunnel

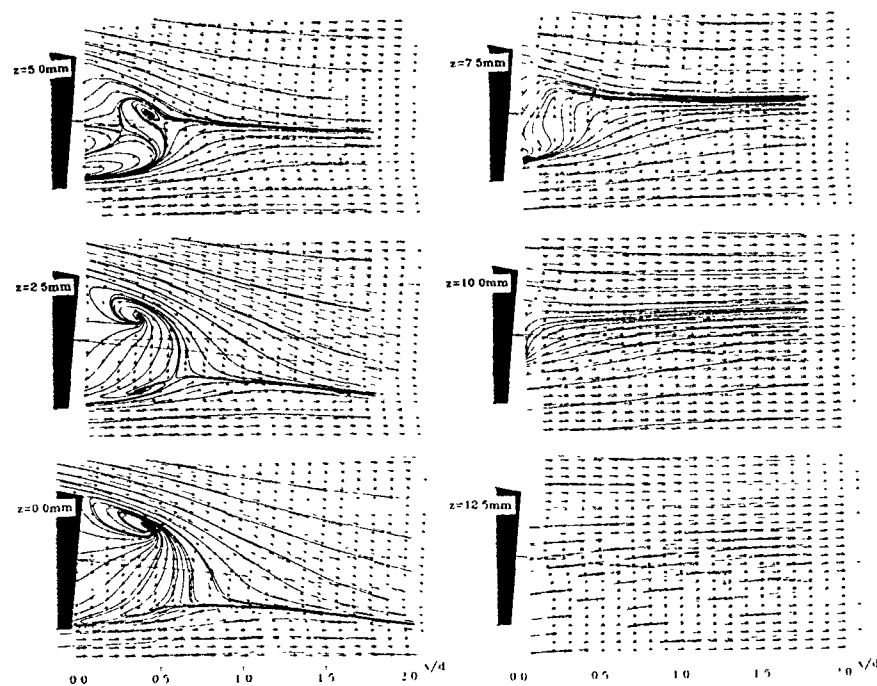


Fig. 22 - Subsonic base flow at incidence (ISL results)  
Mean velocity vector field and streamlines in  
X-Y longitudinal planes

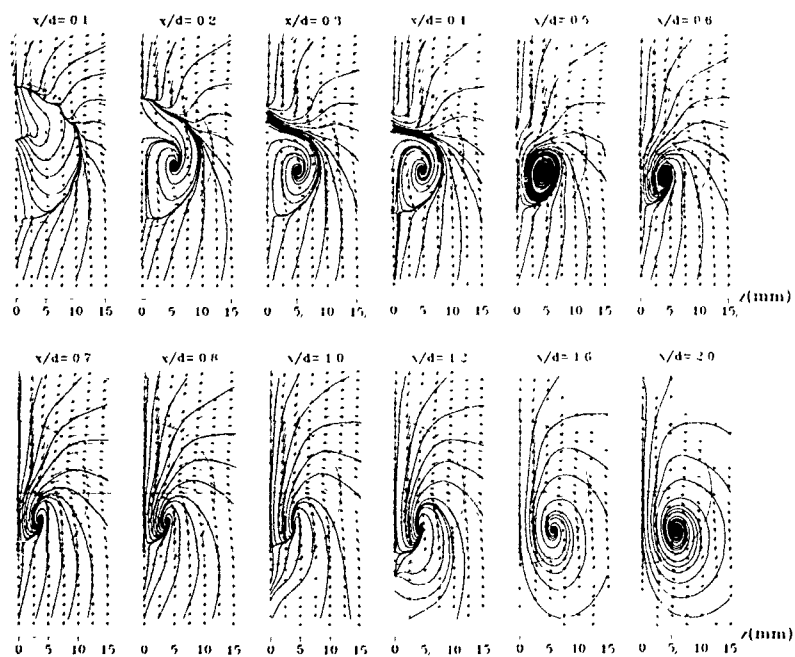
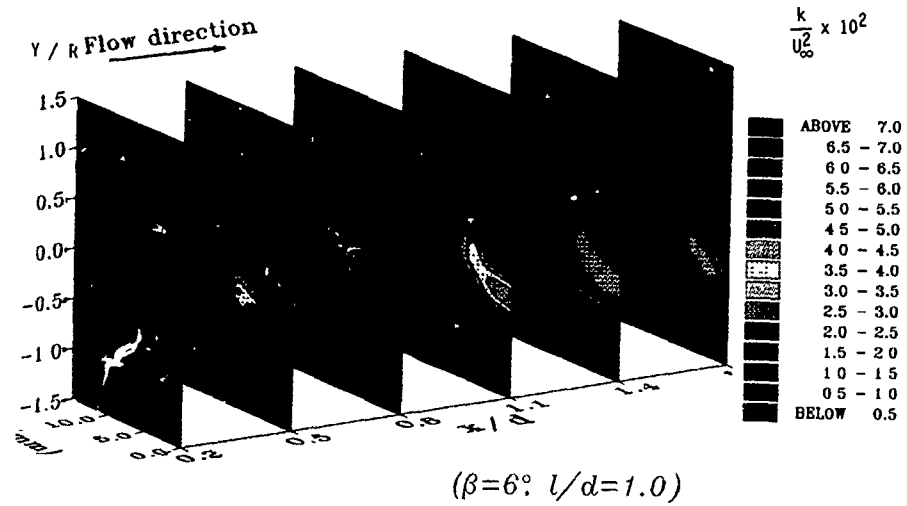
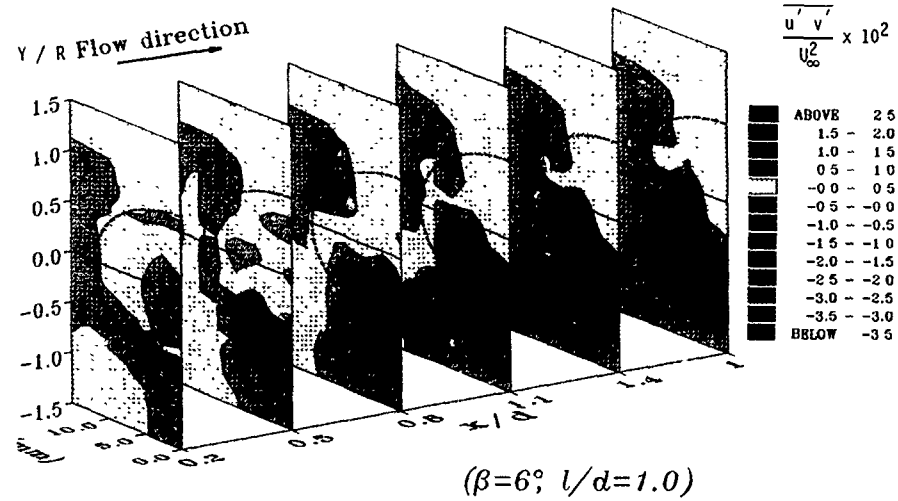


Fig. 23 - Subsonic base flow at incidence (ISL results)  
Mean velocity vector field and streamlines in  
Y-Z transverse planes



a - Contours of turbulent kinetic energy in Y-Z planes



b - Contours of Reynolds shear stress in Y-Z planes

Fig. 24 - Subsonic base flow at incidence (ISL results)  
Turbulent properties

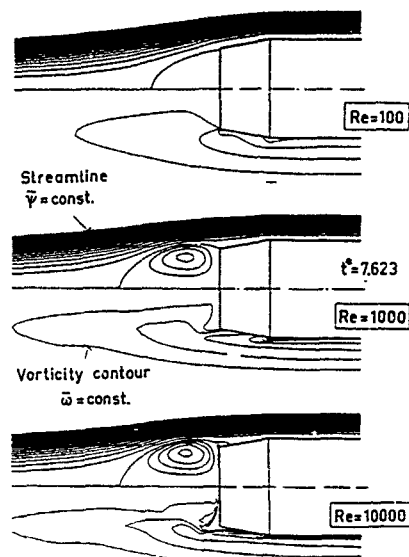


Fig. 25 - Streamlines and vorticity contours downstream of a boattailed afterbody. Influence of Reynolds number Navier-Stokes solution, ISL

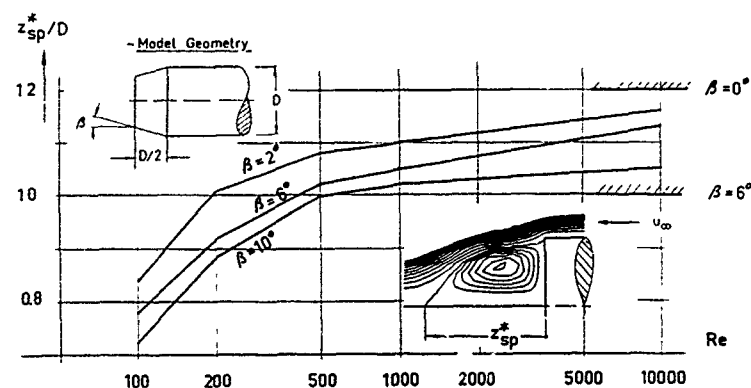


Fig. 26 - Rear free stagnation point position behind a boattailed afterbody. Influence of Reynolds number Navier-Stokes solutions, ISL

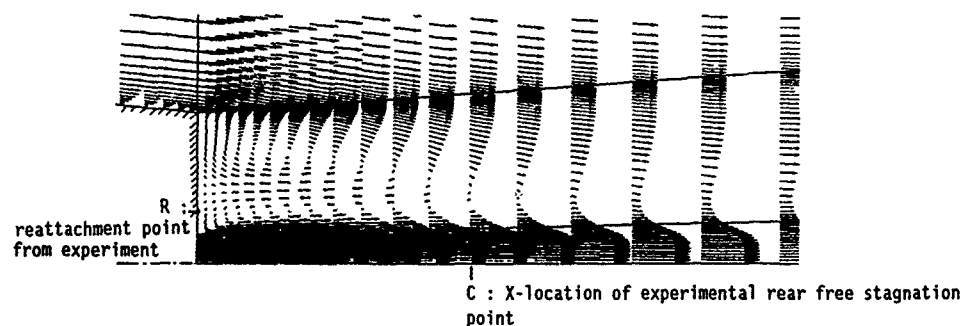


Fig. 27 - Velocity vector field for Test Case 2B Navier-Stokes solution, Dornier



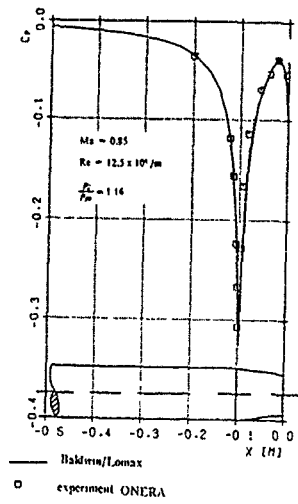


Fig. 28a - Surface pressure distribution along afterbody. Test Case 2B. Navier-Stokes solution, Dornier

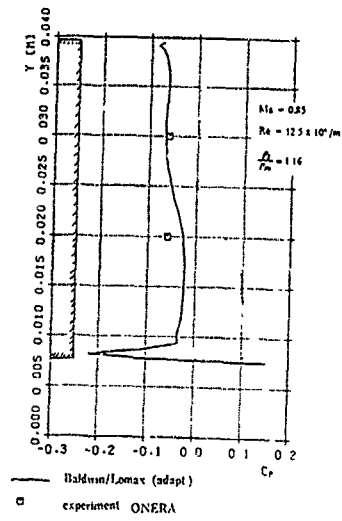


Fig. 28b - Surface pressure distribution at the base. Test Case 2B. Navier-Stokes solution, Dornier

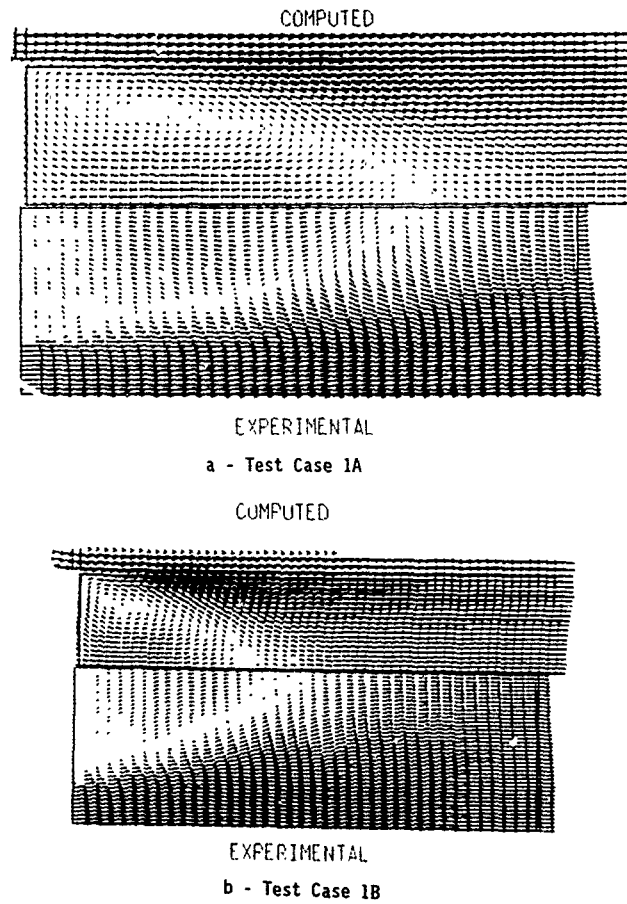
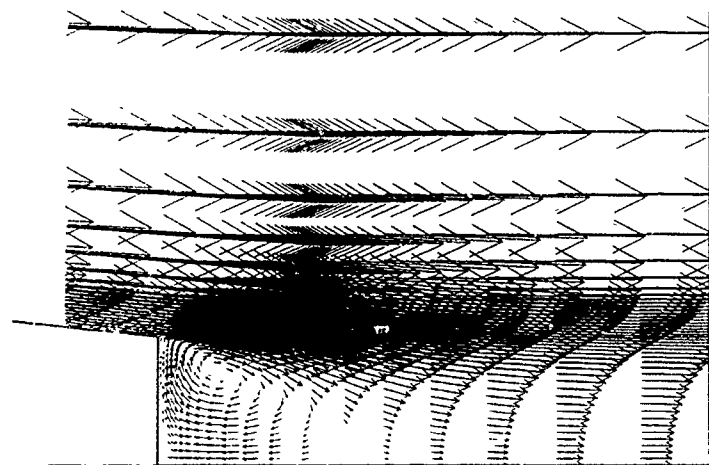
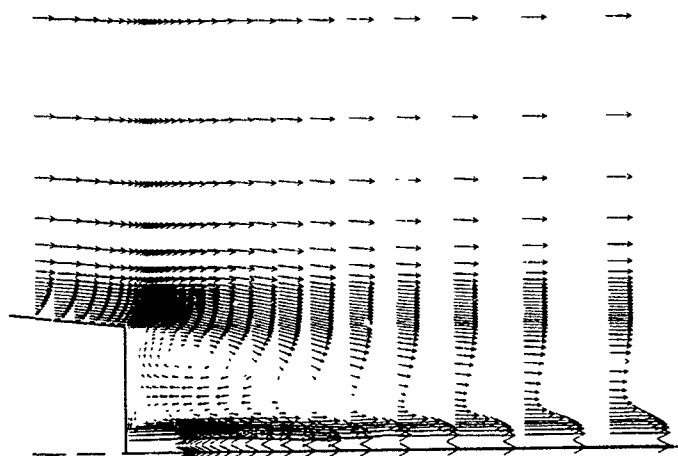


Fig. 29 - Velocity vector field  
Navier-Stokes solutions, BAe



a - Test Case 1B



b - Test Case 2B

Fig. 30 - Velocity vector field  
Navier-Stokes solutions, MATRA

## Experimental Aerodynamics for Hot Gas Jet

### Reaction Control Systems

Dr. H. Schilling  
Rheinmetall GmbH  
Ulmenstr. 125  
D-4000 Düsseldorf

R. Friedrichs & D. Christ  
Deutsche Forschungsanstalt für  
Luft- und Raumfahrt DLR  
Flughafen  
D-3300 Braunschweig

#### SUMMARY

The aerodynamic interferences which arise from the interactions between the flow around a configuration and the flow of lateral blowing thrusters are well-known in the supersonic case due to many missile applications. Here some results and experimental investigations which are planned for the very near future, are reported for the case of a subsonic configuration.

The EPHRAM concept is a terminal guided submunition which is designed to improve the hit accuracy and effectiveness of conventional artillery rounds. The flight condition for this concept is typically Mach 0.5 in low altitudes. EPHRAM is controlled by four lateral hot gas thrusters with a design based on mechanical valve switching technology. By applying lateral forces, the configuration develops an angle of attack which is utilized for flight path corrections.

Extrapolations from the literature show that there might be a negative "jet spoiler effect" reducing the aerodynamic normal forces due to interferences between the lateral jet and the configuration flow field. Therefore, experimental investigations have to be performed in order to learn more about the aerodynamic behaviour of such systems.

In a first test series, the complete model with the operating jet control system was installed in a low speed wind tunnel. The results showed that in the case under investigation there were no severe interferences. However, only a few tests could be performed for a single configuration. So additionally an experimental research program has been launched in order to learn more about the basic effects. This paper reports on the experimental apparatus which shall be used and describes the facilities that are involved in the planned tests.

The investigations show the importance of a thorough understanding of the phenomena. There is some evidence that by a suitable design the performance of subsonic concepts using jet reaction control systems can be improved considerably.

#### SYMBOLS

Symbols have been used according to ISO 1551/Flight Mechanics Standard [1]. Additional symbols are explained in the text.

## 1. INTRODUCTION

The development of new, so-called "brilliant" or "smart" ammunition for artillery applications is very important in order to improve the possibility of an effective defence against future armoured ground vehicles. The hit accuracy and therefore the effectiveness of such concepts increases drastically due to maneuvers in the terminal flight phase (top-attack capability).

One example of such newly developed systems is the EPHRAM ammunition which shall be discussed here. EPHRAM is the German acronym for "Autonomous Precision Guided Munition". Several aspects of this concept were already discussed elsewhere. In [2] the EPHRAM jet reaction control system was presented which is used to obtain the terminal maneuver capability. A trade study was made on actuator systems for artillery applications leading to the chosen concept. Ref. [3] reports on the identification of system and aerodynamic parameters from instrumented drop tests. In this paper considerations about the feasibility of investigations and some results of preliminary tests of the aerodynamic interaction between the hot gas jet reaction control system and the subsonic flowfield around the EPHRAM submunition configuration will be discussed.

In an extensive study of the literature [4] it was found that a lot of research on the interaction problem exists. At supersonic Mach numbers the aerodynamic interferences tend to increase the normal force for suitably designed configurations ("jet spoiler effect", e.g. [5,6]). A lot of experimental investigations and field studies were performed to understand this phenomenon in detail. Especially, there was the need for jet simulation in a well-defined wind tunnel environment [7,8]. In general, there is no valid formula for simulation of hot control jets. Nevertheless requirements and parameters for the simulation can be specified.

The results of the supersonic regime cannot be applied directly to the subsonic EPHRAM case. Therefore, additional experiments have to be carried out to transform and to extrapolate the experiences gained to subsonic velocities. A major problem is the simulation of the EPHRAM hot gas jet reaction control system in the wind tunnel, so that the results of the tests are transferable to free flight conditions. For this purpose a suitable test set-up and test procedures have to be established.

Next the EPHRAM concept is discussed shortly, followed by a presentation of preliminary wind tunnel tests. Then a survey of the experimental research program is presented in which basic aerodynamic effects of the flow phenomena will be investigated. Finally, some results of the programmed flight tests are given showing the effectiveness of the control system for the application discussed here.

## 2. EPHRAM CONCEPT

In different US and European development programs the feasibility of brilliant ammunition concepts is explored. The EPHRAM concept is based on the high hit probability which is characteristic for artillery systems. It is improved by a guided terminal phase of a 2-stage ammunition concept.

Fig. 1 shows a sketch of the EPHRAM projectile structure with the outer thinwall carrier, the first-stage canister, and the submunition for the terminal phase top-attack. The outer shape of the artillery round corresponds to conventional artillery projectiles like the well-known M483A1. Therefore, the usual firing tables can be used with a suitable addendum. Of course, the weight, the moments of inertia, and the position of the center of gravity of the EPHRAM round have to be adjusted properly. The main components of the tactical submunition are indicated additionally.

The overall function of the system is explained in fig. 2. The complete round is fired like a conventional artillery round. The first separation takes place at a certain point on the ballistic trajectory of the shell. The thinwall canister is pulled out at approx. Mach 1 and up to 200 Hz spin rate. It is despun and decelerated by different sets of spin brakes and a parachute, resp. When suitable environmental conditions have been reached (approx. 150 m/sec and less than 10 Hz), the EPHRAM submunition is pulled out of the canister. For initial stabilization the parachute remains attached until the wings of the submunition have been deployed and guarantee stable flight behaviour with almost vanishing spin rate. Then the rear part of the canister is separated, and the submunition starts its controlled terminal maneuver. A variety of flight paths can be preprogrammed; the particular one chosen depends on the seeker performance characteristics and on the constraints of the terminal maneuver.

In fig. 3 a cut through the submunition drop test configuration shows its main components like jet reaction control system, autopilot, instrumentation package, battery, and flight data recorder. The shaped charge warhead is replaced by a soft recovery system, moreover the hemispherical nose is used as a five hole pressure probe.

The submunition is controlled by a lateral blowing jet reaction control system, fig. 4. Its radial thrust forces cause changes in pitch and yaw and, consequently, angle of

incidence and sideslip. This results in high lift from the eight large wings which is sufficient to perform the commanded maneuvers and to achieve the desired footprints. The decision to use a jet reaction control system was made by trade studies and by additional considerations which technology has the potential for next generation designs. This concept offers a growth potential to higher performances, longer flight time as propellants will improve, and increased cost effectiveness by application of fluidic amplifier arrangements.

### 3. AERODYNAMIC CHARACTERISTICS AND DLR WIND TUNNEL TEST RESULTS

The aerodynamic design of the EPHRAM submunition was a very important task in order to achieve the necessary maneuver capability. First a large number of trade studies was performed to optimize the geometric parameters of the configuration. Finally, a fin-body-combination with eight large wings was selected. The high number of wings was chosen in order to maximize lift and to decouple the aerodynamic behaviour from roll position (no dependency of aerodynamic coefficients on roll angle). There have been different approaches for the wing profile, ranging from a NACA0012 profile to a simple flat plate with rounded front corners. Further investigations have been made for various wing positions and nose configurations.

In a second step, five detailed experimental test series have been performed for the case without blowing thrusters in order to establish an aerodynamic model for the 6-DoF-simulations. Two different wind tunnels of the DLR were used, namely the 3.25 m x 2.80 m low speed wind tunnel (NVB) and the 0.8 m x 0.8 m low speed facility (MUB) in Braunschweig. Fig. 5 shows a photo of the NVB test section; this photo was made while the EPHRAM configuration was mounted on a rotary balance. The selection of the large wind tunnel guaranteed an almost perfect simulation with results very close to reality, whereas the smaller tunnel was useful because of its lower costs. The wind tunnel corrections for the MUB were established experimentally.

Some typical aerodynamic results for the EPHRAM drop test configuration are shown in the next figures. For this configuration the simple wing profile was chosen (rounded flat plate). Fig. 6 shows a comparison between 2 and 8 wings with NACA profile and flat plate, resp. The flat plate version shows a better and smoother normal force performance, however, the contrary holds for the glide number, fig. 7. This is due to the differences in the tangential force, which could be expected, fig. 8. The overall normal force and pitching moment of the submunition can be taken from fig. 9. It can be seen that due to the large number of wings there is no sudden breakdown of the normal force (cf. fig. 6). There is a smooth and gradually increasing flow separation from the different wings leading to very smooth characteristics of the configuration.

The EPHRAM concept is not roll-stabilized. For the terminal phase, however, a roll rate of less than 1 Hz is required. The roll damping coefficient of the configuration is expected to be very large due to the large wings. So additional wind tunnel tests have been made to establish the dynamic roll data of the configuration. Fig. 10 shows the roll damping coefficient vs. the angle of attack for different roll rates. The sharp decrease is remarkable, it is due to separation effects.

For system identification purposes, the EPHRAM hemispherical nose was modified as a five-hole pressure probe in order to identify the actual angles of attack and angles of sideslip during the instrumented programmed flight tests [9].

After completion of the various wind tunnel tests the results were verified by drop tests without burning actuation systems. The high quality of the aerodynamic model was substantiated. However, there was the need to learn more about the influence of the working lateral thrusters on the coefficients. Therefore, another program was started at the wind tunnel of the university of Erlangen.

### 4. ERLANGEN WIND TUNNEL TESTS WITH WORKING THRUSTERS

The Erlangen wind tunnel is a horizontal tunnel of the "Goettingen type" with an open 1 m x 1 m test section and a wind speed of 60 m/sec. The aerodynamic coefficients were measured with the help of an external three-component balance which was installed above the test section (cf. fig. 11). The angle of attack could be varied between 0° and +20°. Figs. 12 and 13 show a comparison of the aerodynamic coefficients between this wind tunnel and the NVB. There are only small discrepancies in the test results.

In order to get information about the desired influence of the interference effects, slightly modified lateral thrusters were used which replaced the mechanical switching valve system of the original EPHRAM configuration by a simple nozzle system with mechanical relief valves. These provide a constant pressure in the combustion chamber to ensure optimal propellant burning at a constant burning rate. Moreover, pressure peaks are avoided which would perhaps cause a bursting of the combustion chamber due to material stress.

The EPHRAM actuator block consists of four individually controllable thrusters packaged in one common housing. For the wind tunnel tests, however, only one of them was necessary. It was possible to obtain the influence of the lateral jets on the aerodynamic coefficients in the different directions by blowing out upwards, sideways, or downwards, resp. The case of force-free blowing out could not be simulated.

The item of security, of course, was a major problem during the wind tunnel tests. So additionally to the mentioned relief valve a second safety unit on the basis of stagnation pressure was used. The gas generator used a solid propellant which was designed to act as an end burning constant area type producing a clean hot gas at a comparatively low flame temperature of about 1500 K. The jet Mach number was approximately 3.3.

Fig. 14 shows a typical result of the influence of a lateral blowing jet on the normal force coefficient (10 deg. angle of attack, upwards blowing). The flow velocity was 55 m/sec, the burning time of the motor was roughly 20 sec. The nominal lateral force, which was produced by the jet (without interference from the flowfield), was approx. 60 N. In figs. 15 - 17 the experimental results for the aerodynamic forces in the vertical plane are given neglecting the constant jet thrust force. Fig. 18 shows the normal force and the pitching moment as functions of the configuration roll angle for a fixed angle of attack (roll angle 0°: upwards blowing).

From the diagrams one can draw the following conclusions:

- The tangential force is slightly influenced by the lateral blowing jet. This result could be expected. The strong increase for the case of a sideways blowing jet at 20° angle of attack cannot be explained.
- For the normal force there are small variations as a function of the angle of attack and the position of the lateral jet. No positive jet spoiler effect could be detected. The maximum deviations to the case without interference were obtained at approx. 120° jet roll angle at 10° angle of attack (4 o'clock position). Thus the working thrusters tend to reduce the aerodynamic forces slightly and to induce side forces. Similar results were obtained for the pitching moment data. As a consequence, the position of the center of pressure varies only slightly with engine switched on.
- Under the given conditions the axial position of the radial blowing jet is influenced only a little by the oncoming flow which can be shown with the help of IR-photos.

These first results from an idealized wind tunnel environment show that there are additional forces and moments which arise from the aerodynamic interferences under investigation. However, these tests can only be a first approximation to the real conditions for different reasons. Firstly, an extrapolation of the results to higher flight velocities is very difficult, because the ratio of flight velocity to jet velocity can be larger up to a factor of 5. Secondly, the dynamic effects of the bang-bang characteristics of the actuator system could not be simulated. Thirdly, only a few parameters could be varied in the wind tunnel tests, and due to the high costs the experimental values could not be validated in all cases by repetitions of the tests. Until now there has been no systematic investigation of the problem under controlled realistic conditions. Therefore, a feasibility study has been initiated at the DLR in order to prove the possibility to simulate the interference between a lateral blowing jet and the outer flow in a low speed wind tunnel.

## 5. EXPERIMENTAL RESEARCH PROGRAM AT THE DLR

### 5.1 Basic Considerations on Control Jet Simulation

In order to simulate control jets in a wind tunnel, suitable test conditions have to be established first so that the results of the tests are transferable to free flight conditions.

The characteristic EPHRAM submunition flight velocity is 150 m/sec, which is the basis for the following considerations. Its control jet system has a bang-bang characteristic of 8 msec duration. From a chamber of about 1500 K total temperature the combustion gas flows through a conical nozzle and reaches a Mach number of 3.3 and a temperature of 800 K at the nozzle exit.

For measurements in a low speed wind tunnel, however, it is necessary to generate a continuous and constant control jet due to the length of the needed test period. Thus hot gas thrusters can be used only for comparison. Additionally, in a wind tunnel with a closed circuit like that at Braunschweig only media which are non-corroding and not toxic should be used.

For the jet simulation with the projected EPHRAM submunition configuration both near as well as far-field effects have to be taken into account. In the near field the jet has to be simulated in such a way that the pressure distribution on the model surface in the vicinity of the nozzle is equivalent to that of the original. Because in the present case wind tunnel model and original have the same scale, the jet exit areas of both are equal, however, the initial bell-shaped jet boundary has to be duplicated, too. Moreover, the wings of the submunition can be located near to the control jet. Thus the deflection of the jets caused by the wind tunnel flow (i.e. far-field effects) has to be adjusted as close as possible to free-flight conditions.

There is a strong influence of the combustion gas on the quality of the wind tunnel simulation. The jet exit temperature influences the angle of jet expansion in the bell-shaped part. Furthermore, the decay of the jet occurs earlier with a hot gas than with a cold one. So in wind tunnel tests the hot combustion gas cannot be replaced simply by cold air; this would result in substantial restrictions to the simulation quality.

In order to fulfill the requirements on jet simulation in the near and the long range, essentially three simulation parameters have to be considered which are drawn from the study of literature [4], fig. 19:

- o The geometric similarity, eq. (1), of the model and the original is guaranteed (scaling factor of 1:1), therefore the exit areas are equal.
- o The choice of the simulation gas follows from eq. (2). To reach the required value of the thermodynamic quantity  $(RT)_j$  of the original configuration (left hand side of the equation), it is necessary to choose a high gas constant  $R$  if the exit temperature  $T$  of the simulation gas must be kept low. This holds for helium which is repeatedly stated in the literature as a qualified gas for simulation of a hot combustion gas.

The computation of the required total temperature of the simulation gas in the nozzle chamber at a given Mach number results in a temperature of 310 K for helium. In comparison, for air the resulting temperature would be 1500 K. Thus eq. (2) is fulfilled with helium at ambient temperature, whereas air would have to be heated up very strongly. This would result in large technical problems like a strong heating of the wind tunnel model due to the required long test periods in the low speed wind tunnel. An increase of the temperature of the model surface, however, will effect both the boundary layer and the pressure distribution considerably. Cooling of the model surface is an extremely difficult technical task for wind tunnel force measurements with a strain gauge balance. This problem does not exist for the original configuration, because the propelling charges have a short burning time of only about 10 sec.

For these reasons the use of helium is proposed for the simulation of control jets.

- o The third of the simulation parameters is the momentum ratio between the control jet and the free flow for the original configuration and the model, eq. (3) ( $\rho$ : density,  $V$ : velocity). In the low speed wind tunnel at Braunschweig only a maximum free stream velocity of 85 m/s is available, although the free stream velocity of the original is 150 m/s. Therefore the exit Mach number of the simulation jet has to be calculated such that eq. (3) holds. Assuming total expansion in the nozzle, an exit Mach number of 1.6 for helium is obtained. This corresponds to a jet exit velocity of 1175 m/sec. The total pressure is 4.5 bar with a required mass flow of 0.02 kg/sec. With these data it is possible to simulate the characteristics of the EPHRAM nozzle flow. The nozzle can be designed to have the same exit area and jet exit angle like the original configuration.

From these considerations it can be concluded that there is the possibility to simulate the EPHRAM submunition conditions and nozzle and control jet characteristics, resp., in a low speed wind tunnel, if cold helium is used instead of the original combustion flow.

### 5.2 Test Set-Up and Model Requirements

In order to obtain the influence of control jets on the aerodynamic characteristics of the EPHRAM submunition, overall force and momentum measurements are planned with a six-component strain gauge balance installed inside the model. There are two possibilities for the test set-up: either to separate the gas supply system with the nozzles mechanically from the balance-model-arrangement or to treat it as one unit.

After careful considerations the decision was made for the first possibility. It promises the most exact results, because only the aerodynamic forces and moments are measured without any disturbing reactions and deformations induced by the internal jet supply arrangement. However, the suspensions for both the gas supply system and the model must be designed especially stiff, and a special six-component balance with small deformations has to be chosen.

In addition to the force measurements pressure measurements in the vicinity of the nozzles should be performed to investigate the characteristic features of the aerodynamic interferences at least in the near field.

There is the danger that the interference of the control jets could be falsified indirectly by the gas supply system, because the initial turbulence generated by installations in the supply system has a strong influence on the core length of the jet and therefore on the development of the jet axis and the long-range effects, too. For these reasons the plenum chamber of the jet has to be designed with special care.

For the measurement of the mass flow of the jet medium, which may be difficult due to the small values, turbine gas-meters are recommended. The control of the mass flow and of the necessarily constant level of the pressure in the plenum chamber can be guaranteed only with special control devices. To achieve an uniform and reproducible flow in the gas supply system, a storage tank should be used. To avoid longer adjustment times and larger gas losses a quick shut-off valve with remote control has to be installed in the supply pipe near the model.

Fig. 20 shows a sketch of the planned test set-up which is needed for the jet simulation in the low speed wind tunnel.

### 5.3 Test Program

The test program is divided into pre-tests and main tests, resp. The pre-tests are used for the validation of the method of jet simulation, the measuring techniques, and the test of the flow-field visualization likewise. For this first part cold air will be used due to cost effectiveness, however, the validation of the jet simulation has to be done by comparing hot gas thruster results with helium data. A part of the tests in this early stage can be performed separate from the wind tunnel environment: for the simulation of the near-field effects and the test of the gas supply system the use of a simplified model without outer flow is sufficient.

The objectives of the main tests are force measurements, pressure measurements on the model surface in the vicinity of the jet nozzles, and visual investigations of the flow (e.g. Schlieren and IR pictures). The subsonic jet spoiler effect (if it exists) will be investigated quantitatively and qualitatively. Moreover, a number of different wing-body configurations will be examined to learn more about the influence of geometric parameters. Of course, the EPHRAM configuration itself will be optimized on the basis of the experimental results.

## 6. EPHRAM INSTRUMENTED DROP TESTS / PROGRAMMED FLIGHT

During the development of the EPHRAM system the performance of the overall system could be demonstrated successfully. Parallel to these gun hardening tests drop tests were performed in order to demonstrate the stable flight behaviour of the submunition, the function of the recovery system, and the terminal maneuver capability of the submunition. Fig. 21 shows the profile of the programmed drop tests. EPHRAM was dropped from an instrumented platform which was fixed under a helicopter. This platform had to deliver the necessary initial flight data of the submunition. After a free-flight phase suitable environmental conditions were reached and the actuator was initiated: the submunition flew a controlled lateral maneuver. After the burn-out of the engine the recovery system was activated for a soft landing.

It could be shown in several tests that the EPHRAM control system worked properly and delivered the desired lateral acceleration. Fig. 22 shows cine-theodolite data of one of the drop tests. It can be seen that a footprint of the order of 500 m is delivered which agrees very well with the simulations, fig. 23. All the tests were evaluated with system identification methods [3] which showed a good agreement between the experimental wind tunnel data and the identified parameters.



## 7. CONCLUSIONS

For a smart submunition application the aerodynamic effect of a hot gas jet reaction system on the subsonic aerodynamic characteristics is investigated. On the basis of conventional force and moment measurements without jet a preliminary wind tunnel test series with original thrusters was performed which showed the importance of a thorough understanding of the interaction phenomenon. Therefore a feasibility study on jet simulation in a low speed wind tunnel was accomplished. The results of this study show that such a simulation is possible if the hot combustion gas is replaced by cold helium and if a 1:1 scale model is used. The test set-up and the model requirements are discussed. Finally, an overview on the planned test program is given.

The results of some instrumented drop tests with the EPHRAM submunition indicate the effectivity of the chosen control concept. Until now there are too many open questions about the interaction problem, however. It is hoped that detailed answers can be given when the proposed extensive wind tunnel program has been performed.

## 8. REFERENCES

- [1] LN 9300 Blatt 1: Flugmechanik  
Normenstelle der Luftfahrt, D-7022 Lauffelden, 1970
- [2] Peller, H., Büchele-Buecher, S.  
Jet Reaction Control System for Autonomous Precision Munition  
AGARD CP 411, 1987
- [3] Doherr, K.-P., Lehmann, G., Schilling, H.  
Identification of Stability and Control Parameters of a Brilliant  
Ammunition  
AGARD 72nd FMP-Symp. "Stability & Control of Tactical Missiles",  
Ankara 1988
- [4] Christ, D., Friedrichs, R.  
Studie zur Simulation von Steuerstrahlen an einem Flugkörper im Unterschall  
DFVLR-IB-19111-87 C 16, 1987
- [5] Gilman, B.G.  
Control Jet Interaction  
J. Spacecraft 8 (1971)
- [6] Leplat, M., Champigny, P., Robert, M.  
Interactions Aerodynamiques De Jets Transversaux Sur Missiles  
AGARD/GCP-Symposium, Greece 1987
- [7] Osterhout, D.S.  
An Experimental Investigation of a Cold Jet Emitting from a Body of Revolution  
into a Subsonic Free Stream  
NASA CR-2089, 1972
- [8] Pindzola, M.  
Jet Simulation in Ground Test Facilities  
AGARDograph 79, 1963
- [9] Doherr, K.-P., Weiß, S.  
Mathematisches Modell mit nur einem Parameter für eine halbkugelförmige  
Fünflochsonde  
DLR IB 111-88-51  
to be published in the ZFW

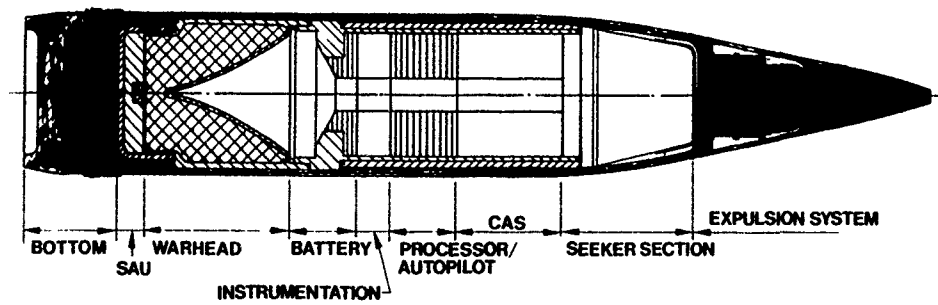


Fig. 1: EPHRAM projectile structure

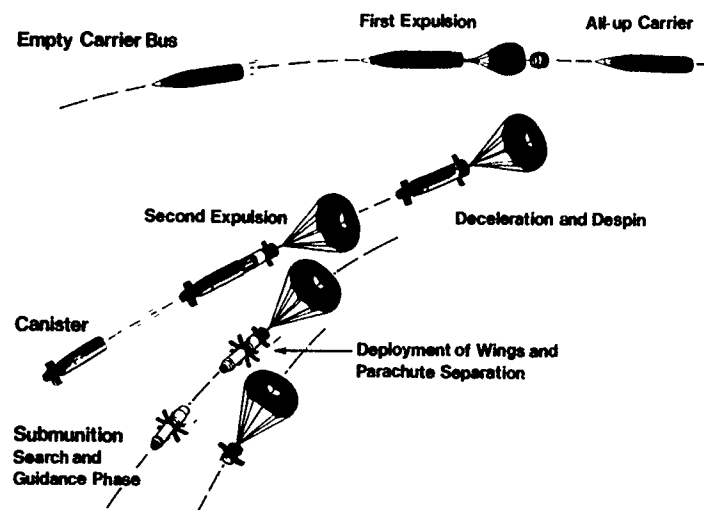


Fig. 2: Functional sequence

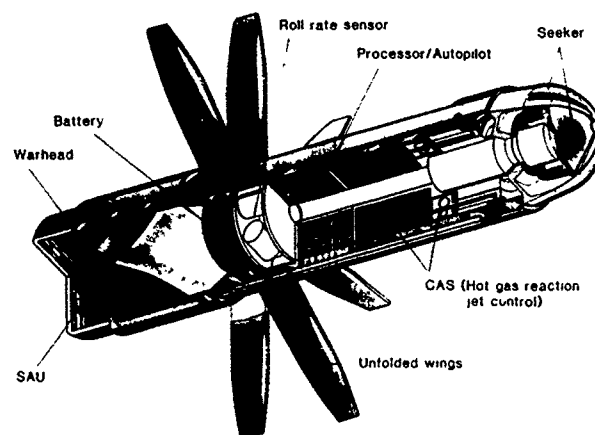


Fig. 3: Drop test submunition configuration

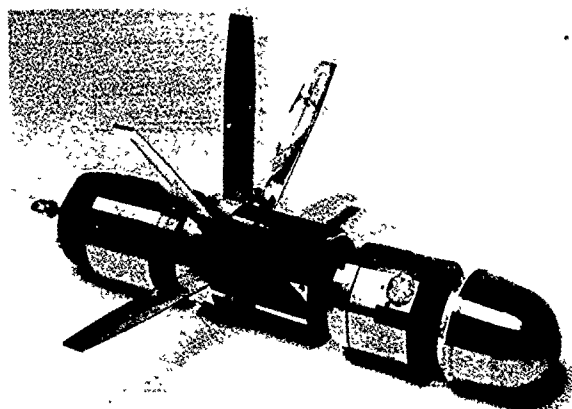


Fig. 4: Main parts of drop test configuration

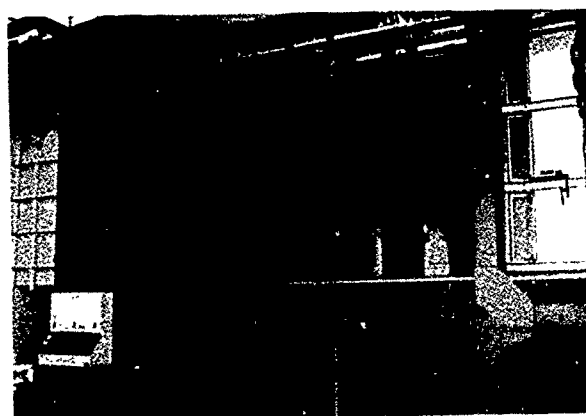


Fig. 5: Closed NWB test section with opened door

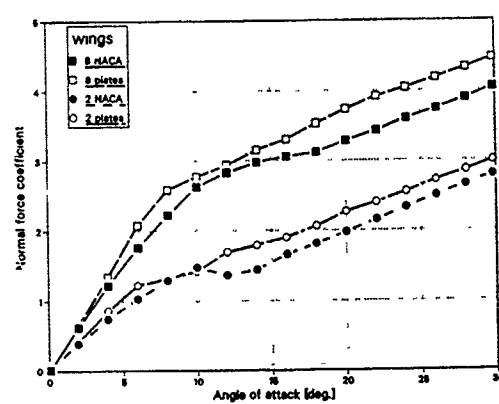


Fig. 6: Comparison of normal force coefficients for different wing profiles and numbers of wings

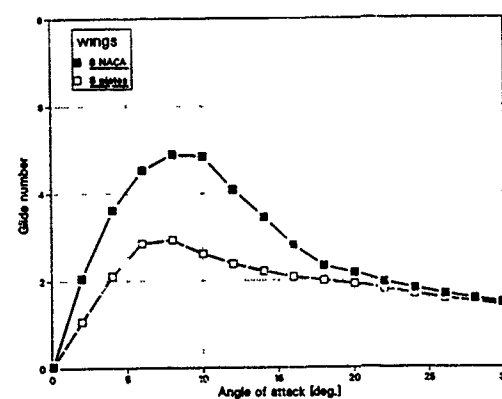


Fig. 7: Glide numbers for different wing profiles

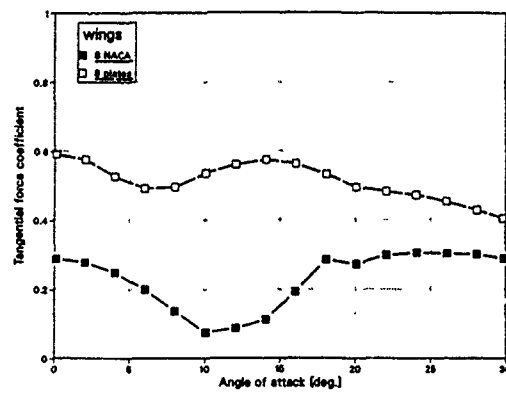


Fig. 8: Tangential force for different wing profiles

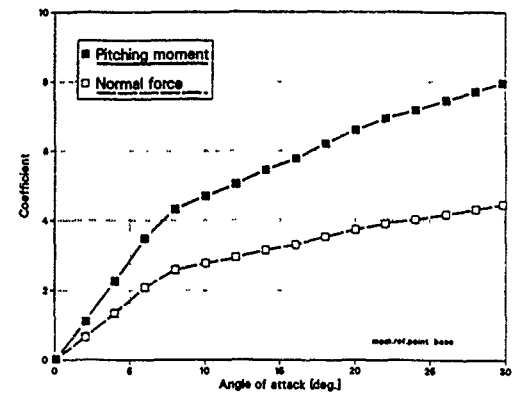


Fig. 9: Pitching moment and normal force

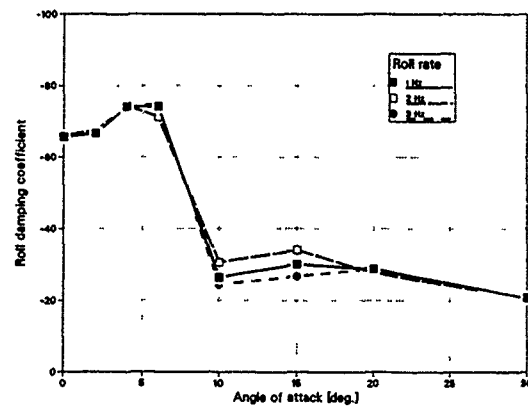


Fig. 10: Roll damping coefficient



Fig. 11: Erlangen wind tunnel test setup

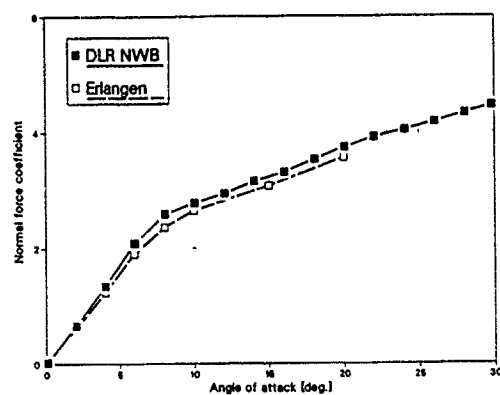


Fig. 12: Comparison of normal force measurements

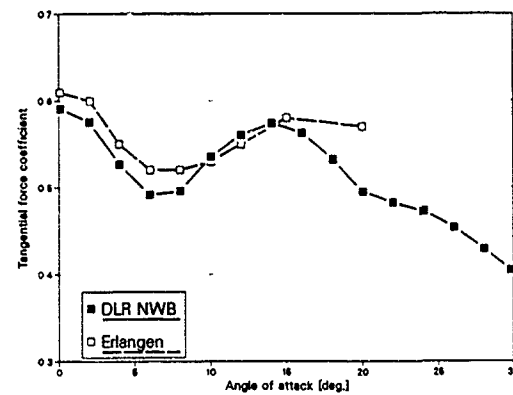


Fig. 13: Comparison of tangential force measurements

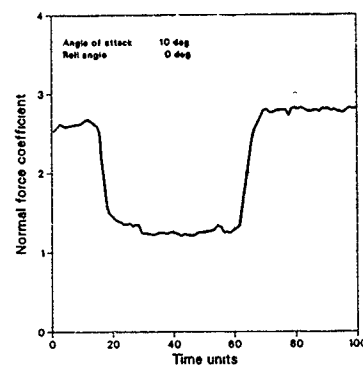


Fig. 14: Time history of wind tunnel test with working motor

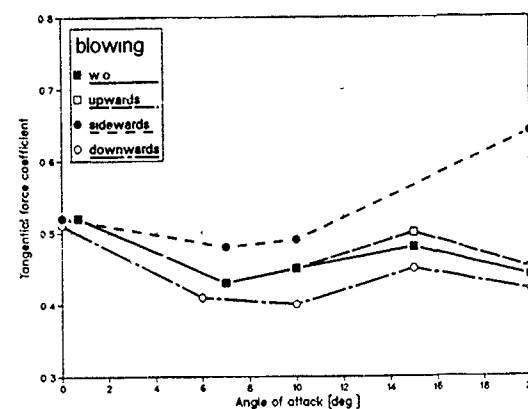


Fig. 15: Influence of aerodynamic interferences on tangential force

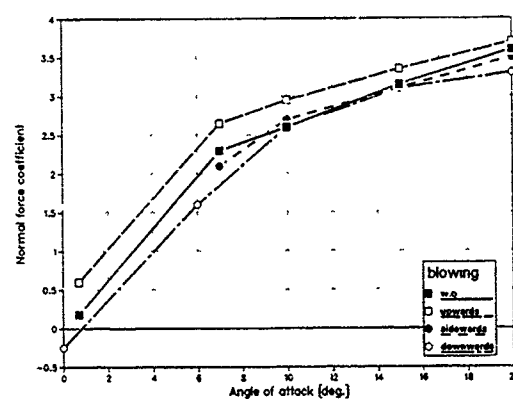


Fig. 16: Influence of aerodynamic interferences on normal force

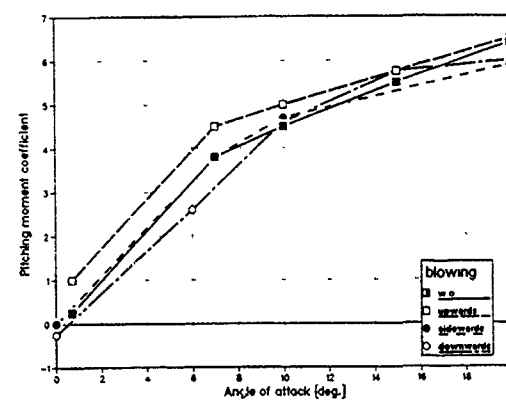


Fig. 17: Influence of aerodynamic interferences on pitching moment

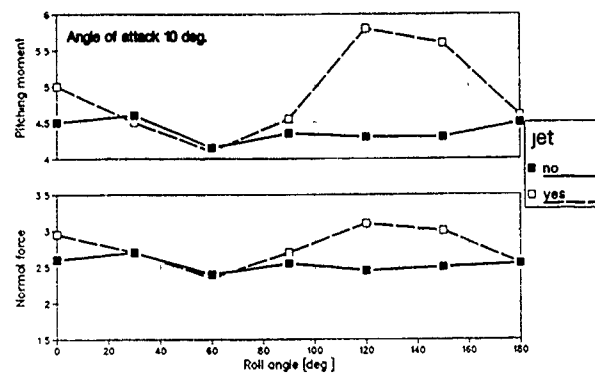


Fig. 18 : Aerodynamic coefficients vs. jet roll angle

$$A_{jf} = A_{jm} \quad (1)$$

$$(R \cdot T)_{jf} \approx (R \cdot T)_{jm} \quad (2)$$

$$(e_j V_j^2 / e_\infty V_\infty^2)_f = (e_j V_j^2 / e_\infty V_\infty^2)_m \quad (3)$$

**Subscripts :**  
 f - full scale, original  
 j - conditions at the jet nozzle exit  
 m - model  
 ∞ - free stream

Fig. 19 : Simulation parameters for hot gas jet reaction control

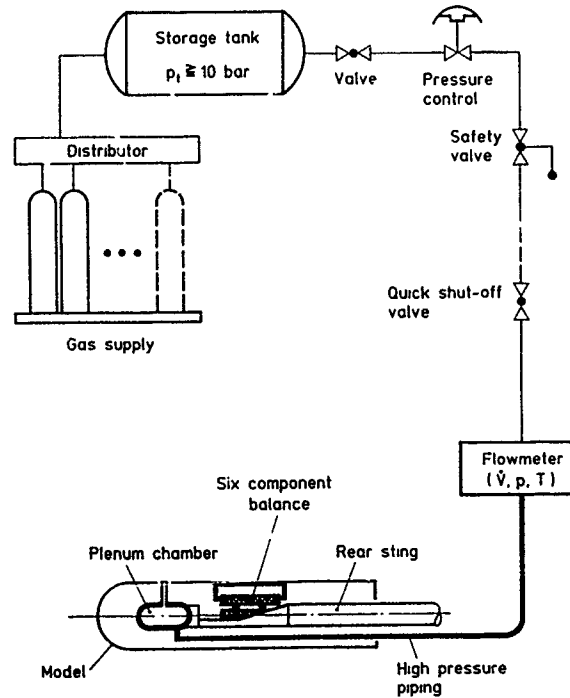


Fig. 20 : Block diagram for jet simulation

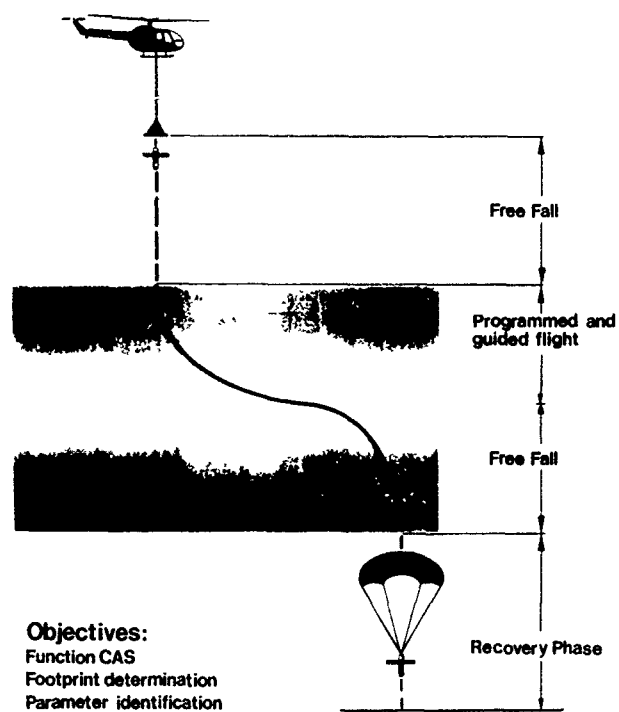


Fig. 21: Sketch of programmed drop test

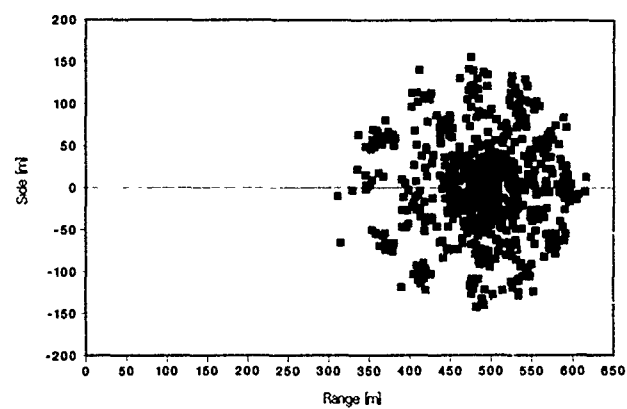


Fig. 23: EPHARAM Monte Carlo simulation results (incl. wind)

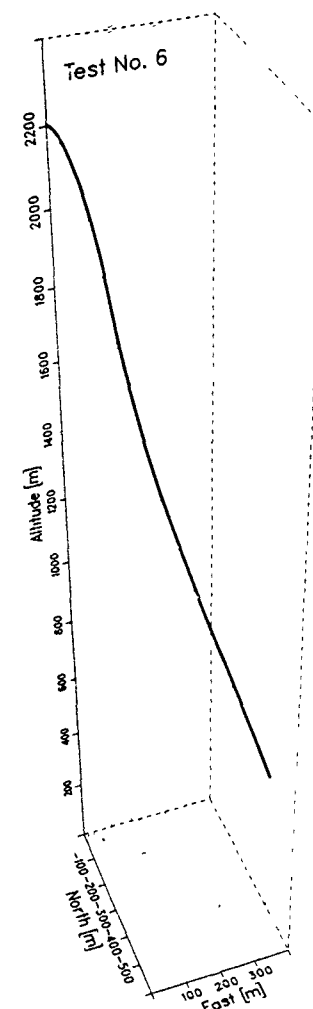


Fig. 22: Typical drop test result

# LAMINAR / TURBULENT FLOW TRANSITION EFFECTS ON HIGH-SPEED MISSILE DOMES

Uwe G. Hingst

BODENSEEWERK GERÄTECHNIK GMBH  
INTELLIGENT SYSTEMS DIVISION  
NUSSDORFER Str. - D-7770 ÜBERLINGEN  
FRG

## SUMMARY

The new generation of high-speed short range missile has to withstand extreme aerokinetic heating. For IR seeking missiles with its fragile domes the aerokinetic heating effects make further velocity increase difficult. The main driving parameter is the aerothermodynamically imposed stress within the IR-window material. The induced thermal stress is a function of the aerodynamic flow properties around the missile dome, the relevant local boundary layer characteristics and the resulting aerokinetic heating. The paper deals with the analysis of the heat transfer coefficients and resulting temperature fields on hemispherical domes for the laminar and turbulent flow and especially for the transient behaviour in between. It will be demonstrated that just the boundary transition from the laminar to the turbulent flow has a significant influence on the imposed window stress. The study investigates the different influences of the characteristic Reynolds-Numbers, start and end of transition zone and the resulting stress parameters. Problems related to the definition of correct transition behaviour are discussed.

## LIST OF SYMBOLS

$c_p$	spec. heat capacity
$D$	dome diameter
$f$	form coefficient
$M$	Mach-Number
$Nu$	Nusselt-Number
$Pr$	Prandtl-Number
$p$	pressure
$\dot{q}$	heat transfer
$r$	Recovery factor
$R$	ideal gas constant, dome radius
$s$	flow length (on dome)
$St$	Stranton-Number
$T$	temperature
$\Delta T$	temperature gradient
$u$	air velocity

## GREEK SYMBOLS

$\alpha$	heat transfer coefficient
$\beta$	velocity gradient

$\beta_o$	pressure gradient
$\rho$	density
$K$	ratio of thermal capacities
$\phi$	dome angle
$\mu$	dynamic viscosity
$\nu$	kinematic viscosity
$\lambda$	heat conductivity
$\gamma$	intermittance factor
$\theta$	momentum thickness
$\tau$	(missile flight) time
$\sigma$	stress (mechanical)

## SUBSCRIPTS

$b$	begin of transition area
$B$	bending
$D$	dome, down stream
$G$	gas
$l$	laminar
$t$	turbulent
$w$	wall, dome surface
$\delta$	edge of boundary layer
$R$	Recovery, radial
$\infty$	ambient environment
$2$	stagnation point

## 1. INTRODUCTION

The new generation of high-speed short range missiles has to withstand extreme aerokinetic heating. The heating effects impose severe thermal stresses onto the dome material in such a way that for IR seeking missiles with its fragile domes the aerokinetic heating makes further velocity increase difficult. To extend the velocity ranges of short range missiles as far as possible a full understanding of all stress imposing parameters must be available and its influence on other missile performance parameters well-known. With this knowledge the best compromise between all missile parameters - including the stress parameter - can be found. This report deals with the transition behaviour of the laminar/turbulent flow onto the imposed thermal stress for hemispherical IR-domes.



## 2. PERFORMANCE REQUIREMENTS

The new requirements for high velocity missiles result in high Ma-Numbers within a very short time, demanding an optimum of aerodynamic design, a tolerable aerokinetic heating and a limited imposed thermal and mechanical stress within the IR-dome.

As a consequence the high velocity profiles have an influence on the performance of the IR-seeker:

- o For the IR performance it is the mean dome temperature and the temperature distribution over the dome which has a strong influence on the IR transmission and detectivity. The radial temperature gradients through the dome material as a function of the transient flow behaviour have a basic influence on the imposed thermal stress.
- o In addition optical effects of the boundary layer and the shock wave-like blurring and foresight errors - have also to be considered.
- o The radiation of gases between the shock wave and the outer surface of the window may influence the infra-red acquisition capabilities of the seeker.
- o Last not least the dome must have sufficient environmental protection to withstand the thermal stress as well as possible hail or rain impact.

From the aerodynamic drag point of view slender bodies with nose cones are the best approach, whereas from thermal point of view blunt bodies reduce the aerokinetic impact and therewith the resulting thermal stress. A large thickness of the IR-window materials promotes the resistance against hail and rain impact, provides slower temperature increase due to the greater material heat capacity, but reduces significantly the thermal stress resistance. A reduced dome thickness allows higher missile velocities due to smaller thermal stress impact. A good missile dome layout results therefore in a compromise between different opposing requirements:

- o LOW AERODYNAMIC DRAG
- o LOW AEROKINETIC HEATING and
- o SMALL IMPOSED THERMAL AND MECHANICAL STRESS

leading to an optimised KINEMATIC MISSILE PERFORMANCE as demonstrated hereafter in Fig. 1.

As an example for such a missile performance optimisation, the missile flight parameters as given in Fig. 2 and 3 and a hemispherical dome layout (Fig. 4) shall

form the basis for our following considerations on dome stress and its influencing parameters.

The Ma-Number ranges - given as function of the flight altitude (Fig. 2) extend for high altitudes into the hypersonic range. The typical velocity profiles for a selected missile layout as function of the flight Ma-Number versus flight time is changing with the launch altitude as demonstrated in Fig. 3. It is obvious that for modern SHORT RANGE MISSILES the max. Ma-Numbers are going up to Ma 6 - 7. The relevant missile flight times are in the order of 15 to 30 secs. The flight profiles are derived for a slender missile with a hemispherical dome and a dome diameter of about 10 cm. The dome is fixed to an ogive structure. Fig. 4 illustrates the wind-tunnel test-model.

## 3. AEROKINETIC HEATING ANALYSIS

One of the main driving parameters in modern missile layout is the correct calculation of the aerothermodynamically imposed stress within the IR-window material for the hemispherical dome shape. The induced stress is a function of the aerodynamic flow around the dome, of the relevant local boundary layer characteristics and the resulting aerokinetic heating. For the heat transfer calculations standard procedures will be used.

The heat transfer  $q$  from the boundary layer to the dome surface for laminar and turbulent flow is calculated via the Stanton- or Nusselt-Number (1) by equation (2) as given by E. R. van Driest [1] and L. Lees [2]:

$$St_{l,t} = \frac{q_w}{\rho_j \cdot u_j \cdot c_{p,j}} = \frac{Nu}{Re_x \cdot Pr} \quad (1)$$

$$\dot{q}_{l,t} = St_{l,t} \cdot \rho_j \cdot u_j \cdot c_{p,j} \cdot (T_R - T_w) \quad (2)$$

$T_R$  is the Recovery-Temperature

$$T_R = T_\infty \left( 1 + r_{l,t} \cdot \frac{K-1}{2} M_\infty^2 \right) \quad (3)$$

The velocity distribution around the dome  $u_\delta$  is

$$u_\delta = \frac{u_\infty}{\gamma} \left\{ \frac{8[(K-1)M_\infty^2+2]}{(K+1)M_\infty^2} \cdot \left[ 1 + \frac{K-1}{2} \cdot \frac{(K-1)M_\infty^2}{2KM_\infty^2-K-1} \right]^{-\frac{1}{K-1}} \right\}^{\frac{1}{2}} \quad (4)$$

The temperature  $T_\delta$ , density  $\rho_\delta$  and pressure  $p_\delta$

$$T_\delta = T_\infty \left( 1 + \frac{K-1}{2} M_\infty^2 \right) \left( \frac{p_\delta}{p_\infty} \right)^{\frac{K-1}{K}} \quad (5)$$

$$p_\delta = p_2 (1 - \sin^2 \phi) + p_\infty \sin^2 \phi \quad (6)$$

$$p_2 = p_\infty \left( \frac{K+1}{2} \right) \cdot M_\infty^2 \cdot \left( \frac{(K+1)^2 M_\infty^2}{4K M_\infty^2 - 2(K-1)} \right)^{\frac{1}{K-1}} \quad (7)$$

$$\rho_\delta = p_\delta / (R_g \cdot T_\delta) \quad (8)$$

The Stanton-Numbers  $St_l$  &  $St_t$  for laminar and turbulent flow are calculated by

$$St_l = f_l \cdot Re_\delta^{-1/2} \quad (9)$$

$$St_t = f_t \cdot Re_\delta^{-1/5} \quad (10)$$

$$\text{with } f_l = 0.763 Pr_\delta^{-3/5} \quad (11)$$

$$f_t = 0.042 Pr_\delta^{-2/3} \quad (12)$$

$$\text{and } Re_\delta = \frac{\rho_\delta \cdot u_\delta \cdot \delta}{\mu_\delta} \quad (13)$$

$$Pr_\delta = \frac{\mu_\delta \cdot c_{p\delta}}{\lambda_\delta} \quad (14)$$

Especially the transient behaviour from the laminar to the turbulent flow creates a significant input onto the thermal stress. Therefore special attention must be given to the transition area. The heat transfer calculations are based on the laminar and turbulent heat flow and a so-called "Intermittence" Factor, introduced by K. K. Chen and N. A. Thyson [3].

$$\dot{q}_{tr} = (1 - \gamma) \dot{q}_l + \gamma \dot{q}_t \quad (15)$$

The intermittence factor will be calculated over the momentum thickness  $\theta$  from K. K. Stetson [4] and the so-called "TURBULENT SPOT THEORY" from H. W. Emmons [5].

Intermittence factor:

$$\gamma = 1 - \exp \left[ -G \sin \left( \frac{S_b}{R} \right) \ln \left( \frac{\tan \left( \frac{S}{2R} \right)}{\tan \left( \frac{S_b}{2R} \right)} \right) \frac{R \ln \frac{S}{S_b}}{\left( \frac{d\mu_\delta}{ds} \right)} \right] \quad (16)$$

Evolution parameters of turbulent spots [5]:

$$G = \frac{3 \cdot u_\delta^2}{\nu^2 \cdot R^2} \cdot Re_\delta^{-2.68} \quad (17)$$

$$A = 60 + 4.68 M_\delta^{1.92} \quad (18)$$

Momentum thickness:

$$\theta = \frac{\sqrt{2 \cdot \xi \cdot \omega}}{S_\delta \cdot u_\delta \cdot R} \left[ 0.494 (1 - 0.09 \beta_\delta^{0.9}) \left( \frac{S_\delta \cdot \mu_\delta}{S_w \cdot \mu_w} \right)^{0.386} \right] \quad (19)$$

$$\xi(s) = \int_0^s S_w \cdot \mu_w \cdot u_\delta \cdot R^2 ds \quad (20)$$

Pressure gradient:

$$\beta_\delta = \frac{\int_0^s S_w \cdot \mu_w \cdot u_\delta \cdot R^2 ds}{S_w \cdot \mu_w \cdot u_\delta^2 \cdot R^2} \cdot \frac{du_\delta}{ds} \quad (21)$$

A significant parameter within the "Turbulent Spot Theory" is the correct introduction of the critical Reynolds-Number for the flow transition from a laminar to turbulent boundary layer

$$Re_{\theta crit} = \frac{S_\delta \cdot u_\delta \cdot \theta}{\mu_\delta} = 250 \div 350$$

based on the momentum thickness  $\theta$ . Normally the values for the critical Reynolds-Number are within the above range. But this range will be influenced and extended by the dome surface properties, mainly surface roughness (polishing) and the temperature difference between dome wall and surrounding air flow ("subcooled wall effect"). The influence of extended critical Reynolds-Numbers will be discussed later on in section 5.

The laminar and even more the turbulent airflow at supersonic velocities creates significant aerokinetic heat inputs as demonstrated in Fig. 5 by the calculated mean dome temperatures as function of the missile flight time for missile velocities similar to those given in Fig. 3. The resulting dome temperatures are going up to 700°C during the missile free flight at high altitude, whereas the adequate velocity profile of the missile at low altitude results in more moderate temperatures. It is remarkable that for high performance short range missiles with hemispherical IR-domes the maximum dome temperature will be achieved at high altitudes far beyond burn-out (of the missile motor), whereas the maximum thermal stress in the window material occurs at low altitudes near the time of burn-out.

To illustrate this fact in more depth the temperatures on the dome in flow direction at the time of motor burn-out is given in Fig. 6. Here the (outer) dome surface temperatures are given as a function of the dome angle measured from the stagnation point up to the dome bonding area for three different altitudes. Most significant is that the flow over the dome for high altitude flights is fully laminar, whereas flights at lower altitude - here at 7 km and at sea level - includes a transition area where the boundary layer changes from laminar to turbulent flow. Due to the great difference of the laminar and turbulent aerokinetic heating a great downstream temperature gradient to higher temperatures will be created by such a boundary layer change. The resulting heat input may differ up to a factor of 2. Due to the rapid velocity increase of the missile also a radial temperature gradient through the material will be imposed. Therefore a radial as well as a downstream temperature gradient has to be considered as demonstrated in Fig. 7 by  $\Delta T_R$  and  $\Delta T_D$ .

The Fig. 7 represents a typical temperature distribution as a function of the dome angle for the inner and outer dome surface. The radial temperature gradient  $\Delta T_R$  is indicated just at the location where the maximum value is generated. This is also the location with maximum dome heating due to the high turbulent heat transfer. The temperature gradient in flow

direction  $\Delta T_D$  between the minimum and maximum values on the outer dome contour is linked to an additional characteristic parameter here indicated as  $\Delta x$ . This is the horizontal distance between the minimum and maximum temperature on the outside contour. The distance  $\Delta x$  can also be expressed as a parameter for the extension of the transition area between the final undisturbed laminar flow and the fully developed turbulent flow. The transition zone starts with the first occurrence of turbulent spots (Emmons [5]).

#### 4. THERMAL STRESS IMPACT

The temperature gradient  $\Delta T_D$  in flow direction over the length  $\Delta x$  causes an additional bending stress on top to the well-known thermal stress caused by the radial temperature gradients  $\Delta T_R$ , generated by the heat flux through the dome thickness. If the radial temperature gradient (through the material) is the main driving influence on the thermal stress, one could assume that the resulting maximum dome stress will be generated at the location of the appearance of the maximum radial temperature gradient. But this is not true as we can see in Fig. 7 (top) where the dome stress has been calculated from the temperature distribution via a finite-element model. The thermally introduced stress is given also as a function of the dome angle at the time of motor burn-out. The peak of the dome (bending) stress occurs just at the beginning of the flow transition, not at the location where the maximum radial temperature gradient  $\Delta T_R$  is produced.

An answer to this remarkable behaviour is easy if we consider the effects which are caused by the downstream temperature gradient  $\Delta T_D$  over the dome length  $\Delta x$ . Normally the radial temperature gradient as given by  $\Delta T_R$  in Fig. 8 over the dome thickness  $L_D$  causes a tensile stress on the inner dome surface during missile acceleration. The increased temperature of the outer parts of the dome structure tend to stretch the inner parts of the dome material, producing a tensile stress. In addition the temperature increase in flow direction - crossing the transition area - causes an additional, superimposed bending of the dome as demonstrated in Fig. 8 by the three arrows illustrating the applied forces. The outer, hotter annular ring section of the dome - located in the turbulent flow region - tends to expand and causes a bending effect on those dome areas which are still on lower temperature. This is the location where the laminar flow starts to change to turbulent flow (beginning of the transition area). This bending stress is superimposed on the still existing tensile stress. This bending stress is the most driving parameter for the thermal stresses in hemispherical IR-domes as it is

illustrated in Fig. 7. In our example, the residual ultimate stress as a function of the sapphire dome temperature is not far away from the calculated maximum bending stress. The difference of both stresses is defined as the residual design margin. This is the reason why further missile velocity increases are difficult to achieve.

Some further calculations shall illustrate and confirm in more depth this additional bending effect: For a significant step increase of the flight Mach-Number the resulting thermal stress and the relevant temperature gradients in flow direction and radial through the dome have been calculated. The main result is that the maximum thermal stress occurs at the time, when the maximum temperature gradient in flow direction  $\Delta T_D$  is generated by the flow field. This maximum thermal stress occurs not at the time of the maximum radial gradient  $\Delta T_R$  through the material. The most remarkable result is that the main driving parameter for the thermal stress is the temperature gradient  $\Delta T_D$  in flow direction as illustrated in Fig. 9.

Another illustrative advice is given in Fig. 10 where both thermal gradients  $\Delta T_R$  and  $\Delta T_D$  are demonstrated by the dome temperature fields at different times. The first temperature field belongs to the time (A) where the radial temperature gradient  $\Delta T_R$  has its maximum value. The curve B is at the time when the maximum downstream gradient  $\Delta T_D$  occurs and the maximum dome stress will be produced (Fig. 9). In Fig 10, curve B, it is obvious that at this time the radial gradient  $\Delta T_R$  is significantly smaller than in curve A. The location of the maximum dome stress is just at the beginning of the transition zone as demonstrated in Fig. 7. In curve B we can clearly see that the downstream temperature gradient must have the most driving effect. Furthermore it will be illustrated that also the rapid change from the laminar to the turbulent flow (length  $\Delta x$  in Fig. 7) may influence the stress, too. The curve C is two times later than the curve B. Both gradients  $\Delta T_D$  and  $\Delta T_R$  as well as the thermal stress are reduced in a significant way.

#### 5. TRANSITION ZONE INFLUENCE, CRITICAL REYNOLDS NUMBER

From both Figures (9 and 10) it is obvious that the bending effect within the dome caused by the temperature gradient in flow direction and within the transition area between laminar and turbulent flow is the main driving parameter for the imposed thermal stress. The characteristics are the temperature gradient  $\Delta T_D$  itself and the length of the transition zone  $\Delta x$ . Both values will be influenced by the critical Reynolds-Number  $Re_g$ . The Reynolds-Number is based on the momentum thickness. Its critical

value - defining the transition from laminar to turbulent flow - varies between 250 and 350 in different references. The influence of variable critical Reynolds-Numbers on the (mean) dome temperatures as well as on the resulting dome stress is given in Fig. 11. With increasing Re-Numbers used for the heat transfer calculations including the turbulent spot theory as described before, the peak temperatures will go down, the beginning of the transition zone will be shifted more and more to larger dome angle. The resulting thermal stress - imposed by the two different temperature gradients - will be reduced to levels which will be generated by radial temperature gradients only.

Higher critical Reynolds-Numbers have the effect to extend the transition zone and to shift it over the dome bonding area so that the bending effect is reduced. Any occurrence of those effects may be helpful to reduce the thermal stress significantly.

The Fig. 12 illustrates the influence of the critical Re-Number on the two driving parameters of the bending stress: The downstream temperature gradient  $\Delta T_D$  and the length  $\Delta x$  between the beginning of the transition zone and the location of its maximum heat input.

The gradient  $\Delta T_D$  as well as  $\Delta x$  are reduced by increasing critical Reynolds-Numbers, but the effect of  $\Delta T_D$  on the stress reduction is more demanding than the lower slope of  $\Delta x$ , as it is illustrated in Fig. 13:  $\Delta T_D$  - decrease results in a significant stress reduction. The location of the maximum stress is shifted to higher dome angles.

The functional dependency between the critical Re-Number and the imposed thermal stress in the dome-material is - as demonstrated in Fig. 11 - also a most remarkable fact. For different critical Reynolds-Numbers the significant stress reduction is given for values greater than 350, which may be valid for highly polished domes and - in relation to the surrounding environment - relatively low (dome-)wall temperatures. But in any case precise information about correct values for the critical Reynolds-Number are difficult to receive neither from the open literature nor from wind-tunnel tests, as it was performed for this purpose at the wind-tunnel test facility at DLR in Porz/Wahn, Germany.

It seems that the KEY PARAMETER for any thermal stress calculation is the CRITICAL REYNOLDS NUMBER. Any stress calculations for the IR-window material seem to be as good as the assumption for the critical Reynolds-Number.

The critical Reynolds-Number used for any dome stress analysis has to take into account all effects resulting from surface polishing, from flow history, and from the relative low wall temperature of the dome at the beginning of missile free flight phase and during the initial boost phase.

Finally, it shall be mentioned that proper dome layout can reduce the induced thermal stress:

Temperature gradients in flow direction in the window material can be avoided by a proper dome layout in such way that the transition at the critical flight phase will be partly or totally outside of the IR-window, either by an increase of the dome radius or by a reduction of the dome aperture (angle  $\phi$ ).

## 6. CONCLUSION

The thermal stress on hemispherical IR-domes is dominated by the boundary layer transient behaviour, i.e. mainly by the beginning of the transition and the length of the transition region. These effects cause significant downstream temperature gradients resulting into a remarkable superposition of an ADDITIONAL BENDING STRESS onto the general existing tensile stress from the radial temperature gradients through the dome material.

The topics for further investigations on the boundary layer (BL) transient behaviour are - from our point of view - the following points:

- o Effects of large temperature differences between the dome material and the boundary layer
- o The effects of the highly polished dome surfaces on the boundary layer transient behaviour.
- o The study of different layouts of IR-windows to optimize the overall performance of the missile.

## REFERENCES

- [1] E. R. van Driest: The problem of aerodynamic heating. Engineering Review 15 (1956), No. 10, page 26-41.
- [2] L. Lees: Laminar heat transfer over blunt-nosed bodies at hypersonic flight speeds. Jet Propulsion 26 (1956), page 259-269.
- [3] K. K. Chen & N. A. Thyson: Extension of Emmon's spot theory to flows on blunt bodies. AIAA Journal 9 (1971), page 821-825.
- [4] K. F. Stetson: Boundary layer transition of blunt bodies with highly cooled boundary layers. Journal of the Aerospace Sciences 27 (1960), page 81-91.
- [5] H. W. Emmons: The laminar-turbulent transition in a boundary layer - Part I. Journal of the Aerospace Sciences, Vol. 18, No. 7, July 1951, page 490-498.

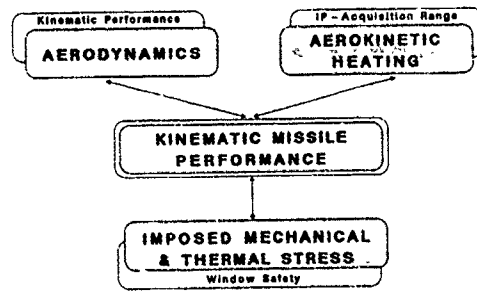


Fig. 1: MISSILE PERFORMANCE WITHIN ITS CONTRARY REQUIREMENTS

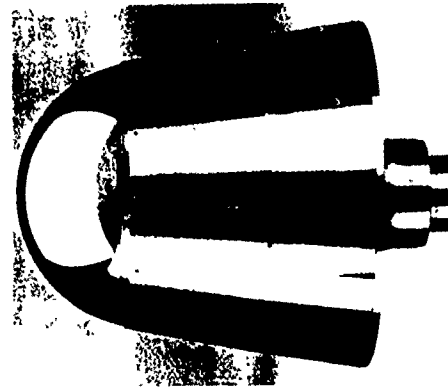


Fig. 4: HEMISPHERICAL DOME LAYOUT FIXED TO AN OGIVE STRUCTURE

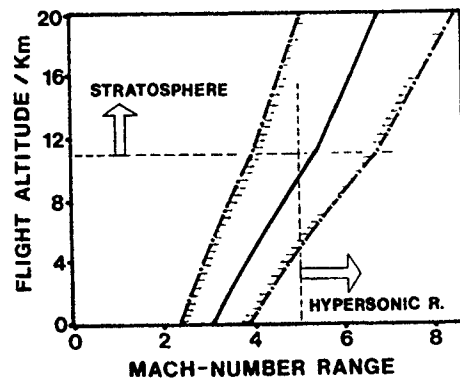


Fig. 2: TYPICAL MA-NUMBER RANGES AS FUNCTION OF ALTITUDE

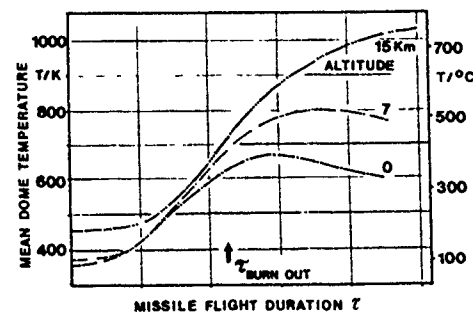


Fig. 5: MEAN DOME TEMPERATURES VERSUS FLIGHT TIME AND ALTITUDE

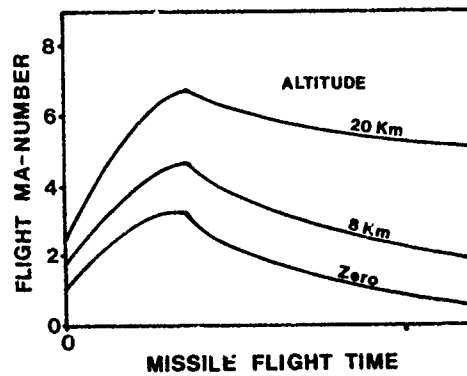


Fig. 3: TYPICAL VELOCITY PROFILES FOR DIFFERENT ALTITUDES

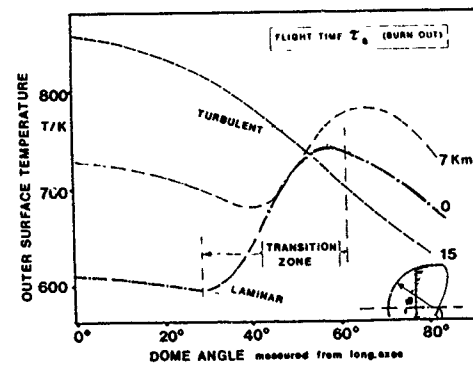


Fig. 6: DOME SURFACE TEMPERATURES AS FUNCTION OF DOME LOCATION

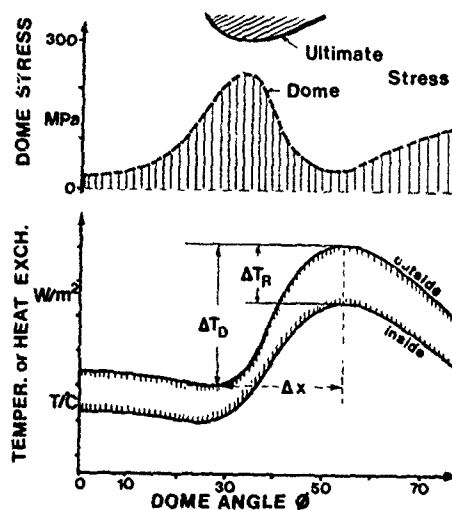
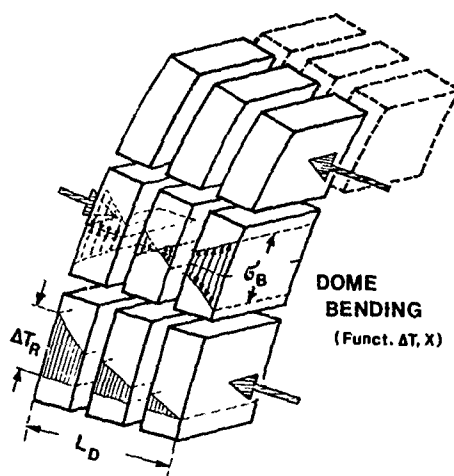


Fig. 7: ILLUSTRATION OF THE RADIAL AND DOWNSTREAM TEMPERATURE GRADIENTS IN THE DOME MATERIAL AND ITS RESULTING STRESS COMPARED WITH THE ULTIMATE STRESS



THERMAL STRESS IMPACT DUE TO

- o TEMPERATURE GRADIENT  $\Delta T_R$  THROUGH THE DOME-MATERIAL
- o DOWNSTREAM TEMPERATURE GRADIENT  $\Delta T_D$

$$\sigma_B = \text{Function}(\Delta T_R, L_D, \Delta T_D, X)$$

Fig. 8: THERMAL STRESS EFFECTS IN THE IR-DOME BY RADIAL- AND DOWNSTREAM TEMPERATURE GRADIENTS

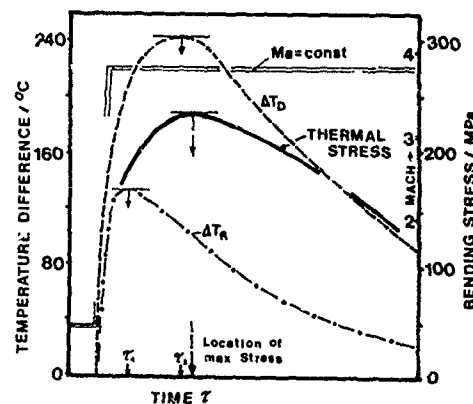
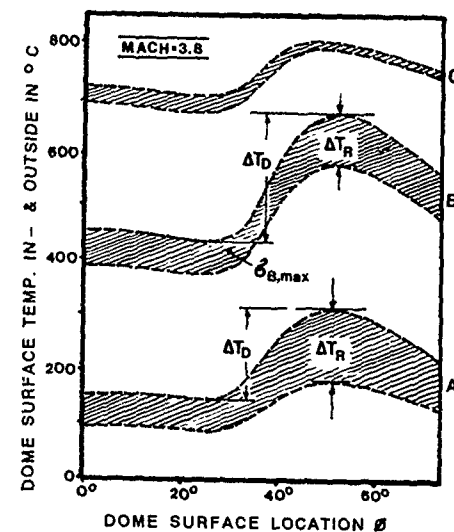


Fig. 9: RELATIONSHIP BETWEEN DOME BENDING STRESS  $\sigma_B$  AND THE DIFFERENT TEMPERATURE GRADIENTS  $\Delta T_R$  &  $\Delta T_D$  FOR A STEP INCREASE OF FLIGHT MACH NUMBER



DOME TEMPERATURE PROFILES AT DIFFERENT TIMES:

- A. --> AT MAX. RADIAL TEMPERATURE GRADIENT  $\Delta T_R$
- B. --> AT MAX. DOWNSTREAM TEMPERATURE GRADIENT  $\Delta T_D$  AT MAX. DOME STRESS
- C. --> AT TIME  $2 \times \tau_{\text{BURN OUT}}$

Fig. 10: DOME TEMPERATURE PROFILES AT DIFFERENT FLIGHT TIMES

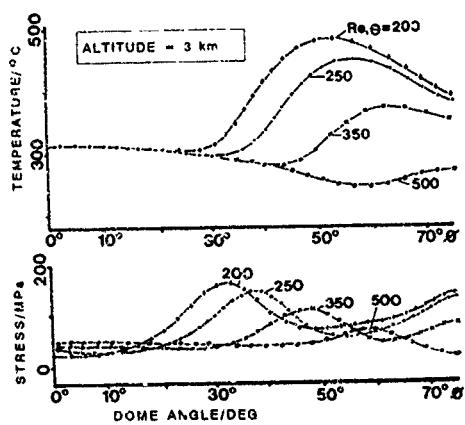


Fig. 11: DOME TEMPERATURES AND DOME STRESS AS FUNCTION OF  $Re,e$  AND DOME ANGLE  $\phi$  (at Motor Burn Out)

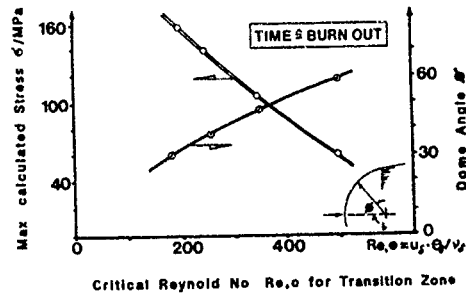


Fig. 13: MAXIMUM STRESS AND ITS LOCATION ON THE DOME AS FUNCTION OF  $Re,e$

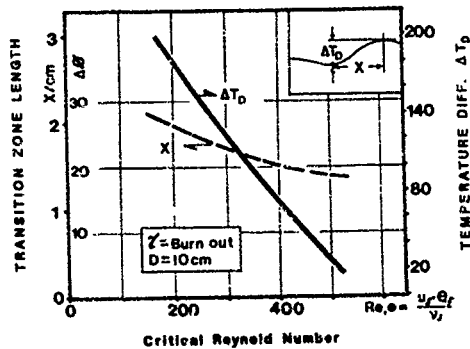


Fig. 12: DOWNSTREAM TEMPERATURE DIFFERENCE  $\Delta T_D$  AND TRANSITION ZONE EXTENSION  $X$  AS FUNCTION OF  $Re,e^{crit}$

# INVESTIGATIONS OF AEROTHERMODYNAMIC EFFECTS ON AXISYMMETRIC BODIES AT HIGH MACH NUMBERS

by

J.D.Regan and T.J.Rooke  
Ministry of Defence  
Royal Aerospace Establishment  
Farnborough, Hampshire GU14 6TD  
United Kingdom

## SUMMARY

This Memorandum describes experimental studies carried out at RAE in the Shock Tunnel and Gun Tunnel to measure the heat transfer rates to a 7° blunted cone, to provide data for validation of flow field prediction codes. The tests were carried out at Mach numbers of 7.1 in the Shock Tunnel and at 12.8 in the Gun Tunnel at angles of incidence of up to 25°. Some observations are made about the general nature of the flow around the body that can be deduced from surface heat transfer contours and flow field photographs and exemplified for 0, 1, 5 and 20° of incidence, and some comparisons between experimental results and theoretical predictions are presented.

## 1 INTRODUCTION

Recent interest in tactical hypersonic missiles has increased the need for aerothermal prediction techniques. These techniques are needed to extrapolate wind-tunnel data to free-flight, and to calculate missile performance for those flight conditions for which wind-tunnel data cannot be obtained. These prediction techniques must be validated by comparison with experimental results.

RAE has long realised this need for good quality experimental heat transfer rate data for the validation of the kinetic heating prediction from available flow field prediction codes. To this end, an extensive experimental programme was undertaken to measure heat transfer rates on simple shapes under various flow conditions. Heat transfer measurements and flow field photographs were taken on a 7° blunt cone for angles of attack from 0 to 25° tested at Mach numbers of 7.1 and 12.8. The purpose of this paper is to present a selection from these results and discuss deductions that can be made of flow field details. Also, selected data are compared with predicted results obtained from two available computer codes KHOMP2D and KHOMP3D.

## 2 DESCRIPTION OF FACILITIES

The tests described in this paper were made in the RAE Gun Tunnel operating at a nominal free-stream Mach number of 12.8, and in the RAE Shock Tunnel operating as a LICH tube at a Mach number of 7.1. The test gas used in both facilities was nitrogen at a stagnation temperature high enough to avoid liquefaction in the working section. The running time of the Shock Tunnel of about 100 ms is to be compared with the 80 ms of the Gun Tunnel, and which are amply sufficient for these heat transfer measurements.

### 2.1 The RAE Gun Tunnel

The RAE Gun Tunnel has a 3.6 m long, 50 mm internal diameter channel section (see Fig 1). The driver section has the same internal diameter as the channel section and is 2.1 m long. At the end of the driver section a perforated plate joins the driver internally to a 0.9 m long, 100 mm internal diameter reservoir. The use of such a section is known as the driver-reservoir technique and allows full use of the available running time by eliminating the reflected head of the expansion wave. This technique also reduces the strength of the reflection, at the plate, of the shock wave produced as the piston slows to rest.

In the Gun Tunnel a light piston is initially placed against the downstream side of the main diaphragm. When the diaphragm bursts the piston is accelerated down the channel section, causing the gas ahead of it to be heated and compressed, partly by the primary shock wave travelling ahead of the light, fast-moving (supersonic) piston and partly by means of an adiabatic compression of the test gas (see Fig 2). When the piston nears the end of the channel, the primary shock wave reflects as a shock wave from the end wall and interacts with the piston causing it to decelerate. There are several shock reflections between the piston and the end wall, and the gas in this volume is compressed non-isentropically to some final pressure and temperature which depends on the initial conditions. The available testing time is then determined by the time it takes for the gas between the piston and the end wall to pass completely through the nozzle.

The subsequent shock reflections, first from the piston then from the end wall, cause a very high peak in pressure in the gas at the end wall, and hence in the test-flow stagnation pressure. These peaks can reach three and four times the original driver gas pressure. Several pressure peaks of lesser magnitude subsequently occur due to further shock reflections between the piston and the end wall, and during this time the piston can execute several oscillations about some mean position a short distance from the end wall.

Reduction of the peak pressure which occurs at the start of a gun tunnel run can be made by operating in the 'dead-beat' piston mode whereby the piston is brought to rest by the first reflected shock from the end wall. The peak pressure is then equal to the final equilibrium pressure, and the technique is therefore called the equilibrium-piston technique. Using this condition it is possible to calculate the piston mass required from the initial conditions in the tunnel and tunnel geometry. More details on the theory and behaviour of gun tunnels may be found, for example, in Ref 1.

For the tests described in this paper, and using nitrogen as driver and channel gases, an 0.025 kg piston was used with a driver pressure of 177 bars and an initial channel section pressure of 4.42 bars. For this pressure ratio of 40 the equilibrium, or stagnation, pressure is 150 bars and the stagnation temperature is 1100 K, just sufficient to avoid liquefaction in the working section. With a free-stream Mach number of 12.8, this gives a tunnel unit Reynolds number of  $5.5 \times 10^6$  per metre.

A 5° semi-angle conical nozzle with a 257 mm exit diameter connects the channel section to the open jet working section, fitted with large Schlieren-quality glass windows. The working section was fitted with a small quadrant-type incidence gear which covered an incidence range from -5° to +35°.

### 2.2 The RAE Shock Tunnel

Some 5 years ago the performance of the RAE Shock Tunnel, in terms of running time as a function of total temperature and nozzle throat area, was enhanced by modifying the facility to run in the so called LICH mode (Ludwig tube with Isentropic Compression Heating) with



the running time increased from 3 to 5 ms to some 100 ms. The tube forming the basic Shock Tunnel facility has an internal diameter through the driver section and channel section of 150 mm. The driver section is 9 m long and the channel section is 18 m long.

In its conversion to a LICH tube (Fig 3), the existing high pressure driver section is used as a reservoir and the diaphragm block replaced by an insert containing a spherically-seated ball valve and a throat. The nozzle diaphragm used to close off the channel section from the nozzle and working section in conventional Shock Tunnel operation is replaced by a fast-acting sliding gate valve. A light piston is fitted into the channel section which runs down the tube in order to compress and pre-heat the test gas. The piston travels relatively slowly down the tube ( $\approx 15$  m/s) so that the gas is heated by isentropic compression, rather than by means of a strong normal shock wave as in a conventional shock tunnel.

In LICH tube operation, the piston starts close to the reservoir throat and travels down the channel section when the ball valve is opened. Thus the test gas ahead of the piston is compressed and hence heated until at a prescribed channel pressure the fast acting valve is opened, whereupon the hot test gas flows through the nozzle.

Because of the low piston speeds involved (15 m/s at  $M = 7.1$ ), the compression process is essentially slow and the pressure throughout the tube is constant and hence when the nozzle fast-acting valve opens and gas flows out through the nozzle, a rarefaction wave (see Fig 4) is generated which travels back up the channel, reflects off the ball valve end of the channel and returns to the nozzle. This process is identical to that in a Ludwieg tube and determines the running time, nozzle stagnation conditions being essentially constant until the rarefaction returns. The presence of the piston, and the fact that the gas behind it has come from the reservoir and is at a lower temperature, cause only slight departure from standard Ludwieg tube operation.

When the nozzle opens, the initial rarefaction wave will produce a drop in the stagnation pressure given by

$$\frac{\Delta p}{P_t} = 0.8102 \frac{A_a^*}{A} \quad \text{for } \gamma = 1.4,$$

which results in a 6% drop for the existing  $M = 7.1$  nozzle.

The pressure in the channel section continues to rise after the fast-acting valve has opened due to the continued reflection of the compression waves. However, as the initial rarefaction proceeds beyond the piston into the driver gas it meets colder gas which results in a continuous reflection of weak waves from this region of non-uniform density. When these reflections hit the nozzle wall, pressure 'doubling' occurs and a very small drop in stagnation pressure results. This small pressure drop may be compensated by the rise in pressure resulting from the continuing compression process. This leads to a compensating condition which is used in the LICH mode to produce very constant stagnation conditions.

The most noticeable deviations from the steady running pressure of the LICH mode are a train of small pulses due to the reflection of the initial rarefaction pulse by the piston. When the initial rarefaction hits the piston, its inertia will prevent it from responding instantaneously and hence the leading edge of the rarefaction will be reflected. This reflected wave will then be reflected repeatedly between the piston and the tube end wall. These pressure pulses will, of course, be doubled in strength by the nozzle end wall total reflections. However, these pulses may be virtually

eliminated by using a fast-acting valve having an opening time greater than the piston mass time constant,

$$\frac{m}{2A\rho a} < 3 \text{ ms}$$

for Shock Tunnel conditions. The opening time for the RAE Shock Tunnel fast-acting valve for  $M = 7.1$  operation is about 10 ms, which is over three times greater than the piston time constant, but still small compared with the tunnel running time of 100 ms. Thus the pressure pulse should be virtually eliminated, and this is borne out in practice. A more detailed discussion of LICH tube operation may be found in the seminal paper<sup>2</sup> (from which Fig 4 was taken).

For the tests described in this paper, the nitrogen gas driver pressure was 375 bar and the initial pressure of the nitrogen in the channel section was 6.46 bar. The test gas in the channel section was processed in the LICH mode using a light piston ( $\approx 0.4$  kg) to give a stagnation pressure of 84 bars and a stagnation temperature of 580 K. A  $5\frac{1}{4}^\circ$  semi-angle conical nozzle with a 356 mm exit diameter and a 38 mm diameter throat section connects the channel section to an open-jet working section fitted with large Schlieren-quality glass windows. The diameter of the usable core is 280 mm in which the free-stream Mach number is 7.1. The unit Reynolds number for these conditions is about  $4 \times 10^7$  per metre, an order of magnitude higher than the Gun Tunnel unit Reynolds number. The working section is fitted with a quadrant-type incidence gear which covers the incidence range from 0 to  $90^\circ$  in  $1^\circ$  intervals.

### 3 DESCRIPTION OF MODELS AND MEASURING TECHNIQUE

The models used in the tests reported in this paper were all based on a generic 13.0 calibre,  $7^\circ$  blunted cone with a nose bluntness ratio of 0.245 (ratio of nose radius to base radius), for which pressure distributions had already been measured at a Mach number of 7.0<sup>3</sup>. The model tested in the Gun Tunnel had a length of 100 mm, giving a Reynolds number based on length of 550,000. Thus the boundary layer was likely to be laminar along the whole length of the body for the Gun Tunnel tests. A larger model (see Fig 5) with a length of 200 mm was used in the Shock Tunnel tests with a correspondingly higher Reynolds number of 8,000,000. For this value of Reynolds number the boundary layer was thought to be laminar over the whole body due to the effect of nose blunting on the stability of the boundary layer. This will be discussed more fully at a later stage.

Heat transfer models were made from the basic model by replacing 75% of the upper surface (based on model length) by a Macor (a trade name for a machinable ceramic glass) insert which formed the semi-infinite substrate for the thin film resistance thermometer gauges. The gauges were produced by painting on to the Macor a proprietary liquid containing platinum, which was then fired in a furnace to fuse the gauges to the Macor substrate. Several coats were applied to give the gauges an electrical resistance of about 50  $\Omega$ . Gold leads are painted on to the Macor, each lead having a resistance of less than 1  $\Omega$ , to connect the gauges to instrumentation wires while avoiding any possible flow disturbance.

The film gauges are fed by a constant current power supply so that any change in gauge resistance  $\delta R$  due to a change in surface temperature will result in a change in gauge voltage which is directly proportional to  $\delta R$ . This

signal is then fed to a high speed analogue circuit to produce a voltage proportional to the heat transfer rate.

The Macor substrate was not taken right up to the nose of models described so far, the first 12% of the models being ungauged. The reason for this is that it is difficult to make gauges less than about  $\frac{1}{2}$  cm in length and so on the slender nose region of the model they would measure a mean circumferential heat transfer rate, not a point value. In order to measure heat transfer rates nearer to the nose, an enlarged model of the first 25% of the original 200 mm long model was made which had a length of 182 mm with a 131 mm Macor insert. It was hoped that measurements on this model would, when properly scaled, be applicable to the original Shock Tunnel model.

#### 4 PREDICTIONS

The only readily available in-house heat transfer prediction codes were those developed by Professor Poll of Manchester University, and his associates, under RAE extramural contracts, viz a zero-incidence two-dimensional code called KHOMP2D and a three-dimensional version called KMOMP3D<sup>4</sup>. For these engineering prediction codes the boundary layer is assumed to be laminar throughout and a simple modified Newtonian pressure distribution prediction method is used to provide the pressure input. The boundary layer thickness, and hence the heat transfer rates, depends on the pressure distribution. Since the modified Newtonian approximation breaks down whenever and wherever the model surface slopes away from the free-stream, the comparisons with the predictions of KHOMP3D have been limited to angles of incidence which do not exceed  $7^\circ$ , the cone half angle, so that the leeward body meridian does not violate this condition.

In their present form these codes can deal only with problems involving air, not nitrogen, as the test medium. However, this limitation is not thought to be a serious source of error. More important is the fact that they can deal only with air as a thermally and calorically perfect gas. Around the noses of the models tested there is a region of high temperature gas in which the specific heats may deviate from the ideal values. The consequent change in the value of the ratio of the specific heats can have a significant effect on the flow field. For instance, the shock stand-off distance can alter quite markedly and this would alter the boundary layer state. Thus the assumption of a calorically perfect gas may introduce errors in the predicted values, although these are thought to be small.

#### 5 TEST AND RESULTS

Heat transfer measurements were made at incidences from  $0$  to  $25^\circ$  in  $5^\circ$  steps, with additional low-incidence tests carried out at  $1^\circ$ ,  $2^\circ$ ,  $3^\circ$  and  $4^\circ$ . At each angle of incidence the model was rotated from  $0^\circ$  of roll, in which the gauges were lying along the leeward generator, to  $180^\circ$  of roll, in which the gauges were along the windward generator of the model.

All the model surface heat transfer measurements presented here have been normalised to the computed value of the stagnation point heat transfer rate based upon the equation proposed by Crabtree, Dommert and Woodley<sup>5</sup>, which was in turn derived from the theory of Fay and Riddell<sup>6</sup>. The results are presented in the form of contour plots of the measured heat transfer distribution around the body.

Photographs of the flow-field pattern were taken at all incidences with a single-pass Schlieren system using an argon-jet spark light source of about 0.2 ms duration. Photographs were taken on Kodak Tri-X Ortho sheet film 4163.

## 6 DISCUSSION OF RESULTS

### 6.1 Experimental measurements

At  $0^\circ$  of incidence, Fig 6a-c, the results from the Gun Tunnel and Shock Tunnel experiments show similar, and expected, patterns of heat transfer contours; viz the isotherms (strictly, iso-heat-transfer values) are approximately  $s = \text{constant}$  curves and their values decrease with distance from the nose. The values of the heat transfer rates are very small, varying from about  $1.5 \text{ W/cm}^2$  near the nose to about  $0.8 \text{ W/cm}^2$  towards the rear of the models. At these low levels systematic errors occur for the small variation of the heat transfer rates with  $\phi$  (the roll angle) for a given value of  $s$ .

In view of the large differences in Reynolds numbers, based on model length, between the tests carried out in the Shock Tunnel at  $M = 7.1$  and those in the Gun Tunnel at  $M = 12.8$  (viz  $8 \times 10^6$  as against  $0.5 \times 10^6$ ), the possibility that for the tests in the Shock Tunnel the boundary layer may be turbulent had to be addressed. However, the heat transfer distribution along the, say,  $\phi = 90^\circ$  line shows no sudden jump to a much higher level at some point along the line as it should do if transition from a laminar to a turbulent boundary layer occurred there, the experimental results showing a monotonic decrease with distance from the nose. This delay in transition is thought to be due to the effect of nose bluntness on transition. This has been studied by many investigators (see, for example, Ref 7) and from their results it would appear that for the Mach number of the tests a small nose bluntness could result in the position of transition being up to five times further aft than the transition position for the sharp cone. It was also noted that the rearward movement of transition stopped after a certain amount of blunting and the location of transition began to move forward when bluntness was further increased. The bluntness experiments referred to in Ref 7 were performed in 'noisy' tunnels and so the measured transition Reynolds numbers for the sharp cones were quite low (between  $2 \times 10^6$  and  $4 \times 10^6$ ) due to the possible effect of high free-stream turbulence. If we take  $(S_{\text{blunt}}/S_{\text{sharp}})_{\text{transition}} = 2.5$  and a sharp-cone transition Reynolds number of  $3 \times 10^6$ , then we would expect the transition Reynolds number for the blunted cone in the Shock Tunnel at  $M = 7.1$  to be  $7.5 \times 10^6$ . This would imply that the boundary layer would be laminar over most, if not all, of the body for the Shock Tunnel experiments.

Additional support for a laminar boundary layer may be obtained from an empirical correlation for hypersonic transition on free-flight vehicles, viz transition occurs when the ratio  $Re_\theta/M_\theta$  equals a value of 100, where  $Re_\theta$  is the Reynolds number based on momentum thickness and  $M_\theta$  is the local Mach number at the edge of the boundary layer. Using the bluntness factor of 2.5 at a free-stream Mach number of 7.1, the value of the ratio at transition for a blunt cone should increase to 250. Values of the ratio  $Re_\theta/M_\theta$  were computed along the surface of the Shock Tunnel model and it was found that the maximum value reached was about 120 and this occurred at the base. It should be mentioned that a value of about 220 for transition at a free-stream Mach number of 7 on a sharp cone model in a tunnel is given by Ref 8. The fact that this value is higher than the free-flight value may be attributed to tunnel turbulence.

As the angle of incidence is increased above zero it is seen that the flow pattern changes very quickly from an axisymmetric flow to one with significant cross flow in the azimuthal direction. This is shown very clearly even for an angle of incidence of  $1^\circ$ , Fig 7a-c, and by  $5^\circ$  of incidence,

Fig 8a-c, the contours are nearly parallel to the model generators. It is perhaps worth pointing out that these low incidence results show that the boundary layer is well and truly laminar over the whole of the model. For it is well known<sup>9</sup> that as the incidence is increased transition moves forward on the leeward side and rearward on the windward side. If transition were to occur in the LICH tube tests at a Reynolds number of  $8 \times 10^6$ , then this should show itself on the leeward generator at small angles of incidence. No evidence of this happening is to be seen.

From about 5° of incidence onwards, however, the surface flow patterns on the two models, as evidenced by the heat transfer contour lines, are no longer similar and will therefore be discussed separately. (Some reference will also be made to the enlarged nose section model, although its flow pattern seems to model that of its parent body.) Isotherms for 20° of incidence are shown on Fig 9a-c. Schlieren photographs for the three models are shown on Fig 10a-c for zero angle of incidence, and Fig 11a-c at 20° of incidence.

We consider first of all the model tested in the Gun Tunnel at a nominal free-stream Mach number of 12.8, Fig 9a. Looking at the heat transfer rate contour maps, we see that the lines bunch together on about the 45° line. This is taken to be evidence of a three-dimensional flow separation found on blunt bodies at high angles of attack, and described by a number of investigators. For example, Stetson<sup>10</sup> measured the surface and pitot pressure distributions in detail over sharp and blunted cones at incidence at a Mach number of 14.2. From these results, Stetson presented a separated flow model with a pair of vortices, which he called "stream ribbons", over the leeward surface.

A comparison of the Gun Tunnel photographs for 0 and 20° of incidence, Figs 10a and 11a, show an unsteady shock wave lying between the bow shock wave and the leeward surface vortices at the higher angle of incidence. This feature does not appear to be present in the Shock Tunnel flow photographs, Fig 11b&c. Although this shock wave must curve around the body in the same way as the bow shock wave, no evidence of its presence is seen in the surface heat transfer plots; that is to say, it is not a surface generated phenomenon, but is a function of flow Mach number only. Upstream of this embedded shock wave the flow Mach number must be very nearly equal to the free-stream value of 12.8; the shock wave is required to match this flow with vortical flow from the windward side. At the lower Mach number tests in the shock tunnel such a shock wave does not appear to be required to match the two flows.

Turning to the Shock Tunnel heat transfer rate contour maps, Fig 9b&c, a separation line is again seen lying approximately on the 45° line, suggesting that the leeward side flow is again vortical in nature. However, the 135° line, the windward surface, shows much more structure than the corresponding Gun Tunnel line, especially towards the base of the model. This is the region where, at hypersonic Mach numbers, the bow shock wave lies very close to body on the windward side, and could cause local heating. However, these high heating rate contours should also be visible on the Gun Tunnel results if their cause was a shock wave-boundary layer type interaction. Also, this phenomenon is seen on the very blunt body where the bow shock is still some distance from the base.

A suggested possible reason for this high base heating region is a stream-wise separation of the laminar boundary layer. If one looks at the  $M = 7.1$  Shock Tunnel results for 20° of incidence, it is seen that on the 135° ray the heat transfer rate decreases in value over the first 15%

on the ray from the nose, then remains virtually constant over the next 35% before rising to higher values over the remaining 50%. This is a typical variation for laminar separation and reattachment and its occurrence is more likely at the higher Reynolds number and lower Mach number of the Shock Tunnel results than for the Gun Tunnel results. The cause could be the pressure gradient along the windward surface caused by an over-expansion and recompression process after the curvature discontinuity at the sphere-cone junction. This is clearly seen in the flow photograph showing an adversely curved shock wave near the nose on the windward surface.

As mentioned above, no embedded shock wave is seen in the Schlieren photographs of the flow in the Shock Tunnel, Fig 11b, comparable to that evident at high angles of incidence in the Gun Tunnel. However, the Shock Tunnel photographs do show an embedded shock wave emanating from the nose region on the leeward surface, at least for angles of incidence from 15° onwards. This shock wave is a stable, fairly weak feature and does not appear in the Gun Tunnel photographs (where, admittedly, the density gradients are much weaker). This embedded shock wave has been reported previously<sup>11</sup> from tests on biconics (on-axis and blunt) and sphere-cones in the Langley 20-inch Mach 6 Tunnel, and was tentatively attributed to a flow expansion around the spherical nose followed by a recompression because of the presence of the cone section.

## 6.2 Comparison of experimental results and theoretical predictions

Fig 12 shows a comparison of experimental data at zero incidence with the predictions of KHOMP2D, shown as solid lines. The code predicts the surface heating rate fairly well over the first half of the 7° blunted cone in both tests, but then over the rear half over-predicts by up to 20%. The code over-predicts the rates on the expanded nose model by some 20-30% over the whole of the body, excluding the nose region for which no experimental results were available.

These discrepancies may be partially attributed to the use of modified Newtonian pressure. Alternatively, it could be attributed to inadequate modelling of the blunt nose region. The flow in the nose region is characterised by a strong near-normal bow shock wave, which generates an entropy gradient inside the shock layer. This entropy gradient results in an entropy layer which prevails over the inviscid region between the shock and the boundary layer. As the shock location approaches the limit of a sharp cone solution, the entropy layer thickness decreases and eventually is swallowed by the boundary layer, which probably occurs about half way along the body for the tests described here. The prediction code may not provide a method to account adequately for the effect of variable entropy on heat transfer rates along blunted bodies, because real gas effects have decreased the shock stand-off distance. This would also explain why the very blunt body heat transfer prediction over-estimates the experimental data.

The plots of heat transfer rate prediction at incidence using KHOMP3D are shown in Fig 13a-d, for both windward and leeward generators. These plots are shown for completeness and indicate that in its present form, the code grossly over-predict measurements along the windward generators. The reasons for this are currently being examined.

## 7 CONCLUSIONS

Heat transfer rate measurements have been made on a 7° blunted cone geometry over a range of incidences at

two hypersonic Mach numbers. Analysis of the data in the form of contour maps of the heat transfer rates over the surface, aided by flow field photographs, have led to the following preliminary conclusions:

- (1) The boundary layer was found to be laminar over all the models tested, even though the Reynolds number for the Shock Tunnel tests was  $8 \times 10^6$  based on model length. This was almost certainly due to the effect of bluntness delaying the onset of transition.
- (2) The appearance of cross flow effects on the results appear even at  $1^\circ$  of incidence.
- (3) By about  $10^\circ$  of incidence there is strong evidence of a cross flow separation over the leeward surface, suggesting that the leeward flow is vortical in nature.
- (4) It is possible that streamwise separation of the boundary layer over the windward surface occurs for the  $M = 7.1$  tests, but not at  $M = 12.8$ .
- (5) An embedded shock wave in the leeside flow is seen in the flow field photographs at  $M = 12.8$  towards the base of the model and which does not appear in the  $M = 7.1$  photographs. This unsteady shock wave is tentatively attributed to a requirement to match the leeside flow with the vortical cross flow.
- (6) An embedded shock wave originating from the region of the join of the spherical nose cap to the cone is seen in the  $M = 7.1$  photographs. There is also some evidence of this shock wave in the  $M = 12.8$  photographs at incidences above  $20^\circ$ .
- (7) The predictions of KHOMP2D, applicable only at zero incidence, are of an acceptable accuracy. KHOMP3D, applicable to non-zero angles of incidence, requires further development before it can yield predictions of acceptable accuracy.
- (8) A wide-ranging data base of flow field photographs and heat transfer contours have been assembled against which current and future flow field prediction methods can be validated.

#### LIST OF SYMBOLS

A	tube cross-sectional area
$A_n$	nozzle throat area
m	piston mass
M	Mach number
$M_0$	Mach number at edge of boundary layer
$P_t$	pressure in front of piston during run
$\Delta p$	rarefaction wave step at start of run
$\dot{q}$	heat transfer rate
$\dot{q}_0$	stagnation point heat transfer rate
r	nose radius
$Re_0$	Reynolds number at edge of boundary layer, based on momentum thickness
$\theta$	momentum thickness
s	surface distance
$\alpha$	angle of incidence
$\gamma$	ratio of specific heats
$\rho$	density of gas
$\phi$	roll angle ( $0^\circ$ - leeward surface)

#### REFERENCES

- 1 Davies, L., Regan, J.D. and Dolman, K.A.; On the equilibrium piston technique in Gun Tunnels, NPL Aero Report 1240, July 1967.
- 2 Oldfield, M.L.G., Jones, T.V. and Schultz, D.L.; A Ludwig tube with light piston isentropic compression heating, ARC 34225 (1972).
- 3 King, J.N.; Details of tests on conical and power law bodies in the ARA M4T and M7T at Mach numbers of 4.25 and 7.0, ARA Model Test Note M154/1, August 1982.
- 4 Hellon, C.M. and Poll, D.I.A.; On the use of the boundary layer integral equation for the prediction of skin friction and heat transfer. College of Aeronautics Report 8625, November 1986.
- 5 Crabtree, L.F., Dommett, R.L. and Woodley, J.G.; Estimation of heat transfer to flat plates, cones and blunt bodies, RAE Technical Report 65137 (1965).
- 6 Fay, J.A. and Riddell, F.R.; Theory of stagnation point heat transfer in dissociated air, *J. Aero Sc.*, 25, 2, (1958).
- 7 Malik, M.R., Spall, R.E. and Chang, C.L.; Effect of nose bluntness on boundary layer stability and transition, AIAA Paper 90-0112, 8-11 January 1990.
- 8 Malik, M.R.; Prediction and control of transition in supersonic and hypersonic boundary layers, *AIAA Journal*, 27, 11, pp 1487-1493, November 1989.
- 9 DiCristina, V.; Three-dimensional laminar boundary layer transition on a sharp  $8^\circ$  cone at Mach 10, *AIAA Journal*, 8, 5, pp 852-856, May 1970.
- 10 Stetson, K.F.; Boundary layer separation on a slender cone at angle of attack, *AIAA Journal*, 10, 5, May 1972.
- 11 Miller, C.G. and Gnoffo, P.A.; Pressure distributions and shock shapes for  $12.84^\circ/7^\circ$  on-axis and bent-nose biconics in air at Mach 6, NASA TM 83222, December 1981.

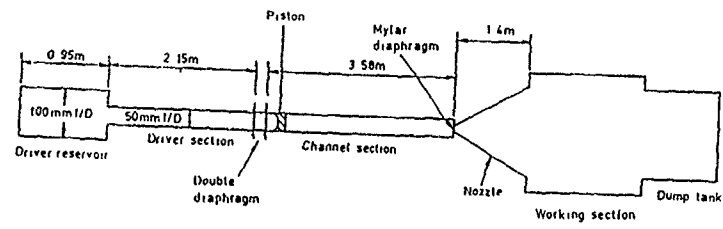


Fig 1 Diagrammatic layout of gun tunnel

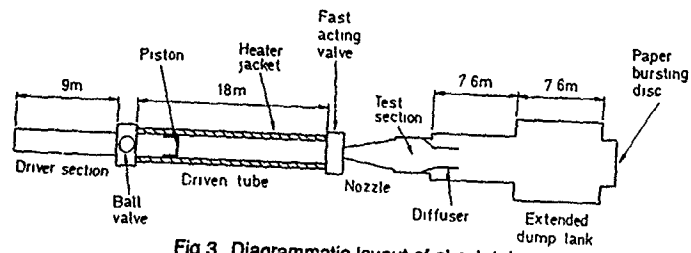


Fig 3 Diagrammatic layout of shock tube

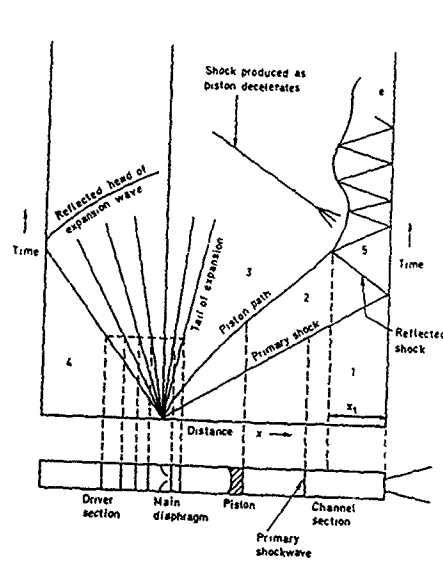


Fig 2 Gun tunnel flow

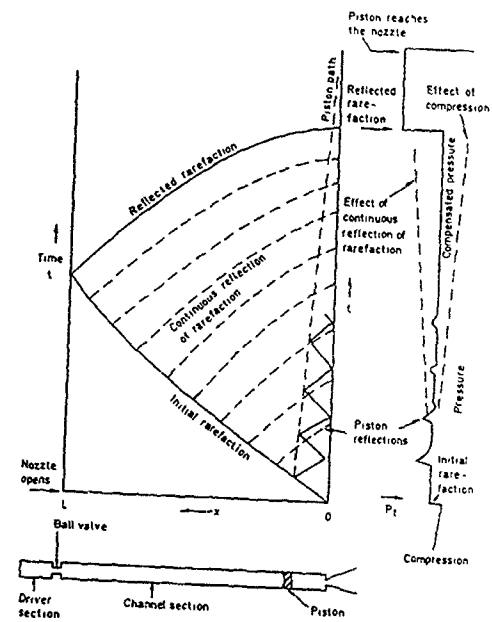


Fig 4 Ludwig tube flow

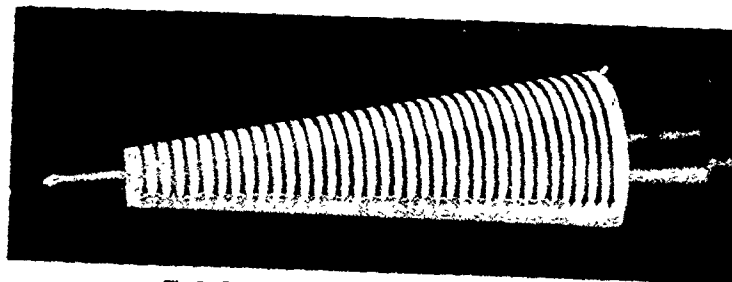


Fig 5 Shock tunnel model showing gauge positions

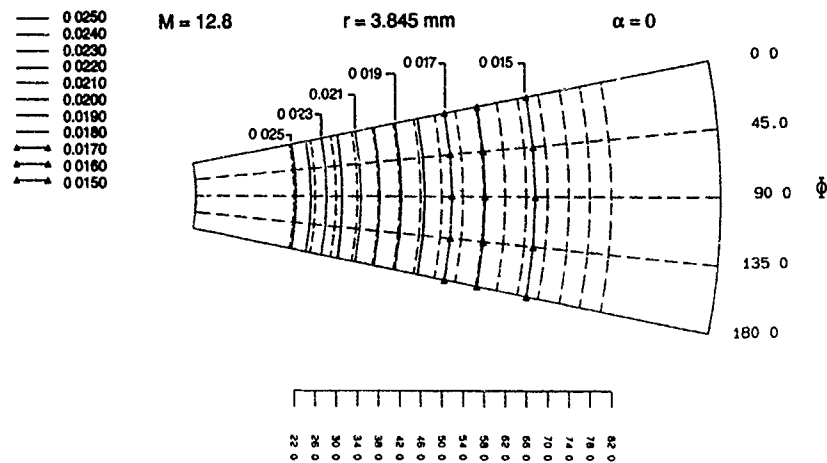


Fig 6a Gun tunnel heat transfer rates

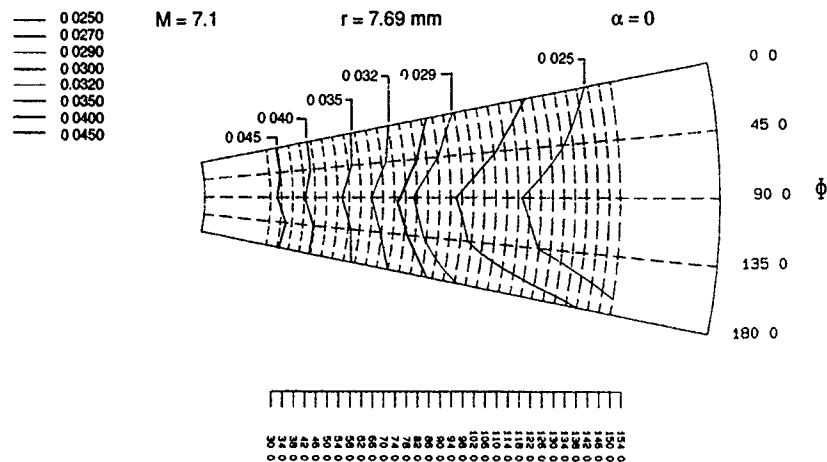


Fig 6b Shock tunnel heat transfer rates

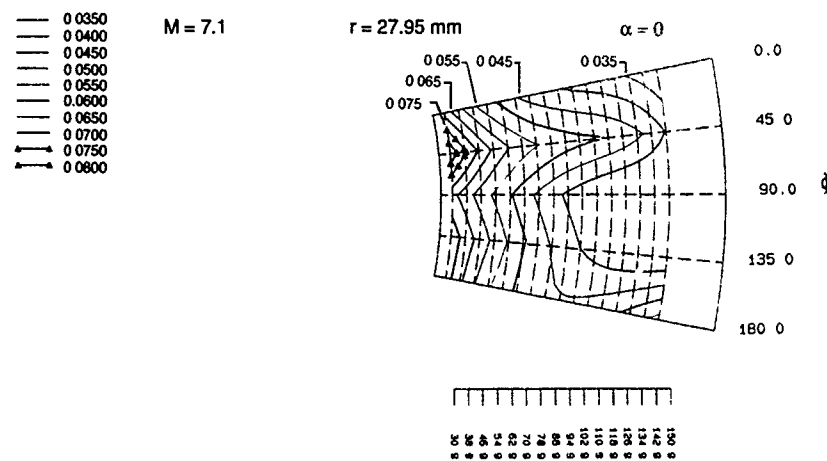


Fig 6c Shock tunnel heat transfer rates

0.0130  
 0.0140  
 0.0150  
 0.0160  
 0.0170  
 0.0180  
 0.0190  
 0.0200  
 0.0210  
 0.0220  
 0.0230  
 0.0240  
 0.0250

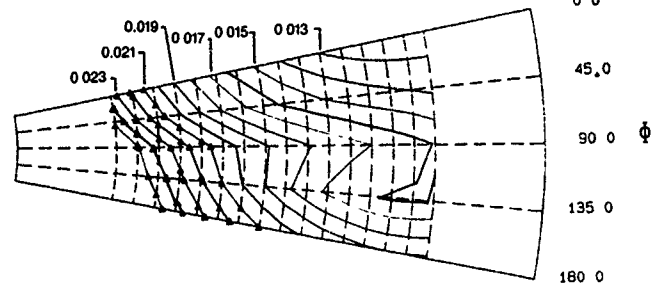
 $M = 12.8$  $r = 3.845 \text{ mm}$  $\alpha = 1$ 

Fig 7a Gun tunnel heat transfer rates

0.0150  
 0.0180  
 0.0200  
 0.0220  
 0.0240  
 0.0260  
 0.0280  
 0.0300  
 0.0350  
 0.0400  
 0.0450  
 0.0500

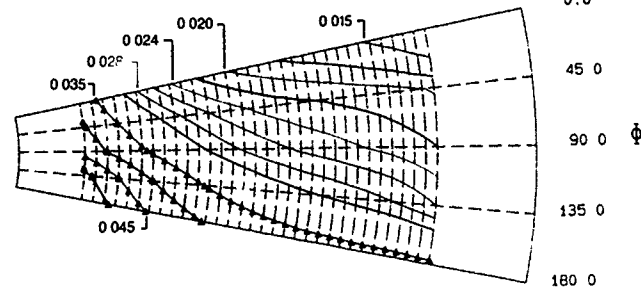
 $M = 7.1$  $r = 7.69 \text{ mm}$  $\alpha = 1$ 

Fig 7b Shock tunnel heat transfer rates

0.0350  
 0.0400  
 0.0450  
 0.0500  
 0.0550  
 0.0600  
 0.0650  
 0.0700  
 0.0750  
 0.0800  
 0.0850  
 0.0900

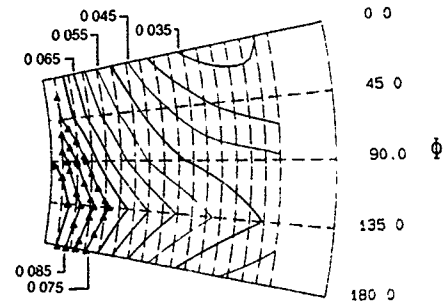
 $M = 7.1$  $r = 27.95 \text{ mm}$  $\alpha = 1$ 

Fig 7c Shock tunnel heat transfer rates

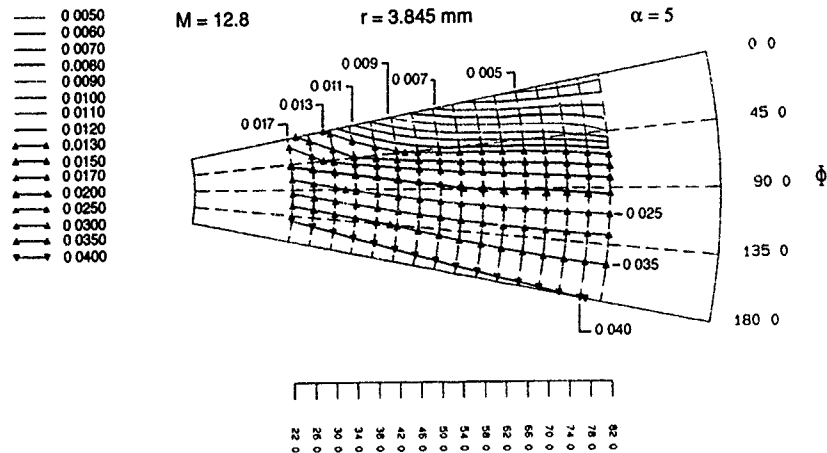


Fig 8a Gun tunnel heat transfer rates

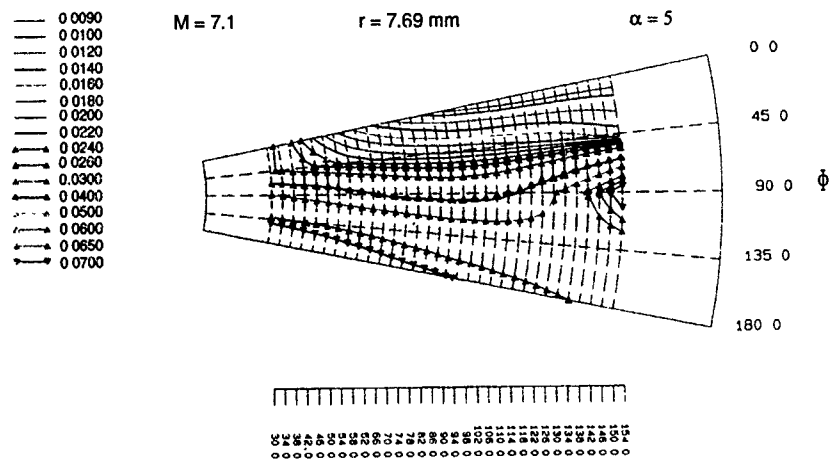


Fig 8b Shock tunnel heat transfer rates

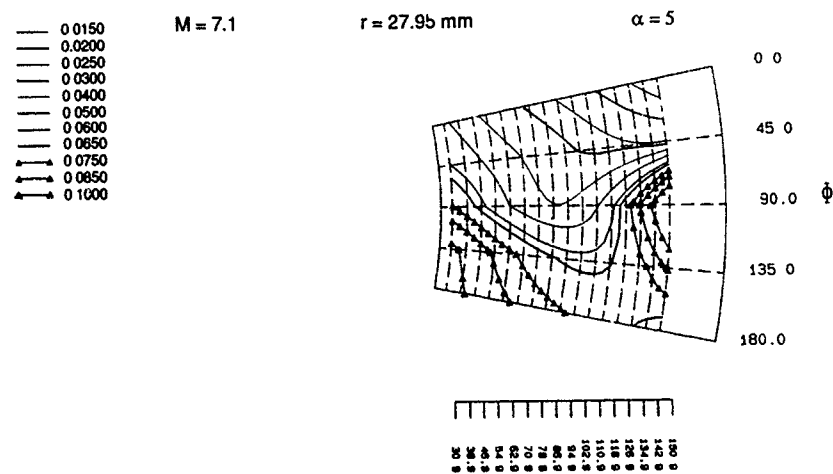
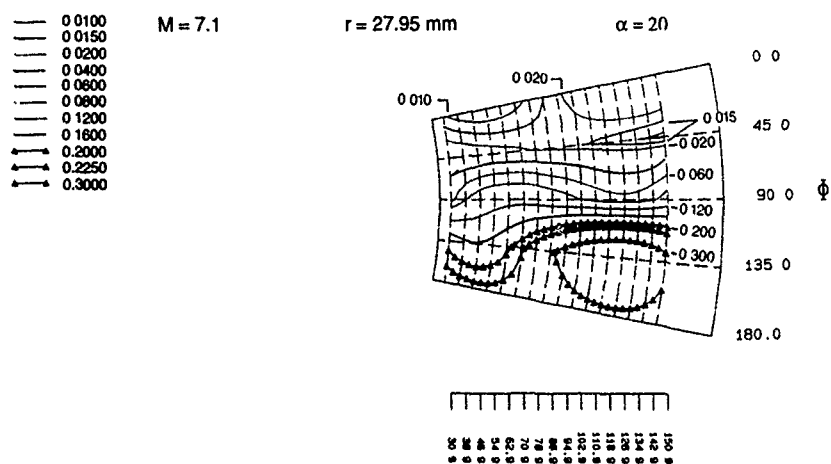
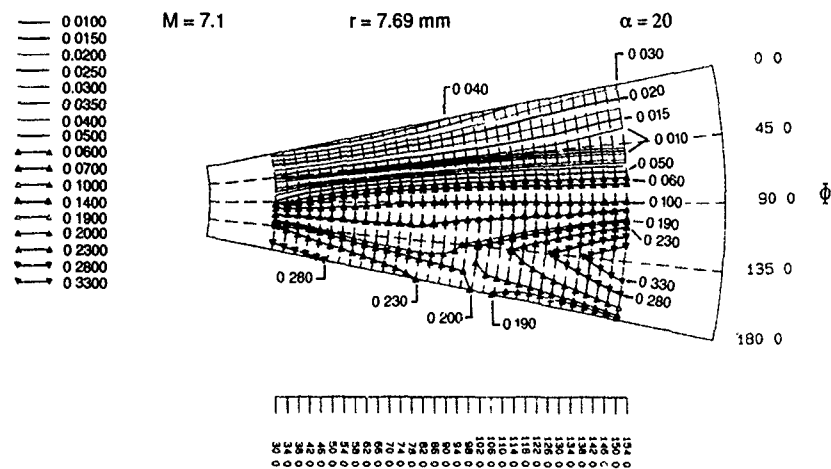
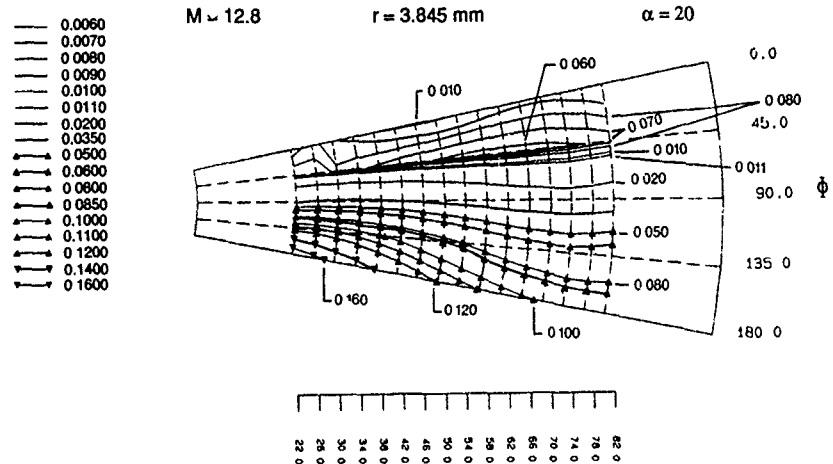


Fig 8c Shock tunnel heat transfer rates





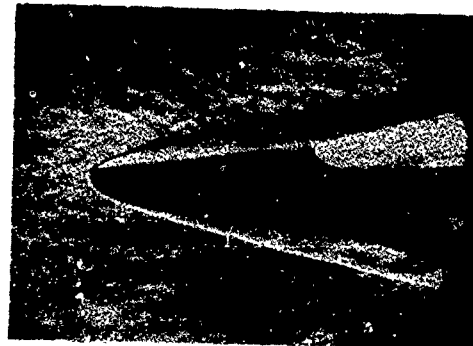
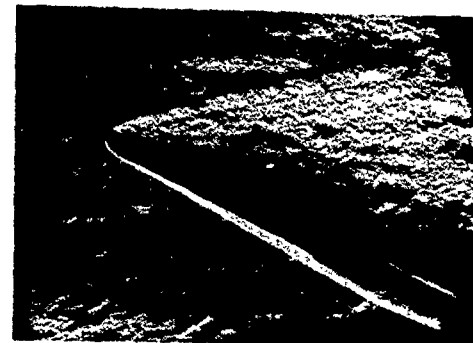
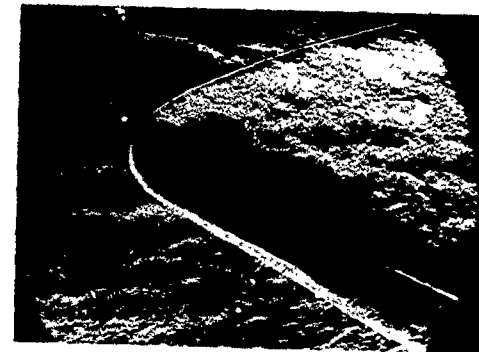
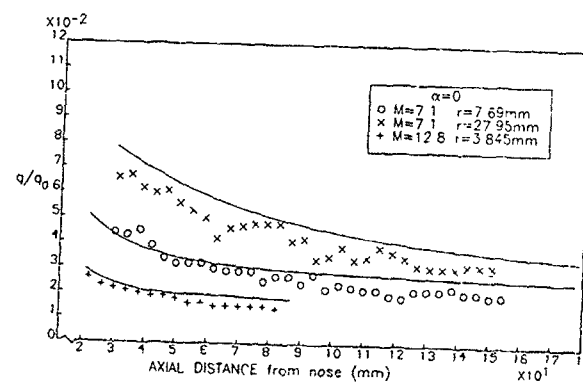
(a) Gun tunnel model:  $r = 3.845$  mm(a) Gun tunnel model:  $r = 3.845$  mm(b) Shock tunnel model:  $r = 7.69$  mm(b) Shock tunnel model:  $r = 7.69$  mm(c) Shock tunnel model:  $r = 27.95$  mm(c) Shock tunnel model:  $r = 27.95$  mmFig 10 Schlieren photographs at  $\alpha = 0^\circ$ Fig 11 Schlieren photographs at  $\alpha = 20^\circ$ 

Fig 12 Comparison of KHOMP2D with experimental data

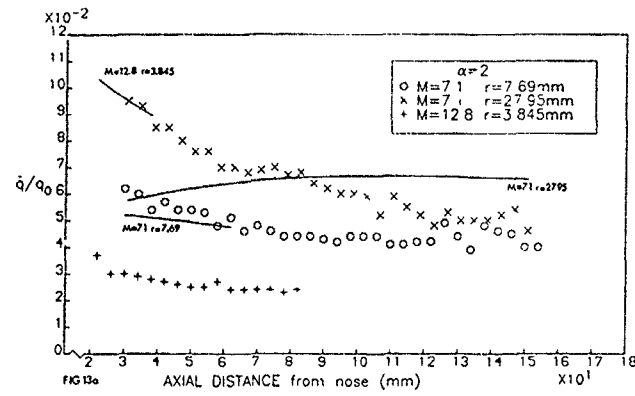


Fig 13a Comparison of KHOMP3D with experimental data Windward generator

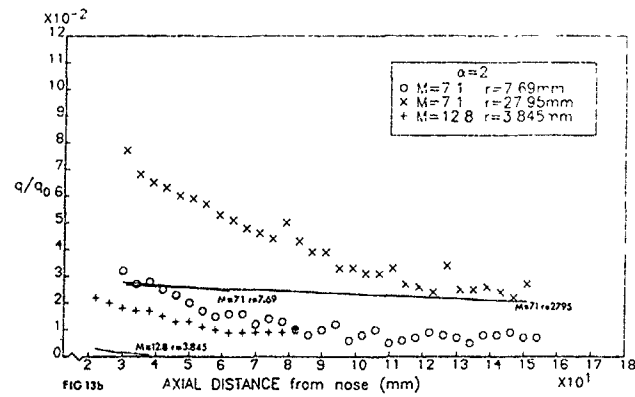


Fig 13b Comparison of KHOMP3D with experimental data Leeward generator

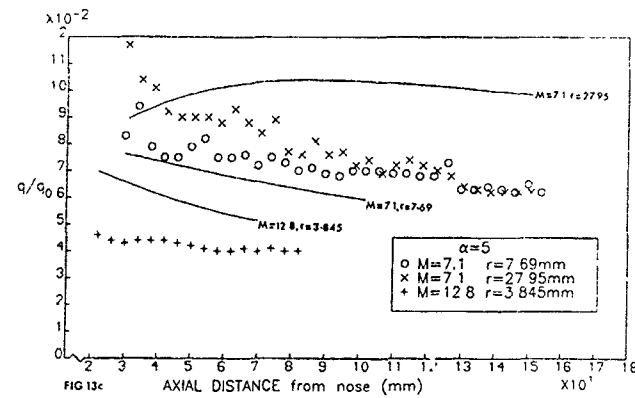


Fig 13c Comparison of KHOMP3D with experimental data Windward generator

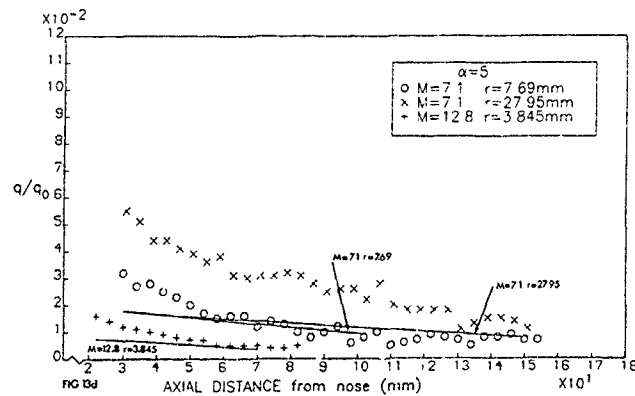


Fig 13d Comparison of KHOMP3D with experimental data Leeward generator

# THERMAL IMAGING ON MISSILES IN HYPERSONIC FLOW

Henning SCHÖLER

DLR Institute for Experimental Fluid Mechanics  
Bunsenstrasse 10, D-3400 Göttingen, F.R.G.

## Summary

The method of thermal imaging with liquid crystals developed at DLR Göttingen is briefly described, and some applications in the DLR Ludwig tube are presented. As the temperature sensor is sprayed on the model no expensive instrumentation is required. Responding to temperature variation the liquid crystals show a colour play which directly visualizes surface temperature fields. For qualitative heat transfer measurements, it is sufficient to photograph or video record the model while it is exposed to the flow.

## 1. Introduction

The increasing speed of missiles and projectiles in the anti-aircraft and armour penetrating classes requires growing attention to aerodynamic heating problems. In many cases the position of hot spots created by shock or vortex impingement or by boundary layer transition cannot be predicted accurately and has to be determined in wind tunnel experiments. Here again, difficulties imposed by extensive model instrumentation with discrete sensors, hamper the accuracy of the results.

Thermal imaging techniques can overcome these problems, as a complete mapping of the model surface is provided. Detailed local information can be obtained later with conventional sensors at the loci of interest, if necessary. Alternatively, after an appropriate calibration procedure, quantitative heat transfer data can be extracted from the thermal maps.

A low cost method of thermal imaging is the liquid crystal technique, which has been developed and established at DLR Göttingen [1].

## 2. Liquid Crystals

Some organic materials form a mesophase between the solid and the liquid phase, where a strongly anisotropic fluid is formed. This mesophase is called the liquid crystal phase. It was first observed in 1888 by Friedrich Reinitzer in Prague.

The melting process of a mesogenic crystal is a gradual loss in order as shown in Fig. 1. At the melting point the three dimensional order of the crystal grid is broken down to a two dimensional one; the material can be imagined as a set of lubricated solid slabs (smectic = soap-like structure). With rising temperature the two dimensional order of each slab is destroyed, and each layer forms a two dimensional fluid. After transition to the nematic (thread-like) phase the position of each molecule is random, however, a long range orientation of the molecules remains.

If the temperature is above the clearing point, the orientation vanishes, the fluid is then isotropic.

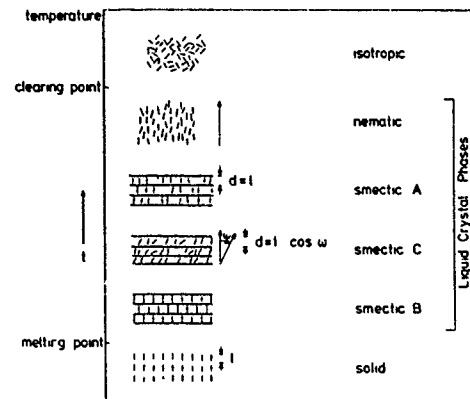


Fig. 1 Phase transitions in a mesogenic material

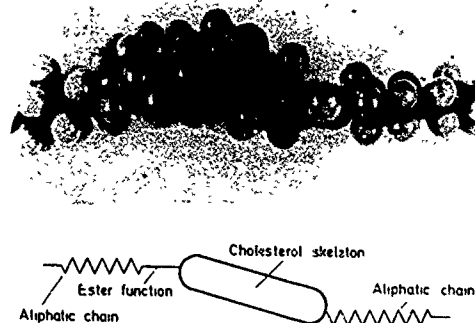


Fig. 2 Chiral structure of cholesterol esters

The cholesteric mesophase can be considered as a special case of the nematics, where chiral molecules are solved in a nematic fluid, or if the molecules of the fluid itself are chiral, i.e. cholesterol esters. The structure of such a molecule is shown in Fig. 2.

The nematic structure undergoes a helical distortion with the spatial period being one half of the pitch  $p$ , which typically is in the order of visible light (Fig. 3).

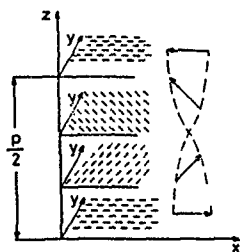


Fig. 3 Structure of cholesteric liquid crystals

This results in Bragg reflection of an incident light beam with  $R = p/2$  showing an extremely brilliant colour. The reflected light is circularly polarized, and the electrical field vector of the light wave forms a helix identical in shape to the cholesteric helix. Oppositely polarized light is fully transmitted. The physical properties of liquid crystals are described in detail in the textbooks by P.G. deGennes [2], and G. Vertogen and W.H. de Jeu [3].

In most cases the pitch  $p$  of cholesteric liquid crystals is decreasing with increasing temperature. There is a colour change from red to blue with rising temperature [4].

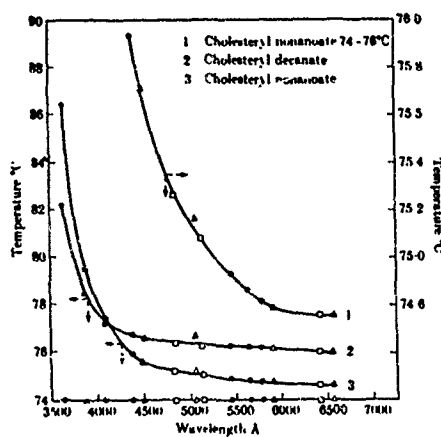


Fig. 4 Relation between pitch and temperature in typical cholesterics [4]

For a given sample at constant pressure the appearing colour is only a function of temperature and the process is fully reversible. The response time is in the order of milliseconds. The dependency of the reflected colour on temperature is highly nonlinear. As shown in Fig. 4, blue colour is displayed over a wide temperature range, therefore the cholesteric liquid crystals are sometimes called "blue phases" in the literature.

Many different materials or composed mixtures are commercially available with temperature spans for the colour play from  $0.05^\circ\text{C}$  to  $30^\circ\text{C}$  in the range from  $-30^\circ\text{C}$  to  $250^\circ\text{C}$ . For wind tunnel testing the choice of the mixture depends on the wind tunnel conditions and the desired experiment. Cholesteric liquid crystals are sensitive to shear stress as well [5]. Shear stress applied to a layer of liquid crystals distorts the helical axis of the orientation (see Fig. 3). Any angle of incidence between the incoming

light beam and the helical axis will shift the Bragg reflection to a shorter wavelength. This shear-stress-induced colour play is in some cases desirable; especially in low speed wind tunnels with negligible temperature effects boundary layer transition can be detected with this method [6, 7], or even in free flight [8].

In hypersonic wind tunnels, however, where temperature effects are dominant, shear stress influence has to be avoided. This can be done by the use of micro-encapsulated thermochromic liquid crystals. A small droplet of thermochromic material is enclosed in a capsule of gelatine and arabic gum which is a reliable shield against shear forces. The diameter of the capsules is in the order of  $10\text{ }\mu\text{m}$ . These micro-encapsulated liquid crystals are commercially available in the temperature range from  $-30^\circ\text{C}$  to  $150^\circ\text{C}$  as a water-based slurry.

In wind tunnel testing the liquid crystals are sprayed on a blackened model surface, as the colour play is best visible against a black background.

### 3. Test Apparatus

The experiments were done in the DLR's Ludwig Tube. A sketch of the tunnel is shown in Fig. 5.

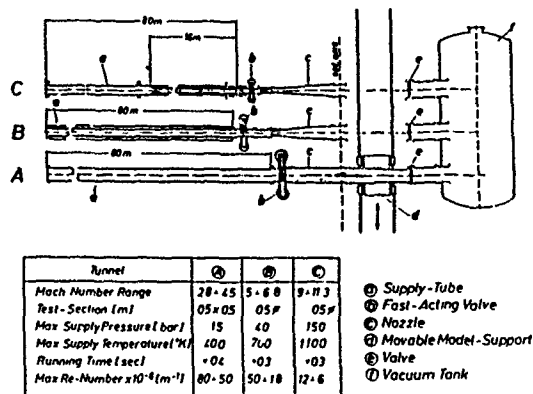


Fig. 5 The Ludwig tube of DLR

The wind tunnel is a downward-blowing tunnel working with the Ludwig principle, where constant stagnation conditions are provided by the state behind a travelling rarefaction wave inside a storage tube, thus disusing any regulation mechanisms. Compressed air is provided in three electrically heated storage tubes of 80 m length each, accelerated in nozzles to the desired Mach number and dumped through the test section into a vacuum tank. The Mach number range is  $3 \leq Ma_\infty \leq 12$  with the Reynolds number extending from  $Re_\infty = 10^6$  to  $Re_\infty = 5 \cdot 10^7$ , based on 1 m length. The test section has a diameter of 0.5 m or, for tube A at  $Ma_\infty = 3 - 4.6$ , a squared test section  $0.5 \times 0.5 \text{ m}^2$ . The running time of the tunnel is limited by the travelling time of the rarefaction wave twice the length of the tube and is around 0.35 s. A detailed description of the Ludwig Tube is given in [9].

The test set-up is sketched in Fig. 6: A model of low heat conductivity is sprayed with liquid crystals of the desired range and then mounted on the support in the test section.

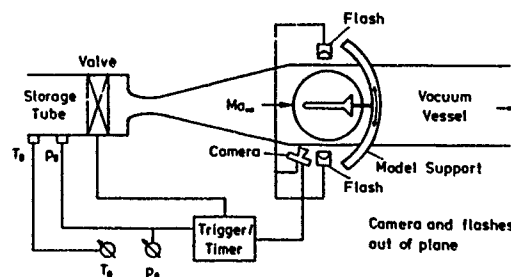


Fig. 6 Test set-up in Ludwieg tube

Low heat conducting material for the models as perspex, Plexiglas® or Ureol® etc. has proven to give the best spacial resolution for thermal imaging. The model is illuminated by a blue flash, a strobe flash, or a circular neon tube, depending on the recording device as i.e. a photo camera, a high speed movie camera, or a video camera. Illumination with spotlights is limited, because the black model surface absorbs all light and converts it into heat. The average power that is radiated by flashing lights is several orders of magnitude smaller. Spotlights are used to heat the models after spraying liquid crystals on the surface to check the quality of the colour play.

#### 4. Examples of Thermal Imaging in Hypersonic Testing

##### 4.1 Boundary layer transition on cones

The expected heat transfer distribution along a cone in hypersonic flow is shown in Fig. 7.

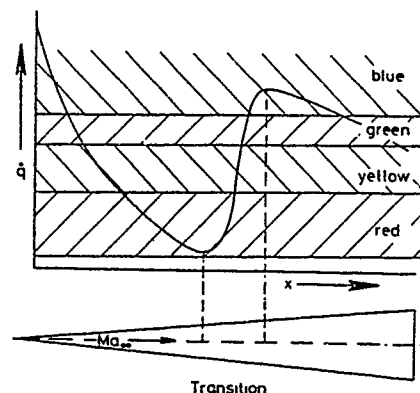


Fig. 7 Heat transfer along a cone

At the vertex there is high stagnation point heating. As the boundary layer grows along the cone the heat transfer reduces. Eventually the laminar boundary layer becomes unstable and undergoes transition to a turbulent state, combined with a steep rise in heat transfer which then with growing turbulent boundary layer thickness gradually reduces again.

If the model is coated with thermochromic liquid crystals a blue colour in the stagnation region will be observed that changes through the whole spectrum to red, and in the transition zone rapidly changes to blue again.

Figures 8-30 are colour photographs which for technical reasons are printed on three pages as an appendix to this contribution. The figure captions are on page 29-A3.

Fig. 8 shows a photograph of a  $10^\circ$ -cone in a  $Ma_\infty = 5$  flow. Between 60 % and 80 % of the cone length we observe a colour change from red to blue, indicating boundary layer transition.

Doubling the free stream Reynolds number from  $1.6 \cdot 10^7$  based on 1 m length to  $3.2 \cdot 10^7$  shifts the transition zone (in Figure 9) forward to 30 % - 40 % of the cone length, thus proving that the transition Reynolds number is independent of the free stream Reynolds number.

The influence of nose radius on transition is shown in Figs. 10 and 11. At the same free stream Reynolds number an increasing nose radius pushes the transition region downstream, due to the fact that the attached conical shock wave now detaches and the subsonic-supersonic flow behind the shock exposes the boundary layer to a more favourable pressure gradient.

Boundary layer transition is very sensitive to small angles of attack, being delayed on the windward side and promoted on the leeward side.

For angles of attack larger than  $\alpha = 3^\circ$ , on the leeward side vorticity effects become pre-dominant [11].

The surface heat transfer pattern induced by leeside vortices is shown in Fig. 12 on a blunt cone in a  $Ma = 5$  flow at  $\alpha = 15^\circ$  angle of attack.

It could be shown that for cones a critical nose radius exists, above which for a given flow situation, the positions of all boundary layer transition and leeside vortex flow phenomena are proportional to the nose radius

##### 4.2 Boundary layer transition on a sphere

The hypersonic flow around domes of self-guiding missiles is similar to the flow around a sphere. As long as the sonic line that limits the subsonic flow behind the detached bow shock is on the spherical part, the shape of the following body is of no evidence to the flow in this region. It is important to know if boundary layer transition occurs in this region giving rise to structural strength problems because of high turbulent heat transfer

A sphere machined from Plexiglas® was coated with liquid crystals and tested in the DLR Ludwieg tube in a  $Ma_\infty = 5$  flow. The test set-up was arranged so that the camera looked from about  $30^\circ$  forward to allow observation of the stagnation region.

The two photographs in Fig. 13 and 14 taken during the same run in a 200 ms time interval, display purely laminar flow around the sphere at a Reynolds number of  $Re_d = 2 \cdot 10^6$ , based on the diameter of the sphere. The first photograph shows a green spot at the stagnation point which quickly fades to red and is colourless where the surface temperature is still below the colour-play band of the liquid crystals.

In Fig. 14 around the stagnation point the temperature has risen to beyond the clearing point of the liquid crystals and decreases continuously towards the equator.

If the Reynolds number is increased to  $Re_d = 3 \cdot 10^6$ , as shown in Fig. 15, some turbulent wakes from surface

roughness appear, the main boundary layer flow still stays laminar.

At a further increase of the Reynolds number to  $Re_d = 3.5 \cdot 10^6$  (Fig. 16) the turbulent wakes become more pronounced and at  $Re_d = 4 \cdot 10^6$  there are only very few areas left where the boundary layer still appears laminar.

Finally at  $Re_d = 4.5 \cdot 10^6$ , the boundary layer transition is complete and can easily be seen in Fig. 18 as a fringed zone encircling the stagnation point.

The wind tunnel conditions at  $Ma_\infty = 5$  simulate flight altitudes of about 14 000 m (Fig. 13, 14) down to 8 000 m in Fig. 18. On the highly polished dome surface of a real missile the boundary layer transition will occur at a somewhat higher Reynolds number, for the liquid crystal layer introduces a surface roughness of about 0.01 - 0.02 mm, hence the prediction is "on the safe side".

#### 4.3 Taylor-Görtler vortices on a short cylinder

On a short cylinder perpendicular in a  $Ma_\infty = 5$  flow thermal imaging reveals two phenomena:

At a Reynolds number of  $Re_d = 2 \cdot 10^6$ , based on the diameter of the cylinder Taylor-Görtler vortices can be observed (Fig. 19) [12]. Their regular structure can still be seen at twice the Reynolds number in Fig. 20. The boundary layer flow, however, is by no means two-dimensional, as the pattern of the vortices might suggest. The boundary layer seems to radiate out from a stagnation point in all directions along the surface of the cylinder and undergoes transition to turbulence.

The three-dimensionality of the boundary layer can also be observed in Fig. 19 by the turbulent wakes of two particles in the flow which have smashed the surface of the cylinder.

#### 4.4 Heating pattern at the window of a missile infrared seeker

A design study for a self-guiding missile was tested in the Ludwig tube. The forebody had a blunt ogive shape with the first part flattened to a ellipsoidal cross section to give space for a plane window for the infrared seeker.

Prior to quantitative heat transfer measurements a flow visualization was made and thermal imaging of the heating pattern.

The flow visualization was done with a differential interferometer, into which a schlieren apparatus is easily changed by adding a pair of Wollaston prisms and a pair of polarizers.

The photograph in Fig. 21 shows the differential interferogram of the duckbill-shaped nose of the missile in a  $Ma_\infty = 5$  flow at  $\alpha = 0^\circ$  angle of attack. Fringe setting was horizontal with infinite spacing and the displacement of the ordinary and extraordinary beam was about 3 mm.

The bow shock is observed from the nose and, on the rostrate part in front of the window, a large separated area, above which a compression wave can be detected. At reattachment of the flow on the window shortly behind the corner a strong plane shock wave is formed.

At  $\alpha = -5^\circ$  angle of attack (Fig. 22) the bow shock is pressed closer to the body. The separation bubble is much smaller and the flow reattaches almost directly behind the corner. The bow shock intersects with the plane shock from the corner. This seems to let the boundary layer separate on the window, as lines of equal density move away from the surface.

This expresses in the appearance of a sharp curved line in the liquid crystal photographs in Fig. 23.

The two photographs are taken during the same wind tunnel run in a 200 ms time interval. Due to the smaller Mach number of  $Ma_\infty = 4.2$  in this test series and hence larger shock angles, the curved line is shifted somewhat towards the rear of the window; the phenomenon, however, is the same. The reason for showing thermal images and interferograms at different Mach numbers is very simple: The photographs became better as we gained experience throughout the tests.

Fig. 23a shows on the window a line of symmetry and number of faintly visible straight lines which focus on the two small dark peaks at the left, just behind the stagnation zone (Fig. 23b). The flow within this region seems to be conical. Note the turbulent wake of a surface roughness in the lower part of the window. The flow outside the conical part expands over the sides of the window and boundary layer transition occurs (see chapter 4.2). The pattern on the model surface resembles a flying bat.

Fig. 24 shows the model at zero angle of attack. The intersection of the bow shock and the window shock does not hit the model. The heat transfer in the window region reduces. In Fig. 24a the line of symmetry is clearly seen as well as the limits of the conical flow region. The flying bat structure is even more pronounced.

Fig. 25 at  $\alpha = +5^\circ$  finally reveals the conical part being the influence of vortices which are developing in the vicinity of the nose and are impinging on the window, expressed by the typical owl face structure.

The thermal imaging allowed a much better interpretation of the results of local quantitative thin skin heat transfer measurements conducted consequently.

#### 4.5 Aerodynamic heating in the fin region of a kinetic energy projectile

In the framework of a data exchange agreement a generic kinetic energy finned projectile was investigated in the DLR Ludwig tube.

The model shown in Fig. 26 had six fins of 4 D length and 1.4 D span each and three different tips with an  $8^\circ$  half angle conical tip of nose radius 0.05 D providing L/D of 10, 15, and 20 respectively for the cylindrical part; D = 20 mm. The aerodynamic heating especially in the finned region was tested by thermal imaging with liquid crystals throughout  $Ma_\infty = 3$  to 6 at  $\alpha = 0^\circ$  and  $4^\circ$ , x-wise and y-wise.

As an example, the heating patterns at  $Ma_\infty = 3$  are presented at L/D = 10 and x-wise orientation.

Fig. 27 shows the model at  $\alpha = 0^\circ$ . The boundary layer is still laminar, as was checked by schlieren visualization. On the fins a number of vortices appear, with a horseshoe vortex around the foot of the fin. Note the high heating at the leading edges, seen by the dark blue colour.

At  $\alpha = 4^\circ$  in Fig. 28 on the suction side we observe the high heating due to the leeward boundary layer transition and vortices on the fuselage and a number of vortices which seem all to originate at the foot of the leading edge. This pattern is typical for the leeward flow over a delta wing.

On the pressure side, however, shown in Fig. 29, the fine vortices on the fins are parallel to the outer flow. A certain large scale periodicity in the heating pattern of these vortices shows up.

The attaching flow heats the fuselage. This is blocked at the beginning of the fins by a separation bubble between the fins, caused by the detached shock waves around the leading edges interfering with the boundary layer on the fuselage. The number of corner vortices between the fins is increasing.

Fig. 30 finally shows the model in side view. Note again the leeward turbulent boundary layer on the fuselage and the different patterns on the inner fins, one displaying the windward, the other the leeward side

## 5. Conclusion

It has been shown that in many cases thermal imaging helps a lot in understanding aerodynamic heating phenomena in hypersonic flow. On the other hand it displays the complexity of boundary layer flow especially in corner flow configurations.

## 6. References

- [1] H. Schöler, *Application of Encapsulated Liquid Crystals on Heat Transfer Measurements in the Fin-Body Interaction Region at Hypersonic Speed*. AIAA Paper No 78-777, AIAA 10th Aerodynamic Testing Conference, San Diego, 1978
- [2] P.G. de Gennes, *The Physics of Liquid Crystals*. Oxford University Press (1974) ISBN 0-19-851285-6.
- [3] G. Vertogen and W.H. de Jeu, *Thermotropic Liquid Crystals, Fundamentals*. Springer Series in Chemical Physics, Vol. 45, 1988 ISBN 3-540-17946-1 Springer-Verlag Berlin, Heidelberg, New York ISBN 0-387-17946-1 Springer-Verlag New York, Berlin, Heidelberg.
- [4] J. Ferguson, N. Goldberg, R. Nadalin, *Molecular Crystals* 1, 315 (1966).
- [5] E.I. Klein, *Liquid Crystals in Aerodynamic Testing*. *Astronautics and Aeronautics* 6, No 7, p. 70 (1968).
- [6] K. Pengel, *Surface Flow Visualization with Shear Stress Sensitive Liquid Crystals*. DNR-WT1-88.039, Oct. 1988.
- [7] L. Gaudet and T.G. Gell, *Use of Liquid Crystals for Qualitative and Quantitative 2-D Studies of Transition and Skin Friction*. Paper prepared for ICIASF '89 DLR Göttingen, 18-21 September 1989. Royal Aerospace Establishment, Technical Memorandum Aero 2159.
- [8] P.D. Gall and B.J. Holmes, *Liquid Crystals for High-Altitude In-Flight Boundary Layer Flow Visualization*. AIAA-86-2592, AIAA General Aviation Technology Conference 1986, Anaheim, California.
- [9] H. Ludwig, Th. Hottner, H. Grauer-Carstensen, *Der Rohrwindkanal der Aerodynamischen Versuchsanstalt Göttingen*. Jahrbuch 1969 der DGLR, pp. 52-58.
- [10] H. Schöler and A. Banerji, *Visualization of Boundary Layer Transition on a Cone with Liquid Crystals*. ICIASF '83 Record - International Congress on Instrumentation in Aerospace Simulation Facilities, September 1983. IEEE Publication 83 CH 1954-7
- [11] H. Schöler and A. Banerji, *Visualization of Separation Effects on Blunt Cones at High Mach Numbers*. DLR-IB 222-84 A 38, Göttingen, 1984.
- [12] M. Van Dyke, *An Album of Fluid Motion*. The Parabolic Press, 1982, p.76. ISBN 0-915760-02-9.



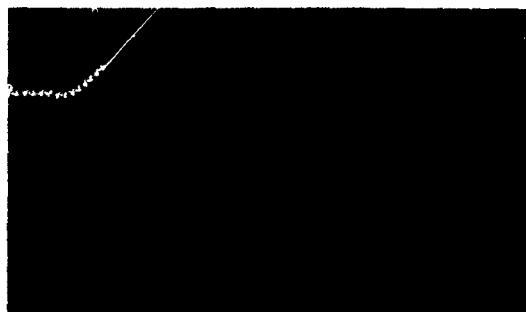


Fig. 8

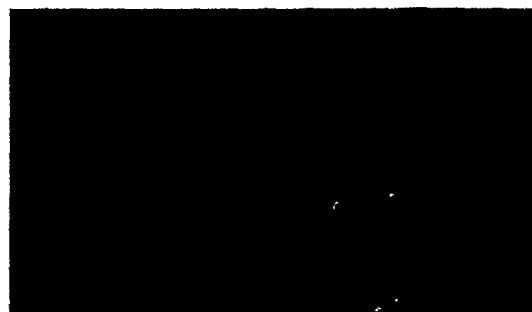


Fig. 13



Fig. 9



Fig. 14

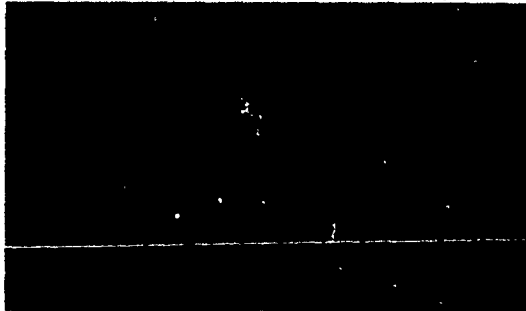


Fig. 10



Fig. 15

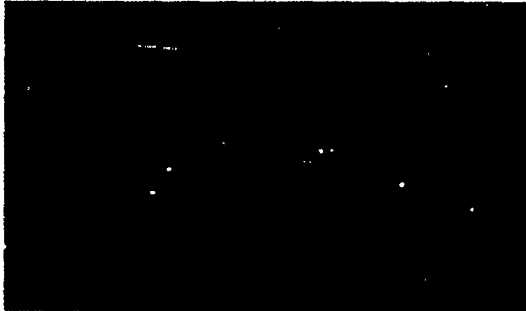


Fig. 11



Fig. 16



Fig. 12



Fig. 17

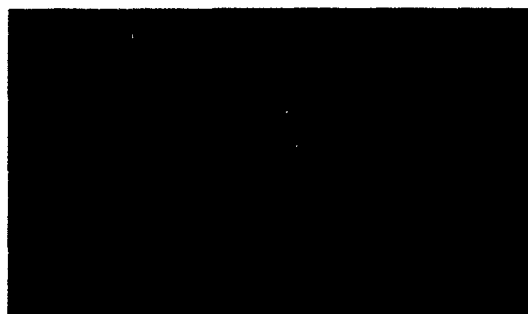


Fig. 18

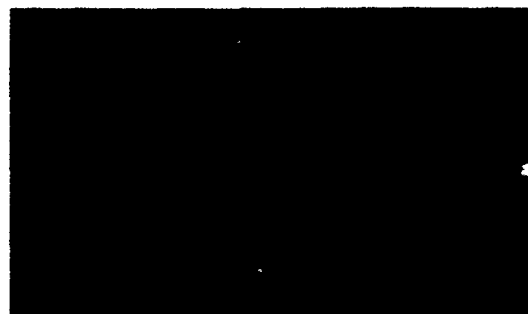


Fig. 23a

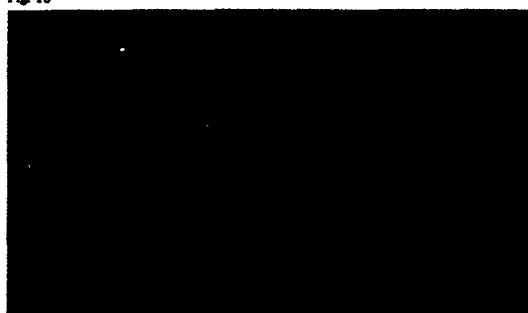


Fig. 19



Fig. 23b

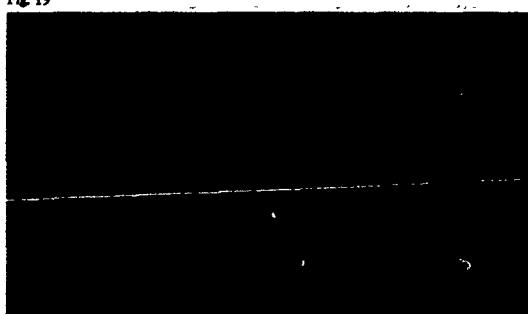


Fig. 20

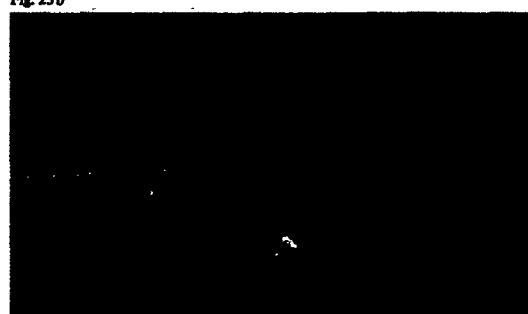


Fig. 24a



Fig. 21



Fig. 24b



Fig. 22

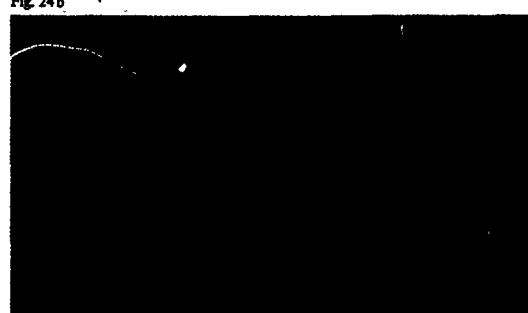


Fig. 25a

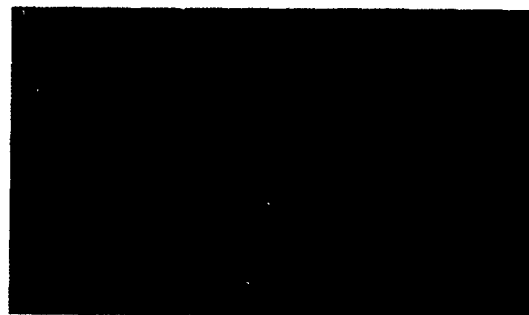


Fig. 25b

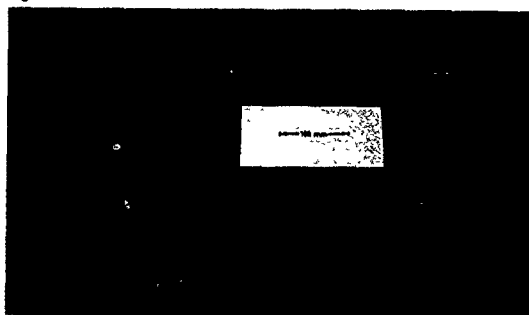


Fig. 26

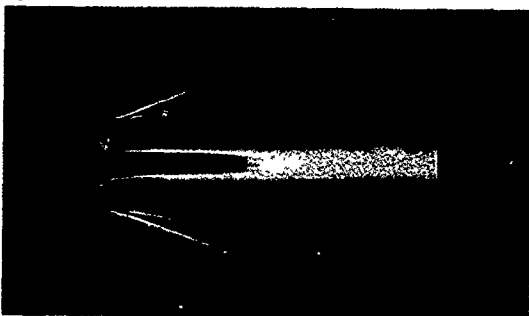


Fig. 27

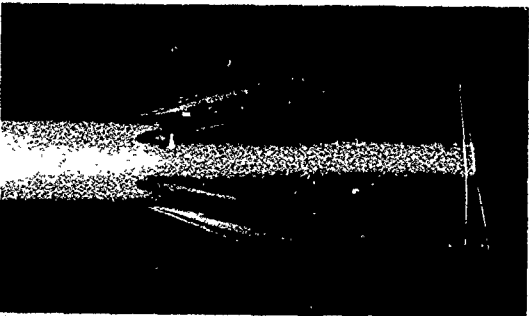


Fig. 28

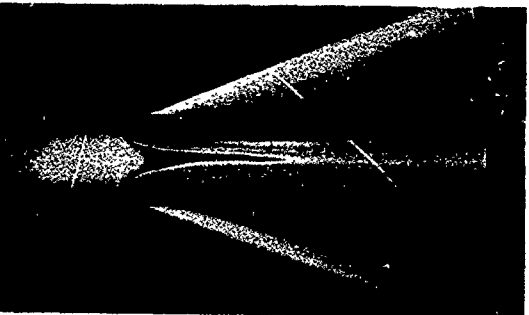


Fig. 29



Fig. 30

Fig. 8 Boundary layer transition on a  $10^\circ$  cone,  $Ma_\infty = 5$ ,  $Re_\infty = 1.6 \cdot 10^7 [m^{-1}]$

Fig. 9 Boundary layer transition on a  $10^\circ$  cone,  $Ma_\infty = 5$ ,  $Re_\infty = 3.2 \cdot 10^7 [m^{-1}]$

Fig. 10 Boundary layer transition on a cone,  $Re_\infty = 2.4 \cdot 10^7 [m^{-1}]$ , nose radius  $r_n = 0.7$  mm.

Fig. 11 Boundary layer transition on a cone,  $Re_\infty = 2.4 \cdot 10^7 [m^{-1}]$ , nose radius  $r_n = 5.25$  mm

Fig. 12 Leeward vortices on a blunt cone,  $Ma_\infty = 5$ ,  $\alpha = 15^\circ$

Fig. 13 Surface temperature distribution on a sphere in a  $Ma_\infty = 5$  laminar flow,  $Re_d = 2 \cdot 10^6$ .

Fig. 14 Same run in Ludwig tube, 200 ms later

Fig. 15 Surface temperature distribution on a sphere in a  $Ma_\infty = 5$  flow,  $Re_d = 3 \cdot 10^6$ , appearance of turbulent spots

Fig. 16 Surface temperature distribution on a sphere in a  $Ma_\infty = 5$  flow,  $Re_d = 3.6 \cdot 10^6$ , increase of turbulent spots

Fig. 17 Surface temperature distribution on a sphere in a  $Ma_\infty = 5$  flow,  $Re_d = 4 \cdot 10^6$ , only few laminar spots remaining

Fig. 18 Surface temperature distribution on a sphere in a  $Ma_\infty = 5$  flow,  $Re_d = 4.5 \cdot 10^6$ , fully turbulent flow

Fig. 19 Taylor-Görtler vortices on a short cylinder,  $Ma_\infty = 5$ ,  $Re_d = 2 \cdot 10^6$

Fig. 20 Taylor-Görtler vortices and boundary layer transition on a cylinder,  $Ma_\infty = 5$ ,  $Re_d = 4 \cdot 10^6$

Fig. 21 Differential interferogram of a missile nose with window for infrared seeker in a  $Ma_\infty = 5$  flow,  $\alpha = 0^\circ$

Fig. 22 Differential interferogram of a missile nose with window for infrared seeker in a  $Ma_\infty = 5$  flow,  $\alpha = -5^\circ$ , shock impinging on window

Fig. 23a Heating pattern on missile nose and window at  $Ma_\infty = 4.2$ ,  $\alpha = -5^\circ$

Fig. 23b Same run, 200 ms later

Fig. 24a Heating pattern on missile nose and window at  $Ma_\infty = 4.2$ ,  $\alpha = 0^\circ$

Fig. 24b Same run, 200 ms later

Fig. 25a Heating pattern on missile nose and window at  $Ma_\infty = 4.2$ ,  $\alpha = +5^\circ$

Fig. 25b Same run, 200 ms later.

Fig. 26 Generic K-E projectile with 3 tips of various L/D

Fig. 27 K-E projectile, aft region,  $Ma_\infty = 3$ ,  $\alpha = 0^\circ$

Fig. 28 K-E projectile, aft region,  $Ma_\infty = 3$ ,  $\alpha = 4^\circ$ , suction side

Fig. 29 K-E projectile, aft region,  $Ma_\infty = 3$ ,  $\alpha = 4^\circ$ , pressure side

Fig. 30 K-E projectile, aft region,  $Ma_\infty = 3$ ,  $\alpha = 4^\circ$ , side view

# CHORDWISE AND SPANWISE CENTERS OF PRESSURE OF MISSILE FINS

Daniel J. Lesieutre  
Research Engineer  
Marnix F. E. Dillenius  
Vice President, Engineering Aerodynamics  
Nielsen Engineering and Research, Inc.  
510 Clyde Avenue  
Mountain View, CA 94043-2287  
U.S.A.

## 1. Summary

The extensive triservice experimental data base has been investigated and used to obtain a fin chordwise and spanwise center of pressure data base for use in the preliminary analysis and design of missile fins. Correlations and curve fits of the center of pressure data have been performed to reduce the storage and computation time required to obtain engineering level predictions of fin hinge and bending moments. The method developed is simple to use and is easily incorporated into comprehensive missile aeroprediction methods. The method is extremely valuable because it includes effects due to real flow and fin-body gaps inherent in the experimental data base.

This paper describes the experimental data base, its manipulation, and its implementation into a prediction method.

## 2. List of Symbols

a	body radius
AR	aspect ratio of wing-alone formed by joining two fins at their root chords
$C_{BM}$	fin bending-moment coefficient; bending moment/ $q_{\infty} S_R$
$C_{HM}$	fin hinge-moment coefficient; hinge moment/ $q_{\infty} S_R c_R$
$C_{NF}$	fin normal-force coefficient; normal force/ $q_{\infty} S_R$
$c_R$	fin root chord
$c_T$	fin tip chord
D	maximum body diameter
$l_R$	reference length
$M_{\infty}$	freestream Mach number
s	exposed fin semispan
$s_m$	semispan of fin-body combination
$S_R$	reference area
$x_{HL}$	chordwise location of fin hinge line measured from leading edge of the fin root chord
$x_{LE}$	axial location of the leading edge of the root chord measured from the nose tip
$x_{cp}$	chordwise location of the fin normal-force center of pressure measured from the leading edge of the fin root chord
$y_{cp}$	spanwise location of the fin normal-force center of pressure measured outboard from the fin root chord
$\alpha_c$	included angle of attack; angle between the body axis and the freestream velocity vector
$\delta$	fin deflection angle
$\lambda$	taper ratio; ratio of fin tip chord to root chord

$\phi_f$  fin orientation angle in data base,  $\phi_f = +90^\circ$  for fin on windward meridian,  $\phi_f = -90^\circ$  for fin on leeward meridian

## 3. Introduction

The preliminary design and analysis of new missile configurations or improvements to existing missiles requires estimates of the fin hinge- and bending-moment coefficients. These estimates are necessary for structural design and for actuator sizing. In addition, a method capable of accurately predicting hinge moments can be used to determine optimum hinge line location for minimum hinge moment.

In order to predict the fin hinge- and bending-moment coefficients and the missile overall rolling, pitching, and yawing moment coefficients, it is necessary to determine the chordwise and spanwise positions of the fin center of pressure. An engineering level method to predict fin center of pressure for preliminary analysis and design of conventional fins in cruciform arrangements has been developed. The method makes use of the extensive systematic fin-on-body force and moment triservice experimental data base (Refs. 1 and 2) which covers a Mach number range from 0.6 to 4.5, fin aspect ratios from 0.25 to 4.0, angles of attack up to  $45^\circ$ , and deflection angles from  $-40^\circ$  to  $40^\circ$ . This paper describes the experimental data base, its manipulation, and its implementation into a prediction method.

### 3.1 Overview Of Triservice Experimental Program

The overall objective of the triservice test program (Ref. 2) was to obtain a high quality systematic force and moment data base for fins mounted on a body. The experimental data fall into two categories: (1) fin loads without fin deflection for all fins in the data base (stability data), and (2) fin loads with fin deflection for a control fin set (control data). The model design and test conditions were based on the utilization of the NASA Langley Remote Control Missile Roll Rig (Ref. 2), and they were intended to reflect as completely as possible the range of flight conditions and fin designs employed by modern high performance missiles.

The Langley body-tail model is 3.0 inches in diameter and 11.5 calibers long. The model allows independent, remote control of four control surfaces and model roll angle and includes three component balances for each of the four fins. All of the data obtained for the data base were for a body with a single cruciform fin set on the body. The body details

including fin hinge line locations are shown in Figures 1(a) and 1(b). The forces and moments for the fins depicted in Figure 1(c) were obtained from force balance measurements. All fins have symmetric double wedge airfoil sections. Geometric details of these fins can be found in Reference 1. All test fins have a body radius to fin semispan ratio,  $a/s_m$ , of 0.5. The tests measured fin normal-force, hinge-moment, and bending-moment coefficients.

Multiple tunnel entries were performed between 1982 and 1984. Intermediate and high Mach number (2.5 - 4.5) tests were conducted in the NASA Langley Unitary Plan Tunnel (Ref. 2), and low and intermediate Mach number (0.6 - 2.0) tests were conducted in the 6-by-6 foot Supersonic Tunnel at NASA Ames.

### 3.2 General Description Of Triservice Data Base

The ranges of parameters in the triservice experimental data base are described in this section. The data base consists of a stability set of data for undeflected fins and a control set of data for deflected fins. The test fins have aspect ratios (aspect ratio of two fins joined together at the root) of 0.25, 0.5, 1, 2, and 4, and the taper ratio ranges from 0 to 1. The fins with aspect ratios of 1, 2, and 4 are the control test fins. Fins with trailing edge sweep and/or swept forward leading edges are not included. The body radius to fin semispan ratio,  $a/s_m$ , is 0.5 for all test fins, and the method and data base consider cruciform sections with identical fins only. Figure 1(c) depicts the fin planforms, and the following table shows the aspect ratio and taper ratio domain of the data base.

		TAPER RATIO, $\lambda$			
		0	1/2	1	
ASPECT RATIO, AR	1/4			12	CONTROL FINS
	1/2	31	32	33	
	1			42	
	2	51	52	53	
	4			62	

TABLE 1. aspect ratio and taper ratio range of the database

The matrix numbers in Table 1 are the test fin designation numbers (Figure 1(c)).

The Mach number range of the data base is from 0.6 to 4.5. Stability test data for Mach numbers of 0.6, 0.8, 0.9, and 1.2 provide detailed loads for the transonic speed regime. The supersonic Mach numbers in the stability data base are 1.5, 2.0, 2.5, 3.0, 3.5, and 4.5. The Mach numbers for the control test data base are 0.8, 1.2, 2.0, 3.0, and 4.5.

The body angle of attack range is  $\alpha_c \leq 45^\circ$  with actual wind tunnel test angles of attack of  $\alpha_c = 0, 2, 5,$

10, ..., 40, and  $45^\circ$ . The fin control deflection angles vary from  $-40^\circ$  to  $40^\circ$  in  $10^\circ$  increments. The data base contains fin loads for  $-90^\circ \leq \phi_f \leq 90^\circ$  in  $10^\circ$  increments, where  $\phi_f$  is the fin orientation angle on the body ( $\phi_f = 90^\circ$  for a fin on the windward meridian,  $\phi_f = -90^\circ$  for a fin on the leeward meridian).

Figure 2 shows the angle of attack, aspect ratio, and Mach number range of the systematic data base.

The stability data base consists of 2090 flow conditions/orientations ( $M_\infty$ ,  $\alpha_c$ , and  $\phi_f$ ) for each of the nine fins. In addition, the fin normal-force, hinge-moment, and bending-moment coefficients are present for each fin and condition. This results in a total of 56,430 individual fin data points measured during the experimental program. The control data base consists of 9405 flow conditions/orientations ( $M_\infty$ ,  $\alpha_c$ ,  $\phi_f$ , and  $\delta$ ) for each of the five control fins. The measurement of the fin normal-force, hinge-moment, and bending moment coefficients for each fin and condition results in a total of 141,075 individual fin data points measured during the experimental program. To develop an efficient prediction method for fin centers of pressure, methods were investigated and developed to correlate the stability and control data thus reducing the required storage and calculations required.

The following sections describe the fin center of pressure data base and correlations. The stability data (undeflected fins) is discussed first followed by a description of the control data (deflected fins).

### 4. Data Base Description

The data base consists of fin-on-body center of pressure data. The centers of pressure in the chordwise and spanwise directions have been correlated to be a function of one or more of the following parameters: AR,  $\lambda$ ,  $M_\infty$ ,  $\alpha_c$ ,  $\phi_f$ ,  $\delta$ , and  $|C_{N_F}|$ , the magnitude of fin normal force. Data for the chordwise and spanwise centers of pressure are included with and without fin deflections for fins with aspect ratios of 0.25 to 4.0 to illustrate the approach.

The measured fin hinge and bending moments have been reduced to obtain the chordwise,  $x_{CP}/c_R$ , and spanwise,  $y_{CP}/s$ , centers of pressure as follows.

$$\frac{x_{CP}(M_\infty, \alpha_c, \phi_f, \delta)}{c_R} = \frac{x_{HL}}{c_R} - \frac{C_{HM}(M_\infty, \alpha_c, \phi_f, \delta)}{C_{NF}(M_\infty, \alpha_c, \phi_f, \delta)} \quad (1)$$

$$\frac{y_{CP}(M_\infty, \alpha_c, \phi_f, \delta)}{s} = \frac{C_{BM}(M_\infty, \alpha_c, \phi_f, \delta)}{C_{NF}(M_\infty, \alpha_c, \phi_f, \delta)} \quad (2)$$

The stability data consist only of  $\delta = 0^\circ$  data. The following sections summarize correlation procedures developed for the stability and control data and examine the behavior of the fin center of pressure with respect to fin geometry and flow conditions.

#### 4.1 Stability Fin Center of Pressure

The correlation procedure for the stability fin centers of pressure is described in Reference 1 and is briefly summarized here. Because the experimental

results correspond to a specific body-tail wind tunnel model, it is desirable to correlate only the center of pressure data which are free of vortex-induced effects. Effects of vorticity in the flow field can be added with the equivalent angle of attack approach described in Reference 1.

When body vortex-induced effects on the fin loads are removed, the fin center of pressure locations depend primarily on the fin normal-force coefficient and therefore are insensitive to roll angle as described in Reference 1. To obtain the centers of pressures as a function of the magnitude of fin normal force  $|C_{NF}|$  without vortex effects, the fin on the windward side of the body ( $0^\circ \leq \phi_f \leq 80^\circ$ ) is considered because the vortex-induced contributions to the fin load are minimal. The measured center of pressure for this case is almost entirely free of vortex effects. A piecewise linear least squares fit applied to the  $x_{CP}/c_R$  ( $M_\infty, \alpha_c, \phi_f, \delta = 0^\circ$ ),  $y_{CP}/s$  ( $M_\infty, \alpha_c, \phi_f, \delta = 0^\circ$ ),  $x_{CP}/c_R$  ( $M_\infty, \alpha_c, \phi_f, \delta = 0^\circ$ ),  $y_{CP}/s$  versus  $|C_{NF}|$  ( $M_\infty, \alpha_c, \phi_f, \delta = 0^\circ$ ) data results in a single curve fit of the windward fin data for  $\phi = 0^\circ$  to  $80^\circ$ . Figure 3 depicts typical fits of the  $x_{CP}/c_R$  and  $y_{CP}/s$  data points for orientation angles  $\phi_f$  from  $0^\circ$  to  $80^\circ$  of fin 52 (Fig. 1(c)). Supersonic conical linear theory predicts the center of pressure to be at the area centroid of the fin. Figure 3 indicates that the chordwise and spanwise centers of pressure measured in the experiment approach the area centroid as the Mach number increases. This is seen by comparing Figures 3(a) through 3(c). Limited representative examples from the data base are shown for selected Mach numbers only. Generally, the centers of pressure for the undeflected fins correlate very well with  $|C_{NF}|$  for all fins and Mach numbers in the data base.

With the dependence on  $\alpha_c$  and  $\phi_f$  reduced to a dependence on  $|C_{NF}|$ ,  $x_{CP}/c_R$  and  $y_{CP}/s$  depend only on AR,  $\lambda$ ,  $M_\infty$ , and  $|C_{NF}|$ . The interpolation procedure in the  $M_\infty$  and  $|C_{NF}|$  parameters is bilinear. The interpolation procedure in the aspect AR and  $\lambda$  parameters is described in Reference 1.

#### 4.2 Control Fin Data Base

The control data base is composed of two parts. (1) transonic center of pressure data, and (2) supersonic center of pressure data.

#### 4.2 Transonic/Low Supersonic Fin Control Center of Pressure

The effect of control deflection on the center of pressure locations in the transonic speed regime is derived from the control test fins at  $\phi_f = 0^\circ$ . Here, the transonic/low supersonic range includes Mach 0.8, 1.2, and 2.0.

For the transonic/low supersonic range, the center of pressure data are plotted versus  $|C_{NF}|$  for each fin. The  $-40^\circ \leq \delta \leq 40^\circ$  data for each fin is plotted on the same graph for each Mach number, and these data are fitted with a piecewise linear curve. Representative examples of these fins are shown in Figure 4 for fin 52 for various Mach numbers. The dependence on  $\alpha_c$  and  $\delta$  is reduced to a dependence on  $|C_{NF}|$ . Thus,  $x_{CP}/c_R$  and  $y_{CP}/s$  depend only on AR,  $\lambda$ ,  $M_\infty$ , and  $|C_{NF}|$ . Note that for  $M_\infty = 3.0$ , this correlation does not collapse the center of pressure data as well as it

does for the lower Mach numbers. Therefore, the correlation described in the next section is used for the higher Mach numbers. The interpolation procedure in the AR- $\lambda$  parameters for the control fin data is described in a later section.

#### 4.3 Supersonic Fin Control Center of Pressure

An extensive effort (Ref. 3) was carried out to correlate the supersonic control fin center of pressure data base. The chordwise and spanwise centers of pressure were correlated for positive and negative deflection angles. During the development, this correlation was made to include the complete range of fin orientation angles; therefore, vortex effects on the centers of pressures were present in the correlations for the higher angles of attack for control fins on the leeward side of the body. This was done in order to give an indication of the magnitude of the body vortex effects present in the experimental tests. These vortex effects were particular to the configuration tested and as such are not applicable to other configurations. Since the vortex location and strength are dependent on the location of the fins on the body as well as upstream fin sets (if any), only the windward side data (nearly vortex free) should be used from the supersonic control fin data base. The equivalent angle of attack scaling method and a separate vortex model should be used to determine the effect of vorticity on the centers of pressure for cases different from those of this data base. Reference 1 describes the procedure used in program MISSILE 3 to accomplish this.

The supersonic control data did not correlate well with the magnitude of the fin normal force  $|C_{NF}|$ ; therefore, an extensive effort was undertaken to correlate these data using one or more of the independent parameters,  $M_\infty$ ,  $\alpha_c$ ,  $\phi_f$ , and  $\delta$  as described below. As a result, the correlations of the  $x_{CP}$  data are within 4% of the root chord, and the correlations for  $y_{CP}$  data are within 4% of the exposed fin span when the fin normal force is of significant value.

The positive deflection data ( $\delta \geq 0^\circ$ ) were plotted against ( $\phi_f - 90^\circ$ ), and the negative deflection data were plotted against ( $90^\circ - \phi_f$ ). This provided a plotting axis system which is zero on the windward meridian and either  $-180^\circ$  or  $180^\circ$  on the leeward meridian. The data were plotted in this manner for the following reasons: (1) on the windward meridian (plane of symmetry), the positive and negative deflection results should be the same for the same magnitude of deflection, (2) the effects of vorticity and dynamic head on the leeward side can be seen, and (3) the compressibility effects due to the body bow shock can be observed.

Representative examples of the correlated data are shown in Figures 5 through 6 for various angles of attack. Figure 5 shows the chordwise center of pressure for fin 52 at  $M_\infty = 4.5$ . Figure 6 shows the spanwise center of pressure for fin 52 at  $M_\infty = 4.5$ .

In Figure 5(a), the chordwise center of pressure shows no unusual behavior in the leeward region ( $\phi_f = -30^\circ$  to  $\phi_f = -90^\circ$ ). Vortical and other nonlinear effects due to angle of attack are minimal for  $\alpha = 2^\circ$ . As shown in Figure 5(b) for  $\alpha = 20^\circ$ , the chordwise center of pressure does not depend greatly on fin deflection

angle (for negative deflection angles) from  $\phi_f = 90^\circ$  to about  $\phi_f = -30^\circ$ . In this region, effects due to body vortices are minimal. On the leeward region, the chordwise center of pressure is influenced by vortical as well as nonlinear effects of reduced dynamic pressure. Largely to the same extent, these effects can also be observed for positive fin deflection angles although in this case some systematic dependence on fin deflection angle is indicated in the region where body vortex effects are minimal. Figure 5(c) illustrates the behavior of  $x_{cp}$  for  $\alpha_c = 45^\circ$ . The effect of the sign of the normal force for negative fin deflections is apparent in this figure.

The effects of the bow shock (and its associated flow field) close to or impinging on the fin can be observed by comparing the spanwise center of pressure locations shown in Figure 6(a) for  $\alpha_c = 2^\circ$  and in Figure 6(c) for  $\alpha_c = 45^\circ$ . For the fin near the windward meridian ( $\phi_f = 90^\circ$ ), the spanwise center of pressure moves inboard as the angle of attack is increased because of the bow shock influence.

The chordwise and spanwise center of pressure correlations shown in Figures 5 and 6 are based on both functional and parameterized correlations. A functional correlation is defined as one for which the effect of one of the independent parameters is described in a functional relationship. A parameterized correlation is defined as one for which the effect of one of the independent parameters is stored as a set of numbers to be used in an interpolation procedure. For the chordwise and spanwise centers of pressure,  $\phi_f$  and  $\delta$  were taken as functional parameters as shown in the next section. For the two high supersonic Mach numbers, 3.0 and 4.5, the experimental angles of attack are used for parameterized correlations. The details of the functional and parameterized correlations for the chordwise and spanwise center of pressure locations are described in Reference 3.

**Chordwise Center of Pressure.** - Figure 7 shows the error between the value from the correlation and the actual data for the chordwise center of pressure as a function of fin normal force magnitude for fin 52 at  $M_\infty = 4.5$  and  $\alpha_c = 20^\circ$ . Note that  $\bar{x}$  ( $\bar{x} = x_{cp}$ ) is the experimental data, and  $\bar{x}_c$  is the correlated quantity. It is seen that the chordwise center of pressure is generally within two percent of the root chord, except at the lower values of fin normal force. The correlations are generally best at low and high angles of attack. The largest deviations occur in the 10 to 20 degree angle of attack range. Maximum hinge moments will generally occur when the fin normal force is large; therefore, errors at the small values of  $C_{NF}$  are not critical for fin structural or actuator design. An extensive investigation of the errors in the correlations with respect to angle of attack and Mach number can be found in Reference 3.

**Spanwise Center of Pressure.** - Figure 8 depicts the error between the results obtained with the correlation and the actual data for the spanwise center of pressure ( $y = y_{cp}$ ) as a function of fin normal force magnitude for fin 52 at  $M_\infty = 4.5$  and  $\alpha_c = 20^\circ$ . It is seen that the spanwise center of pressure is generally within four percent of the exposed fin span, except at the lower values of fin normal force. An extensive investigation

of the errors in the correlations with respect to angle of attack and Mach number can be found in Reference 3.

## 5. Conclusions

The extensive triservice data base has been investigated and used to obtain a fin chordwise and spanwise center of pressure data base for use in the preliminary analysis and design of missile fins. Correlations and curve fits of the center of pressure data have been performed to reduce the storage and computation time required to obtain estimates of fin hinge and bending moments.

The method developed is simple to use and is easily incorporated into comprehensive missile aeroprediction methods. The method is extremely valuable because it includes effects due to fin-body gaps and real flow. Effects due to body vorticity are present for the conditions of the wind tunnel tests, but vortex free results (windward side data) should be used in combination with, for example, the equivalent angle of attack procedure to obtain the effects of vorticity present on the actual configuration and flow conditions of interest.

The correlations and curve fits determined during this investigation are not unique. Other methods of obtaining similar results from the triservice data base are possible. However, it is believed that the developed prediction method is more than adequate for preliminary and design purposes.

## 6. Recommendations

There are several additional investigations which should be performed in order to improve the prediction of fin center of pressure. The supersonic control data were investigated extensively, but the transonic/low supersonic control data were taken directly from previous work described in Reference 1. Additional transonic/low supersonic triservice experimental control data remains to be reduced and examined. This control data should be reevaluated in the manner similar to that used for the supersonic control data. As mentioned previously, a method to include vortex effects for the geometry and flow conditions of interest is required for a more accurate prediction of the centers of pressure. Finally, experimental data should be examined for fins with streamwise sections and planforms different from those in the data base used herein.

## 7. Acknowledgements

The authors wish to acknowledge the United States Air Force, Army, and Navy and the National Aeronautics and Space Administration for their participation in creating the extensive triservice missile data base. The original data correlations for inclusion into the MISSILE 3 prediction program were performed under Contract N00014-80-C-0700. We would also like to thank the Flight Dynamics Laboratory of the Air Force Systems Command, Wright Research & Development Center, Wright-Patterson AFB, OH, for funding an additional effort under Contract F33615-86-C-3626 to examine the center of pressure data in detail for eventual inclusion into prediction methods for Missile DATCOM.

### 8. References

1. Lesieutre, D. J., Mendenhall, M. R., Nazario, S. M., and Hemsch, M. J., "Prediction of the Aerodynamic Characteristics of Cruciform Missiles Including Effects of Roll Angle and Control Deflection," NEAR TR-360, Revised August 1987.
2. Allen, J. M., Slaw, D. S., and Sawyer, W. C., "Analysis of Selected Data From The Triservice Missile Data Base," AIAA Paper No. 89-0478, January 1989.
3. Lesieutre, D. J., Canning, T., Dillenius, M. F. E., Mendenhall, M. R., and Torres, T. T., "Missile Stability and Control Methods, Volume I: Program FINCP for Prediction of Chordwise and Spanwise Centers of Pressure of Missile Control Fins," NEAR TR-396, August 1989.

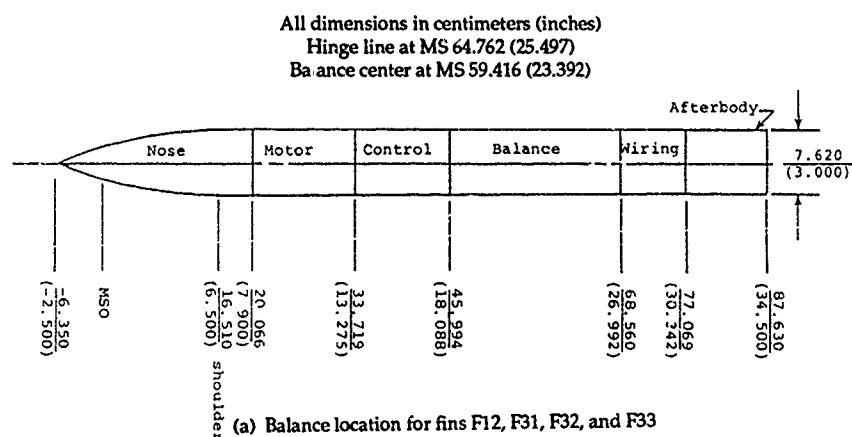


Figure 1. - Body and fin details.

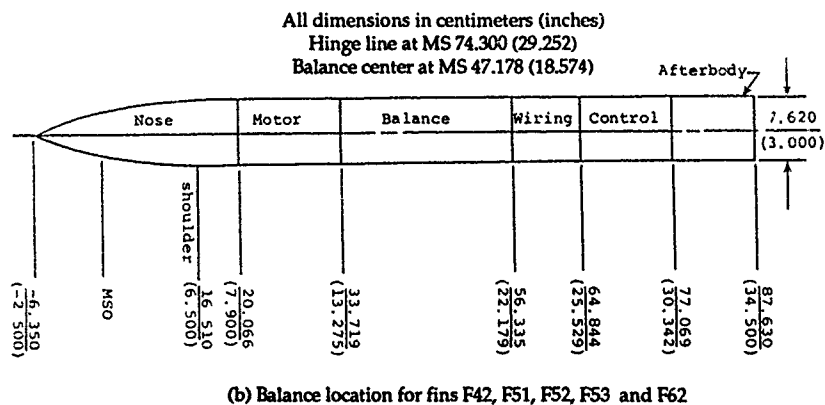


Figure 1. - Continued.



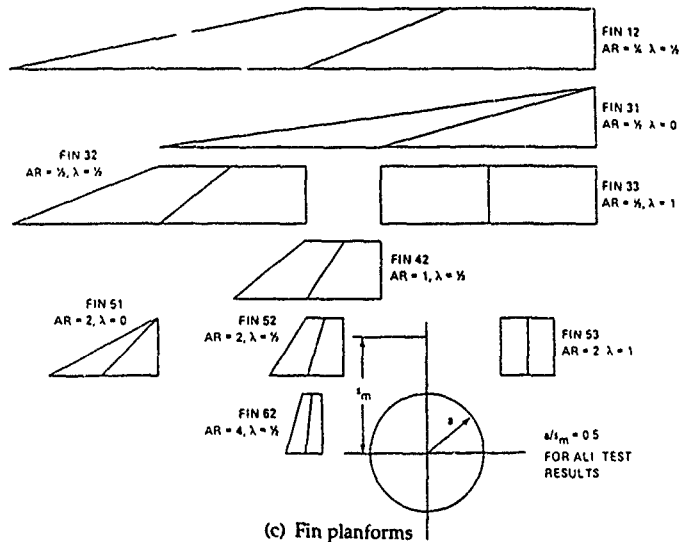


Figure 1. - Concluded.

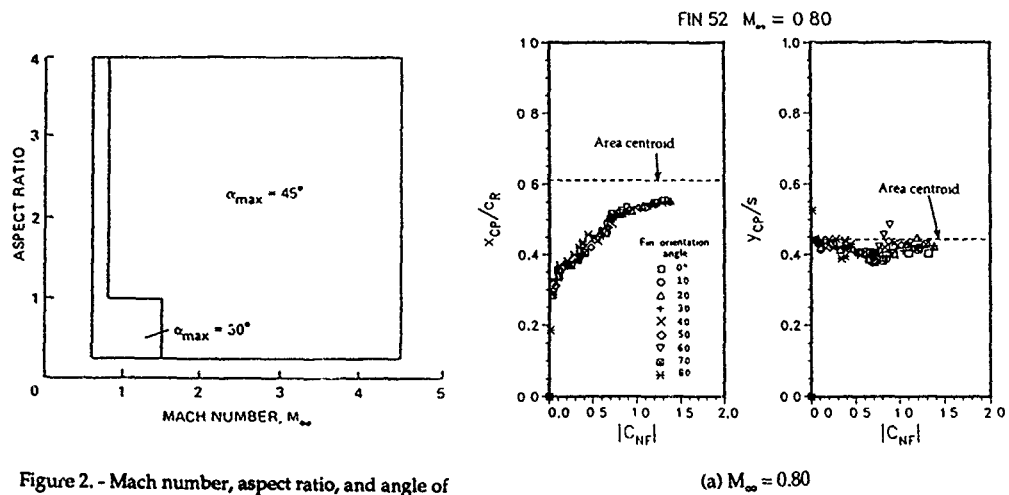


Figure 2. - Mach number, aspect ratio, and angle of attack range of the triservice data base.

Figure 3. -  $x_{cp}/c_R$  and  $y_{cp}/s$  curve fits to the stability data for fin 52.

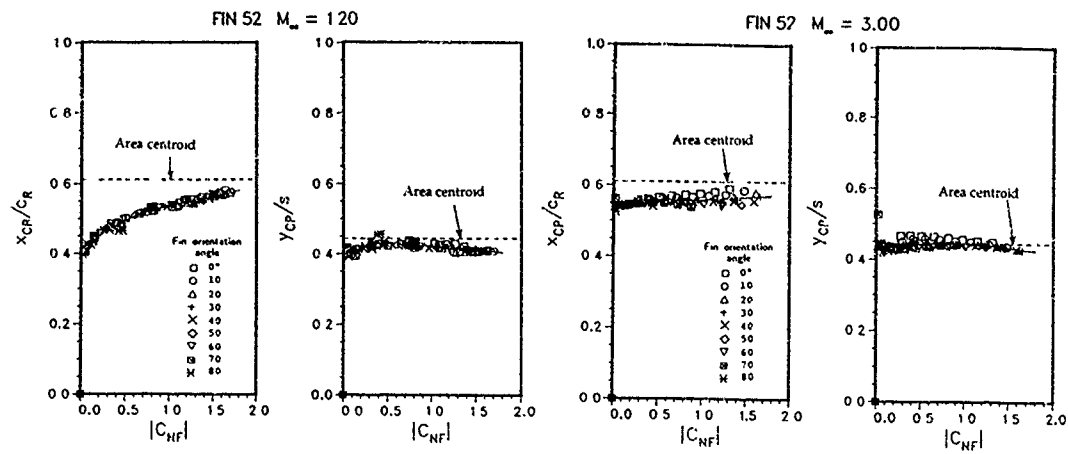
(b)  $M_\infty = 1.20$ (c)  $M_\infty = 3.00$ 

Figure 3. - Continued.

Figure 3. - Concluded.

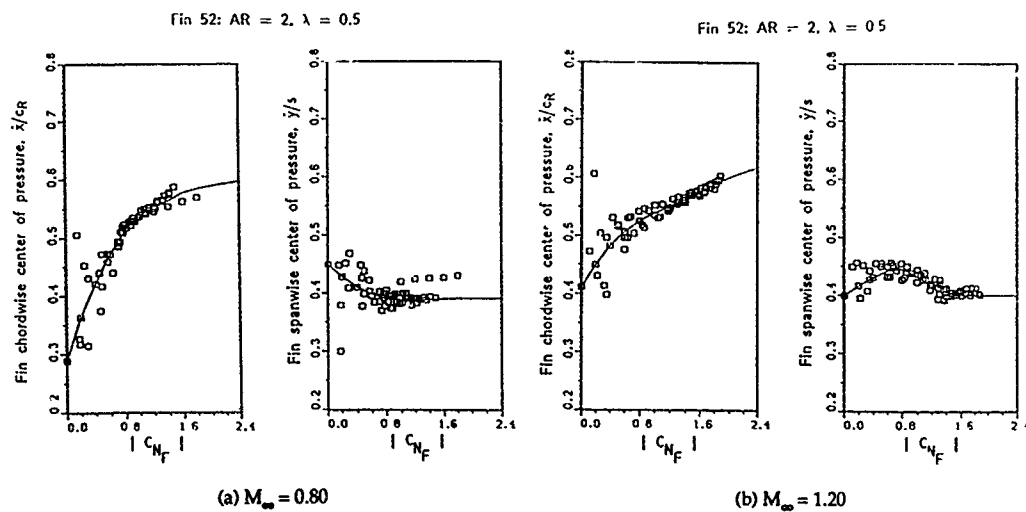
(a)  $M_\infty = 0.80$ (b)  $M_\infty = 1.20$ Figure 4. -  $x_{cp}/c_r$  and  $y_{cp}/s$  curve fits for control deflection effects.

Figure 4. - Continued.

Fin 52: AR = 2,  $\lambda = 0.5$

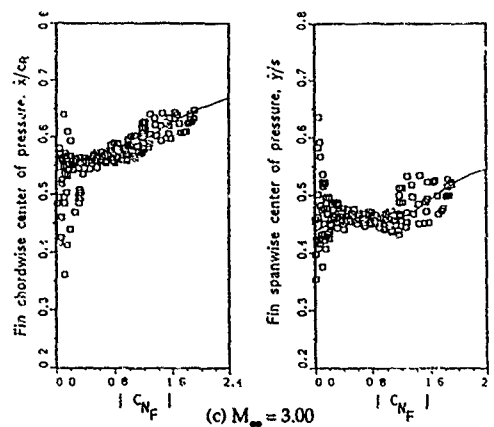


Figure 4. - Concluded.

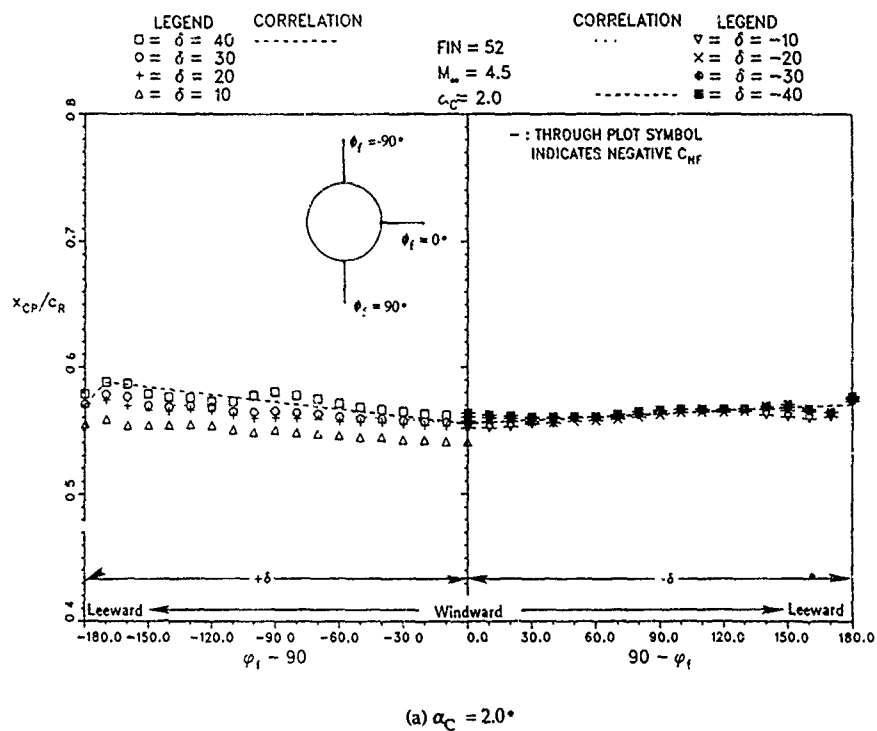


Figure 5. - Chordwise center of pressure for fin 52 at  $M_\infty = 4.5$

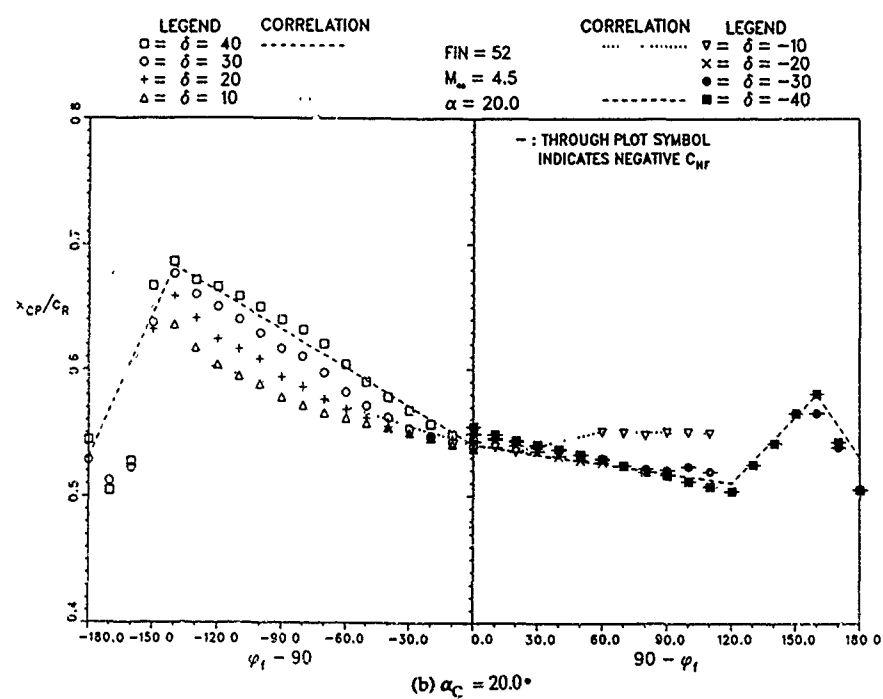


Figure 5. Continued.

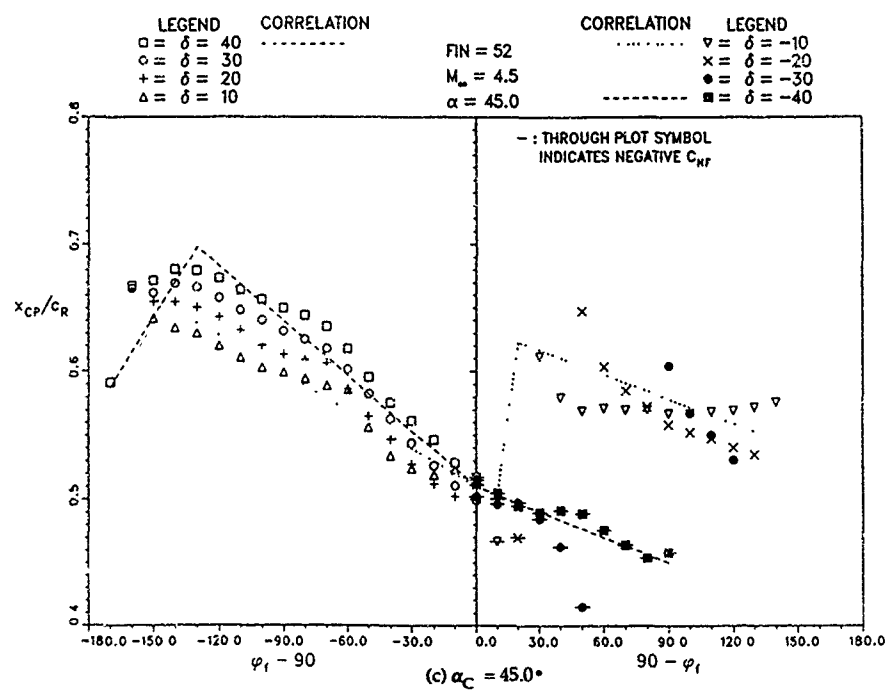


Figure 5. - Concluded.

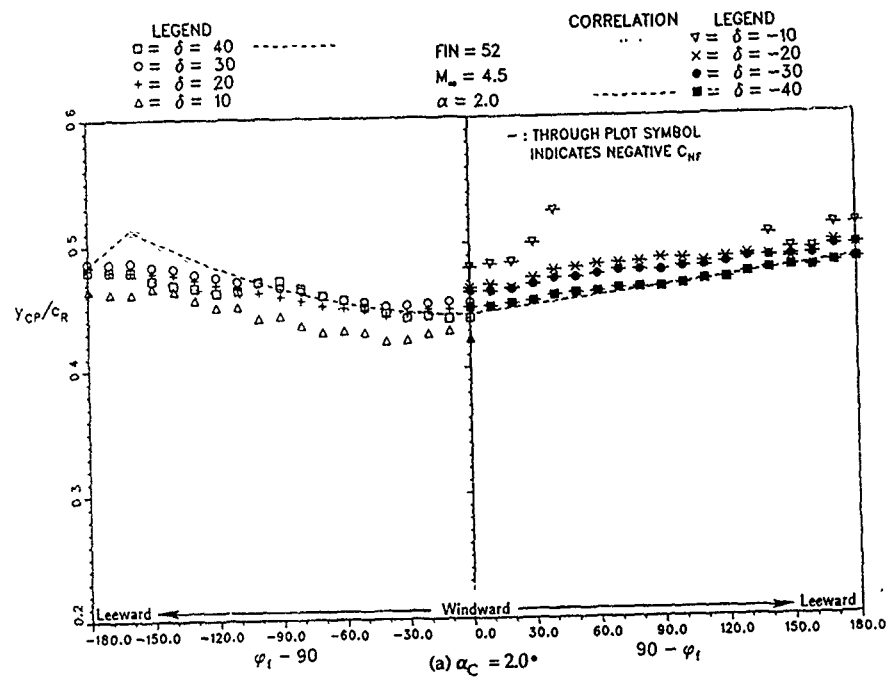
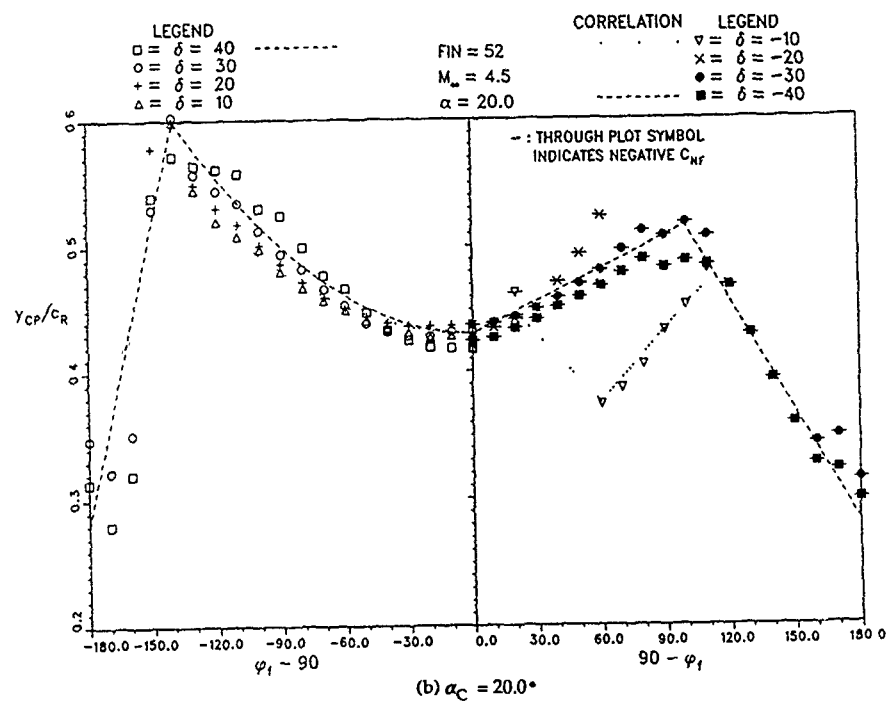
Figure 6. - Spanwise center of pressure for fin 52 at  $M_\infty = 4.5$ .

Figure 6. - Continued.

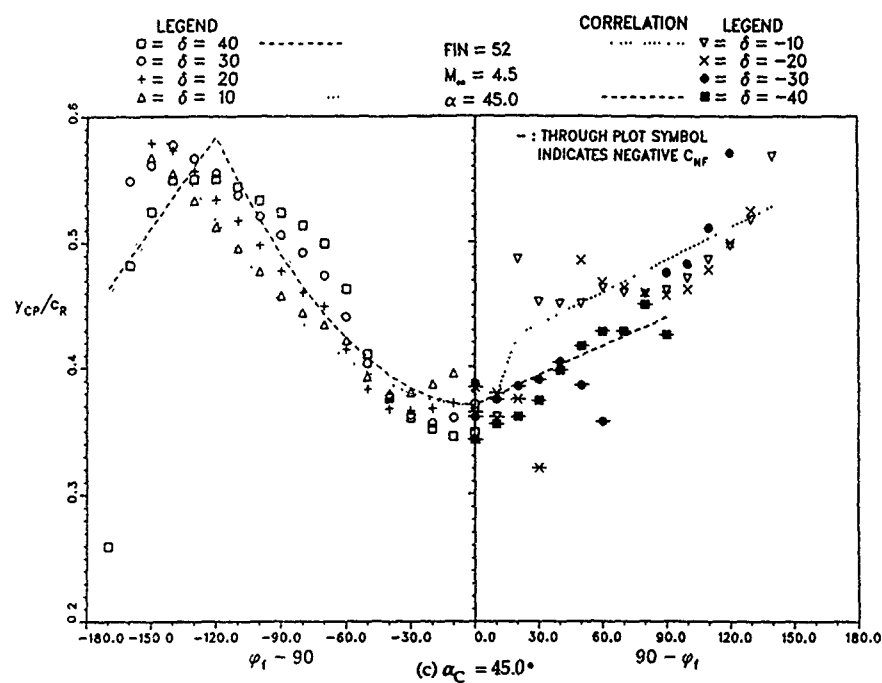
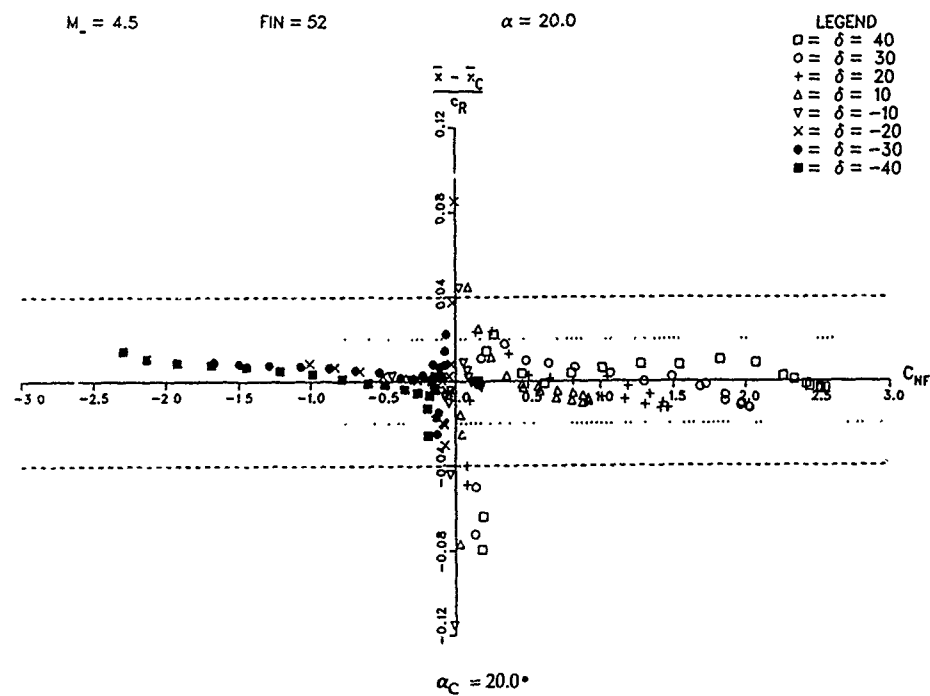


Figure 6. - Concluded.

Figure 7. - Error between correlated  $x_{cp}/c_t$  and data for fin 52 at  $M_\infty = 4.5$  and  $\alpha = 20.0^\circ$ .

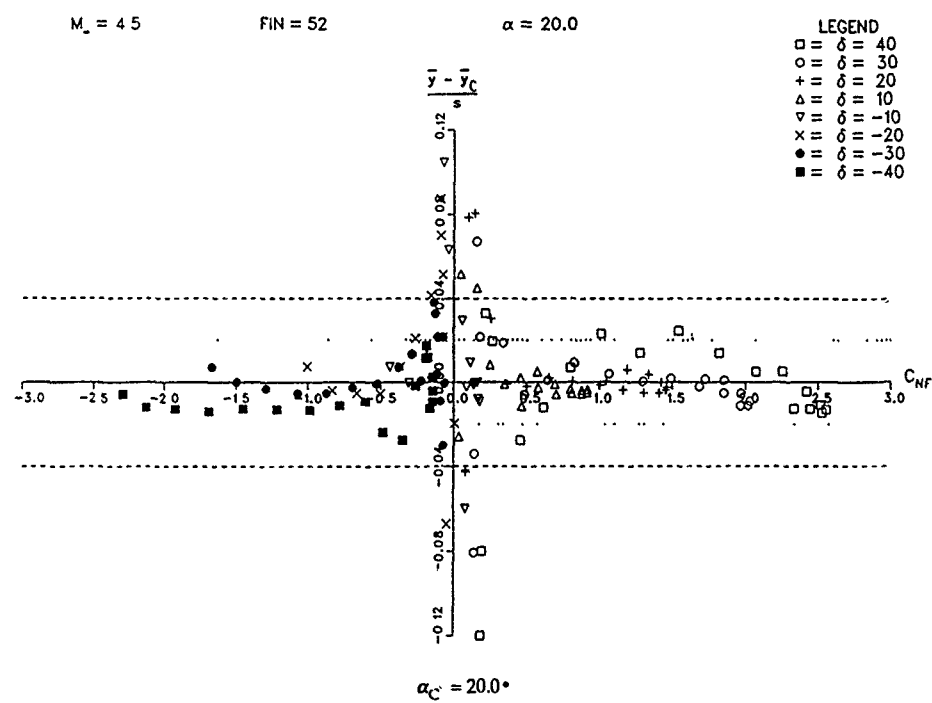


Figure 8. - Error between correlated  $y_{cp}/s$  and data for fin 52 at  $M_\infty = 4.5$  and  $\alpha = 20.0^\circ$ .

# COMPUTATIONAL MODELS WITH ADVANCED THERMOCHEMISTRY FOR THE ANALYSIS OF MISSILE/PLUME FLOWFIELD INTERACTIONS

S.M. Dash, N. Sinha, and B.J. York  
Science Applications International Corporation  
Fluid Sciences Division  
501 Office Center Drive, Suite 420  
Fort Washington, Pennsylvania 19034-3211  
United States

## SUMMARY

Advanced, computational models which solve the full (FNS) and parabolized (PNS) Navier-Stokes equations for the analysis of missile aerodynamic problems with exhaust plume interactions are described. The models utilize conservative implicit algorithms and include finite-rate chemistry, two-equation turbulence models, and preliminary multi-phase flow capabilities. In the tactical missile arena, a 3D Navier-Stokes code, PARCH, has been developed to analyze missile/plume interactions with both conventional nozzle exhausts, as well as with bifurcated/scarfed nozzle exhausts. Our PNS work has focused on supersonic/hypersonic applications utilizing time-iterative upwind numerics for enhanced robustness and accuracy, and has included the analysis of aerodynamic, plume, and propulsive problems for missiles as well as for reentry and aerospace vehicles.

## 1. INTRODUCTION

The ability to analyze missile aerodynamic flowfields has advanced to a level where calculations employing Full Navier-Stokes (FNS) and Parabolized Navier-Stokes (PNS) based computational models can now be performed on a routine basis with some reliability. FNS and PNS models are being utilized in an engineering environment to deal with strongly interactive problems, such as leeside separation or higher altitude flows, that cannot readily be analyzed using coupled viscous/inviscid models [1]. However, including the effects of interactions with propulsive and/or control jets has not heretofore been analyzed at this advanced level due to the complex requirement of incorporating generalized thermochemical capabilities (as well as multi-phase capabilities for solid propellant propulsive systems) into the computational model. Engineering-oriented missile/plume interactive methodology had been restricted to the use of coupled viscous/inviscid methods as surveyed by Dash [2]. Recently, the authors and co-workers have been engaged in programs involving the extension of FNS and PNS computer codes to analyze flowfields with generalized thermochemistry. These extended codes have been applied to a variety of missile flowfield problems with attention focused on missile/plume interaction problems. This paper will provide an overview of these new, extended computer codes and, will highlight applications to a variety of missile/plume interactive problems.

## 2. OVERVIEW OF FNS CODE DEVELOPMENT WORK AND APPLICATIONS

Our primary work with FNS methodology has focused on the computer code, PARCH, for which 2D (planar/axisymmetric) and 3D versions have been developed. PARCH is an outgrowth of the NASA/Ames ARC aerodynamic

code [3] and the AEDC propulsive extension, PARC [4], both of which use Beam-Warming based central-difference numerics. The PARCH code developmental activities have taken place as follows:

- (1) The 2D and 3D versions of ARC and PARC were unified into:

- . a baseline PARCH2D Master Code;
- and,
- . a baseline PARCH3D Master Code.

The baseline PARCH2D/3D Master Codes contain all the desired capabilities available in the ARC and PARC codes. The coding was performed as an upgrade to PARC which had many propulsive-oriented features not available in ARC, particularly, grid blanking/blocking and generalized boundary conditions (see Reference 4).

- (2) As a prerequisite to incorporating extended thermochemical and turbulence modeling capabilities, implicit, approximately factored ADI based scalar solvers were developed to solve the chemical species and turbulence model convective/diffusive equations. These scalar solvers emulated the numerics of the PARCH fluid solver.
- (3) Matrix-split methodology was formulated to incorporate the chemical species equations and finite-rate chemical kinetics into the PARCH codes [5, 6].

Most recently, upgrades in numerical capabilities (e.g., inclusion of Roe/TVD numerics) were incorporated into PARCH [7], and, several specialized versions were developed including: a rocket nozzle version, PARCH/RN [8], with gas/particle nonequilibrium capabilities; a missile hypersonic shock layer version, PARCH/VSL [9], with thermal nonequilibrium capabilities; and, a tactical missile/plume interaction version, PARCH/TMP [10], with very broad-based capabilities. Table 1 exhibits the component ingredients that are incorporated into master versions of PARCH2D/3D along with peripheral modules containing data (Master Data File), providing grids (Grid Generators), and performing post-processing of the data. Also shown in Table 1 are the contents of several specialized versions.

Missile related applications of PARCH2D/3D are summarized in Table 2. The shock layer work has focused on hypersonic, higher altitude, missile nose region studies requiring the inclusion of both chemical and thermal nonequilibrium effects into PARCH. The rocket nozzle work has provided for the inclusion of particulate nonequilibrium capabilities into PARCH, as required for the analysis of solid propellant systems.



Test facility studies have included analytical support for hypersonic missile testing simulating the high enthalpy environment via use of a rocket exhaust blown over the missile airframe. Scramjet applications have focused on Aerospace Plane vehicles, but the computational scheme must be performed for the composite methodology is equally applicable to airbreathing missile systems. Film cooling studies have focused on window cooling environments for hypersonic/high altitude missile systems. The missile/plume interaction work has dealt with a variety of complex problems associated with conventional single-engine and multi-engine nozzle exhausts, as well as with lateral controljets for hypersonic missile problems, and with unconventional scarfed/bifurcated nozzle propulsive systems being utilized on specialized tactical missiles.

### 3. OVERVIEW OF PNS CODE DEVELOPMENT WORK AND APPLICATIONS

Our PNS work is focused on supersonic/hypersonic flowfield problems and several computer codes have been developed which include finite-rate chemistry and advanced turbulence models. Under support of the National Aerospace Plane (NASP) Program, a series of computer codes were developed which provided a complete nose-to-tail flowfield analysis of an aerospace vehicle integrated scramjet and propulsion system [11-13]. The original 2D computer codes, SCAMP, SCRINT, SCORCH, and SCHNOZ, used different numerical techniques. The original versions of the SCAMP forebody code and the SCRINT inlet code employed Beam-Warming based implicit central-difference numerics, and were subsequently upgraded to incorporate Roe/TVD upwind numerics [14]. The SCORCH combustor code employed hybrid implicit/explicit pressure-split methodology [15], while the SCHNOZ nozzle code employed explicit MacCormack numerics [16].

The original versions of SCAMP and SCRINT contained only equilibrium air thermochemistry. A research version, SCRINTX, was upgraded to include finite-rate chemistry into the Beam-Warming numerical framework using a matrix-split approach [5, 17]. SCRINTX was applied to a variety of combustor and nozzle related flowfield problems as well as to inlets. Detailed comparative studies with these codes [18] for scramjet propulsion indicated a clear preference for the SCRINTX methodology with regard to accuracy and robustness.

In our 2D research with SCRINTX, we had incorporated first and second order (TVD) Roe upwind numerics [19] into the code after the matrix-splitting was performed. This 'ad hoc' approach worked quite well for flows with air chemistry, but worked poorly for strongly combusting flow problems where the approximations entailed 'broke down'. For such flows, the formulation of Roe's system of coupled fluid and chemical species equations. For space marching, such an analysis depends upon an eigen-decomposition whose derivation is quite difficult to perform [20]. The Roe (PNS) formulation with chemistry is much easier to develop if

the approximate Riemann problem is posed in time rather than space. For time marching, the eigen-functions of a much simpler matrix are required, and in fact, this analysis has been completed by several researchers, such as Molvik and Merkle [21].

At the 3D level, our recent PNS work has concentrated on the inclusion of time-iterative methodology into existing finite-volume (SCAMP3D) and finite-difference (SCRINT3D) spatial marching codes [22]. Significant improvements in robustness and accuracy, above that provided by the inclusion of upwind numerics, have been obtained by the use of time-iterative relaxation methodology [23]. Also, significant work was performed involving the use of advanced grid generation techniques in the cross-flow plane, and grid blanking for the treatment of cavities and swept surfaces.

Our preliminary 3D PNS work with chemistry had concentrated on the inclusion of chemistry into the SCRINT3DT code which was a 3D extension of the SCRINTX code with time-iterative PNS numerics. SCRINT3DT was made operational with matrix-split chemistry and operated with Beam-Warming central difference numerics or 'ad hoc' real gas Roe upwind numerics (the splitting was done before the Roe decomposition). Its ability to analyze multi-component, chemically reacting flow problems with Roe upwind numerics was found to be problematic and the obvious remedy was a reformulation of the Roe real gas methodology using a large matrix/fully-coupled framework. As this rather ambitious effort was to initiate, the STUFF 3D iterative PNS code of Molvik and Merkle [21] became available which had the large-matrix/fully coupled Roe formulation done properly for clean air chemistry. It was deemed more expeditious to use the STUFF code as our baseline code than to upgrade the SCRINT3DT code, and, the added benefits of the finite volume formulation of STUFF became available with this decision. Our upgraded version of STUFF is called the SCHAFT code, and work to date has involved the generalization of the chemistry and the inclusion of two-equation turbulence models [20, 24, 25].

A companion NS code entitled TUFF has also been developed by Molvik and Merkle [21] with comparable numerics to STUFF. Due to the more generalized geometric capabilities (blanking/blocking) and boundary condition options in the PARCH NS code, we have deemed it more expeditious to upgrade PARCH via including the TUFF strongly-coupled/large matrix methodology for dealing with the Roe chemistry issue, rather than to upgrade the geometric capabilities of TUFF, which would entail a much more substantive effort. PARCH, currently, has the Roe chemistry formulation done in the 'ad hoc' matrix-split manner.

The remainder of this paper will present a brief overview of current capabilities available in the PARCH NS code and our PNS codes, with details of the numerics available in other references. Applications to missile related flow problems will serve to highlight these capabilities and focus

**TABLE 1. PARC2D/3D MASTER CODES AND SUPPORTING MODULES,  
AND CONTENTS OF SPECIALIZED VERSIONS**

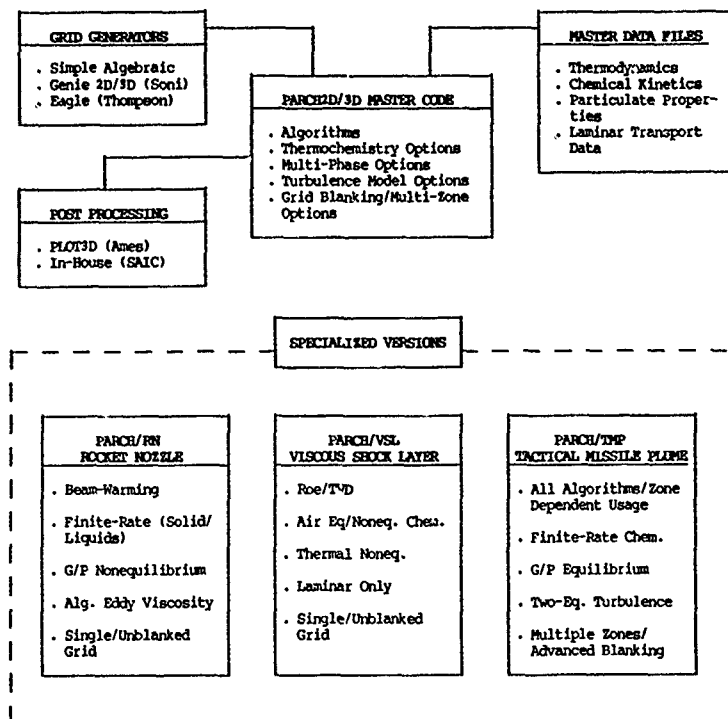


**TABLE 2. PARC2D/3D APPLICATIONS**

APPLICATION	CALCULATIONS	COMMENTS
• HYPERSONIC VISCOUS SHOCK LAYER FLOWFIELDS	- Shock Layer Radiance Studies - AFE Flowfield Studies	- Ionized/Excited State Reactions - Thermal Nonequilibrium Upgrades In Progress
• ROCKET NOZZLE FLOWFIELDS	- Several Large Scale Boosters	- Generalized Finite-Rate Kinetics and Particulate Nonequilibrium
• TEST FACILITY SUPPORT	- Hypersonic Nozzle Calculations for Calspan, AEDC, NSWC, AFVAL	- Thermodynamic (Imperfect Gas) Upgrades - Transitional BL Issues
• MISSILE/PLUME INTERACTIONS	- Conventional (Base Flow Studies) - Lateral Control Jet Studies - Scarfed/Bifurcated Nozzle Plumes - Multi-Engine Base/Plumes (In Progress)	- Turbulence Modeling Issues - 3D Gridding Problems
• SCRAMJET FLOWFIELDS	- Fuel Injector Studies - Scramjet Combustors - Scramjet Nozzles	- Gridding/Turbulence Issues
• HYPERSONIC WAKE FLOWFIELDS	- RV Near Wake Studies With Ablation Product Chemistry	- Transitional Issues - Complex Chemistry Mechanisms
• JET/PLUME RESEARCH	- Axisymmetric Jets Into Still Air - 3D Jet Mixing Problems	- TVD Numerics Required for Acoustic Applications - Vortical/Large Scale Structure Issues
• FILM/WINDOW COOLING STUDIES	- Window Cavity Coolant Studies	- Turbulent Issues Keyed to Scalar Fluctuation Predictions/Compressibility Effects

attention on needed upgrades in the areas of turbulence modeling [26, 27] and grid generation, which are generally the limiting factors in obtaining good agreement with the data.

#### 4. PARCNS FNS CODE

##### 4.1 Gas-Phase Fluid Dynamic Equations

PARCNS solves the Reynolds averaged, compressible flow equations, cast in strong conservation form in generalized curvilinear coordinates:

$$\frac{\partial Q}{\partial \xi} + \frac{\partial E}{\partial \xi} + \frac{\partial F}{\partial \eta} + \frac{\partial G}{\partial \zeta} - H = 0 \quad (1)$$

A detailed description of the fluid dynamic elements in the above vector arrays and the transformation to generalized coordinates is provided in refs. 3 and 4. The PARCNS code contains options for solving the thin layer equations and Euler equations in addition to the full NS equations.

With the addition of NS chemical species equations ( $i = 1, 2, 3, \dots, NS$ ) and the 2  $k$  turbulence model equations to the continuity, momentum and energy equations, the  $(5 + NS + 2)$  vector array of dependent variables is given by:

$$Q = \frac{1}{J} \begin{bmatrix} \rho \\ \rho u \\ \rho v \\ \rho w \\ E_t \\ \rho a_1 \\ \rho k \\ \rho \epsilon \end{bmatrix} \quad (2)$$

The inviscid ( $E_i, F_i, G_i$ ) and viscous ( $E_v, F_v, G_v$ ) flux vectors take the form:

$$E_i = \frac{1}{J} \begin{bmatrix} \rho U \\ \rho U + \xi_x P \\ \rho V + \xi_y P \\ \rho W + \xi_z P \\ (E_t + P)U \\ \rho U a_i \\ \rho U k \\ \rho U \epsilon \end{bmatrix} \quad (3a)$$

$$E_v = \frac{1}{J} \begin{bmatrix} 0 \\ \xi_x \tau_{xx} + \xi_y \tau_{xy} + \xi_z \tau_{xz} \\ \xi_x \tau_{yx} + \xi_y \tau_{yy} + \xi_z \tau_{yz} \\ \xi_x \tau_{zx} + \xi_y \tau_{zy} + \xi_z \tau_{zz} \\ \xi_x q_x + \xi_y q_y + \xi_z q_z \\ \mu (\xi_x a_{ix} + \xi_y a_{iy} + \xi_z a_{iz}) \\ \mu (\xi_x k_x + \xi_y k_y + \xi_z k_z) \\ \mu (\xi_x \epsilon_x + \xi_y \epsilon_y + \xi_z \epsilon_z) \end{bmatrix} \quad (3b)$$

where  $E = E_i - E_v$ . Analogous expressions are obtained for the  $F$  and  $G$  arrays, and, the source term vector  $H$  takes the form:

$$H = \frac{1}{J} \begin{bmatrix} 0 \\ H_{p_u} \\ H_{p_v} \\ H_{p_w} \\ H_{p_h} \\ \dot{\omega}_i \\ \underline{P} - \rho \epsilon \\ \frac{\epsilon}{k} (C_1 P - C_2 \rho \epsilon) \end{bmatrix} \quad (4)$$

In the above equations  $\xi(x, y, z)$ ,  $\eta(x, y, z)$  and  $\zeta(x, y, z)$  represent the curvilinear coordinates in the transformed computational domain;  $\xi_x, \xi_y, \xi_z, \eta_x, \eta_y, \eta_z, \zeta_x, \zeta_y, \zeta_z$  and  $J$  represent the metrics and Jacobian of the transformation;  $\rho$  is the fluid density;  $P$  is the pressure;  $u, v$ , and  $w$  are the Cartesian velocity components in the  $x, y$ , and  $z$  directions;  $a_i$  represents the mass fraction of the  $i$ th chemical species,  $\mu$  is the laminar viscosity;  $q_x, q_y, q_z$  is the heat flux;  $k$  is the turbulent kinetic energy; and  $\epsilon$  is the turbulence dissipation rate.  $U, V$  and  $W$  are the contravariant velocity components.

For turbulent flow simulation the laminar viscosity and thermal conductivity are replaced by their respective sums of laminar and turbulent values. (i.e.  $\mu + \mu_t, k + k_t$ ). Additionally, the source term  $H$  is comprised of the chemical production terms  $\dot{\omega}_i$ ; the turbulent production  $\underline{P}$ , and the dissipation of turbulent kinetic energy,  $\epsilon$ ; and the gas/particle interaction terms  $H_{p_u}, H_{p_v}, H_{p_w}$  and  $H_{p_h}$  required for multi-phase flow simulation [8, 28].

##### 4.2 Matrix-Split Methodology

Applying the conventional Beam-Warming algorithm to equation (1), utilizing Euler

implicit time-differencing, yields the 'delta' form finite-difference expression [3, 4, 29] written below for the 2D system of equations:

$$[I + \Delta t(\delta_\xi A^N + \delta_\eta B^N - M^N)] \Delta Q^N = -\Delta t(\delta_\xi E^N + \delta_\eta F^N - H^N) = R^N \quad (5)$$

In equation (5),  $\delta$  is a central difference operator,  $\Delta Q^N = Q^{N+1} - Q^N$  where  $N$  denotes the time step level, and, the flux vectors  $E$  and  $F$ , (which are nonlinear functions of  $Q$ ) have been linearized about  $Q^N$ , viz.,  $E^{N+1} = E^N + A \Delta Q^N$  where  $A = \partial E / \partial Q$ . Equation (5) is the unfactored form of the block algorithm and represents a system of 4 fluid (5 for 3D flows),  $n$  ( $= NS$ ) species equations, and 2 turbulence model equations (which we will now dismiss to simplify our discussion of matrix splitting). We thus seek to decompose an  $n+4$  system of coupled equations to a system of 4 coupled fluid dynamic equations, and  $n$  scalar chemical species equations. Using the nomenclature

$$Q_f = (\rho, \rho u, \rho v, E_t)^T$$

$$Q_c = (a_1, a_2, a_3, \dots, a_n)^T \quad (6)$$

the  $n+4$  system is decomposed as:

$$\left[ I + \Delta t \begin{array}{c|c} \delta_\xi & \\ \hline \delta_\eta & \end{array} \begin{array}{c|c} A_{ff} & A_{fc} \\ \hline A_{cf} & A_{cc} \end{array} \right] \begin{array}{c|c} B_{ff} & B_{fc} \\ \hline B_{cf} & B_{cc} \end{array} \begin{array}{c} \Delta Q_f \\ \hline \Delta Q_c \end{array} = \begin{array}{c} R_f \\ \hline R_c \end{array} \quad (7)$$

where  $A_{ff} = \partial E_f / \partial Q_f$ ,  $A_{cf} = \partial E_c / \partial Q_f$ , etc.

The above system of matrices is split about the horizontal (indicated by the dashed lines) leading to a fluid dynamic system written as:

$$[I + \Delta t(\delta_\xi A_{ff}^N + \delta_\eta B_{ff}^N)] \Delta Q_f^N = R_f^N - \Delta t(\delta_\xi A_{fc}^N + \delta_\eta B_{fc}^N) \Delta Q_c^N \quad (8)$$

(where the source term  $M_c$ , having particulate contributions is treated explicitly, and has thus been incorporated into  $R_c$ ).

This exercise in matrix partitioning recovers the original  $4 \times 4$  block structure of the perfect-gas fluid dynamic formulation, with addition of a forcing function on the explicit right hand side and revised elements of the  $A_{ff}$  and  $B_{ff}$  matrices on the implicit left hand side to account for generalized multi-component species and calorically imperfect behaviour (see refs. 5 and 17 for details). The elements of the

forcing function term,  $\Delta Q_c$ , contain the net influence of the chemical species change (due to convection/diffusion/kinetics) on the fluid dynamic solution through pressure/species derivatives [5, 17]. The inclusion of this term on the right hand side is not essential to obtain a converged steady state solution and it can be discarded. However, it cannot be discarded for time accurate computations. For the same reason, it can not be discarded for a space marching PNS computation unless time-iterative methodology is incorporated. The removal of the forcing function from the right hand side can impact the rate of convergence and this is an area of current investigation.

#### 4.3 Numerical Methodology

All work with PARCH to date has focussed on the analysis of steady flow problems using non-time accurate procedures to expedite convergence to steady state. The block unfactored, matrix-split, fluid dynamic equations (eq. 8) (with the explicit species term,  $\Delta Q_c$ , removed), are approximately factored as follows:

$$[I + \Delta t \delta_\xi A_{ff}^N] [I + \Delta t \delta_\eta B_{ff}^N] \Delta Q_f^N = R_f^N \quad (9)$$

Equation (9) can be solved by block tridiagonal inversion [3, 29], which is computationally expensive per time step, but generally permits taking large time steps (e.g., Courant numbers of 5 - 10) and obtaining converged solutions in a very reasonable number of iterations (e.g., 300 - 3,000, depending on the problem at hand, the grid, the initial and boundary conditions, etc.). Equation (9) can more efficiently be solved by using the diagonalized scheme of Chaussee and Pulliam [30] which uncouples the block system and reduces the work to the inversion of a scalar tridiagonal system. However, the implicit diagonalized solution is restricted to the Euler equations (the viscous terms do not diagonalize and must thus be treated explicitly), and, the path to convergence for complex, viscous dominated flows can be slow and sometimes problematic.

The choice of the block tridiagonal inversion or diagonalized solution procedure for the fluid dynamic equations is available as a user option in PARCH and is very problem dependent. With multi-zone versions, the diagonalized option can be used in some zones and the blocked option in others (e.g., for a missile/plume interactive problem, the zone of strongly interactive flow can be handled by the block procedure with all other flow zones analyzeable by the generally more efficient diagonalized method). With central difference numerics employed, artificial dissipation is required in nonviscous regions to ensure stability and diagonal dominance. The implicit/explicit second and fourth order dissipation model of Jameson, et al., [31] is employed in PARCH. Independent time steps are used to advance the equations based on a user-specified Courant

number (locally applied at each grid point) with a flux change limiter (e.g., 20 percent change in  $\Delta Q/Q$ ), which cuts back on the local time step in regions of severe change (see ref. 4 for details).

#### 4.4 Chemical Species/Rate Kinetics Algorithm

Upon matrix splitting and decomposition of equation (7), the lower half contains the chemical species transport equations, written as:

$$[I + \Delta t(\delta_{\xi}^N A_{CC}^N + \delta_{\eta}^N B_{CC}^N - M^N) \Delta Q_C = R_C^N - \Delta t(\delta_{\xi}^N A_{Cf}^N + \delta_{\eta}^N B_{Cf}^N) \Delta Q_f \quad (10)$$

The second term on the right hand side contains the forcing functions from the fluids upon the species, which is discarded for time-asymptotic steady-state solutions. Subsequent factorization leads to:

$$[(I - \Delta t M^N) + \Delta t \delta_{\xi}^N A_{CC}^N] [(I - \Delta t M^N) + \Delta t \delta_{\eta}^N B_{CC}^N] \Delta Q_C = R_C^N \quad (11)$$

Equation (11) represents the numerically intensive task of inverting block  $N \times N$  tridiagonal matrices. CPU costs and memory requirements can become prohibitive as the number of chemical species gets large. An efficient alternative solution strategy has been devised, which breaks up the solution sequence into two steps:

- (1) a point implicit solution of the chemical kinetic rate equations with diffusion and convection treated explicitly; and,
- (2) a globally implicit time integration of the species equations sequentially with the chemical source term specified from step (1).

The details of this methodology are provided in Reference 32.

#### 4.5 Turbulence Modeling

In the earlier 2D versions of PARCH [5, 6, 8, 33], the high Reynolds number form of the  $k$ - $\epsilon$  model was utilized and near wall matching was achieved by coupling the  $k$ - $\epsilon$  solution to a mixing length - Van Driest formulation at a location corresponding to  $y^+ \sim 50$ . The low Reynolds number extension of the  $k$ - $\epsilon$  model, as proposed by Chien [34], has been implemented in the 3D code. In the Chien low Re extension, the convective/diffusive terms are the same, but the source terms for  $k$  and  $\epsilon$  are given by:

$$H_k = P - \rho \epsilon - \frac{2\mu k}{y^+} \quad (12)$$

$$H_{\epsilon} = \frac{\epsilon}{k} (C_1 P - C_2 \rho \epsilon f) - \frac{2\mu \epsilon}{y^+} \exp(-C_3 y^+) \quad (13)$$

where:

$$f = 1 - \frac{0.4}{1.8} \exp(-\rho k^2 / 6\mu \epsilon) \quad (14)$$

and:

$$\mu_t = C_{\mu} \rho k^2 / \epsilon [1 - \exp(-C_4 y^+)] \quad (15)$$

In eqs. (12) and (13),  $y$  represents the distance from the nearest wall and is used for computing the corresponding  $y^+$ . The model constants are  $C_{\mu} = 0.09$ ,  $C_1 = 1.35$ ,  $C_2 = 1.8$ ,  $C_3 = 0.0115$  and  $C_4 = 0.5$ .  $P$  is the turbulent production term.

The turbulence model equations are solved as independent, uncoupled equations using the approximately-factored ADI solver of eq. (11). The source terms are treated implicitly using the linearization described in refs. 26 and 27. Corrections to the  $k$ - $\epsilon$  equations for compressibility, curvature, etc., are incorporated in a zonal manner on a problem dependent basis [26, 27]. The initialization of the turbulence model variables is case dependent and often, a simpler algebraic eddy-viscosity model is used to initiate the calculation until the flow structure becomes somewhat established; then  $k$  and  $\epsilon$  are initialized assuming the turbulence to be in equilibrium.

#### 4.6 Multi-Phase Flow Capabilities

The PARCH code contains multi-phase flow capabilities for the simulation of solid propellant rocket nozzle/exhaust plume flowfields where the dilute particle assumption applies and eliminates particle volumetric effects [35]. Gas/particle interactions [35] can be treated in both the equilibrium limit (where particle velocities and temperatures are taken to be the same as that of the gas-phase) and the nonequilibrium limit (where particle velocities and temperatures differ from those of the gas-phase). In the nonequilibrium limit, the analysis is presently restricted to flows with a primary streamwise direction where the particulate equations can be spatially integrated.

The particulate equations, cast in strong conservation form in generalized curvilinear coordinates, are listed below for two dimensions.

$$\frac{\partial \mathcal{E}_P}{\partial \xi} + \frac{\partial \mathcal{F}_P}{\partial \eta} - H_P = 0 \quad (16)$$

The inviscid flux ( $\mathcal{E}_P$ ,  $\mathcal{F}_P$ ) vectors take the following form:

$$\mathcal{E}_P = \frac{1}{J} \begin{bmatrix} \rho_P U_P \\ \rho_P U_P U_P \\ \rho_P v_P U_P \\ \rho_P h_P U_P \end{bmatrix} \quad (17a)$$

$$F_P = \frac{1}{J} \begin{bmatrix} \rho_P v_P \\ \rho_P u_P v_P \\ \rho_P v_P v_P \\ \rho_P h_P v_P \end{bmatrix} \quad (17b)$$

The source term vector  $H_P$  takes the form:

$$H_P = \begin{bmatrix} 0 \\ H_{Pu} \\ H_{Pv} \\ H_{Ph} \end{bmatrix} \quad (18a)$$

$$= \frac{1}{J} \begin{bmatrix} 0 \\ -\rho_P (u_P - u)/\tau_u \\ -\rho_P (v_P - v)/\tau_v \\ -\rho_P (h_P - h)/\tau_h \end{bmatrix} \quad (18b)$$

Particulate equations are solved for different particulate types (e.g.,  $Al_2O_3$ ) and for several representative sizes (e.g., 1  $\mu m$ , 3  $\mu m$ , 5  $\mu m$ , ...). The nomenclature to designate types and sizes has been eliminated for simplicity. In the above equations,  $u_P$  and  $v_P$  are the Cartesian particulate velocity components in the x and y directions and  $u_P$  and  $v_P$  are the contravariant velocity components.  $\tau_u$ ,  $\tau_v$ , and  $\tau_h$  represent characteristic particle times for velocity and thermal equilibration. Details of the explicit predictor-corrector based particle space marching algorithm utilized is provided in ref. 36. Coupling between the gas and solid phases is provided through the gas/particle interaction source terms in both the gas-phase and particulate equations [35]. In nozzle/plume applications, the particle solution is typically updated (by marching down the length of the nozzle or the exhaust plume) every 50 iterations of the gas-phase solution.

The highly efficient particle spatial marching technique is, of course, limited to flows where there are no recirculating features. Applications include rocket nozzle flow or the farfield of rocket exhaust plumes. The nearfield is significantly more complex, being characterized by large base regions, plume induced separation and a significant amount of recirculating flow. The analysis of particulates in this region requires the usage of a time-asymptotic, elliptic solver.

#### 4.7 Grid Blanking, Multi-Zone Blocking, and Generalized Boundary Conditions

In the PARC code [4], which preceded PARCH, significant effort was expended in

the development of coding logic which permits patching the overall flowfield to 'blank out' grid points occupied by embedded obstacles (rather than contour the grid about such obstacles as would be required in conventional codes). This facilitates the treatment of embedded boundaries such as steps, struts, cavities, etc., which would be difficult to deal with if blanking capabilities were not available. With blanking, the overall grid is broken down into a set of 'patches' for each of the mapped coordinate directions (viz., patching is done in mapped computational coordinates, not in physical coordinates). The patches are automatically constructed from boundary inputs. Figure 1 illustrates the patching concept for a simple 2D problem. Boundary conditions are applied along the outer computational boundaries as well as on the embedded boundaries, and are generalized to permit varied fluxes to cross the boundaries.

The analysis of geometrically complex, three-dimensional, chemically reacting flowfields can require several million node points with memory requirements well in excess of those available on modern day super computers. To overcome the memory limitation imposed by machines, a generalized multi-zone blocking procedure has been made operational in PARCH3D. The flowfield is split into several zones and only one zone is permitted to reside in the memory while the flowfield variables from the other zones are saved (i.e., on SSD, an I/O device available on CRAY). The zones are rolled in and out of memory in a sequential fashion and specialized logic has been written to ensure communication between adjacent zones in a manner consistent with the second order accuracy of the implicit algorithm. The details of the multi-zone blocking is discussed in ref. 37 and closely parallels that recently implemented by Sirbaugh, et al. [38], in the AEDC PARC code.

#### 4.8 Recent Numerical Upgrades

PARCH implements central-difference numerics with second/ fourth order artificial dissipation. Its application to hypersonic problems with strong shock waves can be problematic. Roe/ TVD upwind numerics [19] has recently been incorporated [7] to integrate the matrix-split fluid dynamic equations. With this upwind methodology, issues arise with regard to the scalar solver equations for the chemical species and turbulence model equations, and with regard to the Roe/TVD real gas manipulations, which are 'ad hoc' if performed after the matrix-splitting. Successful results for problems with non-combustion chemistry have been obtained using nonconservative forms of the scalar equations. Future work is geared towards developing a non-matrix split upwind version of PARCH (with all equations strongly-coupled) with a finite-volume discretization. Such upgrades will borrow from the methodology incorporated in the TUFF NS code [21].

## 5. PARCH CODE VALIDATION AND REPRESENTATIVE APPLICATIONS

### 5.1 Observations on Code Validation Process

The validation of a Navier-Stokes code, which contains generalized thermochemical capabilities and advanced turbulence models, must be performed in a very systematic manner, and, must be restricted to a very specific category of flowfield problems. The performance of the 'basic code' (algorithm, boundary conditions) must be distinguished from the performance of the incorporated submodules for turbulence and thermochemistry, and, will be dependent on the quality and resolution of the grid utilized.

A detailed discussion of the code validation process for scramjet propulsive flowfields was given by Dash [39], with four distinct levels of validation identified, as summarized below.

**LEVEL 1 - Performance Of The 'Basic Code'.** This entails code to code comparisons, serves to remove 'bugs', establishes run parameters (e.g., artificial damping coefficients), and defines the operational range of the code using the existing algorithms and boundary conditions.

**LEVEL 2 - Analysis Of 'Fundamental' Unit Problems.** This entails analyzing unit problems such as simple shear layers, laminar/turbulent diffusion flames, etc., to ensure that the advanced turbulence models and thermochemistry were incorporated into the code correctly, and, that the coefficients are appropriate (e.g., turbulence model coefficients, thermodynamic curve fits, chemical rates, etc.).

**LEVEL 3 - Analysis Of 'Component' Problems.** This entails the analysis of 'advanced' unit problems which are subsets of the overall flowfield problems, and for which detailed data are generally available. For a missile airframe/plume interaction problem, component problems would include:

- missile aerodynamic problems sans plume; viz., blunt nose region thermochemistry, treatment of wings/fins/ control surfaces, angle-of-attack issues, etc.
- plume interaction problems sans missile airframe; viz., straight-back jets, transverse jets, angled jets with simple approach flows, etc.
- unit plume/airframe interaction problems; viz., conventional plume/base flow interaction problems for single/ multiple nozzles; angled/transverse plume/airframe interaction problems sans wings/fins, etc.

**LEVEL 4 - Analysis Of 'Complete' Flow-field Problem.** This entails the analysis of a problem which could involve

additional complexities such as multi-zone blocked grids, zonal turbulence modeling, etc. Validation on this level should proceed initially to establish a baseline operational capability (e.g., to get all the pieces in place), recognizing that the Level 3 unit problems may not be easily resolved to support the Level 4 analysis (e.g., turbulence modeling issues may preclude obtaining good agreement with Level 3 unit problem data).

### 5.2 PARCH Code Validation Studies

PARCH derives from ARC [3] and PARC [4] which have been very popular aerodynamic and propulsive NS codes in the United States, and reflect a ten year history of development, upgrade, validation and application - restricted to single component, single phase, perfect gas flows with simple algebraic turbulence models. ARC code aerodynamic validation studies have been widely reported in the open literature, by Pulliam and coworkers [3, 40, 41] and many other investigators. ARC code derivatives have been successfully applied to projectile flowfield problems [42] and have incorporated upwind (TVD) upgrades [43, 44]. PARC code plume/propulsive validation studies have also been widely reported in the open literature by Cooper and various coworkers at Sverdrup [45 - 51].

Level 1 validation issues with PARCH have been largely resolved by previous and ongoing studies with ARC and PARC. Our PARCH validation work was initiated with Level 2 studies which emphasized a checkout of the new code with inclusion of advanced turbulence models, multi-component species, real gas thermodynamics and finite-rate chemistry. The unit problems studied have included:

- (1) turbulent free shear flows for streams of different composition, using the  $k_\epsilon$  turbulence model and variants with high Mach number compressibility-corrections [52];
- (2) laminar/turbulent shock-boundary layer interaction problems;
- (3) laminar premixed flame problems; and,
- (4) turbulent combustor shear layers in a duct.

These Level 2, fundamental unit problem studies have been described in refs. 5 - 8 and 33. They have ensured us that the  $k_\epsilon$  turbulence model and the finite-rate chemistry are working properly in PARCH via comparisons with results of other (already validated) computer codes, and with fundamental data. At Level 3, some of the fundamental studies performed, oriented towards missile/plume interactive flowfield problems, will be summarized below.

### 5.3 Jet Interaction Studies

Jet interaction unit problem studies have included the analysis of: conventional (straight-back) propulsive jets, with uniform low and high speed approach flow - with and

without base regions; transverse and angled jets; and, wall jets (to simulate missile film cooling problems as well as wall bounded propulsive jet interactions). For straight-back jets, we have used the data of Seiner which has served to validate our earlier PNS jet model, SCIPVIS [53, 54]. Figure 2 exhibits predicted density contours for an underexpanded ( $P_0/P_\infty = 1.44$ ) Mach 2 axisymmetric jet exhausting into a Mach .25 external stream, while Figure 3 compares PARC and SCIPVIS predictions. Numerical studies showing comparisons of SCIPVIS predictions with data, using various two-equation turbulence models ( $k_\epsilon$ ,  $k_W$ ,  $k_{\epsilon c}$ ), are described in refs. 53 and 54 - the  $k_W$  model performed the best for this unit problem which has not yet been incorporated into PARC. Comparative studies with PARC, TUFF, and SCIPVIS of such jet flows, using a new matrix of data, will be the subject of a forthcoming paper [55].

A PARC prediction for an underexpanded ( $P_0/P_\infty = 2$ ) Mach 2 jet exhausting into a Mach 2 external stream, in the presence of a base (base height is 1.5 nozzle exit radius) is exhibited in Figure 4. This prediction simulated an experiment of Reed and Hastings [56], and the predicted base pressure agreed quite well with the experimental measurement despite the uniform, coarse mesh employed (50 by 50 over 4x4 numerical domain), and the use of a basic  $k_\epsilon$  model with no compressibility-correction. This calculation is being repeated with an adaptive mesh [57], using a compressibility-corrected turbulence model [52] for the base region shear layers. A comparable PARC prediction with an  $H_2$  jet instead of an air jet is exhibited in Figure 5, which demonstrates the ability of PARC to deal with base combustion - the base pressure levels were elevated from those of the noncombusting case and appear qualitatively reasonable, although no data is available to quantify the prediction.

Predictions for a 2D transverse jet interaction flowfield simulating the helium fuel injection experiment of Kraemer and Rogers (described in ref. 58) are exhibited in Figure 6 along with the experimental setup. Predictions made with the  $k_\epsilon$  turbulence model underestimated the lateral extent of the approach separation zone indicating too fast a rate of mixing. A 'capped' version of the  $k_\epsilon$  model which did not allow the turbulent viscosity,  $\mu_t$ , to exceed  $1000 \mu$ , produced results in better agreement with the data indicating the requirement to incorporate compressibility effects and possibly strong nonequilibrium effects (correction for  $P/\rho \gg 1$ ) into the turbulence model. Gridding was not an issue as ascertained by both grid convergence studies on both rectangular and adaptive [57] grids. Predictions by Weidner and Drummond for this problem using an algebraic turbulence model also underestimated the lateral extent of the separation zone [58].

For high speed wall jets, the Burrows and Kurkov data [59] are among the few sets of data available that provide the detailed initial conditions required to analyze this

problem properly. The case involves the sonic, tangential, balanced pressure injection of a Mach 1, cold ( $T = 254^\circ K$ )  $H_2$  jet into a Mach 2.44, hot ( $T = 1270^\circ K$ ) vitiated airstream in a near-parallel wall combustor. The airstream has a thick boundary layer, which was about three times the size of the initial  $H_2$  jet (jet slot height was 0.4 cm). Figure 7 shows the experimental set up and compares predictions (performed imposing a turbulent Prandtl number of 0.9 and utilizing the hybrid  $k_\epsilon$ /Van Driest turbulence model) of  $H_2$ ,  $N_2$ ,  $O_2$ , and  $H_2O$  mole fractions at the combustor exit (36 cm downstream of the injection plane) with the measured data. The results are quite reasonable and accurately locate the flame position (peak  $H_2O$ ) although they slightly under predict the peak level of  $H_2O$  observed (this may require use of adaptive gridding that concentrates points in the flame zone).

The above 'Level 3' validation studies exhibit the ability of PARC to analyze various types of jet interactions using a two-equation turbulence model, and the chemical kinetic capabilities incorporated in the code. Issues with regard to the turbulence modeling still have not been resolved at this 2D component problem level, and adaptive grid requirements are indicated to achieve adequate resolution with a reasonably sized mesh. Analogous Level 3 jet interaction studies for 3D problems will be performed in the near future.

#### 5.4 Missile Rocket Nozzle Studies

A complete missile calculation requires the analysis of the rocket nozzle/propulsive flowfield. For some problems, there can be strong coupling between the nozzle exhaust and the missile aerodynamic flowfields. A specialized version of PARC (PARC/RN) has been developed to analyze rocket nozzle flowfields, starting from nonequilibrium conditions in the combustion chamber. This version deals with multi-phase (gas/particle) nonequilibrium, as well as chemical nonequilibrium and is described in refs. 8 and 28.

Validation sans nonequilibrium effects is provided via data such as that of Back and Cuffell [59]. The test case chosen is a popular one for validation of nozzle codes since both wall and profile data are available, and the large throat curvature poses a distinct numerical challenge to simulate the flowfield in this conical nozzle. The reservoir conditions were  $P_0 = 70$  psia and  $T_0 = 540^\circ R$ . The nozzle is a conical geometry with  $45^\circ$  converging and  $15^\circ$  diverging half angles. The throat radius is 0.8 in. with a small throat radius of curvature ( $R_c/R_{th} = .625$ ). Figure 8 shows the grid utilized and comparisons between the measured and computed pressures on the wall and axis, for an Euler calculation. The agreement with data is seen to be good upstream of the nozzle throat; however the comparison is poorer downstream of the throat. The cause of the discrepancy may be inadequate grid resolution in the throat region and failure to resolve the significant gradients produced by the small throat radius of curvature. The agreement with data is comparable to



that achieved by most other investigators (see e.g. the recent work of Marcum and Hoffman in ref. 61).

To illustrate gas/particle nonequilibrium capabilities in PARCH, a solid propellant rocket motor nozzle calculation was performed with H/C/O chemistry (12 species, 16 reactions), and with  $\text{Al}_2\text{O}_3$  particulates (30% mass loading). Preliminary calculations were performed assuming all the particulates to have radii of 3  $\mu\text{m}$ . Computations were performed with and without particles to illustrate the strong influence of particulates on the gas-phase flowfield. Figure 9 compares the Mach number contours from the gas only calculation with that of the multi-phase calculation. As shown by the Mach number contours, the presence of particles has a dramatic influence on the flowfield. The reflected shock disappears; the particles peel away from the nozzle at the throat and the limiting particle streamline effect is clearly seen. Figure 10 shows the temperature distributions along the nozzle centerline. Notice the particulate temperatures lagging the gas temperature. At the nozzle exit plane, the thermal nonequilibrium between the gas and particles is almost 300 °K. Also, the particles begin to solidify with the onset of phase changes indicated by the particle temperature remaining constant. Comparisons with an earlier spatial marching two-phase code, SPFNOZ code [62] are also shown, downstream of the throat.

This case was also computed with three particle size groups. The total mass loading of particulates remained the same, however it was distributed into particles of 3, 5 and 10 microns with respective mass fractions of .6, .3 and .1. Pressure, temperature, and Mach number contours are shown in Figure 11. The striations evident in the contours of temperature and Mach number coincide with the limiting particle streamline locations of the three particle size groups (3  $\mu$  is uppermost, 5  $\mu$  is next, 10  $\mu$  is lowest). Further details of this calculation and other rocket nozzle calculations are provided in refs. 8 and 28.

### 5.5 Tactical Missile Airframe/Plume Interaction Studies

Much of our recent work has concentrated on the difficult interaction problem of a tactical missile with scarfed (bifurcated) nozzles [63] where the nozzle exhaust issues from the sides of the missile (Fig. 12). Calculations for a tactical missile ( $M = 0.6$  sea level) with a liquid (amine) propellant and no wings/ fins are presented. Figure 13 shows the grid utilized. The 3D problem was performed with half plane symmetry and had two engines whose centerlines are on the plane  $\phi = 0$  and  $\phi = 180^\circ$ , with grid points clustered in the vicinity of the nozzle exit plane and base, as well as on the missile body surface to resolve the boundary layers. Note that the 'blanking' capabilities of PARCH greatly simplify the analysis of the base region. Contours of temperature, velocity and turbulent kinetic energy (the full flow was taken to be turbulent and solved using the low  $Re/\text{Chien}$

variant of the  $k\epsilon$  model) are exhibited in Figure 14, in the symmetry plane which includes the centerline of both engines. Axial cuts of  $x/R_b = 18$  (just downstream of nozzle),  $= 25$  (in base) and  $= 30$  (in plume wake flow) are shown in Fig. 15 for the temperature.

The problem described above was repeated for a missile flying at an angle-of-attack of  $10^\circ$ . Contours of Mach number and turbulent kinetic energy are exhibited in Figures 16 and 17 in a plane containing the two nozzle axes (e.g., top view) and in a plane rotated  $180^\circ$  (e.g., side view). The side view contours show a thin turbulent boundary layer on the windward (bottom) side of the missile, and indicate separated flow on the leeward (upper) side. The upstream influence of the propulsive jets is readily evident in the top view Mach number contours. Cross flow contours of Mach number (and/or velocity) temperature, and turbulent kinetic energy are exhibited: at  $x = 22.9$  (at the missile base) in Figure 18; and, at  $x = 23$  (just downstream of the base) in Figure 19. Note that the plumes heat up the base as evident from the base temperature contours shown in Figure 18. Note also that the flow downstream of the missile base represents a complex interaction of 3 free shear flows, namely the two exhaust plumes and the missile wake.

Work is currently in progress towards analyzing a tactical missile with wings/fins (Fig. 20) and towards analyzing a missile with nonflush scarfed nozzle (Fig. 21). Attempts are being made to analyze these problems with a single grid to minimize CPU costs (the use of contiguous blocked grids entails more operations, e.g., the transfer of information from one blocked grid to the next, and will slow down the path to convergence).

### 5.6 Hypersonic/Higher Altitude Missile Applications

Much of this work has entailed the upgrade of PARCH to incorporate thermal nonequilibrium effects, and, advanced ground state and excited state air chemistry [9]. Thermal nonequilibrium work has included the performance of sensitivity studies to assess the dependency of reaction rates on temperature (viz. which temperature is utilized in the chemical reactions). Other work in this area has explored the ability of the PARCH NS code to simulate very high Mach number/high altitude shock layer problems such as the Mach 37, 80 km case (simple perfect gas conditions were used here to first explore numerical issues) whose pressure contours are exhibited in Fig. 22 for 2 nose radii ( $R_n = 2.5$  in. and  $R_n = 7.9$  in.). Note the marked differences in the shock thickness for these two cases, which is clearly exhibited in the pressure variation along the stagnation streamline (Figure 23). In such cases, the inclusion of rotational nonequilibrium effects in the thick shock may be required [64] as will be the inclusion of slip flow surface boundary conditions. Comparisons of such hypersonic calculations

with direct simulation Monte Carlo code predictions are currently in progress.

#### 6. SCHAFT PNS CODE AND PRELIMINARY CALCULATIONS

##### 6.1 SCHAFT Code Overview

The SAIC SCHAFT Code [20, 24, 25] represents an upgrade of the 3D PNS STUFF code of Molvik and Merkle [21] whose features are summarized in Table 3 below.

TABLE 3. STUFF CODE OVERVIEW

- . 3D Thin Layer PNS Code Developed For Hypersonic External Aerodynamics With Advanced Thermochemistry By Molvik And Merkle (AIAA Paper 89-0199)
- . Roe/TVD - Convective, Central Difference - Diffusive
- . Iterative Spatial Marching Procedure
- . Vectorization on CRAY-2
- . Fully-Coupled/Fully Implicit Finite-Rate Clean Air Chemistry (5 + NS - 1) Matrix Inversion Where NS = 7 For Clean Air Chemistry
- . Laminar Transport Data For Air

##### Recent Upgrades By Molvik

- . Generalization Of Matrix Size To 5 + NS - 1 Where NS Is Number Of Chemical Species
- . Perfect Gas/Equilibrium Air (Tannehill Fits) Run Options

The work to date in developing SCHAFT from STUFF is described below in Table 4. The user-friendly aspects of dealing with generalized H/C/N/O chemistry parallel the methodology in earlier SAIC codes (SCORCH, SCHNOZ, etc.) and PARCH, in that data banks contain the generalized thermochemical data, and varying mechanisms, rates, etc., is quite straightforward. STUFF utilizes forward/backward rate data whereas the earlier SAIC codes utilized forward data only, with backward rates obtained from the equilibrium coefficient.

##### 6.2 SCHAFT Equations

The finite-volume equations in the SCHAFT3D code are given in Table 5 below. Note that SCHAFT integrates a system of 5 (fluid) + NS - 1 (species) + 2 (turbulence) equations in a fully-coupled manner with all source terms treated fully-implicitly. The complete details of the numerics, including the Roe upwind manipulations, performed with the real gas behavior accounted for in a rigorous manner, are given in ref. 21.

TABLE 4. SCHAFT3D CODE DEVELOPMENT FROM STUFF CODE FRAMEWORK

- . 3D PNS Extension Of STUFF For Plume/Propulsive Applications
- . Generalization Of Boundary Conditions
  - No Slip/Slip/Symmetry/Free-stream On Any Of 4 Boundaries
- . Full Cross-Flow Stress/Diffusive Terms Incorporated
- . Generalization Of Clean Air Finite-Rate Chemistry For Arbitrary H/C/N/O Systems
  - User Friendly Coding To Vary Reactions Employed, Rate Coefficients, etc.
  - Data Bank Of Reaction Mechanisms And Rate Data
  - Transport Data For H/C/N/O Chemical Species
  - Full Coupling/Fully Implicit Methodology
- . Inclusion Of Two-Equation Turbulence Models
  - $k\epsilon$ , Low Re Chien Terms
  - Strong Coupling/Extension Of Matrix Size
  - Implicit Treatment Of Source Terms

TABLE 5. SCHAFT3D EQUATIONS

$$\frac{d}{dt} \left( \int \rho Q d\Omega + \int \rho E d\Omega + \int \rho F d\Omega + \int \rho G d\Omega \right) = \frac{1}{Re} \int \rho S d\Omega + \frac{1}{Re} \int \rho T d\Omega + \int \rho Q d\Omega$$

$$\left. \begin{aligned} \text{Where } S &= S_1(Q, Q_h) + S_2(Q, Q_f) \\ T &= T_1(Q, Q_f) + T_2(Q, Q_h) \end{aligned} \right\}$$

[ORIGINAL STUFF CODE HAD ONLY  $S_1$  TERM]

$$Q = \underbrace{[\rho, \rho U, \rho V, \rho W, \rho E_t, \rho a_1, \rho a_2, \dots, \rho a_{NS-1}]}_{\substack{5 \text{ FLUID} \\ \text{VARIABLES}}} \underbrace{[\rho k, \rho \epsilon]}_{\substack{2 \text{ TURBULENCE} \\ \text{VARIABLES}}} \underbrace{[\rho S_1, \rho S_2, \dots, \rho S_{NS-1}]}_{\substack{NS - 1 \text{ CHEMICAL} \\ \text{SPECIES}}}$$

##### SOURCE TERM

$$D = [0, 0, 0, 0, 0, \dot{\omega}_1, \dot{\omega}_2, \dots, \dot{\omega}_{NS-1}, D_k, D_\epsilon]^T$$

CHEMISTRY SOURCE TERM      TURBULENCE SOURCE TERMS

$D_k, D_\epsilon$  - LOW RE CHIEN FORM OF  $k\epsilon$  FORMULATION

ALL SOURCE TERMS - LINEARIZED/FULLY IMPLICIT TREATMENT

The source terms in SCHAFT are all linearized and treated in a fully-implicit manner - a detailed description of the treatment of the chemical source term,  $\dot{\omega}_i$ , is provided in ref. 21.

### 6.3 Numerical/Validation Studies

The STUFF PNS code has concentrated on hypersonic external aerodynamic applications, with validation studies [65] emphasizing the clean air chemistry capabilities. SCHAFT has involved an extension of STUFF for plume/propulsive applications, and the validation studies performed to date have included:

- (1) Laminar Premixed  $H_2$ /Air Flame
- (2) 2D Shear Layers
- (3) 2D Shock Propagation In Duct
- (4) 2D Shock Induced Combustion
- (5) 2D CD Nozzle
- (6) 3D CD Nozzle
- (7) 3D Combustor/Nozzle
- (8) 2D/3D Plumes

Many of these validation studies have involved 'Level 1' comparisons with predictions made utilizing PARCH, as well as with earlier PNS codes such as SCRINTX [5, 17] and SCRINT3DT [20, 22]. While PARCH, and its predecessors, ARC and PARC, have a long validation history, STUFF is a new code, and our extended version, SCHAFT, has been operational for less than 1 year. Hence, validation to date has been limited and has emphasized 'Level 1' comparisons, some of which will be briefly summarized below.

### 6.4 2D Shock Propagation in Duct

SCHAFT can run in an Euler mode as well as a PNS mode and a numerical study of a simple 2D shock propagation problem is presented and compared with SCRINTX results in Figure 24. The conditions and grid for this perfect gas calculation are described below, along with a comparison of predicted pressures along the upper and lower duct walls. Results of the two codes, both implementing second-order Roe upwind numerics, are in good agreement, with the SCHAFT predictions showing somewhat crisper waves. Comparisons of pressure contours for this case more clearly exhibit the superior shock-capturing characteristics of SCHAFT which utilizes an iterative, finite-volume discretization in comparison to the non-iterative finite-difference discretization utilized in SCRINTX.

### 6.5 Shock-Induced Combustion

A solution of flow in the same duct with the same grid as the previous case is shown in Figure 25, where the approach flow now contains two uniform streams - a lower  $H_2$  stream, and an upper air stream both at the same pressure (1 atm), temperature (750 °K), and Mach number ( $M = 2.9$ ). The initial temperature and pressure levels are too low for combustor to ignite the initial shear layer. The shock emanating from the lower compression surface is sufficient to initiate combustion as shown in the temperature

contours and the water contour of Figure 26. Combustion initiates when the shock penetrates the  $H_2$ /air shear layer. SCHAFT performed this analysis with a 7 species/8 reaction representation of the  $H_2$ /O chemistry.  $H_2$  contours serve to indicate the extent of the shear layer - notice the very crisp response of the shear layer streamlines to wave interactions.  $H_2O$  contours clearly indicate the combustion process and its onset just downstream of where the shock from the lower wall penetrates the shear layer.

### 6.6 SCHAFT Analysis of 3D Combustor/Nozzle Problem

SCRINT3DT calculations [22] were performed earlier using first order Roe upwind numerics. Attempts to analyze this problem using second order upwind numerics failed. The Beam-Warming second order central-difference run option was not sufficiently robust to deal with the shocks generated by the underexpanded jets while the ad hoc real gas Roe upwind formulation would not operate with second order accuracy. The SCRINT3DT calculation could NOT be started from the initial data plane 'top hat' profiles. The solution was initiated 1 duct height downstream with profiles provided by a PARCH NS solution (the complete PARCH solution for this case is described in refs. 8 and 28). The first order SCRINT3DT results were found to be overly diffusive, and flux/species conservation was not satisfactory. To exhibit that the fluid/chemistry matrix split coupling in the Roe formulation was the source of the problems encountered by SCRINT3DT, the calculation had been repeated with air/air mixing (perfect gas) using second order Roe/TVD numerics. It was found that the calculation could be initiated at  $x=0$  and flux balances were excellent (see ref. 22 for details).

The SCHAFT analysis of this flowfield (Fig. 28) was extremely promising. The calculation could be started from 'top hat' profiles at  $x=0$  and no problems were encountered using the second order Roe/TVD numerics. Contours in a vertical plane passing through the center of the inner  $H_2$  jet are shown in Fig. 29. This plane initially exhibits more of a 2D like solution. The initial growth of the  $H_2$ /air shear layer is depicted in the temperature contours. The pressure contours exhibit the underexpansion shock propagating outward from the jet and the Prandtl-Meyer fan propagating inward. Figure 30 exhibits SCHAFT cross-flow contours of  $H_2O$  at planes  $x=5, 10$ , and  $15$ . Note the deformation of the original square shapes by the expansion waves emanating from the upper wall and side wall.

### 6.6 Axisymmetric Underexpanded Plume

The calculation simulated a uniform Mach 2, hot ( $T = 1000$  °K), underexpanded air jet exhausting into a uniform Mach 5 external air stream ( $P_0/P_\infty = 10/1$ ). A relatively crude grid was employed for this jet interaction calculation with 50 radial grid points extending from the axis to upper

boundary ( $r/r_0 = 5$ ), and an axial step size of  $\Delta x = .1 \frac{1}{2}$ , employed (where  $r_0$  is the nozzle exit radius). With this crude grid, a step-like initial profile at the nozzle exit plane, and no special treatment of the lip interaction region or the Mach disc region, the results exhibited in Figure 31 were obtained. With twice the grid resolution, the nearfield pressure contours shown in Figure 32 were obtained which show a clear definition of the lip Prandtl-Meyer expansion fan, the barrel and reflected shocks, and the plume underexpansion shock. The upper boundary at  $r/r_0 = 5$  is 'non-reflective' and permits waves such as the plume underexpansion shock to pass out of the computational domain with no reflections. The improvement provided by enhanced nearfield grid resolution is readily evident by the pressure variations along the plume centerline, also shown in Figure 32.

A series of calculations for 3D square and rectangular plumes are described in refs. 20, 24 and 25. For 3D problems, a cross-flow adaptive grid is required which conforms to the evolving plume shape - such adaptive gridding will be added to SCHAFT in the near future.

#### CONCLUDING REMARKS

Significant progress towards analyzing 3D tactical missile/exhaust plume interaction flowfields has been made using the PARC NS code. Current capabilities provide for the analysis of complete 3D interactive flowfields with finite-rate chemistry and equilibrated multi-phase flow. Efforts are now concentrated on grid generation for protruding nozzles and for missile wings/fins. Two-equation turbulence models, such as  $k_\epsilon$ , are now operational in PARC. Their calibration and upgrade for complex 3D, compressible flows requires detailed and systematic comparisons with available data. Such work, as well as the upgrade of multi-phase flow capabilities to provide for gas/particle nonequilibrium effects, is envisioned for the near future. PARC has incorporated chemistry using a matrix-split formulation which works effectively and efficiently with central-difference numerics, but not with Roe/TVD upwind numerics. Modifications to PARC to make the chemistry consistent with the Roe/TVD formulation are in progress which will employ a strongly-coupled, large matrix formulation.

The SCHAFT PNS code has such a strongly-coupled chemistry formulation, which, along with its finite-volume numerics, provides very accurate results and extremely robust performance. SCHAFT has run all the calculations described in an effortless manner without the need to include special start-up procedures, or, to pack grid points in regions of extreme gradients. Clearly, adaptive gridding will greatly improve the accuracy of the calculations described, but 'robustness' problems were never encountered - a statement we cannot make about any previous spatial marching PNS code we have ever worked with. SCHAFT operates in both a 2D

(planar or axisymmetric) or 3D mode, presently includes finite-rate chemistry, two-equation turbulence models, and generalized implicit boundary conditions. Its excellent performance to date clearly warrants its application to supersonic/hypersonic missile aerodynamic and plume propulsive flowfield problems and we plan to use it for such purposes in upcoming programs.

#### ACKNOWLEDGEMENTS

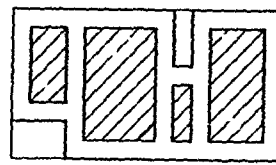
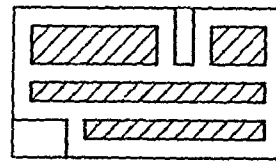
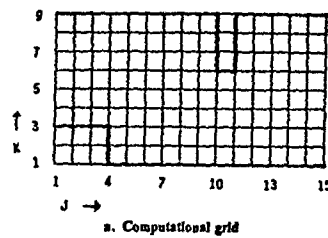
Portions of this work were performed under ONR Contract N0014-87-C-0549 (monitored by Dr. Spiro Lekoudis), with funds provided by MICOM (monitored by Dr. Billy Walker) and by NASP (monitored by Dr. Joseph Shang).

#### REFERENCES

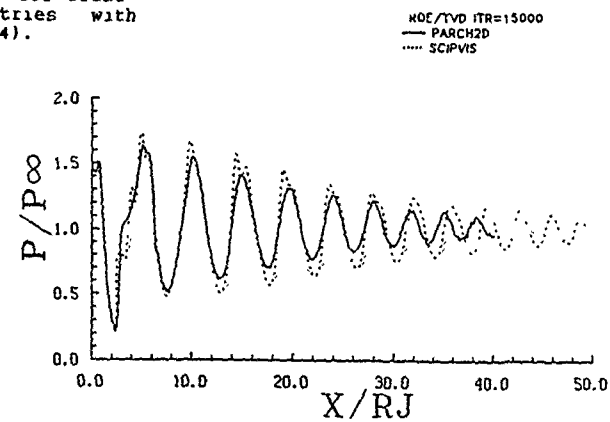
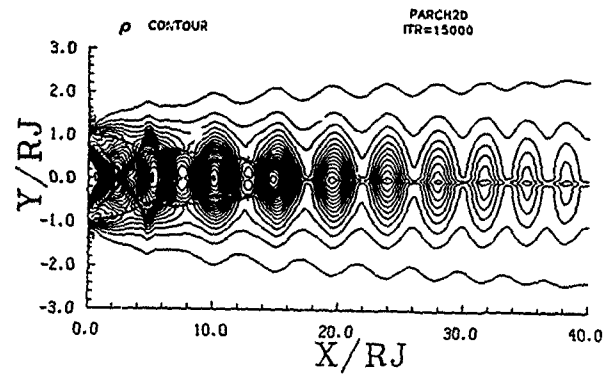
1. Hall, D.W., Hines, R.W., Baltakis, F.P. and Wardlaw, A.B., 'Coupled Inviscid/Viscous Aerodynamic Predictions for Supersonic Tactical Missiles', AIAA Paper 90-0617, Jan. 1990.
2. Dash, S.M., 'Exhaust Plumes and Their Interaction With Missile Airframes', *Tactical Missile Aerodynamics*, Vol. 104, Progress in Aeronautics, ed. J.N. Nielson and M.J. Hemmich, AIAA, New York, 1986, Chapter XVII, pp. 778-851.
3. Pulliam, T.H., 'Euler and Thin-Layer Navier-Stokes Codes: ARC2D, ARC3D', *Notes for Computational Fluid Dynamics User's Workshop*, The University of Tennessee Space Institute, Tullahoma, TN UTSI Pub. E02-4005-023-84, March 1984, pp. 14.1 - 15.85.
4. Cooper, G.K., 'The PARC Code: Theory and Usage', AEDC-TR-87-24, October 1987.
5. Dash, S.M., Sinha, N. and York, B.J., 'Matrix Split Approach for Inclusion of SPF Thermochemical Capabilities Into Beam-Warming Based PNS and NS Models', *JANNAF 17th Plume Technology Meeting*, CPIA Pub. 487, Vol. I, April 1988, pp. 91-110.
6. Sinha, N., York, B.J. and Dash, S.M., 'Applications of a Generalized Implicit Navier-Stokes Code, PARC, to Supersonic and Hypersonic Propulsive Flowfields', AIAA Paper 88-3278, Boston, MA, July 1988.
7. Sinha, N., York, B.J., Ong, C.C., Stowell, G.M. and Dash, S.M., '3D Navier-Stokes Analysis of High-Speed Propulsive Flowfields Using The PARC Code', AIAA Paper 89-2796, Monterey, CA, July 1989.
8. York, B.J., Sinha, N., Ong, C.C. and Dash, S.M., 'PARC Navier-Stokes Reacting/Multi-Phase Analysis of Generalized Nozzle Flowfields', AIAA Paper 89-1765, Buffalo, NY, June 1989.
9. Sontowski, J., Sinha, N., Stowell, G.M. and Krawczyk, W.J., 'Analysis of Nosecap Shock Layer UV Signatures', Final Report for SDIO, Contract SDIO84-88-C-0016, April 1989.
10. Dash, S.M., Sinha, N., York, B.J. and Ong, C.C., '3D Navier-Stokes Analysis of Tactical Missile External/Plume Interaction Flowfields', *JANNAF 18th Plume Technology Meeting*, Monterey, CA, November 1989.

11. Dash, S.M., Sinha, N., Wolf, D.E. and York, B.J., 'Computational Models for the Analysis/Design of Hypersonic Scramjet Components, Part I: Combustor and Nozzle Models', AIAA Paper 86-1595, Huntsville, AL, June 1986.
12. Krawczyk, W.J., Rajendran, N., Harris, T.B., York, B.J. and Dash, S.M., 'Computational Models for the Analysis/Design of Hypersonic Scramjet Components, Part II: Inlet and Ramp/Forebody Models', AIAA Paper 86-1596, Huntsville, AL, June 1986.
13. Dash, S.M., 'Design-Oriented PNS Analysis of Complete Scramjet Propulsive System', Second National Aerospace Plane Technology Symposium, NASP CP-2012, November 1986, pp. 287-324.
14. Krawczyk, W.J. and Harris, T.B., 'Analysis of Aerospace Vehicle Scramjet Propulsive Flowfields: 2D Forebody/Inlet Code Development - Phase I', NASP CR 1003, August 1987.
15. Sinha, N. and Dash, S.M., 'Parabolized Navier-Stokes Analysis of Ducted Supersonic Combustion Problems', J. Propulsion, Vol. 3, No. 5, Sept. - Oct. 1987, pp. 455-464.
16. Wolf, D.E., Lee, R.A. and Dash, S.M., 'Parabolized Navier-Stokes Analysis of Scramjet Hypersonic Nozzle Flowfields', AIAA Paper 87-1897, San Diego, CA, June - July 1987.
17. Sinha, N., Krawczyk, W.J. and Dash, S.M., 'Inclusion of Chemical Kinetics into Beam-Warming PNS Models for Hypersonic Propulsion Applications', AIAA Paper 87-1898, San Diego, CA, June - July 1987.
18. Lee, R.A., Sinha, N. and Dash, S.M., 'PNS Code Assessment Studies for Scramjet Combustor and Nozzle Flowfields', AIAA Paper 89-1827, Buffalo, NY, June 1989.
19. Chakravarthy, S. and Osher, S., 'A New Class of High Accuracy TVD Schemes for Hyperbolic Conservation Laws', AIAA Paper 85-0363, Reno, NV, January 1985.
20. Dash, S.M., Sinha, N. and Lee, R.A., 'Time Iterative Upwind/Implicit 3D PNS Codes for the Analysis of Chemically-Reacting Plume/Propulsive Flowfields', JANNAF 18th Plume Technology Meeting, November 1989.
21. Mølvik, G.A. and Merkle, C.L., 'A Set of Strongly Coupled Upwind Algorithms for Computing Flows in Chemical Non-equilibrium', AIAA Paper 89-0199, Reno, NV, Jan. 1989.
22. Dash, S.M., Harris, T.B., Krawczyk, W.J., Rajendran, N., Sinha, N., York, B.J. and Carlson, D., 'Three-Dimensional Upwind/Implicit PNS Computer Codes for Analysis of Scramjet Propulsive Flowfields', Sixth NASP Technology Symposium, NASP CP 6035, April 1989, pp. 129-172.
23. Krawczyk, W.J., Harris, T.B., Rajendran, N. and Carlson, D., 'Progress in the Development of Parabolized Navier-Stokes Methodology for External and Internal Supersonic Flows', AIAA Paper 89-1828, Buffalo, NY, June 1989.
24. Sinha, N. and Dash, S.M., 'Implicit/Upwind 3D PNS Scramjet Propulsive Flowfield Code: SCRAFT3D', Seventh NASP Technology Symposium, NASP CP 7041, Oct. 1989, pp. 151-180.
25. Sinha, N., Dash, S.M. and Lee, R.A., '3D PNS Analysis of Scramjet Combustor/Nozzle and Exhaust Plume Flowfields', AIAA Paper 90-0094, Reno, NV, January 1990.
26. Dash, S.M., 'Turbulence Modeling for Computations of High Speed Flows - State-of-the-Art', Fifth NASP Technology Symposium, NASP CP 5029, Oct. 1988, pp. 287-320.
27. Dash, S.M., 'Turbulence Model Validation for High Speed Propulsive Applications', Fifth NASP Technology Symposium, NASP CP 5029, Oct. 1988, pp. 467-504.
28. York, B.J., Sinha, N. and Dash, S.M., 'PARCH Navier-Stokes Code Analysis of Rocket and Airbreathing Nozzle/Propulsive Flowfields', JANNAF 18th Plume Technology Meeting, Monterey, CA, November 1989.
29. Anderson, D.A., Tannehill, J.C. and Fletcher, R.H., Computational Fluid Mechanics and Heat Transfer, Hemisphere Publishing Co., USA, 1984.
30. Chaussee, D.S. and Pulliam, T.H., 'Two Dimensional Inlet Simulation Using a Diagonal Implicit Algorithm', AIAA J., Feb. 1981, pp. 153-159.
31. Jameson, A., Schmidt, W. and Turkel, E., 'Numerical Solutions of Euler Equations by Finite-Volume Methods Using Runge-Kutta Time Stepping Schemes', AIAA Paper 81-1259, June 1981.
32. Dash, S.M., Sinha, N., York, B.J., 'Tactical Missile/Plumes Interaction Flowfield Analyses with the PARCH Computer Code', U.S. Army Missile Command, Report in preparation.
33. York, B.J., Sinha, N. and Dash, S.M., 'Computational Models for Chemically-Reacting Hypersonic Flows', AIAA Paper 88-0509, AIAA 26th Aerospace Sciences Meeting, Reno, NV, January 1988.
34. Chien, K.Y., 'Predictions of Channel and Boundary Layer Flows With a Low Reynolds Number Turbulence Model', AIAA J., Jan. 1982, pp. 33-38.
35. Dash, S.M., Wolf, D.E., Beddini, R.A. and Pergament, H.S., 'Analysis of Two-Phase Flow Processes in Rocket Exhaust Plumes', J. Spacecraft and Rockets, May - June 1985.
36. Dash, S.M. and Thorpe, R.D., 'Shock Capturing Model for One and Two-Phase Supersonic Exhaust Flow', AIAA Journal, Vol. 19, July 1981, pp. 842-851.
37. Hvidock, T.R., 'Blocked', RCH3D Code, Science Applications International Corporation, Ft. Washington, PA, TP-196, May 1989.
38. Sirbaugh, J., Personal Communication, Sverdrup, Inc., AEDC, Tullahoma, TN, 1989.
39. Dash, S.M., 'Turbulence Modeling, Chemical Kinetics and Algorithm Related Issues in CFD Analysis of Scramjet Components', Second National Aerospace Plane Technology Symposium, NASP CP-2012, John Hopkins University Applied Physics Lab., Laurel, MD, Nov. 1986, pp. 39-80.
40. Pulliam, T.H., 'Efficient Solution Methods for the Navier-Stokes Equations', Numerical Techniques for Viscous Flow Computations in Turbomachinery Bladings, Von Karman Institute Lecture Series, Brussels, Belgium, Jan. 1986.

41. Pulliam, T.H. and Steger, J.L., 'Recent Improvements in Efficiency, Accuracy, and Convergence for Implicit, Approximate Factorization Algorithms', AIAA Paper 85-0360, Reno, NV, Jan. 1985.
42. Nietubicz, C.J., Inger, G.R. and Danberg, J.E., 'A Theoretical and Experimental Investigation of a Transonic Projectile Flowfield', AIAA Paper 82-0101, Jan. 1982.
43. Shian, N.H. and Hsu, C.C., 'A Diagonalized TVD Scheme for Turbulent Transonic Projectile Aerodynamic Computation', AIAA Paper 88-0217, Reno, NV, Jan. 1988.
44. Hsu, C.C., Shian, N.H. and Reed, C.W., 'Numerical Simulation of Transonic Turbulent Flow Past a Real Projectile', AIAA Paper 88-0218, Jan. 1982.
45. Cooper, G.K., Gerrard, G.D. and Phares, W.J., 'PARC Code Validation for Propulsion Flows', AEDC, TR-88-32, Jan. 1989.
46. Cooper, G.K., Jordan, J.L. and Phares, W.J., 'Analysis Tools for Application to Ground Testing of Highly Underexpanded Nozzles', AIAA Paper 87-2015, June-July 1987.
47. Reddy, D.R. and Harloff, G.J., 'Three-Dimensional Viscous Flow Computations of High Area Ratio Nozzles for Hypersonic Propulsion', AIAA Paper 88-0474, Jan. 1988.
48. Harloff, C.J., Lai, H.T. and Nelson, E.S., '2D Viscous Flow Computations of Hypersonic Scramjet Flowfields', NASP CR 1018, July 1988.
49. Lai, H. and Nelson, E., 'Comparison of 3D Computation and Experiment for Nonaxisymmetric Nozzles', NASP CR 1047, June 1989.
50. Hsu, A.T., 'Effect of Adaptive Grid on Hypersonic Nozzle Flow Calculation', NASP CP 1045, June 1989.
51. Harloff, G.J. and Lytte, J.K., 'Three-Dimensional Viscous Flow Computations of a Circular Jet in Subsonic and Supersonic Cross Flow', NASP CP 1021, Aug. 1988.
52. Dash, S.M., Weilerstein, G. and Vaglio-Laurin, R., 'Compressibility Effects in Free Turbulent Shear Flows', Air Force Office of Scientific Research, TR-75-1436, August 1975.
53. Dash, S.M., Wolf, D.E. and Seiner, J.M., 'Analysis of Turbulent Underexpanded Jets - Part I: Parabolized Navier-Stokes Model, SCIPVIS', AIAA Journal, Vol. 23, April 1985, pp. 505-514.
54. Seiner, J.M., Dash, S.M. and Wolf, D.E., 'Analysis of Turbulent Underexpanded Jets - Part II: Shock Noise Features Using SCIPVIS', AIAA Journal, Vol. 23, May 1985, pp. 669-677.
55. Dash, S.M., Sinha, N., York, B.J. and Lee, R.A., 'Progress in the Development of Advanced Computational Models for the Analysis of Generalized Supersonic Jet Flowfields', to be presented at AIAA 13th AeroAcoustics Conference, Tallahassee, FL, Oct. 1990.
56. Reid, J. and Hastings, R.C., 'The Effect of a Central Jet on the Base Pressure of a Cylindrical Afterbody in a Supersonic Stream', Aero Res. Council, R+M No. 3224, Dec. 1989.
57. Davies, C. and Venkatapathy, E., 'A Simplified Self-Adaptive Grid Method, SAGE', NASA TM 102198, Oct. 1989.
58. Weidner, E.H. and Drummond, J.P., 'Numerical Study of Staged Fuel Injection for Supersonic Combustion', AIAA J., Oct. 1982, pp. 1426-1431.
59. Burrows, M.C. and Kurkov, A.P., 'Analytical and Experimental Study of Supersonic Combustion of Hydrogen in a Vitiated Airstream', NASA TM X-2828, Sept. 1973.
60. Cuffel, R.F., Back, L.H., and Massier, P.F., 'Transonic Flowfield in a Supersonic Nozzle with a Small Throat Radius of Curvature', AIAA J., Vol 7, No. 7.
61. Marcum, D.L. and Hoffman, J.D., 'Calculation of Three-Dimensional Inviscid Flowfields in Propulsive Nozzles with Centerbodies', AIAA Paper 86-0449, Reno, NV, Jan. 1986.
62. Wolf, D.E., Dash, S.M. and Pergament, H.S., 'A Shock-Capturing Model for Two-Phase, Chemically Reacting Flow in Rocket Nozzles', AIAA Paper 85-0306, Reno, NV, January 1985.
63. Lilley, J.S., 'The Design and Optimization of Propulsion Systems Employing Scarfed Nozzles', AIAA Paper 85-1308, AIAA/SAE/ASME/ASCE 21st Joint Propulsion Conference, Monterey, CA, July 1985.
64. Lumpkin, F. and Chapman, D., 'A New Rotational Relaxation Model for Use in Hypersonic Computational Fluid Dynamics', AIAA Paper 89-1737, June 1989.
65. Strawa, A.W., Molvik, G., Yates, L. and Cornelison, C., 'A Comparison of Experiment and Computation for Slender Cones at High Mach Numbers', NASP CP 6035, April 1989, pp. 251-264.



**Fig. 1:** Grid Blanking Capability in PARC (Patched Grid Approach) for Treating Irregular Geometries with Simple Grids (see Ref. 4).



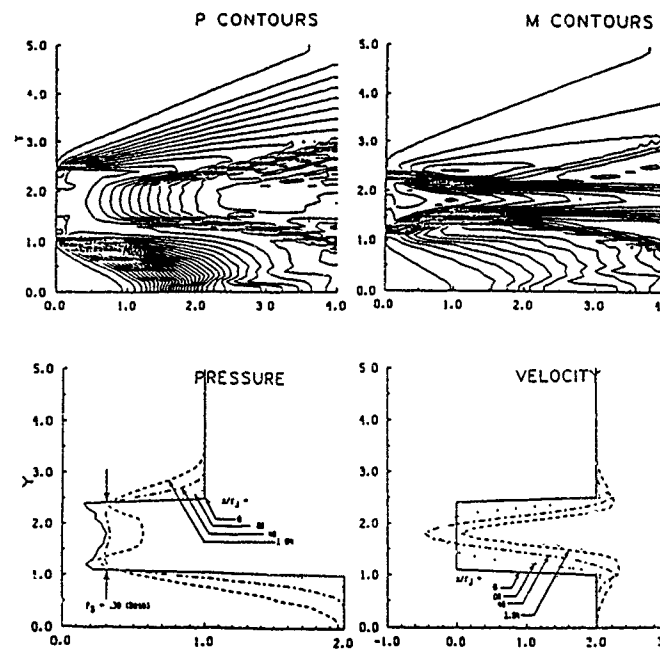


Fig. 4: PARCH Analysis of Reid and Hastings Experiment.

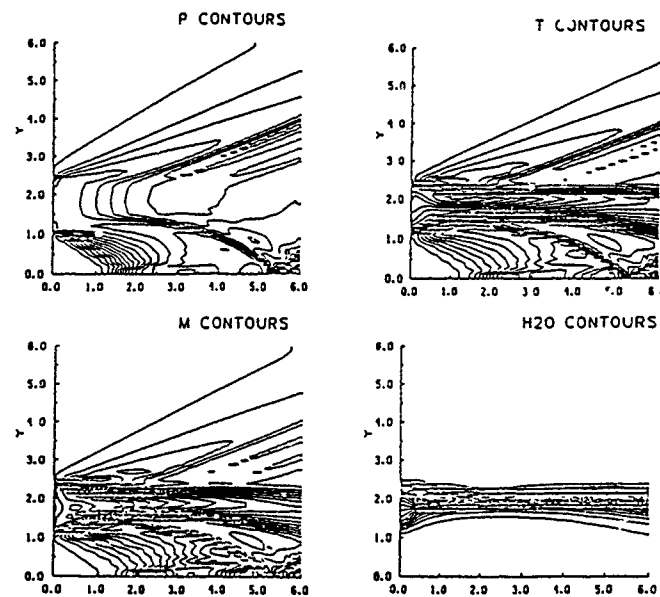


Fig. 5: PARCH Analysis of Jet/External Flow Interaction Problems with Base Combustion.



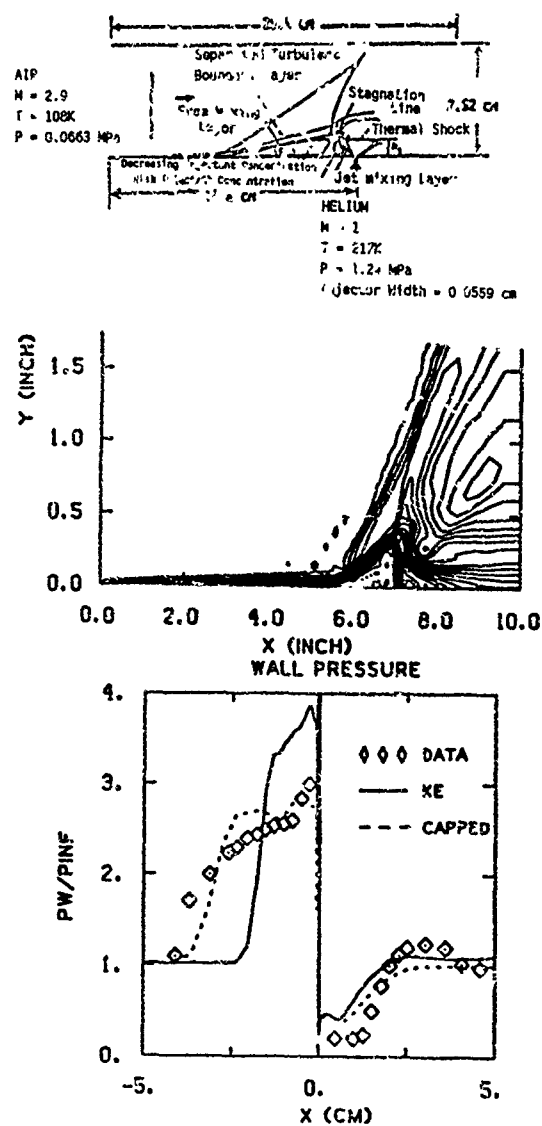


Fig. 6: 2D Transverse Jet Injection Problem, and PARCH Predictions Compared with Experimental Data.

	Hydrogen jet	Free stream
Mach number, $M$ . . . .	1.00	2.44
Temperature, $T$ , K . . .	254	1270
Velocity, $u$ , m/s . . .	1216	1764
Pressure, $p$ , MPa . . .	0.1	0.1
Mass fraction:		
$\phi_{H_2}$ . . . . .	1.000	0
$\phi_{O_2}$ . . . . .	0	0.250
$\phi_{H_2}$ . . . . .	0	0.406
$\phi_{H_2O}$ . . . . .	0	0.256

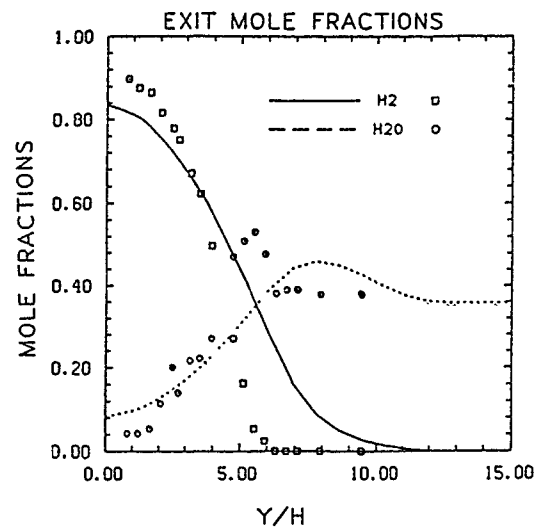
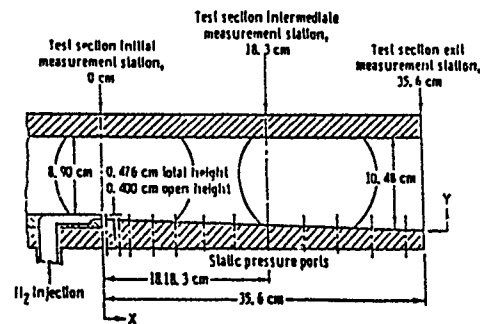


Fig. 7: PARCH Prediction of Exit Species Mole Fraction Profiles vs Burrows and Kurkov Data.

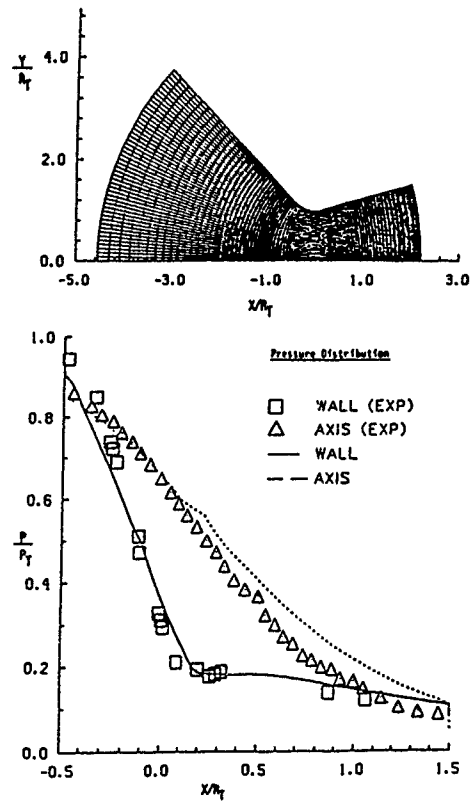


Fig. 8: Axial Pressure Distribution for Back and Cuffel Nozzle.

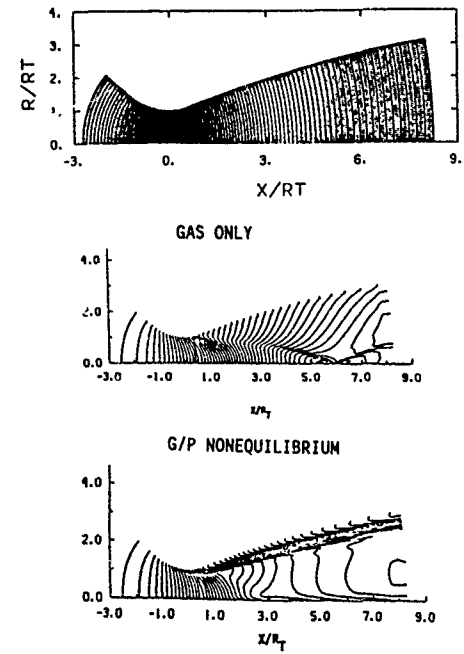


Fig. 9: PARCH Analysis of Solid Propellant Rocket Nozzle Flowfield; Gas Only and G/P Nonequilibrium with 30%  $\text{Al}_2\text{O}_3$ , 3  $\mu\text{m}$ .

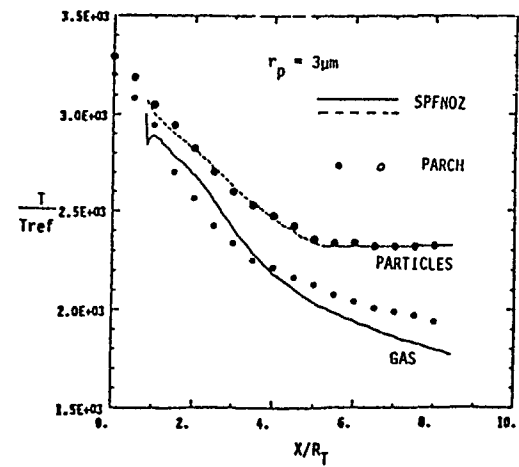
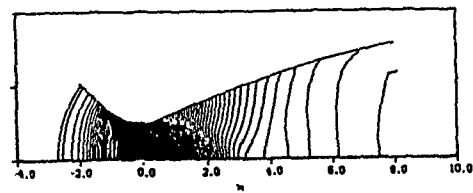
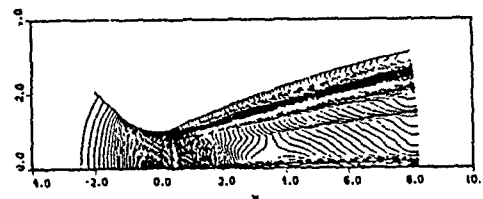


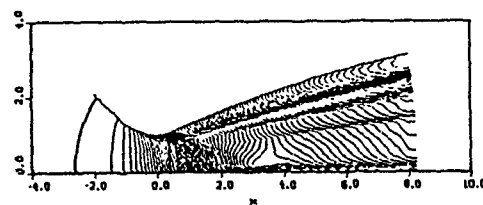
Fig. 10: Centerline Temperature Variations for Solid Propellant Rocket Nozzle Prediction.



Pressure Contours



Mach Number Contours



Temperature Contours

**Fig. 11:** Contours for Solid Propellant Rocket Nozzle Calculation with 3 Size Groups.

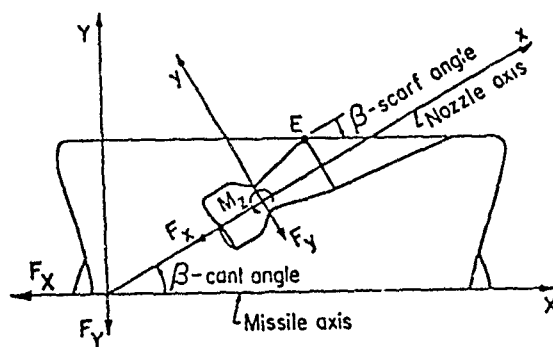


**Fig. 12:** Schematic of Bifurcated/Scarfed Nozzle Canted at an Angle  $\beta$  Relative to the Missile Axis (from Ref. 63.).

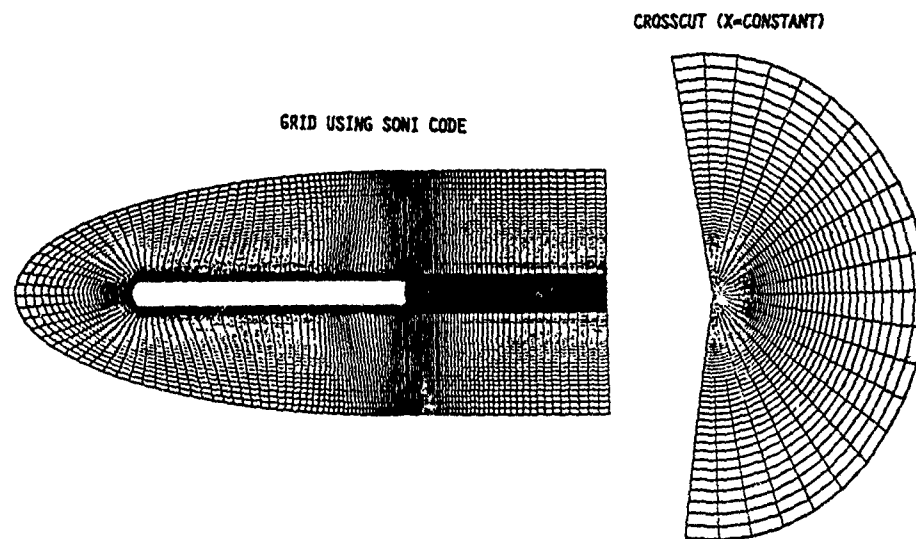
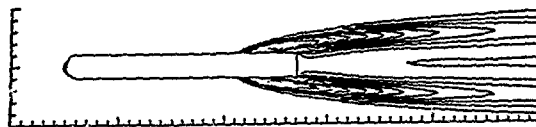
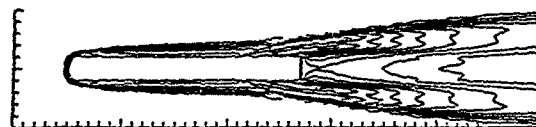


**Fig. 13:** Grid Utilized for Tactical Missile Analysis with Bifurcated Nozzle Exhaust.

### T CONTOURS



### TURB LEVEL CONTOURS



### U CONTOURS

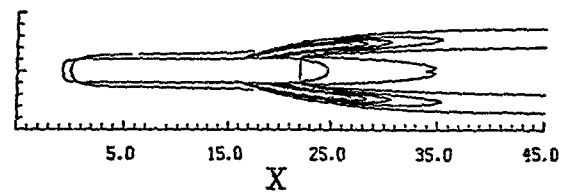


**Fig. 14:** Contours at Symmetry Plane Containing Missile and Nozzle Axes.

### T CONTOURS

X = 13



X = 25



X = 30

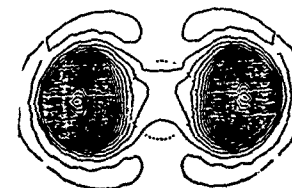


**Fig. 15:** Temperature Contours at Several Axial Stations.

## M CONTOURS

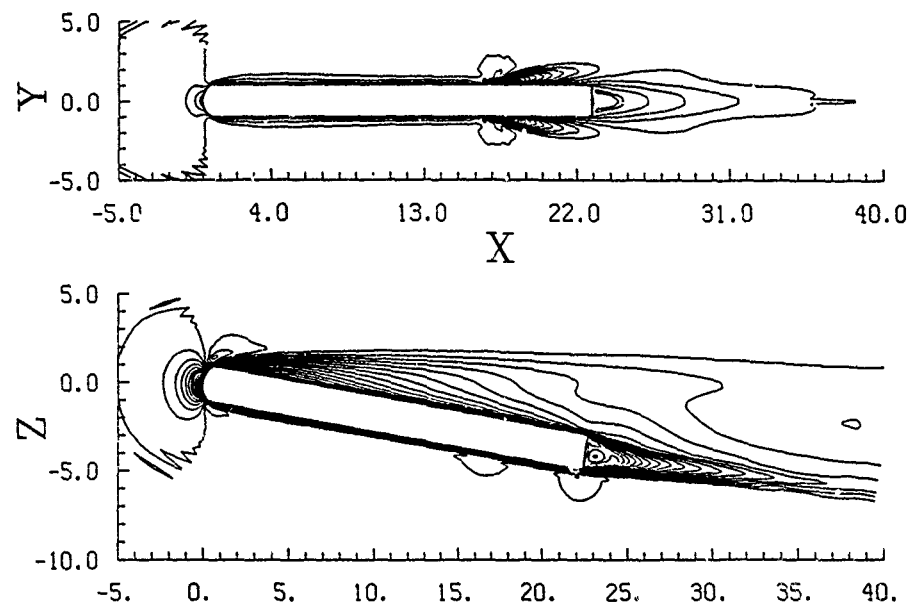


**Fig. 16:** Mach Number Contours for Angle-of-Attack Case.

## TURBULENCE CONTOURS

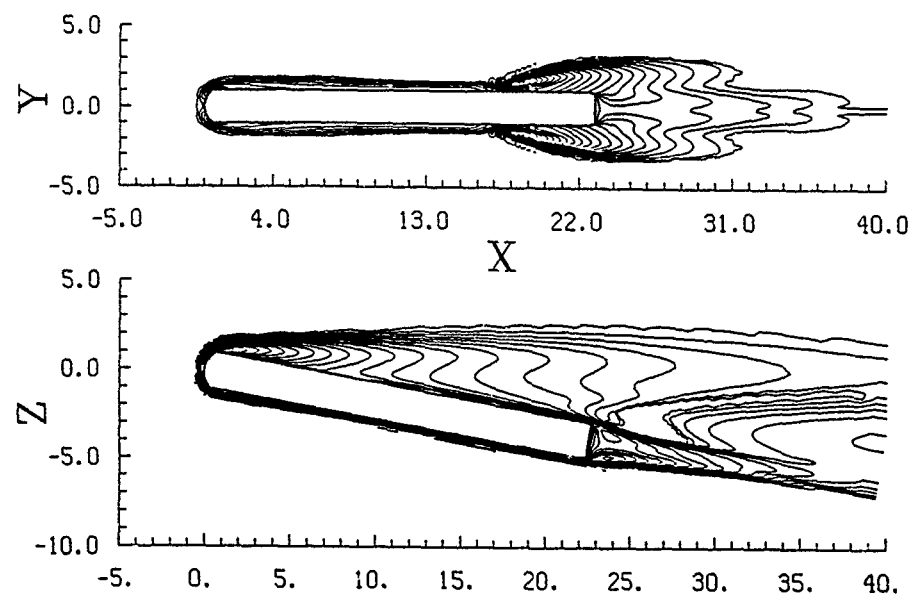


**Fig. 17:** Turbulent Kinetic Energy Contours for Angle-of-Attack Case.

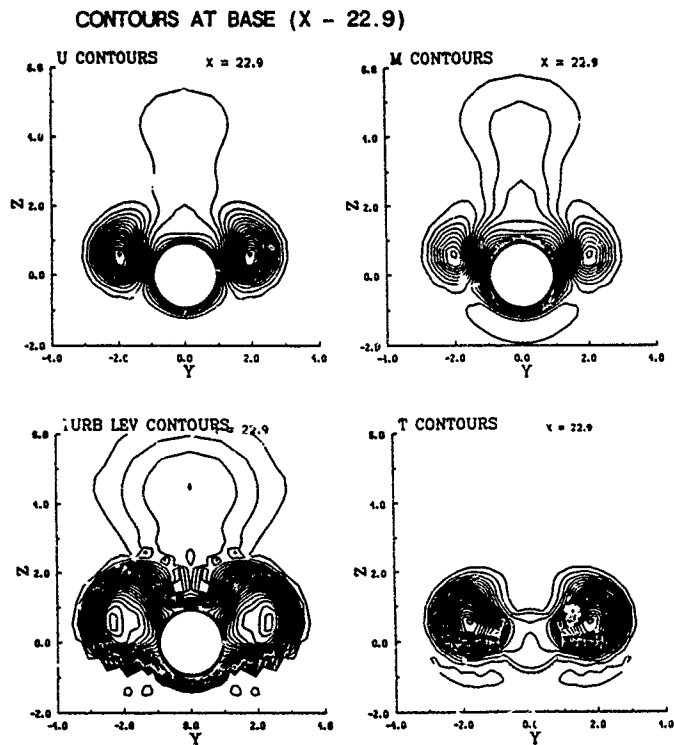


**Fig. 18:** Cross-Flow Contours at  $X = 22.9$   
(Plane of Missile Base) for Angle-of-Attack Case.

**DOWNSTREAM OF BASE (X = 23.3)**

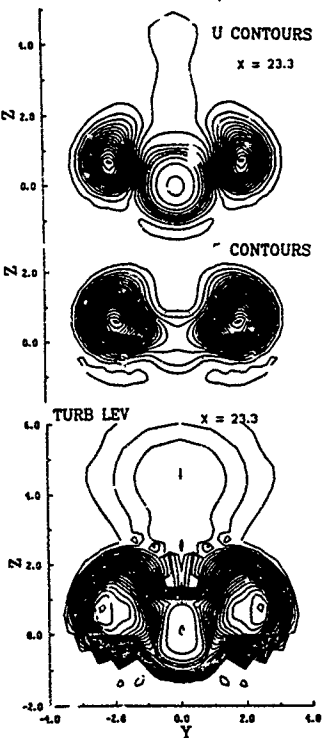


**Fig. 19:** Cross-Flow Contours at  $X = 23.2$   
(Just Downstream of Base) for Angle-of-Attack Case.

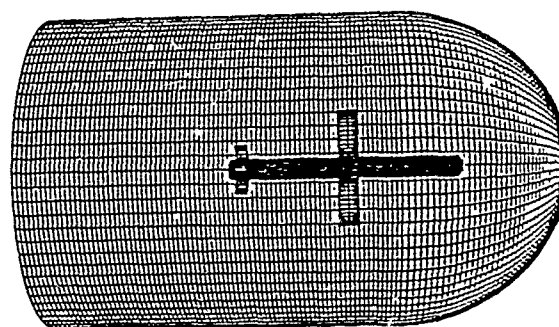
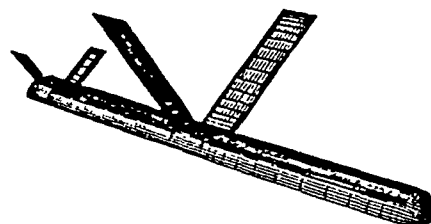


**Fig. 20:** Grid Details for Tactical Missile with 'Non-Flush' Bifurcated/Scarfed Nozzle.

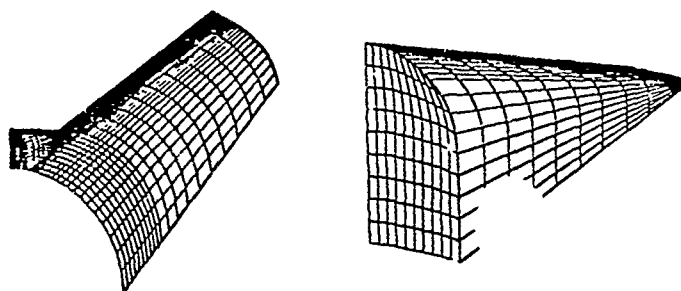
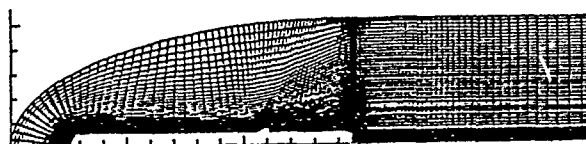


**Fig. 21:** Grid for Tactical Missile with Wings and Fins.



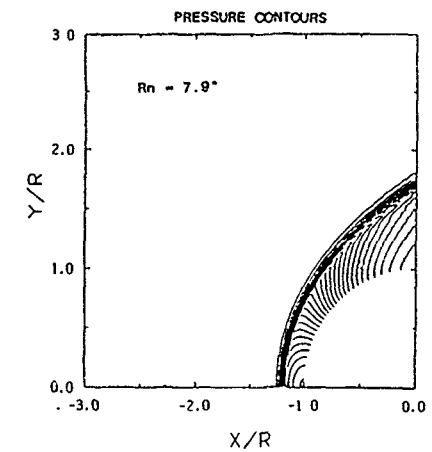
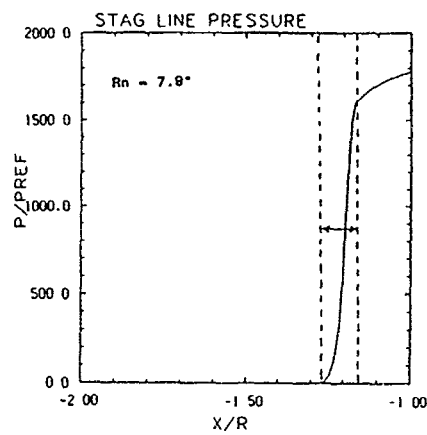
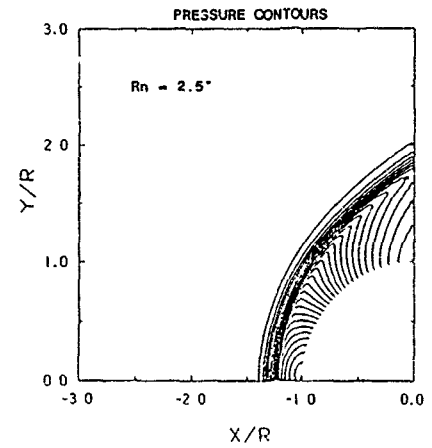
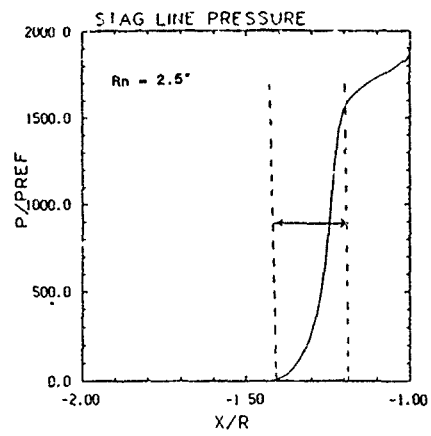


Fig. 22: Viscous Shock Layer Pressure Contours for Mach 37, 80 km Conditions Showing Influence of Nose Radius.

Fig. 23: Viscous Shock Layer Stagnation Pressure Variation Showing Influence of Nose Radius on Shock Thickness.

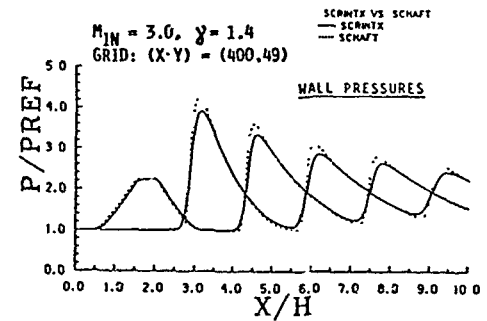
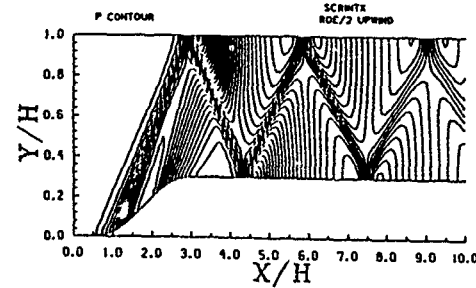
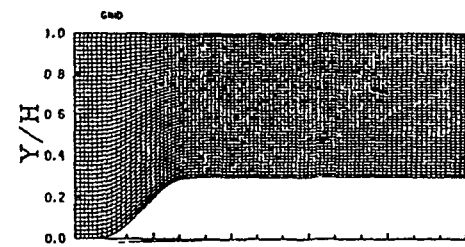
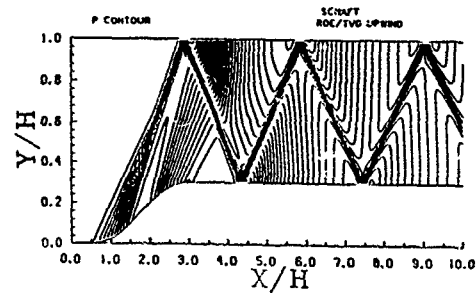


Fig. 24: Shock Propagation in a Duct: SCHAFT vs SCRINTX.

LOWER STREAM  
 $H_2$ ,  $M = 2.9$ ,  
 $P = 0.1 \text{ atm}$ ,  $T = 750 \text{ K}$

UPPER STREAM  
 Air,  $M = 2.9$ ,  
 $P = 0.1 \text{ atm}$ ,  $T = 750 \text{ K}$   
 $U_{Air}/U_{H_2} = 4$

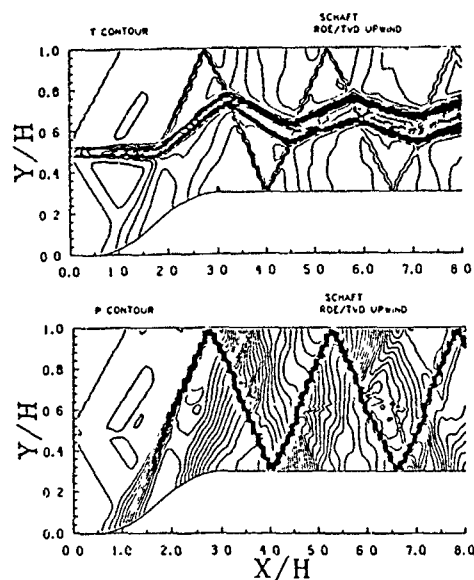


Fig. 25: Shock Induced Combustion Problem:  
 Temperature and Pressure Contours.

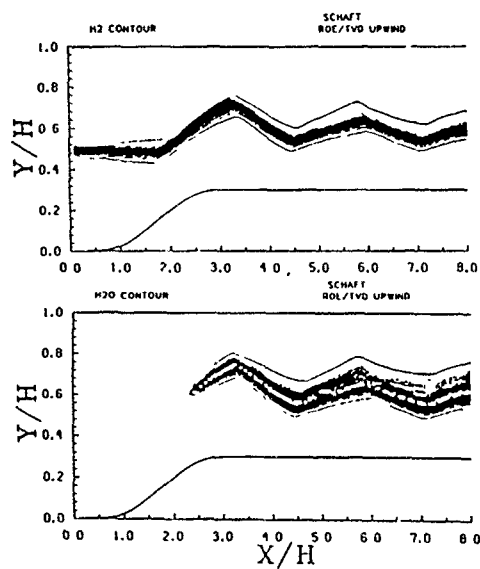


Fig. 26: Shock Induced Combustion Problem:  
 H2 and H2O Contours.

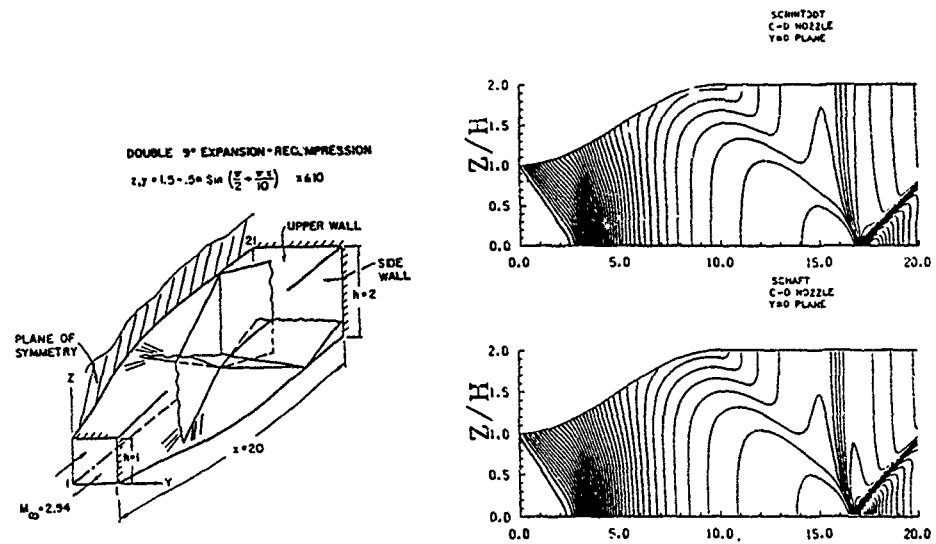
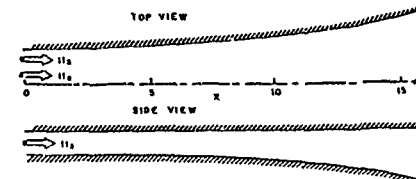


Fig. 27: SCHAFT and SCRINT3DT 3D Analyses of Square CD Nozzle.

INITIAL CONDITIONS:

$H_2$      $U = 13000 \text{ ft/s}$   
           $M = 3.0$   
           $T = 300 \text{ K}$   
           $P = 0.45 \text{ atm}$

AIR     $U = 15000 \text{ ft/s}$   
          $M = 7.0$   
          $T = 1100 \text{ K}$   
          $P = 0.15 \text{ atm}$



CALCULATION: 2ND ORDER ROR UPWIND/TVD

GRID : NX=300, NY=49, NZ=34  
 Chemistry : Hydrogen-Air Finite Rate

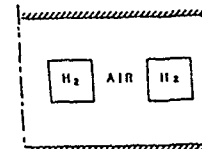


Fig. 28: SCHAFT Combustor/Nozzle Problem.

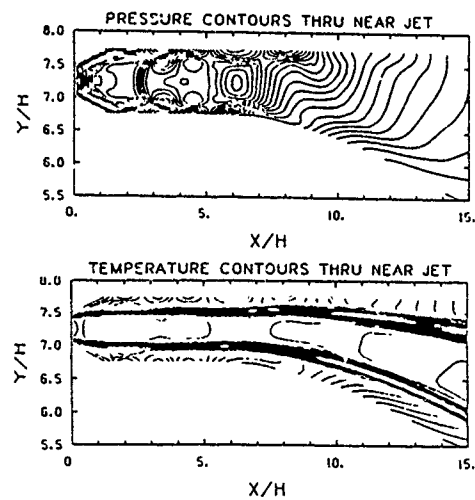


Fig. 29: SCHAFT Vertical Plane (Passing Through Center of Inner Jet) Pressure and Temperature Contours for Combustor/Nozzle Problem.

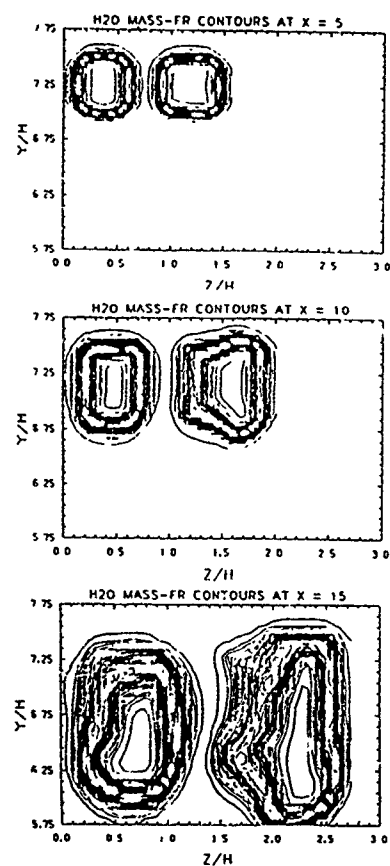
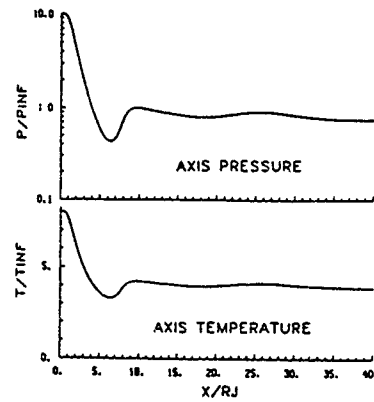
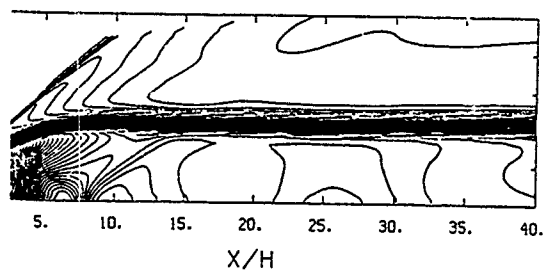


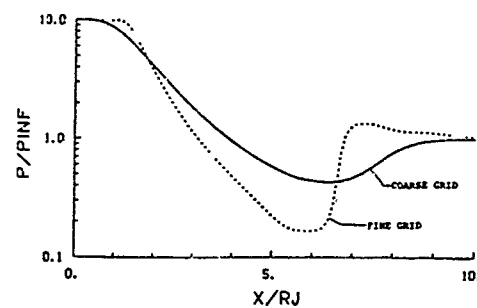
Fig. 30: Cross-Flow Contours of  $H_2O$  at  $X = 15, 10$ , and 5.



PLUME TEMPERATURE CONTOURS



**Fig. 31:** SCHAFT Axis Pressure and Temperature Variations for Axisymmetric Underexpanded Plume with Coarse Grid.



PLUME PRESSURE CONTOURS

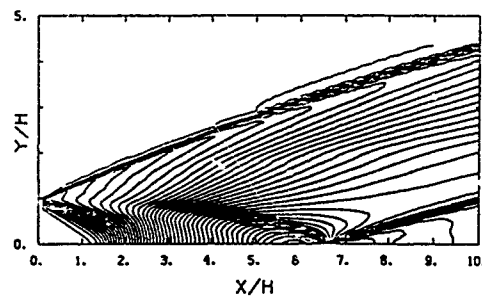


**Fig. 32:** Comparison of Axis Pressure Variations with Coarse and Fine Grids.

ROUND TABLE DISCUSSION  
FDP SYMPOSIUM "MISSILE AERODYNAMICS"  
Friedrichshafen, Germany 23 - 26 April 1990

P.R. Bignell, Chairman

So we are on the last lap of this conference with a substantial time allotted for discussion. In the programme, you will see reference to the Round Table Discussion after the remarks by the Technical Evaluator. That isn't strictly what will happen; it won't be a Round Table Discussion in the true sense, it really is a free-for-all. For those of you who went to Trondheim, the discussion was done slightly differently there in that the session chairmen played a major part in the Round Table Discussion, it was a genuine Round Table Discussion. I would have expected three of the session chairmen to be here, unfortunately one of them has had to go, Mr. Lacau. But there were two other session chairmen from Trondheim, Professor Gersten and our Technical Evaluator. As I said on Monday, we were all sorry that Jack Nielsen had to pull out only a week or so ago. It was a bit of a problem for me for about 5 minutes. I walked into the office next door to mine and spoke to Paul Herring and as he was coming to Friedrichshafen I asked him if he would be prepared to take on this job, which he readily agreed to do. I was extremely grateful, as you can imagine given that sort of notice but I was aware that Dr. Nielsen had been unwell for some considerable time. Anyway, Paul is a colleague of mine, has been for some 25 years or so, during which he has worked solely really in missile aerodynamics. So he is well able to comment on a Symposium entitled "Missile Aerodynamics". He has worked in the Guided Weapons Division of what was Bristol Aircraft Ltd, which then became British Aircraft Corporation and finally British Aerospace, and he is now head of an Aerodynamics Department within the Corporate Research Center of British Aerospace in Bristol. He has presented AGARD papers, as you well know, he presented one this week, papers at AIAA meetings on missile aerodynamics and for those of you yesterday afternoon who were still awake, and quite a lot of you were awake when Mr. Delery was speaking, you will have noticed that Paul is a member of the GARTEUR Action Group 09 on flows past missile afterbodies. While you have all been enjoying yourselves during the evenings, out on the town as it were, Paul has been locked away in his hotel room. He has missed all the functions, the boat trip, the jazz band, this is what I believe, I don't really know, while he has been preparing his comments for you. Without more ado, I will ask Paul to give you his evaluation.

P.G.C. Herring, British Aerospace

I want to start by saying that I am very much aware, and I think more aware than anybody sat down there, that I am here standing in for Jack Nielsen, Mr. Missile Aerodynamics himself. There is no way that I can compete either in physical or mental stature with Jack. I know that if Jack was doing this technical evaluation all of his remarks would be technically sound, they would be extremely perceptive and they would be honest. All I can promise is that my remarks will be honest. One of the nice things about AGARD meetings is the fact that they bring together people who are working in a common field. Those of you who attended this meeting and other meetings will know that a lot of the technical discussions and information exchange takes place outside this hall, be it in the room out there, over in the lunch hall, or even, rumor has it, in the local bars and cafes. That to me is one of the most useful and interesting parts of a meeting like this.

Turning to what has been happening inside these four walls, I have been generally very impressed with the very high standard of presentation of the papers. I don't think we have had a bad presentation all week. I would like to congratulate all the speakers. One comment I would like to make before I actually go on to the technical evaluation is about the human brain. You may know that the human brain is a marvelous piece of machinery. It starts working a couple of weeks after conception and continues functioning until the moment that you stand up to talk in public. Bearing that in mind, I shall start my evaluation.

On the green card that we received announcing this meeting, the stated purpose of this symposium is to review current progress and achievements, highlight outstanding problems and establish pointers for planning future research programs. That is, a follow-on from the 1982 meeting which was held in Trondheim.

At the end of the 1982 meeting, as you heard, we had a Round Table Discussion and I have selected half a dozen topics which came out of that Round Table Discussion, and I want initially to see if we have achieved any of the aims that were raised at that RTD. One of the points that was raised in Trondheim was that exact prediction methods are beginning to account for the major flow features about weapon configurations. I think to some extent that statement is still true, though obviously we are now able to account for more of those features and some of the minor flow features. So in that sense we as a community have made a lot of progress over the last 8 years. The second point that was raised was that advanced panel methods were beginning to show promise but were not yet ready to be used as engineering tools. That is one thing that we can definitely cross off our list. Advanced panel methods are used day-to-day, routinely for the design and evaluation of missile configurations. The next point that was made was that CFD was too costly in terms of run costs and set-up time to be used on a day-to-day basis. I think that most people would agree that this is still true. I think that it will be so for a long time to come. A further point that was made is that we needed to undertake trade off studies between aerodynamics and stealth requirements. I have no doubt that such studies have been taking place, but obviously for security reasons, one can imagine that those studies won't be discussed at a meeting like this. Those of you who were in Trondheim in 1982 will remember that during the Round Table Discussion there were some fairly heated debates about the usefulness of experimental data, semi-empirical prediction methods and CFD methods. It was Jack Nielsen who said that we need to continue to develop the computational methods, the semi-empirical methods and to do more tests, both for method development and validation. It is good to see that in this conference we have lots of new computational methods, new semi-empirical methods and more experimental data. Now I don't intend to go through all the papers that were presented this week and give an assessment of each paper. What I have done is divide the papers of the week into a number of topic areas. What I would like to do is go through those topics. In addition to those, I think that I will start by first looking at the three papers we had Monday morning, the survey papers. I think that people would generally agree that those three survey papers were very interesting and very informative. But a couple of points on each of them. In Mr. Lacau's paper he concentrated on the evaluation of missile aerodynamics using computational methods.

The thing that surprised me is that he didn't mention Navier-Stokes. Mr. Lacau seemed to indicate that the future, perhaps as far as Aerospatiale is concerned, lies with the Euler solvers. Barry Haines gave an excellent overview of the Bath conference. I wasn't at the Bath conference, but talking to people who were there, I understand he gave a very fair and very full overview of what went on. He showed some very impressive viewfoils from that conference showing CFD solutions for very complex stores installations and the installation of the multiple stores on the F-15 was a very good example of that. I wonder how often you can actually grid up a configuration like that for aerodynamic assessment? One comment that Barry made that came from that conference, which I think ought to be borne in mind, is the point that we can use CFD as a guide to good design. Howard Torode gave us some comments on the conference that was held a couple of years ago in Ankara. One of the points that he made is that, at the Ankara conference, aerodynamicists were concerned that although they had been asked to produce accurate aerodynamic information for missile configurations, when that information is used by the system engineers, they end up putting straight lines into their models and he assured us that that system was now changing. I will believe it when I see it. Certainly as far as the people that we work with are concerned, the aerodynamic models that they use in their simulation studies are not yet capable, as far as I know, of taking aerodynamic data as detailed as we could provide. The other point that Howard made was on unsteady aerodynamics and I don't think that we as a community have looked at unsteady aerodynamics in the detail that we ought to.

Going on now to the first topic on my list, Euler methods. This was to me a disappointment. There were several papers which described the same problem, that is, smooth bodies at supersonic speeds and the use of empirical experimental data to determine how and where the flow separates from a smooth body at incidence at supersonic speeds. Nothing was presented on Euler solutions for subsonic and transonic speeds. This is an area where the computational methods like Euler need to be applied. Because of the three papers that we had which discussed supersonic Euler, all basically looking at the same problem, some of which used the same experimental data, I wonder to what extent the committee who selected the papers were deceived by the abstracts. It was suggested just before I came up here that it would be interesting to do a correlation between what appears in the abstract and what appears in the paper.

It seems to me that the Euler solution can be used at supersonic speeds to provide good estimates of overall forces and moments for some configurations. But how people can expect non-viscous codes to represent highly separated flows in the lee of bodies is beyond me. I will, with Mr. Delery's permission, quote from his paper where he was talking about the CARTEUR Action Group activities. Initially the Action Group was going to look at the use of semi-empirical, multi-component and Euler methods as applied to missile afterbodies. The action group very soon decided to drop the Euler activity, because, as Mr. Delery said, "the use of Euler for highly separated flows is science fiction, not science". One of the concerns that I have about Euler methods and CFD methods in general, is the problem of grid generation for real configurations. Some of the grids that Mr. Lacau showed for example - in particular for the complex airbreathing configuration - obviously took a considerable amount of time and research to generate. But in my experience, particularly at sub-sonic speeds, it is often the small features of a configuration which can have a profound effect on the aerodynamic characteristics. I remember many instances of missiles at sub-sonic speeds for example, where the presence of a launch rail can produce quite profound changes to the aerodynamic characteristics. If we are going to use CFD methods we are going to have to represent, through the grid, those small excrescences. Are we going to be able to do that? I don't know.

Moving on to the Navier-Stokes papers, I was very impressed to see how Navier-Stokes is now being used for practical problems. Navier-Stokes obviously has a tremendous promise for the future. It is obviously the future of CFD. As the last paper this morning indicated, Navier-Stokes is not limited by the algorithm, it is limited by the computer power that is currently available. Because Navier-Stokes is the future, we need to be developing the Navier-Stokes solvers now so that we have the algorithms available when the computers become available. Those computers are going to become available perhaps a lot quicker than we think. Computer power has a way of going up in quantum leaps. Who knows, in five years time we may have a hundred times the computer power we have available now. I think that we need to be ready to use those machines when they come.

Going on to general comments about CFD, I think that we need, as a community, to use CFD sensibly. The paper by Mike Mendenhall was, if you like, the epitome of how we as a missile aerodynamics community should use prediction codes. You use the right code for the right application. If you can use a semi-empirical code, use it; if you have to go to a panel code, use it; for some other features of the flow you may have to go to Navier-Stokes, so use Navier-Stokes, but use the right code for the right application. Again I go back to the comment that Barry Haines made that CFD can be used as a good design guide and can help to solve some specific problems, but we don't want to end up using CFD in a blanket fashion; it is not cost effective.

Going on to semi-empirical methods, as I said earlier, it is nice to see that semi-empirical methods are still being developed. People who actually are involved with missile design realize that semi-empirical methods are always going to be used in the same way that the experience of an engineer is used. An engineer can give an off-the-top-of-the-head figure for an aerodynamic coefficient, perhaps. As long as there are missiles we are going to have semi-empirical methods because they provide basic information at minimum cost.

Some of the methods that were presented were fairly naive. I was particularly concerned with the Dornier paper. They are, if I understood correctly, hoping to represent the load on a panel as a function of the zero roll angle panel load and roll angle. I tried this myself once many years ago, I suspect the Nielsen organisation may have tried it once many years ago, and although it looks attractive initially, I think people soon realize that it doesn't work and you have to start using the now well-known equivalent angle-of-attack approach.

Going to the experimental papers, it is obvious that there are still many problems which can only be investigated in the wind tunnel. It is obvious to me from the papers we have had this week that there is currently a very great deal of care and attention to model design and care in execution of experiments, that the experiments and tests are obviously very carefully planned, very carefully thought out and have obviously been done by professionals. This is something that is good and necessary, simply because of the cost of wind tunnel tests these days. It is nice to see that we are getting such high quality data on all sorts of things from the papers that were presented by ARA and the more recent papers we have had on heating for example. We must make sure that we are just as careful when we come to analyze these data.

Coming on to some of the general papers, we had some very useful reviews and descriptions of how the data that we as a community provide are being used for current project investigations. It is nice to see that the prediction methods that are being developed are actually used. That is something that we need to remember. We are here to provide methods that will be used.

In conclusion I think that what I would like to end with is a concern that has been with me for a long time in that, I intimated as much when I was talking about Mike Mendenhall's paper, we need to be aware of what is available both in terms of methods and experimental data and that those tools need to be used sensibly. You don't use a screw driver on a nut, you use a spanner. In the same way we need to use the right prediction tool for the right application. That application and the tool is determined by factors such as: - how accurate do we need the solution to be; - how much money have we got available to find that solution; how quickly do we need that solution; - how many times are we going to require that particular information for however many configurations.

So in summary, generally I thought the conference was very good, very informative. The big disappointment to me was the Euler sessions, and the fact that all those papers was so similar was a surprise to me and I hope that it was a surprise to the Panel who selected the papers. If the papers were selected in that fashion deliberately, I must say that I am disappointed. Finally, I would like to end by saying that we all come here to learn by listening to presentations, exchanging views, discussions, even being shot down in flames occasionally, it all helps, we learn from our mistakes. Finally, I remind people why we are here. We are here as an aerodynamic community to develop aerodynamic prediction techniques which are used to design more effective weapon systems. We are not here to sit around playing with interesting problems, we are here to provide solutions to real problems which will increase the effectiveness of weapons systems and our work must have a practical application and with that I would like to finish.

P.R. Bignell, Chairman

Thank you very much, Paul, for that evaluation. I had in fact made an additional list of 6 points which have already been covered in the evaluation and it would only be a complete waste of time to add to what has already been suggested. So really, now it is over to you. I would ask that because this session is being recorded, it will be included in the Conference Proceedings, you must give your name and affiliation when you speak. The session is now open for discussion.

D.S. Woodward, RAE

I might take issue with Mr. Herring slightly on his comments over Navier-Stokes. I think it is not true to say that the application of Navier-Stokes is limited solely by the power of the computers that are available, there is a very fundamental problem with the application of Navier-Stokes and that is the turbulence modelling that is incorporated in those codes. We are going to have a technical status review this afternoon on the state of turbulence modelling, but I think it is fair to say that there is no turbulence model currently available on which one can rely to provide accurate calculations of the flow, particularly when the flow is partially separated. I think there is a very fundamental advance that we need to make before we can take advantage of any advance in computer power that may come in the future. The two things need to go together.

P.G.C. Herring, British Aerospace

One of the things that I think I said was that we need to develop the algorithms including the turbulence models so that they are available for use on real problems when the computing power is available. I agree there are areas where we have got to improve the algorithms. We need to develop the algorithms and not wait until the computers which will enable them to be used become available.

K. Gersten, Univ. Bochum

I would like to clarify something about the nomenclature. Navier-Stokes - I saw from the papers that most of these Navier-Stokes codes were actually not Navier-Stokes, not full Navier-Stokes but more partially parabolized Navier-Stokes, so in principle, these are hidden boundary layer equations really because you parabolize these equations so I wonder why people are afraid to use the word boundary layers. We have learned about boundary layers for about 80 years or so and Euler methods are of any value only in combination with boundary layer equations to get the separation line etc. I think Euler methods per se, are not of any value except when you combine them with boundary layer equations or any other equations where the viscous effect comes into play. I would like to see more of the fundamental work on boundary layers applied to even more complicated three-dimensional flows. In the list, boundary layer methods would be very good to see.



RTD-4

P.R. Bignell, Chairman

While you are giving the microphone to Prof. Lilley, perhaps I could ask a question myself on Euler methods, that is the application of Euler methods to missile aerodynamics. I am somewhat puzzled at the level of agreement there seems to be between Euler methods and experiment. but I wonder if we have got a situation here where two wrongs are making a right, where you may well have deficiencies in the equations in the Euler equations being combined with deficiencies in the numerical schemes and the overall result is that you get good agreement. I would like somebody to tell me if that is true or not. If it is true it suggests that you are getting good agreement for the wrong reasons.

G.M. Lilley, Univ. of Southampton

Mr. Chairman, you have more or less stated one of my questions. My first question however, is in the form of a statement. It is a minor point, and it is one in which I would not wish it to be seen that I am making any criticism on all of the excellent computations that have been presented at this conference under the name Navier-Stokes. My statement is that it is wrong to call these solutions of the Navier-Stokes equations; they are solutions of the Reynolds averaged Navier-Stokes equations, which were referred to some years ago as RANS, Reynolds Averaged Navier-Stokes equations. I would suggest it is better to use this notation and would avoid any confusion with the very large computing power that is available today one can obtain at low Reynolds numbers the full simulation of the Navier-Stokes equations and such solutions involve none of the approximations and simplifications associated with RANS. If in future meetings we are going to refer to these solutions from full simulation or from large eddy simulation (LES) there will be confusion if they are to be compared also with Navier-Stokes solutions which are strictly Reynolds averaged Navier-Stokes solutions. At this meeting as far as I am aware, the solutions presented have been from the Reynolds averaged Navier-Stokes equations. The second point is the point that Chairman has just made with regard to the problems of numerics. Here I would just like to remind the audience that at the Stanford Conference in 1980-81 we attempted the comparison between calculations made on the various turbulence models for complex turbulent flows and good reliable experimental data. Let me remind the audience here that the complex turbulent flows that we were concerned with at the Stanford meeting were very much simpler than some of the very complex flows that we have at this meeting with missiles incorporating wing body interference, main wing and tail/fin interference. All of these are much more complex than treated at the Stanford meeting. At that meeting it was very difficult to see in many cases the differences between one turbulence model and another because in the main the solutions suffered from numerical inaccuracies, centered on a lack of grid independence and problems associated with numerical diffusion. Earlier in this meeting I made the point that indeed in many of the calculations presented here a lot of numerical diffusion has been incorporated. Thus, when a certain turbulence model is employed it is easy to miss the differences between using one type of turbulence model such as an algebraic stress model, k-epsilon, or full Reynolds stress equation model from another if strong numerical diffusion is present. Some of it of course is grid generated, some of it is by the numerical algorithm used. I stress that it is important to make full use of the power of the computers we have today in obtaining accurate solutions of the Reynolds averaged Navier-Stokes equations with the current turbulence models. This will enable us to see more clearly the deficiencies in these models and will assist in the development of improved turbulence models, which address more adequately the physics of turbulence. A review of current turbulence models is being discussed this afternoon.

W. Schmidt, Dornier

I would like to come back to the question that Mr. Woodward raised earlier. I am a little bit concerned about the fact that in many cases the matter of the turbulence models is not the real problem. The very bad resolution of the flow physics due to coarse meshes and due to the high numerical viscosity is the real problem. It might not be a matter of having the best turbulence model in the first place since we are lacking many, many other things. Many people just use the turbulence model as an umbrella for all those things they do not understand when they do real practical applications. The second argument was along with Mr. Gersten. If you use large computers the most efficient way to incorporate boundary layer methods in Euler methods is to use the parabolized Navier-Stokes equations.

J. Slooff, NLR

A change of subject, Mr. Chairman, if you will allow me. The technical evaluator very briefly mentioned the fact that very little attention was paid to unsteady effects at this meeting. It is my impression that increased manoeuvrability or agility, at least for certain classes of missiles, is something that is being pursued fairly strongly. Therefore, that raises the question of whether or not we should pay more attention to time accurate simulation of flowfields about missiles both computationally as well as experimentally. I wonder whether somebody from the missile community would comment on that and perhaps give some indications in particular for what sort of experimental means that they would hope to be available for that purpose in the future.

P.R. Bignell, Chairman

Anybody want to comment on that? I believe that at the Missile Aerodynamics Conference that was organized to celebrate Jack Nilsens 70th birthday in 1988 there was quite a lot of discussion on unsteady aerodynamics. This is one of the points that I wanted to raise here that we have had very little on unsteady aerodynamics and I wonder if there is some sort of scope for having a meeting in the not too distant future covering that aspect of missile aerodynamics, looking at unsteady aerodynamics, dynamic effects, aeroelasticity, etc.

M. Mendenhall, Nielsen Engineering

Joop, I think that you hit upon the problem. We are all trying to stick our heads in the sand and avoid unsteady aerodynamics because it is a difficult problem. We at NEAR have been trying to use the engineering methods to look at unsteady aerodynamic and hydrodynamic effects, in particular, long slender bodies going through rapid pitching maneuvers. What we are finding, interestingly enough some of it has been published, some of it hasn't, is that the vortex shedding effects in unsteady motion are critical to the non-linear aerodynamics. We have seen some very interesting effects of unsteady vortex shedding induced effects on control fins. There is almost no data for us to compare with, but what we have seen is a reversal of the hysteresis loop for the fin normal force as a function of changing angle in a steady pitching maneuver. I don't know if this is correct or not, but if it is, it has great implications on the design of control systems. We are also doing some work which Marnix could probably talk about better than I. He is looking at unsteady effects of sea skimming missiles flying at low altitudes, essentially flying over a wavy wall, if you will, and some of the dominant non-linear effects that can occur there. I think that the problem in my work in the last number of years in unsteady aerodynamics and hydrodynamics of missiles and submersible bodies is the problem that there are no data available to find out if what we are calculating makes any sense. You can calculate a lot of things. You turn on the code, and as they say, if it doesn't blow up the answer is right. I think we all realize that is not true. I think that what we need to do is to get some people interested, and we need to get some data together to evaluate some of these unsteady methods.

M.F.E. Dillenius, Nielsen Engineering

Our dear VP mentioned my name, so I would like to say that in the application to missiles the aspect of unsteady aerodynamics will become intimately coupled with resonances or the frequencies of the structure and the automatic pilot and that we are finally getting down to where you have to have the aerodynamicist and the system guy come together and understand the problem. The thing of it is that the natural frequencies influence one another and will affect the final performance of the whole thing and that is, as a matter of fact, the missile engineer's nightmare. That is why during one of the talks we listened to describing a Navier-Stokes solution I popped up the question that maybe it is important that you consider the unsteady aspects. At NASA Ames they show big differences in the transonic range, the shock formation can be quite different and introduce frequencies again that you miss when you do it in time asymptotic solution. The costs are horrendous, and is it right? I don't know. Experiments and tests are just as important today in view of this unsteady problem that we are faced with next. So don't forget the tests and experimentation. What to do? I don't know how you do experimentation for unsteady effects.

P.R. Signell, Chairman

Could I ask Dr. Orlik-Ruckemann to consider making a comment. I am surprised he has not stood on the table waiting to get in on this.

Dr. K. Orlik-Ruckemann, NAE

I am rather on the production end of all those aerodynamic data, not a person who applies them, and before I say how you can get them, let me pose a question to people who actually use aerodynamic data for predicting stability and, generally speaking, behavior of missiles. Research of this nature is often driven by a documented need and in the aircraft community we have had cases where there was clear evidence that, if you do not include some non-linear and unsteady effects, the correct prediction of an aircraft maneuver at high angles of attack and high rates of motion was not a very precise procedure. I wonder whether anybody here has had any experience with predicting missile behavior under such conditions and whether he could point out, without necessarily mentioning what missile it was or without revealing too many details, whether there were any large discrepancies between the predicted behavior and the actually observed one.

M.E. Dillenius, Nielsen Engineering

It just so happened that I saw a bit of a propaganda tape from NASA Ames. They show calculations done for the shuttle fuel tank going through a fairly rapid acceleration through the transonic range, and there are appreciable differences because of the shock motion and the wake moving back and forth on the bottom of the tank. That is one example that I can think of.

W.B. Brooks, ITV

I don't know whether it is just personal ignorance or not, but I am often embarrassed by the hinge moments on the control fins measured in flight as opposed to those measured in wind tunnel.

Dr. K. Orlik-Ruckemann, NAE

I would now like to get back to how to provide unsteady and especially non-linear unsteady data. Several speakers have mentioned that this is a formidable computational problem and I agree with that. In our laboratory we have been pursuing experimental methods to obtain this information and we have developed some non-linear types of experiments with an associated non-linear method of representing the data obtained. So far, this has never been applied to a missile configuration, but rather to a wing or wing body configuration, and it consists of presenting various kinds of aerodynamic data, such as detailed pressures as well as forces and moments, in terms of the various motion variables and their time derivatives. We have also used that kind of data obtained experimentally in a wind tunnel to predict the actual free behavior of a model, in this case in roll, and we have shown that there was a very good agreement between the prediction based on those non-linear data and a free-to-roll motion of the same

RTD-6

model in the same wind tunnel. When standard linear data were used instead, that agreement was often rather poor. I stress that this was for a particular, rather high, angle of attack of  $35^\circ$  or  $45^\circ$ , for a large amplitude (up to  $40^\circ$ ) and also high frequency (up to 10 Hz) motion of a delta wing with approximately 2 foot span. I am still looking for somebody who could give me such information regarding missiles.

W.B. Brooks, LTV

If I could mix the two topics we have been discussing, and maybe someone knows the answer much better than I do, as we move to unsteady solutions, does the Reynolds averaged approach break down? I know in fundamental turbulence measurements, sometimes the averaging process takes days, which we generally don't have for our flow fields.

G.M. Lilley, University of Southampton

In general it is accepted that solutions of the unsteady form of the Reynolds averaged Navier-Stokes equations will be correct provided the frequencies are small or the unsteady time is long compared with the turbulence time scales. Unsteady solutions from the Reynolds averaged Navier-Stokes equations would be applicable in finding unsteady derivatives, etc.

W.B. Brooks, LTV

How would this then relate to subjects such as the last paper which involved chemical reactions?

S.M. Dash, SAIC

No influence if the chemistry rates are still representable. The same comments that Dr. Lilley has made should apply to chemically reacting flows. We do typically solve unsteady time accurate solutions of a large number of chemically reacting flows using Reynolds averaged equations, and I say the comment does apply to those flows also.

Dr. K. Orlik-Ruckemann, NAE

I would like to make a further comment regarding the unsteady effects. We should distinguish between high-frequency phenomena which affect the structural and control responses and more low-frequency phenomena which affect the dynamic behavior of the complete missile. In this second case it should be realized that, if we get into significantly non-linear situations, the standard method of superimposing the effects of various motions, such as represented by the stability derivative approach (I believe there was one or two papers on that in the meeting) is, strictly speaking, not valid any longer. In fact, it could lead to substantial errors. So it is important to investigate more complex motions, not just pitching motions and rolling motions separately.

J.B. Berry, Aircraft Research Association

I think that unsteady effects are very difficult to set up experiments to study and get quantitative data for. But I think where the experimentalist can help is getting a better understanding of the physics of the flow processes which are causing the unsteady responses and here I think non-intrusive techniques, e.g., lasers, for flow visualization and flowfield surveys are going to be much more important from now on.

P.R. Bignell, Chairman

Mr. Lacau on Monday was talking about accuracy, and he said the use of semi-empirical methods would give center of pressure to within half a caliber but the use of CFD methods would give center of pressures to within a quarter of a caliber, but is that good enough? Are there applications of missiles where you would need to get even more accurate than that, say highly agile air-to-air missiles, would anybody like to comment on that?

G. Moretti, British Aerospace

I think the overall accuracy is very important. The more accurate the data is, quite obviously, the better is the job we may do and the better is the envelope we can produce at the end of the day on various missile or various stores. So, yes, it is important to increase the accuracy, but we have got to balance that with the costs, and it is not very simple to do that. I was surprised to see that we use Navier-Stokes for so many CPU hours. Perhaps with less money we can achieve similar results. I think this is very important, I would like more accuracy, but I am not so sure the costs warrant it.

W. Schmidt, Dornier

Along with accuracy I have a question that is coming from the application standpoint and might be very pragmatic. As you know missiles and rockets are built to be used once and are manufactured in large quantities at a rather bad manufacturing accuracy. How can we talk about accuracy in tools if we don't know the accuracy of the final product?

R. Deslandes, MBB

Since about 5 years I am using Euler codes for missiles, for missile separation and for trajectory prediction, and I am quite happy about the accuracy. I do not think that we will ever apply any Navier-Stokes code on it because we are happy with about 80% agreement between Euler and full-scale aerodynamics. We are not looking at flow phenomena, such as vortex tracks and so on, but we have to quantify the coefficients, and so I think we should say also a little bit good about Euler, because these

equations are the unique physical solutions we have now available in CFD. Panel methods and potential theory are mathematically tuned solutions. Navier-Stokes codes now available are for me science fiction because of the lack of appropriate turbulence modelling.

S. Dash, SAIC

I would like to comment on that last remark. I think that the Navier-Stokes codes serve a very useful purpose even in preliminary design of very unconventional systems. All the problems that we are dealing with are not strictly aerodynamic problems with pressures. In fact in some of the advanced missile concepts with unconventional propulsive systems, we are talking about hot reacting plumes with particulates impinging over large portions of the aerodynamic surfaces. For those types of calculations only Navier-Stokes types of codes will be applicable. The turbulence models for aerodynamic predictions in Navier-Stokes codes are really no different than the turbulence models you would be using in boundary layer codes. So if a KE model works in a boundary code, you will have the same accuracy in a Navier-Stokes code. The real problems are dealing with the heavily separated flow regions and some of those effects, and there we do need upgrades in turbulence modelling.

M. Mendenhall, Nielsen Engineering

I will bring up a topic that came out of the Missile Aerodynamics Conference in Monterey in November 1988. We had a Missile Aerodynamics Panel session. A comment that was made and recorded in the proceedings of that Conference was that the quality or the sophistication of the missiles that are being designed today are limited by the capability of the codes that are available to design those missiles. As long as your missile design is evolutionary and the missile that you are going to build for next year is going to look 99.44% like the missile you designed last year, we are probably O.K., and the semi-empirical methods are in good shape. But I think a group of people in this audience maybe should be considering, what is the missile 20 years from today going to look like, and what kind of methods or predictions methods are required for a dramatic change in missile configuration, something totally different than we have seen at this point.

P.R. Bignell, Chairman

If you go to a completely different shape then that could prove to be a very much more expensive solution. Maybe it doesn't, I don't know. However, in the missile fraternity there has been a lot of thinking that it may be better to go for something cheap and cheerful than something that is extremely sophisticated and complicated. Maybe if you wanted to make the latter, you would never sell it in the sense of industry having to make a profit. So there must be a trade off between something that is pretty conventional and something which is very sophisticated but which may have problems in manufacturing. Thank you for that comment Dr. Mendenhall.

M. Ahmet, British Aerospace

I have more of a general comment to make rather than a technical one. It appears to me that although there is agreement that all methods discussed have their practical applications, yet arguments develop about Euler vs. Navier-Stokes vs. empiricism or analytical methods. I think that it may be an idea for our colleagues involved in these specific fields, to look at in more detail at the other techniques, so they can appreciate the applications and limitations in a bit more detail.

P.R. Bignell, Chairman

One thing that concerns me, coming from industry, relative to CFD is that there is always a great deal of debate between the people in the research laboratories developing the codes and the people at what I would call the sharp end, who have to apply these codes in real life, whether that be to a missile or to an aircraft. Is there anybody who would care to comment from the missile industry, that there is this rapport, which is obviously quite necessary, between the code developers and the people who actually have to use these codes in the end to design missiles?

D. Hughes, British Aerospace

I have been involved over the past nine years or so in using semi-empirical prediction methods for the design of missiles. The particular application that I have been looking at involves a semi-automated approach whereby missiles can be designed very quickly using semi-empirical techniques so that when used in the concept feasibility stages you can produce many, many configurations in a very short space of time, which are the sort of time-scales that you need at this level for use in simulation modelling. One of the things that I have noticed is that invariably no matter how careful the semi-empirical method designers are in developing the codes, the project aerodynamicist will always come up with a configuration that doesn't quite meet the code that he has got. Therefore, bearing in mind the fact that expanding the data bases of these codes is likely to be very costly in the future if wind tunnel testing is involved, perhaps a marriage between the semi-empirical approach and the computational fluid dynamics approach could be postulated whereby the results of computational fluid dynamics runs could be used to expand the semi-empirical method data bases. Perhaps people would like to comment on that.

S. McDougall - British Aerospace

We are already doing it. I presented some results in my paper using a semi-empirical method and compared these with a panel method. We have already incorporated panel method results into the technique. As I said, the new inviscid calculation is being expanded to Mach numbers up to 5, and we will be using Euler methods to extend the data base of the semi-empirical method in order to do that.

RTD-8

D. W. Hughes, British Aerospace

Then I would like to ask if the code has been validated against experimental data.

S. McDougall, British Aerospace

Yes.

S. Dash, SAIC

That path has been taken quite a bit. I have been involved in the National Aerospace Plane program in the United States, and preliminary design of the scram jet propulsion system is routinely done by one-dimensional cycle codes. One-dimensional cycle codes contain information such as skin friction, the amount of combustion that takes place and tries to simply represent very complex processes. The CFD community has gotten involved and we have taken these large full-scale computer codes, we have attempted validation as best as possible and we have transferred the CFD information into the cycle decks. We have put information relevant to combustion efficiency, to A to KE's for inlet performance and all these types of information have been fed in to improve the cycle decks information for preliminary design.

P.R. Bignell, Chairman

I would like to get back to Mr. Deslandes. You commented on the use you make of Euler methods. Did I understand it correctly that these you use in the context of store carriage and release, because that is an incredibly complicated aerodynamic situation where you are releasing a store into an aircraft flow field so can you comment that you still get good comparisons with experiment?

R. Deslandes, MBB

With the panel method I was using 10 years ago, I never succeeded in producing a full agreement for installed flows of a store on an aircraft. With the Euler method we get more than 90% of appropriate measurements. Calculating separation and comparing the results with flight tests, we never get more than 80 - 90% agreement, but we don't know where this difference exactly occurs. Some mistakes are probably provided by the analysis of the flight test data itself. Not knowing perfectly where we are, we are happy about the 80% accuracy provided by the Euler equations. You cannot reach this degree of accuracy with other data than higher order methods like the Euler method.

P.R. Bignell, Chairman

One comment I was going to address to Howard Torode, but he has just left the room. He said to me as we were walking back one afternoon that he was extremely disappointed that there was so little on sub-sonic aerodynamics and I thought he would be addressing the hall on this. Would anybody else like to make a comment on why we didn't seem to get too much in the way of sub-sonic aerodynamic papers or issues being discussed at the meeting. I would have thought that people still work on high sub-sonic, maybe transonic, missile applications.

R. Deslandes, MBB

I was also very surprised to see that the Euler applications in this meeting were only referring to super-sonic speeds. I think that the reason is that for sub-sonic speeds, you cannot use space-marching schemes which are very good, but you have to use time-marching procedures. We have a very good experience in missile aerodynamic calculations with the Euler code in sub-sonic regions and also there, the accuracy is much higher than attainable with potential theory even within the transonic regime. There are some problems for the base pressures predictions. However, still now, we cannot specify who is right, the wind tunnel with small scale models, or the Euler calculations which for instance provided a very good approximation for a crew escape module which we were analyzing last year.

G.M. Lilley, University of Southampton

I accept everything the last speaker has said with regard to solutions of the Euler equations, but I would welcome his telling us of his experience in using the Euler equations in the case of separated flows.

R. Deslandes, MBB

I was expecting this. Perhaps I should say that Euler is not able to calculate smooth surface separation. It is impossible with an inviscid code. We have seen in this session possibilities to take this kind of separation into account by fixing the transition line and the separation line. However, wherever you have surface singularities, this means a kink or a sharp edge, Euler will produce a physical separation. We have very good results for such separation effects, which are matching wind tunnel measurements by more than 90%.

G.M. Lilley, University of Southampton

Mr. Chairman, I really wanted to change the subject, so if you are still continuing this particular area of discussion, perhaps I had better let somebody else speak.

W. Schmidt, Dornier

Since you are talking about Euler and separation, I think I have to add one point. If we deal with a high speed inviscid flow, high supersonic flow over a smooth surface and the flow has to pass a strong shock due to discontinuities, then this can cause separation as a fully inviscid problem. Similarly, we deal with an inviscid vortex and a shock, namely a vortex passing through a shock, then we will experience on a fully inviscid basis, that this vortex will burst. There is not only this viscosity causing separation, but also inviscid phenomena. In some cases the inviscid phenomena are causing separations that are looking very similar to the very physical ones. This is the only reason why sometimes Euler can succeed in predicting flows that originally are viscous flows with separation.

M.F.E. Dillenius, Nielsen Engineering

One thing that we didn't bring up here was the work that was done, I believe, at NASA Langley by Newsome. I am not a CFD'er, but it has worried me to no end. He did convergence studies with the grid using an Euler on a fin and Navier-Stokes of some kind on the fin, and with the Euler he kept getting different results as he kept refining the grid. It never converged. So sharp edge vortical formation Euler is highly questionable, I think. Perhaps you do have to use a cut-off or such thing to make sure that it is physically correct. With regard to Mr. Deslandes' comments on him being very happy with Euler, which is nice, in his store separation work. Remember we saw the case here of the F-15 which took 6 man months to set up and using the Euler. Guess what they didn't get - the inlet vortex flow that came out of it. So there are still problems with that if you are dealing with a specific aircraft with big inlets. There is also the wind tunnel problem of course. Does the inlet work in the wind tunnel the way it does in full flight. Apart from that, the vortical flow that comes out of an inlet under certain conditions is not modeled.

R. Deslandes, MBB

Mr. Dillenius, to be honest, I would like to remark that the grid they have shown is representing a closed intake. Therefore, they had no chance to produce any vorticity there. Some other Euler codes and grid generators are available, which can simulate open inlets as also done at MBB for the Tornado or with the EFA aircraft.

G.M. Lilley, University of Southampton

The point I wished to make is in relation to experiments and what one can deduce from them. In many of the test results that were discussed at this conference, the model was mounted in the wind tunnel with an ordinary sting, and hence there was the problem of deriving the base pressure that would exist on the actual case of the missile. I wonder whether any of our experimentalists would like to comment on this problem in predicting the kind of base flow and the accuracy in deriving that base flow on the missile model, which would exist in the absence of the sting.

J. Delery, ONERA

I would like to speak in French. The problem of the model support which is used for base flow studies is a basic problem. It has been studied a very long time ago as well in Europe as in the USA. However, for all the test cases in the case of GARTEUR for instance, with a view to test the Navier-Stokes codes, we have chosen an upstream support (nose sting system). In this case there are no disturbances due to three-dimensional effects coming from a lateral strut placed in the high speed flow. So since the computing codes can take account of the upstream boundary layer, we find ourselves in a validation situation which I would call healthy.

P.R. Bignell, Chairman

It is almost exactly 12:30 so I think we must bring our discussion to a halt. I would like to thank the program committee who helped me to put the program together and the session chairmen also. More particularly I would like to thank the authors, especially the invited speakers and if I could say a special thank you to Dr. Graham from Imperial College, to Marnix Dillenius from Nielsen and to M. Champigny from ONERA who were prepared to present papers at the very last minute on withdrawals. This has meant that we were able to stick to our schedule of 31 papers. I think that that was particularly appreciated. Above all I would like to thank the delegates to the conference who have participated so well during the week and to this discussion here this morning. It has been a delight to have the meeting so well attended. I thank you very much for that and I now hand over to the Panel Chairman to draw the meeting to a close.

J. McCroskey, FDP Chairman

Thank you Bob. Now it is time to bring our 66th Meeting of the Fluid Dynamics Panel to a close. Whether you prefer Euler or Navier-Stokes or Lieberkase or Wiernerschnitzel, I hope that you have found this Symposium both informative and stimulating and that you have enjoyed the Duchy of Wuertemberg and the Bodensee environment as much as I have.

Now as we say in the U.S., a word from our sponsor. I would like to call your attention to some events that you can find on the AGARD cable channel in the months ahead. We have a fall Symposium in the Netherlands on Vortex Flow Aerodynamics, a four day symposium followed by some Panel business meetings. In the spring of 1991, we have two specialists meetings on the topics you see, Effects of Adverse Weather on Aerodynamics and Manoeuvring Aerodynamics to be held in France. In the fall we have a full blown Symposium on Airframe Engine Integration, and then in the spring we will have two special courses presented at von Karman Institute and other locations to be determined precisely on Aircraft Dynamics at High Angles of Attack and Engineering Methods in Aerodynamic Analysis and Design of Aircraft, with I am sure some attention paid to missiles. So I would ask you to please contact me or the AGARD office or your countrymen on the Panel for further details.

RTD-10

This Symposium on Missile Aerodynamics was intended to review the current state of affairs, to highlight outstanding problems and to guide future research programs. I will leave it to you to determine the extent to which these goals were met, but I would say on this subject or any of the other AGARD functions if you find them useful, and I certainly hope you do, I would urge you to relay your positive impressions to your colleagues and to your management. If you don't like what you have seen, we would appreciate your constructive criticism, preferably directed to Panel members and we will strive to improve. Assuming you have found something to cheer about, I would like on your behalf to thank the Program Committee and especially the Program Chairman, Mr. Robert Bignell, and the Technical Evaluator and of course the speakers for their contributions for making this in my view a very successful Symposium.

Next I am sure you will join me in thanking our warm and efficient German hosts. These include a number of people, I will just mention a few, Herr Guenther, the German National Coordinator and of course a lot of support from the German Ministry of Defense. Here in Friedrichshafen Buergermeister Sigg, Herr Haupt, Herr Fischer, the personnel in town in Friedrichshafen and the Graf Zeppelin house, Dornier and Deutsche Aerospace, you recall Herr Ambos was joining us on the boat ride and certainly His Royal Highness Carl Duke of Wuertemberg. His presence will linger with us beyond this morning's session.

Please join me in thanking our good friend and colleague Dr. Wolfgang Schmidt, also people working with him, Frau Berkel, Frau Bower and other Dornier personnel who have been here on the site, and I am sure that they will certainly be ready for a vacation after this exhausting week.

Successful meetings rely heavily on the staff of AGARD and it is even more difficult when we have these classified meetings such as this. We must acknowledge first and foremost our Panel Executive Winston Goodrich, our Panel secretary Anne Marie Rivault, and others including the technicians who have operated this projection and audio equipment in this rather difficult environment so efficiently all during the week and including Mr. Fischer from the local organization.

This could go on and on, but I will now say last and by no means least, our interpreters who have worked very hard all week keeping up with our supersonic conversations. I can hardly even pronounce their names and they have kept the dialogue going bi-lingually; Madame Kudick, Madame des Susby and M. Sherer. Thank you very much.

Now unless Wolfgang has some further remarks or surprises, you never know,

W. Schmidt, Dornier

I would like to thank all of you for being so active in here and the whole thing worked out very nicely.

J. McCroskey, FDP Chairman

Thank you, Wolfgang, thanks to you ladies and gentlemen, have a safe trip home and a pleasant trip too, and we hope to see you at future AGARD activities.

RTD-11

REPORT DOCUMENTATION PAGE															
1. Recipient's Reference	2. Originator's Reference	3. Further Reference	4. Security Classification of Document												
	AGARD-CP-493	ISBN 92-835-0589-1	UNCLASSIFIED												
5. Originator	Advisory Group for Aerospace Research and Development North Atlantic Treaty Organization 7 rue Ancelle, 92200 Neuilly sur Seine, France														
6. Title	MISSILE AERODYNAMICS														
7. Presented at	the Symposium of the Fluid Dynamics Panel in Friedrichshafen, Germany, 23rd—26th April 1990.														
8. Author(s)/Editor(s)	Various		9. Date October 1990												
10. Author's/Editor's Address	Various		11. Pages 402												
12. Distribution Statement	This document is distributed in accordance with AGARD policies and regulations, which are outlined on the Outside Back Covers of all AGARD publications.														
13. Keywords/Descriptors	<table border="0"> <tbody> <tr> <td>Missiles</td> <td>Boundary layer separation</td> </tr> <tr> <td>External stores</td> <td>Hypersonic flow</td> </tr> <tr> <td>Aerodynamics</td> <td>Supersonic flow</td> </tr> <tr> <td>Numerical analysis</td> <td>Transonic flow</td> </tr> <tr> <td>Design</td> <td>Subsonic flow</td> </tr> <tr> <td>Aerothermodynamics</td> <td>Aerodynamic characteristics</td> </tr> </tbody> </table>			Missiles	Boundary layer separation	External stores	Hypersonic flow	Aerodynamics	Supersonic flow	Numerical analysis	Transonic flow	Design	Subsonic flow	Aerothermodynamics	Aerodynamic characteristics
Missiles	Boundary layer separation														
External stores	Hypersonic flow														
Aerodynamics	Supersonic flow														
Numerical analysis	Transonic flow														
Design	Subsonic flow														
Aerothermodynamics	Aerodynamic characteristics														
14. Abstract	<p>The Fluid Dynamics Panel of AGARD organised this Symposium on Missile Aerodynamics to (i) review current progress and achievements, (ii) highlight outstanding problems and (iii) establish pointers for planning future research programmes.</p> <p>→ The Symposium addressed many aspects of the aerodynamic design and performance of missiles for the subsonic through to the hypersonic flight regimes and reviews were included covering the stability and control of tactical missiles and the progress made in the field of store carriage and release. 31 papers were presented in seven sessions with contributions from Canada, France, Germany, Turkey, United Kingdom and United States. Topics considered in the Symposium were: computational methods and validation, empirical tools and experimental techniques, flow separation and interference effects, unconventional shapes and projectiles, propulsion and base flows, aerothermodynamics and hypersonics.</p> <p>The volume includes all the unclassified papers presented at the Symposium together with a transcript of the discussion which took place at the conclusion of the meeting.</p>														



<p>AGARD Conference Proceedings No.493 Advisory Group for Aerospace Research and Development, NATO MISSILE AERODYNAMICS Published October 1990 402 pages</p> <p>The Fluid Dynamics Panel of AGARD organised this Symposium on Missile Aerodynamics to (i) review current progress and achievements, (ii) highlight outstanding problems and (iii) establish pointers for planning future research programmes.</p> <p>The Symposium addressed many aspects of the aerodynamic design and performance of missiles for the subsonic through to the hypersonic flight regimes and P.T.O.</p>	<p>AGARD-CP-493</p> <p>Missiles External stores Aerodynamics Numerical analysis Design Aerothermodynamics Boundary layer separation Hypersonic flow Supersonic flow Transonic flow Subsonic flow Aerodynamic characteristics</p>	<p>AGARD-CP-493</p> <p>Missiles External stores Aerodynamics Numerical analysis Design Aerothermodynamics Boundary layer separation Hypersonic flow Supersonic flow Transonic flow Subsonic flow Aerodynamic characteristics</p>	<p>AGARD-CP-493</p> <p>Missiles External stores Aerodynamics Numerical analysis Design Aerothermodynamics Boundary layer separation Hypersonic flow Supersonic flow Transonic flow Subsonic flow Aerodynamic characteristics</p>
<p>AGARD Conference Proceedings No.493 Advisory Group for Aerospace Research and Development, NATO MISSILE AERODYNAMICS Published October 1990 402 pages</p> <p>The Fluid Dynamics Panel of AGARD organised this Symposium on Missile Aerodynamics to (i) review current progress and achievements, (ii) highlight outstanding problems and (iii) establish pointers for planning future research programmes.</p> <p>The Symposium addressed many aspects of the aerodynamic design and performance of missiles for the subsonic through to the hypersonic flight regimes and P.T.O.</p>	<p>AGARD-CP-493</p> <p>Missiles External stores Aerodynamics Numerical analysis Design Aerothermodynamics Boundary layer separation Hypersonic flow Supersonic flow Transonic flow Subsonic flow Aerodynamic characteristics</p>	<p>AGARD-CP-493</p> <p>Missiles External stores Aerodynamics Numerical analysis Design Aerothermodynamics Boundary layer separation Hypersonic flow Supersonic flow Transonic flow Subsonic flow Aerodynamic characteristics</p>	<p>AGARD-CP-493</p> <p>Missiles External stores Aerodynamics Numerical analysis Design Aerothermodynamics Boundary layer separation Hypersonic flow Supersonic flow Transonic flow Subsonic flow Aerodynamic characteristics</p>

<p>reviews were included covering the stability and control of tactical missiles and the progress made in the field of store carriage and release. 31 papers were presented in seven sessions with contributions from Canada, France, Germany, Turkey, United Kingdom and United States. Topics considered in the Symposium were: computational methods and validation, empirical tools and experimental techniques, flow separation and interference effects, unconventional shapes and projectiles, propulsion and base flows, aerothermodynamics and hypersonics.</p> <p>The volume includes all the unclassified papers presented at the Symposium together with a transcript of the discussion which took place at the conclusion of the meeting.</p> <p>ISBN 92-835-0589-1</p>	<p>reviews were included covering the stability and control of tactical missiles and the progress made in the field of store carriage and release. 31 papers were presented in seven sessions with contributions from Canada, France, Germany, Turkey, United Kingdom and United States. Topics considered in the Symposium were: computational methods and validation, empirical tools and experimental techniques, flow separation and interference effects, unconventional shapes and projectiles, propulsion and base flows, aerothermodynamics and hypersonics.</p> <p>The volume includes all the unclassified papers presented at the Symposium together with a transcript of the discussion which took place at the conclusion of the meeting.</p> <p>ISBN 92-835-0589-1</p>
<p>reviews were included covering the stability and control of tactical missiles and the progress made in the field of store carriage and release. 31 papers were presented in seven sessions with contributions from Canada, France, Germany, Turkey, United Kingdom and United States. Topics considered in the Symposium were: computational methods and validation, empirical tools and experimental techniques, flow separation and interference effects, unconventional shapes and projectiles, propulsion and base flows, aerothermodynamics and hypersonics.</p> <p>The volume includes all the unclassified papers presented at the Symposium together with a transcript of the discussion which took place at the conclusion of the meeting.</p> <p>ISBN 92-835-0589-1</p>	<p>reviews were included covering the stability and control of tactical missiles and the progress made in the field of store carriage and release. 31 papers were presented in seven sessions with contributions from Canada, France, Germany, Turkey, United Kingdom and United States. Topics considered in the Symposium were: computational methods and validation, empirical tools and experimental techniques, flow separation and interference effects, unconventional shapes and projectiles, propulsion and base flows, aerothermodynamics and hypersonics.</p> <p>The volume includes all the unclassified papers presented at the Symposium together with a transcript of the discussion which took place at the conclusion of the meeting.</p> <p>ISBN 92-835-0589-1</p>

**AGARD**  
 NATO  OTAN  
 7 RUE ANCELLE · 92200 NEUILLY-SUR-SEINE  
 FRANCE  
 Téléphone (1)47.38.57.00 · Telex 610 176

**DIFFUSION DES PUBLICATIONS  
 AGARD NON CLASSIFIEES**

L'AGARD ne détient pas de stocks de ses publications, dans un but de distribution générale à l'adresse ci-dessus. La diffusion initiale des publications de l'AGARD est effectuée auprès des pays membres de cette organisation par l'intermédiaire des Centres Nationaux de Distribution suivants. Ces Centres disposent parfois d'exemplaires additionnels; dans les cas contraire, on peut se procurer ces exemplaires sous forme de microfiches ou de microcopies auprès des Agences de Vente dont la liste suit.

**CENTRES DE DIFFUSION NATIONAUX**

**ALLEMAGNE**  
 Fachinformationszentrum,  
 Karlsruhe  
 D-7514 Eggenstein-Leopoldshafen 2

**BELGIQUE**  
 Coordonnateur AGARD-VSL  
 Etat-Major de la Force Aérienne  
 Quartier Reine Elisabeth  
 Rue d'Evere, 1140 Bruxelles

**CANADA**  
 Directeur du Service des Renseignements Scientifiques  
 Ministère de la Défense Nationale  
 Ottawa, Ontario K1A 0K2

**DANEMARK**  
 Danish Defence Research Board  
 Ved Idrætsparken 4  
 2100 Copenhagen Ø

**ESPAGNE**  
 INTA (AGARD Publications)  
 Pintor Rosales 34  
 28008 Madrid

**ETATS-UNIS**  
 National Aeronautics and Space Administration  
 Langley Research Center  
 M/S 180  
 Hampton, Virginia 23665

**FRANCE**  
 O.N.E.R.A. (Direction)  
 29, Avenue de la Division Leclerc  
 92320, Châtillon sous Bagneux

**GRECE**  
 Hellenic Air Force  
 Air War College  
 Scientific and Technical Library  
 Dekelia Air Force Base  
 Dekelia, Athens TGA 1010

**ISLANDE**  
 Director of Aviation  
 c/o Flugrad  
 Reykjavik

**ITALIE**  
 Aeronautica Militare  
 Ufficio del Delegato Nazionale all'AGARD  
 3 Piazzale Adenauer  
 00144 Roma EUR

**LUXEMBOURG**  
 Voir Belgique

**NORVEGE**  
 Norwegian Defence Research Establishment  
 Attn: Biblioteket  
 P.O. Box 25  
 N-2007 Kjeller

**PAYS-BAS**  
 Netherlands Delegation to AGARD  
 National Aerospace Laboratory NLR  
 Kluyverweg 1  
 2629 HS Delft

**PORTUGAL**  
 Portuguese National Coordinator to AGARD  
 Gabinete de Estudos e Programas  
 CLAFIA  
 Base de Alfragide  
 Alfragide  
 2700 Amadora

**ROYAUME UNI**  
 Defence Research Information Centre  
 Kentigern House  
 65 Brown Street  
 Glasgow G2 8EX

**TURQUIE**  
 Milli Savunma Bakanlığı (MSB)  
 ARGE Daire Başkanlığı (ARGE)  
 Ankara

**LE CENTRE NATIONAL DE DISTRIBUTION DES ETATS-UNIS (NASA) NE DETIENT PAS DE STOCKS  
 DES PUBLICATIONS AGARD ET LES DEMANDES D'EXEMPLAIRES DOIVENT ETRE ADRESSEES DIRECTEMENT  
 AU SERVICE NATIONAL TECHNIQUE DE L'INFORMATION (NTIS) DONT L'ADRESSE SUIT.**

**AGENCES DE VENTE**

National Technical Information Service  
 (NTIS)  
 5285 Port Royal Road  
 Springfield, Virginia 22161  
 Etats-Unis

ESA/Information Retrieval Service  
 European Space Agency  
 10, rue Mario Nikis  
 75015 Paris  
 France

The British Library  
 Document Supply Division  
 Boston Spa, Wetherby  
 West Yorkshire LS23 7BQ  
 Royaume Uni

Les demandes de microfiches ou de photocopies de documents AGARD doivent comporter le numéro de série AGARD, le titre, le nom de l'auteur ou du rédacteur-coordonnateur et la date de publication. Les demandes adressées au NTIS doivent comporter le numéro matricule NASA du rapport. Des références bibliographiques complètes ainsi que des résumés des publications AGARD figurent dans les journaux suivants:

Scientific and Technical Aerospace Reports (STAR)  
 publié par la NASA Scientific and Technical  
 Information Branch  
 NASA Headquarters (NT-40)  
 Washington D.C. 20546  
 Etats-Unis

Government Reports Announcements (GRA)  
 publié par National Technical Information Services.  
 Springfield  
 Virginia 22161  
 Etats-Unis



Imprimé par Specialised Printing Services Limited  
 40 Chigwell Lane, Loughion, Essex IG10 3TZ